Inter-lab Quantum Microwave Teleportation

Dissertation

Michael Renger
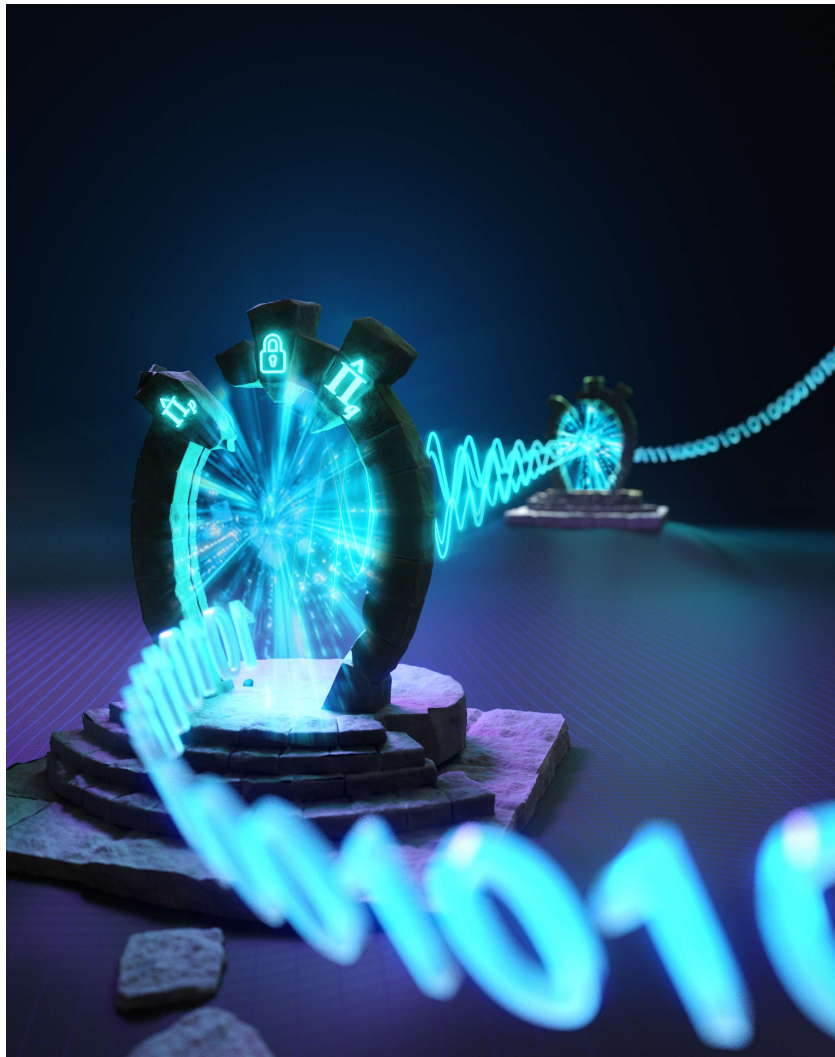
TECHNISCHE UNIVERSITÄT MÜNCHEN

TUM School of Natural Sciences

Inter-lab Quantum Microwave Teleportation

Michael Uwe Renger

Vollständiger Abdruck der von der TUM School of Natural Sciences der Technischen Universität München zur Erlangung des akademischen Grades eines

Doktors der Naturwissenschaften

genehmigten Dissertation.

Vorsitz: Prof. Dr. Frank Pollmann

Prüfer*innen der Dissertation: 1. Priv.- Doz. Dr. Frank Deppe

                                     2. Prof. Dr. Andreas Reiserer

Die Dissertation wurde am 26.04.2023 bei der Technischen Universität München eingereicht und durch die TUM School of Natural Sciences am 24.08.2023 angenommen.

Abstract

The rapidly growing field of quantum communication relies on the laws of quantum physics to optimize efficiency and security of information exchange between different communication parties. Quantum networks have the potential to lift our communication abilities to completely new levels. This conclusion has inspired the Nobel Committee to honor pioneering research in this field with the physics prize in 2022. Of obvious relevance to a realization of quantum networks are the aspects of scaling the number of communication parties and the communication distance. Consequently, these two issues are considered key to a quantum-secured transfer of classical information, as it is done in quantum key distribution. Here, optical frequencies have a longstanding tradition because their properties favor exactly these two key aspects. In a scenario, where quantum states should be exchanged between two parties, however, there are important material platforms working in the microwave domain. Key examples are spins in solid state systems and, most noteworthy, the heavily industrially developed quantum computing platform of superconducting circuits. Unfortunately, the necessary near-unity conversion efficiency for quantum states from microwave to optics and back faces, despite heavy research efforts, still major material challenges and a realization within the next years would require unpredictable breakthroughs. The obvious alternative is conversion-free microwave quantum communication. In this field, tremendous experimental progress has been made over the last decade. One major challenge is that even quantum local area network (QLAN) settings will require a cryogenic environment over meter-scale distances. Hence, setting up and such a QLAN demonstrator and performing a benchmark quantum communication protocol with it is the main objective of this thesis.

Specifically, we investigate quantum communication with propagating microwave states. The main building block for our protocols is provided by entangled two-mode squeezed (TMS) states. We generate these states with Josephson parametric amplifiers (JPAs). These nonlinear superconducting circuits can also be used as measurement devices. To this end, we experimentally and theoretically study the quantum efficiency of our JPAs. In addition, we investigate quantum correlations, shared between both modes of our TMS states, with respect to information flow towards environment. The main novelty of this thesis consists of two experimental results. First, we demonstrate the successful experimental realization of continuous-variable quantum teleportation of coherent microwave states. Quantum teleportation stands out as one of the most fundamental and, simultaneously, most famous quantum communication protocols. In this protocol, we employ shared quantum correlations and a classical communication channel for disembodied and unconditionally secure transfer of unknown quantum states. We perform a systematic

analysis of the resulting teleportation fidelity as a function of experimental parameters. We demonstrate security of the protocol by exceeding the asymptotic no-cloning limit for fidelity of teleported coherent states. Second, we design, build, and optimize a cryogenic microwave link operating at millikelvin temperatures with which we connect two dilution cryostats located in remote laboratories. The cryogenic link contains superconducting coaxial transmission lines which form an inter-lab microwave quantum channel. Finally, we combine our two main results to demonstrate microwave quantum teleportation between two remote laboratories and show that our protocol provides a quantum advantage in terms of teleported states fidelity and feedforward channel security towards eavesdropping.

Kurzzusammenfassung

In dem sich in enormem Tempo entwickelnden Gebiet der Quantenkommunikation machen wir uns die Gesetze der Quantenphysik zunutze, um den Informationsaustausch zwischen den verschiedenen Kommunikationsteilnehmern im Hinblick auf Effizienz und Sicherheit zu optimieren. Quantennetzwerke bergen hierbei ein enormes Potential, um Kommunikationskapazitäten auf eine höhere Ebene zu bringen. Unter anderem hat diese Tatsache das Nobelpreiskomitee dazu bewegt, die wegbereitende Forschung auf diesem Gebiet mit dem Physik-Nobelpreis 2022 auszuzeichnen. Sowohl bezüglich Vergrößerung der Kommunikationsteilnehmerzahl, als auch der Übertragungsweglänge, ist die Verwirklichung von leistungsfähigen Quantennetzwerken von äußerster Dringlichkeit. Infolgedessen stellen diese beiden Aspekte zentrale Elemente für quantengeschützte Übertragung klassischer Information dar, beispielsweise im Rahmen des Quantenschlüsselaustauschs. Üblicherweise wird insbesondere die letztgenannte Anwendung im optischen Frequenzspektrum verwirklicht, da optische Quantennetzwerke den beiden oben genannten Ansprüchen genügen. Nichtsdestotrotz existieren Fälle, in denen Quantenzustände auf Materialplattformen, die im Mikrowellenbereich arbeiten, übertragen werden müssen. Relevante Beispiele sind Festkörperspins, und, am bemerkenswertesten, industriell entwickelte Quantenrechner, basierend auf supraleitenden Schaltkreisen. Um jedoch materialtechnisch in den kommenden Jahren die notwendige annähernd perfekte und reversible Frequenzkonvertierung von Quantenzuständen im Mikrowellenregime in den optischen Frequenzbereich zu realisieren, müssten trotz aktiver und umfassender Forschung unvorhersehbare Durchbrüche erfolgen. Der offensichtliche alternative Ansatz ist die konversionsfreie Mikrowellenkommunikation. In diesem Forschungsfeld gab es über das vergangene Jahrzehnt enorme experimentelle Fortschritte. Eine wesentliche Herausforderung ist hierbei die Tatsache, dass für Mikrowellen selbst ein lokales Quantennetzwerk (QLAN) im Meterbereich in eine kryogene Umgebung einebettet werden muss. Aufgrund dieser Tatsache stellt die Realisierung eines Mikrowellen QLAN-Demonstrators sowie dessen Nutzung zur erfolgreichen Durchführung eines Referenzquantenkommunikationsprotokolls das Hauptziel dieser Doktorarbeit dar.

Im Rahmen dieser Doktorabeit untersuchen wir die Quantenkommunikation mit propagierenden Mikrowellenzuständen. Der grundlegende Baustein unserer Protokolle ist hierbei der verschränkte zwei-Moden gequetschte (TMS) Zustand. Wir erzeugen diese Zustände mittels parametrischer Josephson-Verstärker (JPAs). Zudem verwenden wir diese nichtlinearen supraleitenden Schaltkreise als analoge Messgeräte. Wir untersuchen die Quanteneffizienz unserer JPAs, sowohl experimentell als auch theoretisch. Zudem betrachten wir die zwischen beiden TMS-Moden vorherrschenden Quantenkorrelationen im Bezug auf den Informationsfluss zur Umgebung. Die zentrale wissenschaftliche Neuheit innerhalb

dieser Doktorarbeit setzt sich aus zwei experimentellen Resultaten zusammen. Unser erstes Hauptergebnis ist die erfolgreiche experimentelle Umsetzung der Quantenteleportation von Quantenmikrowellenzuständen der kontinuierlichen-Variablen. Quantenteleportation sticht als eines der grundlegendsten und zugleich berühmtesten Quantenkommunikationsprotokolle hervor. In diesem Protokoll verwenden wir verteilte Quantenkorrelationen sowie einen klassischen Kommunikationskanal für die bedingungslos sichere Übertragung unbekannter Quantenzustände. Wir führen eine systematische Analyse der sich ergebenden Teleportationsgüte als Funktion der experimentellen Parameter durch. Zudem zeigen wir die Sicherheit des Protokolls auf, indem wir die asymptotische No-Cloning-Grenze für kohärente Zustände überschreiten. Unser zweites Hauptergebnis stellt die Realisierung eines kryogenen Links dar, welcher im Millikelvinbereich betrieben wird. Hierfür verbinden wir zwei Mischungskryostaten, die in zwei voneinander getrennten Laboren aufgestellt sind. Im Inneren des kryogenen Links befindet sich eine supraleitende Koaxialleitung, welche als Hardwareplattform für die Realisierung eines laborübergreifenden Mikrowellenquantenkanals fungiert. Schlussendlich verbinden wir unsere beiden Hauptergebnisse, um Mikrowellenquantenteleportation zwischen zwei getrennten Laboren zu demonstrieren. Zudem zeigen wir, dass unser Protokoll einen Quantenvorteil sowohl hinsichtlich Güte, als auch Sicherheit bietet.

Contents

List of Figures

List of Tables

Chapter 1

Introduction

Since the beginning of its development in the early 20th century, quantum mechanics has proven to be one of the most successful physical theories [1–3]. Among the most impressive results of quantum physics are the emerging paradoxes in case we combine a quantum description of nature with the classical concept of locality [4, 5]. A remarkable consequence of quantum theory is the effect of quantum entanglement, which implies that correlated quantum systems, under certain conditions, can be fully described only as one combined entity [6, 7]. Notably, key experimental demonstrations of nonlocality and the usefulness of quantum entanglement have recently been awarded with the Nobel Prize in physics [8–10]. Apart from numerous fundamental effects [11–14], quantum physics has caught significant level of interest with respect to practical applications in information science over the previous years [15–19]. This stems from the fact that quantum properties such as quantum superposition or quantum entanglement provide additional useful and unique properties for information processing purposes [20]. Consequently, the laws of quantum physics enable improvements of efficiency and security of classical protocols and allow to solve tasks for which a reasonable implementation is impossible on classical machines [21–24]. Such quantum information processing (QIP) tasks can be implemented on various hardware platforms such as trapped ions [25], polarized photons [26], quantum dots [27], nuclear spins [28], or nitrogen-vacancy centers [29], among others. In this thesis, we focus on QIP based on superconducting quantum circuits employing Josephson junctions [30–35]. In these circuits, we can reach a favorable compromise between the strength of the light-matter interaction and the system nonlinearity by means of engineering [36, 37]. In many other approaches involving natural atomic systems, the nonlinearity is predetermined by nature and cannot be significantly changed [38]. During the time at which we have developed our results, superconducting quantum technology had made a major breakthrough by demonstrating quantum supremacy [39], as well as successful quantum error correction [40, 41]. These results are widely expected to be the kickoff into a soon-to-arrive era of practically useful noisy intermediate-scale quantum devices [42].

In QIP, there are two fundamental approaches. In the first approach, one employs systems with a discrete-variable (DV) spectrum of eigenstates, described within a finite Hilbert space [15]. The simplest DV system is realized by a quantum bit (qubit) [43]. Such

a digital approach is conventionally desired in many quantum computing applications as well as in quantum simulation, e.g., of protein molecules [44–46]. In the second approach, one uses quantum systems with a continuous spectrum of eigenstates [47]. Such a continuous-variable (CV) system is naturally realized by a quantum harmonic oscillator or propagating electromagnetic fields [48]. In CV systems, one can employ the quantized electromagnetic field quadratures for QIP purposes [49]. Furthermore, CV quantum states are particularly useful for transmitting quantum information between different parties and are important candidates for distributed quantum computing and quantum communication platforms.

The goal of quantum communication is the exploitation of quantum resources to realize efficient and secure communication channels which can eventually be connected to form quantum networks [50–57]. Precisely the second aspect of the aforementioned 2022 Nobel prize, the usefulness of quantum entanglement, has been awarded for the experimental demonstration of quantum teleportation in the late 1990s [8, 9]. Ever since, teleportation is one of the most fundamental quantum communication protocols and quantum communication with CV states is a vivid field with pioneering theoretical [47, 58–60] and experimental work. The latter features the implementation of quantum key distribution [61, 62], dense coding [59, 63], analog quantum computing [64], remote-state preparation (RSP) [65, 66], and coherent state quantum teleportation, a milestone experiment, conducted by Furusawa *et al.* in 1998 [67].

All experiments quoted above were investigated at optical frequencies. However, if one aims to combine the CV quantum communication with superconducting quantum processors operating at microwave frequencies [68], the enormous energy mismatch of five orders of magnitude must be overcome. The comparably low energy scale of the superconducting systems is defined by the energy gap of the superconductor and cannot be adapted easily. Furthermore, microwave frequencies imply that experiments need to be performed at temperatures $T \ll 100\,\mathrm{mK}$ [69], a practical engineering challenge. This energy mismatch between microwave and optics requires cumbersome frequency conversion techniques which tend to destroy the valuabe quantum coherence. The conversion is often realized via an intermediate nanomechanical mode [70]. The related material problems to date result in typical bidirectional quantum conversion efficiencies on the order of 10^{-5} on the single-photon level [71, 72] which is far away from being sufficient for any practical applications in QIP protocols. Hence, we follow a different approach and implement CV quantum communication directly with superconducting circuits in the microwave regime. Resulting from the cryogenic expertise gathered over decades, Walther-Meißner-Institut (WMI) has taken a pioneering role in the field of quantum communication with propagating microwaves. Here, significant milestones include development of the photon number calibration technique, based on Planck spectroscopy [73], realization of advanced signal reconstruction techniques which enable microwave Wigner tomography [74], implementation of microwave squeezing [75] and displacement

operations [76], demonstration of microwave path entanglement [77], as well as realization of remote-state preparation as a first advanced quantum communication experiment with propagating microwaves [66].

In this work, we demonstrate the first experimental realization of deterministic CV quantum teleportation with propagating microwave states [78]. The main building block of our experiments is the Josephson parametric amplifier (JPA) [79–81]. Such JPAs are widely known as quantum-limited amplifiers employed for single-shot dispersive qubit readout [82]. Here, we employ them for generation of entangled two-mode squeezed (TMS) states [83]. We implement our quantum teleportation experiment in a fully analog way [84]. In our experiment, we realize an analog Bell measurement in phase-space with two JPAs generating a classical analog feedforward signal. The performance of the Bell measurements crucially depends on quantum efficiency of our JPAs. Consequently, we perform a systematic study of the JPAs' quantum efficiency [85]. In addition, we investigate effects of noise on quantum correlations within our TMS resource states [86]. We put a special focus on quantum discord, which plays a fundamental role in concepts such as quantum Darwinism [87], and, furthermore, is a practically useful quantity to describe information flow and correlation consumption in quantum communication protocols [88]. Finally, we implement a cryogenic hardware platform for inter-lab microwave quantum communication experiments at WMI [89], which we later employ for successful realization of microwave quantum teleportation between two separate laboratories.

This thesis is structured as follows. In chapter 2, we review the fundamental theory of JPAs as well as Gaussian quantum optics. In addition, we provide a description of analog CV quantum teleportation and related quantum communication protocols. We introduce criteria which quantify quantum advantage, as well as unconditional security. In the following chapter 3, we describe the relevant experimental techniques with respect to the cryogenic setup, JPA samples, and standard characterization and calibration measurements. We describe our Wigner tomography setup, which is based on a field-programmable gate array. In chapter 4, we present measurement results on the quantum efficiency of our JPAs. We demonstrate that we can exceed the standard quantum limit for sufficiently broadband input signals even in the phase-insensitive case, as predicted by theory. In addition, we investigate how one can improve quantum efficiency by chaining multiple JPAs. Next, in chapter 5, we employ the concept of quantum discord to investigate information flow between a noisy TMS state and environment. In chapter 6, we present our results for coherent state quantum teleportation and investigate the protocol with respect to security and communication bit rate. In addition, we interpret analog CV quantum teleportation as an error correction scheme for certain Gaussian imperfections in the feedforward channel. In chapter 7, we describe the cryogenic millikelvin link which connects two dilution refrigerators. These two cryostats are located in separate laboratories at a distance of 6.6 m. The cryogenic link contains three superconducting transmission lines, making the link act as a microwave quantum local area network (QLAN) cable.

We describe the design, assembly, and operation of the cryolink system. Finally, in chapter 8, we present results on quantum communication experiments using the QLAN cable. We demonstrate entanglement distribution between the distant fridges and verify the fluctuation-dissipation theorem. Finally, we perform inter-lab microwave quantum teleportation and interpret our results within a practical security analysis. In chapter 9, we provide a summary of our results as well as an outlook on microwave quantum teleportation via a room temperature or open-air feedforward channel.

Chapter 2

Superconducting circuits and propagating quantum microwaves

In this chapter, we introduce a theory related to the experiments conducted throughout this work. Section 2.1 is dedicated to JPAs which form the fundamental hardware platform for our experiments. The following Sec. 2.2 introduces Gaussian quantum optics. Based on this framework, we discuss continuous variable (CV) quantum communication with special focus on Gaussian quantum teleportation. Considering that we implement all our experiments in the microwave regime, we find that we can significantly reduce technological effort if we implement the protocol by solely employing analog signals. We focus on an analog formulation in Sec. 2.3, with a special emphasis on implementation of the Bell measurements.

2.1 Josephson parametric amplifier

In this section, we formulate the general theory of linear quantum amplifiers. In Sec. 2.1.1, we introduce the JPA as a superconducting circuit and provide its quantum description. In Sec. 2.1.2, we apply the input-output formalism to the JPA. In Sec. 2.1.3, we investigate the fundamental quantum limits on parametric amplification and demonstrate in Sec. 2.1.4 that these fundamental limitations can be overcome by employing sufficiently broadband input signals.

2.1.1 JPA circuit

Figure 2.1(a) shows the circuit diagram for our JPA [79, 90]. The JPA consists of a superconducting $\lambda/4$ resonator, terminated by a direct current (DC) superconducting quantum interference device (SQUID) [91]. In the following, we discuss these two building blocks as well as the dynamics of the resulting superconducting circuit. To form the resonator, we employ superconducting coplanar waveguides (CPWs) as two-dimensional structures which form quasi one-dimensional transmission lines for signal propagation [92]. A characteristic quantity for the CPW is its impedance $Z = \sqrt{L_0/C_0}$, where L_0
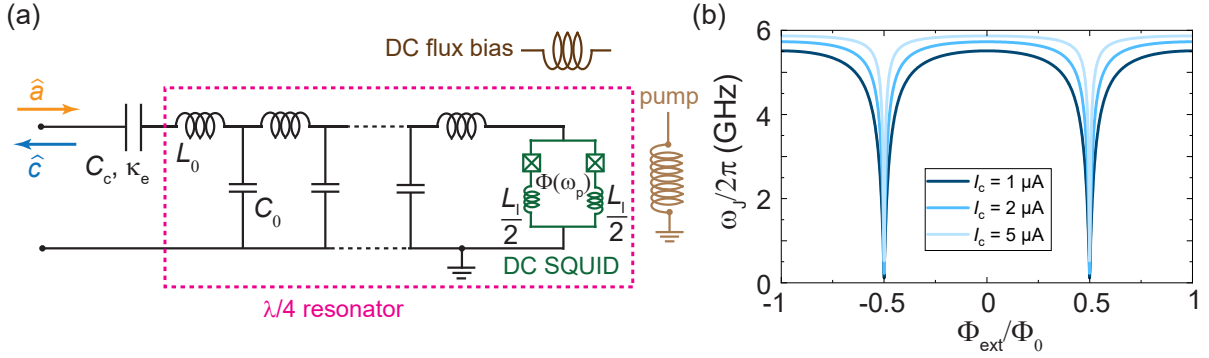
Figure 2.1: (a) Circuit diagram for the JPA, consisting of a superconducting $\lambda/4$ resonator with inductance (capacitance) L_0 (C_0) per unit length. The resonator is terminated by a DC SQUID with loop inductance L_l. Input (output) modes $\hat{a}$ ($\hat{c}$) are coupled into the resonator via the rate κ_e, determined by the coupling capacitance C_c. (b) Flux-tunable JPA resonance frequency $\omega_J(\Phi_{ext})$, according to Eq. (2.3), as a function of external DC flux Φ_{ext} for various critical currents I_c. The results correspond to the bare resonator frequency $\omega_r/2\pi = 6\,\text{GHz}$, resonator inductance $L_r = 2\,\text{nH}$ and loop inductance $L_l = 50\,\text{pH}$.

(C_0) denotes the inductance (capacitance) per unit length [93]. The impedance can be determined from the CPW geometry using conformal mapping techniques [94, 95]. Next, we apply boundary conditions to the CPW, as shown in Fig. 2.1(a). The coupling capacitance C_c on the left side leads to a current node, whereas the ground short on the right hand implies a voltage node. In case the resonator has a length d, these boundary conditions allow for the modes [96]

$$\omega_r^{(n)} = \frac{\pi}{2d\sqrt{L_0 C_0}}(1 + 2n), \qquad n \in \mathbb{N}_0. \tag{2.1}$$

Throughout this work, we restrict our considerations to the fundamental mode, implying a bare resonator frequency $\omega_r \equiv \omega_r^{(0)}$, which corresponds to a wavelength $d = \lambda/4$. We describe our superconductors within the phenomenological macroscopic quantum model, implying a single phase-coherent wave function to describe the collective dynamics of Cooper pairs [69, 97]. We form a Josephson junction by weakly coupling two bulk superconducting electrodes via a thin insulating barrier. The gauge-invariant phase difference across the junction then induces a net supercurrent due to tunneling of Cooper pairs between the superconductors. The junction current, as well as the corresponding voltage drop associated with these coherent tunneling dynamics are governed by the Josephson equations [98]. The Josephson equations imply that the Josephson junction forms a lossless and nonlinear inductance [69]. A DC SQUID consists of two identical Josephson junctions in a closed superconducting ring geometry [91]. In case the loop inductance L_l of this geometry is sufficiently small to neglect the flux induced by the circulating current in the SQUID loop, the DC SQUID acts like a single Josephson junction with flux-tunable Josephson inductance $L_s(\Phi_{ext})$, where Φ_{ext} denotes the external flux

threading the SQUID loop.

Next, we describe the JPA by the circuit scheme in Fig. 2.1(a), where we assume that the SQUID is located at $z = d$ [99]. Neglecting the capacitive energy of the SQUID, the equation of motion (EOM) for the Josephson phase difference $\varphi(z)$ in the system is determined by the Lagrangian

$$\mathcal{L} = \left(\frac{\Phi_0}{2\pi}\right)^2 \int_0^d dz \left\{ \frac{C_0}{2} \left[\dot{\varphi}(z,t)\right]^2 - \frac{1}{2L_0}\left[\partial_z\varphi(z,t)\right]^2 \right\} + E_{\mathrm{J}}\cos\varphi(d,t), \qquad (2.2)$$

where the integral describes the massless Klein-Gordon field in the resonator [2, 100–102]. The quantity E_{J} denotes the tunable Josephson coupling energy associated with the SQUID and $\Phi_0 = h/(2e) \simeq 2.0678 \times 10^{-15}\,\mathrm{Wb}$ is the magnetic flux quantum [103, 104]. The magnetic flux in the system is determined by $\Phi(z,t) = \varphi(z,t)\Phi_0/2\pi$. When discretizing Eq. (2.2) [99], the boundary condition at $z = d$ implies that the inductance of the resonator becomes flux-dependent [96]. Consequently, the DC-biased system can be approximately described as a harmonic oscillator with frequency

$$\omega_{\mathrm{J}}(\Phi_{\mathrm{ext}}) = \omega_{\mathrm{r}}\left[\frac{L_{\mathrm{r}}}{L_{\mathrm{r}} + L_{\mathrm{l}}/4 + L_{\mathrm{s}}(\Phi_{\mathrm{ext}})}\right], \qquad L_{\mathrm{s}}(\Phi_{\mathrm{ext}}) = \frac{\Phi_0}{4\pi I_{\mathrm{c}}\left|\cos\left(\pi\frac{\Phi_{\mathrm{ext}}}{\Phi_0}\right)\right|}, \qquad (2.3)$$

where $L_{\mathrm{r}} = L_0 d$ corresponds to the bare resonator inductance and I_{c} is the critical current of the equal Josephson junctions in the SQUID [105]. In Fig. 2.1(b), we plot the JPA frequency $\omega_{\mathrm{J}}(\Phi_{\mathrm{ext}})$, according to Eq. (2.3), as a function of DC flux Φ_{ext} for various critical currents I_{c}. The general solution of the Euler-Lagrange equation, resulting from Eq. (2.2), can be separated into a time-dependent and a z-dependent contribution and corresponds to a linear superposition of all resonator modes, compatible with the $\lambda/4$-boundary conditions, Eq. (2.1). Next, we insert the general solution into the Lagrangian and only keep the fundamental mode, leading to $\Phi(z,t) = \phi(t)\cos(kz)$, $k = \pi\omega_{\mathrm{J}}(\Phi_{\mathrm{ext}})/(2d\omega_{\mathrm{r}})$. We furthermore neglect the loop inductance L_{l} of the SQUID. From Eq. (2.2), we determine the effective capacitance C and inductance L, associated with this solution,

$$C = C_0 \int_0^d \cos^2(kz)dz = C_0\frac{2dk + \sin(2dk)}{4k} = \frac{C_{\mathrm{r}}}{2}\left[1 + \mathrm{sinc}\left(\frac{\omega_{\mathrm{J}}}{\omega_{\mathrm{r}}}\right)\right], \qquad (2.4)$$

$$\frac{1}{L} = \frac{1}{L_0}\int_0^d k^2\sin^2(kz) = \frac{k[2dk - \sin(2dk)]}{4L_0} = \frac{\pi^2}{8L_{\mathrm{r}}}\left(\frac{\omega_{\mathrm{J}}}{\omega_{\mathrm{r}}}\right)^2\left[1 - \mathrm{sinc}\left(\frac{\omega_{\mathrm{J}}}{\omega_{\mathrm{r}}}\right)\right], \qquad (2.5)$$

where $C_{\mathrm{r}} = C_0 d$ and $\mathrm{sinc}(x) \equiv \sin(\pi x)/(\pi x)$.

So far, apart from employing the phenomenological macroscopic quantum model, the treatment of our circuit has been fully classical. In the next step, we use the Faraday law to determine the charge in the resonator, $Q = -C\dot{\phi}$. Following that, we perform the first quantization by treating charge and flux as complex conjugate variables, $Q \to \hat{Q}$, $\phi \to \hat{\phi}$, satisfying the commutation relation $[\hat{\phi}, \hat{Q}] = i\hbar$ [106]. The corresponding Hamiltonian of

the JPA is obtained from Eq. (2.2) by Legendre transformation [107],

$$\hat{H}_{\text{JPA}} = E_{\text{C}}\left(\frac{\hat{Q}}{e}\right)^2 + E_{\text{L}}\left(\frac{\hat{\phi}}{\Phi_0}\right)^2 - E_{\text{J}}\cos\left(2\pi\cos(kd)\frac{\hat{\phi}}{\Phi_0}\right), \tag{2.6}$$

where we define the capacitive energy, $E_{\text{C}} = e^2/(2C)$, as well as the inductive energy $E_{\text{L}} = \Phi_0^2/(2L)$. The energy scales E_{C} and E_{L}, together with the Josephson energy $E_{\text{J}} = \Phi_0^2/[4\pi^2 L_{\text{s}}(\Phi_{\text{ext}})]$ [107, 108], determine the circuit dynamics. For JPAs, we typically aim for large Josephson coupling energy, $E_{\text{J}}/E_{\text{C}} \simeq 10^3$ [79]. In contrast, $E_{\text{J}}/E_{\text{C}} \simeq 50$ corresponds to the transmon qubit regime [109]. Since our JPAs are weakly nonlinear devices [108], we can expand the cosine term up to quadratic order and find

$$\hat{H}_{\text{JPA}} = \frac{\omega_{\text{J}}(\Phi_{\text{ext}})\hat{Q}^2}{\omega_{\text{r}}C_{\text{r}}} + \frac{\omega_{\text{J}}(\Phi_{\text{ext}})\pi^2\hat{\phi}^2}{16L_{\text{r}}\omega_{\text{r}}} + \mathcal{O}(\hat{\phi}^4). \tag{2.7}$$

In the derivation of Eq. (2.7), we furthermore use the approximation $\omega_{\text{r}}/\omega_{\text{J}}(\Phi_{\text{ext}}) \simeq 1$ [96]. Next, we apply the external flux $\Phi_{\text{ext}} = \Phi_{\text{dc}} + \Phi_{\text{rf}}(t)$, consisting of the DC bias Φ_{dc} and a time-dependent low amplitude radio frequency (RF) modulation $\Phi_{\text{rf}}(t)$. We assume $\Phi_{\text{rf}}(t) \ll \Phi_0$ and perform a Taylor expansion of the flux-tunable resonance frequency around $\Phi_{\text{rf}}(t) = 0$, leading to

$$\hat{H}_{\text{JPA}} = \frac{\omega_0\hat{Q}^2}{\omega_{\text{r}}C_{\text{r}}} + \frac{\omega_0\pi^2\hat{\phi}^2}{16L_{\text{r}}\omega_{\text{r}}} + \left(\frac{\partial\omega_{\text{J}}}{\partial\Phi_{\text{ext}}}\right)_{\Phi_{\text{dc}}}\left[\frac{\hat{Q}^2}{\omega_{\text{r}}C_{\text{r}}} + \frac{\pi^2\hat{\phi}^2}{16L_{\text{r}}\omega_{\text{r}}}\right]\Phi_{\text{rf}}(t), \tag{2.8}$$

where we choose the energy reference such that zero order terms can be neglected and define $\omega_0 \equiv \omega_{\text{J}}(\Phi_{\text{dc}})$. Next, we express the JPA Hamiltonian in the framework of the second quantization and define the annihilation (creation) operators $\hat{a}_{\text{r}}$ ($\hat{a}_{\text{r}}^\dagger$) for the resonator field as

$$\hat{a}_{\text{r}} \equiv \frac{1}{4}\sqrt{\frac{2\pi}{\hbar Z}}\hat{\phi} + i\sqrt{\frac{2Z}{\pi\hbar}}\hat{Q}, \qquad \hat{a}_{\text{r}}^\dagger \equiv \frac{1}{4}\sqrt{\frac{2\pi}{\hbar Z}}\hat{\phi} - i\sqrt{\frac{2Z}{\pi\hbar}}\hat{Q}. \tag{2.9}$$

Annihilation and creation operator obey the bosonic commutation relation, $[\hat{a}_{\text{r}}, \hat{a}_{\text{r}}^\dagger] = 1$ [110]. We drop the charge modulation term in Eq. (2.8) [1] and obtain

$$\hat{H}_{\text{JPA}} = \hbar\omega_0\left[\hat{a}_{\text{r}}^\dagger\hat{a}_{\text{r}} + \frac{1}{2} + \frac{\Phi_{\text{rf}}(t)}{4\omega_0}\left(\frac{\partial\omega_{\text{J}}}{\partial\Phi_{\text{ext}}}\right)_{\Phi_{\text{dc}}}(\hat{a}_{\text{r}}^\dagger + \hat{a}_{\text{r}})^2\right]. \tag{2.10}$$

From Eq. (2.10), we observe that the DC bias shifts the resonance frequency of the circuit,

---

[1]In a high-frequency limit, this approximation can be justified by the fact that charge needs to be fundamentally associated with mass [111], implying that we can neglect charge modulation in case the modulation frequency exceeds the plasma frequency of the resonator [69]. However, even if this is not the case, dropping the RF charge term is legit since the effect of charge and flux modulation are interchangeable. This can be seen by transforming $\hat{H}_{\text{JPA}}$ into the interaction picture [2, 112].

according to Eq. (2.3) [96, 99, 113]. Next, we apply an RF field $A_{\mathrm{p}}(t) = A_0 \cos(\alpha\omega_0 t)$ via the pump line, where we assume the amplitude A_0 to be sufficiently large such that quantization effects are negligibly small (i.e. $|A_0|^2 \gg \hbar\alpha\omega_0/2$) [108]. The pump field $A_{\mathrm{p}}(t)$ proportionally translates into oscillatory flux modulation $\Phi_{\mathrm{rf}}(t)$ via the mutual inductance between the SQUID loop and pump line antenna [114, 115]. Thus, we can rewrite Eq. (2.10) as

$$\hat{H}_{\mathrm{JPA}} = \hbar\omega_0 \left[\hat{a}_{\mathrm{r}}^\dagger \hat{a}_{\mathrm{r}} + \frac{1}{2} + \epsilon \cos(\alpha\omega_0 t)(\hat{a}_{\mathrm{r}}^\dagger + \hat{a}_{\mathrm{r}})^2 \right] + \hbar\gamma(\hat{a}_{\mathrm{r}}^\dagger + \hat{a}_{\mathrm{r}})^4, \qquad (2.11)$$

where the parameter ϵ contains the pump amplitude and the relevant geometric parameters and the constant γ specifies the next higher-order nonlinearity [90] which we have neglected in Eq. (2.7) and Eq. (2.10). We observe from Eq. (2.10) that ϵ depends on the JPA resonance frequency, and can thus be tuned by frequency engineering. In addition, ϵ depends on the slope of the flux-characteristic at the specific DC bias point. This slope needs to be chosen sufficiently large. Only then, a desired flux modulation with sufficiently small pump amplitude A_0 can be achieved. In practice, A_0 is often restricted by the dynamic range of a pump generator. In the following theory considerations and in our experiments, we choose $\alpha = 2$ for the modulation parameter.

2.1.2 Input-output formalism for the JPA

So far, we have considered the Hamiltonian of the isolated circuit. To obtain a relation between JPA input and output modes, we couple the resonator to a signal transmission line via a coupling constant κ_{e} as well as to a bosonic environmental bath via κ_{i} [90]. We assume a continuous mode spectrum described by the coupling Hamiltonians

$$\frac{\hat{H}_{\mathrm{s}}}{\hbar} = \int dk \left[v_k k \hat{a}_k^\dagger \hat{a}_k + i \sqrt{\frac{v_k \kappa_{\mathrm{e}}}{2\pi}} \left(\hat{a}_{\mathrm{r}}^\dagger \hat{a}_k - \hat{a}_k^\dagger \hat{a}_{\mathrm{r}} \right) \right], \qquad (2.12)$$

$$\frac{\hat{H}_{\mathrm{e}}}{\hbar} = \int dk \left[v_k k \hat{b}_k^\dagger \hat{b}_k + i \sqrt{\frac{v_k \kappa_{\mathrm{i}}}{2\pi}} \left(\hat{a}_{\mathrm{r}}^\dagger \hat{b}_k - \hat{b}_k^\dagger \hat{a}_{\mathrm{r}} \right) \right], \qquad (2.13)$$

where $k = \omega_k/v_k$ is the wave number and v_k corresponds to the phase velocity of mode k. The annihilation operators $\hat{a}_k$ ($\hat{b}_k$) in Eq. (2.12) correspond to the input signal (loss) port. The coupling constant κ_{e} in Eq. (2.12) is determined by the capacitance C_{c}. The internal loss κ_{i} results from imperfections in the system, such as quasiparticles or environmental two-level fluctuators [116]. Next, we investigate the frequency spectrum of a harmonic resonator, where the system Hamiltonian corresponds to Eq. (2.11) for $\epsilon = \gamma = 0$ and $\omega_0 = \omega_{\mathrm{r}}$. The Heisenberg EOM in a single-mode approximation, $v_k = v$, is then given by

$$\frac{d\hat{a}_{\mathrm{r}}}{dt} = -\hbar \left(i\omega_0 + \frac{\kappa}{2} \right) \hat{a}_{\mathrm{r}} + \underbrace{\hbar \sqrt{v\kappa_{\mathrm{e}}} \hat{a}(t)}_{\text{coupled input}} + \underbrace{\hbar \sqrt{v\kappa_{\mathrm{i}}} \hat{b}(t)}_{\text{environmental bath}}, \qquad (2.14)$$

where $\hat{a}(t)$ [$\hat{b}(t)$] corresponds to the input (environmental) field, and $\kappa \equiv \kappa_e + \kappa_i$. The steady-state solution can be obtained by transforming Eq. (2.14) into a frame rotating with ω_0, followed by the Fourier transform. By comparing input and output signals, we can determine the complex reflection coefficient, S_{11}. Consequently, the power spectrum of the resonator is given by

$$|S_{11}(\Delta)|^2 = 1 - \frac{4\kappa_i \kappa_e}{\kappa^2 + (2\Delta)^2}, \tag{2.15}$$

where $\Delta \equiv \omega - \omega_0$. In addition, the resonator phase is given by

$$\varphi(\Delta) = \text{atan2}\left(\frac{\kappa_i^2 - \kappa_e^2 + (2\Delta)^2}{(\kappa_i + \kappa_e)^2 + (2\Delta)^2}, \frac{-4\kappa_e\Delta}{(\kappa_e - \kappa_i)^2 + (2\Delta)^2}\right), \tag{2.16}$$

where atan2 denotes the 2-argument arctangent function [117]. From the coupling constants, we can define an external quality factor Q_e, an internal quality factor Q_i as well as a loaded quality factor Q_l,

$$Q_e \equiv \frac{\omega_0}{\kappa_e}, \qquad Q_i \equiv \frac{\omega_0}{\kappa_i}, \qquad Q_l \equiv \frac{\omega_0}{\kappa} = \frac{\omega_0}{\kappa_e + \kappa_i}. \tag{2.17}$$

The quality factor measures the ratio between the energy stored in the resonator and the energy lost during one cycle [93]. The resonator response for various coupling constants is depicted in Fig. 2.2. Figure 2.2(a) shows the reflected power spectrum and Fig. 2.2(b) the phase shift induced by the resonator. We clearly observe the distinction between the overcoupled ($Q_e < Q_i$) and undercoupled ($Q_e > Q_i$) regimes. At critical coupling, $Q_e = Q_i$, signal loss is maximal due to impedance matching [93]. Since the Lorentzian $|S_{11}(\Delta)|^2$ is symmetric with respect to to κ_i and κ_e, it looks similar for overcoupled and undercoupled resonators, we use the resonator phase to distinguish between these different regimes. Overcoupled resonators show a phase $\pi < \varphi < 2\pi$ at resonance, whereas undercoupled resonators are characterized by $0 < \varphi < \pi$ [92]. Next, we apply the input-output formalism to the driven JPA. As shown in Fig. 2.3(a), we tune the JPA resonance frequency by a DC flux bias and apply a flux modulation with frequency $\alpha\omega_0$, $\alpha = 2$, leading to the Hamiltonian Eq. (2.11) [90]. The resulting Heisenberg EOM is given by

$$\frac{d\hat{a}_r}{dt} = -\hbar\left(i\omega_0 + \frac{\kappa}{2} - 2\epsilon\omega_0 \cos(2\omega_0 t)\right)\hat{a}_r + 2i\hbar\omega_0 \cos(2\omega_0 t)\hat{a}_r^\dagger$$
$$- \underbrace{i\hbar\gamma[(\hat{a}_r^\dagger + \hat{a}_r)^4, \hat{a}_r]}_{\text{Kerr term}} + \underbrace{\hbar\sqrt{v\kappa_e}\hat{a}(t)}_{\text{coupled input}} + \underbrace{\hbar\sqrt{v\kappa_i}\hat{b}(t)}_{\text{bath}}. \tag{2.18}$$

Next, we write $\cos(2\omega_0 t)$ in terms of complex exponential functions and apply the rotating wave approximation. In addition, we perform the stiff pump approximation in which we assume that energy in the pump signal is conserved [108, 118]. Consequently, we neglect loss of resonator excitations to the pump line, implying that we drop the term
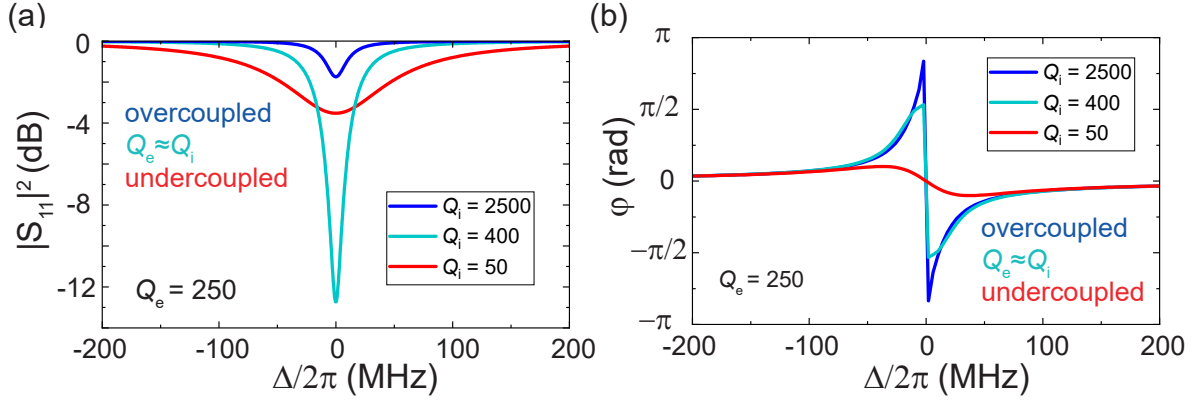
Figure 2.2: (a) Reflected power spectrum $|S_{11}|^2$ for an overcoupled (blue) and an undercoupled (red) harmonic resonator with an external quality factor $Q_e = 250$ as a function of detuning Δ, according to Eq. (2.15). The cyan curve corresponds to the regime $Q_e \simeq Q_i$. Power loss to environment is maximal for critical coupling, $Q_i = Q_e$, whereas in the limit $Q_i \gg Q_e$, the reflected energy equals the incoming energy. (b) Corresponding phase response φ of the reflected signal, according to Eq. (2.16). In case $Q_i \gg Q_e$, the phase shifts at resonance by roughly 2π, whereas for $Q_e \gg Q_i$, the phase is preserved. The critical coupling case $Q_e = Q_i$ corresponds to a phase shift of $\pi/2$.

$2\hbar\omega_0\epsilon\cos(2\omega_0 t)\hat{a}_r$. For simplicity, we also neglect the next higher-order nonlinearity, γ, although this nonlinearity, entering via the Kerr term in Eq. (2.18), combined with the finite energy of the pump tone, determines compression of the JPA [90, 107]. With these approximations, Eq. (2.18) becomes linear. In a frame rotating with ω_0, the corresponding homogeneous equation is solved by exponential functions with a time constant λ,

$$\lambda_{1,2} = -\frac{\kappa}{2}\left(\frac{\epsilon_c - \epsilon}{\epsilon_c}\right), \qquad \epsilon_c = \frac{\kappa}{2\omega_0}. \tag{2.19}$$

The quantity ϵ_c resembles the critical driving force of a Duffing oscillator [119]. Convergence to a steady-state solution requires the condition $\epsilon \leq \epsilon_c$. In the following, we neglect the transient solution Eq. (2.19) and assume that we operate the JPA in a steady state. This steady-state solution corresponds to a special solution of the Heisenberg EOM, which we obtain by taking the Fourier transform of Eq. (2.18) as well as of the respective complex conjugated equation [90]. From the resulting linear system of equations connecting input and output fields, we find the steady-state input-output relation

$$\hat{c}(\omega_s) = \underbrace{M(\omega_s)\hat{a}(\omega_s)}_{\text{signal}} + \underbrace{L(\omega_s)\hat{a}^\dagger(\omega_i)}_{\text{idler}} + \underbrace{M_b(\omega_s)\hat{b}(\omega_s) + L_b(\omega_s)\hat{b}^\dagger(\omega_i)}_{\text{noise}}, \tag{2.20}$$

with the signal frequency ω_s and idler frequency $\omega_i = 2\omega_0 - \omega_s$. The mode $\hat{c}(\omega_s)$ describes the steady-state output field [48]. The noise contribution in Eq. (2.20) corresponds to environmental modes, coupled to the system via κ_i [116]. In the nondegenerate case,

$\Delta \neq 0$, signal and idler modes are separated as depicted in Fig. 2.3(b) [105]. In this case, the complex signal gain $M(\omega_s)$ and the idler (or intermodulation) gain $L(\omega_s)$ are given by

$$M(\omega_s) = 1 + \kappa_e \frac{-i\omega_s + \kappa/2}{[\omega_s + i\kappa/2]^2 + \epsilon^2\omega_0^2}, \qquad L(\omega) = -\frac{i\epsilon\kappa_e\omega_0}{[\omega_s + i\kappa/2]^2 + \epsilon^2\omega_0^2}. \qquad (2.21)$$

We observe from Eq. (2.21) that in the overcoupled regime, the JPA acts as an amplifier for all $0 < \epsilon < \epsilon_c$. In the undercoupled case, there is a second critical pump field $0 < \epsilon_{c2} < \epsilon_c$, which can be expressed as $\epsilon_{c2} = \sqrt{\kappa_i^2 - \kappa_e^2}/(2\omega_0)$ close to resonance [90]. For $0 < \epsilon < \epsilon_{c2}$, the undercoupled JPA acts as an attenuator. Throughout this work, we only employ overcoupled JPAs and thus assume $\kappa_i \ll \kappa_e$. For this case, signal gain $G_s(\Delta) = |M(\omega_s)|^2$ and idler gain $G_i(\Delta) = |L(\omega_s)|^2$ are plotted in Fig. 2.3(c) as a function of detuning $\Delta = \omega_s - \omega_0$ for various internal loss rates κ_i. Signal and idler gain are related via

$$G_s(\Delta) - G_i(\Delta) = 1 + \kappa_i\kappa_e \frac{\Delta^2 + \epsilon^2\omega_0^2 - \kappa_i\kappa_e/4}{\kappa^2\Delta^2 + [\kappa^2/4 - \epsilon^2\omega_0^2 - \Delta^2]^2} \simeq 1. \qquad (2.22)$$

Thus, we can find u such that $G_s(\Delta) = \cosh^2 u$ and $G_i(\Delta) = \sinh^2 u$. Consequently, output signal and idler fields are connected to input signal and idler via a Bogoliubov transformation [120, 121]. Close to resonance, the nondegenerate gain can be expressed as

$$G_s(\Delta) = 1 + \frac{4\epsilon^2\epsilon_c^2\omega_0^4}{(\epsilon^2 - \epsilon_c^2)^2\omega_0^4 + 2\omega_0^2(\epsilon^2 + \epsilon_c^2)\Delta^2 + \Delta^4} \simeq 1 + \frac{G_0 b_J^2}{b_J^2 + \Delta^2} + \mathcal{O}\left(\frac{\Delta}{\omega_0}\right)^4, \quad (2.23)$$

with

$$G_0 = \frac{4z^2}{(1 - z^2)^2}, \qquad b_J = \frac{\kappa_e}{2} \frac{z^2 - 1}{\sqrt{2(z^2 + 1)}}, \qquad (2.24)$$

where $z \equiv \epsilon/\epsilon_c$. As a result, Eq. (2.23) can be well approximated by a Lorentzian with full width at half maximum (FWHM) bandwidth b_J. Note that an exact Lorentzian gain function in Eq. (2.23) would be unphysical since it would not preserve the bosonic commutation relations. From Eq. (2.24), we can calculate the gain-bandwidth product (GBP) [75, 108]

$$\tau = \sqrt{G_0}b_J = \sqrt{\frac{2}{\epsilon^2 + \epsilon_c^2}}\epsilon\epsilon_c\omega_0 = \frac{\epsilon_c\omega_0}{2}\left(1 + \frac{1}{z}\right) + \mathcal{O}\left(z^2 - 1\right) \simeq \frac{\omega_0}{2Q_e}. \qquad (2.25)$$

We observe that from a mathematical point of view, the GBP would become constant in the limit $\epsilon \gg 1$, as expected for classical operational amplifiers [122]. However, the corresponding solution for the JPA is not physical because for $\epsilon > \epsilon_c$ we can no longer neglect the time-dependent solution corresponding to Eq. (2.19) and the JPA starts entering the parametric oscillator regime [90, 123, 124]. In case we operate our JPAs with high gain, we vary the dimensionless pump power z^2 within a small range around a value z_0^2, slightly below the critical field, corresponding to $z^2 = 1$. We can then approximate
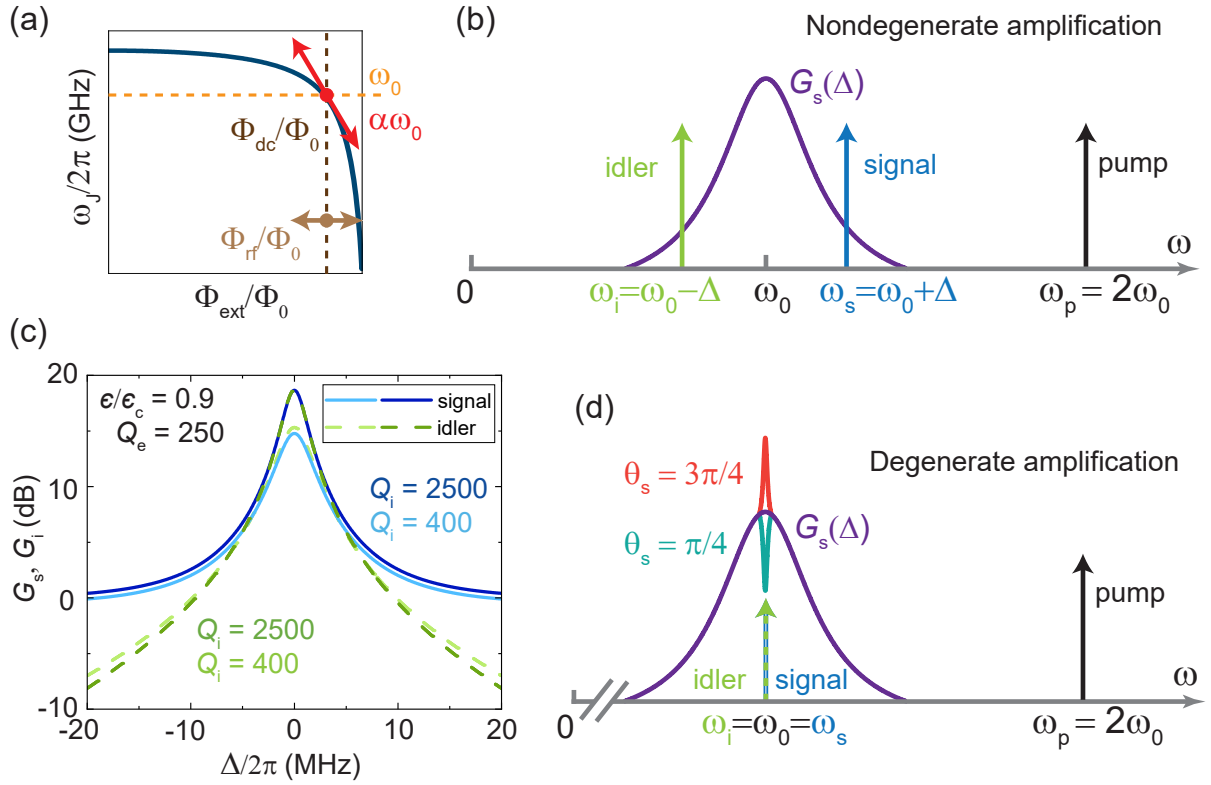
Figure 2.3: (a) Operation principle of the JPA. We combine a DC flux bias $\Phi_{\rm dc}$ with RF flux modulation at the frequency $\alpha\omega_0$, $\alpha \simeq 2$ induced by the pump signal. (b) Scheme for nondegenerate parametric amplification, characterized by $\Delta \neq 0$, leading to spectral separation between signal and idler. Consequently, the JPA acts as a phase-insensitive amplifier. (c) Theoretical nondegenerate signal and idler gain according to Eq. (2.23) and Eq. (2.22) for the overcoupled and the undercoupled scenario. (d) Degenerate amplification for an input signal at resonance, $\Delta = 0$. Depending on the relative phase $\theta_{\rm s}$ with respect to the pump, the JPA either amplifies or attenuates the signal and, thus, realizes a phase-sensitive amplifier.

the gain in Eq. (2.24) as

$$\ln G_0 = \underbrace{\ln 4z^2}_{\simeq 2\ln 2} - 2\ln(1 - z^2) \simeq 2\ln 2 - 2\ln\left(1 - z_0^2\right) - 2\frac{z^2 - z_0^2}{z_0^2 - 1} + \mathcal{O}\left[(z^2 - z_0^2)^2\right], \quad (2.26)$$

where in the first approximation, we exploit the fact that logarithm is a flat function in the region of $z^2 \simeq z_0^2 \simeq 1$. As a result, in the high-gain limit, the asymptotic pump power dependence of G_0 close to criticality can be well approximated by an exponential function. Next, we operate the JPA in the degenerate regime, $\Delta = 0$, as illustrated in Fig. 2.3(d). In this case, signal and idler exactly coincide [125]. Depending on the phase θ of the input signal, we can either achieve constructive or destructive interference between signal and idler, resulting in either amplification or attenuation of the input field. The phase of the pump field thereby provides the phase reference. The resulting degenerate gain can be

expressed as [90]

$$
G_{\mathrm{d}}(\theta) = \frac{\left(\frac{\kappa_{\mathrm{e}}^2 - \kappa_{\mathrm{i}}^2}{4} + \epsilon^2\omega_0^2\right)^2 + \kappa_{\mathrm{e}}^2\epsilon^2\omega_0^2 - 2\kappa_{\mathrm{e}}\epsilon\omega_0\left(\frac{\kappa_{\mathrm{e}}^2 - \kappa_{\mathrm{i}}^2}{4} + \epsilon\omega_0^2\right)\sin 2\theta}{\left(\frac{\kappa^2}{4} + \epsilon^2\omega_0^2\right)^2}
$$
$$
\overset{\kappa_{\mathrm{i}} \ll \kappa_{\mathrm{e}}}{\simeq} 1 + G_0\left[2z - (1 + z^2)\sin 2\theta\right]. \tag{2.27}
$$

The gain function has an elliptic shape. In the overcoupled case, we achieve maximal gain for $\theta = 3\pi/4 + n\pi$ and maximal attenuation for $\theta = \pi/4 + n\pi$, $n \in \mathbb{Z}$. According to Eq. (2.27) in the limit $\kappa_{\mathrm{e}} \gg \kappa_{\mathrm{i}}$, the corresponding maximal/minimal gain is given by

$$
G_{\mathrm{max}} = \left(\frac{z + 1}{z - 1}\right)^2, \qquad G_{\mathrm{min}} = \left(\frac{z - 1}{z + 1}\right)^2, \tag{2.28}
$$

satisfying $G_{\mathrm{max}}G_{\mathrm{min}} = 1$. Consequently, we can find r such that $G_{\mathrm{max}} = e^{2r}$, $G_{\mathrm{min}} = e^{-2r}$. The parameter r is conventionally referred to as squeezing parameter [126]. Note that the demonstrated input-output description of the JPA is mainly valid for finding steady-state solutions. An alternative description of the JPA in terms of master equations is provided in Ref. 90, which is especially useful to describe transient effects. In case $\epsilon > \epsilon_{\mathrm{c}}$ the JPA enters the parametric oscillator regime, where the wave function collapses into one of two possible steady states [127].

2.1.3 Standard quantum limit

In the following, we review the fundamental quantum mechanical treatment of linear amplification, focusing on amplification noise. A practical quantity to characterize this noise is quantum efficiency η [107], which is defined as the ratio between the input and output signal-to-noise ratios (SNRs), and therefore, coincides with the overall noise factor of the system [93]. Using η as a measure for the amplifier performance is beneficial since it is restricted to the interval between 0 and 1, in contrast to other noise quantifiers, such as noise photon number or noise temperature. The crucial difference between classical amplifiers and quantum amplifiers is described by the Haus-Caves theorem [128, 129], which states that noiseless linear phase-preserving amplification is not possible due to the bosonic commutation relations [130, 131]. To ensure that both input signal $\hat{a}$ and the output signal $\hat{c}$ are bosonic modes, the steady-state input-output relation, Eq. (2.20), needs to have the form of a Bogoliubov transformation [120],

$$
\hat{c} = \sqrt{G_{\mathrm{s}}}\,\hat{a} + \sqrt{G_{\mathrm{s}} - 1}\,\hat{f}^\dagger. \tag{2.29}
$$

Here, $G_{\mathrm{s}} \geq 1$ represents the signal gain and the mode operator $\hat{f}$ results from the fact that the amplifier needs to be coupled to an energy reservoir [130] and guarantees that input and output modes satisfy the bosonic commutation relation. The total power

corresponding to $\hat{f}$ is determined by

$$\langle|\hat{f}|^2\rangle = \frac{1}{2}\langle\hat{f}^\dagger\hat{f} + \hat{f}\hat{f}^\dagger\rangle = \langle\hat{f}^\dagger\hat{f}\rangle + \frac{1}{2}. \tag{2.30}$$

According to Eq. (2.29), we have

$$\langle|\hat{c}|^2\rangle = G_\mathrm{s}\langle|\hat{a}|^2\rangle + (G_\mathrm{s} - 1)\langle|\hat{f}|^2\rangle, \tag{2.31}$$

under the assumption that $\hat{a}$ and $\hat{f}$ are uncorrelated. We choose the amplifier input as a gain-independent reference for the noise photon number n_f and find

$$n_\mathrm{f} = \langle|\hat{f}|^2\rangle\frac{G_\mathrm{s} - 1}{G_\mathrm{s}} \geq \frac{1}{2}\left(1 - \frac{1}{G_\mathrm{s}}\right), \qquad \eta = \frac{1}{1 + 2n_\mathrm{f}} \leq \frac{G_\mathrm{s}}{2G_\mathrm{s} - 1}. \tag{2.32}$$

These inequalities are conventionally known as the standard quantum limit (SQL) [129, 130, 132]. Thus, for $G_\mathrm{s} \gg 1$, the amplifier broadens the signal variance by at least the vacuum variance and limits the quantum efficiency to $1/2$ and the noise temperature to $T_\mathrm{f} \geq \hbar\omega_\mathrm{s}/(k_\mathrm{B}\ln 3)$ [130, 133]. This can be understood by the fact that the output of such an amplifier is classical, implying that both signal quadratures have been measured. Resulting from the Heisenberg uncertainty relation, such a simultaneous measurement is only possible if the detector adds at least vacuum fluctuations to the signal [132, 134]. For the parametric amplifier, $\hat{f}$ corresponds to the input idler mode. A schematic illustration of the nondegenerate parametric amplifier as a 4-port device is shown in Fig. 2.4(a). The signal photons, n_s, and the input variance, σ_s^2, are amplified with gain G_s. The idler noise σ_i^2 is converted to the signal frequency with intermodulation gain $G_\mathrm{i} = G_\mathrm{s} - 1$ [80]. Thus, bimodal input fluctuations are amplified in a different linear superposition than the input signal, which gives rise to a constant additive noise contribution by the idler port. In addition, the phase-conjugated signal as well as the signal fluctuations are mixed into the idler band with gain G_i. Throughout the rest of this work, the idler output is not considered. Figure 2.4(b) shows the idler noise contribution at an exemplary frequency of 5.5 GHz for various environmental temperatures and demonstrates the importance of cooling down the system as low as possible. The respective noise is determined by including thermal statistics [cf. Eq. (2.100)] into Eq. (2.30). The situation changes when the amplifier is operated in the degenerate regime. Without loss of generality, we assume that the p-quadrature is amplified with gain G_p and the q-quadrature is simultaneously deamplified with G_q. In this case, Eq. (2.32) holds if we replace noise and gain with the respective geometric means, $n_\mathrm{f} = 2\sqrt{n_q n_p}$ and $G = \sqrt{G_q G_p}$, where n_q (n_p) is the noise, added to the q (p) quadrature. Since $G_q G_p = 1$ for an ideal degenerate amplifier, noiseless amplification is allowed by quantum mechanics in this regime. The absence of the SQL in this case results from the fact that the input signal can be effectively regarded as a frequency-degenerate two-mode state, consisting of signal and idler.

(a)

(b)
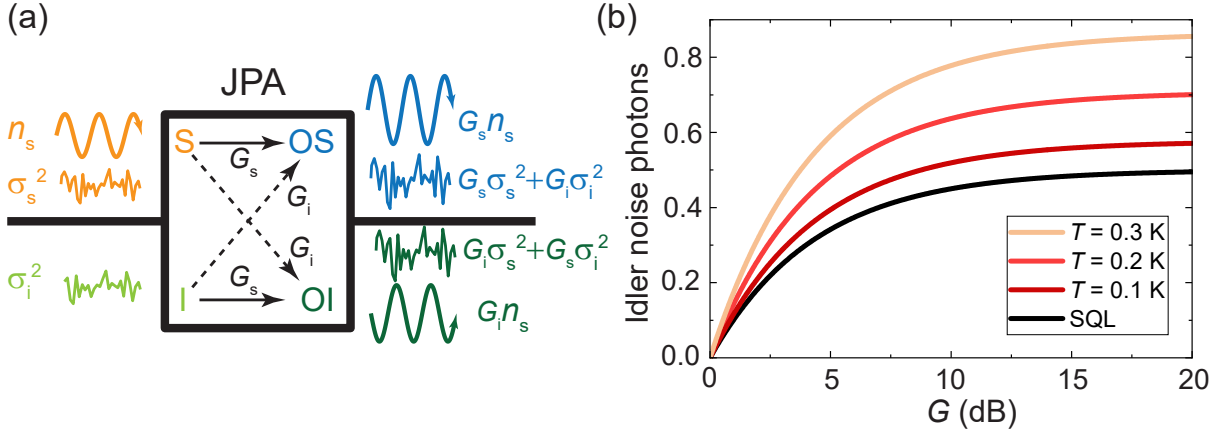
Figure 2.4: (a) Illustration of the origin of the SQL for nondegenerate parametric amplification. The amplifier is described as a 4-port device with signal and idler inputs (S, I) and respective (OS, OI) output ports. The input signal, carrying n_s photons, as well as the input fluctuations, σ_s^2, is amplified with gain G_s. The uncorrelated idler fluctuations, σ_i^2, are mixed into the signal band with gain $G_\mathrm{i} = G_\mathrm{s} - 1$ and act as additive noise. (b) Idler noise floor for various environmental temperatures, determined from thermal statistics, as described in the main text. The limit $T \to 0$ corresponds to the SQL.

2.1.4 Parametric amplification of broadband signals

So far, our consideration of the SQL relies on the assumption of a single-mode signal. In the next step, we analyze the SQL for a multimode input spectrum in the nondegenerate case and find that, for sufficiently broadband signals noiseless amplification becomes possible. Intuitively, this can be seen from Eq. (2.31). In the high gain limit, $G_\mathrm{s} \gg 1$, the output becomes classical, $\langle \hat{c}^\dagger \hat{c} \rangle \gg 1/2$. Thus, we can approximate

$$\frac{\langle \hat{c}^\dagger \hat{c} \rangle}{G_\mathrm{s}} = \left(\langle \hat{a}^\dagger \hat{a} \rangle + \frac{1}{2} \right) + \frac{1}{2}. \tag{2.33}$$

As a result, the power of the amplified signal, referred to the input, consists of the input signal, as well as of the input vacuum fluctuations at signal and idler port. In the broadband case, the input signal also couples to the idler port. Under the assumption of $\langle \hat{a}^\dagger \hat{a} \rangle = \langle \hat{f}^\dagger \hat{f} \rangle$, we have

$$\frac{\langle \hat{c}^\dagger \hat{c} \rangle}{2G_\mathrm{s} - 1} = \langle \hat{a}^\dagger \hat{a} \rangle + \frac{1}{2}, \tag{2.34}$$

implying that the signal is amplified with an effective broadband gain $G_\mathrm{b} = 2G_\mathrm{s} - 1$ without additional noise. In the following, we perform a strict quantum mechanical calculation, based on the input-output formalism and derive the dependence of the SQL on the input signal bandwidth b_s. This theory has been published in Ref. 85 and parts of the text as well as from the figures have been adopted from this publication.

Neglecting any transient effects [135], the multimode steady-state input-output relation

for a set $\mathcal{I}$ of input modes can be written as

$$\hat{c}(\omega) = \int_{\mathcal{I}} d\tilde{\omega} \left[M(\omega, \tilde{\omega})\hat{a}(\tilde{\omega}) + L(\omega, \tilde{\omega})\hat{a}^\dagger(\tilde{\omega}) \right] + \hat{f}(\omega), \qquad (2.35)$$

where $\hat{c}(\omega)$ corresponds to the amplified output mode, $\hat{a}(\tilde{\omega})$ is the input mode at frequency $\tilde{\omega}$ which is amplified with gain $M(\omega, \tilde{\omega})$, and $\hat{a}^\dagger(\tilde{\omega})$ is a phase-conjugated input mode which is amplified with signal gain $L(\omega, \tilde{\omega})$ [129]. The gain functions account for power conversion as well as for possible frequency conversion between input and output modes, $\tilde{\omega} \to \omega$. The bosonic mode $\hat{f}(\omega)$ represents the noise added by the amplifier, referred to the amplifier output. This mode is assumed to be uncorrelated with the input signal and can be a result from technical noise, fundamental quantum noise or potential noise contributions from higher order nonlinearities [107]. The output as well as the input modes fulfill the continuum bosonic commutation relations

$$[\hat{a}(\omega), \hat{a}^\dagger(\omega')] = \delta(\omega - \omega'), \qquad [\hat{a}(\omega), \hat{a}(\omega')] = [\hat{a}^\dagger(\omega), \hat{a}^\dagger(\omega')] = 0, \qquad (2.36)$$

$$[\hat{c}(\omega), \hat{c}^\dagger(\omega')] = \delta(\omega - \omega'), \qquad [\hat{c}(\omega), \hat{c}(\omega')] = [\hat{c}^\dagger(\omega), \hat{c}^\dagger(\omega')] = 0. \qquad (2.37)$$

As shown by Eq. (2.19), in the parametric three-wave mixing process, every input mode $\hat{a}(\tilde{\omega})$ can be associated with a corresponding phase-conjugated idler mode at frequency $\tilde{\omega}_{\mathrm{i}} = 2\omega_0 - \tilde{\omega}$ [134], where ω_0 is the resonance frequency of the parametric amplifier. The amplitude gain for the output mode at frequency ω is then given by

$$M(\omega, \tilde{\omega}) = M(\tilde{\omega})\delta(\omega - \tilde{\omega}), \qquad L(\omega, \tilde{\omega}) = L(\tilde{\omega}_{\mathrm{i}})\delta(\omega - \tilde{\omega}_{\mathrm{i}}). \qquad (2.38)$$

We now assume that the input signal is centered around the signal reconstruction frequency ω_{s} with a single-side bandwidth b_{s} (total bandwidth $2b_{\mathrm{s}}$). Thus, Eq. (2.35) yields

$$\hat{c}(\omega) = \int_{\omega_{\mathrm{s}}-b_{\mathrm{s}}}^{\omega_{\mathrm{s}}+b_{\mathrm{s}}} \left[M(\tilde{\omega})\delta(\omega - \tilde{\omega})\hat{a}(\tilde{\omega}) + L(\tilde{\omega}_{\mathrm{i}})\delta(\omega - \tilde{\omega}_{\mathrm{i}})\hat{a}^\dagger(\tilde{\omega}) \right] d\tilde{\omega} + \hat{f}(\omega). \qquad (2.39)$$

We make use of the relation

$$\int_a^b f(x)\delta(x)dx = f(0)\mathbb{1}[a, b](0), \qquad \mathbb{1}[a, b](x) \equiv \begin{cases} 1 & a \leq x \leq b \\ 0 & \text{else} \end{cases} \qquad (2.40)$$

for any function $f(x)$ and obtain

$$\hat{c}(\omega) = M(\omega)\mathbb{1}_{\mathrm{s}}(\omega)\hat{a}(\omega) + L(\omega_{\mathrm{i}})\mathbb{1}_{\mathrm{i}}(\omega)\hat{a}^\dagger(\omega_{\mathrm{i}}) + \hat{f}(\omega), \qquad (2.41)$$
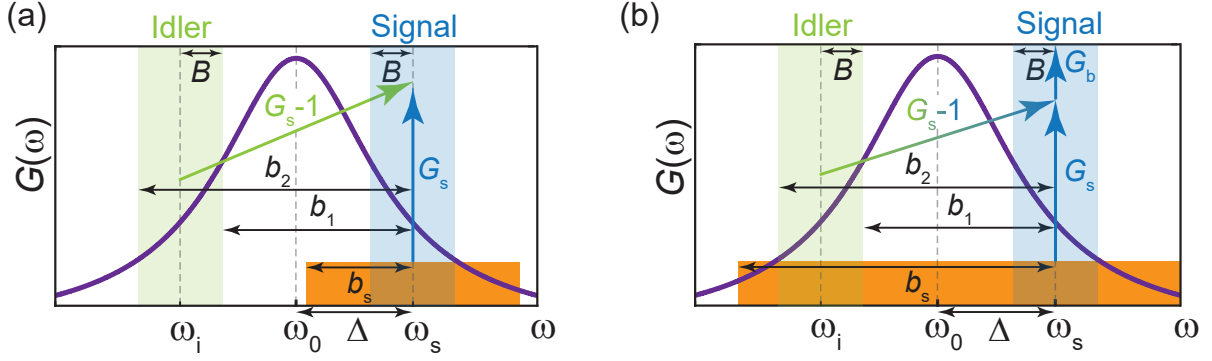
Figure 2.5: (a) Spectrum of nondegenerate parametric amplification of narrow signals with bandwidth b_{s}. The signal is schematically depicted by the orange rectangle. The solid purple line illustrates the gain function, which is approximately Lorentzian. The blue-shaded and green-shaded regions show the measurement bands with full bandwidth $2B$ around signal and idler modes, respectively. For input signals $b_{\mathrm{s}} \leq b_1$, the idler modes add at least vacuum fluctuations to the output. (b) Spectrum of nondegenerate parametric amplification of a broadband signal. If $b_{\mathrm{s}} \geq b_2$, each mode in the signal bandwidth corresponds to a respective input mode at the idler sideband, resulting in amplification with an overall broadband gain G_{b} and absence of the SQL.

where $\omega_{\mathrm{i}} = 2\omega_0 - \omega$ and

$$\mathbb{1}_{\mathrm{s}}(\omega) \equiv \mathbb{1}[\omega_{\mathrm{s}} - b_{\mathrm{s}}, \omega_{\mathrm{s}} + b_{\mathrm{s}}](\omega) = \Theta(\omega - \omega_{\mathrm{s}} + b_{\mathrm{s}}) - \Theta(\omega - \omega_{\mathrm{s}} - b_{\mathrm{s}}), \tag{2.42}$$

$$\mathbb{1}_{\mathrm{i}}(\omega) \equiv \mathbb{1}[2\omega_0 - \omega_{\mathrm{s}} - b_{\mathrm{s}}, 2\omega_0 - \omega_{\mathrm{s}} + b_{\mathrm{s}}](\omega) = \Theta(\omega - \omega_{\mathrm{i}} + b_{\mathrm{s}}) - \Theta(\omega - \omega_{\mathrm{i}} - b_{\mathrm{s}}), \tag{2.43}$$

where $\Theta(x)$ is the Heaviside step function. We calculate the commutators

$$\begin{aligned}
[\hat{c}(\omega), \hat{c}^\dagger(\omega')] &= M(\omega)M^*(\omega')\mathbb{1}_{\mathrm{s}}(\omega)\mathbb{1}_{\mathrm{s}}(\omega')[\hat{a}(\omega), \hat{a}^\dagger(\omega')] \\
&\quad - L(\omega_{\mathrm{i}})L^*(\omega_{\mathrm{i}}')\mathbb{1}_{\mathrm{i}}(\omega)\mathbb{1}_{\mathrm{i}}(\omega')[\hat{a}(\omega_{\mathrm{i}}'), \hat{a}^\dagger(\omega_{\mathrm{i}})] + [\hat{f}(\omega), \hat{f}^\dagger(\omega')].
\end{aligned} \tag{2.44}$$

After inserting the bosonic commutation relations Eq. (2.36) and Eq. (2.37), we find

$$[\hat{f}(\omega), \hat{f}^\dagger(\omega')] = \delta(\omega - \omega')(1 - M(\omega)M^*(\omega')\mathbb{1}_{\mathrm{s}}(\omega)\mathbb{1}_{\mathrm{s}}(\omega') + L(\omega_{\mathrm{i}})L^*(\omega_{\mathrm{i}}')\mathbb{1}_{\mathrm{i}}(\omega)\mathbb{1}_{\mathrm{i}}(\omega')). \tag{2.45}$$

For the symmetrized fluctuations describing the variance associated with $\hat{f}(\omega)$, and therefore the additive noise, we find [129]

$$\langle|\Delta\hat{f}|^2\rangle \equiv \frac{1}{2}\langle\hat{f}(\omega)\hat{f}^\dagger(\omega') + \hat{f}^\dagger(\omega')\hat{f}(\omega)\rangle - \underbrace{\langle\hat{f}(\omega)\rangle\langle\hat{f}^\dagger(\omega')\rangle}_{=0} = G_{\mathrm{s}}(\omega)S_{\mathrm{f}}(\omega)\delta(\omega - \omega'), \tag{2.46}$$

where $G_{\mathrm{s}}(\omega) = |M(\omega)|^2 = |L(\omega_{\mathrm{i}})|^2 + 1$ is the parametric signal gain and $S_{\mathrm{f}}(\omega)$ is the input noise power spectral density in units of photons per bandwidth [129]. In Eq. (2.46),

we have assumed that the expectation value of the fluctuations vanishes. We use the Heisenberg uncertainty principle $\langle|\Delta\hat{f}|^2\rangle \geq 1/2|\langle[\hat{f}(\omega), \hat{f}^\dagger(\omega')]\rangle|$ [2, 48] and integrate over ω', finding

$$S_{\mathrm{f}}(\omega) \geq \frac{1}{2G_{\mathrm{s}}(\omega)}|\mathbb{1}_{\mathrm{i}}(\omega) - 1 + G_{\mathrm{s}}(\omega)(\mathbb{1}_{\mathrm{s}}(\omega) - \mathbb{1}_{\mathrm{i}}(\omega))|. \qquad (2.47)$$

We obtain the number of noise photons n_{f}, added by the mode $\hat{f}(\omega)$, by integrating Eq. (2.47) over the output mode frequencies $[\omega_{\mathrm{s}} - \gamma, \omega_{\mathrm{s}} + \gamma]$. The output mode bandwidth γ is limited by the single-sided detection bandwidth B,

$$\gamma = \begin{cases} b_{\mathrm{s}} & b_{\mathrm{s}} \leq B \\ B & \text{else} \end{cases}. \qquad (2.48)$$

We obtain

$$\int_{\omega_{\mathrm{s}}-\gamma}^{\omega_{\mathrm{s}}+\gamma} S_{\mathrm{f}}(\omega)d\omega = 2\gamma n_{\mathrm{f}} \geq \frac{1}{2}\int_{\omega_{\mathrm{s}}-\gamma}^{\omega_{\mathrm{s}}+\gamma}(\mathbb{1}_{\mathrm{s}}(\omega) - \mathbb{1}_{\mathrm{i}}(\omega))d\omega + \frac{1}{2}\int_{\omega_{\mathrm{s}}-\gamma}^{\omega_{\mathrm{s}}+\gamma}\frac{1}{G_{\mathrm{s}}(\omega)}(\mathbb{1}_{\mathrm{i}}(\omega) - 1)d\omega. \qquad (2.49)$$

Equation (2.49) gives the general constraint on the added noise, depending on the bandwidth of the signal. For $b_{\mathrm{s}} \leq b_1 \equiv 2\Delta - B$, we have $\mathbb{1}_{\mathrm{i}}(\omega) = 0$, whereas for $b_{\mathrm{s}} \geq b_2 \equiv 2\Delta + B$, we always find $\mathbb{1}_{\mathrm{i}}(\omega) = 1$, resulting in $n_{\mathrm{f}} \geq 0$. For narrow signals at ω_{s}, we can assume $b_{\mathrm{s}} \ll B$ and thus $\gamma = b_{\mathrm{s}}$. We use the approximation of a frequency independent gain within the signal bandwidth $G_{\mathrm{s}}(\omega) \simeq G_{\mathrm{s}}(\omega_{\mathrm{s}}) \equiv G_{\mathrm{s}}$. Furthermore, we have $\mathbb{1}_{\mathrm{i}}(\omega) = 0$ and $\mathbb{1}_{\mathrm{s}}(\omega) = 1$. Thus, we find

$$2b_{\mathrm{s}}n_{\mathrm{f}} \geq \frac{1}{2}\int_{\omega_{\mathrm{s}}-b_{\mathrm{s}}}^{\omega_{\mathrm{s}}+b_{\mathrm{s}}}\left(1 - \frac{1}{G_{\mathrm{s}}}\right)d\omega \simeq \frac{1}{2}\left(1 - \frac{1}{G_{\mathrm{s}}}\right) \cdot 2b_{\mathrm{s}} \qquad (2.50)$$

which recovers the SQL from Eq. (2.32) for narrowband signals. To find a more general solution for a realistic spectral gain function, we rewrite Eq. (2.49) as

$$n_{\mathrm{f}} \geq \frac{1}{4\gamma}\int_{\omega_{\mathrm{s}}-\gamma}^{\omega_{\mathrm{s}}+\gamma}\left(1 - \frac{1}{G_{\mathrm{s}}(\omega)}\right)d\omega + \frac{1}{4\gamma}\int_{\mathcal{I}_{\mathrm{i}}}\mathbb{1}_{\mathrm{i}}(\omega)\left(\frac{1}{G_{\mathrm{s}}(\omega)} - 1\right)d\omega, \qquad (2.51)$$

where $\mathcal{I}_{\mathrm{i}}$ is the set of all input signal modes which overlap with the idler sideband measurement bandwidth. Equation (2.51) can be regarded as the generalized SQL in the multimode description and allows for the calculation of the fundamental quantum limit for arbitrary frequency-dependent gain $G_{\mathrm{s}}(\omega)$. In the following, we solve Eq. (2.51) for the JPA gain function under the Lorentzian approximation, where a closed analytical solution

can be found. First, we determine the frequency intervals

$$
\begin{aligned}
\mathcal{I}_{\mathrm{i}} &= [2\Delta + \omega_{\mathrm{s}} - b_{\mathrm{s}}, 2\Delta + \omega_{\mathrm{s}} + b_{\mathrm{s}}] \cap [\omega_{\mathrm{s}} - B, \omega_{\mathrm{s}} + B] \\
&= [\max(2\Delta + \omega_{\mathrm{s}} - b_{\mathrm{s}}, \omega_{\mathrm{s}} - B), \min(2\Delta + \omega_{\mathrm{s}} + b_{\mathrm{s}}, \omega_{\mathrm{s}} + B)] \\
&= \begin{cases}
\varnothing & b_{\mathrm{s}} \leq B, \\
\varnothing & B \leq b_{\mathrm{s}} \leq b_1, \\
[2\Delta + \omega_{\mathrm{s}} - b_{\mathrm{s}}, \omega_{\mathrm{s}} + B] & b_1 \leq b_{\mathrm{s}} \leq b_2, \\
[\omega_{\mathrm{s}} - B, \omega_{\mathrm{s}} + B] & b_{\mathrm{s}} \geq b_2,
\end{cases}
\end{aligned}
\tag{2.52}
$$

where $\varnothing$ denotes the empty set. Equation (2.52) implies that we need to distinguish between the four cases $b_{\mathrm{s}} \leq B$, $B \leq b_{\mathrm{s}} \leq b_1$, $b_1 \leq b_{\mathrm{s}} \leq b_2$ and $b_{\mathrm{s}} \geq b_2$. We describe the JPA gain curve as a Lorentzian centered at ω_0 with half width at half maximum bandwidth b_{J} [79, 90],

$$
G_{\mathrm{s}}(\omega) = 1 + \frac{G_0 b_{\mathrm{J}}^2}{b_{\mathrm{J}}^2 + (\omega - \omega_0)^2}.
\tag{2.53}
$$

In the first case, we have $b_{\mathrm{s}} \leq B$, which implies $\gamma = b_{\mathrm{s}}$, according to Eq. (2.48). Thus, we find

$$
2 b_{\mathrm{s}} n_{\mathrm{f}} \geq \frac{1}{2} \int_{\omega_{\mathrm{s}} - b_{\mathrm{s}}}^{\omega_{\mathrm{s}} + b_{\mathrm{s}}} \left(1 - \frac{1}{G_{\mathrm{s}}(\omega)} \right) d\omega = \frac{G_0}{2(G_0 + 1)} \int_{\omega_{\mathrm{s}} - b_{\mathrm{s}}}^{\omega_{\mathrm{s}} + b_{\mathrm{s}}} \frac{1}{1 + \left(\frac{\omega - \omega_0}{b \sqrt{G_0 + 1}} \right)^2} d\omega.
\tag{2.54}
$$

Evaluating the integral yields

$$
n_{\mathrm{f}} \geq \frac{G_0 b_{\mathrm{J}}}{4 b_{\mathrm{s}} \sqrt{G_0 + 1}} \arctan \left(\frac{2 b_{\mathrm{s}} b_{\mathrm{J}} \sqrt{G_0 + 1}}{b_{\mathrm{J}}^2 (G_0 + 1) + \Delta^2 - b_{\mathrm{s}}^2} \right).
\tag{2.55}
$$

With the gain-bandwidth product, $\tau = b_{\mathrm{J}} \sqrt{G_0}$ [cf. Eq. (2.25)] [75], and the large-gain approximation $G_0 + 1 \simeq G_0$, we obtain

$$
n_{\mathrm{f}} \geq \frac{1}{4 \beta_{\mathrm{s}}} \arctan \left(\frac{2 \beta_{\mathrm{s}}}{1 + \delta^2 - \beta_{\mathrm{s}}^2} \right),
\tag{2.56}
$$

where $\beta_{\mathrm{s}} \equiv b_{\mathrm{s}} / \tau$ and $\delta \equiv \Delta / \tau$. For the typical values $\tau / 2\pi \simeq 20\,\mathrm{MHz}$, $\Delta / 2\pi \simeq 0.3\,\mathrm{MHz}$, $B / 2\pi \simeq 0.2\,\mathrm{MHz}$ we find [75]

$$
n_{\mathrm{f}} \geq \frac{1}{2} \frac{1}{1 + \delta^2} + \mathcal{O}(\beta_{\mathrm{s}}^2) = 0.4999 \simeq \frac{1}{2}.
\tag{2.57}
$$

As a result, the Lorentzian shape of the gain curve only implies a small correction to the SQL of $1/2$ in the narrowband case $\beta_{\mathrm{s}} \ll 1$. In the second case, we have $\gamma = B$. Thus, we

need to solve

$$2Bn_\mathrm{f} \geq \frac{1}{2} \int_{\omega_\mathrm{s}-B}^{\omega_\mathrm{s}+B} \left(1 - \frac{1}{G_\mathrm{s}(\omega)}\right) d\omega. \tag{2.58}$$

A similar calculation as in the first case gives

$$n_\mathrm{f} \geq \frac{1}{4\beta} \arctan\left(\frac{2\beta}{1 + \delta^2 - \beta^2}\right), \tag{2.59}$$

where $\beta \equiv B/\tau$ and $G_0 \simeq G_0 + 1$. In the third case, $b_1 \leq b_\mathrm{s} \leq b_2$, we have

$$2Bn_\mathrm{f} \geq \frac{1}{2} \int_{\omega_\mathrm{s}-B}^{\omega_\mathrm{s}+B} \left(1 - \frac{1}{G_\mathrm{s}(\omega)}\right) d\omega + \frac{1}{2} \int_{2\Delta+\omega_\mathrm{s}-b_\mathrm{s}}^{\omega_\mathrm{s}+B} \left(\frac{1}{G_\mathrm{s}(\omega)} - 1\right) d\omega$$
$$= \frac{1}{2} \int_{\omega_\mathrm{s}-B}^{2\Delta+\omega_\mathrm{s}-b_\mathrm{s}} \left(1 - \frac{1}{G_\mathrm{s}(\omega)}\right) d\omega, \tag{2.60}$$

which yields

$$n_\mathrm{f} \geq \frac{1}{4\beta} \arctan\left(\frac{2(\delta + \beta - \beta_\mathrm{s})}{1 + \beta\beta_\mathrm{s} + \delta(\beta_\mathrm{s} - \beta) - \delta^2}\right). \tag{2.61}$$

The fourth case is trivial,

$$2Bn_\mathrm{f} \geq \int_{\omega_\mathrm{s}-B}^{\omega_\mathrm{s}+B} \left(1 - \frac{1}{G_\mathrm{s}(\omega)}\right) d\omega + \frac{1}{2} \int_{\omega_\mathrm{s}-B}^{\omega_\mathrm{s}+B} \left(\frac{1}{G_\mathrm{s}(\omega)} - 1\right) d\omega = 0 \tag{2.62}$$

and implies the absence of the SQL if the input signal completely covers the idler port. In summary, the quantum limit n_ql, corresponding to the minimal value of n_f, is given by

$$n_\mathrm{ql} = \frac{1}{4\beta} \begin{cases} \frac{\beta}{\beta_\mathrm{s}} \arctan\left(\frac{2\beta_\mathrm{s}}{1+\delta^2-\beta_\mathrm{s}^2}\right) & b_\mathrm{s} \leq B, \\ \arctan\left(\frac{2\beta}{1+\delta^2-\beta^2}\right) & B \leq b_\mathrm{s} \leq b_1, \\ \arctan\left(\frac{2(\delta+\beta-\beta_\mathrm{s})}{1+\beta\beta_\mathrm{s}+\delta(\beta_\mathrm{s}-\beta)-\delta^2}\right) & b_1 \leq b_\mathrm{s} \leq b_2, \\ 0 & b_\mathrm{s} \geq b_2. \end{cases} \tag{2.63}$$

The corresponding quantum efficiency $\eta_\mathrm{ql} = 1/(1 + 2n_\mathrm{ql})$ is plotted in Fig. 2.6(a) for $\tau/2\pi = 15\,\mathrm{MHz}$ for varying detuning Δ with $B/2\pi = 30\,\mathrm{kHz}$. Figure 2.6(b) displays η_ql as a function of B for $\Delta/2\pi = 37.5\,\mathrm{kHz}$. We observe a narrowband region with $\eta_\mathrm{ql} = 1/2$ and a broadband regime where $\eta_\mathrm{ql} = 1$. Both regimes are connected by a smooth transition region, where only a part of the input signal modes overlaps with the mirrored detection bandwidth on the idler sideband. It is worth mentioning that so far, our treatment of the first case in Eq. (2.52) corresponds to an artificial scenario, where the detection bandwidth is perfectly adjusted to the signal bandwidth. This consideration is necessary since we are interested in the actual quantum limit, which requires that we have to make B as small as possible without losing any signal modes. However, in a realistic experiment, B is always a fixed quantity. As a result, the case distinction Eq. (2.48) is not required. In the case

(a)

(b)
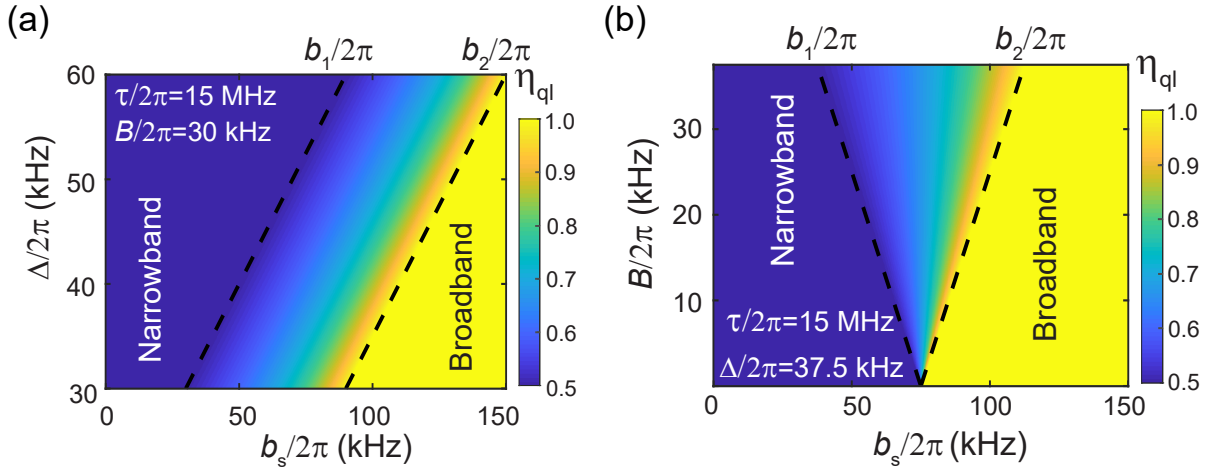
Figure 2.6: Theoretical limit $\eta_{ql} = 1/(1 + 2n_{ql})$ for the quantum efficiency η as a function of the input signal bandwidth b_s for $\tau/2\pi = 15\,\mathrm{MHz}$, where the noise limit n_{ql} is given by Eq. (2.63). Panel (a) shows η_{ql} for varying detuning Δ and $B/2\pi = 30\,\mathrm{kHz}$ and panel (b) shows η_{ql} as a function of B for fixed detuning $\Delta/2\pi = 37.5\,\mathrm{kHz}$. For $b_s \geq b_2$, noiseless amplification is possible.

$b_s < B$, the modes with frequencies $\omega_s - B \leq \omega \leq \omega_s - b_s$ and $\omega_s + b_s \leq \omega \leq \omega_s + B$ do not correspond to the input signal although they are within the detection bandwidth. This effect needs to be taken into account in Eq. (2.47) by adding the corresponding vacuum power spectral density $S_{vac} = 1/2$ for these modes to the right hand side. Furthermore, we have $\mathbb{1}_i(\omega) = 0$ in this case, we obtain

$$\int_{\omega_s-B}^{\omega_s+B} S_f(\omega)d\omega = 2Bn_f \geq \frac{1}{2}\int_{\omega_s-B}^{\omega_s+B} \mathbb{1}_s(\omega)\left(1 - \frac{1}{G_s(\omega)}\right)d\omega + \int_{\omega_s-B}^{\omega_s-b_s} \frac{1}{2}d\omega + \int_{\omega_s+b_s}^{\omega_s+B} \frac{1}{2}d\omega,$$

(2.64)

and consequently

$$n_f \geq \frac{1}{4\beta}\arctan\left(\frac{2\beta_s}{1 + \delta^2 - \beta_s^2}\right) + \frac{1}{2}\frac{\beta - \beta_s}{\beta}.$$

(2.65)

Thus, the result of Eq. (2.63) does not fundamentally change and, in the limit $b_s \ll B$, Eq. (2.65) still reproduces the SQL, $n_f \geq 1/2$.

2.1.5 Chained Josephson parametric amplifiers

In case parametric amplifiers are employed for quantum experiments, it is crucial to reduce the amplifier noise as much as possible. So far, we have seen that fundamental quantum noise can be suppressed by operating the JPA either in the degenerate or in the broadband nondegenerate regime. However, especially for high-gain applications such as classical feedforward generation or preamplification for single-shot measurements, gain-dependent technical noise $n_J(G_s)$ becomes a main limitation for the quantum efficiency. There are

various models explaining the origin of this noise [85, 90, 107, 136]. Within the JPA theory introduced in Sec. 2.1.2, it is assumed that the gain-dependent JPA noise temperature is described by the amplified environmental noise coupling to the resonator due to finite internal quality factors [90]. However, this theory predicts that the resulting noise photon number is a monotonically decreasing function of G_s, which is not observed in experiments. This discrepancy implies that in our case, $n_J(G_s)$ is dominated by alternative noise sources, such as flux noise in the SQUID [137], pump-induced noise or higher-order nonlinearities [107]. We can attempt to lower $n_J(G_s)$ by connecting N JPAs in series and compare to a case with a single JPA, as depicted in Fig. 2.7 [138, 139]. We assume g_i to be the gain of the ith amplifier, and demand $g_1 g_2 \cdots g_N = G_s$. The effective input noise added by the whole JPA chain is denoted as $n_N(G_s)$. A gain partition $\{g_i\}$ then reduces the overall noise if we satisfy the inequality

$$G_s \cdot n_N(G_s) = \sum_{i=1}^{N} n_J(g_i) \prod_{j=i}^{N} g_j \leq G_s \cdot n_J(G_s), \tag{2.66}$$

which is obtained from the Friis equation [93, 140, 141]. Since the exact functional shape of $n_J(G_s)$ is not yet specified, we distribute the gain equally over all amplifiers. Equation (2.66) then becomes a geometric sum and we find the closed expression

$$\frac{G_s - 1}{G_s - G_s^{(N-1)/N}} \leq \frac{n_J(G_s)}{n_J(\sqrt[N]{G_s})}. \tag{2.67}$$

Next, while still not assuming any specific functionality of $n_J(G_s)$, we make three physically legit assumptions which are compatible with experimental findings:

1. In case the amplifier is switched off, $G_s = 1$, we do not add any noise, $n_J(1) = 0$.

2. $n_J(G_s)$ increases monotonically with the gain G_s.

3. $n_J(G_s) \to \infty$ for $G_s \to \infty$.

In addition, we focus on the case $N = 2$, since chaining $N > 2$ amplifiers can be deduced inductively from this case. To keep equations simple, we define $x \equiv \sqrt{G_s}$ and $n_J(G_s) \equiv f(x^2)$. Thus, resulting from Eq. (2.67), we gain an SNR advantage by chaining if we fulfill the inequality

$$f(x) \leq \frac{x}{x+1} f(x^2). \tag{2.68}$$

We then obtain the following general statements:

Statement 1. *For sufficiently large gain, there are always regions where chaining is advantageous*

Proof. We assume that this statement is wrong, i.e., there is $\xi > 0$ such that chaining is

(a)

(b)
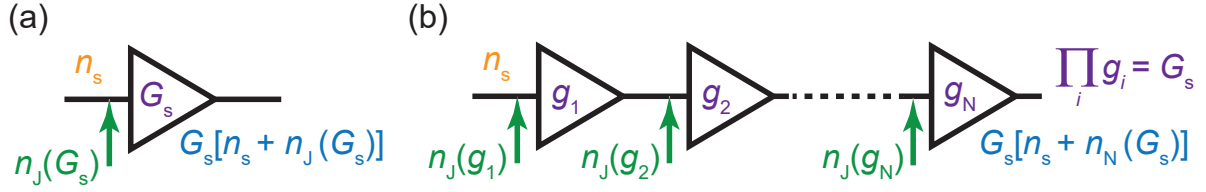
Figure 2.7: (a) Noise model for a single JPA. The gain-dependent noise $n_{\mathrm{J}}(G_{\mathrm{s}})$ is added at the amplifier input and amplified with gain G_{s} along with the input signal photons n_{s} (b) Scheme for N serially connected JPAs with the gain distribution $\{g_i\}$. The ith JPA adds $n_{\mathrm{J}}(g_i)$ noise photons at the input, which are amplified by the following JPAs. Chaining provides an advantage if the effective noise $n_{\mathrm{N}}(G_{\mathrm{s}})$, referred to the input of the fist amplifier, is lower than $n_{\mathrm{J}}(G_{\mathrm{s}})$.

not advantageous for all $x > \xi$. Since f is monotonically increasing, we find for $x > \xi$ that

$$\frac{x}{x+1} \leq \frac{f(x)}{f(x^2)} \leq 1. \tag{2.69}$$

Induction then yields that we have $f(x) \to f(x^2) \to \cdots \to f(x^{2n})$ $\forall n \in \mathbb{N}$ in the limit $x \to \infty$, according to the squeeze theorem. As a result, the sequence $(a)_n \equiv f(x^{2n})$ is a real Cauchy sequence, implying convergence, $\lim_{x \to \infty} f(x) \in \mathbb{R}$ [142], which is a contradiction to the third assumption, stating $f(x) \to \infty$. □

Statement 2. *If $f(x)$ is convex, we always achieve an advantage by chaining*

Proof. Since f is convex, we have

$$f(\lambda x_1 + (1 - \lambda)x_2) \leq \lambda f(x_1) + (1 - \lambda)f(x_2) \tag{2.70}$$

for any x_1, x_2 and $0 \leq \lambda \leq 1$. We set $x_1 = x^2$, $x_2 = 1$ and $\lambda = 1/(1 + x)$ and obtain

$$f(x) \leq \frac{1}{x+1}f(x^2) + \underbrace{\frac{1}{x+1}f(1)}_{=0} \leq \frac{x}{x+1}f(x^2). \tag{2.71}$$

□

Statement 3. *There exists a region where chaining is not advantageous if $f''(1) + 2f'(1) < 0$, where f' (f'') denotes the first (second) order derivative of f.*

Proof. We rewrite Eq. (2.68) by defining the auxiliary function

$$F(x) = \frac{x}{x+1}f(x^2) - f(x). \tag{2.72}$$

Regions with a disadvantage are then characterized by $F(x) < 0$. Furthermore, we always have $F(1) = 0$. From statement 1, we know that we can always find sufficiently large x

such that $F(x) > 0$. As a result, there is a gain region where chaining is not advantageous if F has an additional zero $x_* > 1$. In this case, we have a disadvantage for $x < x_*$ and an advantage for $x > x_*$ in vicinity of x_*. From direct calculation, we obtain that $F'(1) = 0$, i.e., $F(x)$ takes an extremum or a saddle point at $x = 1$. Thus, a region with $F(x) < 0$ exists if F has a local maximum at $x = 1$, yielding the condition of negative curvature,

$$F''(1) < 0. \tag{2.73}$$

A straightforward calculation gives

$$\begin{aligned} F''(x) = {} & \frac{-2f(x^2)}{(x+1)^3} + \frac{2x}{(x+1)^2}f'(x^2) \\ & + \frac{2x^2 - 1}{(x+1)^2}f'(x^2) + \frac{4x^3}{x+1}f''(x^2) - f''(x), \end{aligned} \tag{2.74}$$

which directly implies

$$F''(1) = 2f'(1) + f''(1) < 0. \tag{2.75}$$

$\square$

The previous statement 3 gives us a direct tool for evaluating whether a given noise function provides a disadvantage for chaining or not. However, for many concave functions f, the first and second derivative diverges at $x = 1$. This is the case for concave power law functions such as $\sqrt{x}$ or, in general, for functions $f(x) = k(x)^\epsilon$ with $0 < \epsilon < 1$ and concave $k(x)$. In this case, we need to take

$$\lim_{x \to >1} (2f'(x) + f''(x)) \tag{2.76}$$

and investigate under which conditions this limit approaches $-\infty$ or $+\infty$. As an example, if we take logaritmic behavior, $f(x) = \ln x$, we have $2f'(1) + f''(1) = 1 > 0$. Thus, we always obtain an advantage. For a power law, $f(x) = (x-1)^\epsilon$, we obtain

$$\lim_{x \to >1} [2f'(x) + f''(x)] = \lim_{x \to >1} \underbrace{\epsilon(x-1)^{\epsilon-2}}_{>0} \cdot \underbrace{(2\epsilon x - 1 - \epsilon)}_{\to \epsilon - 1}, \tag{2.77}$$

which is always negative for concave power laws. As a result, for such a power law dependence, there is always a region for low gains for which chaining increases the noise. In fact, it turns out that from an empirical point of view, a power law

$$n_{\mathrm{J}}(G_{\mathrm{s}}) = \chi_1 (G_{\mathrm{s}} - 1)^{\chi_2} \tag{2.78}$$

describes the JPA noise with reasonable accuracy in the limit $G_{\mathrm{s}} \gg 1$ [78, 85]. In Sec. 4.1.1, we show how pump-induced noise can result in such a dependence. For weak concave dependence, $\chi_2 \ll 1$, the threshold gain G_{t} beyond which we reach an advantage by
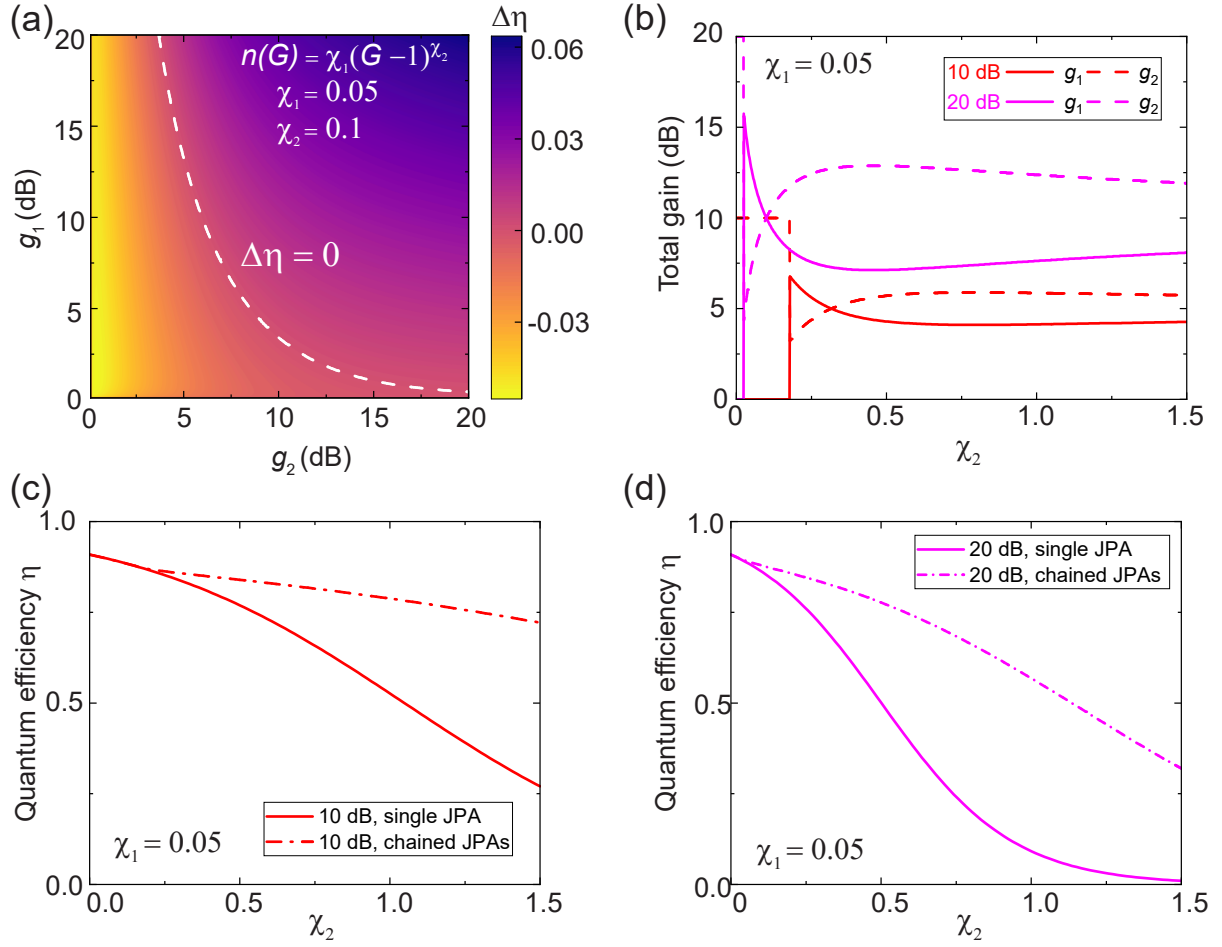
Figure 2.8: (a) Theoretically predicted difference $\Delta\eta$ in quantum efficiency between the scenario of two chained JPAs with respective gains g_1 and g_2 and single JPA amplification with $G_s = g_1 g_2$. The noise is assumed to follow the power law dependence Eq. (2.78) with $\chi_1 = 0.05$ and $\chi_2 = 0.1$. The white contour line corresponds to the threshold beyond which chaining provides an advantage. (b) Optimal gain distribution for a total gain of 10 dB (red) and 20 dB (magenta) to maximize quantum efficiency for two chained amplifiers as a function of χ_2 for fixed $\chi_1 = 0.05$. We find that chaining is only beneficial if χ_2 exceeds a certain threshold. (c) Quantum efficiency for a total gain of 10 dB as a function of χ_2, corresponding to the optimal gain distribution in (b). (d) Optimal quantum efficiency for a total gain of 20 dB.

chaining can be approximated by

$$G_t \simeq \frac{1}{\chi_2^2 W(1/\chi_2)^2}, \tag{2.79}$$

where $W(z)$ denotes the product logarithm function.

Optimal gain distribution   The previously assumed equal gain distribution might not be the optimal choice for reducing the total noise of the amplification chain. This is a direct result from the Friis equation, which states that the gain-dependent noise at a certain amplifier stage is amplified by all the following amplifiers. [141]. As long as $n_\mathrm{J}(G_\mathrm{s})$ is monotonic, the optimal gain partition can be found by reformulating Eq. (2.66) as a constrained convex minimization problem [143]. For the case of two amplifiers, the corresponding Lagrangian is given by

$$\mathcal{L}(g_1, g_2, \lambda) = g_1 g_2 n_1(g_1) + g_2 n_2(g_2) + \lambda(g_1 g_2 - G_\mathrm{s}), \tag{2.80}$$

where λ is introduced as a Lagrangian multiplier. We then search the minimum

$$\nabla \mathcal{L}(g_1, g_2, \lambda) = 0. \tag{2.81}$$

We now make the model assumption that both JPAs are equal and that the noise obeys linear gain-dependence $n_1(g) = n_2(g) = n'g$, where n' is a constant.[2] Equation (2.81) provides

$$\frac{g_2}{2} + 2n' g_2 g_1 + \lambda g_2 = 0, \tag{2.82}$$

$$\frac{g_1}{2} + n' g_1^2 + 2n' g_2 + \lambda g_1 = 0, \tag{2.83}$$

$$g_1 g_2 - G_\mathrm{s} = 0. \tag{2.84}$$

The same system of equations is obtained for the narrowband nondegenerate regime in case we additionally take the idler noise into account,

$$n_1(g) = n_2(g) = \frac{1}{2}\left(1 - \frac{1}{g}\right) + n'g. \tag{2.85}$$

A straightforward calculation gives the solution

$$g_1 = \sqrt[3]{2} G_\mathrm{s}^{\frac{1}{3}}, \qquad g_2 = \frac{1}{\sqrt[3]{2}} G_\mathrm{s}^{\frac{2}{3}}. \tag{2.86}$$

For the total input noise, we find $n_*(g_1, g_2) = 3\sqrt[3]{2} n' G_\mathrm{s}^{\frac{1}{3}}/2$. The relative improvement, compared to the single JPA case (n_single) and equal gain distribution (n_eq), is given by

$$\frac{n_*(g_1, g_2)}{n_\mathrm{single}} = \frac{3\sqrt[3]{2}}{2 G_\mathrm{s}^{\frac{2}{3}}}, \qquad\qquad \frac{n_*(g_1, g_2)}{n_\mathrm{eq}} = \frac{3\sqrt[3]{2}}{2}\frac{1}{\sqrt[6]{G_\mathrm{s}}}. \tag{2.87}$$

---

[2]We note that even with these rough assumptions, the data corresponding to complex experiments can be accurately fitted [66].

We observe that knowledge of the exact gain scaling and choosing the correct gain distribution can drastically improve the performance. As an example, compared to the equal distribution, we obtain a relative improvement of $58\,\%$ for $G_\mathrm{s} = 100\,\mathrm{dB}$ if we use Eq. (2.86). With decent effort, we can also find an analytical solution for the general case of N amplifiers under the approximation of linear noise. Since the corresponding analysis is rather technical, we provide the full solution in Appendix C. We note that, despite the simple assumptions, the result Eq. (2.86) is already nontrivial.

Next, we analyze the more realistic gain-dependent noise function Eq. (2.78) with realistic parameters $\chi_1 = 0.05$ and $\chi_2 = 0.1$. In Fig. 2.8(a) we plot the difference $\Delta\eta$ between the quantum efficiency $\eta_\mathrm{chain}(g_1, g_2)$ in the chained case with gain distribution g_1 and g_2 and $\eta_\mathrm{single}(G_\mathrm{s})$, corresponding to the quantum efficiency of a single JPA with gain $G_\mathrm{s} = g_1 g_2$. We observe that, for low gains, chaining provides a disadvantage, as predicted by statement 3. In addition, we find that the threshold defined by $\Delta\eta = 0$ is asymmetric with respect to g_1 and g_2. In most of the cases, choosing $g_2 > g_1$ leads to a higher quantum efficiency. As discussed previously, this observation can be explained by the structure of the Friis equation. In Fig. 2.8(b)-(d), we plot the optimal gain distribution between both amplifiers to achieve a total gain $G_\mathrm{s} = 10\,\mathrm{dB}$ (red) and $G_\mathrm{s} = 20\,\mathrm{dB}$ (magenta) as a function of χ_2. The corresponding gain values have been determined numerically by a brute-force comparison of the single JPA case with the chained JPA scenario for all possible gain distributions. We observe that, for concave noise ($\chi_2 < 1$), there is always a region where chaining decreases the quantum efficiency, in accordance with statement 3. Furthermore, we find that, in a small region of χ_2, choosing $g_1 > g_2$ is advantageous.

2.2 Continuous-variable quantum information processing

So far, we have introduced the JPA as a device which enables us to realize either phase-dependent or phase-independent amplification for arbitrary input fields $\hat{a}$. In Sec. 2.2.1, we investigate the quantum statistical description of these steady-state fields in terms of phase space quasiprobability distributions. In Sec. 2.2.2, we focus on the practically relevant case where this distribution is Gaussian and we introduce fundamental classes of single-mode Gaussian states. Following that, we introduce the two-mode squeezed (TMS) state as a Gaussian state which gives rise to bipartite nonlocal quantum correlations. We discuss two categories of such CV quantum correlations, entanglement and quantum discord, in Sec. 2.2.3. Following that, we introduce fundamental Gaussian channels, implementing transitions between different Gaussian states, in Sec. 2.2.4. We can concatenate multiple Gaussian channels to form quantum communication protocols. In Sec. 2.2.5, we discuss CV quantum teleportation as a particular example. To evaluate the performance of such a Gaussian quantum communication protocol, we introduce the Uhlmann-fidelity and certain fidelity thresholds in Sec. 2.2.6.

2.2.1 Phase space representation of quantized electromagnetic fields

Complete quantum mechanical description of an arbitrary quantum system is provided by the density operator $\hat{\rho}$, which enables to determine the expectation value of any observable $\hat{O}$, according to the Born rule $\langle \hat{O} \rangle = \mathrm{Tr}(\hat{\rho}\hat{O})$ [2]. In case we select one mode of our propagating electromagnetic field, described by signal operators $\hat{a}$ and $\hat{a}^\dagger$, the observables correspond to the orthogonal field quadratures [48]

$$\hat{q}_\theta = \frac{\hat{a}e^{-i\theta} + \hat{a}^\dagger e^{i\theta}}{2}, \qquad \hat{p}_\theta = \frac{\hat{a}e^{-i\theta} - \hat{a}^\dagger e^{i\theta}}{2i}. \tag{2.88}$$

As discussed in Sec. 2.1.2, the phase reference θ is determined by the JPA pump and conventionally set to zero, $\hat{q} \equiv \hat{q}_0$, $\hat{p} \equiv \hat{p}_0$. In analogy to quantized flux and charge in a superconducting circuit, the quadrature operators do not commute due to the bosonic commutation relation satisfied by $\hat{a}$ and $\hat{a}^\dagger$. Consequently, the field quadratures satisfy the Heisenberg uncertainty relation [47, 144]

$$(\Delta q)^2 (\Delta p)^2 \equiv \left(\langle \hat{q}^2 \rangle - \langle \hat{q} \rangle^2 \right) \left(\langle \hat{p}^2 \rangle - \langle \hat{p} \rangle^2 \right) \geq \frac{1}{4} \left| \left\langle \, [\hat{q}, \hat{p}] \, \right\rangle \right|^2 = \frac{1}{16}. \tag{2.89}$$

In case of an ℓ-mode state, each mode satisfies such a respective uncertainty relation. Complete information about the corresponding propagating quantum state can be obtained by determining the statistical quadrature moments $\langle \hat{q}_1^{m_1} \cdots \hat{q}_\ell^{m_\ell} \hat{p}_1^{n_1} \cdots \hat{p}_\ell^{n_\ell} \rangle$, $m_j, n_k \in \mathbb{N}_0$. However, due to the continuous energy spectrum emerging from the absence of boundary conditions a direct calculation of moments via $\hat{\rho}$ is cumbersome since the corresponding Hilbert space is of infinite dimension [145]. Instead, we determine the signal moments

by introducing a phase space quasiprobability distribution function $W(q_1, ..., q_\ell, p_1, ..., p_\ell)$ [48, 146]. We can then employ the Weyl correspondence principle to determine the symmetrized quadrature moments [47, 147],

$$
\begin{aligned}
\operatorname{Tr}\left[\hat{\rho}\mathcal{S}(\hat{q}_1^{m_1}\cdots\hat{q}_\ell^{m_\ell}\hat{p}_1^{n_1}\cdots\hat{p}_\ell^{n_\ell})\right] &= \int W(q_1, p_1, \cdots, q_\ell, p_\ell) \prod_{j,k=1}^{\ell} q_j^{m_j} p_k^{n_k} dq_j dp_k \\
&= \langle q_1^{m_1} p_1^{n_1} \cdots q_\ell^{m_\ell} p_\ell^{n_\ell}\rangle,
\end{aligned} \tag{2.90}
$$

where $\mathcal{S}(\cdots)$ denotes the symmetrization operator [148]. Weyl correspondence enables to calculate the quadrature moments as known from classical statistics. The quasiprobability distribution $W(q_1, p_1, \cdots, q_\ell, p_\ell)$ is conventionally known as Wigner function [149]. The prefix "quasi" emerges from the fact that the distribution can become negative, in contrast to conventional probability distributions [150]. For general CV quantum states, the Wigner function can be determined from the density operator via Fourier transform of the characteristic function [151]. The marginal phase space distribution with respect to a certain set of m field quadratures can be obtained by integrating $W(q_1, p_1, \cdots, q_\ell, p_\ell)$ with respect to the remaining $2\ell - m$ quadratures [47]. In experiment, detecting all marginal single-quadrature distributions then enables us to reconstruct the complete quantum state via the Radon transform [152]. Aside from the Wigner function, there are alternative phase space distributions such as the Husimi Q-function [153] or the Glauber-Sudarshan P-function [154, 155].

For a multi-mode state, it is useful to introduce the notation $\hat{\mathbf{R}} \equiv (\hat{q}_1, \hat{p}_1, \cdots, \hat{q}_\ell, \hat{p}_\ell)^{\mathrm{T}}$. We can then write the corresponding commutation relations as [47]

$$
[\hat{R}_j, \hat{R}_k] = \frac{i}{2}\Lambda_{jk}, \qquad \mathbf{\Lambda} = -i\bigoplus_{n=1}^{\ell}\sigma_y, \tag{2.91}
$$

where σ_y denotes the Pauli $y-$matrix. In addition, we define the displacement vector $\mathbf{d}$ and the covariance matrix $\boldsymbol{V}$, according to

$$
d_j \equiv \langle\hat{R}_j\rangle, \qquad V_{jk} \equiv \frac{1}{2}\langle\{\hat{R}_j, \hat{R}_k\}\rangle - \langle\hat{R}_j\rangle\langle\hat{R}_k\rangle. \tag{2.92}
$$

The displacement vector corresponds to the average electromagnetic field amplitude of the propagating state. The diagonal elements of the covariance matrix measure local variance and therefore uncertainty for the respective mode. Off-diagonal elements describe non-local covariances and thus correlations between different modes. The physicality criterion for an ℓ-mode state can be expressed as the positive-definiteness condition [156]

$$
\boldsymbol{V} - \frac{i}{4}\mathbf{\Lambda} \geq 0. \tag{2.93}
$$

We note that from the quadrature moments, we can furthermore determine the statistical
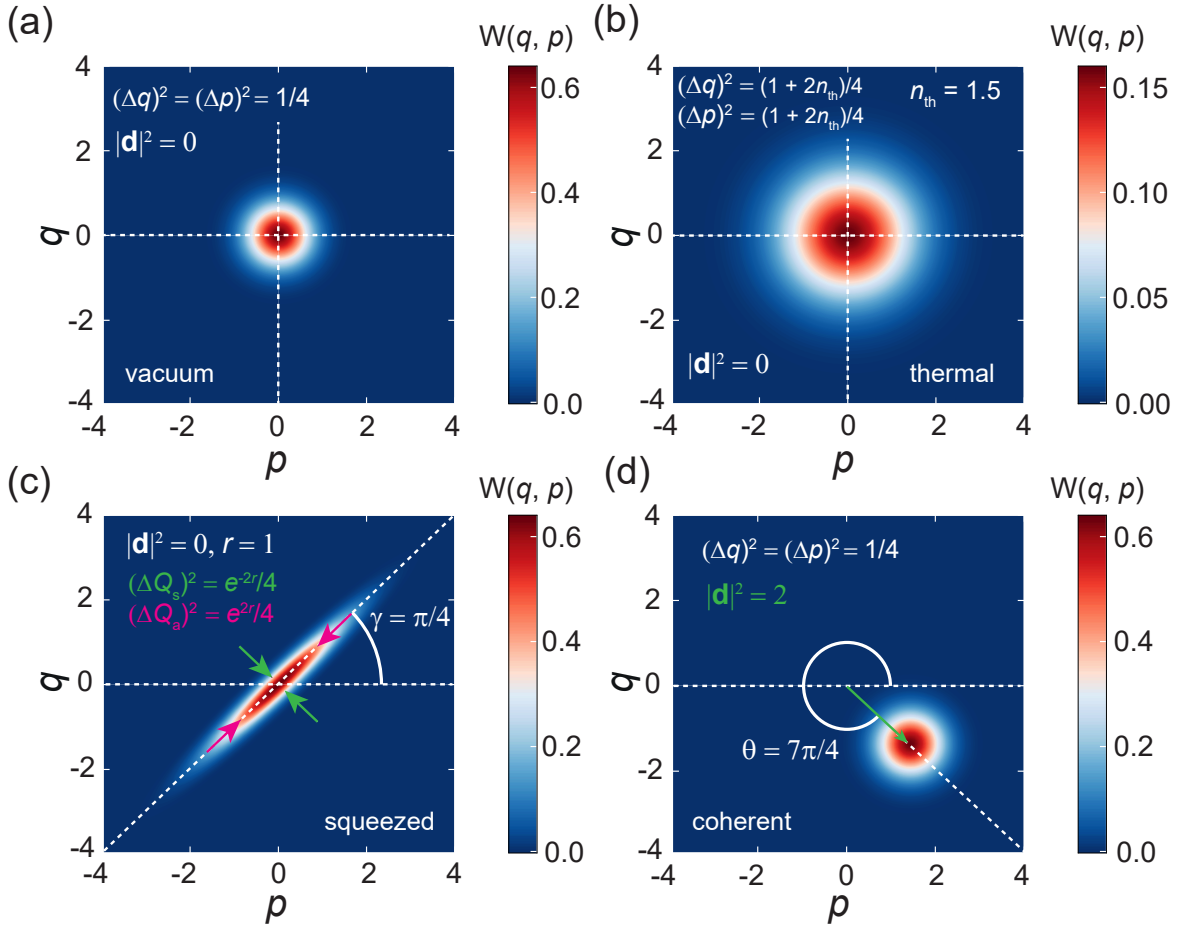
Figure 2.9: Wigner function of (a), the vacuum state, (b), a thermal state containing $n_{\text{th}} = 1.5$ photons, (c), a squeezed state with squeeze factor $r = 1$ and squeezing angle $\gamma = \pi/4$ and (d), a coherent state with displacement angle $\theta = 7\pi/4$ and 2 displacement photons.

signal moments $\langle \hat{a}_1^{m_1} \cdots \hat{a}_\ell^{m_\ell} (\hat{a}_1^\dagger)^{n_1} \cdots (\hat{a}_\ell^\dagger)^{n_\ell} \rangle$, $m_j, n_k \in \mathbb{N}_0$ via the binomial theorem [157, 158].

2.2.2 Gaussian states of light

In the following, we focus on quantum states described by a Gaussian phase space distribution [159]. These Gaussian states are fully determined by their displacement vector $\mathbf{d}$ and covariance matrix $\boldsymbol{V}$, and, therefore, by moments up to second order. By defining the vector $\mathbf{R} \equiv (q_1, p_1, \cdots, q_\ell, p_\ell)^{\text{T}}$ the Wigner function of an ℓ-mode Gaussian state can be generally expressed as

$$W(\mathbf{R}) = \frac{1}{(2\pi)^\ell \sqrt{\det \boldsymbol{V}}} \exp\left[-\frac{1}{2} (\mathbf{R} - \mathbf{d}) \, \boldsymbol{V}^{-1} (\mathbf{R} - \mathbf{R})^{\text{T}} \right]. \tag{2.94}$$

Equation (2.94) enables direct calculation of purity [160]

$$\mu = \text{Tr}\hat{\rho}^2 = \pi^\ell \int [W(\mathbf{R})]^2 \, d^{2\ell}\mathbf{R} = \frac{1}{4^\ell \sqrt{\det \boldsymbol{V}}}. \tag{2.95}$$

Pure CV states satisfy $\mu = 1$ and correspond to states with minimal uncertainty, according to Eq. (2.93). Mixed states show purities $0 \leq \mu < 1$, where $\mu = 0$ corresponds to maximally mixed states.[3] Furthermore, for any Gaussian state, we can determine the quadrature moments via the moment generating function [161]

$$M(\boldsymbol{\xi}) = \exp\left[\mathbf{d}^\text{T}\boldsymbol{\xi} + \frac{1}{2}\boldsymbol{\xi}^\text{T}\boldsymbol{V}\boldsymbol{\xi}\right]. \tag{2.96}$$

We then have

$$\langle q_1^{n_1} p_1^{n_2} \cdots q_\ell^{n_{2\ell-1}} p_\ell^{n_{2\ell}}\rangle = \frac{\partial^{n_1}}{\partial \xi_1^{n_1}} \cdots \frac{\partial^{n_{2\ell}}}{\partial \xi_{2\ell}^{n_{2\ell}}} M(\boldsymbol{\xi})\Big|_{\boldsymbol{\xi}=\mathbf{0}}. \tag{2.97}$$

The partial derivatives can be successively evaluated by using the relation [162]

$$\frac{\partial^n}{\partial x^n} \exp\left[\frac{(x-x_0)^2}{2\sigma^2}\right] = \exp\left[\frac{(x-x_0)^2}{2\sigma^2}\right] \left[\sum_{k=0}^n \binom{n}{k} B_{(2n+k)\frac{1-(-1)^k}{2}} \frac{2^{\frac{k}{2}}\Gamma\left(\frac{k+1}{2}\right)}{\sigma^n \Gamma\left(\frac{1}{2}\right)} \left(\frac{x-x_0}{\sigma}\right)^{n-k}\right], \tag{2.98}$$

where B_j denote the Bernoulli numbers and $\Gamma(x)$ is the gamma function [163]. Alternatively, arbitrary moments of Gaussian states can be determined using Wick's theorem [164]. Next, we respectively introduce vacuum, thermal, coherent and squeezed states as the four fundamental single-mode Gaussian states [48]. To distinguish between the photon statistics of these different states, we employ the $g^{(2)}$-correlation function, which can be expressed as [165]

$$g^{(2)}(0) = \frac{\langle(\hat{a}^\dagger)^2\hat{a}^2\rangle}{\langle\hat{a}^\dagger\hat{a}\rangle^2}. \tag{2.99}$$

From a practical point of view, this quantity is particularly useful to distinguish among different types of statistics since it is solely determined by the relationship between fourth and second order moments and does not require any photon number calibration.

Vacuum and thermal states   The vacuum state $|0\rangle$ corresponds to the state with minimal energy which satisfies the bosonic commutation relations [166]. Consequently, it contains half a quantum of noise, which symmetrically splits between both signal quadratures due to the absence of phase coherence, manifesting in variances $(\Delta q)^2 = (\Delta p)^2 = 1/4$. The corresponding Wigner function is plotted in Fig. 2.9(a). A thermal state is characterized by its equilibrium photon number distribution at temperature $T > 0$ [167]. The corresponding

---

[3]This is in strong contrast to qubits, where maximally mixed states have purity $\mu = 1/2$ [15]. The difference results from the fact that for a statistical mixture between j eigenstates in a Hilbert space $\mathcal{H}$ with classical probability p_j, the state is maximally mixed if $p_j = 1/\dim \mathcal{H}$.

density operators can be determined from the canonical partition sum [168], according to

$$\hat{\rho}_{\text{th}} = \sum_n \frac{n_{\text{th}}^n}{(1 + n_{\text{th}})^{n+1}} |n\rangle\langle n|, \qquad n_{\text{th}} = \langle \hat{a}^\dagger \hat{a} \rangle = \frac{1}{e^{\frac{\hbar\omega}{k_{\text{B}}T}} - 1}, \qquad (2.100)$$

where the thermal photon number n_{th} is determined by the Planck distribution and $k_{\text{B}} = 1.38 \times 10^{-23}\,\text{J}\,\text{K}^{-1}$ denotes the Boltzmann constant. A thermal state has zero displacement, $\mathbf{d} = \mathbf{0}$, and a diagonal covariance matrix with variances

$$(\Delta q)^2 = (\Delta p)^2 = \frac{1 + 2n_{\text{th}}}{4}. \qquad (2.101)$$

At absolute zero, a thermal state corresponds to vacuum and, in the limit $n_{\text{th}} \gg 1$, the state is maximally mixed with ensemble probability $1/n_{\text{th}}$, according to Eq. (2.100). The normally ordered signal moments of a thermal state can be expressed as

$$\langle (\hat{a}^\dagger)^m \hat{a}^n \rangle = n! n_{\text{th}}^n \delta_{nm}, \qquad (2.102)$$

implying that $g^{(2)}(0) = 2$ [47]. The quadrature moments satisfy

$$\langle q^m p^n \rangle = \frac{(m-1)!!(n-1)!!}{2^{m+n}} \frac{(1 + 2n_{\text{th}})^{\frac{m+n}{2}}}{4} \left[1 + (-1)^m + (-1)^n + (-1)^{m+n} \right]. \qquad (2.103)$$

In Fig. 2.9(b), we plot the Wigner function of a thermal state for $n_{\text{th}} = 1.5$.

Squeezed state Vacuum and thermal state have symmetric variances and a diagonal covariance matrix. However, as we have seen Sec. 2.1.2, we can implement a JPA for phase-sensitive amplification, which leads to an elliptical distortion of the Wigner function. As we have seen in Eq. (2.28), such a process leads to deamplification of one field quadrature. We create a squeezed state by suppressing the fluctuations in the attenuated quadrature below the vacuum limit [48]. It can be shown that for $\gamma = 0$, the JPA Hamiltonian, Eq. (2.11), implements a squeezing operation in the Dirac interaction picture,

$$\hat{S}(\xi) = \exp\left[\frac{1}{2}\xi^* \hat{a}^2 - \frac{1}{2}\xi \left(\hat{a}^\dagger\right)^2 \right], \qquad (2.104)$$

where $\xi = re^{i\varphi}$. The quanity r thereby denotes the squeeze factor, defined in the scope of Eq. (2.28), and φ corresponds to the phase, relative to the phase reference (pump) [112]. The squeezing operator, Eq. (2.104), implements the Bogoliubov transformation

$$\hat{S}^\dagger(\xi)\hat{a}\hat{S}(\xi) = \hat{a}\cosh r - \hat{a}^\dagger e^{i\varphi}\sinh r, \qquad (2.105)$$

which corresponds to the transformation between signal and idler fields introduced in Sec. 2.1.2. In case we apply $\hat{S}(\xi)$ to vacuum, we find [48]

$$|\xi\rangle = \hat{S}(\xi)|0\rangle = \sum_n (-1)^n \frac{\sqrt{(2n)!}}{2^n n!} \frac{(e^{i\varphi}\tanh r)^n}{\sqrt{\cosh r}} |2n\rangle, \tag{2.106}$$

implying that the ideal squeezed state contains only even photon numbers due to a pairwise emergence of signal and idler photons. However, a practically generated squeezed state also contains odd photon numbers due to impurities in the initial state. The squeezing operator keeps the displacement at $\mathbf{d} = \mathbf{0}$ and transforms the covariance matrix, yielding

$$\boldsymbol{V}_{\rm sq} = \frac{1}{4}\begin{pmatrix} e^{-2r}\cos^2\frac{\varphi}{2} + e^{2r}\sin^2\frac{\varphi}{2} & -\sinh 2r\sin\varphi \\ -\sinh 2r\sin\varphi & e^{2r}\cos^2\frac{\varphi}{2} + e^{-2r}\sin^2\frac{\varphi}{2} \end{pmatrix}. \tag{2.107}$$

It is convenient to describe the squeezing direction via the squeezing angle $\gamma = -\varphi/2$, where factor of $1/2$ is a result from the 2-fold rotational symmetry of the Wigner function. We observe that one quadrature, $Q_{\rm s}$, is squeezed with variance $(\Delta Q_{\rm s})^2 = e^{-2r}/4$ and the orthogonal quadrature $Q_{\rm a}$ is antisqueezed with variance $(\Delta Q_{\rm a})^2 = e^{2r}/4$. We define the squeezing level S of a squeezed vacuum state by comparing $(\Delta Q_{\rm s})^2$ to vacuum variance of $1/4$ [75],

$$S = -10\log_{10}\left[\frac{(\Delta Q_{\rm s})^2}{0.25}\right] = 10\log_{10}\left[\frac{(\Delta Q_{\rm a})^2}{0.25}\right] = 20r\log_{10}e \simeq 8.69r. \tag{2.108}$$

The squeezed variance for the JPA resonator field is limited by $(\Delta Q_{\rm s}^{\rm (r)})^2 \geq 1/8$, restricting the intra-resonator squeezing level $S_{\rm r}$ to $S_{\rm r} \lesssim 3\,{\rm dB}$ [169]. For the output field, we have $(\Delta Q_{\rm s})^2 \to 2\epsilon_{\rm c}(\Delta Q_{\rm s}^{\rm (r)})^2$, implying that there is no fundamental limit for the maximally achievable squeezing for the squeezing level, apart from the resonator bandwidth. Furthermore, the moments with respect to the squeezed (antisqueezed) quadrature $Q_{\rm s}$ ($Q_{\rm a}$) can be expressed as

$$\langle Q_{\rm s}^m Q_{\rm a}^n \rangle = \frac{(m-1)!!(n-1)!!}{2\sqrt{2}^{m+n}} e^{r(m-n)} \left[1 + (-1)^m + (-1)^n + (-1)^{m+n}\right]. \tag{2.109}$$

In Fig. 2.9(c), we plot the Wigner function for a squeezed state for $r = 1$ and $\gamma = \pi/4$.

Coherent state   To introduce coherent states, we map the phase space to a complex plane and introduce the complex displacement $\alpha = d_p + id_q$ from the displacement vector $\mathbf{d} = (d_p, d_q)^{\rm T}$. We can then generate a coherent state via [154]

$$|\alpha\rangle = \hat{D}(\alpha)|0\rangle = e^{-\frac{|\alpha|^2}{2}} \sum_n \frac{\alpha^n}{\sqrt{n!}}|n\rangle, \tag{2.110}$$
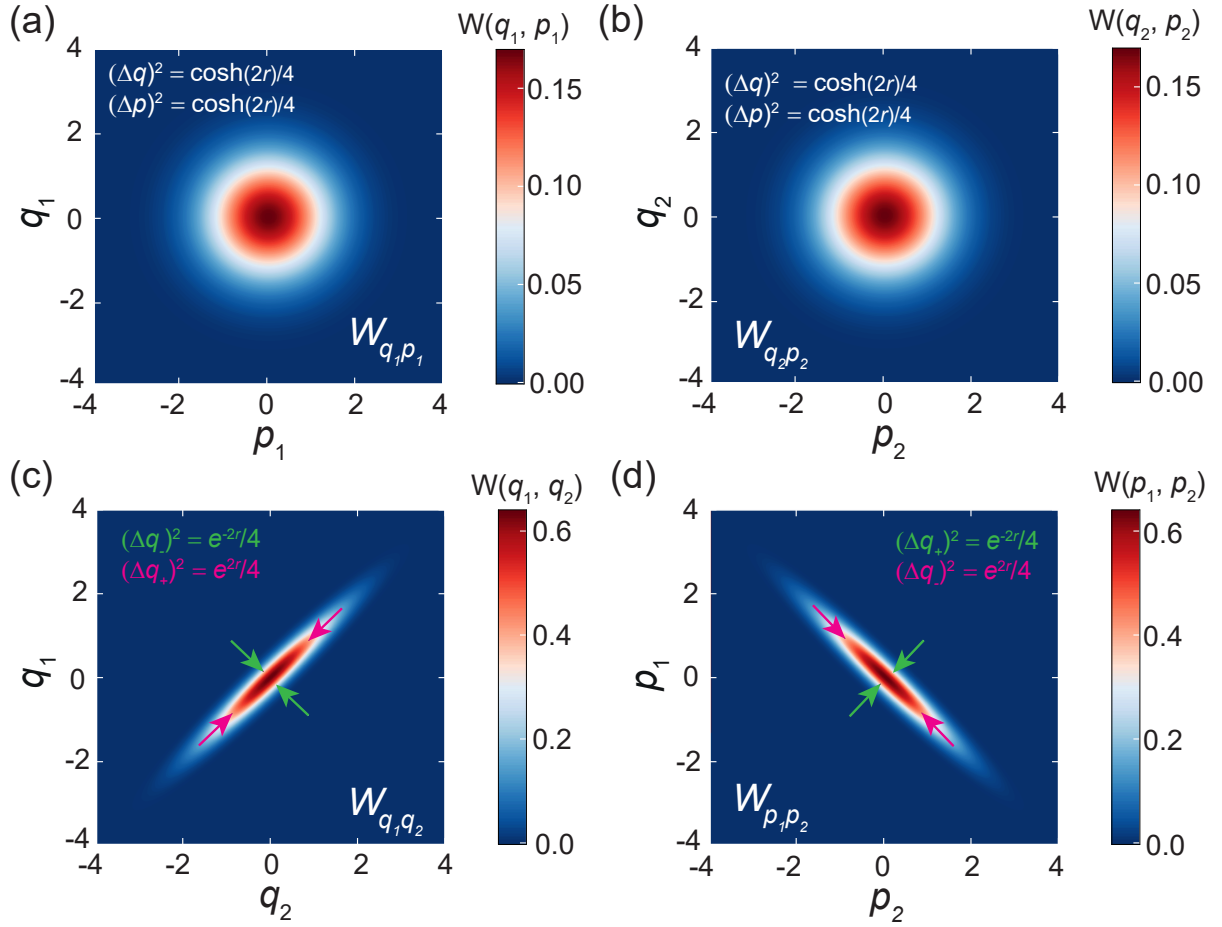
Figure 2.10: Wigner function for the TMS state for $r = 1$, $\varphi = 0$. Panels (a) and (b) correspond to the marginal distributions for the local modes, which resemble thermal noise with photon number $n_{\mathrm{th}} = \sinh^2 r$. Panels (c) and (d) show the respective marginal distributions, corresponding to nonlocal quadratures. We observe that nonlocal q (p)-quadratures are correlated (anticorrelated).

where $\hat{D}(\alpha) = \exp\left(\alpha\hat{a}^\dagger - \alpha^*\hat{a}\right)$ denotes the displacement operator [170]. The displacement operator changes the expectation value of the quasiprobability distribution to $\mathbf{d}$ and keeps the covariance matrix unaffected, $\hat{D}^\dagger(\alpha)\hat{a}\hat{D}(\alpha) = \hat{a} + \alpha$. Consequently, $|\alpha\rangle$ is a pure state with minimal uncertainty and photon number $n_{\mathrm{coh}} = |\alpha|^2 = |\mathbf{d}|^2$. A coherent state can be regarded as a quantum mechanical analogue of a classical sinusoidal signal with in-phase contribution d_p and orthogonal component d_q. Simultaneously, the coherent state is an eigenstate of the annihilation operator $\hat{a}$ [48]. It is convenient to write $\mathbf{d} = |\alpha|^2(\cos\theta, \sin\theta)^{\mathrm{T}}$, where θ denotes the displacement angle. As can be seen from Eq. (2.110), coherent states satisfy Poissonian photon statistics, implying $g^{(2)}(0) = 1$ [171]. The quadrature moments can be calculated by

$$\langle q^m p^n \rangle = \frac{2}{\pi} \left[M_m(|\alpha|\cos\theta) + \tilde{M}_m(|\alpha|\cos\theta) \right] \left[M_n(|\alpha|\sin\theta) + \tilde{M}_n(|\alpha|\sin\theta) \right], \quad (2.111)$$

where

$$M_j(x) = \frac{2^{-\frac{j}{2}}}{4}x[1-(-1)^j]\Gamma\left(1+\frac{j}{2}\right){}_1F_1\left(\frac{1-j}{2};\frac{3}{2};-2x^2\right),\qquad(2.112)$$

$$\tilde{M}_j(x) = \frac{2^{-\frac{j}{2}}}{2\sqrt{2}}[1+(-1)^j]\Gamma\left(\frac{j+1}{2}\right){}_1F_1\left(-\frac{j}{2};\frac{1}{2};-2x^2\right),\qquad(2.113)$$

with the confluent hypergeometric function ${}_1F_1(a;b;x)$ [163]. The Wigner function for a coherent state with two displacement photons and displacement angle $\theta = 7\pi/4$ is shown in Fig. 2.9(d).

Two-mode squeezed state   In the following, we introduce the TMS state as the CV analogue to qubit Bell states [15, 172]. We generate a TMS state between modes $\hat{a}_1$ and $\hat{a}_2$ by applying the TMS operator $\hat{S}_{\mathrm{TMS}} = \exp\left[\xi^*\hat{a}_1\hat{a}_2 - \xi\hat{a}_1^\dagger\hat{a}_2^\dagger\right]$ with $\xi = re^{i\varphi}$, to two-mode vacuum [47],

$$|\mathrm{TMS}\rangle = \hat{S}_{\mathrm{TMS}}|0\rangle_1|0\rangle_2 = \frac{1}{\cosh r}\sum_{n=0}^{\infty}\left(e^{-i\varphi}\tanh r\right)^n|n\rangle_1|n\rangle_2.\qquad(2.114)$$

The TMS state has purity $\mu = 1$ and can be described by the covariance matrix

$$\boldsymbol{V}_{\mathrm{TMS}} = \frac{1}{4}\begin{pmatrix} \cosh 2r\mathbb{1}_2 & \sinh 2r\,(\sigma_z\cos\varphi + \sigma_x\sin\varphi) \\ \sinh 2r\,(\sigma_z\cos\varphi + \sigma_x\sin\varphi) & \cosh 2r\mathbb{1}_2 \end{pmatrix},\qquad(2.115)$$

where $\mathbb{1}_2$ denotes the (2×2) unity matrix and σ_z (σ_x) denotes the Pauli-z (x) matrix [15]. The global phase φ is normally set to zero since the TMS is conventionally used as the phase reference in our quantum communication experiments. After defining the nonlocal quadrature superpositions $q_\pm \equiv (q_1 \pm q_2)/\sqrt{2}$, $p_\pm \equiv (p_1 \pm p_2)/\sqrt{2}$, we can express the corresponding Wigner function as [48]

$$W_{\mathrm{TMS}}(q_+,p_+,q_-,p_-) = \frac{4}{\pi^2}\exp\left[-\frac{2(q_+^2+p_-^2)}{e^{2r}} - \frac{2(q_-^2+p_+^2)}{e^{-2r}}\right]$$

$$\xrightarrow{r\gg 1}\frac{4}{\pi e^{2r}}\exp\left[-\frac{2(q_+^2+p_-^2)}{e^{2r}}\right]\delta(q_-)\delta(p_+).\qquad(2.116)$$

Consequently, the TMS operator implements a respective squeezing operation for the nonlocal quadrature superpositions q_- and p_+. In the limit $r \to \infty$, the nonlocal q (p)-quadratures become perfectly correlated (anticorrelated) [84]. In contrast, the local states, described by Eq. (2.115), resemble thermal noise with photon number $n_{\mathrm{th}} = \sinh^2 r$. It can furthermore be shown that a TMS state with two-mode squeeze factor r is equivalent to the symmetric superposition of two orthogonal squeezed states with respective squeeze factor r [83]. Without quoting the lengthy and technical derivation, we give the result for

the quadrature moments for a TMS state,

$$\langle q_1^k p_1^l q_2^m p_2^n \rangle = M_{klmn}(r) \left[1 + (-1)^{k+m} + (-1)^{l+n} + (-1)^{k+l+m+n} \right], \tag{2.117}$$

where we define

$$M_{klmn}(r) \equiv \sum_{i_1=0}^{k} \sum_{i_2=0}^{l} \sum_{i_3=0}^{\lfloor \frac{m}{2} \rfloor} \sum_{i_4=0}^{\lfloor \frac{n}{2} \rfloor} c_{i_1 i_2 i_3 i_4} \exp \left[8r(i_1 + i_3 - i_2 - i_4 - \lfloor \tfrac{i_1}{2} \rfloor - \lfloor \tfrac{i_2}{2} \rfloor) \right], \tag{2.118}$$

where $\lfloor x \rfloor$ denotes the floor function. The coefficients are given by

$$c_{i_1 i_2 i_3 i_4} = \frac{1}{4^{k+l+m+n+1}} \binom{k}{i_1} \binom{l}{i_2} \binom{m}{i_1 + 2i_3 - 2\lfloor \frac{i_1}{2} \rfloor} \binom{n}{i_2 + 2i_4 - 2\lfloor \frac{i_2}{2} \rfloor} \tag{2.119}$$

$$\times [4(i_1 + i_3 - \lfloor \tfrac{i_1}{2} \rfloor) - 1]!![2(k + m - 2i_1 - 2i_3 - 2\lfloor \tfrac{i_1}{2} \rfloor) - 1]!! \tag{2.120}$$

$$\times [4(i_2 + i_4 - \lfloor \tfrac{i_2}{2} \rfloor) - 1]!![2(k + m - 2i_2 - 2i_4 - 2\lfloor \tfrac{i_2}{2} \rfloor) - 1]!!. \tag{2.121}$$

We can produce any pure single-mode Gaussian state by a concatenation of displacement and squeezing operations, where the order of these operations is crucial since displacement and squeezing operators do not commute [173, 174]. Local variance broadening and therefore mixed states can be modelled by the TMS operator, $\hat{S}_{\mathrm{TMS}}$. Thereby, we need to consider the environment as an ancillary mode which needs to be traced out in case we are interested in the local mode. Simultaneously, the TMS operator is realized by the nondegenerate JPA and can be used to model phase-insensitive amplification of the mode $\hat{a}_1$ [175]. The SQL, Eq. (2.32), then emerges from the presence of the uncorrelated input mode, $\hat{a}_2$.

2.2.3 Gaussian quantum correlations and entanglement

For many quantum communication protocols, the quantum advantage arises from the exploitation of quantum correlations shared by the communication parties [47]. Here, we introduce quantum entanglement and quantum discord as quantum correlation quantifiers [176]. Since the description of quantum correlations between two quantum systems is closely related to their shared nonlocal information, we first discuss the concept of entropy [15]. According to the Williamson theorem, we can find a symplectic transformation for any covariance matrix $\boldsymbol{V}$ under which it becomes diagonal [177, 178]. Consequently, entropic quantities and nonlocal correlations can be expressed in terms of symplectic invariants [179]. In particular, by employing a linear unitary Bogoliubov transformation [47], we can write any two-mode covariance matrix in the form

$$\boldsymbol{V} = \begin{pmatrix} a\mathbb{1}_2 & c\boldsymbol{\Pi}_p + c'\boldsymbol{\Pi}_q \\ c\boldsymbol{\Pi}_p + c'\boldsymbol{\Pi}_q & b\mathbb{1}_2 \end{pmatrix}, \tag{2.122}$$

with the phase space projection operators

$$\mathbf{\Pi}_p = \begin{pmatrix} 1 & 0 \\ 0 & 0 \end{pmatrix}, \qquad \mathbf{\Pi}_q = \begin{pmatrix} 0 & 0 \\ 0 & 1 \end{pmatrix}. \qquad (2.123)$$

The real numbers a and b describing the respective local modes, and c (c') describing the nonlocal correlation between p (q)-quadratures need to satisfy the relation [177, 180]

$$a^2 + b^2 + 2cc' \leq 8(ab - c^2)(ab - c'^2) + \frac{1}{8}, \qquad (2.124)$$

according to Eq. (2.93). In case of Bell-like states, such as the TMS state, one type of nonlocal quadratures is correlated and the orthogonal quadratures are anticorrelated, $c = -c'$. The symplectic invariants then correspond to [47]

$$I_1 = a^2, \qquad I_2 = b^2, \qquad I_3 = cc', \qquad I_4 = \det \mathbf{V} = I_1 I_2 + I_3^2 - \sqrt{I_1 I_2}(c^2 + c'^2). \ (2.125)$$

In addition, it is useful to define the quantity $\Delta \equiv I_1 + I_2 + 2I_3$, which enables us express the symplectic eigenvalues of $\mathbf{V}$ as [181]

$$\nu_\pm = \sqrt{\frac{\Delta \pm \sqrt{\Delta^2 - 4I_4}}{2}}. \qquad (2.126)$$

Entropic measures   Entropy measures the statistical ordering of a physical system and cannot decrease if the system is isolated, according to the second law of thermodynamics [182]. For a classical information processing system, described by a random variable X taking outcomes $\{x_i\}$ with respective probabilities $\{p_i\}$, the fundamental entropic quantity is Shannon entropy $H(X) = -\sum_i p_i \ln p_i$ [183]. According to Shannon's source coding theorem, $H(X)$ describes how many classical bits are required for the optimal compression of the system and thereby measures the system's actual information content [184].[4] By taking the continuum limit of the summation, we can express the Shannon entropy of an n-mode Gaussian state from the corresponding phase space quasiprobability distribution $W(\alpha)$, according to [151]

$$H(X) = -\int W(\alpha) \ln W(\alpha) d^2\alpha = \frac{1}{2} \ln\left[(2\pi e)^n \det \mathbf{V}\right], \qquad (2.127)$$

where $\alpha = p + iq$. A closely related quantity is the Shannon mutual information $I_s(X, Y)$ between two random variables X and Y. In general, $I_s(X, Y)$ measures the maximal amount of information which can be obtained about Y if we assume complete knowledge of X. In case X (Y) is described by a phase space probability distribution $P(\alpha)$ [$P'(\alpha')$],

---

[4]For this interpretation, all logarithms need to be taken with basis 2. Throughout this work, we usually use the natural logarithm as this often simplifies the calculations. Actual information in units of bits can be obtained by multiplying entropic quantities with $1/\ln 2 \simeq 1.44$.

mutual information can be calculated by [183]

$$I_{\mathrm{s}}(X,Y) = \int d^2\alpha\, d^2\alpha'\, P'(\alpha'|\alpha) P(\alpha) \ln\left(\frac{P'(\alpha'|\alpha)}{P'(\alpha')}\right),\qquad(2.128)$$

where $P'(\alpha'|\alpha)$ corresponds to the conditional probability distribution for α'. The order of α and α' can be swapped using Bayes' rule. One possible quantum mechanical generalization of Eq. (2.127) for a given density operator $\hat{\rho}$ is given by the Rényi-α_{r} entropy [185], which is defined as

$$S_{\alpha_{\mathrm{r}}}(\hat{\rho}) = \frac{1}{1-\alpha_{\mathrm{r}}} \ln \mathrm{Tr}(\hat{\rho}^{\alpha_{\mathrm{r}}}).\qquad(2.129)$$

The limiting case $\alpha_{\mathrm{r}} \to 1$ is called von Neumann entropy $S(\hat{\rho})$ and represents the natural extension of the classical thermodynamic entropy to statistical quantum mixtures [186]. For n-mode Gaussian states, the von Neumann entropy can be directly calculated from the symplectic eigenvalues ν_i [187],

$$S(\hat{\rho}) = -\mathrm{Tr}(\hat{\rho} \ln \hat{\rho}) = \sum_{i=1}^{n} f(\nu_i),\qquad(2.130)$$

where we define the entropic function

$$f(x) = \left(2x + \frac{1}{2}\right) \ln\left(2x + \frac{1}{2}\right) - \left(2x - \frac{1}{2}\right) \ln\left(2x - \frac{1}{2}\right).\qquad(2.131)$$

For $n = 1$, Eq. (2.130) simplifies to $f(\sqrt{\det \boldsymbol{V}})$ [49]. The von Neumann entropy is directly related to purity μ. For pure states, $\mu = 1$, we have $S = 0$ and for maximally mixed states, $\mu = 0$, von Neumann entropy diverges. As we further discuss in Sec. 2.3.1, Rényi entropy for the case $\alpha_{\mathrm{r}} = 2$ in Eq. (2.129) is commonly used in the context of quantum phase transitions [188]. For an n-mode Gaussian state, this Rényi-2 entropy is directly linked to the Shannon entropy via [189]

$$S_2(\hat{\rho}) = H(X) - n \ln \sqrt{\frac{\pi e}{8}}\qquad(2.132)$$

and straightforwardly allows for the distinction of ordered phases ($S_2 = 0$) and disordered phases ($S_2 > 0$).

Entanglement   Entanglement represents a specific category of quantum correlations and emerges from a nonseparability of a multipartite quantum system [15]. Throughout this work, we focus on two-mode states shared by parties A and B. In case such a quantum system is described by the joint density operator $\hat{\rho}_{\mathrm{AB}}$, the system is separable if $\hat{\rho}_{\mathrm{AB}}$ can be decomposed into a sum of tensor products between density operators fully describing the respective local subsystems A and B. In general, the separability of a multimode Gaussian

state is characterized by the Peres-Horodecki PPT criterion [190], which states that the partially transposed density matrix needs to be positive [191]. Thereby, transposition of a Gaussian state is equal to reflection of a certain quadrature eigenvalue with respect to the corresponding phase space axis [180]. Resulting from that, it can be shown that a suitable monotonic non-separability measure which is easy to calculate is provided by the negativity N [192]. In case $\tilde{\rho}_{AB}$ is the partially transposed density operator, normalization guarantees $\mathrm{Tr}(\tilde{\rho}_{AB}) = 1$. If one of the eigenvalues is negative, we thus must have $\mathrm{Tr}|\tilde{\rho}_{AB}| > 1$. Negativity effectively measures the difference of $\mathrm{Tr}|\tilde{\rho}_{AB}| - 1$. For bipartite Gaussian states, negativity can be expressed as

$$N = \max\left(0, \frac{1}{8\tilde{\nu}_-} - \frac{1}{2}\right), \tag{2.133}$$

where $\tilde{\nu}_-$ corresponds to the smallest symplectic eigenvalue of the partially transposed state. Another relevant entanglement monotone is provided by entanglement of formation (EoF). For bipartite Gaussian states described by a joint covariance matrix $\boldsymbol{V}_{AB}$, EoF is defined as [193]

$$\mathcal{E}_F(\boldsymbol{V}_{AB}) = \inf_{\boldsymbol{V}'_{AB} \leq \boldsymbol{V}_{AB}, \det \boldsymbol{V}'_{AB} = 1/16} f(\sqrt{A'}), \tag{2.134}$$

where A' is the symplectic invariant corresponding to the local subsystem A, which is derived from $\boldsymbol{V}_{AB}$ by tracing out B. EoF is significantly harder to calculate than negativity, but has multiple intriguing properties and interpretations. As an example, Gaussian EoF quantifies the minimal amount of two-mode squeezing needed to prepare an entangled state, starting from a classical one by using local operations and classical communication [194]. In general, the minimization procedure in Eq. (2.134) needs to be done numerically. However, an analytical lower bound E_F has been derived in Ref. 195,

$$E_F = \mathrm{sign}(\gamma)\left[\cosh^2\gamma \ln(\cosh^2\gamma) - \sinh^2\gamma \ln(\sinh^2\gamma)\right] \leq \mathcal{E}_F, \tag{2.135}$$

where γ corresponds to the minimally required amount of two-mode squeezing to disentangle the bipartite state. Although the bound Eq. (2.135) only becomes exact in case of symmetric local states A and B, we approximate $E_F \simeq \mathcal{E}_F$ throughout the rest of this work.[5] An entangled state is called maximally entangled if the local states in the subsystems have purity $\mu = 0$ and maximal entropy [196]. The TMS state becomes asymptotically maximally entangled, as the state locally looks like a thermal state with temperature $T = \hbar\omega/[2k_B \ln(\coth r)] \to \infty$ in the limit of $r \to \infty$. The presented entanglement monotones diverge for maximally entangled states. In addition, maximally entangled states satisfy the Tsirelson bound and maximally violate the CHSH inequality [197–199]. These states are suspected to provide maximal quantum nonlocality [200].

---

[5]The quantity E_F actually bounds the kernel $\mathcal{E}_k$ of EoF $\mathcal{E}_F$, $\mathcal{E}_F = \max[\mathcal{E}_k, 0]$. As a result, vanishing entanglement is indicated by $E_F \leq 0$.

Quantum discord   Entanglement only measures correlations emerging from the non-separability of joint quantum systems. However, even separable quantum systems can share quantum correlations. In this work, we use quantum discord as a general correlation quantifier, including entanglement [201]. Quantum discord is defined as the difference between the full quantum mutual information and the classical correlation. In analogy to Eq. (2.128), bipartite quantum mutual information is defined as the intersection between the full quantum information of system A and B, respectively. This intersection is given by the discrepancy of the sum of the von Neumann entropies, corresponding to the individual subsystems, and the joint entropy S_{AB} [179, 202]

$$I(\mathrm{A} : \mathrm{B}) = S_{\mathrm{A}} + S_{\mathrm{B}} - S_{\mathrm{AB}} = I(\mathrm{B} : \mathrm{A}). \tag{2.136}$$

The classical correlation $J(A|B)$ describes the maximum amount of accessible information which can be extracted by performing a projective measurement on one of the subsystems, in our case B. It is defined as [203]

$$J(\mathrm{A}|\mathrm{B}) = \sup_{\{\hat{\Pi}_{\mathrm{B}}\}} \left[S_{\mathrm{A}} - \sum_i p_i S(\hat{\rho}_{\mathrm{A}}|i) \right] = S_{\mathrm{A}} - C_{\min}(\mathrm{A}|\mathrm{B}), \tag{2.137}$$

where the supremum is taken over all positive operator valued measures (POVMs) $\{\hat{\Pi}_{\mathrm{B}}\}$ [15]. This maximization procedure is necessary since the measurement outcome depends on the choice of the measurement operators. The quantities p_i describe the probability of a certain measurement outcome and $C_{\min}(\mathrm{A}|\mathrm{B})$ is the minimized conditional entropy. Note that Eq. (2.137) is not symmetric in general, $J(\mathrm{A}|\mathrm{B}) \neq J(\mathrm{B}|\mathrm{A})$. The A-quantum discord and the B-quantum discord are then defined as the discrepancy between the quantum mutual information and the classical correlation [176]

$$D_{\mathrm{A}} = I(\mathrm{A} : \mathrm{B}) - J(\mathrm{A}|\mathrm{B}), \qquad D_{\mathrm{B}} = I(\mathrm{A} : \mathrm{B}) - J(\mathrm{B}|\mathrm{A}). \tag{2.138}$$

Resulting from the asymmetry of Eq. (2.137), in general, we have $D_{\mathrm{A}} \neq D_{\mathrm{B}}$. Although the calculation of D_{A} and D_{B} is nontrivial for general bipartite quantum systems, there exist closed analytical expressions for Gaussian quantum states in terms of symplectic invariants. According to Ref. 204, the bipartite Gaussian quantum discord can be expressed as

$$D_{\mathrm{A}} = f\left(\sqrt{I_2}\right) - f(\nu_+) - f(\nu_-) + f\left(\sqrt{E_{\mathrm{A}|\mathrm{B}}^{\min}}\right), \tag{2.139}$$

where

$$E_{\mathrm{A}|\mathrm{B}}^{\min} = \begin{cases} \left[\dfrac{4|I_3| + \sqrt{16 I_3^2 - (I_1 - 16 I_4)(16 I_2 - 1)}}{16 I_2 - 1} \right]^2 & \text{if } \xi_{\mathrm{A}} \leq 0 \\[2ex] \dfrac{I_1 I_2 + I_4 - I_3^2 - \sqrt{(I_1 I_2 + I_4 - I_3^2)^2 - 4 I_1 I_2 I_4}}{2 I_2} & \text{else} \end{cases}, \tag{2.140}$$

with

$$\xi_A \equiv \frac{16(I_1 I_2 - I_4)^2}{(I_1 + 16 I_4)(16 I_2 + 1) I_3^2} - 1. \tag{2.141}$$

We can furthermore calculate the B-discord by formally exchanging the systems $A \longleftrightarrow B$, which is mathematically equivalent to replacing $I_1 \longleftrightarrow I_2$. It can furthermore be shown that, for pure states, EoF exactly coincides with quantum discord. Therefore, entanglement already captures all quantum correlations in this case, implying that the investigation of quantum discord is only reasonable for mixed states [204]. As pointed out in Ref. 112, quantum discord is directly related to the fact that it is, in general, not possible to uniquely distinguish between non-orthogonal quantum states with one single projection. This is especially intuitive in the single qubit case since the Bloch sphere is a volumetric object [15]. As a result, the necessity of elaborate reconstruction techniques such as quantum process tomography [205–207] or randomized benchmarking, [208] can eventually be regarded as a consequence of quantum discord. For pure bipartite states, quantum discord coincides with EoF [204]. However, in contrast to entanglement, quantum discord shows asymptotic stability against noise [209].

2.2.4 Gaussian quantum channels

So far, we have analyzed how to describe Gaussian quantum states of light. In the following, we investigate Gaussian quantum channels, i.e., transformations between Gaussian states [210]. In case our Gaussian state is described by the density operator $\hat{\rho}_G$, a general Gaussian quantum channel Φ can be expressed as a completely positive trace-preserving (CPTP) map

$$\hat{\rho}'_G = \Phi(\hat{\rho}_G) = \text{Tr}_E \left[U(\hat{\rho}_G \otimes \hat{\rho}_E) U^\dagger \right], \tag{2.142}$$

where U is a unitary operator, corresponding to a quadratic Hamiltonian which describes the propagating electromagnetic field and $\hat{\rho}_E$ corresponds to a Gaussian environment [211]. Next, we apply the Weyl correspondence principle to Eq. (2.142) for an n-mode Gaussian state, described by the $2n$-dimensional displacement vector $\mathbf{d}$ and the $(2n \times 2n)$ covariance matrix $\boldsymbol{V}$ [147]. In this case, the effect of Φ is schematically depicted in Fig. 2.11(a) and can be generally expressed as

$$\mathbf{d}' = \boldsymbol{X}\mathbf{d} + \mathbf{d}_\Phi, \qquad \boldsymbol{V}' = \boldsymbol{X}\boldsymbol{V}\boldsymbol{X}^\dagger + \boldsymbol{Y}\boldsymbol{Y}^\dagger, \tag{2.143}$$

where $\boldsymbol{X}$ is a real $(2n \times 2n)$ matrix which describes rotations, amplification or attenuation [212]. The vector $\mathbf{d}_\Phi$ corresponds to a constant displacement induced by Φ, and the matrix $\boldsymbol{Y}$ describes the noise, added by the environment.

Single-mode Gaussian quantum channels   In the following, we investigate some of the most relevant fundamental Gaussian quantum channels [210, 212]. The first channel

(a)

(b)

Classical feedforward

(c)

Entanglement distribution
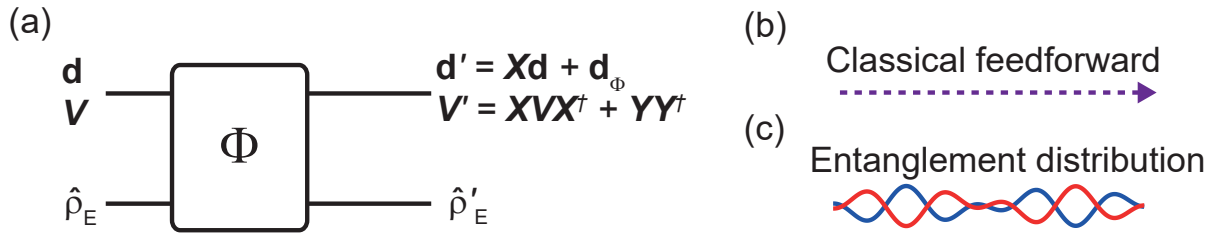
Figure 2.11: (a) Schematic illustration of a general Gaussian quantum channel Φ. The left side corresponds to the input displacement $\mathbf{d}$, input covariance matrix $\boldsymbol{V}$ and environment $\hat{\rho}_{\mathrm{E}}$, which is treated as an ancilla system. The right side depicts how the respective input quantities transform under Φ. (b) Schematic depiction of a classical feedforward channel. (c) Schematic depiction of an entanglement distribution channel.

is the *phase-preserving amplification channel* $\Phi_{\mathrm{pp}}(G)$ which describes quantum-limited phase-insensitive amplification with gain G. It is characterized by

$$\mathbf{d}_\Phi = \mathbf{0}, \qquad \boldsymbol{X} = \sqrt{G}\mathbb{1}_2, \qquad \boldsymbol{Y} = \frac{1}{2}\sqrt{\frac{G-1}{G}}\mathbb{1}_2. \qquad (2.144)$$

The last term in Eq. (2.144) corresponds to the SQL. As we have seen in Sec. 2.1.4, the same channel can be rewritten without any additive $\boldsymbol{Y}$ contribution if we treat it as a multimode channel. Next, we discuss the ideal *phase-sensitive amplification channel* $\Phi_{\mathrm{ps}}(G, \varphi)$ of a quadrature. The arguments are the amplification angle φ and the gain G. This channel corresponds to a squeezing operation described by

$$\mathbf{d}_\Phi = \mathbf{0}, \qquad \boldsymbol{X} = \boldsymbol{R}(\varphi)\boldsymbol{J}(G)\boldsymbol{R}^{\mathrm{T}}(\varphi), \qquad \boldsymbol{Y} = \mathbb{0}_2, \qquad (2.145)$$

where the rotation matrix $\boldsymbol{R}(\varphi)$ and $\boldsymbol{J}(G) = \mathrm{diag}\left(\sqrt{G}, 1/\sqrt{G}\right)$ are (2×2) matrices. For the *attenuation channel* $\Phi_{\mathrm{att}}(\varepsilon)$, we assume that the signal is lost to an environment at zero temperature with a power loss parameter $0 \leq \varepsilon \leq 1$. This loss is modelled by

$$\mathbf{d}_\Phi = \mathbf{0}, \qquad \boldsymbol{X} = \sqrt{1-\varepsilon}\mathbb{1}_2, \qquad \boldsymbol{Y} = \frac{\sqrt{\varepsilon}}{2}\mathbb{1}_2. \qquad (2.146)$$

Equation (2.146) describes losses to the environment with a simple beam splitter model. Throughout all our experiments, the beam splitter model is a valid approximation since we do not consider any non-Markovian effects [213]. This model then corresponds to the ensemble average of photon loss with probability ε with simultaneous excitation of Markovian environment $\hat{t}$ via the beam splitter relation $\hat{a}' = \sqrt{1-\varepsilon}\hat{a} + \sqrt{\varepsilon}\hat{t}$ [48]. For our measurements at millikelvin temperatures, the attenuation channel provides an accurate tool to model path losses. However, since the third law of thermodynamics forbids to reach the limit $T \to 0$ [214], a more realistic model is provided by the *thermal noise channel* $\Phi_{\mathrm{th}}(\varepsilon, n_{\mathrm{th}})$. In this case, we need to assign a finite temperature T to the mode $\hat{t}$

and assume that this mode satisfies Boltzmann statistics with mean photon number n_{th} [168]. Thus, we have

$$\mathbf{d}_\Phi = \mathbf{0}, \qquad \boldsymbol{X} = \sqrt{1-\varepsilon}\,\mathbb{1}_2, \qquad \boldsymbol{Y} = \frac{1}{2}\sqrt{\varepsilon(1+2n_{\text{th}})}\,\mathbb{1}_2. \qquad (2.147)$$

During the experiments presented in chapter 8, we artificially generate a thermal noise channel by heating local sections of the experimental setup in a controlled way. Such experiments are of particular fundamental interest, since Eq. (2.147) is directly related to the fluctuation-dissipation theorem, which generally states that fluctuation spectrum and dissipation spectrum are linearly related to each other in an ergodic system [215, 216]. Thus, by ensuring lossless transmission of quantum signals through a thermal environment, we expect to avoid the otherwise destructive impact of thermal noise on fragile quantum properties such as entanglement [217]. In particular, the fluctuation-dissipation theorem in units of photons is given by

$$\mathcal{S}(\omega) = 2\coth\left(\frac{\hbar\omega}{2k_{\text{B}}T}\right)\varepsilon(\omega) = 4\mathcal{S}_{\text{th}}(\omega)\varepsilon(\omega), \qquad (2.148)$$

where $\mathcal{S}(\omega)$ denotes the coupled power spectrum in units of photons per bandwidth (positive and negative sideband), $\mathcal{S}_{\text{th}}$ corresponds to the power spectrum of the environmental thermal noise and $\varepsilon(\omega)$ is the dissipation spectrum, associated with the signal losses.[6] Thus, the detected noise power within a small bandwidth, according to the fluctuation-dissipation theorem, exactly corresponds to the additive noise contribution in Eq. (2.147). The thermal noise channel is a combination of the beam splitter model and a classical noise channel, which would simply broaden the quadrature variances. However, a correct quantum description of noise coupling requires that a part of the signal is lost to the environment to preserve the bosonic commutation relations [48]. Next, we exploit the fact that any concatenation of Gaussian channels forms again a valid Gaussian channel to implement the classical noise channel by attenuation, followed by phase-insensitive amplification, according to the function composition $\Phi_{\text{cl}} = \Phi_{\text{pp}}[1/(1-\varepsilon)] \circ \Phi_{\text{att}}(\varepsilon)$, which leads to

$$\mathbf{d}_\Phi = \mathbf{0}, \qquad \boldsymbol{X} = \mathbb{1}_2, \qquad \boldsymbol{Y} = \frac{1}{2}\sqrt{\frac{\varepsilon(2-\varepsilon)}{1-\varepsilon}}\,\mathbb{1}_2. \qquad (2.149)$$

Since the prefactor function of $\boldsymbol{Y}$ has range $[0,\infty)$, any classical noise channel can be written as such a composition and we employ such a channel to model our gain-dependent JPA noise [85]. Throughout our quantum communication experiments, an important Gaussian quantum channel is the *classical feedforward channel*. Such a channel is formed by concatenation of an amplification channel (phase-insensitive or phase-sensitive) with gain $G \gg 1$, followed by a thermal noise channel. The graphical notation chosen for this

---

[6]Note that we effectively only couple $1/4$ of the full thermal power spectral density since we assume ideal power matching with respect to the circuit impedance [93].

channel is shown in Fig. 2.11(b). A Gaussian quantum channel connecting pure single-mode states can always be expressed as a concatenation of displacement, squeezing, and rotation operations. Note that these unitary single-mode operations are already sufficient to describe large parts of ideal (loss- and noiseless) Gaussian quantum communication protocols. However, these ideal protocols also require non-unitary operations such as (projective) measurements [159]. As we discuss in Sec. 2.3, a unitary approximation of such an operation in its analog form can be realized by an interplay of unitary components.

Entanglement distribution   So far, we have investigated single-mode Gaussian channels. Nevertheless, all entanglement-based protocols necessarily require the use of multi-mode channels [158]. To create bipartite quantum correlations between modes l and m in an n-mode system, we employ beam splitter operations of the form $\boldsymbol{B}^{(l,m)}(T) = \tilde{\boldsymbol{B}}^{(l,m)}(T) \otimes \mathbb{1}_2$ with

$$\tilde{\boldsymbol{B}}_{ij}^{(l,m)}(T) = \delta_{ij}(1 - \delta_{im} - \delta_{jl}) + \sqrt{1 - |T|}(\delta_{il}\delta_{jm} + \delta_{im}\delta_{jl}) + \sqrt{|T|}\delta_{ij}(\delta_{im} + \delta_{jl}), \quad (2.150)$$

where δ_{ij} denotes the Kronecker delta and T describes the transmissivity. In Eq. (2.150), we assume a phase reference of zero and a relative phase shift of π between the outputs. To describe the entanglement distribution channel Φ_{TMS} via a TMS state with squeeze factor r, we define $\boldsymbol{S}_{lm}(r)$ as the $n-$mode operation which applies the phase-sensitive channel $\boldsymbol{J}_l(e^{2r}, 0)$ to mode l and $\boldsymbol{J}_m(e^{2r}, \pi/2)$ to mode m. The channel Φ_{TMS} is then realized by

$$\mathbf{d}_\Phi = \mathbf{0}, \qquad \boldsymbol{X} = \boldsymbol{B}^{(l,m)}(1/\sqrt{2})\boldsymbol{S}_{lm}(r), \qquad \boldsymbol{Y} = \mathbb{0}_{2n}. \qquad (2.151)$$

Our schematic symbol for the entanglement distribution channel is depicted in Fig. 2.11(c).

2.2.5 Continuous-variable quantum teleportation

Now we introduce quantum teleportation as the central quantum communication protocol which is extensively investigated throughout this work. A schematic illustration of a general quantum teleportation experiment is shown in Fig. 2.12. In general, quantum teleportation enables the disembodied transfer of an unknown quantum state $\hat{\rho}_{\mathrm{in}}$ between two communication parties, usually referred to as Alice and Bob [218]. Prior to performing the experiment, Alice and Bob share an entangled resource state. Next, Alice entangles her part of the resource with $\hat{\rho}_{\mathrm{in}}$ and performs a projective Bell measurement on the resulting state. She then sends the classical outcome of this measurement to Bob, who performs a unitary operation $\hat{U}$ to his part of the predistributed resource state. Bob's operation comes from a well-defined set but the exact choice depends on the classical measurement result communicated by Alice [9, 219]. Bob's final state $\hat{\rho}_{\mathrm{out}}$ then ideally coincides with $\hat{\rho}_{\mathrm{in}}$ without actually transmitting the input state. Simultaneously, the quantum state on Alice's side is erased in agreement with the no-cloning theorem. The
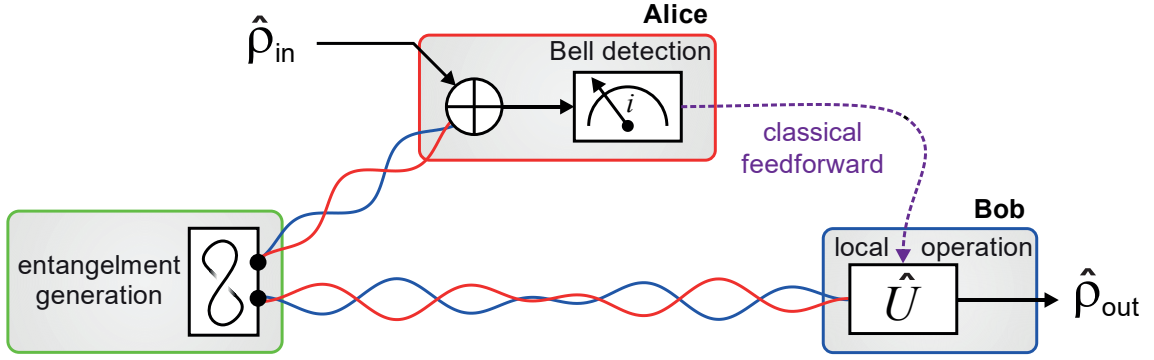
Figure 2.12: Schematic illustration of a general quantum teleportation setup. Prior to the experiment, an entangled resource state is generated and distributed to the communication parties Alice and Bob. Next, Alice entangles the input state $\hat{\rho}_{\mathrm{in}}$, which can be unknown to her, with her part of the resource and performs a Bell measurement on the resulting bipartite state. The classical result is forwarded to Bob who performs a conditioned unitary operation to his state, leading to the final state $\hat{\rho}_{\mathrm{out}}$, which coincides with $\hat{\rho}_{\mathrm{in}}$ for ideal teleportation.

protocol is fully compatible with special relativity theory since the classical information transfer in the feedforward channel is limited by the speed of light. Although quantum teleportation is conventionally discussed in the scope of DV quantum systems such as qubits, we focus on the CV implementation here as it is the suitable formulation of the protocol to describe our experiments [47, 58, 67]. For the teleportation of single-mode CV states, we need three modes in total. Throughout this work, we use the convention that the first (second) mode corresponds to the entanglement resource, distributed to Bob (Alice) and the third mode corresponds to the input state. For a TMS state as entanglement resource in the limit $r \gg 1$ used to teleport a state described by the Wigner function $W_{\mathrm{in}}(q_3, p_3)$, the Wigner function of the initial three-mode state is given by [220]

$$W(q_1, p_1, q_2, p_2, q_3, p_3) = \delta(q_1 - q_2)\delta(p_1 + p_2)W_{\mathrm{in}}(q_3, p_3), \qquad (2.152)$$

where we neglect any prefactor for normalization. In an ideal Bell detection, we measure the quadrature superpositions $q_- = (q_3 - q_2)/\sqrt{2}$ and $p_+ = (p_3 + p_2)/\sqrt{2}$ with respective measurement outcomes a and b and obtain

$$W'(q_1, p_1, q_3, p_3) = \int dq_- dp_+ \delta(q_1 - q_2)\delta(p_1 + p_2)\delta(q_- - a)\delta(p_+ - b)W_{\mathrm{in}}(q_3, p_3) \quad (2.153)$$

$$= \delta(q_1 - q_3 + \sqrt{2}a)\delta(p_1 - p_3 + \sqrt{2}b)W_{\mathrm{in}}(q_3, p_3). \qquad (2.154)$$

Next, we calculate the marginal distribution with respect to Bob's phase space coordinates, q_1 and p_1, and find the Wigner function associated with the final mode

$$W_{\mathrm{out}}(q_1, p_1) = W_{\mathrm{in}}(q_1 + \sqrt{2}a, p_1 + \sqrt{2}b). \qquad (2.155)$$

We thus observe that Bob's final state coincides with the input state up to a displacement of $\sqrt{2}a$ ($\sqrt{2}b$) in the q_1 (p_1) quadrature [58]. The two real numbers a and b are transmitted from Alice to Bob through the classical feedforward channel. Bob then uses this classical information to perform a conditioned displacement operation on his state which compensates the displacement offset in Eq. (2.155). Furthermore, we have not yet made any assumptions about $W_{\text{in}}(q_3, p_3)$, implying that neither Alice nor Bob need any information about the input state. We note that ideal quantum teleportation is an unconditionally secure protocol, which can be regarded as a quantum implementation of the classical one-time pad encryption technique by exploiting quantum fluctuations as a perfect random number generator [221]. An elegant diagrammatic proof can be found in Ref. 222.

2.2.6 Fidelity and codebook

Uhlmann fidelity   In the previous section, we have discussed the ideal CV quantum teleportation protocol where the output state of Bob perfectly coincides with the input state. Nevertheless, in a practical implementation, we cannot realize the limit $r \to \infty$ as it would require an infinite amount of energy. In addition, in any realistic implementation, all quantum states are subject to losses and noise, which eventually lead to deviations in Bob's final state from the input state. A suitable measure for the performance of the protocol is the Uhlmann fidelity F, which measures the statistical overlap of two density operators $\hat{\rho}_1$ and $\hat{\rho}_2$ [223]. In the CV case, it can be shown that F simultaneously measures the statistical phase space overlap of the quasiprobability distributions, $W_1(\alpha_1)$ and $W_2(\alpha_2)$, associated with $\hat{\rho}_1$ and $\hat{\rho}_2$. The fidelity can be expressed as [15, 224, 225]

$$F = \text{Tr} \sqrt{\sqrt{\hat{\rho}_1} \hat{\rho}_2 \sqrt{\hat{\rho}_1}} = \pi \int d^2\alpha_1 d^2\alpha_2 W_1(\alpha_1) W_2(\alpha_2). \tag{2.156}$$

The fidelity is bound by $0 \leq F \leq 1$ and can be regarded as a monotone for the performance of a quantum protocol, where $F = 1$ corresponds to an ideal protocol [226]. Before discussing relevant limits of F for quantum teleportation, we provide a more practical evaluation of fidelity in case the states are Gaussian and described by displacement $\mathbf{d}_1$ ($\mathbf{d}_2$) and covariance matrix $\boldsymbol{V}_1$ ($\boldsymbol{V}_2$). In this case, the integral in Eq. (2.156) can be evaluated explicitly, yielding

$$F(\mathbf{d}_1, \boldsymbol{V}_1, \mathbf{d}_2, \boldsymbol{V}_2) = \frac{1}{2} \frac{\exp\left(-\frac{1}{2}\boldsymbol{\beta}^{\text{T}}(\boldsymbol{V}_1 + \boldsymbol{V}_2)^{-1}\boldsymbol{\beta}\right)}{\sqrt{\Lambda + \Delta} - \sqrt{\Delta}}. \tag{2.157}$$

Here, $\Lambda \equiv \det(\boldsymbol{V}_1 + \boldsymbol{V}_2)$, $\Delta \equiv 16(\det\boldsymbol{V}_1 - 1/16)(\det\boldsymbol{V}_2 - 1/16)$ and $\boldsymbol{\beta} \equiv \mathbf{d}_1 - \mathbf{d}_2$ [227]. In case one of the two states is pure, we have $\Delta = 0$, which leads to a significant simplification of Eq. (2.157). Next, we discuss the requirements to observe a quantum advantage in the protocol when we employ entanglement. For coherent input states, this
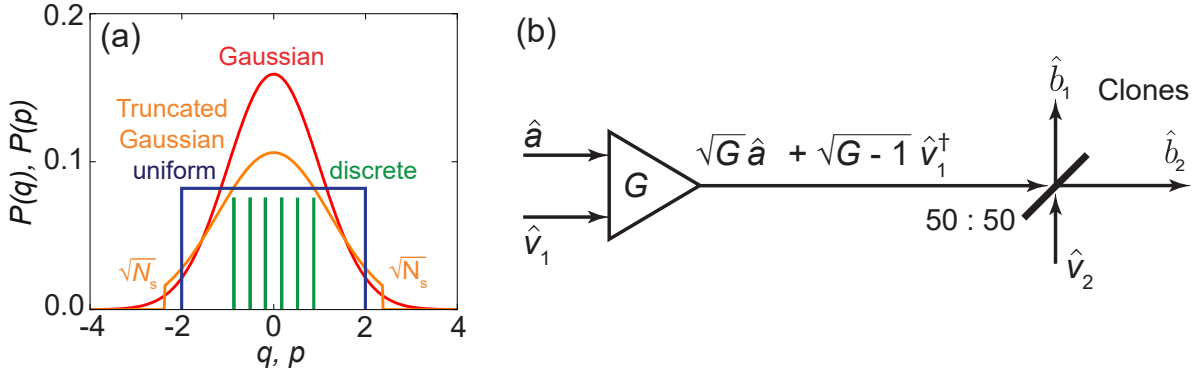
Figure 2.13: (a) Various types of input codebooks for quantum communication protocols. (b) Scheme for the optimal cloning machine for a Gaussian codebook according to Ref. 229. The cloning machine consists of a phase-insensitive amplifier acting on the unknown input mode $\hat{a}$ with weak gain G, followed by a symmetric beam splitter, which produces the clones $\hat{b}_1$ and $\hat{b}_2$. For an infinitely large codebook, $\sigma \to \infty$, the optimal gain exactly compensates for the beam splitter loss, $G_{\mathrm{opt}} = 2$.

is the case if the fidelity exceeds the classical threshold $F_{\mathrm{c}} = 1/2$ (in contrast to $2/3$ for qubits). Without the use of entanglement, we always have $F \leq F_{\mathrm{c}}$. As can be seen from Eq. (2.157), F_{c} exactly corresponds to the case where the protocol broadens the variance by twice the vacuum fluctuations, referred to as *quduties* by Braunstein and Kimble [47, 58]. The emerging quduties can be intuitively explained by reconsidering Eq. (2.152) for the case where we do not employ a TMS state. In this case, we have to replace the Dirac delta functions by two uncorrelated Gaussian vacuum modes. The first quduty is a result from Alice's simultaneous measurement of two signal quadratures during the Bell detection. One of the input vacuum modes thereby forms the SQL for Alice's detection process. The second quduty emerges when Bob uses the information from this noisy Bell measurement to perform the conditioned unitary operation on his uncorrelated vacuum mode. The fluctuations induced by the quduties, can only be suppressed by destructive interference of pre-shared quantum correlations. Thus, measuring fidelities $F > 1/2$ is a proof that our entanglement resource leads to a purification of the teleported state [228]. In addition, fidelity can also act as a security quantifier for quantum teleportation. For this interpretation of fidelity, we need to introduce the concept of input codebooks [229].

Codebook In the next step, we assume that the teleported input states are drawn from a specific probability distribution $P(\alpha)$. The existence of such a codebook is necessary to form an alphabet among the communication partners, which eventually enables calculation of bit rates and security. Figure 2.13(a) illustrates various types of codebooks in phase space. Any practical codebook is discrete due to the finite resolution of our microwave devices, and truncated at a maximal photon number N_{s}, which is determined by the JPA compression. However, for such a codebook we do not know the optimal attack by a

potential eavesdropper, which restricts us from performing a general security analysis. Nevertheless, the optimal cloning attack scheme is known for bivariate Gaussian codebooks of the form

$$P_{\mathrm{G}}(\alpha) = \frac{1}{2\pi\sigma^2} e^{-\frac{|\alpha|^2}{2\sigma^2}} \tag{2.158}$$

and has been widely studied in literature [229]. This optimal cloning machine is shown in Fig. 2.13(b) and consists of phase-preserving amplification with gain G, followed by a symmetric beam splitter [229, 230]. The goal of such a machine is to create a copy of an unknown input state $\hat{a}$ with maximal fidelity. The output modes ("clones") are given by

$$\hat{b}_1 = \frac{1}{\sqrt{2}} \left(\sqrt{G}\hat{a} + \sqrt{G-1}\hat{v}_1^\dagger + \hat{v}_2 \right), \tag{2.159}$$

$$\hat{b}_2 = \frac{1}{\sqrt{2}} \left(\sqrt{G}\hat{a} + \sqrt{G-1}\hat{v}_1^\dagger - \hat{v}_2 \right), \tag{2.160}$$

where $\hat{v}_1$ and $\hat{v}_2$ are the respective vacuum modes added by amplifier and beam splitter. In case of coherent input states, the fidelity between input and one of the resulting clones is given by [231]

$$F(\alpha) = \frac{2}{G+1} \exp\left[-\frac{2(1-\sqrt{G/2})|\alpha|^2}{G+1} \right]. \tag{2.161}$$

Next, we calculate the average fidelity with respect to $P_{\mathrm{G}}(\alpha)$ and optimize the result with respect to G. The result is the no-cloning limit [229]

$$F_{\mathrm{nc}} = \begin{cases} \frac{4\sigma^2+2}{6\sigma^2+1} & \sigma^2 \geq \frac{1}{2} + \frac{1}{\sqrt{2}} \simeq 1.207, \\ \frac{1}{(3-2\sqrt{2})\sigma^2+1} & \sigma^2 \leq \frac{1}{2} + \frac{1}{\sqrt{2}} \simeq 1.207. \end{cases} \tag{2.162}$$

We plot the solution Eq. (2.162) as well as the optimal gain in Fig. 2.14(a). The case distinction at $\sigma^2 \simeq 1.207$ emerges from the constraint $G \geq 1$ since attenuation would require a different mathematical model and lead to lower fidelities. For arbitrary coherent input states with equal probability, $\sigma^2 \to \infty$, it is optimal to choose G such that it compensates for the beam splitter loss, $G = 2$. Then, Eq. (2.161) becomes independent of $|\alpha|^2$. In this case, we obtain a bound of $F_{\mathrm{nc}} = 2/3$, conventionally known as the asymptotic no-cloning limit [232].[7] Whenever we mention the no-cloning limit throughout this work, we always refer to this asymptotic no-cloning limit, unless explicitly stated otherwise. Whenever we reach a teleportation fidelity F above the no-cloning limit, we know that F exceeds the fidelity between $\hat{\rho}_{\mathrm{in}}$ and any clone a potential eavesdropper may possess [234]. In this sense, the protocol is unconditionally secure since Bob's state contains a fraction of information about the input state which is not available to any eavesdropper as long as the laws of quantum physics are assumed to be valid. In the

---

[7]For qubits, this limit would be 5/6 [233].
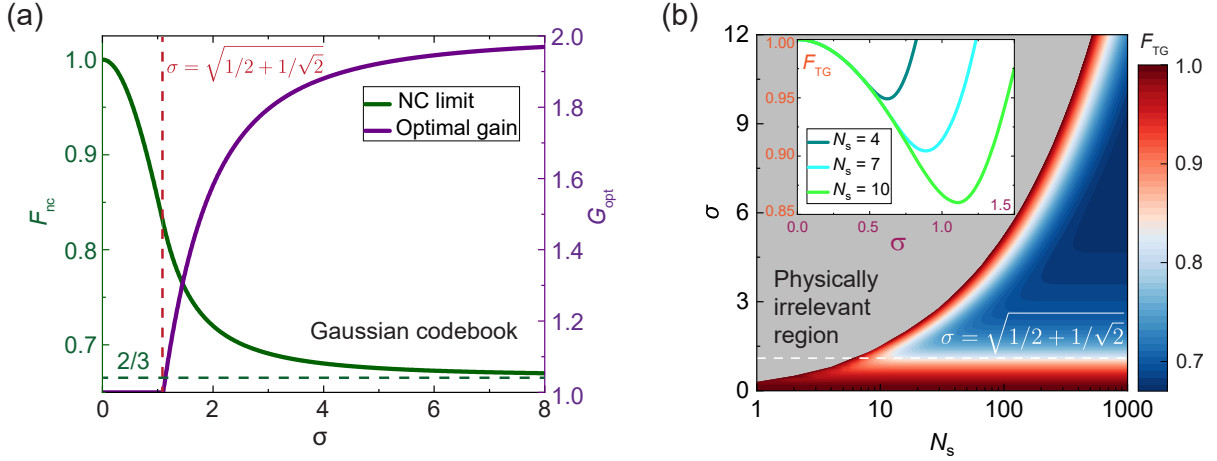
Figure 2.14: (a) No-cloning limit for fidelity, F_{nc}, and optimal gain G_{opt} for the Gaussian codebook as function of standard deviation σ, according to Ref. 229. (b) Upper bound F_{TG} for the no-cloning limit for a truncated Gaussian codebook as function of truncation photon number N_{s} and standard deviation σ. The gray region corresponds to unphysical results $F_{\mathrm{TG}} > 1$. The inset shows F_{TG} for fixed $N_{\mathrm{s}} = 4, 7, 10$ photons as a function of σ. We observe that for each N_{s}, we can choose σ in a way such that F_{TG} is minimized.

regime $1/2 < F < 2/3$, sometimes referred to as "quantum faxing" regime, we properly employ our quantum resource to purify for up to one quduty, but communication is not unconditionally secure due to the possibility of an eavesdropper (or a dishonest Alice) who might have cloned the state and transmitted the worse clone to Bob [235]. Note that there are non-Gaussian attacks which produce clones with higher fidelity than Eq. (2.162) [236]. However, such an attack can be ruled out by Bob if he checks for Gaussianity of his state. In addition, we remark that unconditional security requires the codebook to consist of a set of non-orthogonal states [237]. Next, we investigate truncated codebooks. They provide a more realistic alphabet since it can be realized with finite energy. In this case, the cloning attack described by Eq. (2.159) is not necessarily optimal, implying that the eavesdropper can change strategy or exploit knowledge of the codebook to perform Bayesian statistics. Thus, we choose the specific shape of a truncated Gaussian codebook

$$P(\alpha) = \frac{e^{-\frac{|\alpha|^2}{2\sigma^2}}}{2\pi\sigma^2(1 - e^{-N_{\mathrm{s}}/2\sigma^2})}\Theta(N_{\mathrm{s}} - |\alpha|^2), \tag{2.163}$$

where $\Theta(x)$ represents the Heaviside-function, N_{s} is the cutoff photon number, and σ^2 is the corresponding Gaussian codebook variance. We can derive an upper bound for the no-cloning limit by exploiting our knowledge of the exact no-cloning limit for the infinite Gaussian codebook.[8] We treat the optimal cloning machine for the truncated Gaussian

---

[8]The calculations related to the truncated Gaussian codebook have been performed in close collaboration with Dr. Roberto Di Candia and are shown here with his friendly permission.

codebook as an arbitrary Gaussian channel $\mathcal{N}$ and calculate the average fidelity [229, 238]

$$\bar{F}(\mathcal{N}) = \int F(\mathcal{N}, \alpha) P(\alpha) d^2\alpha. \tag{2.164}$$

We then have

$$\bar{F}(\mathcal{N}) = \int F(\mathcal{N}, \alpha)[P(\alpha) - P_{\mathrm{G}}(\alpha)]d^2\alpha + \underbrace{\int F(\mathcal{N}, \alpha) P_{\mathrm{G}}(\alpha) d^2\alpha}_{\equiv \bar{F}_\infty(\mathcal{N})}$$

$$\leq \|P(\alpha) - P_{\mathrm{G}}(\alpha)\|_1 + \bar{F}_\infty(\mathcal{N}), \tag{2.165}$$

where $\|f(\alpha)\|_1 = \int |f(\alpha)|d^2\alpha$ is the 1-norm and $\bar{F}_\infty(\mathcal{N})$ represents the average fidelity with respect to the limit $N_{\mathrm{s}} \to \infty$. The maximal fidelity $\mathcal{F}_{\mathrm{TG}}$ that can be obtained by the cloner is then found by optimizing with respect to $\mathcal{N}$,

$$\mathcal{F}_{\mathrm{TG}} = \max_{\mathcal{N}} \bar{F}(\mathcal{N}) \leq F_{\mathrm{TG}} \equiv \|P(\alpha) - P_{\mathrm{G}}(\alpha)\|_1 + F_{\mathrm{nc}}, \tag{2.166}$$

where $F_{\mathrm{nc}} = \max_{\mathcal{N}} \bar{F}_\infty(\mathcal{N})$ is the well known no-cloning limit for the Gaussian codebook, according to Eq. (2.162) [229]. Thus, the truncation adds the correction term

$$\|P(\alpha) - P_{\mathrm{G}}(\alpha)\|_1 = \int_0^\infty \frac{e^{-\frac{|\alpha|^2}{2\sigma^2}}}{2\pi\sigma^2} \left(\frac{\Theta(N_{\mathrm{s}} - |\alpha|^2)}{1 - e^{-\frac{N_{\mathrm{s}}}{2\sigma^2}}} - 1 \right) d^2\alpha = 2e^{-\frac{N_{\mathrm{s}}}{2\sigma^2}}. \tag{2.167}$$

We plot F_{TG} as a function of σ and N_{s} in Fig. 2.14(b) and observe that, in the limits $\sigma \to \infty$ and $N_{\mathrm{s}} \to \infty$ with $\sigma^2 \neq N_{\mathrm{s}}$, we reproduce $F_{\mathrm{TG}} = F_{\mathrm{nc}} = 2/3$. In a realistic experiment, the truncation number N_{s} is determined by physical boundary conditions such as finite energy supply or compression. For fixed N_{s}, we then minimize F_{TG} with respect to σ to find the optimal codebook [229]. The analytical solution can be expressed in terms of product logarithm functions and is not shown here since it is a bulky expression. In the cutoff range of $1 - 10$ photons, we reach minimal values $F_{\mathrm{TG}} \simeq 0.86$. Note that F_{TG} is an upper bound for the actual no-cloning limit $\mathcal{F}_{\mathrm{TG}}$. The quantitative deviation between F_{TG} and $\mathcal{F}_{\mathrm{TG}}$ is not known and requires a more detailed investigation.

Besides the classical limit and the no-cloning limit, there are several other fidelity thresholds to benchmark the performance of the protocol. As an example, if we employ a single squeezed state as a resource, fidelity is limited by $F \leq 1/\sqrt{2}$ [239]. Even higher thresholds than the no-cloning limit emerge in case we want to rule out that the teleportation results can be explained by local hidden variables. For qubit teleportation, this limit is given by [240]

$$F_{\mathrm{lhv}} = \frac{1}{2} + \sqrt{\frac{3}{2}} \frac{\arctan\sqrt{2}}{\pi} \simeq 0.87. \tag{2.168}$$

However, we are not aware of such a limit for CV systems. Throughout this work, our gold standard to benchmark the success of our teleportation experiments is $F > 1/2$ to demonstrate a quantum advantage and $F > 2/3$ to demonstrate security.

2.3 Gaussian analog projector formalism

Throughout this work, we realize quantum teleportation using an analog feedforward channel, implying that we transmit the feedforward from Alice to Bob as a classical propagating signal without digitization. In this section, we discuss the general formulation of Gaussian quantum communication protocols as analog quantum channels. The central component of this discussion is the Gaussian analog projector (GAP) formalism, which explains the mechanism of approximating a phase space projection of a quantum signal with Gaussian operations. This effect is realized by an interplay of strong phase-sensitive amplification of one signal quadrature with gain $G \gg 1$ to increase the power in the to-be-measured quadrature to a degree that the vacuum fluctuations become negligibly small. The signal can then be treated as classical with respect to this quadrature, implying that the quadrature has been detected. The resulting process resembles a homodyne detection (projection onto infinitely squeezed states) [48, 204, 241]. To retrieve the measurement outcome, we need to attenuate the signal back to its original energy level. If one realized this attenuation by a simple attenuation channel, as provided by Eq. (2.146), the vacuum fluctuations, coupled in from the environment would degrade the measurement result. Thus, we realize this attenuation by weakly coupling the amplified mode into an auxiliary mode using a directional coupler [84]. With this artificial multi-mode extension, which we realize by employing quantum-correlated auxiliary modes, we can implement an effective classical attenuation channel and keep the attenuated state pure. In Sec. 2.3.1, we discuss this mechanism at the example of analog quantum teleportation. The results of the corresponding experimental realization are discussed in chapter 6. We investigate analog RSP and analog dense coding in Sec. 2.3.2 and thereby verify that the GAP formalism provides a general tool to implement analog CV quantum protocols.

2.3.1 Gaussian quantum teleportation with analog feedforward

A schematic illustration of the Gaussian analog teleportation protocol is provided in Fig. 2.15. The entangled resource is formed by a TMS state, which is generated by superimposing two orthogonally squeezed states at a symmetric beam splitter [83]. The analog Bell detection setup is realized by a frequency-degenerate Josephson mixer (JM) [242–244]. The JM consists of two symmetric beam splitters forming a Mach-Zehnder interferometer [245–248]. Each of the respective interferometer paths contains a JPA. These two JPAs perform strong phase-sensitive amplification of orthogonal quadratures with degenerate gain G. The resulting action of the JM on two input modes, $\hat{a}_1$ and $\hat{a}_2$ is given by the expression [249]

$$\hat{M}^{\dagger} \begin{pmatrix} \hat{a}_1 \\ \hat{a}_2 \end{pmatrix} \hat{M} = \begin{pmatrix} \sqrt{G}\hat{a}_1 + \sqrt{G-1}\hat{a}_2^{\dagger} \\ \sqrt{G}\hat{a}_2 + \sqrt{G-1}\hat{a}_1^{\dagger} \end{pmatrix}. \tag{2.169}$$
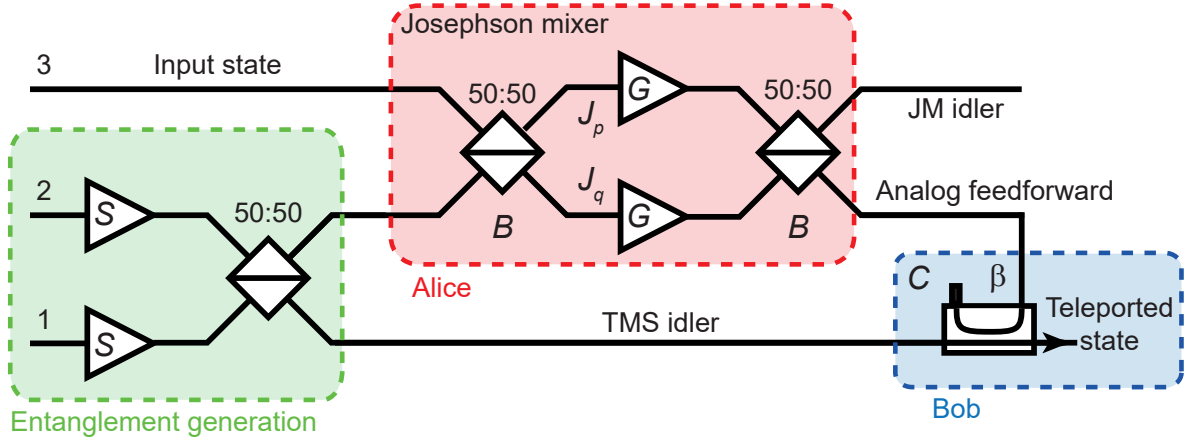
Figure 2.15: Scheme for the analog Gaussian quantum teleportation protocol. The entanglement resource is formed by a TMS state generated by the entanglement JPAs. Two additional measurement JPAs, amplifying orthogonal quadratures with gain $G \gg 1$, implement the Bell detection. Subsequently, the measurement outcome is transmitted to Bob as a classical analog signal. Conditioned on the feedforward, Bob displaces his TMS mode using a directional coupler C with a coupling parameter β.

Thus, the JM acts like a single JPA with spatially separated signal and idler ports. In a teleportation experiment, we employ the JM as a heterodyne detector and the vacuum fluctuations at the input idler mode lead to the first quduty. One of the JM outputs provides the analog feedforward signal, which is directly transmitted to Bob. Bob then couples the signal to his mode of the predistributed entanglement using a directional coupler with coupling $\beta \ll 1$ [84]. The directional coupler realizes Bob's analog displacement operation. The displacement factor is $\sqrt{\beta}\alpha$ and α is the displacemet in the feedforward [76]. However, the directional coupler fulfills the second purpose of realizing the phase space projection in joint action with Alice's JM [78]. Next, we formulate the protocol as a Gaussian quantum channel. We start with the three-mode Gaussian state

$$\mathbf{d} = \begin{pmatrix} 0 \\ 0 \\ \mathbf{d}_{\mathrm{in}} \end{pmatrix}, \qquad \mathbf{V} = \frac{1}{4} \begin{pmatrix} \mathbb{1}_2 \cosh 2r & \sigma_z \sinh 2r & \mathbb{0}_2 \\ \sigma_z \sinh 2r & \mathbb{1}_2 \cosh 2r & \mathbb{0}_2 \\ \mathbb{0}_2 & \mathbb{0}_2 & \mathbb{1}_2 \end{pmatrix}, \qquad (2.170)$$

consisting of the predistributed TMS state with squeeze factor r in paths 1 and 2 and a coherent state with displacement vector $\mathbf{d}_{\mathrm{in}}$ in the third path. The quantity $\mathbb{0}_2$ denotes the (2×2) zero matrix. According to Eq. (2.150), we describe the symmetric beam splitters by $\boldsymbol{B} = \boldsymbol{B}^{(2,3)}(1/\sqrt{2})$ and the coupler by $\boldsymbol{C} = \boldsymbol{B}^{(1,2)}(\sqrt{1-\beta})$. The phase-sensitive amplification of the measurement JPAs in the JM is described by [78]

$$\boldsymbol{J} = \begin{pmatrix} \mathbb{1}_2 & \mathbb{0}_2 & \mathbb{0}_2 \\ \mathbb{0}_2 & \boldsymbol{J}_q & \mathbb{0}_2 \\ \mathbb{0}_2 & \mathbb{0}_2 & \boldsymbol{J}_p \end{pmatrix}, \qquad \boldsymbol{J}_q = \begin{pmatrix} 1/\sqrt{G} & 0 \\ 0 & \sqrt{G} \end{pmatrix}, \qquad \boldsymbol{J}_p = \begin{pmatrix} \sqrt{G} & 0 \\ 0 & 1/\sqrt{G} \end{pmatrix}. \qquad (2.171)$$

The teleportation protocol from Fig. 2.15 can then be expressed by the matrix

$$\boldsymbol{T} = \boldsymbol{CBJB} = \frac{1}{2} \begin{pmatrix} 2\sqrt{1-\beta}\mathbb{1}_2 & \sqrt{\beta}(\boldsymbol{J}_q - \boldsymbol{J}_p) & \sqrt{\beta}(\boldsymbol{J}_q + \boldsymbol{J}_p) \\ -2\sqrt{\beta}\mathbb{1}_2 & \sqrt{1-\beta}(\boldsymbol{J}_q - \boldsymbol{J}_p) & \sqrt{1-\beta}(\boldsymbol{J}_q + \boldsymbol{J}_p) \\ \mathbb{0}_2 & -\boldsymbol{J}_q - \boldsymbol{J}_p & -\boldsymbol{J}_q + \boldsymbol{J}_p \end{pmatrix}. \quad (2.172)$$

We can formulate the protocol as a Gaussian quantum channel, according to Eq. (2.143), by letting $\boldsymbol{X} = \boldsymbol{T}$ and by setting the additive contributions $\boldsymbol{Y}$ and $\mathbf{d}_\Phi$ to zero. We apply this Gaussian channel to Eq. (2.170) and divide the resulting covariance matrix $\boldsymbol{V}'$ into nine (2×2) blocks $\boldsymbol{V}'_{ij}$. The diagonal elements $\boldsymbol{V}'_{ii}$ correspond to the local covariance matrix in path i and the off-diagonal elements $\boldsymbol{V}'_{ij}$, $i \neq j$ correspond to the remaining correlations between path i and j after the protocol. The teleported output state is given by the final state in path 1 and reads

$$\mathbf{d}_{\text{out}} = \frac{\sqrt{\beta}}{2}(\boldsymbol{J}_q + \boldsymbol{J}_p)\mathbf{d}_{\text{in}}, \quad (2.173)$$

$$\boldsymbol{V}_{\text{out}} = \boldsymbol{V}'_{11} = \frac{1}{16}\Big\{ 4(1-\beta)\cosh 2r\mathbb{1}_2 + 2\sqrt{1-\beta}\sqrt{\beta}\sinh 2r(\boldsymbol{J}_q - \boldsymbol{J}_p)\sigma_z$$
$$+ 2\sqrt{1-\beta}\sqrt{\beta}\sinh 2r\sigma_z(\boldsymbol{J}_q - \boldsymbol{J}_p) + \beta\cosh 2r(\boldsymbol{J}_q - \boldsymbol{J}_p)^2 + \beta(\boldsymbol{J}_q + \boldsymbol{J}_p)^2 \Big\}. \quad (2.174)$$

From Eq. (2.173), we find the power matching condition for the displacement

$$G = \frac{2\sqrt{1-\beta}+2}{\beta} - 1 = \frac{4}{\beta} + \mathcal{O}(1). \quad (2.175)$$

In the next step, we drop terms $\mathcal{O}(\beta^2)$ and thus approximate $\sqrt{1-\beta} \simeq 1$. In addition, we take the projective limit

$$\beta \to 0, \qquad G \to \infty, \qquad k \equiv \frac{G\beta}{4} = \text{const.} \quad (2.176)$$

I.e., we increase the gain and simultaneously reduce the coupling in a way that their product remains constant. The parameter k describes the effective amplification or attenuation of the input state during the protocol and takes the role of the feedforward gain in the framework of Gaussian quantum teleportation [47]. In the following, we assume $k = 1$, which implies that the measurement gain G exactly compensates for the coupling β and the beam splitters. In the limit described by Eq. (2.176), the quantity $\sqrt{\beta/G}$ converges rapidly to zero and the renormalized operators $\boldsymbol{J}_q$ and $\boldsymbol{J}_p$ asymptotically transform into the quadrature projection operators:

$$\frac{\sqrt{\beta}}{2}\boldsymbol{J}_q \to \boldsymbol{\Pi}_q, \qquad\qquad \frac{\sqrt{\beta}}{2}\boldsymbol{J}_p \to \boldsymbol{\Pi}_p. \quad (2.177)$$

Aside from power matching between input and output states, the projection condition, $k = 1$, guarantees that we satisfy the requirement $\left(\sqrt{k}\mathbf{\Pi}_{q,p}\right)^2 = \sqrt{k}\mathbf{\Pi}_{q,p}$, necessary for any projector. The interferometer geometry of the JM rotates phase space by $\pi/4$, which implies that the measurement is performed in the hybridized Bell basis [20]

$$\tilde{q}(q,p) = \frac{q+p}{\sqrt{2}}, \qquad \tilde{p}(q,p) = \frac{q-p}{\sqrt{2}}. \tag{2.178}$$

Thus, the measurement operators transform to $\mathbf{\Pi}_+ = (\mathbf{\Pi}_q + \mathbf{\Pi}_p)/2 = \mathbb{1}_2/2$ and $\mathbf{\Pi}_- = (\mathbf{\Pi}_q - \mathbf{\Pi}_p)/2 = -\sigma_z/2$. The teleported state can then be expressed in terms of projection operators by reordering them into the (2×6) block matrix $\mathbf{\Pi}$ according to

$$\mathbf{d}_{\text{out}} = \mathbf{d}_{\text{in}}, \qquad \boldsymbol{V}_{\text{out}} = \mathbf{\Pi}\boldsymbol{V}\mathbf{\Pi}^\dagger, \qquad \mathbf{\Pi} = (\mathbb{1}_2\,\mathbf{\Pi}_-\,\mathbf{\Pi}_+). \tag{2.179}$$

If we insert the TMS state, the final covariance matrix can be expressed in the form

$$\boldsymbol{V}_{\text{out}} = \frac{1}{4}\mathbb{1}_2 + \text{Tr}\left(\boldsymbol{\mathcal{O}}_\Pi \boldsymbol{V}_{\text{TMS}}\right)\mathbb{1}_2, \qquad \boldsymbol{\mathcal{O}}_\Pi = \begin{pmatrix} \mathbf{\Pi}_+ & \mathbf{\Pi}_- \\ \mathbf{\Pi}_- & \mathbf{\Pi}_+ \end{pmatrix}, \tag{2.180}$$

where $\boldsymbol{V}_{\text{TMS}}$ denotes the covariance matrix of the TMS input state and $\boldsymbol{\mathcal{O}}_\Pi$ is an effective measurement operator for $\boldsymbol{V}_{\text{TMS}}$. The second term on the right hand side of $\boldsymbol{V}_{\text{out}}$ measures the interference between the symmetrically projected local elements of the TMS resource and the antiymmetrically projected off-diagonal elements. Throughout this work, we refer to this additive term as the interference function. In case the beam splitter and amplification phases are suitably chosen, the interplay between symmetric and antisymmetric projection leads to destructive interference which corrects for the two quduties and leads to a trace of zero in Eq. (2.180) in the limit $r \to \infty$, which purifies the state. In particular, we obtain

$$\boldsymbol{V}_{\text{out}} = \frac{1}{4}(1 + 2e^{-2r})\mathbb{1}_2, \tag{2.181}$$

leading to the well-known result $F = 1/(e^{-2r} + 1)$ [58]. As expected, we find $F = 1/2$ and $\boldsymbol{V}_{\text{out}} = 3\mathbb{1}_2/4$ in the classical case, $r = 0$. Remembering that these results are obtained from the assumptions stated in Eq. (2.176), we repeat the calculations with the exact expressions. For $r = 0$, we find the simple exact result

$$\boldsymbol{V}_{\text{c}} = \underbrace{\frac{k}{4}\mathbb{1}_2}_{\text{(I)}} + \underbrace{\frac{k}{4}\mathbb{1}_2}_{\text{(II)}} + \underbrace{\frac{1}{4}(1-\beta)\mathbb{1}_2}_{\text{(III)}} + \underbrace{\frac{\beta^2}{32k}\mathbb{1}_2}_{\text{(IV)}}. \tag{2.182}$$

One finds $\boldsymbol{V}_{\text{c}} = 0.74\mathbb{1}_2$ for typical experimental parameters $\beta = -15\,\text{dB}$, $G = 21\,\text{dB}$, implying that the error due to the projective limit approximation is of the order of $1 - 2\,\%$. Term (I) in Eq. (2.182) corresponds to the amplified vacuum fluctuations in the

input state. Term (II) is the first quduty from the idler input of the JM and term (III) corresponds to the second quduty emerging from the uncorrelated vacuum fluctuations at the directional coupler input. Term (IV) results from the vacuum fluctuations in the deamplified quadratures and rapidly converges to zero in the projective limit. Next, we investigate the final states in the residual paths. The final three-mode displacement vector is given by

$$\mathbf{d}' = \boldsymbol{T} \cdot \mathbf{d} \simeq \frac{1}{2} \begin{pmatrix} 2\mathbf{d}_{\text{in}} \\ \sqrt{G}\mathbf{d}_{\text{in}} \\ \sqrt{G}\sigma_z\mathbf{d}_{\text{in}} \end{pmatrix}, \tag{2.183}$$

and for the covariance matrices, we obtain

$$\boldsymbol{V}'_{22} = \frac{1}{16}\left[\underbrace{\beta\cosh 2r}_{(\text{I})} + \underbrace{4\sinh 2r}_{(\text{II})} + \underbrace{G\cosh 2r}_{(\text{III})} + \underbrace{G}_{(\text{IV})}\right]\mathbb{1}_2, \tag{2.184}$$

$$\boldsymbol{V}'_{33} = \frac{1}{16}\left[\underbrace{G\cosh 2r}_{(\text{V})} + \underbrace{G}_{(\text{VI})}\right]\mathbb{1}_2 = \frac{G\cosh^2 r}{8}\mathbb{1}_2. \tag{2.185}$$

Expression (I) describes the coupling of Bob's part of the TMS state to path 2 with coupling β. Term (II) describes the constructive interference between the quantum correlations of Alice's and Bob's TMS state. This term compensates for the energetic loss, resulting from the destructive interference on Bob's side. Terms (III) and (V) describe Alice's part of the TMS state which is amplified by the JM. The origin of terms (IV) and (VI) are the amplified first quduty and the amplified vacuum fluctuations of the input state. The states $\boldsymbol{V}'_{22}$ and $\boldsymbol{V}'_{33}$ contain all energetic contributions, emerging from the TMS state resource and the JM amplification, such that the overall energy balance is fulfilled, which is also reflected by the fact that $\det \boldsymbol{T} = 1$ before taking the projective limit. The remaining elements $\boldsymbol{V}'_{ij} = \boldsymbol{V}'_{ji}$ are given by

$$\boldsymbol{V}'_{12} = \frac{\sqrt{G}}{8}(e^{-2r} + 1)\mathbb{1}_2, \qquad \boldsymbol{V}'_{13} = \frac{\sqrt{G}}{8}(1 - e^{-2r})\mathbb{1}_2, \qquad \boldsymbol{V}'_{23} = \frac{G\cosh^2 r}{8}\sigma_z. \tag{2.186}$$

So far, we have investigated the idealized case $k = 1$ for coherent state teleportation. However, in a realistic experiment, this condition cannot be realized. Instead, we fix the gain G (and therefore k) at a desired value and treat it as an independent parameter [47, 250]. We can now repeat the previous calculation for an arbitrary Gaussian input state $(\mathbf{d}_{\text{in}}, \boldsymbol{V}_{\text{in}})$. In the projective limit, we find

$$\mathbf{d}_{\text{out}} = \sqrt{k}\mathbf{d}_{\text{in}}, \qquad \boldsymbol{V}_{\text{out}} = k\boldsymbol{V}_{\text{in}} + \frac{1}{4}C(r,k)\mathbb{1}_2, \tag{2.187}$$

where in analogy to Eq. (2.180), we define the interference function [251]

$$C(r,k) \equiv (1+k)\cosh 2r - 2\sqrt{k}\sinh 2r. \qquad (2.188)$$

The interference function superimposes the two diagonal elements with the respective off-diagonal elements of the TMS resource in a destructive interference process. The structure of Eq. (2.188) reveals the importance of choosing $k = 1$. In this case, the e^{2r} contributions exactly compensate and we can reach $C(r,k) \to 0$ by increasing the squeezing. In the case $k \neq 1$, a fraction of the e^{2r} terms does not cancel, which leads to a maximally mixed output state, $C(r,k) \to \infty$, in the limit $r \to \infty$. The structure of Eq. (2.188) reveals that the fundamental physical origin of this fact is that amplification is a local process, which allows us to uniquely identify the mode which has been amplified. On the other hand, the correlations are perfectly delocalized over the system, implying perfect indistinguishability of the paths and hence perfect symmetry between the paths with respect to amplification. Thus, in case Alice's mode is amplified with gain k, the gain splits up asymmetrically over the local states, according to $(1+k)$, but symmetrically according to $2\sqrt{k}$ over the two nonlocal contributions. The interference function superposes the average local part and the average nonlocal part. However, resulting from the different symmetry with respect to amplification, these averages correspond to an arithmetic mean for local part and a geometric mean for the nonlocal contribution. The AM-GM inequality then implies that the only way to cancel all e^{2r} contributions is to balance both modes in the TMS with respect to power [142]. In case $k \neq 1$, this implies that Bob needs to either attenuate $(k < 1)$ or amplify $(k > 1)$ his state. Both options do not lead to an improved teleportation performance, either because of the SQL or because of the vacuum noise coupled in from the environment during the attenuation process. This finding stresses the necessity of $k = 1$ for optimal performance of the protocol. However, we can only ensure $k \simeq 1$ in any practical realization. Thus, as discussed in the following paragraph, there is a finite optimum r_* in resource squeezing which maximizes the experimental teleportation fidelity. As a practical consequence, optimal exploitation of a highly-squeezed TMS resource state requires to satisfy $k \to 1$ as close as possible.

Occasionally, e.g., for the calculation of Δ in Eq. (2.157), resource squeezing r enters the fidelity expression via the function

$$C_\Delta(r,k) = (1 + 6k + k^2)\cosh 4r - 4\sqrt{k}(1+k)\sinh 4r + (k-1)^2. \qquad (2.189)$$

This second interference function can be expressed as $C_\Delta = 2C^2(r,k)$. For a coherent state $|\alpha\rangle$, the fidelity can be expressed as [231]

$$F_{\mathrm{q}} = \frac{2}{C(r,k)+k+1}\exp\left[-2\frac{(\sqrt{k}-1)^2}{C(r,k)+k+1}|\alpha|^2\right]. \qquad (2.190)$$

In the classical case, $r = 0$, one then obtains

$$F_{\mathrm{c}} = \frac{1}{k+1} \exp\left[-\frac{(\sqrt{k}-1)^2}{k+1}|\alpha|^2\right],\tag{2.191}$$

which reproduces the $F = 1/2$ limit for $k = 1$. An interesting scenario occurs if we allow for $k \neq 1$. In this case, we can optimize Eq. (2.191) with respect to k for fixed $|\alpha|^2$. This optimum always exists and can be described by a third order polynomial in $\sqrt{k}$. For typical photon numbers $|\alpha|^2 = 1$, this optimum is located at $k = 1/3$, leading to an optimal fidelity $F = 3\sqrt{3}/8 \simeq 0.65$, which significantly exceeds the $1/2$ limit although we do not employ entanglement. In the limit $|\alpha|^2 \ll 1$, we can approximate $F_{\mathrm{c}} = 1/(1+k)$. Indeed, it is then optimal to choose $k \to 0$. In this case, Alice "cheats" and simply switches off her measurement devices. Since Alice and Bob then both compare the statistical overlap of their respective uncorrelated vacuum fluctuations, they reach $F = 1$. Nevertheless, no information can be transferred in this case since the codebook size is limited to effectively one state. In addition, the resulting protocol can no longer be considered to be quantum teleportation as it does not involve any projective measurement. As a result of the above discussion we have to fix $k \simeq 1$ in a realistic teleportation experiment. Otherwise, the $F = 1/2$ limit is not valid. Although we have not performed such experiments within this work, we can also use Eq. (2.187) to determine the teleportation fidelity for a squeezed state with squeeze factor r_{s} [226],

$$F_{\mathrm{sq}} = 2\left(\frac{2}{3k^2 + 2k + 3 + C_\Delta(r,k) + 4(k+1)C(r,k)\cosh 2r_{\mathrm{s}}}\right)^{\frac{1}{2}}.\tag{2.192}$$

For the sake of completeness, we also give the expression for teleportation of a thermal state with photon number n_{th} [252],

$$F = \frac{2}{A(r,k,n_{\mathrm{th}}) - \sqrt{B(r,k,n_{\mathrm{th}})}},\tag{2.193}$$

with

$$A(r,k,n_{\mathrm{th}}) = 2 + 4n_{\mathrm{th}}(1 + n_{\mathrm{th}}) + (1 + 2n_{\mathrm{th}})C(r,k),$$
$$B(r,k,n_{\mathrm{th}}) = 2n_{\mathrm{th}}(n_{\mathrm{th}} + 1)\left[8n_{\mathrm{th}}(n_{\mathrm{th}} + 1) + 4(1 + 2n_{\mathrm{th}})C(r,k) + C_\Delta(r,k)\right].$$

In the previous considerations, we have seen that it is not beneficial to aim for the limit $r \to \infty$ unless k exactly equals 1. As a verification, we plot $C(r,k)$ in Fig. 2.16 for various values of k and clearly observe that $C(r,k)$ has a finite minimum $r_*(k)$ for $k \neq 1$ and fidelity depends on $|\alpha|^2$ [253]. We now perform a similar optimization procedure as in Ref. 250, where the effective feedforward gain has been optimized for fixed squeezing. However, in contrast to the discussion in this reference, we now fix k and optimize with
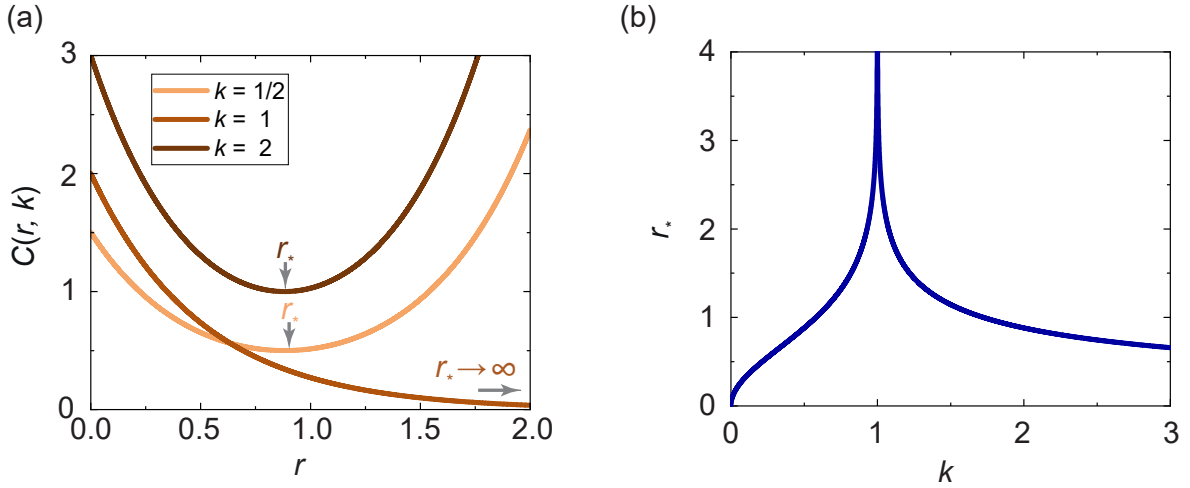
Figure 2.16: (a) Interference function $C(r,k)$ as a function of resource squeeze factor r for various gains k. For $k \neq 1$, $C(r,k)$ is minimal at finite r_*. For $k \to 1$, $C(r,k)$ asymptotically approaches zero in the limit $r \to \infty$. (b) Optimal resource state squeezing r_* of the interference function as a function of k. We find a logarithmic divergence at $k=1$.

respect to r [254]. This simplifies the optimization problem since according to Eq. (2.187), r only implicitly enters in $\boldsymbol{V}_{\text{out}}$ and thus in all fidelity quantities via the interference function. We find

$$\left(\frac{\partial C}{\partial r}\right)_k = 0 \implies r_*(k) = \frac{1}{2}\operatorname{arctanh}\left(\frac{2\sqrt{k}}{k+1}\right) \xrightarrow[k\to 1]{k>1} \ln\left(\frac{2}{\sqrt{k-1}}\right) + \mathcal{O}(k-1). \quad (2.194)$$

We observe that a finite r_* exists for any $k \neq 1$, $k > 0$ and that $r_*(k)$ shows a logarithmic divergence at $k = 1$, indicating that the regimes $0 < k < 1$ and $k > 1$ behave fundamentally different. We find that each r_* always corresponds to two distinct coexisting values of k, one in the regime $0 \leq k \leq 1$ and one solution $k > 1$. At the optimum r_*, the interference function takes the simple shape $C(r_*, k) = |k - 1|$. At $k = 1$, $C(r_*, k)$ becomes non-differentiable and we observe critical behavior which resembles a first-order phase-transition with an ordered phase at $0 \leq k \leq 1$ and a disordered phase at $k > 1$. This can be seen by determining the Rényi-2 entropy [185, 255],

$$S_2(r_*, k) \equiv \begin{cases} 0 & 0 \leq k \leq 1, \\ \ln(2k - 1) & k > 1. \end{cases} \quad (2.195)$$

We clearly observe that we obtain an ordered and a disordered regime. Equation (2.195) enables us to define the order parameter $O = e^{S_2} - (2k - 1)$, which shows a critical exponent of 1 [256]. The transition happens when we cross the border between attenuation and amplification regime. The physical reason for this phase-transition like behavior is the fact that the TMS state can correct for quantum noise up to two qudities in the limit
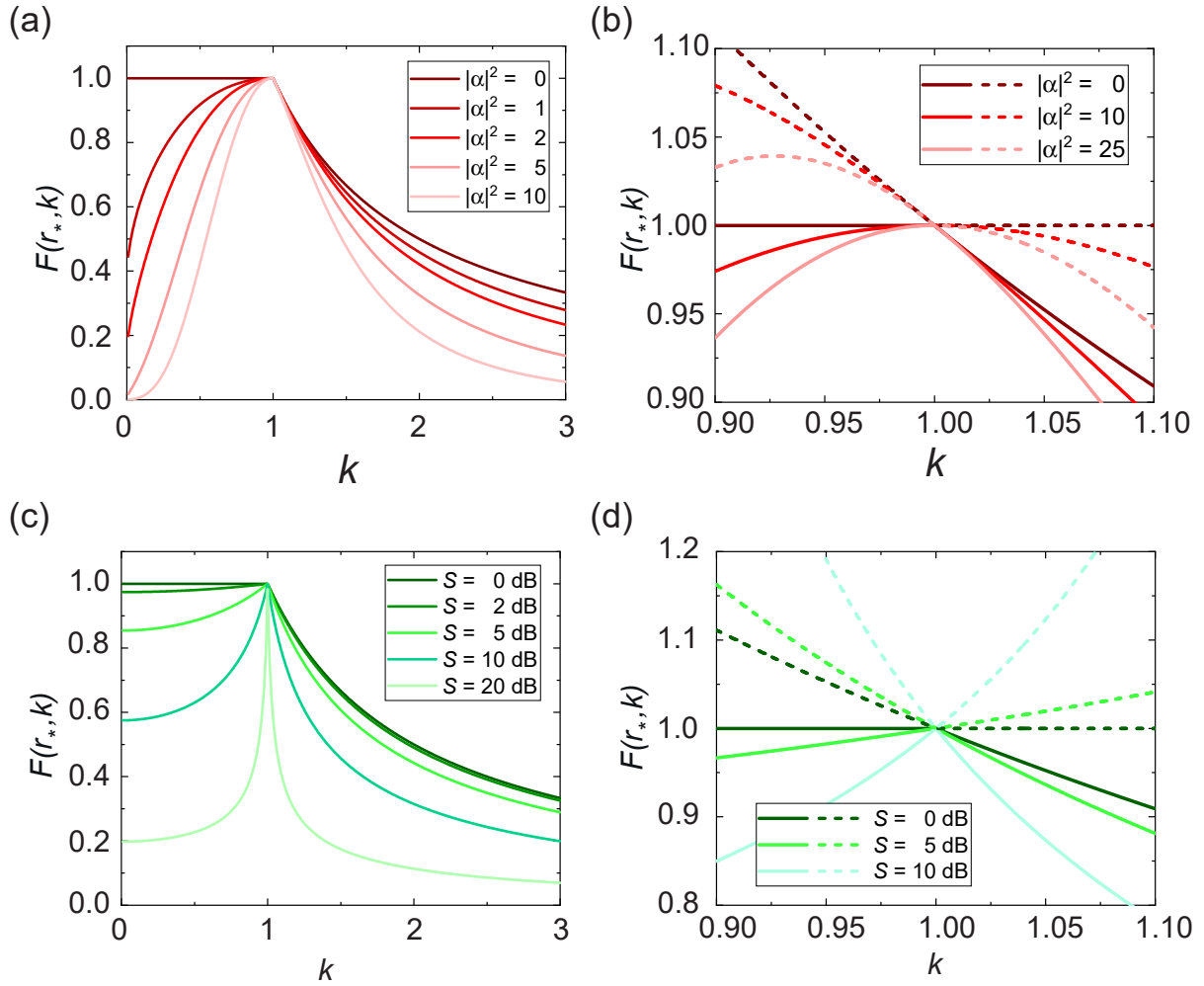
Figure 2.17: (a), (b) Maximally achievable teleportation fidelity $F_{\mathrm{q}}(r_*, k)$ as a function of k for a coherent state. (c), (d) Maximally achievable fidelity for $F_{\mathrm{sq}}(r_*, k)$ squeezed state teleportation. At $k = 1$, we observe that the solution is non-differentiable, which indicates a separation between two different teleportation regimes. At this point, the coexisting solutions from Eq. (2.196) and Eq. (2.197) intercept. The physically relevant solution thereby always corresponds to the minimum. The second solution is indicated by the dashed lines in panels (b) and (d).

of a maximally entangled state, $r \to \infty$. This is equivalent to saying that each ancillary introduced path can be used to correct for half a quantum of noise. For $0 \le k \le 1$, the quantum noise in the teleported state corresponds to $3/2$ photons and we can always adjust r properly in a way such that we achieve perfect correction for the quduties in the system. For $k > 1$, the energy of the quantum noise in the system exceeds $3/2$ photons and the quduties can no longer be fully compensated, even by a maximally entangled state. Instead, it is more beneficial to reduce the resource squeezing with increasing k due to the imbalance in the interference function. For the optimal fidelity of coherent state

teleportation, we find

$$F_{\mathrm{q}}(r_*, k) = \begin{cases} \exp\left(-|\alpha|^2(\sqrt{k}-1)^2\right) \equiv F^\flat & 0 \le k \le 1, \\ \frac{1}{k}\exp\left(-|\alpha|^2\frac{(\sqrt{k}-1)^2}{k}\right) \equiv F^\sharp & k > 1. \end{cases} \tag{2.196}$$

This fidelity is plotted in Fig. 2.17(a) and Fig. 2.17(b) for various displacement photon numbers $|\alpha|^2$. We observe that for $|\alpha|^2 = 0$, the solution $F^\flat$ remains flat until $k = 1$, where we observe sharp decline, according to $F^\sharp$. Mathematically, the two solutions $F^\flat$ and $F^\sharp$ both exist for all $k \ge 0$. At $k = 1$, both solutions intersect and the physically relevant solution always corresponds to the smaller value. In the analogy of phase-transitions, this fact resembles the principle of minimal Gibbs free energy [257]. Panel (c) and panel (d) of Fig. 2.17 show the corresponding result for squeezed state teleportation. In this case, the optimum fidelity is given by

$$F_{\mathrm{sq}}(r_*, k) = \sqrt{2}\begin{cases} \frac{1}{1+k^2+(1-k^2)\cosh 2r_{\mathrm{s}}} & 0 \le k \le 1, \\ \frac{1}{\sqrt{1+k^2+(k^2-1)\cosh 2r_{\mathrm{s}}}} & k > 1, \end{cases} \tag{2.197}$$

according to Eq. (2.192).

2.3.2 Application to other quantum communication protocols

So far, we have used the example of quantum teleportation to show that the interplay between phase-sensitive amplifiers and directional couplers can asymptotically realize analog projective measurement operations if we take the projective limit Eq. (2.176). Next, we demonstrate that the GAP formalism can be used to describe the analog implementation of other quantum communication protocols based on projective measurements and classical feedforward. In particular, we investigate the specific type of decoding protocols depicted in Fig. 2.18(a) and the encoding protocols shown in Fig. 2.18(b). In decoding protocols $\boldsymbol{P}_{\mathrm{d}}$, Alice transmits a potentially unknown quantum state to Bob by employing $n-1$ ancilla modes and Bob decodes the state using a unitary operation $\boldsymbol{U}$. Encoding protocols $\boldsymbol{P}_{\mathrm{e}}$ correspond to the reverse scheme, where Alice employs a unitary operation to encode a message which is then forwarded to Bob who performs a measurement. Correlations between different modes are realized by beam splitters [48], generally described by the blocks $\boldsymbol{B}_1$ and $\boldsymbol{B}_2$ and the block $\boldsymbol{M}$ corresponds to analog projective measurement by phase-sensitive amplification with gain G. We assume that the signal passes b_1 (b_2) beam
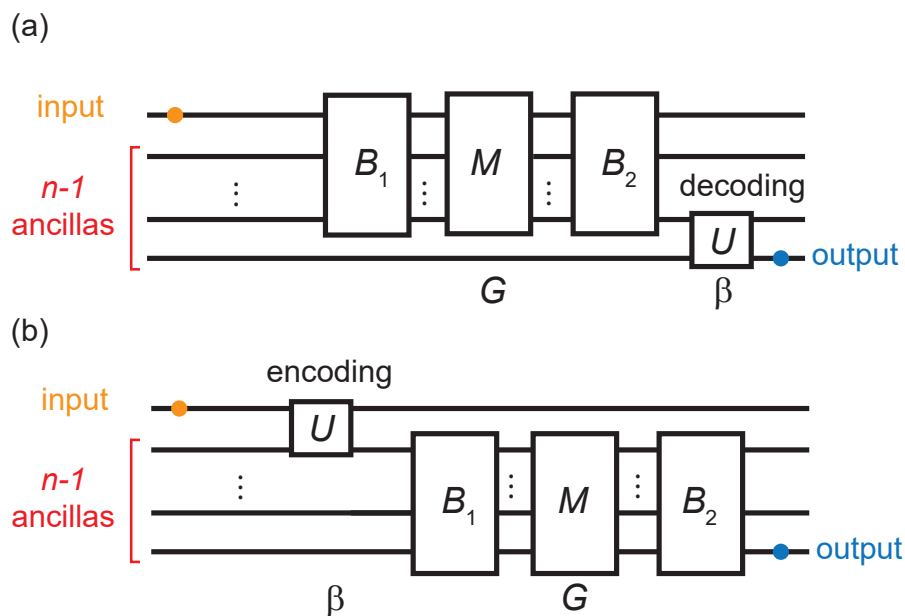
Figure 2.18: (a) Schematic quantum circuit for a certain class of analog decoding protocols, such as quantum teleportation or RSP. For such a protocol, an unknown input state is correlated with $n-2$ ancilla modes using a beam splitter block $\boldsymbol{B}_1$. Next, the joint state is measured by block $\boldsymbol{M}$, and we allow for potential superposition of the measurement results by a second set of beam splitters, $\boldsymbol{B}_2$. The measurement results are transmitted to Bob via an analog feedforward, who then decodes the state using a unitary operation $\boldsymbol{U}$ such as a directional coupler. (b) Schematic quantum circuit for a certain class of analog encoding protocols, such as dense coding. In such a scenario, the state is encoded by Alice and measured by Bob.

splitters in block $\boldsymbol{B}_1$ ($\boldsymbol{B}_2$). As for quantum teleportation, the unitary decoding/encoding displacement operation is realized by a directional coupler with coupling $\beta \ll 1$. Both types of protocols then implement a respective Gaussian channel,

$$\boldsymbol{P}_{\mathrm{d}}(G, \beta, \{\boldsymbol{J}_i\}) = \boldsymbol{U}(\beta)\boldsymbol{B}_2\boldsymbol{M}(G, \{\boldsymbol{J}_i\})\boldsymbol{B}_1, \tag{2.198}$$

$$\boldsymbol{P}_{\mathrm{e}}(G, \beta, \{\boldsymbol{J}_i\}) = \boldsymbol{B}_2\boldsymbol{M}(G, \{\boldsymbol{J}_i\})\boldsymbol{B}_1\boldsymbol{U}(\beta). \tag{2.199}$$

The analog measurement operation $\boldsymbol{M}$ depends on operators $\boldsymbol{J}_i$, which describe a phase-sensitive amplification in path i with gain G. Next, we take the projective limit, i.e. we let $G \to \infty$ and $\beta \to 0$ while the product of these quantities remains constant. The joint action of the amplifiers and the unitary operation then leads to the transformation

$$\sqrt{\frac{\beta}{2^{b_1+b_2}}}\boldsymbol{J}_i \to \sqrt{k}\boldsymbol{\Pi}_i, \tag{2.200}$$

where $\boldsymbol{\Pi}_i$ is a phase space projector. The performance of the protocol is then determined by the projectivity

$$k_{b_1+b_2} = \left(\frac{1}{2}\right)^{b_1+b_2} G\beta. \tag{2.201}$$

In Sec. 2.3, we have extensively studied the theory of analog quantum teleportation. In this case, we have set $k = k_2$ [cf. Eq. 2.176]. In the following, we use the additional examples of analog RSP as a decoding protocol and analog dense coding as an encoding protocol to verify that our framework can be applied to general analog quantum communication schemes.

Remote state preparation   As a first example, we can consider the CV-RSP protocol [258], extensively described in Ref. 112. This protocol is similar to quantum teleportation and the goal of RSP is Alice's entanglement-assisted preparation of a known squeezed state at Bob's side. For this purpose, Alice strongly amplifies one signal quadrature and Bob performs a conditioned unitary operation using a directional coupler, in direct analogy to quantum teleportation. It can be shown that this protocol can become unconditionally secure and simultaneously reduces the amount of bits which needs to be sent by Alice through the classical channel. In contrast to teleportation, RSP is a two-path protocol with $b_1 = b_2 = 0$ and thus, the projectivity is $k_0 = \beta G$, according to Eq. 2.201. Inserting the RSP protocol into Eq. (2.198) gives the covariance matrix of the remotely prepared state as

$$\boldsymbol{V}_{\mathrm{RSP}} = \frac{1}{4}\left[\cosh 2r\mathbb{1}_2 + \sqrt{\beta}\sinh 2r\left(\boldsymbol{J}\sigma_z + \sigma_z\boldsymbol{J}^\dagger\right) + \beta\cosh 2r\boldsymbol{J}\boldsymbol{J}^\dagger\right], \tag{2.202}$$

where $\boldsymbol{J}$ describes the phase-sensitive amplification of Alice's measurement JPA with gain G and r is the resource squeezing. We now assume that Alice amplifies the q-quadrature

and take the projective limit, which yields

$$\boldsymbol{V}_{\text{RSP}} = \frac{1}{4}\left[\cosh 2r\boldsymbol{\Pi}_p + \boldsymbol{\Pi}_q C(r, k_0)\right], \tag{2.203}$$

where $C(r, k_0)$ corresponds to the interference function. As a result, the analog RSP is equivalent to quantum teleportation if we replace the heterodyne JM with a single homodyne detector and the existence of squeezing in the final state relies on the same interference mechanism as the purification of the final state in quantum teleportation. If we fulfill the projection condition $k_0 = 1$, we immediately find the well known result for RSP [259],

$$\boldsymbol{V}_{\text{RSP}} = \frac{1}{4}\left[\cosh 2r\boldsymbol{\Pi}_p + 2e^{-2r}\boldsymbol{\Pi}_q\right]. \tag{2.204}$$

Analog dense coding protocol   So far, we have only discussed decoding protocols. Next, we apply the GAP formalism to analog dense coding, which can be regarded as the reverted quantum teleportation protocol [59]. In dense coding, quantum correlations are exploited to improve classical data transfer rates [15]. In the CV case, Alice and Bob share a classical channel and exploit a TMS state to improve the classical channel capacity up to a factor of two. Like for teleportation, a TMS state is distributed as ancillary modes in the first two paths and the coherent input signal is coupled into the second path by Alice using a directional coupler. Following that, the TMS state is measured by two orthogonal phase-sensitive amplifiers in the configuration of a heterodyne detector [260]. The dense coding protocol is then given by

$$\boldsymbol{D} = \boldsymbol{JBC}, \tag{2.205}$$

where $\boldsymbol{J}$ corresponds to orthogonal strong phase-sensitive amplification, $\boldsymbol{J}_q$ and $\boldsymbol{J}_p$, by two measurement JPAs and $\boldsymbol{B}$ is a symmetric beam splitter operation between path one and path two. Thus, we have $b_1 = 0$ and $b_2 = 1$ in Eq. (2.200). The protocol can be expressed as

$$\boldsymbol{D} = \frac{1}{\sqrt{2}}\begin{pmatrix} \boldsymbol{J}_q & \sqrt{1-\beta}\boldsymbol{J}_q & \sqrt{\beta}\boldsymbol{J}_q \\ -\boldsymbol{J}_p & \sqrt{1-\beta}\boldsymbol{J}_p & \sqrt{\beta}\boldsymbol{J}_p \\ \mathbb{0}_2 & -\sqrt{2\beta}\mathbb{1}_2 & \sqrt{2(1-\beta)}\mathbb{0}\mathbb{1}_2 \end{pmatrix}. \tag{2.206}$$

Next, we take the projective limit $\beta \ll 1$, $G \gg 1$ and define $k_1 \equiv G\beta/2$ [cf. Eq. 2.201], and determine the final two-mode covariance matrix after the detector, which takes the form

$$\boldsymbol{V}' = \frac{1}{4}\begin{pmatrix} (e^{-2r}G + k_1)\boldsymbol{\Pi}_p & \mathbb{0}_2 \\ \mathbb{0}_2 & (e^{-2r}G + k_1)\boldsymbol{\Pi}_q \end{pmatrix}. \tag{2.207}$$

In case we combine the measurement for the displacement, we find

$$\mathbf{d}' = \sqrt{k_1}\mathbf{d}_0, \tag{2.208}$$

where $\mathbf{d}_0$ denotes the input displacement. We observe that in this limit, we lose all information about respective orthogonal field quadratures in both paths. We assume a Gaussian codebook with variance σ^2 for the coherent input state [cf. Eq. (2.158)]. For the photon number in the first mode, we then find

$$\bar{n} = 2\beta\sigma^2 + \sinh^2 r, \tag{2.209}$$

which enables us to determine the Shannon mutual information between Alice and Bob, according to Eq. (2.128). We approximate homodyne detection of q- and p-quadrature by the two phase-sensitive JPAs and obtain

$$I_\mathrm{s}(\mathrm{A:B}) = \underbrace{\frac{1}{2}\ln\left(1 + \frac{4k_1\sigma^2 e^{2r}}{G + k_1 e^{2r}}\right)}_{q-\text{quadrature}} + \underbrace{\frac{1}{2}\ln\left(1 + \frac{4k_1\sigma^2 e^{2r}}{G + k_1 e^{2r}}\right)}_{p-\text{quadrature}} \simeq \ln\left(1 + \frac{4k_1\sigma^2 e^{2r}}{G}\right). \tag{2.210}$$

In Eq. (2.210), we use the approximation $G \gg k_1 e^{2r}$. This approximation is valid since we work in the projective limit for G and keep r and k_1 finite. In the following, we set $k_1 = 1$, which enables us to directly extract the initial displacement. We now optimize the mutual information for fixed $\bar{n}$, in analogy to the Braunstein-Kimble scheme [59]. The maximized mutual information is then equivalent to the classical channel capacity C_cl. In a similar way as in Ref. 59, we find $2\beta\sigma^2 = \sinh r \cosh r$ and $\bar{n} = e^r \sinh r$. This directly provides the well-known result

$$C_\mathrm{cl} = \ln(1 + \bar{n} + \bar{n}^2) \to 4r. \tag{2.211}$$

We furthermore obtain the classical capacity, according to photon counting from an ensemble of number states with maximum entropy [261, 262],

$$C_\mathrm{cl} = (1 + \bar{n})\ln(1 + \bar{n}) - \bar{n}\ln\bar{n} \to 2r. \tag{2.212}$$

We therefore obtain the expected improvement by a factor of two, which demonstrates the possibility of fully analog dense coding using phase-sensitive JPAs and directional couplers. The physical intuition behind this improvement is that we employ the TMS state to compensate for the prefactor of $1/2$ in Shannon mutual information in Eq. (2.210). This factor arises when we only detect one quadrature and thereby lose all information about the orthogonal field quadrature. Correcting for this factor of $1/2$ is only possible if we additionally measure the orthogonal quadrature. This requires to connect the two orthogonal JPAs in a heterodyne configuration using a symmetric beam splitter. Since a beam splitter is an intrinsic 4-port device [73], we lose the information advantage of detecting both quadratures by decreasing the SNR due to one added quduty resulting from the input vacuum fluctuations at the second input port of the beam splitter [263]. We can compensate for this quduty by using entanglement. In case we keep the coupling

β finite, we obtain the local covariance matrices

$$\boldsymbol{V}'_{11} = \frac{\boldsymbol{J}_q^2}{8} \left[C(1-\beta, -r)\boldsymbol{\Pi}_p + C(1-\beta, r)\boldsymbol{\Pi}_q + \beta\mathbb{1}_2 \right], \tag{2.213}$$

$$\boldsymbol{V}'_{22} = \frac{\boldsymbol{J}_p^2}{8} \left[C(1-\beta, r)\boldsymbol{\Pi}_p + C(1-\beta, -r)\boldsymbol{\Pi}_q + \beta\mathbb{1}_2 \right]. \tag{2.214}$$

A numerical investigation then reveals that we obtain a quantum advantage in classical channel capacity for squeezing $r > 0.7808 + 0.5049\beta$. Note that further improvement by a factor exceeding two can be obtained by employing multimode correlations, as shown in Ref. 264.

2.3.3 Wigner function formulation of analog quantum teleportation

So far, we have treated analog quantum teleportation and related protocols as Gaussian channels. Next, we provide a generalized alternative formulation of our protocol in terms of Wigner functions [259]. To verify that such a Wigner function formulation is particularly useful to describe non-Gaussian protocols, we analyze analog teleportation of Fock states [251]. Fock state teleportation is of particular relevance in the scope of hybrid schemes which employ TMS states to teleport qubit states [265, 266]. In the first step, we investigate the transformation of the Wigner function in the projective limit. We consider general linear ℓ-mode phase space operations $\hat{O}$, transforming $\hat{R}' = \hat{O}\hat{R}$. We obtain the corresponding transformation of the Wigner function, $W_{\text{in}} \to W_{\text{out}}$, by applying the Weyl correspondence, Eq. (2.90). The quadrature moments of the transformed phase space coordinates satisfy

$$\text{Tr}\left(\hat{\rho}'\hat{R}'\right) = \int W_{\text{out}}(\mathbf{R})\mathbf{R}d^{2\ell}\mathbf{R}. \tag{2.215}$$

Simultaneously, we have

$$\text{Tr}\left(\hat{\rho}'\hat{R}'\right) = \text{Tr}\left[\hat{\rho}(\hat{O}\hat{R})\right] = \int W_{\text{in}}(\mathbf{R})\boldsymbol{O}\mathbf{R}d^{2\ell}\mathbf{R} = \frac{1}{\det \boldsymbol{O}} \int W_{\text{in}}(\boldsymbol{O}^{-1}\tilde{\mathbf{R}})\tilde{\mathbf{R}}d^{2\ell}\tilde{\mathbf{R}}. \tag{2.216}$$

By comparing Eq. (2.215) and Eq. (2.216), we find

$$W_{\text{out}}(\mathbf{R}) = \frac{1}{\det \boldsymbol{O}} W_{\text{in}}(\boldsymbol{O}^{-1}\mathbf{R}). \tag{2.217}$$

Since we treat our protocol as unitary, we let $\det \boldsymbol{O} = 1$ in the following.

Interplay of a phase-sensitive JPA and a directional coupler   Before investigating the full teleportation protocol, we analyze the effect of the interplay between phase-sensitive amplifiers and weak directional couplers. In this case, we start with the separable two-mode Wigner function

$$W(\mathbf{R}) = W_{\mathrm{a}}(q_1, p_1) W_{\mathrm{in}}(q_2, p_2), \tag{2.218}$$

where $W_{\mathrm{a}}(q_1, p_1)$ denotes an ancillary mode at the coupler input (conventionally assumed to be the vacuum state) and $W_{\mathrm{in}}(q_2, p_2)$ is an unknown input state. We apply a phase-sensitive amplification $\boldsymbol{J}$, followed by an asymmetric beam splitter operation $\boldsymbol{C}$,

$$\boldsymbol{J} = \begin{pmatrix} \mathbb{1}_2 & \mathbb{0}_2 \\ \mathbb{0}_2 & \boldsymbol{J}_q \end{pmatrix}, \qquad \boldsymbol{C} = \begin{pmatrix} \sqrt{1-\beta} & \sqrt{\beta} \\ -\sqrt{\beta} & \sqrt{1-\beta} \end{pmatrix} \otimes \mathbb{1}_2, \tag{2.219}$$

where we assume without loss of generality that we amplify the q-quadrature. After approximating $\sqrt{1-\beta} \simeq 1$, we can express the resulting Wigner function as

$$W(\boldsymbol{J}^{-1}\boldsymbol{C}^{-1}\mathbf{R}) = W_{\mathrm{a}}(q_1 - \sqrt{\beta}q_2, p_1 - \sqrt{\beta}p_2) W_{\mathrm{in}}\left(\sqrt{\frac{\beta}{G}}q_1 + \frac{q_2}{G}, \sqrt{\beta G}p_1 + \sqrt{G}p_2\right). \tag{2.220}$$

The final Wigner function at the output of the coupler is given by

$$W_{\mathrm{out}}(q_1, p_1) = \int_{-\infty}^{\infty} dq_2 \int_{-\infty}^{\infty} dp_2 W(\boldsymbol{J}^{-1}\boldsymbol{C}^{-1}\mathbf{R}). \tag{2.221}$$

Next, we use the substitutions

$$q_2' = \sqrt{\frac{\beta}{G}}q_1 + \frac{q_2}{\sqrt{G}}, \qquad p_2' = \sqrt{\beta G}p_1 + \sqrt{\beta}p_2, \tag{2.222}$$

define $k_0 \equiv \sqrt{\beta G}$ and take the projective limit, implying that we neglect terms $\mathcal{O}(\beta)$ and $\mathcal{O}(\sqrt{\beta/G})$. The result can be rewritten as

$$\begin{aligned} W_{\mathrm{out}}(q_1, p_1) &= \int_{-\infty}^{\infty} dq_2' \int_{-\infty}^{\infty} dp_2' W_{\mathrm{a}}(q_1 - \sqrt{k_0}q_2', p_1) W_{\mathrm{in}}(q_2', p_2'), \\ &= \int_{-\infty}^{\infty} dq_2' W_{\mathrm{a}}(q_1 - \sqrt{k_0}q_2', p_1) w_{\mathrm{in}}^{(q)}(q_2') \\ &= \frac{1}{\sqrt{k_0}} W_{\mathrm{a}}(q_1, p_1) \star w_{\mathrm{in}}^{(q)}\left(\frac{q_1}{\sqrt{k_0}}\right), \end{aligned} \tag{2.223}$$

where $w_{\mathrm{in}}^{(q)}(q)$ denotes the marginal distribution of the input state with respect to the q-quadrature and $\star$ denotes the convolution operator. The final state is thus the convolution of $w_{\mathrm{in}}^{(q)}(q)$ with the ancillary input state and k_0 acts as a scaling factor for the final quasiprobability distribution. We especially observe that in the asymptotic limit, $G \to \infty$,

the action of phase-sensitive amplification can be expressed as

$$W\left(\frac{p}{\sqrt{G}}, \sqrt{G}q\right) \to \frac{W\left(\frac{p}{\sqrt{G}}, d_q\right)}{\sqrt{G}w^{(q)}(d_q)}\delta\left(q - \frac{d_q}{\sqrt{G}}\right), \qquad (2.224)$$

where d_q denotes the displacement along the q-axis and $w^{(q)}(d_q)$ is the marginal probability distribution with respect to the q-quadrature. If the ancilla would be a Dirac δ with respect to q_1, and p_1, Eq. (2.223) would correspond to an ideal projective phase space measurement if we let $k_0 = 1$. Nevertheless, according to quantum mechanics, $W_a(q_1, p_1)$ needs to be at least in the vacuum state. In the case of Gaussian input states, this implies that the variance of the output state is broadened by the vacuum fluctuations, according to the Gaussian convolution theorem. In the general case where we add n vacuum fluctuations to the state, fidelity reduces to $F = 2/(2+n)$. Thus, the maximal fidelity which we can reach by only measuring one quadrature, according to the scheme described by Eq. (2.223) coincides with the asymptotic no-cloning limit, $F = 2/3$. In quantum teleportation, we exploit that, although the Heisenberg uncertainty relation prevents a Dirac δ-correlation between local field quadratures [267], it allows for perfect correlation between different quadrature superpositions in nonlocal modes. As such, we need to introduce a second ancillary mode. This second mode can be regarded as an "investment" since it reduces the fidelity which we can classically achieve from 2/3 to 1/2. This is a result from the necessity of a heterodyne detection scheme in this case, which implies that we need to add a second quduty. However, as we have extensively studied in Sec. 2.3, introducing two ancillary modes simultaneously enables us to reach $F \to 1$ by properly employing quantum correlations. Thus, CV quantum teleportation can be regarded as entanglement-assisted ideal projective measurement of both quadratures of an unkwon input state [259].

Analog quantum teleportation   Next, we study the full teleportation protocol and start with the three-mode Wigner function

$$W(q_1, p_1, q_2, p_2, q_3, p_3) = W_{\text{TMS}}(q_1, p_1, q_2, p_2)W_{\text{in}}(q_3, p_3). \qquad (2.225)$$

By using the definition $G \equiv e^{2\phi}$ and Eq. (2.217), the argument in the initial Wigner function transforms according to

$$\boldsymbol{T}^{-1} = \begin{pmatrix} \mathbb{1}_2 & -\sqrt{\beta}\mathbb{1}_2 & \mathbb{0}_2 \\ \sqrt{k}\sigma_z & \sinh\phi\sigma_z & -\cosh\phi\mathbb{1}_2 \\ \sqrt{k}\mathbb{1}_2 & \cosh\phi\mathbb{1}_2 & -\sinh\phi\sigma_z \end{pmatrix}, \qquad (2.226)$$

where $k \equiv G\beta/4$. The final covariance matrix is obtained by

$$W_{\text{out}}(q_1, p_1) = \int W(\boldsymbol{T}^{-1}\mathbf{R})dq_2 dp_2 dq_3 dp_3. \qquad (2.227)$$

We now perform the substitution

$$\begin{pmatrix} \tilde{q}_2 \\ \tilde{p}_2 \\ \tilde{q}_3 \\ \tilde{p}_3 \end{pmatrix} = \underbrace{\begin{pmatrix} \sinh\phi & 0 & -\cosh\phi & 0 \\ 0 & -\sinh\phi & 0 & -\cosh\phi \\ \cosh\phi & 0 & -\sinh\phi & 0 \\ 0 & \cosh\phi & 0 & \sinh\phi \end{pmatrix}}_{\equiv \boldsymbol{M}} \begin{pmatrix} q_2 \\ p_2 \\ q_3 \\ p_3 \end{pmatrix}. \qquad (2.228)$$

The matrix $\boldsymbol{M}$ is unitary and skew-involuntary, $\boldsymbol{M}^{-1} = -\boldsymbol{M}$, which reflects the fact that it describes the Bogoliubov transformation, induced by the JM and therefore belongs to the Lorentz group [268]. We observe that if we take the projective limit, this full rank matrix becomes degenerate with rank 2, implying that we lose all information about two field quadratures, as expected. However, this limit can only be approached asymptotically in a realistic experiment with finite energy.[9] Thus, we still assume that $\boldsymbol{M}$ preserves full rank. For the phase space coordinates (q_1', p_1') of the final state, we make the approximation

$$q_1' = q_1 + \tilde{q}_2\sqrt{\beta}\sinh\phi - \tilde{q}_3\sqrt{\beta}\cosh\phi \simeq q_1 + \sqrt{k}(\tilde{q}_2 - \tilde{q}_3), \qquad (2.229)$$

$$p_1' = p_1 - \tilde{p}_2\sqrt{\beta}\sinh\phi - \tilde{p}_3\sqrt{\beta}\cosh\phi \simeq p_1 - \sqrt{k}(\tilde{p}_2 + \tilde{p}_3). \qquad (2.230)$$

We then find

$$W_{\text{out}}(q_1, p_1) = \int W(q_1 + \sqrt{k}(\tilde{q}_2 - \tilde{q}_3), p_1 - \sqrt{k}(\tilde{p}_2 + \tilde{p}_3), \tilde{q}_2, \tilde{p}_2, \tilde{q}_3, \tilde{p}_3)d\tilde{q}_2 d\tilde{p}_2 d\tilde{q}_3 d\tilde{p}_3. \ (2.231)$$

This is the central result for the analog quantum teleportation protocol in terms of Wigner functions which enables us to extend our analysis to non-Gaussian states. As an example, we evaluate the teleportation of Fock states [251]. This consideration is of high impact for the concept of hybrid quantum teleportation [265, 266], in case a TMS resource is used for teleportation of a qubit state. Teleportation of a Fock state $|n\rangle$ is thereby possible since the TMS resource contains contributions from all possible photon numbers, according to Eq. (2.114). The Wigner function of Fock state $|n\rangle$ is given by

$$W_n(\alpha) = \frac{2}{\pi}(-1)^n e^{-2|\alpha|^2} L_n(4|\alpha|^2) \qquad \Longrightarrow \qquad W_1(\alpha) = \frac{2}{\pi}e^{-2|\alpha|^2}(1 - 4|\alpha|^2), \quad (2.232)$$

with the Laguerre polynomials $L_n(x)$ [48]. Next, we use Eq. (2.231) to exemplary demonstrate teleportation of Fock state $|1\rangle$ using a TMS state with squeeze factor r as a

---

[9]Note that despite taking the projective limit, we still treat the protocol as unitary since all our operations are Gaussian. Otherwise, we would have $\det \boldsymbol{O} = 0$ in Eq. (2.217).

resource. The four Gaussian integrals in Eq. (2.231) can be determined in a lengthy but straightforward calculation. For the final Wigner function, we find

$$W_{\mathrm{out}}(\alpha) = \frac{\exp\left(-\frac{2|\alpha|^2}{k+C(r,k)}\right)}{\pi[k+C(r,k)]^3}\left[8k|\alpha|^2 - g(r,k)\right], \qquad g(r,k) = 2k^2 - C_\Delta(r,k), \quad (2.233)$$

where $C(r,k)$ and $C_\Delta(r,k)$ represent the interference functions. Next, we calculate the fidelity

$$\begin{aligned}
F &= \frac{4}{[k+C(r,k)]^3}\int_0^\infty \exp\left(-2|\alpha|^2\frac{1+k+C(r,k)}{k+C(r,k)}\right)\left[8k|\alpha|^2 - g(r,k)\right]|\alpha|d|\alpha| \\
&= \frac{12k - 2k^2 - 2 + C_\Delta(r,k)}{[C(r,k)+1+k]^3}.
\end{aligned} \qquad (2.234)$$

Teleportation of Fock state $|n\rangle$ is successful if F exceeds the limit [269]

$$F_{|n\rangle}^* = \frac{(2n)!}{2^{2n+1}(n!)^2}, \qquad (2.235)$$

which leads to a fidelity threshold of $1/4$ in our case. Equation (2.234) simplifies significantly in the limiting cases of zero resource squeezing. For this classical case, we find the simple formula

$$F(0,k) = \frac{2k}{(1+k)^3}. \qquad (2.236)$$

We thereby find $F(0,0) = 0$ due to orthogonality, $\langle 0|1\rangle = 0$ [48], in contrast to the expected result $\langle 0|\alpha\rangle = \exp\left(-|\alpha|^2/2\right) \to 1$ for coherent states in the limit $|\alpha| \to 0$. Thus, Alice's cheating strategy of switching off the Bell measurement does not work for Fock states. Fidelity then takes a nontrivial maximum of $F = 8/27 \simeq 0.296$ at $k = 1/2$ before dropping to 0 in the high gain limit. For $k = 1$, we obtain the threshold value, described by Eq. (2.235). In the ideal scenario, $k = 1$, Eq. (2.234) simplifies to

$$F(r,1) = \frac{1}{4}\left(1+\tanh r\right)\left(1+\tanh^2 r\right), \qquad (2.237)$$

which takes the expected classical limit of $1/4$ for $r = 0$ and then quickly rises to the asymptotic ideal value of 1 with increasing r. Next, we analyze the conditions under which we can reconstruct a negative region in the final Wigner function. This requires the prefactor of the Gaussian function in Eq. (2.234) to be negative for certain values of $|\alpha|^2$, which is the case if $g(r,k) > 0$. In the classical case, we have $g(0,k) = -2(1+2k) < 0$ and therefore, the Wigner function is completely positive due to the two quduties. Due to $g(r_*,k) = 4k - 2$, we can only obtain a negative region in case we let $k > 1/2$. Next, we

determine the negativity indicator

$$
\begin{aligned}
N(r,k) &= \int \left[|W_{\text{out}}(\alpha)| - W_{\text{out}}(\alpha) \right] d^2\alpha \\
&= \frac{2\pi}{\pi[k + C(r,k)]^3} \int_0^\infty \exp\left(-\frac{2|\alpha|^2}{k + C(r,k)} \right) \\
&\quad \times \left(|8|\alpha|^2 - g(r,k)| - 8|\alpha|^2 + g(r,k) \right) |\alpha| d|\alpha| \\
&= \frac{4}{[k + C(r,k)]^3} \int_0^{\sqrt{\frac{g(r,k)}{8k}}} \exp\left(-\frac{2|\alpha|^2}{k + C(r,k)} \right) [8k|\alpha|^2 - g(r,k)]|\alpha| d|\alpha| \\
&= \frac{g(r,k) + 4k \left[\exp\left(-\frac{g(r,k)}{4k[k + C(r,k)]} \right) - 1 \right] C(r,k)}{[k + C(r,k)]^2}.
\end{aligned}
\tag{2.238}
$$

By defining the normalized interference function $\xi \equiv C(r,k)/k$, the result can be finally expressed as

$$
N(\xi) = -2 + (N_0 + 2)\frac{e^{\frac{\xi}{2}}}{1 + \xi}, \qquad N_0 = -2 + \frac{4}{\sqrt{e}} \simeq 0.4261.
\tag{2.239}
$$

For $\xi = 0$ (i.e., for ideal destructive interference), we reproduce the well-known negativity indicator N_0 for Fock state $|1\rangle$ [270]. Furthermore, $N(\xi) = 0$ for $\xi = 1$. Note that Eq. (2.239) is only valid under the assumption $C(r,k) \leq k$ and thus $k \geq 1/2$. In general, Eq. (2.231) can also be used to analyze Fock state teleportation in case we do not take the projective limit, implying that we treat $\sinh\phi$ and $\cosh\phi$ in Eq. (2.229) and Eq. (2.230) as separate quantities. Alternatively, hybrid quantum teleportation can be directly described in terms of density operators. However, such a consideration requires truncation of Hilbert space at finite dimension [271], similar as in density matrix renormalization group approaches [272]. Details about a formulation of hybrid quantum teleportation in terms of Wigner functions is provided in Appendix D [266, 273].

2.3.4 Shannon mutual information for different codebooks

To employ our analog quantum teleportation protocol for future communication applications, it is necessary to determine the Shannon mutual information $I_{\text{s}}(\text{A} : \text{B})$ between Alice and Bob. In protocols such as teleportation-based QKD [274, 275], the resulting $I_{\text{s}}(\text{A} : \text{B})$ is then compared to a suitable Holevo quantity [276]. In this way, one can calculate the dependence of the maximally achievable secret key rate on the input alphabet [263]. In particular, we determine the final unconditioned probability distribution $P'(\alpha')$ for our quantum teleportation protocol for an infinite Gaussian, a truncated Gaussian, a uniform, and a discrete codebook of input states. In these cases, we can find analytical expressions for $P'(\alpha')$, which can then be used to determine $I_{\text{s}}(\text{A} : \text{B})$ [47]. Finding an analytical expression for $P'(\alpha')$ is particularly useful since this solution can be directly

used to determine $I_\text{s}(\text{A} : \text{B})$ numerically via Eq. (2.128).

Infinite Gaussian codebook First, we demonstrate the corresponding calculation for the infinite Gaussian codebook, Eq. (2.158). Let v_out define the variance of the teleported output state, given by Eq. (2.187) in the loss- and noiseless case. The corresponding conditioned phase space probability distribution for the output state α' is given by the Wigner function in Eq. (2.231) and can be expressed as

$$P'(\alpha'|\alpha) = \frac{1}{2\pi v_\text{out}} \exp\left(\frac{-|\alpha' - \sqrt{k}\alpha|^2}{2v_\text{out}} \right). \tag{2.240}$$

We now sample the input state α from the Gaussian input codebook and apply Bayes' theorem. The unconditioned final probability distribution is then given by the marginal distribution

$$P'(\alpha') = \int P'(\alpha'|\alpha) P_\text{G}(\alpha) d^2\alpha = P'(\alpha'|\alpha) \star P_\text{G}. \tag{2.241}$$

Thus, we convolute the conditioned probability distribution with the input codebook. According to the Gaussian convolution theorem, the resulting probability distribution corresponds to a Gaussian with variance given by the sum of the individual variances,

$$P'(\alpha') = \frac{1}{2\pi(v_\text{out} + k\sigma^2)} \exp\left[\frac{-|\alpha'|^2}{2(v_\text{out} + k\sigma^2)} \right]. \tag{2.242}$$

In that case, the mutual information can be analytically calculated via

$$I_\text{s}(\text{A} : \text{B}) = \int P'(\alpha'|\alpha) P_\text{G}(\alpha) \ln\left(\frac{P'(\alpha'|\alpha)}{P'(\alpha')} \right) d^2\alpha \, d^2\alpha' \tag{2.243}$$

$$= \ln\left(1 + \frac{k\sigma^2}{v_\text{out}} \right) \underbrace{\int P'(\alpha'|\alpha) P_\text{G}(\alpha) d^2\alpha \, d^2\alpha'}_{=1} \tag{2.244}$$

$$+ \underbrace{\int \left[\frac{|\alpha'|^2}{2(v_\text{out} + k\sigma^2)} - \frac{|\alpha' - \sqrt{k}\alpha|^2}{2v_\text{out}} \right] P'(\alpha'|\alpha) P_\text{G}(\alpha) d^2\alpha \, d^2\alpha'}_{=0} \tag{2.245}$$

$$= \ln\left(1 + \frac{k\sigma^2}{v_\text{out}} \right), \tag{2.246}$$

which corresponds to the well-known Shannon mutual information for Gaussian distributions [47, 277]. The second term is zero since α' is unconditionally distributed with variance $v_\text{out} + k\sigma^2$ and, conditionally on α, distributed with variance v_out. Thus, the corresponding expectation values coincide. Consequently, removing the quduties using the TMS resource increases the mutual information between Alice and Bob, as expected. In the ideal case, mutual information is optimized by r_* [cf. Eq. (2.194)] for fixed k and we obtain an optimal $I_\text{s}(\text{A} : \text{B}) = \ln(1 + 4\sigma^2)$ for $k = 1$. In the limit of a broad codebook,

$4\sigma^2 + 1 \simeq 4\sigma^2$, employing entanglement thus increases mutual information by an addend of $\ln 3$, compared to the classical protocol.

Truncated Gaussian codebook   Next, we repeat the previous consideration for a truncated Gaussian codebook, Eq. (2.163). As in the Gaussian case, we first need to determine the unconditioned probability distribution $P'(\alpha')$ for the output state by evaluating the convolution integral in Eq. (2.241). The mutual information can then be determined from Eq. (2.128) by numerical integration. In this case, we cannot apply the Gaussian convolution theorem, implying that we need to explicitly determine the integral in Eq. (2.241), which can be expressed as

$$P'(\alpha') = \mathcal{N}(|\alpha'|) \int \Theta(N_{\mathrm{s}} - |\alpha|^2) \exp\left[-w|\alpha|^2 + \frac{\sqrt{k}}{2v_{\mathrm{out}}}\left(\alpha^*\alpha' + \alpha'^*\alpha\right)\right] d^2\alpha, \qquad (2.247)$$

where

$$\mathcal{N}(|\alpha'|) = \frac{\exp\left[-\frac{|\alpha'|^2}{2v_{\mathrm{out}}}\right]}{4\pi^2\sigma^2 v_{\mathrm{out}}\left(1 - e^{-\frac{N_{\mathrm{s}}}{2\sigma^2}}\right)}, \qquad w = \frac{1}{2\sigma^2} + \frac{k}{2v_{\mathrm{out}}}. \qquad (2.248)$$

Next we decompose, $\mathrm{Re}(\alpha) = |\alpha|\cos\varphi$, $\mathrm{Im}(\alpha) = |\alpha|\sin\varphi$, define $q' \equiv \mathrm{Re}(\alpha')$ and $p' \equiv \mathrm{Im}(\alpha')$, which yields

$$\alpha^*\alpha' + \alpha'^*\alpha = 2|\alpha|(q'\cos\varphi + p'\sin\varphi). \qquad (2.249)$$

This allows us to explicitly perform the polar integration in Eq. (2.247), according to [278]

$$P'(\alpha') = 2\pi\mathcal{N}(|\alpha'|) \int_0^{\sqrt{N_{\mathrm{s}}}} |\alpha| \exp\left(-w|\alpha|^2\right) I_0\left(\frac{\sqrt{k}|\alpha||\alpha'|}{v_{\mathrm{out}}}\right) d|\alpha|$$

$$= 2\pi \frac{v_{\mathrm{out}}^2}{k|\alpha'|^2}\mathcal{N}(|\alpha'|) \int_0^{\frac{\sqrt{kN_{\mathrm{s}}}|\alpha'|}{v_{\mathrm{out}}}} x e^{-ux^2} I_0(x)dx, \qquad (2.250)$$

where $u \equiv wv_{\mathrm{out}}^2/k|\alpha'|^2$ and $I_0(x)$ is the modified Bessel function of the first kind. The integral can be expressed in closed form in terms of a hypergeometric series by expanding $I_0(x)$ in a Taylor series, followed by treating u like a Feynman parameter [110] and application of the generalized Leibniz product rule [279]. We eventually obtain

$$P'(\alpha') = \frac{1}{2\pi(v_{\mathrm{out}} + k\sigma^2)(1 - e^{-N_{\mathrm{s}}/2\sigma^2})} \exp\left[-\frac{|\alpha'|^2}{2(v_{\mathrm{out}} + k\sigma^2)}\right]$$

$$\times \left\{1 - \exp\left[-wN_{\mathrm{s}} - \frac{k|\alpha'|^2}{4wv_{\mathrm{out}}^2}\right] \Phi_3\left(1, 1; \frac{k|\alpha'|^2}{4wv_{\mathrm{out}}^2}, \frac{kN_{\mathrm{s}}|\alpha'|^2}{4v_{\mathrm{out}}^2}\right)\right\}, \qquad (2.251)$$

where $\Phi_3(a, b; x, y)$ denotes the third Humbert hypergeometric function [280].

Uniform codebook   In the next step, we determine $P'(\alpha')$ for a uniform polar symmetric codebook with cutoff photon number N_s,

$$P_\mathrm{u}(\alpha) = \frac{1}{\pi N_\mathrm{s}} \Theta(|\alpha|^2 - N_\mathrm{s}).$$
(2.252)

The calculation is analogue to the truncated Gaussian case and leads to the result

$$P'(\alpha') = \frac{1}{\pi N_\mathrm{s}} \exp\left(-\frac{|\alpha'|^2}{2v_\mathrm{out}}\right) \left\{ \exp\left(\frac{k|\alpha'|^2}{2v_\mathrm{out}}\right) - \exp\left(-\frac{N_\mathrm{s}}{2v_\mathrm{out}}\right) \Phi_3\left(1, 1; \frac{k|\alpha'|^2}{2v_\mathrm{out}}, \frac{kN_\mathrm{s}|\alpha'|^2}{4v_\mathrm{out}^2}\right) \right\}.$$
(2.253)

Discrete Gaussian codebook   A realistic codebook is limited by finite phase resolution of the input state. We can determine the resulting effect on the final probability distribution by considering the Gaussian codebook with discretized phase,

$$P_\mathrm{d}(\alpha) = \frac{1}{N\sigma^2} \exp\left(-\frac{|\alpha|^2}{2\sigma^2}\right) \sum_{l=0}^{N-1} \delta\left(\varphi - \frac{l}{N} 2\pi\right).$$
(2.254)

The final probability distribution can then be expressed as

$$P'(\alpha') = \frac{e^{-\frac{|\alpha'|^2}{2v_\mathrm{f}}}}{4\sqrt{\pi}N\sigma^2 v_\mathrm{f} w} \sum_{l=0}^{N-1} \left[c_l e^{c_l^2} \left(\mathrm{erf}(c_l) + 1\right)\right] + \frac{e^{-\frac{|\alpha'|^2}{2v_\mathrm{f}}}}{4\pi w\sigma^2 v_\mathrm{f}},$$
(2.255)

where we define the sequence

$$c_l = \frac{1}{2}\sqrt{\frac{k}{w}}\left[q'\cos\left(2\pi\frac{l}{N}\right) + p'\sin\left(2\pi\frac{l}{N}\right)\right].$$
(2.256)

In the continuous limit, $N \to \infty$, the sum becomes a Riemann sum [142] and reproduces the result for the infinite Gaussian codebook.

Discrete truncated uniform codebook   The most realistic codebook involves discretized phase and power as well as a power limitation to a maximal photon number N_s. Such a discretized truncated codebook can be realized by

$$P_\mathrm{dt} = \frac{1}{N^2} \sum_{j,l=0}^{N-1} \delta\left(\varphi - 2\pi\frac{l}{N}\right) \delta\left(|\alpha| - \sqrt{N_\mathrm{s}}\frac{j}{N-1}\right).$$
(2.257)

In this case, we find

$$P'(\alpha') = \frac{1}{N^2 v_\mathrm{out}} \exp\left(-\frac{|\alpha'|^2}{2v_\mathrm{out}}\right) \sum_{j,l=0}^{N-1} \exp\left[a_{jl}\right],$$
(2.258)

with

$$a_{jl} = -\frac{k}{2v_{\text{out}}}\frac{j^2}{(N-1)^2} - 2\frac{\sqrt{w}}{v_{\text{out}}}\frac{j}{N-1}c_l.$$

(2.259)

Chapter 3

Experimental techniques

Realization of quantum microwave communication requires a significant level of inter-disciplinary knowledge and advanced technology. In Sec. 3.1, we introduce our basic cryogenic setups as well as the reference-state reconstruction method for our quantum state tomography scheme based on a field-programmable gate array (FPGA).[1] In addition, we describe our photon number calibration method based on Planck spectroscopy. Next, we dedicate Sec. 3.2 to the sample preparation of our JPA chips as well as to fundamental characterization measurements. Following that, we introduce 2D Planck spectroscopy as a novel and more accurate calibration method in Sec. 3.3.[2]

3.1 Reconstruction of propagating quantum microwave states

Quantum state tomography of propagating quantum microwave states requires environmental temperatures below $100\,\mathrm{mK}$. This requirement results from the fact that the energy of microwaves photons, typically at approximately $5\,\mathrm{GHz}$ in our experiments, is lower by a factor of $\simeq 10^5$ compared to that of photons in the optical regime. Thus, our experiments require cryogenic setups based on $^3\mathrm{He}/^4\mathrm{He}$ dilution cooling, which we introduce in Sec. 3.1.1. Since our experiments are typically performed at the level of a few microwave photons, these quantum signals need to be amplified strongly before detection. This amplification procedure drastically reduces the SNR due to broadband noise added by the first amplification stage. Thus, we need to employ elaborate state tomography procedures which we introduce in Sec. 3.1.2. Due to the low SNR, advanced measurements can take multiple days since we need to record a significant amount of averages. To speed the experiments, we perform both data acquisition and *in-situ* data processing within the FPGA-based framework described in Sec. 3.1.3.

---

[1]The FPGA image has been collaboratively developed within a Master's thesis project of R. Neagu. The resulting Master's thesis can be found in Ref. 281.

[2]2D Planck spectroscopy has been collaboratively developed within a Master's thesis project of S. Gandorfer. The resulting Master's thesis can be found in Ref. 282.

3.1.1 Cryogenic setup

In order to cool down our microwave experimental setup to millikelvin temperatures, we employ ^{3}He/^{4}He dilution cryostats [283], where we exploit the spontaneous phase separation of a ^{3}He/^{4}He mixture at $860\,$mK in a first order phase-transition [284–286]. Dilution cooling then results from endothermic diffusion of ^{3}He atoms though the phase
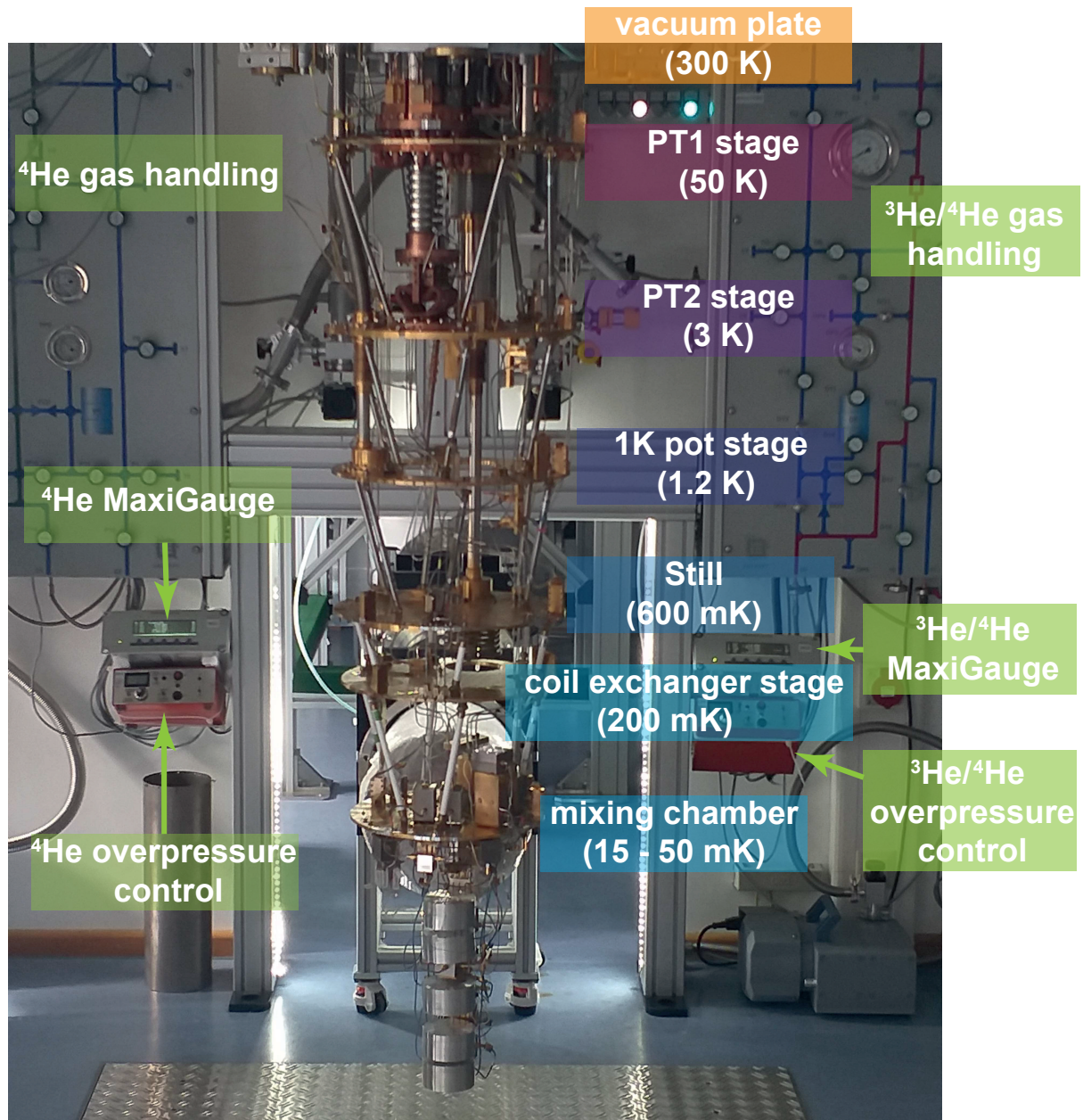

Figure 3.1: Photograph of the Alice dilution cryostat and indication of corresponding temperature stages. The ^{4}He gas handling system on the left side is used for precooling and operation of a dry 1K pot. The ^{3}He/^{4}He gas handling system on the right side is employed to control the dilution cooling.

boundary. The experiments presented in this thesis have been performed in two different laboratories, in the following referred to as the Alice lab or the Bob lab. This nomenclature arises from the fact that within the scope of this work, both labs have been connected for joint quantum communication experiments using a cryogenic link, as extensively discussed in chapter 7.

Alice cryostat   The central component of the Alice lab is the home-built dry dilution refrigerator [287], in the following referred to as Alice. Alice is manually operated using two distinct gas handling systems. Details about the Alice cryostat are provided in Ref. 288. A photograph with labels of the different temperature stages is shown in Fig. 3.1. Alice is equipped with eight stainless steel (SS) microwave input lines [3] and four output lines. From transmission measurements, we estimate the attenuation of these input cables to be $\simeq 16\,\mathrm{dB}$ at room temperature. This value does not include additional attenuation, explicitly added to the different temperature stages to suppress the input thermal noise. Between the mixing chamber stage and the first amplification stage, which is realized with cryogenic HEMT amplifiers, [4] the output lines consist of superconducting coaxial NbTi cables to minimize losses. [5] The experimental setup is protected from the HEMT amplifier noise by two circulators. [6] Between the HEMT amplifiers and the room temperature flange, the output lines consist of silver-plated stainless steel (SSS) cables. [7] The HEMT amplifiers in Alice are operated using a custom built power supply which is temperature-stabilized to $26.0 \pm 0.2\,°\mathrm{C}$. [8] In addition, two separate DC anchors are installed in Alice, one for supply of DC currents or low frequency voltage pulses and another for a four-wire readout of resistance thermometers. [9] More details about the wiring of Alice and the thermometry are provided in Ref. 112.

Bob cryostat   The dilution cryostat ("Bob") in Bob lab is a commercial `Triton` system, provided by Oxford Instruments (OINT). In contrast to Alice, the precooling and mixture circuits are not separated in this cryostat. The precooling of Bob is performed using the $^3\mathrm{He}/^4\mathrm{He}$ mixture under a pressure of up to 3 bar. The precooling of the mixture is realized by a pulse tube refrigerator (PTR) and a Joule-Thompson (JT) impedance. [10] The $^3\mathrm{He}$ gas is pumped out of the mixing chamber (MC) using a turbo-molecular pump (TMP) with a scrolls backing pump and recondensed at a pressure of 500 mbar using the precooling compressor. The mixture is kept clean by guiding it through an external liquid

---

[3]We use `SC-219/50-SS-SS` stainless steel cables from `Coax Co., Ltd` for this purpose.

[4]We use `LNF-LNC4_8A` HEMT amplifiers from `Low Noise Factory` for this purpose.

[5]We use `SC-219/50-NbTi-NbTi` superconducting cables from `Coax Co., Ltd` for this purpose.

[6]We use `CTH1184-KS18` circulators from `Quinstar`, followed by `RADC-4-8-Cryo` circulators from `Raditek` for this purpose.

[7]We use `SC-219/50-SSS-SS` stainless steel cables from `Coax Co., Ltd` for this purpose.

[8]We use a `TECPak 585-05-12` temperature controller from `Arroyo Instruments` for that purpose.

[9]We use a `Lakeshore370` resistance bridge for Alice thermometry.

[10]We use a `PT415-RM` PTR from `Cryomech` for this purpose.

nitrogen (LN$_2$) cold trap. Bob's gas handling and the pumps are controlled electronically, so Bob can be cooled down via a fully automated script. Since Bob has been installed in the framework of this thesis, we describe its wiring and the thermometry in more detail. In analogy to Alice, we add four custom-made SS microwave input lines to Bob, where stainless steel has been chosen for better thermal decoupling of the respective stages due its comparably low thermal conductivity [283]. Significant losses of SS cables around several dB/m at gigahertz frequencies at cryogenic temperatures are not critical for input lines, as long as the radiofrequency (RF) sources are capable of providing sufficient output power and the cryostat can sustain the dissipated heat. The cables are cut using a diamond saw [11] and bent in a loop-shaped way to compensate for the thermal contraction during cooldowns. On each temperature stage, we add a well-defined and well-thermalized attenuator into each input line. This attenuation is chosen such that the noise temperature in the RF lines matches the temperature of the respective cryostat stage. Suitable attenuation values are 20 dB for the first PTR stage (PT1), 10 dB for the second PTR (PT2) and still stages, and 6 dB for the cold plate and MC stages. For JPA pump lines, we use a lower attenuation of 2 dB on cold plate and MC stage due to the limited dynamical range of our microwave sources. This reduced pump line attenuation enables us to apply pump tones which can be regarded as classical signals with photon number $n_{\mathrm{p}} \gg 1$ at the MC stage. For all input lines we use either soldered [12] or crimped [13] SMA connectors. We determine characteristic impedance of each connection using the time domain reflectometry (TDR) and verify 50 Ω matching with a tolerance of ±3 Ω.[14] Crimping of the cables takes less time and effort, compared to soldering. However, there could be the potential drawback that crimped connectors might be more fragile and, thus, suffer from impedance changes due to distorted geometry over multiple cool downs. We typically perform a thermal stress test for our crimped input lines by dipping the connector into LN2, followed by crude heating using a heat gun. After 10 repetitions, we do not observe any further change in impedance, and TDR reveals a tolerable maximal mismatch of 7 Ω. During the measurements, no difference between crimped and soldered lines has been observed. In addition, Bob is equipped with two output lines which are designed analogously to those of Alice. Since our superconducting coaxial cables are more ductile in comparison to their SS counterparts, we do not include a loop but compensate for the thermal contraction by bending them in an S-shaped way. The superconducting coaxial wires are thermalized by annealed silver wires,[15] which are gently wrapped around the cable and fixed with oxygen-free high conductance (OFHC) copper clamps. Thermalization of the SSS cables between the HEMT amplifiers and the room temperature flange is realized with Cu-braids.

---

[11]We use a `11-180` low speed saw from `Buehler Ltd.` for this purpose.

[12]We use `11_SMA-50-2-15/111_NE` connectors from `Huber+Suhner` for this purpose.

[13]We use `R125.052.90` SMA connectors from `Radiall` for crimping.

[14]We use a `DSA8200` digital serial analyzer from `Tektronix` for this purpose.

[15]We use 1.5 mm thick wires with a purity of 99.99 % from `WIELAND Edelmetalle GmbH` annealed in an `Austromat3001` furnace from `Dekema GmbH` for that purpose.

In addition to the commercial OINT thermometry,[16] we install two distinct DC looms, each consisting of 12 twisted wire pairs. One loom is supposed to be used for additional thermometers and the second one for the supply of DC power to avoid crosstalk, which could otherwise especially affect the sensitive four-wire sensor readout. Between room temperature and PT2 stage, we use twisted-pair BeCu-looms which are soldered to a 24 pin `LEMO` connector at the room temperature stage. Below the PT2 stage, we use a 12-twisted-pair wire NbTi-loom. The transition from BeCu to NbTi is realized by 24 pin male and female connectors in a way that each loom can be replaced individually. At the mixing chamber stage, each loom is soldered to a 24 pin `Buerklin` microconnector using custom soldering sleeves made from CuNi capillaries with inner diameter of 0.8 mm.[17] A layer of nonconducting polymer is inserted between the pins to prevent galvanic shorts. Thermalization of the DC wires is realized by carefully clamping the looms between two layers of `Kapton` foil using gold-plated OFHC-Cu slabs at each temperature stage. Thermalization of all DC cables is especially relevant for the thermometer readout, since an insufficient thermal contact would falsify measured temperatures of the sensor. Thus, the `Buerklin` connector at the MC stage is tightly pressed inside an OFHC-Cu housing which is directly screwed to the MC plate and glued with blue `stycast 2850 FT` epoxy. For the HEMT amplifiers, located at 3 K, an additional BeCu-loom has been installed, which allows for direct connection using female nano-D connectors. The HEMT amplifiers are powered by a commercial power supply.[18]

Like in Alice, our central superconducting elements of the setups for quantum microwave experiments are fixed at the MC stage and connected to the input and output lines using SMA connectors. A proper installation of an advanced quantum communication setup is described in detail in chapter 6 during the discussion of our quantum teleportation experiment. The experiments presented in chapters 4-6 have been performed in the Alice lab, whereas the measurements in chapter 8 have been realized over our cryogenic link. In chapter 7, we discuss the cryogenic properties of Alice and Bob in more detail, due to their high relevance for performance of the cryogenic link.

3.1.2 Reference-state reconstruction method

Resulting from the comparably low single photon energies at microwave frequencies, quantum state tomography of propagating microwave signal requires the use of low-noise amplifiers [74]. In the following, we discuss how we can experimentally extract a two-mode quantum state $\hat{a}_i$, $i \in \{1, 2\}$ from noisy measurements. In our experiments, we employ HEMT amplifiers with an approximate gain of $G_i = 40$ dB and a noise temperature of

---

[16]We use a `Lakeshore372` resistance bridge for this purpose.

[17]Cutting segments off such a fragile and soft capillary works optimally by carefully cutting a trench using a scalpel, and then gently breaking the capillary with a tweezer.

[18]We use an `LNF-PS3B` power supply for control of drain voltage and current control, powered by a `LNF-PBA` power block.

2 K at typical frequencies of $5 - 6\,\text{GHz}$. Due to the high gain, the HEMT amplifier noise dominates the overall noise figure of the amplification chain. The resulting complex envelope function, corresponding to the detected signal at room temperature is then given by $\hat{S}_i = \sqrt{G_i}\left(\hat{a}_i + \hat{h}_i^\dagger\right)$. The amplification process results in a low SNR for the detected signal, $\langle\hat{a}_i^\dagger\hat{a}_i\rangle \ll \langle\hat{h}_i^\dagger\hat{h}_i\rangle$, implying that the tomography of propagating microwave states requires elaborate signal reconstruction schemes. Throughout most of this work, we make use of the reference-state reconstruction method, where we use the detected moments $\langle(\hat{S}_1^\dagger)^k(\hat{S}_1)^l(\hat{S}_2^\dagger)^m(\hat{S}_2)^n\rangle_{\text{ref}}$ from a well-known reference signal to eliminate the unknown noise moments $\langle(\hat{h}_1^\dagger)^k(\hat{h}_1)^l(\hat{h}_2^\dagger)^m(\hat{h}_2)^n\rangle$. The reference signal is usually a weak thermal state with a photon number $n_{\text{th}} \ll 1/2$ per mode, which can be approximately considered as vacuum. In this case, reference-state and noise moments are related by a simple proportionality relation [289]. For measurements with higher reference temperatures, $T_{\text{ref}} \gtrsim 60\,\text{mK}$, the thermal statistics can no longer be neglected. In this case, the noise moments can be obtained from the reference moments by inversion of a linear system of equations. The statistical signal moments $\langle(\hat{a}_1^\dagger)^k(\hat{a}_1)^l(\hat{a}_2^\dagger)^m(\hat{a}_2)^n\rangle$, and the quadrature moments $\langle I_1^k Q_1^l I_2^m Q_2^n\rangle$, are linearly related to the detected moments of the complex envelope function and the reference moments. We obtain the quadrature moments by inversion of the corresponding system of linear equations [158].

The reference-state scheme is not the only way to perform tomography of quantum microwaves. Alternative schemes exist, such as the dual-path reconstruction method which requires an additional hybrid ring beam splitter and is implemented with a relative phase shift of 180° between the two paths [74]. The dual-path method has the advantage that it does not require knowledge or existence of the reference state and is slightly more accurate regarding the standard deviation of reconstructed moments [157]. However, the reference-state method requires only one output channel per reconstructed mode which makes it the preferred reconstruction technique throughout most of this work. Nevertheless, we sometimes employ the dual-path technique as an alternative reconstruction method to check for consistency of our results. For future experiments, it is furthermore desired to improve quantum microwave detection by employing single microwave photon detectors [290], e.g., based on Josephson parametric converters [291, 292].

3.1.3 Quantum microwave receiver setup

In this section, we describe our microwave setup and our procedure for Wigner tomography. The latter includes an analog heterodyne downconversion scheme, followed by a digital FPGA-based data processing setup [281, 293]. We discuss the required hardware components as well as the necessary steps for determining the photon statistics of the reconstructed signal.
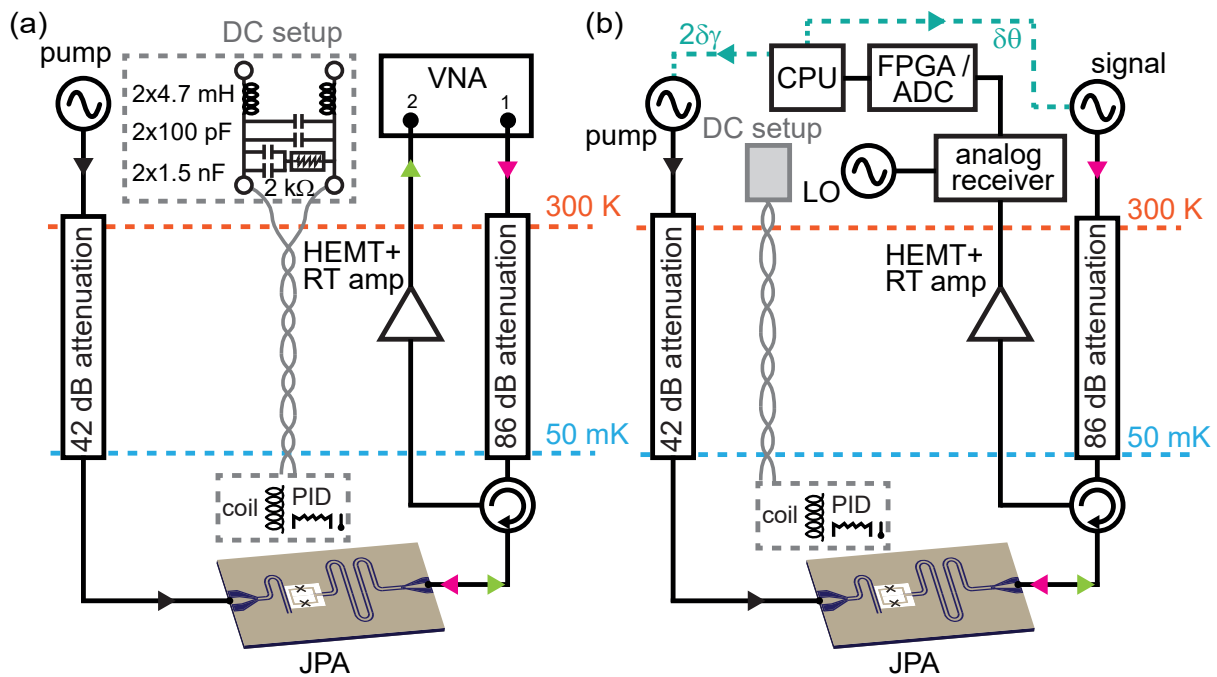
Figure 3.2: (a) Fundamental setup for measuring S_{11} (reflection) and S_{21} (transmission) parameters. The probe signal entering the cryostat is strongly attenuated to suppress the thermal noise and interacts with the JPA. The output (reflected) signal is amplified at multiple stages and detected. The JPA is pumped using a separate RF source ("pump"). Coils, heaters, and sensors are controlled by a DC setup, which includes an analog low-pass at room temperature, shown in the dashed gray box. (b) Fundamental setup for Wigner tomography. A coherent input signal can be provided by an RF source ("signal"). The amplified output signal is detected by the analog receiver, digitized, and further processed. The quantum state is reconstructed on a CPU. The RF sources are phase-stabilized with closed feedback loops (green dashed arrows).

Fundamental measurement setup Before introducing our microwave receiver, we discuss our general measurement setup for fundamental experiments. We synchronize all RF devices using a 10 MHz Rubidium (Rb) clock.[19] For frequency resolved measurements [93, 294], we employ a vector network analyzer (VNA) [295], as schematically depicted in Fig. 3.2(a).[20] The JPA is pumped with a separate RF source.[21] To suppress high-frequency noise in the DC lines and enable sensitive proportional-integral-derivative (PID) control, we use an analog low-pass filter with a cutoff frequency at 100 kHz to remove any high frequency noise contributions in each pair of DC wires as well as in the sensor lines [245, 296]. The basic setup for quantum microwave state reconstruction is depicted in Fig. 3.2(b). In this case, separate RF sources generate the JPA pump tone and potentially required coherent input signals. The RF sources can be amplitude-modulated using a

---

[19]We use a S725 atomic clock from `Stanford Research Systems` for this purpose.

[20]We use a ZVA24 from `Rohde&Schwarz` and a ZNA26 from `Rohde&Schwarz` for this purpose.

[21]We use SGS100A sources from `Rohde&Schwarz` for this purpose.

data timing generator (DTG) [22] in Alice lab or by an 8-port arbitrary waveform generator (AWG) in Bob lab.[23] However, the setup for pulse-modulation is not shown in Fig. 3.2 for simplicity. Full experimental schemes including the modulation setup are provided in Appendix A. One of the RF sources acts as a local oscillator (LO) for the detection chain and is directly referenced to our 10 MHz frequency standard. The remaining RF sources are daisy-chained to the LO source at the reference frequency of 1 GHz. The output phases of our RF sources are stabilized *in-situ* during the experiment via a closed feedback loop. This loop is realized by determining the experimental squeezing (displacement) angle γ_{exp} (θ_{exp}) within each measurement cycle. The RF phase is then corrected by $2\delta\gamma$ ($\delta\theta$), where $\delta\gamma = \gamma_{\text{exp}} - \gamma_{\text{target}}$ ($\delta\theta = \theta_{\text{exp}} - \theta_{\text{target}}$) denotes the deviation from the target phase. The full RF setup is controlled by a custom written LabVIEW code [297].

Heterodyne microwave receiver   Figure 3.3 depicts our microwave receivers in the Alice and Bob labs. Both receivers are constructed in an equivalent way, implying that we do not distinguish between them throughout this work. The receiver is designed for two-mode tomography and enables the reconstruction of bipartite quantum correlations. Before entering the receiver, the signals exiting the cryostat undergo a second amplification stage consisting of two independently controllable RF amplifiers [24] which are temperature-stabilized to $19.5 \pm 0.1\,^{\circ}\text{C}$ by a Peltier cooler.[25] Next, the RF signal is filtered in a bandwidth of $4.9 - 6.2\,\text{GHz}$.[26] For the downconversion to intermediate frequency (IF), ω_{if}, we use a strong independent LO signal, implying that the receiver implements a heterodyne detector. The LO signal is filtered with a pass band of $3 - 7\,\text{GHz}$.[27] In the Alice (Bob) lab, we use $\omega_{\text{if}}/2\pi = 11\,\text{MHz}$ ($\omega_{\text{if}}/2\pi = 12.5\,\text{MHz}$) since these values are well-detuned from the 10 MHz reference within the reconstruction bandwidth. In addition, the choice of 11 MHz in the Alice lab reduces the risk of any impact from technical microwave tones, such as the 10 MHz reference, since 11 is a prime number. However, the frequency choice in the Bob lab has the advantage of being commensurable with the FPGA sampling frequency $\tilde{\omega}/2\pi = 125\,\text{MHz}$. The IF frequency is chosen such that effects of the $1/f$-noise are still negligible, while we are simultaneously well below the Nyquist-Shannon limit with respect to $\tilde{\omega}$ [277, 298]. In the next step, we use image rejection mixers to filter out the blue sideband created during the downconversion process, which otherwise would limit the reconstructed squeezing level to 3 dB [158].[28] Following that, we balance the power in both signal paths using step attenuators [29] and filter the signal within the bandwidth of

---

[22]We use a `DTG 5334` from `Tektronix` for this purpose.

[23]We use an 8-port `HDAWG` AWG from `Zurich Instruments` controlled by the `labOne` interface.

[24]We use `AMT-A003` amplifiers from `Agile MwT` for this purpose.

[25]We use a `Laird` DA-075-12-02-00-00 Peltier cooler and a PT100 thermometer for this purpose.

[26]We use `VPFZ-5500-S+` band-pass filters from `Mini-Circuits` for this purpose.

[27]We use `VHP_26 15542` from `Mini-Circuits` for this purpose.

[28]We use `IRM4080B` mixers from `Polyphase` for this purpose.

[29]We use `ESA2-1-10/8-SFSF` attenuators from `EPX microwave Inc.` for this purpose.
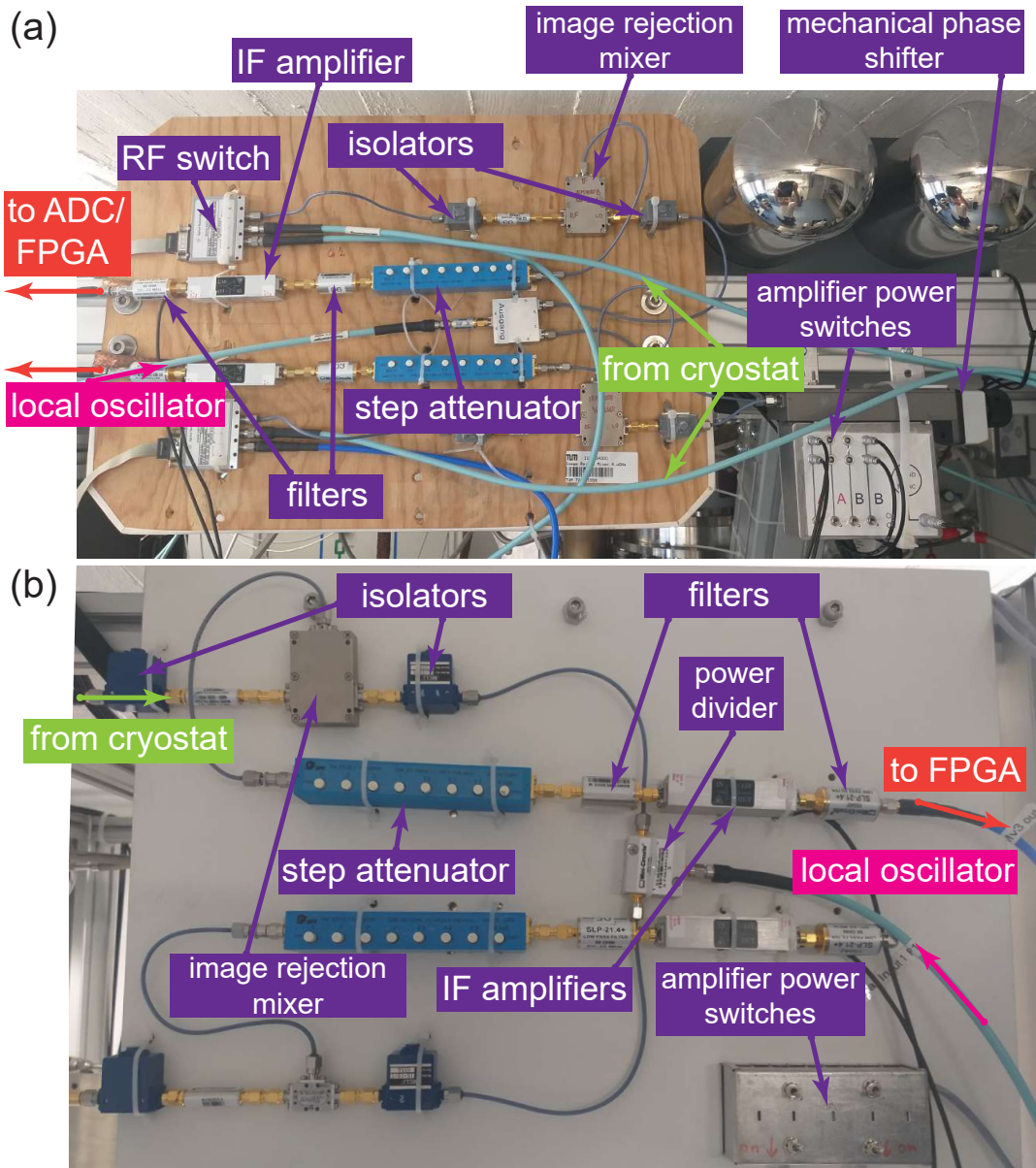
Figure 3.3: (a) Heterodyne microwave receiver in the Alice lab and amplifier control electronics. The receiver is designed for $\omega_{\mathrm{if}}/2\pi = 11\,\mathrm{MHz}$ and enables two-mode tomography. (b) Heterodyne microwave receiver in the Bob lab, designed for $\omega_{\mathrm{if}}/2\pi = 12.5\,\mathrm{MHz}$.

$9.5 - 11.5\,\mathrm{MHz}$ ($0 - 22\,\mathrm{MHz}$) in the Alice (Bob) lab.[30] Next, we employ IF amplifiers[31] and additional low-pass filtering with a cutoff frequency at $22\,\mathrm{MHz}$ before digitizing the signal in the next step.[32] The relative phase between both paths can be adjusted using a

---

[30]We use a `SBP-10.7+` filter from `Mini-Circuits` for Alice lab and a `SLP-21.4+` filter from `Mini-Circuits` for Bob lab.

[31]We use `AU-1447-R` amplifiers from `Miteq` for this purpose.

[32]We use a `SLP-21.4+` filter from `Mini-Circuits` for this purpose.
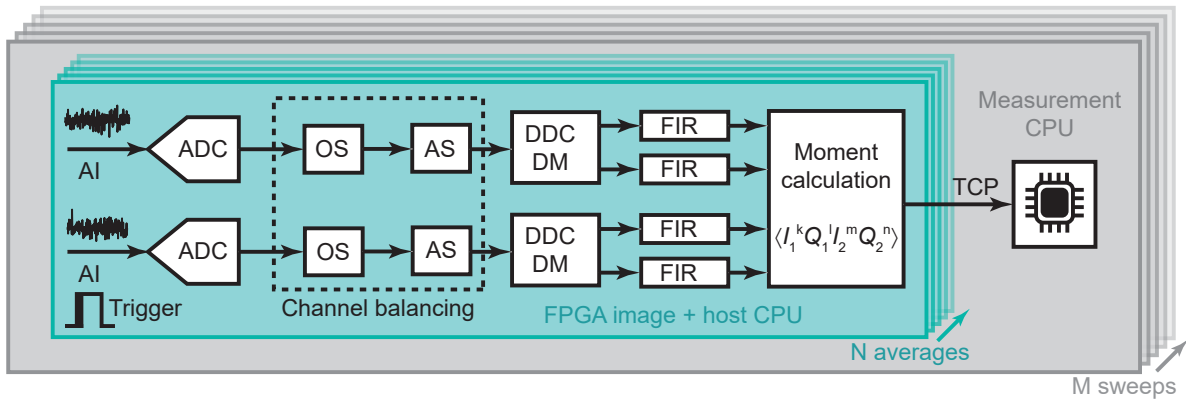
Figure 3.4: Scheme for the FPGA-based digital data processing routine. After starting a measurement with an external trigger pulse, the analog input (AI) signal in both paths is digitized by an ADC. We correct for possible offsets between the paths (OS) and scale the amplitudes to equivalent values (AS). Then, the signal is digitally downconverted (DDC), demodulated (DM), and filtered (FIR) before we calculate the quadrature moments up to the fourth order. The routine is repeated for N averages before the moment data is transmitted to the measurement CPU. The whole procudure can be repeated for M sweeps to extend the total number of averages.

mechanical phase-shifter.[33]

FPGA image   After the heterodyne downconversion step, the signal is digitized and further processed to extract its statistical moments. For the measurements presented in chapter 4 and chapter 5, we use the analog-to-ditital conversion (ADC) setup described in Ref. 112 and Ref. 158, which relies on an `Acqiris DC440` digitizer card, connected to a CPU by a PXI-to-PCI interface. The signal moments are computed on the CPU using a custom C++ code. In this configuration, all acquired raw data is transmitted from the Acqiris card to the CPU without any further compression. Hence, the measurement speed is rather low and can be significantly increased by employing an FPGA-based ADC scheme. The latter allows for parallel signal detection and on-board processing. For the quantum communication experiments discussed in chapter 6 and chapter 8, we have developed a real-time digitizer scheme based on a `National Instruments` NI-5782 transceiver module for signal recording and a `National Instruments` PXIe-7975R FPGA for parallel data processing. Our FPGA image is originally written in LabVIEW FPGA, which makes it fully compatible with our measurement code. For logical operations and buffer storage, we employ block random access memory (BRAM) and look-up tables (LUTs) as resources. The on-board dynamical random access memory (DRAM) is difficult to use due to a significant clock frequency mismatch. A schematic illustration of our two-path FPGA image is given in Fig. 3.4. The FPGA is syncronized with our 10 MHz

---

[33]We use a `PNR P1506D` phase shifter from `ATM` for our purposes.

reference and the measurement of a time trace is triggered by the DTG (8-port AWG) in the Alice (Bob) lab. The incoming IF signal is sampled at the frequency $\tilde{\omega}/2\pi = 125\,\text{MHz}$. Next, we correct for a potential offset between the channels and ensure proper amplitude scaling by balancing with respect to the detected noise level in the cryostat output lines corresponding to both detected paths. In this step, the balancing is performed with the step attenuators in the analog receiver, which allows for a simultaneous check whether the attenuation is sufficiently high to avoid clipping effects. Then we repeat amplitude balancing with a weak coherent signal. Although reference-state reconstruction does not require a specific phase relation between the paths, we calibrate for a relative 180° phase shift, which allows to check whether we can sustain a stable phase over longer time frames. In the next step, we perform digital downconversion and demodulation of the signal. In this digital homodyning step, we determine the I-(Q)-quadrature of the digitized signal $A(t)$ by numerical integration over a full period of a digitally created cosine (sine) function at demodulation frequency [297],

$$I = \frac{\omega_{\text{if}}}{\pi} \int_t^{t+\frac{2\pi}{\omega_{\text{if}}}} A(t') \cos(\omega_{\text{if}} t') dt' \simeq \frac{\omega_{\text{if}}}{\tilde{\omega}} \sum_{i=0}^{\lfloor \frac{\tilde{\omega}}{\omega_{\text{if}}} \rfloor} A(t_i) \cos(\omega_{\text{if}} t_i), \tag{3.1}$$

$$Q = \frac{\omega_{\text{if}}}{\pi} \int_t^{t+\frac{2\pi}{\omega_{\text{if}}}} A(t') \sin(\omega_{\text{if}} t') dt' \simeq \frac{\omega_{\text{if}}}{\tilde{\omega}} \sum_{i=0}^{\lfloor \frac{\tilde{\omega}}{\omega_{\text{if}}} \rfloor} A(t_i) \sin(\omega_{\text{if}} t_i), \tag{3.2}$$

where $t_i = t_0 + 2\pi i/\tilde{\omega}$ and $\lfloor x \rfloor$ denotes the floor function.[34] Next, the demodulated signal is filtered by a digital finite impulse response (FIR) filter [299], which is based on the Hamming window function and consists of 90 filter coefficients for our desired SSB of $200\,\text{kHz}$.[35] The impact of using a filter is shown in Fig. 3.5. Figure 3.5(a) shows the amplitude transmission as a function of detuning $\Delta\omega$ from the demodulation frequency $11\,\text{MHz}$ without any filter. In comparison, three FIR filters with different SSBs are illustrated in Fig. 3.5(b).[36] The measured asymmetry in the filter response is a result of the fact that the sampling frequency and the IF frequency are non-commensurable.

---

[34]Note that despite the signal quadratures containing the statistical information about our quantum state, we can demodulate I and Q simultaneously although these quadrature values correspond to incompatible observables. A potential explanation is a collapse of the wave function inside the HEMT amplifier, which implements a permanent cycle of projective measurements on the signal and adds noise beyond the SQL. In case we want to digitally measure two entangled modes, we need to amplify them with respective gain $G \gg 1$, which requires two phase-insensitive amplifiers. Due to the SQL, both amplifiers add a combined noise of at least one photon, which is the threshold for sudden death of entanglement [217]. Consequently, entanglement is lost and the delocalized wave function needs to have collapsed. However, the information on the (potentially entangled) state present before the collapse is not lost. Thus, we do not violate any bosonic commutation relation.

[35]The filter has been designed using the `DSP System Toolbox` toolbox in `Matlab`. The choice of 90 coefficients emerges from a compromise between small measurement bandwidth and sufficiently short filter ringing [299].

[36]We gratefully acknowledge the experimental contribution of S. Pogorzalek, who performed this measurement.
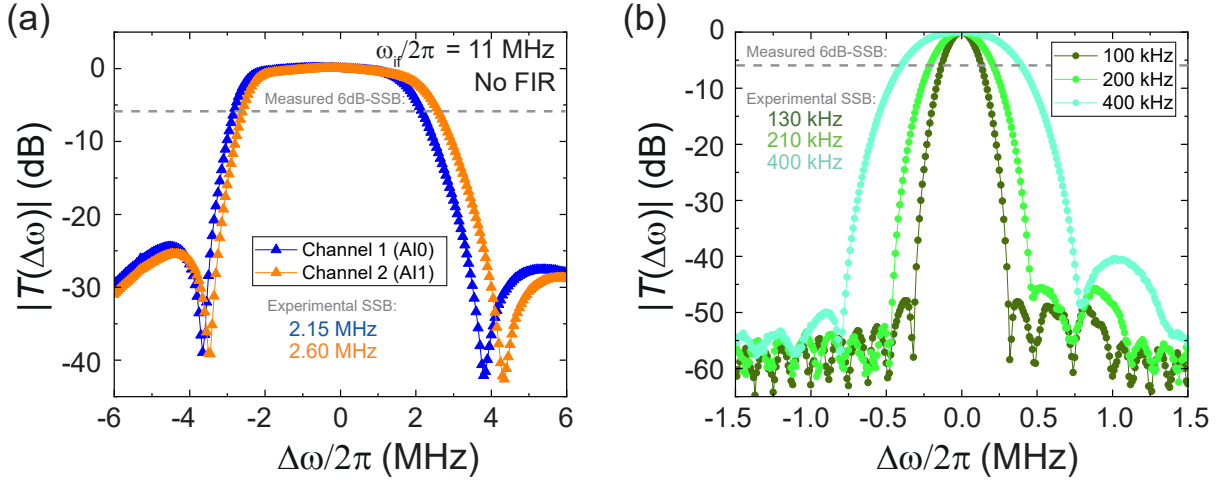
Figure 3.5: (a) Amplitude transmission for the FPGA-based setup without a digital filter as a function of detuning $\Delta\omega$ from the reconstruction frequency. The gray dashed line indicates the $-6\,\mathrm{dBc}$ cutoff. (b) Amplitude transmission with FIR filters, designed with respective SSBs of $100\,\mathrm{kHz}$, $200\,\mathrm{kHz}$, and $400\,\mathrm{kHz}$, as well as experimentally determined filter bandwidths. The measured $-6\,\mathrm{dBc}$ cutoff matches well with the design parameters.

Throughout all experiments described in this work, we use the filter corresponding to a SSB with $B/2\pi = 200\,\mathrm{kHz}$. After filtering, we determine the statistical moments. To estimate the required BRAM resources for moment calculation, we determine the number of moments $M_N^{(\ell)}$ of moments up to order N for ℓ-mode tomography. For this, we consider $\mathcal{M}_n^{(\ell)} \equiv \{\langle I_1^{j_1} Q_1^{k_1} \cdots I_\ell^{j_\ell} Q_\ell^{k_\ell}\rangle \,|\, j_1 + k_1 + ... + j_\ell + k_\ell = n\}$. The number of elements in this set can be determined by drawing an analogy to the combinatoric urn model of unordered sampling with replacement [300]. The total number $M_N^{(\ell)}$ is then given by

$$M_N^{(\ell)} = \left|\bigcup_{n=1}^{N} \mathcal{M}_n^{(\ell)}\right| = \sum_{n=1}^{N} \binom{n + 2\ell - 1}{n} = \frac{(2\ell + N)!}{(2\ell)!N!} - 1. \tag{3.3}$$

This leads to $M_4^{(1)} = 14$ for single-path tomography and $M_4^{(2)} = 69$ for two-mode reconstruction. We furthermore observe that Eq. (3.3) is a polynomial with leading term $\mathcal{O}(N^{2\ell})$. Due to this drastic scaling, reconstructing moments up to fourth order is a good compromise between saving memory and sufficient Gaussianity checks. In fact, our moment calculation requires approximately $90\,\%$ of the $16\,\mathrm{kbit}$ BRAM. During a single measurement, we average the moments over N time traces and the experiment is then repeated over M sweeps. The moment data is transmitted from the FPGA to a host-CPU via a bus consisting of two first-in-first-out (FIFO) buffers on the FPGA and CPU sides, respectively. The data is received and routed by a permanently running LabVIEW program on the host CPU. This program simultaneously controls the FPGA parameters such as the number of averages. The host CPU also acts as a TCP/IP server for our measurement routine. During experiments, the FPGA and host CPU are always in
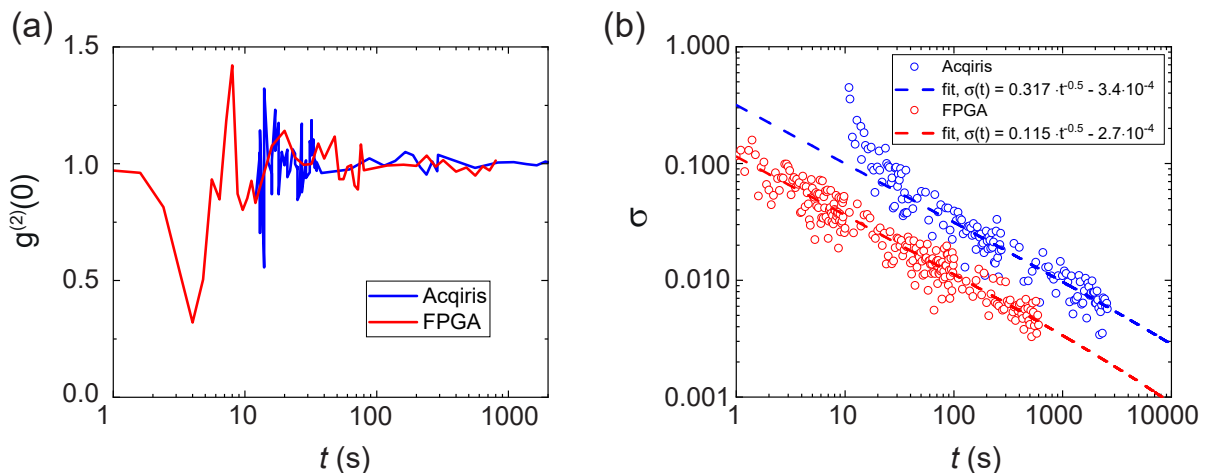
Figure 3.6: (a) Dependence of the $g^{(2)}$ correlation function on measurement time t for a noisy coherent input signal, measured with the FPGA and the Acqiris card. In both scenarios, we observe the expected behavior $g^{(2)} \to 1$. (b) Standard deviations σ for $g^{(2)}$, measured with the FPGA and the Acqiris card. We observe that using the FPGA measurement, σ decreases 7.6 times faster in comparison to the Acqiris card.

operation and wait for commands from the measurement CPU. With our FPGA image, we reach an overall duty cycle of 88 % and observe only small phase drifts of $0.1 \pm 0.01\,^\circ\,\mathrm{h}^{-1}$. To quantify the FPGA performance, we measure the $g^{(2)}(0)$-correlation function since this quantity provides a self-consistent description of the photon statistics and does not require an exact photon number conversion factor (PNCF). For a digitized thermal coherent state $\hat{\rho}(\alpha, n_{\mathrm{th}})$, the second order correlation function can be expressed as

$$g^{(2)}(0) = 1 + \frac{10|\alpha|^2(n_{\mathrm{th}} + n_{\mathrm{d}}) + 5(n_{\mathrm{th}} + n_{\mathrm{d}})^2 - n_{\mathrm{d}}^2}{5(|\alpha|^2 + n_{\mathrm{th}} + n_{\mathrm{d}})^2}, \tag{3.4}$$

where the digitization error is taken into account as a white noise contribution [301], consisting of n_{d} photons, satisfying a uniform distribution. For our ADCs transforming the IF signal into fixed point representation with a resolution of $\Omega_{\mathrm{q}} = 16$ bits, we find $n_{\mathrm{d}} \simeq 10^{-5}$ for our typical PNCF values, implying that the digitization noise can be neglected. The finite resolution of our ADCs leads to a digitization SNR of $1.761\,\mathrm{dB} + \Omega_{\mathrm{q}} \cdot 6.02\,\mathrm{dB} \simeq 98\,\mathrm{dB}$ [301]. This value is approximately $24\,\mathrm{dB}$ higher compared to the digitization SNR of the Acqiris card which measures with 12-bit resolution. In the next step, we directly compare the performance of the FPGA and the Acqiris card. As described in Ref. 281, we have constructed a test setup at room temperature. It consists of an RF source to generate a coherent signal which is superposed with an artificial Gaussian noise created by an AWG.[37] This allows us to sensitively control the SNR and benchmark our averaging procedure. We verify that the detected Gaussian voltage fluctuations in the system decay

---

[37]We use a `81160A` AWG from `Keysight` for this purpose.

with the expected $1/\sqrt{N}$-dependence, where N is the number of averages [281]. Next, we generate an amplitude-modulated coherent signal with $\mathrm{SNR} = 2.5 \times 10^{-7}$ and determine $g^{(2)}$ as a function of averaging time t with the FPGA and the Acqiris card. We reconstruct the state by taking the AWG noise in the first pulse as a reference. The result is shown in Fig. 3.6(a), where we observe that we measure $g^{(2)} \to 1$ after $\simeq 100\,\mathrm{s}$, as expected for a coherent signal. In Fig. 3.6(b), we plot the standard deviation $\sigma = \sqrt{\langle [g^{(2)}]^2 \rangle - \langle g^{(2)} \rangle^2}$. Our data can be fitted using the central limit theorem, $\sigma(t) \sim 1/\sqrt{t}$. We find a ratio of 2.76 for the corresponding standard deviations, implying that in order to achieve a fixed σ, we need to average for approximately 7.6 times longer with the Acqiris card than with the FPGA setup [293]. This significant speedup is going to be crucial for our quantum teleportation experiment as explained in Sec. 6.3. More technical details about the FPGA card and implementation of its image are provided in Ref. 281.

In addition, using an FPGA will become crucial as soon as we want to create digital feedforward signals. These signals must be realized within a significantly shorter time frame compared to the coherence time of employed quantum correlations. In addition, for upcoming experiments with non-Gaussian states, it is of high relevance to implement an FPGA-based detection of histograms, which allows for direct measurement of the Husimi Q-function [302].

3.1.4 Photon number calibration

To relate the detected moments $\langle I_1^k Q_1^l I_2^m Q_2^n \rangle$ to quantum statistics inside the cryostat, we need a proper photon number calibration for each output line. The basic idea of such a calibration is to install a photon source which emits a signal with a well-defined and simultaneously well-known photon number. The detection of this signal with our receiver setup allows us to map the ADC room temperature voltage to the photon number at the source location. The proportionality factor provides the PNCF. Examples for widely used photon sources are shot-noise tunnel junctions [303], qubits [304], or Johnson-Nyquist noise resulting from heating of the sample stage [305]. Since heating of the full sample stage can affect the characteristics of our JPAs, we employ Planck spectroscopy using the black body radiation emitted by a standalone heatable microwave attenuator in the input line. Here, the attenuation value of $30\,\mathrm{dB}$ is a reasonable compromise between realization of a black body and damping of input signals [73]. The attenuator is clamped into an OFHC-Cu frame and wrapped with a flattened silver ribbon thermally anchored to the MC stage. This weak-thermalization assembly provides a reasonable trade-off between the ability to sustain a significant temperature gradient to the mixing chamber when heating is on and cooldown time of the attenuator in the absence of heating. For a PID-controlled temperature stabilization, a $\mathrm{RuO_2}$ sensor and a heater are fixed at opposite sides of the attenuator, as can be seen in the photograph in Fig. 3.7(a). The heater is realized by a $100\,\Omega$ strip-resistor soldered to a custom-made twisted pair of multi-filament

superconducting NbTi wires and glued to an annealed flat silver strip using a blue `stycast 2850 FT` epoxy bead. The resistor is galvanically separated from the silver strip by a layer of cigarette paper. The sensor is read out via a custom drilled double-twisted pair of superconducting wire, glued with `GE varnish`, in a four-wire configuration. To minimize losses and heating of the sample stage, we exclusively use superconducting cables after the heatable attenuator. Depending on the attenuator temperature T_a, we measure the power [73]

$$P(T_\mathrm{a}) = \frac{\kappa}{Z_0} \left[\frac{1}{2} \coth \left(\frac{\hbar \omega_\mathrm{s}}{2 k_\mathrm{B} T_\mathrm{a}} \right) + n_\mathrm{H} \right], \tag{3.5}$$

where ω_s denotes the signal frequency, κ is the PNCF for a given detection bandwidth B, effective amplification gain G, and the impedance $Z_0 = 50\,\Omega$. The quantity n_H describes the amplification noise, dominated by the HEMT amplifier noise. In case we change the detection bandwidth to B', and the gain to G', the PNCF changes by a factor $B'G'/(BG)$. In Fig. 3.7(b), we show the result from such a Planck spectroscopy measurement, where we find $\kappa/Z_0 = 27 \pm 2\,\mathrm{nW}$ per photon and $n_\mathrm{H} = 14.8 \pm 0.8$ from a fit based on Eq. (3.5). For $T \gtrsim 100\,\mathrm{mK}$, we measure linear Johnson-Nyquist noise.[38] For low temperatures, we observe the saturation effect resulting from vacuum fluctuations. Especially with respect to our measurements over the cryogenic link in chapter 8, it is a practically relevant question at which point the finite temperature of the environment needs to be included in the reference-state reconstruction method. A conventional quantifier is the crossover temperature $T_\mathrm{cr} = \hbar \omega_\mathrm{s}/(2 k_\mathrm{B})$ [306], which quantifies the transition from the saturated regime to the Johnson-Nyquist regime. However, T_cr depends on the losses between the heatable attenuator and the HEMT amplifier since these losses impact the linear slope but not the vacuum fluctuations. An alternative loss-independent quantifier is the temperature T_κ, corresponding to maximal curvature of the Planck curve. Numerically, we find $T_\kappa \simeq 0.223 \hbar \omega_\mathrm{s}/k_\mathrm{B}$, which corresponds to roughly $60\,\mathrm{mK}$. For environmental temperatures $T \le T_\kappa$, the reference state can be well approximated by vacuum.

The quantum state can be reconstructed at an arbitrary point inside the setup by compensating for the losses between the photon source and the reconstruction point [112]. In our case, we model these losses with a beam splitter model. In the experiment, these losses are estimated from the datasheet values of the passive microwave components and from TDR measurements of the respective connectors of our custom made cables. To properly compensate for these losses, we additionally need to know the corresponding bath temperature. To obtain a stable thermal background, we stabilize our samples to a

---

[38]Note that in case we perform a Taylor expansion of Eq. (3.5) in the limit $T \gg 1$, the resulting power spectral density is only $1/4$ of the well known Johnson-Nyquist relation $\langle V^2 \rangle = 4 k_\mathrm{B} T Z_0$. The reason for this is the assumed ideal impedance matching to $50\,\Omega$, implying that the observable voltage drop is only $V/2$ [93].
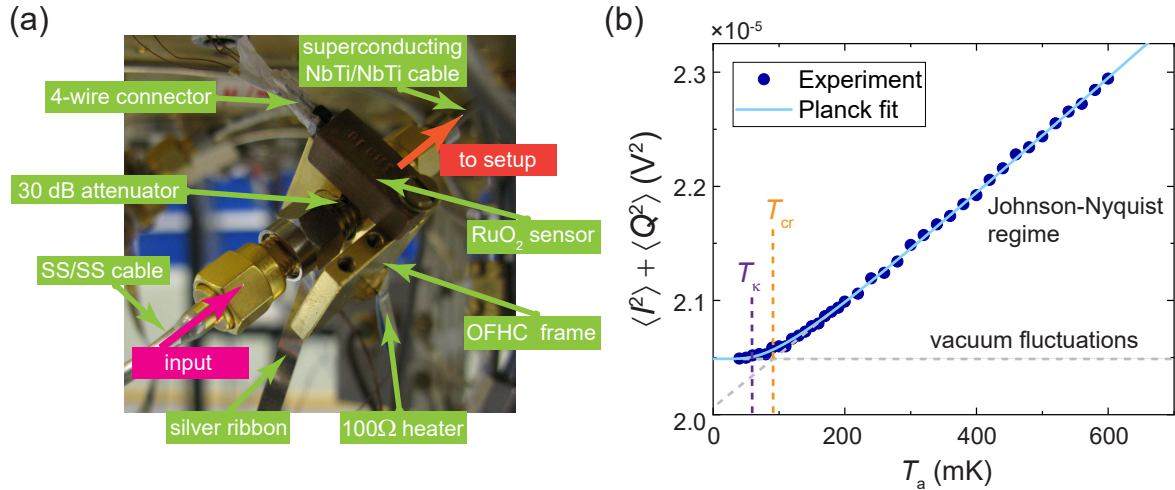
(a)

(b)

Figure 3.7: (a) Photograph of the heatable 30 dB attenuator for Planck spectroscopy installed in one of our cryogenic setups. (b) Measured Planck curve for photon number calibration with a detection bandwidth $B/2\pi = 200\,\text{kHz}$. The temperature threshold T_{cr} corresponds to the crossover temperature between the quantum saturation, dominated by vacuum fluctuations, and the linear Johnson-Nyquist regime. The threshold T_κ marks the temperature at which the Planck curve shows maximal curvature.

temperature slightly above the cryostat base temperature, typically to 50 mK.[39] However, the attenuator heating necessarily implies the existence of temperature gradients in our system. Consequently, the bath temperature of the dissipative environment depends on the temperature of the heatable attenuator. One possibility to account for this effect, suggested in Ref. 158 and Ref. 112 is to assume a linear temperature gradient and a linear distribution of losses between the attenuator and the temperature stabilized JPA. These losses are then modelled via 100 equidistantly spaced fictitious beam splitters. This is an accurate approach for setups constructed with normal conducting RF cables. However, in our superconducting setup it is more accurate to couple the attenuator temperature to the loss attributed to the first SMA connector and the stable JPA temperature to the remaining connector and circulator losses. This effect of nonhomogeneous bath temperature only adds a small correction to the PNCF, which does not impact any experimental results within the error bars.

3.2 JPA sample characterization

In this section, we discuss our JPA chips as well as the results from basic calibration measurements, including flux tuning, gain, compression and squeezing. The setup, used

---

[39]In Alice lab, we use two `AVS-47B` resistance bridges, combined with two `TS-530A` temperature controllers from Picowatt for this purpose. In Bob lab, we use a `AVS-48SI Picobridge®` resistance bridge from Picowatt for this puspose.

for these fundamental characterization measurements, coincides with the corresponding setups described in Ref. 158 and Ref. 112.

3.2.1 Sample preparation of single- and double-SQUID JPAs

In the experiments described in this work, we use JPA chips from two different sets. The first set has been fabricated at NEC Smart Energy Research Laboratories, Japan and RIKEN, Japan [79]. Each of these JPAs consists of a superconducting $\lambda/4$ microwave resonator in a CPW geometry. The resonator is terminated to the ground plane via a DC SQUID [105]. A $300\,\mu\mathrm{m}$ thick silicon chip, covered by a thermal oxide, is used as substrate and an aluminum shadow evaporation technique is used to fabricate the DC SQUID with electrode thickness of $50\,\mathrm{nm}$. The resonator and the pump line are formed by a $50\,\mathrm{nm}$ thick layer of sputter-deposited niobium. Details about the fabrication as well as about the device geometry are provided in Ref. 75 and in Ref. 79. A microscope image [40] of the NEC JPA chip is shown in Fig. 3.8(a). Figure 3.8(b) shows the aluminum SQUID of size $4.2 \times 2.4\,\mu\mathrm{m}^2$. Figure 3.8(c) shows the coupling capacitance, which is designed to yield an external quality factor $Q_\mathrm{e} = 200$ in this case. The second set of JPAs has been manufactured at VTT Technical Research Center of Finland Ltd. This JPA geometry generally coincides with the NEC design, with the difference that a $525\,\mu\mathrm{m}$ thick silicon wafer has been used. In addition, the SQUIDs for this type of JPA are fabricated from Niobium. A photograph of the chip is provided in Fig. 3.8(d). Throughout this work, we employ double-SQUID JPAs and single-SQUID JPAs. A photograph of the double-SQUID loops is shown in Fig. 3.8(d) and the single SQUID is depicted in Fig. 3.8(e). The respective loop area is $3.9 \times 3.9\,\mu\mathrm{m}^2$.[41] Our sample boxes are milled from OFHC-Cu and gold-plated. A photograph of a fully prepared sample box is shown in Fig. 3.9(a). The JPA chip is glued into the roughened center of the box using GE varnish glue. The RF connections to pump and signal line are then established by K-connectors.[42] The interface between the sample and the RF connector is formed by gold-plated alumina printed circuit boards (PCBs),[43] which host a $50\,\Omega$ matched CPW. Signal and pump lines are connected to the inner connector of the CPW using aluminum bonds. Additional dense aluminum bonds are added for grounding the chip and the PCB to the sample box. The body of the K-connector and the PCB are connected via a glass bead, which is soldered into the OFHC-Cu housing by heating up the box using a hot plate.[44] The glass bead is then soldered to the inner CPW connector. To reduce the risk of creating ground shorts, it is beneficial to use a flux-free solder for this purpose.[45] Alternatively, the DC

---

[40]We use a `Keyence VHX-7000` microscope for this purpose.

[41]We show the photos of the chips with friendly permission from VTT.

[42]We use `K102F-R` connectors from `Anritsu` for this purpose.

[43]The PCBs have been fabricated at `Rohde&Schwarz GmbH`.

[44]We use `K-100` glass beads from `Anritsu` for this purpose.

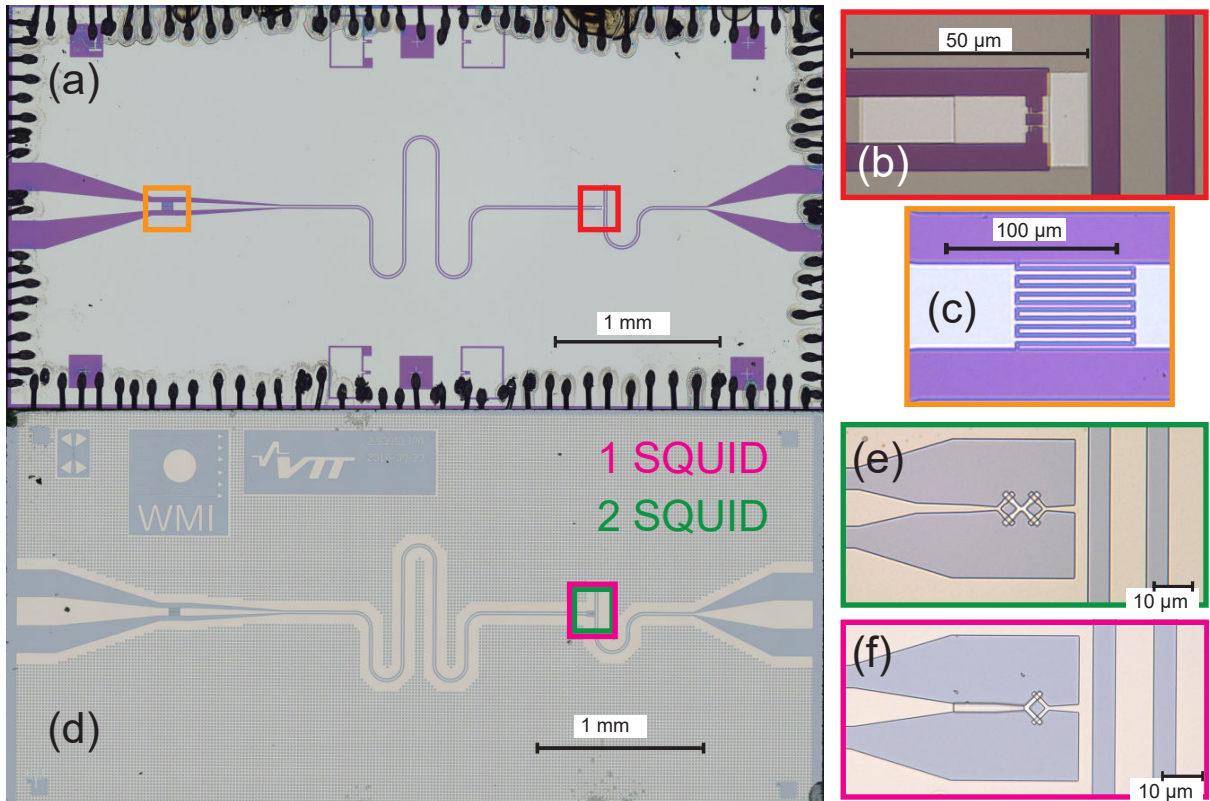[45]A suitable solder is `L-PbSn40(Sb)/zh` solder from `Felder GmbH`.

Figure 3.8: (a) Microscope image of an NEC JPA sample. The pump line is located on the right side and the DC SQUID is indicated by the red rectangle. The DC SQUID is shown in (b) in higher resolution. The orange rectangle indicates the coupling capacitance between the $\lambda/4$ resonator and the signal port (left). An enlarged picture of this capacitor is shown in (c). Panel (d) shows a microscope image of a VTT chip. The geometry coincides with the NEC design and we clearly observe the periodic flux trapping structures. High resolution pictures of the single-SQUID and double-SQUID loops are provided in panels (e) and (f), respectively.

connection can be established by clamping a small piece of indium between glass bead and inner CPW connector, followed by local heating. The resulting soldering contact to the PCB is purely mechanical due to the gold-plating. In future experiments, a more stable contact can be established by employing solders with gold content or by using gold bonds between PCB and glass bead. On the connector side, we ground the PCB to the sample box using silver glue which improves the impedance matching to $50 \pm 3\,\Omega$. The dimensions of the recess holding the chip are originally designed for the NEC JPAs. For the VTT JPAs, we adjust the lateral dimensions. These adaptations are necessary since the VTT wafers are broken along the (110)-direction on one long edge, leading to tilt angles of $45°$ which thereby increases the effective chip area. Consequently, we cut the VTT chips to a suitable dimension.[46] For flux tuning, we employ custom-made superconducting coils which consist of a gold-plated OFHU-Cu body and single-filament NbTi-wire [47] with

---

[46]We use a `DAD3221` dicing saw from `Disco Corporation` for this purpose.

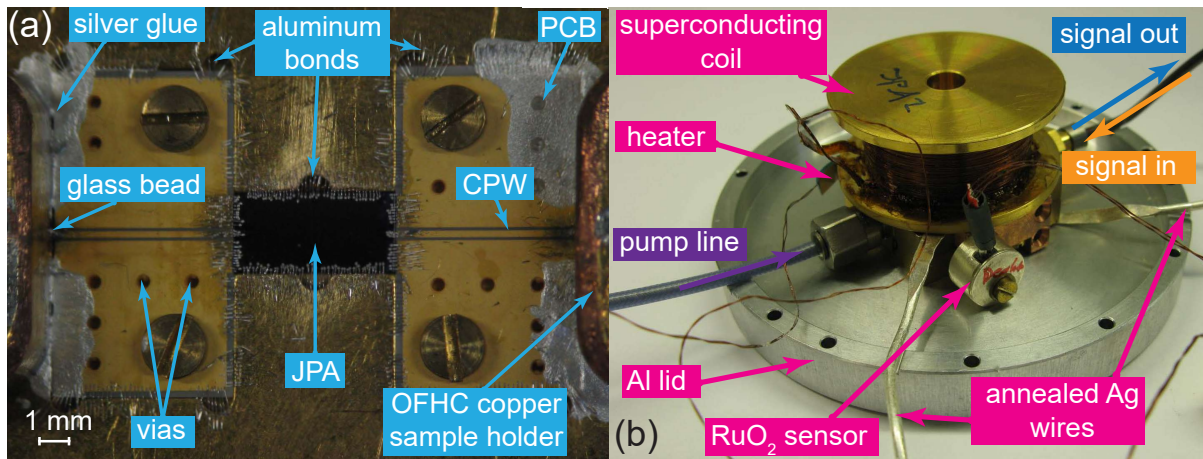[47]We use `C510/NbTi` wire from `Supercon Inc.` for this purpose.

Figure 3.9: (a) Photograph of a prepared sample box. The bonded JPA chip is located in the center. Signal (pump) line are connected via a gold-plated alumina PCB, as depicted on the left (right) side. Top and bottom part of the PCB are connected by vias. The PCB is grounded to the sample box with aluminum bonds and silver glue. (b) Photograph of the closed sample box with connected signal and pump lines. A superconducting coil for DC flux bias is mounted on top of the box. A RuO$_2$ temperature sensor and a 100 Ω heater are installed to enable temperature stabilization. The sample box is thermalized with two silver wires and fixed inside an aluminum box for magnetic shielding.

approximately 3800 windings, which are fixated and thermalized with `GE varnish` glue. The coil is fixed onto the top of the sample box as shown in Fig. 3.9(b). We attach two annealed flattened silver wires for thermalization at the top and bottom of the sample box. For temperature stabilization, we add a 100 Ω heater and a RuO$_2$ sensor to opposite sides of the sample box. We connect the pump line with a flexible RF cable [48] and the signal line with a superconducting coaxial NbTi cable. Each pump line contains an additional DC block at room temperature. For magnetic shielding, we place the sample box inside a cylindrical aluminum box. Since we measure the JPA in reflection, we use an input circulator to separate input and output modes. As the circulator employs an internal ferromagnet to break time-reversal symmetry [307], it is crucial to space it reasonably far away from the JPA. In addition, the circulator should be installed such that its permanent magnetic field is oriented in parallel to the JPA ground plane. For additional protection from external magnetic fields, the cryogenic setup is surrounded by a cryoperm shield.

3.2.2 Fundamental characterization measurements

In this section, we discuss basic characterization measurements of our JPA samples. Within these experiments, we measure flux tuning, nondegenerate and degenerate gains, compression, and squeezing. These fundamental measurements are necessary before realization of any advanced quantum communication experiment with JPAs.

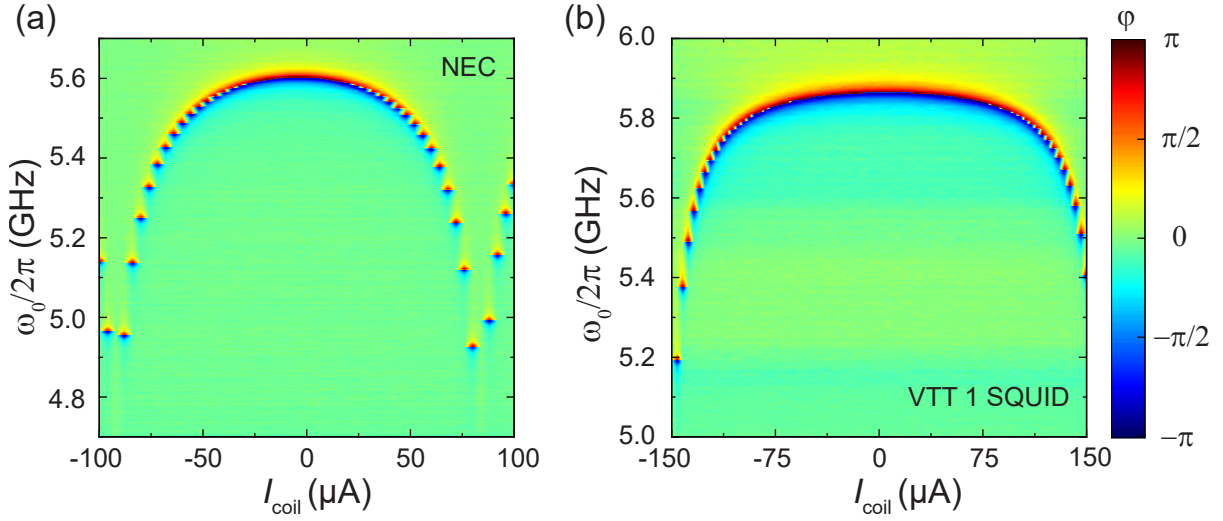[48]We use `Minibend` cables from Huber+Suhner for this purpose.

Figure 3.10: (a) Flux tuning of an NEC JPA. The phase shift from $-\pi$ to π demonstrates that the JPA resonator is overcoupled. (b) Flux tuning of a VTT single-SQUID JPA. Compared to the NEC JPAs, we observe that the flux characteristic is flatter around the DC flux $\Phi_{\mathrm{dc}} \simeq 0$, implying a larger critical current I_{c} for VTT samples.

JPA flux characteristic   Here, we investigate the DC flux tuning of the JPA resonance frequency and measure the phase φ of the resonator transmission as a function of the applied coil current I_{coil} using a VNA. We apply the DC flux with DC sources [49] via custom made cables. They are connected to the setup with 2-pin `LEMO` connectors at room temperature. To reduce the risk of magnetic flux trapping, it is beneficial to keep the current sources connected during the cooldown and set them to $0\,\mathrm{mA}$. As shown in Fig. 3.10, both the NEC and VTT JPAs show the expected periodic flux tuning, corresponding to Eq. (2.3). In addition, JPAs from both sets show the expected phase shift for overcoupled resonators, according to Eq. (2.16). By comparing to Fig. 2.1, we find higher critical currents for the VTT SQUIDs. The VTT double-SQUID JPAs show similar flux characteristics (data not shown). Next, we fit Eq. (2.3) to the measured flux characteristic of each JPA. A list of the fitted parameters, corresponding to one exemplary sample of each JPA type, used within this work, can be found in Tab. 3.1. For all the fits, we have fixed the resonator inductance $L_{\mathrm{r}} = 2\,\mathrm{nH}$. The fit is performed iteratively. In the first step, we fit the flux periodicity and offset Φ_{off}. For the NEC JPAs, we find $\Phi_{\mathrm{dc}}/\Phi_0 = 6.24 I_{\mathrm{coil}}/\mathrm{mA}$ and an offset flux $\Phi_{\mathrm{off}} = -0.023\,\Phi_0$. For the single (double)-SQUID VTT JPAs, we obtain $\Phi_{\mathrm{dc}}/\Phi_0 = 3.62 I_{\mathrm{coil}}/\mathrm{mA}$ ($\Phi_{\mathrm{dc}}/\Phi_0 = 3.56 I_{\mathrm{coil}}/\mathrm{mA}$) and $\Phi_{\mathrm{off}} = 0.016\,\Phi_0$ ($\Phi_{\mathrm{off}} = -0.014\,\Phi_0$). In the next step, we fix all quantities at approximately expected values and only fit L_{l}. Following that, we fit ω_{r} and I_{c}. This iterative procedure is necessary since the problem is numerically badly conditioned due to $L_{\mathrm{l}} \ll L_{\mathrm{r}}$. Our procedure significantly lowers the fit uncertainty [308]. Note that we give a conservative lower bound for Q_{i}, since

---

[49]We use `SourceMeter 240` current sources from `Keithley` for this purpose, controlled via a `GPIB` interface.

Table 3.1: Table of characteristic JPA parameters for NEC, VTT single-SQUID and VTT double-SQUID JPAs. Quantities Q_e (Q_i) denote the the external (internal) quality factors. Values for Q_i represent a conservative lower bound. In addition, we provide the bare resonator frequency ω_r, the critical current I_c, the effective loop inductance L_l and the Josephson coupling energy E_J.

Sample	Q_e	Q_i	$\omega_r/2\pi$ (GHz)	I_c (μA)	L_l (pH)	E_J/h (THz)
NEC JPA	256-373	>5000	5.83 ± 0.01	2.31 ± 0.02	45.0 ± 0.2	1.15 ± 0.01
VTT 1 SQUID	157-215	>9800	6.00 ± 0.01	4.72 ± 0.03	44.1 ± 0.1	2.35 ± 0.02
VTT 2 SQUID	101-138	>10000	5.96 ± 0.01	9.01 ± 0.12	63 ± 2	4.48 ± 0.06

internal quality factor fitting can become inaccurate, e.g., due to Fano interference, for overcoupled resonators [309]. We find that the critical current for double-SQUID JPAs is approximately twice as high as for the single-SQUID samples. This relation has been designed on purpose to match the Josephson inductance of both samples. For all JPAs, we find a screening factor $\beta_L < 2/\pi$ [91]. However, since it has been shown in Ref. 105 that the flux characteristic can be hysteretic also in this regime, we use the convention that we perform all flux sweeps with increasing current.

Nondegenerate and degenerate gain To measure gain and eventually squeezing, we need to carefully choose a suitable DC flux working point. The flux sweet spot is determined by the optimal trade-off between flux noise $S_\Phi(\omega)$ at low frequency and pump noise at high frequency. The reason for that can be seen in Fig. 3.10. Flux variations impact the resonance frequency proportionally to the slope $\partial_\Phi \omega_0$. Furthermore, this slope also determines the coupling strength to the RF flux modulation drive [cf. Eq. (2.10)]. This implies that with increasing frequency, we need to pump the JPA stronger to achieve a certain gain, which also, in turn, implies increasing influence of pump-induced noise. Models for the dependence of $S_\Phi(\omega)$ on the SQUID geometry, are given in Ref. 137 and Ref. 310, and a model for the pump-induced noise is provided in Sec. 4.1.1. From an empirical point of view, we prefer to go to rather high frequencies, where an eventual technical upper frequency limit is determined by the dynamic range of our pump RF sources. This limit results from the fact that the pump power needs to be sufficiently large to provide a reasonable parametric gain while we simultaneously compensate for the cryostat attenuation in the pump line. In addition, the MC needs to provide sufficient cooling power to sustain the dissipated pump power. An additional constraint for quantum communication experiments with multiple JPAs is compatibility of the working point with all other JPAs used in the setup. Since dependence of the parametric gain on the DC flux can be very sensitive, we have increased the precision of the `Keithley` sources by shunting them with a $100\,\Omega$ resistance in some of our measurements. Since all our JPAs are overcoupled, $\kappa_e \gg \kappa_i$, we expect them to show parametric gain as described by Eq. (2.23) [90]. Figure 3.11(a) shows the spectral nondegenerate gain function G of the NEC JPA, detected in a transmission experiment, for various pump powers. For this
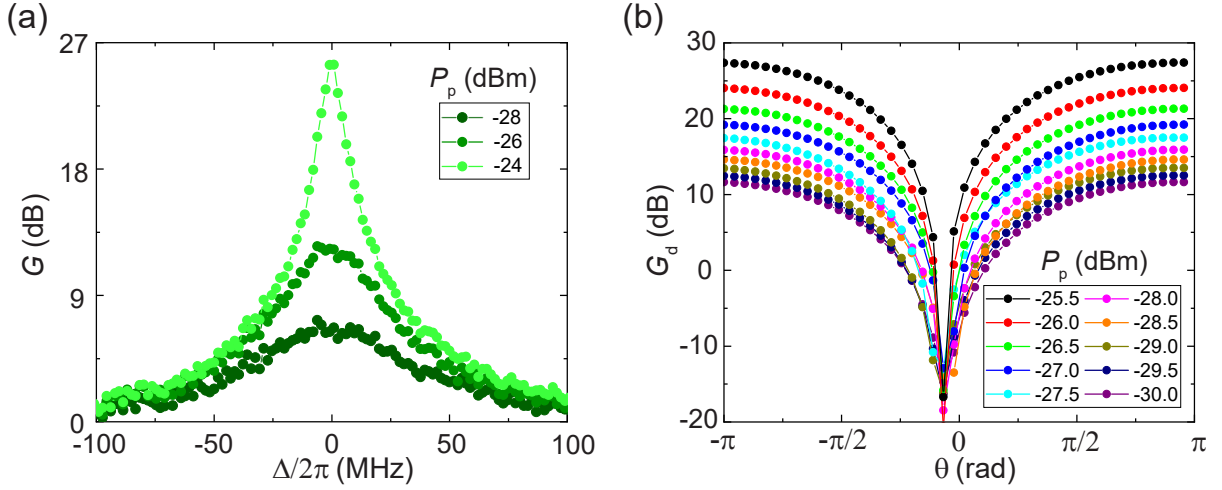
Figure 3.11: (a) Experimentally measured nondegenerate gain for the NEC JPA as a function of detuning Δ from resonance for three different pump powers P_p, referred to the JPA input. (b) Experimentally determined degenerate (phase-sensitive) gain for the NEC JPA for 10 different pump powers. The phase-offset of the minimum with respect to zero is a result from a relative phase delay between pump tone and signal.

measurement, we have chosen a resonance frequency $\omega_0/2\pi = 5.45\,\mathrm{GHz}$ and a pump drive at $\omega_\mathrm{p} = 2\omega_0$. The quantity $\Delta = \omega_\mathrm{s} - \omega_0$ corresponds to the relative detuning of the input signal frequency ω_s from ω_0. Next, we measure the phase-sensitive degenerate gain G_d. We fix the pump power and apply a weak coherent signal at frequency $\omega_\mathrm{s} = \omega_\mathrm{p}/2$ and with input power in the single-photon regime. We sweep the coherent phase θ, which we stabilize relatively to the pump phase. We determine G_d by comparing the coherent output power detected with our microwave receiver setup to a reference measurement during which the pump has been switched off. In Fig. 3.11(b), we plot the degenerate gain for an NEC JPA at $\omega_\mathrm{s}/2\pi = 5.435\,\mathrm{GHz}$ for various pump powers. In this particular parameter range, we measure a maximal $G_\mathrm{d} \simeq 27\,\mathrm{dB}$ at $\theta \simeq \pm\pi$ and strong attenuation of the signal at $\theta \simeq 0$, in accordance with Eq. (2.27) in case we choose the reference phase $2\theta - \pi/4$. As discussed in Sec. 2.3, a high degenerate gain is of particular importance for realizing an analog projective detection in quantum communication experiments.

1dB compression point   For sufficiently large signal power P_s, the output power of a realistic amplifier tends to saturate [311]. In a classical approximation, this compression effect can be modelled by a gain which depends on the signal power.[50] In case of our JPAs, the dynamical range is determined by two effects: a pump depletion and higher-order nonlinearities [108]. The 1 dB compression point is defined as the power P_s at which the amplifier response starts saturating and is reduced with respect to the ideal linear

---

[50]We note that quantum-mechanical treatment of compression is tedious since modelling of a power-dependent gain does not necessarily preserve the bosonic commutation relations. In Appendix F, we provide a simplistic compression model for our JPAs.
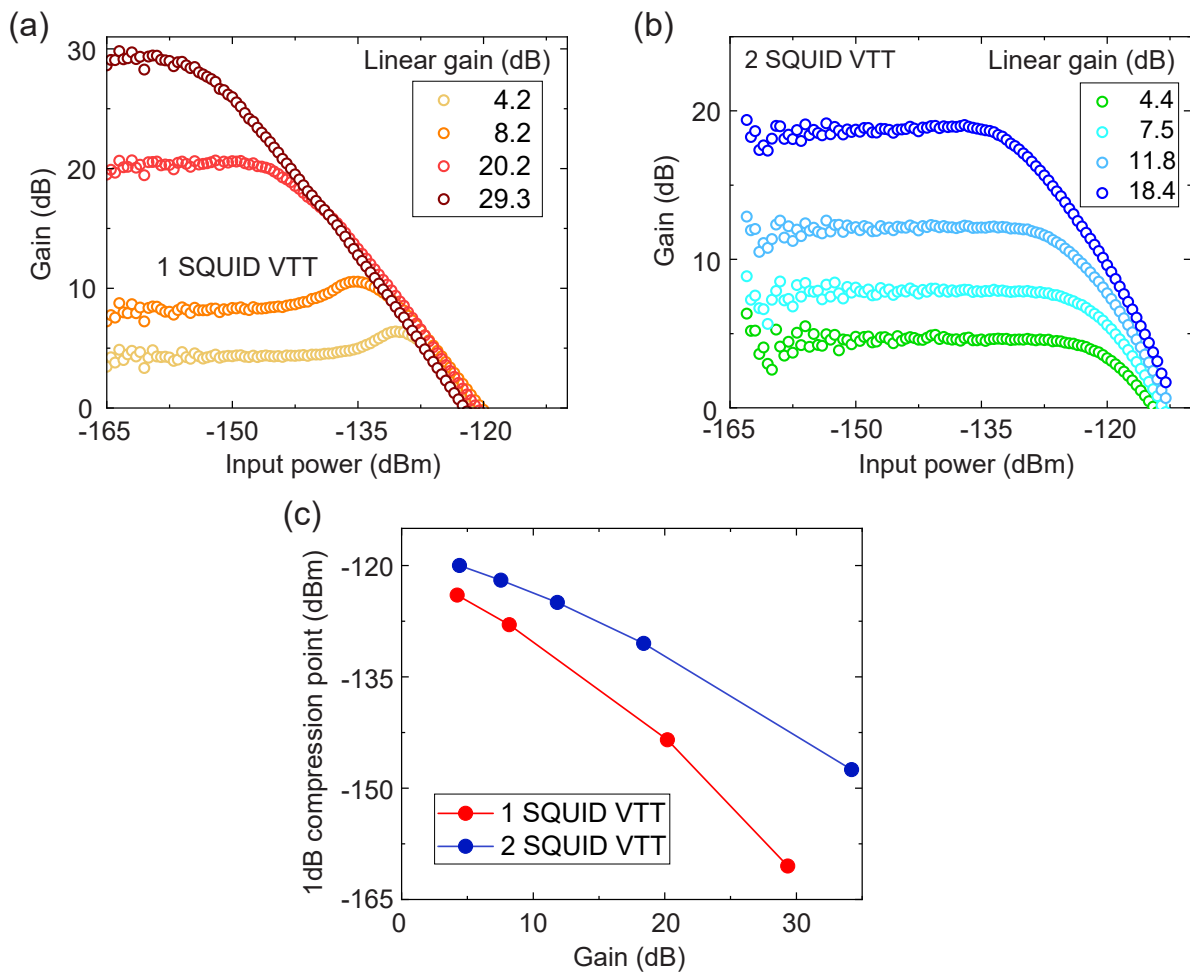
Figure 3.12: Normalized nondegenerate power gain as a function of applied power at the input port
of the VTT single-SQUID JPA (a) and the double-SQUID JPA (b). For sufficiently high
input powers, the amplifiers enter the compression regime which manifests as a decrease of
the effective gain with the input power. (c) Experimentally determined 1 dB compression
point corresponding to the measurements in (a) and (b) as a function of gain. We clearly
observe that the double-SQUID JPA has significantly better compression properties. Among
others, deviations from the expected 6 dB difference in compression between the JPAs can
be explained by different gain-dependent noise which effectively contributes to the input
power. Solid lines are a guide to the eye.

behavior by 1 dB. The investigation of the multi-SQUID JPAs is of particular interest for
our experiments since employing an N-SQUID array delocalizes the gauge-invariant phase
difference over multiple Josephson inductors [312] and lowers the impact of higher-order
nonlinearities by a factor $1/N$. Indeed, by employing N SQUIDs, theory predicts an
improvement by a factor N^2 under the assumption of equal critical current [119, 313].
Thus, we expect that for double-SQUID JPAs, the 1 dB compression point is increased by
6 dB compared to the single-SQUID samples. We measure compression using a VNA set
to a bandwidth of 10 Hz. We fix the JPA pump power at frequency $\omega_\mathrm{p}/2\pi = 11.1$ GHz
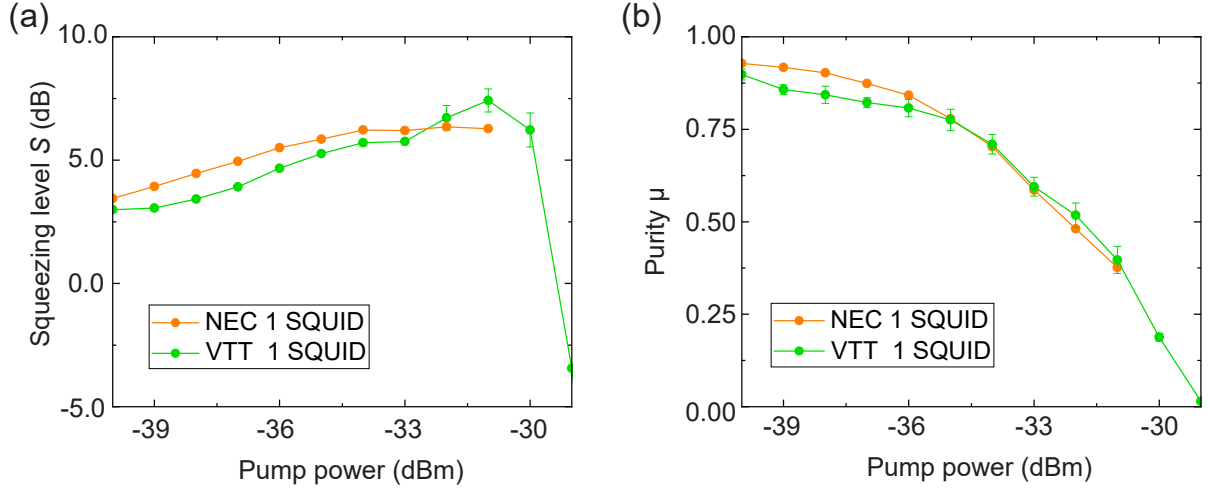
Figure 3.13: (a) Experimentally determined squeezing level S for the NEC JPA and a VTT single-SQUID JPA as a function of pump power at the input of the JPA pump port. Panel (b) shows the experimentally determined purity μ of the squeezed states as a function of pump power. Statistical error bars are only shown when they exceed the data point size. Lines are a guide to the eye.

while we simultaneously increase the power of the input signal. In Fig. 3.12, we plot the amplifier response at $5.55\,\text{GHz}$ for the case of the single- and double-SQUID JPAs. Here, flat gain regions imply that the amplifier is linear. As a reference for the linear gain, we use the average over the first 10 input powers, where compression can still be neglected. The experimentally determined $1\,\text{dB}$ compression point as a function of gain is is plotted in Fig. 3.12(c). In the region of $G \lesssim 10\,\text{dB}$, we observe an improvement close to the predicted $6\,\text{dB}$ limit. One possible explanation for the larger improvement at higher gains can be different gain-dependence of the amplifier noise. Since this noise effectively contributes to the input signal, it also affects the $1\,\text{dB}$ compression. To substantiate this conjecture, we compare the noise extracted in a separate squeezing measurement with the respective gain $G \simeq 20.2\,\text{dB}$ ($\simeq 18.4\,\text{dB}$) for the single- (double)-SQUID JPAs. We find that the amplified output state contains 5.61 ± 0.03 (3.47 ± 0.01) noise photons, implying that we expect a mismatch of $2.1\,\text{dB}$ in compression, in addition to the $6\,\text{dB}$. However, this noise alone cannot explain the measured deviation of $17.5\,\text{dB}$ for the $1\,\text{dB}$ compression points and additional effects need to be involved. The overall $1\,\text{dB}$ compression power of the VTT JPAs is similar to the values obtained for the NEC JPAs in Ref. 112. However, in contrast to our measurement, compression has been measured in the degenerate regime there. Increasing the dynamical range is of special relevance for our analog projection measurements in order to allow for higher photon numbers in the detected signal and, therefore, for larger input codebooks in quantum communication experiments. Thus, it is beneficial to employ multi-SQUID JPAs for the analog feedforward generation (cf. Sec. 8.3).

Squeezed state generation In the next step, we compare the NEC and single-SQUID VTT JPAs with respect to their squeezing performance. Measuring squeezing is similar to the degenerate gain measurement. The difference is that we do not apply any coherent tone here, but, instead, phase-sensitively amplify the weak thermal state emitted by the heatable attenuator at cryostat base temperature, which can be well approximated by vacuum. Like for degenerate amplification, the pump phase is stabilized using the phase-locked loop. The squeezing level S is then determined by the second order moments detected with our microwave receiver [75]. We perform the measurement within a finite bandwidth set by our digital FIR filter. Thus, more precisely speaking, we measure two-mode squeezing between symmetrically distributed signal and idler modes around resonance [112]. As a consequence, great care needs to be taken to obtain a symmetric gain function in Fig. 3.11(a) to generate symmetric signal and idler sidebands. This symmetry is necessary to optimize for balanced interference between signal and idler modes. Achieving this signal-idler symmetry requires sensitive tuning of the JPA DC flux to precisely meet the condition $2\omega_0 = \omega_{\mathrm{p}}$. In Fig. 3.13(a), we plot the experimentally determined S for the NEC JPA and the single-SQUID VTT JPA as a function of the applied pump power. In this measurement, we reach a maximal squeezing level of $S = 6.35 \pm 0.11\,\mathrm{dB}$ ($S = 7.42 \pm 0.47\,\mathrm{dB}$) for the NEC (single-SQUID VTT) JPA. For the VTT JPA, we explore a larger pump power range and observe that S strongly decreases beyond a pump power P_{p} of $-31\,\mathrm{dB}$. At this value, there is an optimal trade-off between gain-dependent noise and phase-sensitive attenuation. For $P_{\mathrm{p}} \gtrsim -31\,\mathrm{dB}$, the deamplified variance broadens significantly due to the added noise. The corresponding purity μ of the reconstructed squeezed states is plotted in Fig. 3.13(b). The monotonic decrease of μ is a result from pump-induced noise and gain-dependent environmental noise [85]. The latter is coupled into the JPA due to the finite internal quality factor of the resonator [90]. Another reason for decreasing purity is the effect of higher-order nonlinearities [107].

3.2.3 Gaussianity and physicality checks

Our experiments rely on the assumption that the reconstructed quantum states are Gaussian and can thus be completely described by signal moments up to second order. Simultaneously, we need to ensure that the states are physical, i.e., they need to fulfill the bosonic commutation relations. In the following, we discuss how we verify Gaussianity as well as physicality in our experiments.

Gaussianity As a measure for Gaussianity, we use the absolute value of the cumulants, associated with the phase space quasiprobability distribution [77, 314],

$$\kappa_{mn} = \left| \frac{\partial^n}{\partial x^n} \frac{\partial^m}{\partial y^m} \ln \sum_{k,l} \frac{\langle (\hat{a}^\dagger)^k \hat{a}^l \rangle}{k!l!} x^k y^l \Big|_{x=y=0} \right|. \tag{3.6}$$

To demonstrate Gaussianity, it is necessary to show that $\kappa_{mn} \to 0$ for $m + n = 3$ (skewness) and sufficient to verify that $\kappa_{mn} \to 0$ for $m + n = 4$ (sharpness) [315]. Since measuring zero is not possible in practice, we treat our state as Gaussian if third and fourth order cumulants are significantly smaller than cumulants of first and second order. Although we compare absolute values of cumulants throughout this work, a potentially suitable normalization is given by $\langle \hat{a}^\dagger \hat{a} \rangle^{(m+n)/2}$. The cumulants allow to qualitatively verify Gaussianity, but do not allow for estimating the impact of the Gaussian approximation on relevant quantities such as purity. A general theory for arbitrary microwave states in terms of bosonic field moments is provided in Ref. 316. As an example, purity can be expressed as

$$\mu = \sum_{n,m,k,l} \frac{(-1)^{m+k}(n+k)!}{n!m!k!l!} \delta_{n+k,m+l} \langle (\hat{a}^\dagger)^n \hat{a}^m \rangle \langle (\hat{a}^\dagger)^k \hat{a}^l \rangle. \tag{3.7}$$

Since Eq. (3.7) requires knowledge of an infinite number of moments while we reconstruct moments up to the fourth order, we can only estimate the impact of non-Gaussianity using a perturbative approach. One possibility is to define $\mu^{(N)}$ as the sum Eq. (3.7) of all terms which contain moments up to the Nth order. For a thermal state, we obtain

$$\mu^{(4)} = 1 - 2\langle \hat{a}^\dagger \hat{a} \rangle - 3\langle (\hat{a}^\dagger)^2 \hat{a}^2 \rangle \langle \hat{a}^\dagger \hat{a} \rangle + \frac{3}{2} \langle (\hat{a}^\dagger)^2 \hat{a}^2 \rangle^2 + \langle (\hat{a}^\dagger)^2 \hat{a}^2 \rangle. \tag{3.8}$$

We can now insert experimental results into this equation and compare the resulting $\mu^{(4)}$ to the value $\mu_{\text{th}}^{(4)}$ of an ideal thermal state solely determined by the measured photon number $\langle \hat{a}^\dagger \hat{a} \rangle$ according to Eq. (2.102). As an example, we use reference-state tomography to reconstruct a thermal state at one of our heatable attenuators with a temperature $600\,\text{mK}$ at $5.435\,\text{GHz}$. Since amplitude modulation is not possible in such a measurement, the reference state has been recorded separately. We measure the moments $\langle \hat{a}^\dagger \hat{a} \rangle = 1.803 \pm 0.001$ and $\langle (\hat{a}^\dagger)^2 \hat{a}^2 \rangle = 6.487 \pm 0.059$. The reconstructed photon number coincides well with the expected value $n_{\text{th}} = 1.835$ obtained from the Planck distribution. We then obtain a relative deviation $\epsilon \equiv |(\mu_{\text{th}}^{(4)} - \mu^{(4)})/\mu_{\text{th}}^{(4)}| \simeq 0.69\,\%$. In an alternative ansatz, we assume that effects from non-Gaussianity are small and can be described by a perturbation parameter $\lambda \simeq 1$ which modifies thermal statistics according to

$$\langle (\hat{a}^\dagger)^n \hat{a}^m \rangle = n! \lambda^{n-1} \delta_{n,m} \langle \hat{a}^\dagger \hat{a} \rangle^n. \tag{3.9}$$

The parameter λ can be related to the reconstructed $g^{(2)}$-function via $\lambda = g^{(2)}(0)/2$. We find

$$\mu = \sum_{n,k} \frac{(-1)^{n+k}(n+k)!}{n!k!} \lambda^{n+k-2} \langle \hat{a}^\dagger \hat{a} \rangle^{n+k} = \frac{1}{\lambda^2} \frac{1}{1 + 2\lambda \langle \hat{a}^\dagger \hat{a} \rangle}. \tag{3.10}$$

We can compare this purity with the purity μ_{th} under the assumption of an ideal thermal state with moments satisfying Eq. (3.9) and $\langle \hat{a}^\dagger \hat{a} \rangle$ corresponding to the measured photon number. For our exemplary measurement, we find $\lambda = 0.9978$ and $\epsilon \equiv |(\mu_{\text{th}} - \mu)/\mu_{\text{th}}| =$

0.60 % in good agreement with the above result. We conclude that, in this specific example, the error from the Gaussian approximation is less than 1 %. Finally, we note that the general treatment of quantum microwave states in terms of moments is tedious since the series of the form of Eq. (3.7) converges only conditionally. Hence, the result depends on the order of the terms, according to the Riemann rearrangement theorem [142]. In practice, we treat our states as Gaussian in case we measure $\kappa_{mn} \ll \kappa_{lj}$ for $m + n \geq 3$ and $l + j \leq 2$. In addition, we take particular care that the statistical error bars of κ_{mn} cross zero. However, the cumulant method does not provide any quantitative measure of non-Gaussianity.

Physicality checks and maximum-likelihood estimation   Resulting from the low SNR, it can happen that the reconstructed covariance matrix is not physical. An ℓ-mode Gaussian state, described with a covariance matrix $\boldsymbol{V}$, is only physically valid if the positive definiteness condition Eq. (2.93) is fulfilled. In particular, we can demand

$$\det \boldsymbol{V} \geq \frac{1}{16^\ell}, \qquad 2\ell = \dim \boldsymbol{V}, \tag{3.11}$$

which corresponds to the conventional Heisenberg uncertainty relation in case of single mode states. Equation (2.93) can be rewritten in terms of inequalities between reconstructed moments [317]. Our reconstruction routine includes a step which sorts out the unphysical states. However, the effect of "unphysicality" is often a result of insufficient averaging. Thus, these states can still be taken into account to decrease the overall measurement uncertainty in large enough ensembles. A more detailed study about the impact of our physicality checks is provided in Ref. 112. In case the measurement is so noisy that a significant part of the reconstructed covariance matrices $\boldsymbol{V}$ becomes unphysical, it is beneficial to find the optimal approximation of the reconstructed quasiprobability distribution by a physically valid distribution. In the simplest approach of such a maximum-likelihood estimation [318], we parametrize a general real and symmetric covariance matrix $\boldsymbol{V}'$ by a parameter set $\{t_i\}$ and determine

$$\min \|\boldsymbol{V} - \boldsymbol{V}'\|_{\mathrm{F}}, \qquad \det \boldsymbol{V}' \geq \frac{1}{16^\ell}, \tag{3.12}$$

where $\|\cdot\|_{\mathrm{F}}$ denotes the Frobenius norm. For pure states, we minimize the likelihood-functional

$$\mathcal{L}(V', \lambda) = \|\boldsymbol{V} - \boldsymbol{V}'\|_{\mathrm{F}}^2 + \lambda \left(\det \boldsymbol{V}' - \frac{1}{16^\ell} \right), \tag{3.13}$$

where λ is introduced as a Lagrangian multiplier. A suitable way to solve this problem in Matlab is the `fminsearch` function, which makes use of the Nelder-Mead algorithm [319]. Since this optimization problem does not have to be convex in general, we need to construct a proper initialization matrix $\boldsymbol{V}_0$ in order to avoid convergence to a local

minimum. This can be realized by rescaling the measured covariance matrix $\boldsymbol{V}$ to

$$\boldsymbol{V}_0 = \frac{1}{4\sqrt[2\ell]{\det \boldsymbol{V}}}\boldsymbol{V}. \tag{3.14}$$

3.3 Two-dimensional Planck spectroscopy

In Sec. 3.1.4, we have discussed our photon number calibration measurement, relying on Planck spectroscopy. However, our state reconstruction requires knowledge of the losses between the photon source and the reconstruction point. In practice, we carefully estimate these losses from the corresponding data sheet values and from our TDR characterization at room temperature. However, this procedure does not take into account that these losses could be different at millikelvin temperatures. An accurate prediction of the temperature dependence of the losses is generally difficult. One possible way to solve this problem is a two-dimensional Planck spectroscopy, where we use losses ε between the calibrated photon source and the HEMT amplifier as a third fitting parameter. This can be done by variation of the mixing chamber temperature T_{mc} in addition to the attenuator temperature sweep T_{a}. The detected power at the ADC is then given by

$$P(T_{\mathrm{a}}, T_{\mathrm{mc}}) = \frac{\langle I^2\rangle + \langle Q^2\rangle}{Z_0} = \frac{\kappa}{Z_0}\left[\frac{1-\varepsilon}{2}\coth\left(\frac{\hbar\omega_{\mathrm{s}}}{2k_{\mathrm{B}}T_{\mathrm{a}}}\right) + \frac{\varepsilon}{2}\coth\left(\frac{\hbar\omega_{\mathrm{s}}}{2k_{\mathrm{B}}T_{\mathrm{mc}}}\right) + n_{\mathrm{H}}\right]. \tag{3.15}$$

In Fig. 3.14(a), we plot Eq. (3.15) for $\omega_{\mathrm{s}}/2\pi = 5.5\,\mathrm{GHz}$, $n_{\mathrm{H}} = 7$, $\varepsilon = 1\,\mathrm{dB}$ and the arbitrary choice $\kappa/Z_0 = 50\,\Omega^{-1}$. We clearly observe that the offset of each Planck curve depends on T_{mc}.

In the next step, we experimentally perform the two-dimensional Planck spectroscopy in the Bob cryostat. We record a respective Planck curve at $\omega_{\mathrm{s}}/2\pi = 5.5\,\mathrm{GHz}$ for PID-stabilized values up to $T_{\mathrm{mc}} = 350\,\mathrm{mK}$. The result of this measurement is shown in Fig. 3.14(b). The number of recorded points decreases since, in Eq. (3.15), we treat T_{a} and T_{mc} as independent control quantities. Thus, we measure the mutual temperature response of T_{a} and T_{mc} in a separate calibration measurement and only use data points where this independence is valid. The Planck curves are simultaneously fitted in a weighted least-square fit routine, according to Eq. (3.15). The weights for each Planck curve are chosen proportionally to the amount of data points. From the fit, we obtain $\varepsilon = 2.79\,\mathrm{dB}$ and $n_{\mathrm{H}} = 6.83$. The HEMT amplifier noise fits well with the specified data sheet value of $n_{\mathrm{H}} = 6.2$ photons. We compare the result to a 1D PNCF measurement, where we estimate $\varepsilon = 2.1\,\mathrm{dB}$ and measure $n_{\mathrm{H}} = 9.59$. We observe that the HEMT amplifier noise significantly deviates from the data sheet value in this case. This results from the fact that any 4-port device in front of the first amplifier increases the effective noise by the inverse transmissivity. This reasoning also holds for losses since they are described with a beam splitter model. Thus, the determination of the amplifier noise crucially depends
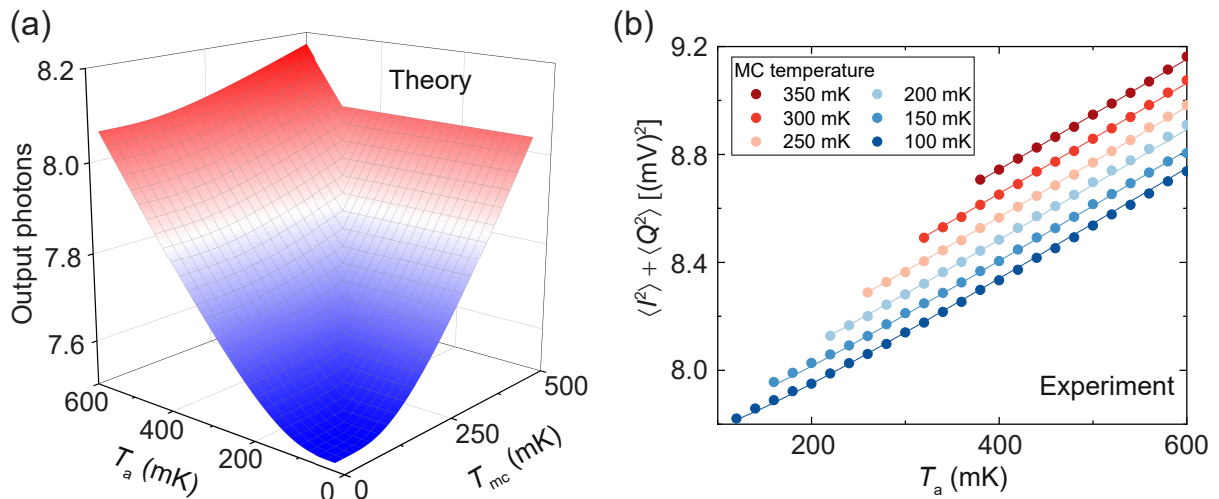
Figure 3.14: (a) Theoretical expectation of 2D Planck spectroscopy at $\omega_s/2\pi = 5.5\,\text{GHz}$ under the approximation of infinitely weak thermal coupling between MC and heatable attenuator. For the calculation, we assume the HEMT amplifier noise $n_H = 7$, losses $\varepsilon = 1\,\text{dB}$ between attenuator and HEMT amplifier, and an arbitrary PNCF $\kappa/Z_0 = 50\,\Omega^{-1}$. (b) Experimental 2D Planck spectroscopy. The offset of each Planck curve depends on the stabilized mixing chamber temperature T_{mc}. The number of data points decreases with increasing T_{mc} since we only consider data points where the decoupling assumption is valid.

on a correct loss estimation.[51] Consequently, the 2D Planck spectroscopy can be used to accurately and self-consistently determine the noise temperature of amplifiers. We expect the Planck curves to be equidistantly spaced by $\Delta P \simeq \kappa\varepsilon k_B\Delta T/(Z_0\hbar\omega_s)$, which is observed in experiment for $T_{mc} \lesssim 250\,\text{mK}$. At higher temperature, the offset increases, which might be a result from emerging temperature dependence of ε and from the fact that the effective bath temperature, which couples via the losses, differs from T_{mc}. The deviation of $0.69\,\text{dB}$ between measured and estimated ε results from the fact that, in this specific experiment, we have installed a Josephson travelling wave parametric amplifier (JTWPA) between heatable attenuator and HEMT amplifier, which has not been taken into account in the loss estimation [304, 305]. The JTWPA has been provided by VTT and is based on three-wave mixing, induced by a pumped Josephson metamaterial formed by an array of superconducting nonlinear asymmetric inductive elements (SNAILs).[52] To benchmark whether we can accurately fit the losses, we exploit the flux tuning of the SNAIL to vary ε. The orange line in Fig. 3.15(a) shows the JTWPA transmission at $5.5\,\text{GHz}$ as a function of the DC flux, which is proportional to the current applied to the inductance on top of the JTWPA. The transmission is recorded relative to zero

---

[51]This is also the reason why the effectively determined noise temperature of the HEMT amplifiers is setup-dependent. A long term study in which we investigate this phenomenon for the years $2014-2020$ can be found in Ref. 282.

[52]We do not discuss the theory of SNAILs and the JTWPA in this work since we have not employed the TWPA in any of our quantum communication experiments. More information about SNAILs is provided in Ref. 305.
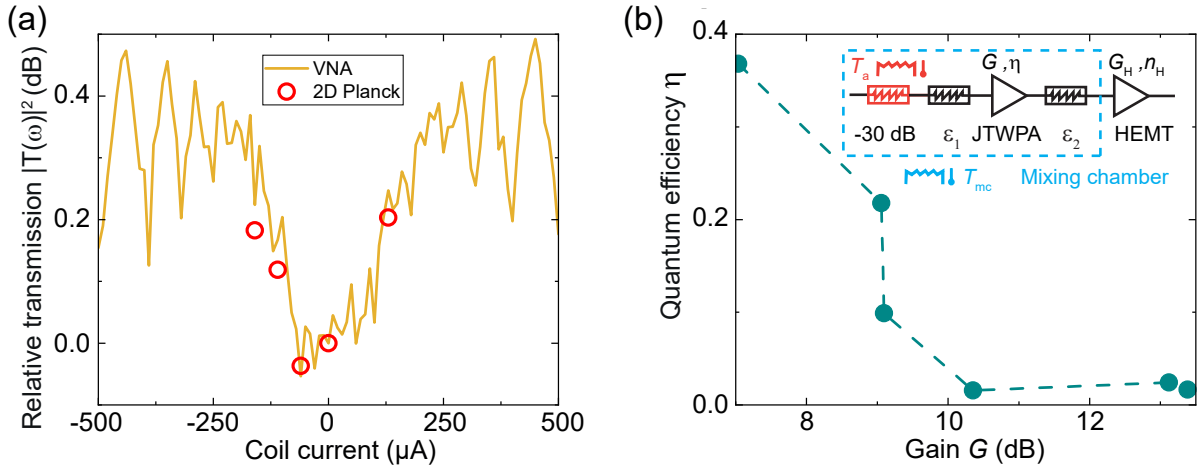
Figure 3.15: (a) Flux tuning of the transmission of a JTWPA. The solid orange line corresponds to a VNA measurement. Transmission is measured relative to zero coil current. The red dots correspond to separate 2D PNCF measurements and have been determined from the fitted losses. A good agreement with the VNA transmission demonstrates that 2D Planck spectroscopy can be used for sensitive loss measurements. (b) Quantum efficiency of the JTWPA determined with 2D Planck spectroscopy, where we exploit that the noise measurement does not depend on any loss estimation. The inset shows the measurement scheme consisting of the heatable attenuator, the JTWPA, and the HEMT amplifier. Dashed lines are a guide to the eye.

current. Next, we perform our 2D Planck spectroscopy for five distinct flux points. We then determine the relative transmission from the fitted losses $\varepsilon = 2.79\,\mathrm{dB}$ at zero current. The results are depicted by the red circles and are in good agreement with the VNA measurement, proving that our method can be employed for self-calibrated loss measurement. Next, we couple a pump tone at $12\,\mathrm{GHz}$ to the JTWPA[53] and employ the 2D Planck spectroscopy to measure its nondegenerate quantum efficiency η as a function of gain G. The result of this measurement is shown in Fig. 3.15(b). The effect of the HEMT amplifier is removed by using the Friis equation. We observe a significant decrease of η as a function of gain. This effect is potentially related to the fact that the JTWPA is a broadband device which enters compression already at comparably low gain in case of broadband input signals. A technically relevant aspect of employing multiple amplifiers is the fact that, in case we modulate the gain of the amplifiers in a pulsed measurement, we can independently determine the losses ε_1 before the first amplifier, as well as total losses $\varepsilon_1 + \varepsilon_2$. In case the amplifier gain becomes sufficiently large, only losses before the first amplification stage are relevant. Thus, the 2D Planck spectroscopy enables us to sensitively measure the loss of an RF component by installing it between two high-gain amplifiers. Apart from providing an accurate photon number calibration method, the

---

[53]We use a `Miteq` CPL-4-8GHz coupler with $-20\,\mathrm{dBm}$ coupling for this purpose. Although this device is only specified up to $8\,\mathrm{GHz}$, it still works at our pump frequency of $12\,\mathrm{GHz}$ with reduced coupling of $-33\,\mathrm{dBm}$.

2D Planck spectroscopy enables the possibility of studying temperature-dependent losses, e.g., in Kondo physics [320]. A more detailed analysis of the 2D Planck spectroscopy can be found in Ref. 282. Throughout the rest of this work, the term "Planck spectroscopy" always refers to the 1D method, described in Sec. 3.1.4, if not explicitly specified further.

Chapter 4

Quantum efficiency of Josephson parametric amplifiers

Various experiments have demonstrated that a JPA can be operated as a quantum-limited phase-preserving amplifier [79–81], as well as a phase-sensitive amplifier with quantum efficiency exceeding the SQL [75, 321]. Furthermore, in Sec. 2.1.4, we have predicted that quantum efficiency of a nondegenerate parametric amplification process can exceed the standard quantum limit if the signal spectrum is sufficiently broad. In this chapter, we experimentally validate this prediction by directly comparing quantum efficiencies corresponding to the amplification of broadband thermal states and narrowband coherent states. These measurements are performed with two distinct JPAs, to check for reproducibility of our results. The results of this chapter have been published in Ref. 85. Parts of the figures as well as from the text have been adopted from this publication. The results of this section are of special relevance for protocols which require efficient state reconstruction, such as quantum illumination [322, 323], quantum communication, dispersive qubit readout [109], dark matter axion detection [324], or sensing of the cosmic microwave background [325].

4.1 Experimental broadband and narrowband quantum efficiency

Experimental setup Our experimental setup is schematically depicted in Fig. 4.1. Our amplification chain consists of a flux-driven JPA,[1] serially connected to a cryogenic high-electron-mobility transistor (HEMT) amplifier with a gain of $G_\mathrm{H} = 41\,\mathrm{dB}$. The JPA is operated in the nondegenerate regime. This is realized by detuning the signal frequency ω_s by $\Delta/2\pi = 300\,\mathrm{kHz}$ from the resonance frequency $\omega_0 = \omega_\mathrm{p}/2$. A circulator at the JPA input separates the resonator input and output fields.[2] The statistical moments of the output signal are detected within the single-side bandwidth $B/2\pi = 200\,\mathrm{kHz}$

---

[1]We use NEC JPAs in this experiment.
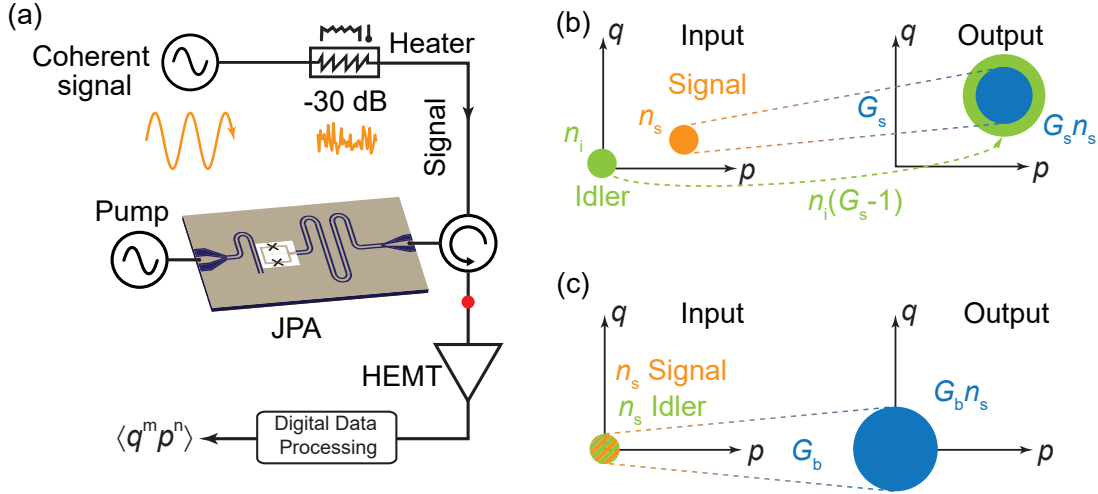[2]We use Quinstar CTH1184-KS18 circulators for this purpose.

Figure 4.1: (a) Experimental scheme for nondegenerate narrowband and broadband amplification. The amplification chain consists of a JPA and a cryogenic HEMT amplifier. Coherent states can be applied via a microwave source at room temperature and a heatable 30 dB attenuator enables the generation of broadband thermal states. The red dot indicates the signal reconstruction point. (b) Phase space representation of narrowband amplification. Colored circles depict the respective variance of the input signal (orange), output signal (blue) and input idler (green). (c) phase space representation of broadband amplification. The idler no longer acts as a noise port and effectively contributes to the signal, leading to a total broadband gain $G_{\mathrm{b}} = 2G_{\mathrm{s}} - 1$.

using the reference-state reconstruction method at the reconstruction point [83, 289]. The experiment is performed for two JPA devices, labelled JPA 1 and JPA 2, which are operated at different DC flux spots to check for reproducibility of our results. For JPA 1 (JPA 2), we reconstruct the signal at $\omega_{\mathrm{s}}/2\pi = 5.500\,\mathrm{GHz}$ (5.435 GHz). A continuous coherent tone can be applied via a microwave input line and a heatable 30 dB attenuator allows for the generation of thermal states as broadband input signals. Thus, we can directly compare narrowband amplification, depicted in Fig. 4.1(b) and the broadband regime, shown in Fig. 4.1(c) via the same input and output line without the need of any modifications in the setup.

Measurement of broadband and narrowband quantum efficiency   To extract the noise added by the amplification chain for broadband input signals, we vary the JPA gain and perform Planck spectroscopy, as described in Sec. 3.1.4.[3] The total power $P(T_{\mathrm{a}})$ is determined by the sum $\langle I^2 \rangle + \langle Q^2 \rangle$ of the second order moments and follows a Planck curve

$$P(T_{\mathrm{a}}) = \frac{\langle I^2 \rangle + \langle Q^2 \rangle}{Z_0} = \frac{\kappa G_{\mathrm{b}}}{Z_0} \left[\frac{1}{2} \coth\left(\frac{\hbar \omega_{\mathrm{s}}}{2 k_{\mathrm{B}} T_{\mathrm{a}}} \right) + n_{\mathrm{f,b}} \right], \tag{4.1}$$

---

[3]We use a `Lakeshore370` resistance bridge for this purpose.

where $n_{\mathrm{f,b}}$ corresponds to the total noise added by the overall amplification chain referred to the input, $Z_0 = 50\,\Omega$ is the impedance, and κ is the PNCF (cf. Sec. 3.1.4) at the reconstruction point. The gain dependence of $n_{\mathrm{f,b}}$ is extracted by measuring Planck curves for broadband gains ranging between $5\,\mathrm{dB}$ and $25\,\mathrm{dB}$. To obtain a calibration reference for the broadband amplification gain G_{b} as a function of pump power, we directly probe the pump power dependence of the narrowband signal gain G_{s} at the signal reconstruction frequency using a VNA. We expect $G_{\mathrm{b}} \simeq G_{\mathrm{s}} + 3\,\mathrm{dB}$, according to Eq. (2.34). The Planck spectroscopy is performed in a two-pulse scheme, where the JPA pump is only switched on during the second pulse and the first pulse acts as a reference. Thus, the actual broadband gain can be directly extracted by determining the slope ratio of the linear sections of the Planck curves for the second and first pulses. The detected output photon numbers, $n_{\mathrm{b}} = P(T_{\mathrm{a}})/\kappa$, corresponding to these measurements, are shown as a function of the attenuator temperature in Fig. 4.2(a) for JPA 2. To determine the quantum efficiency for narrowband amplification, the JPA pump is initially switched off and the resonance frequency is tuned out of the measurement bandwidth using a DC flux bias such that the JPA does not impact the calibration procedure. In the next step, we perform Planck spectroscopy to obtain the PNCF at the signal reconstruction point. We then sweep the power P_{coh} of a coherent input signal in a two-pulse measurement to determine the photon number n_{in} at the JPA input using reference-state reconstruction. The result is linearly fitted according to

$$n_{\mathrm{in}}(P_{\mathrm{coh}}) = c_1 P_{\mathrm{coh}} + c_2, \tag{4.2}$$

where c_1 and c_2 are treated as fit parameters. Next, we measure the additive noise photon number. We tune the JPA into resonance and sweep the coherent input power in a two-pulse scheme, where the JPA pump is switched on during the second pulse. The output photon number n_0 (n_{n}), corresponding to the first (second) pulse, is then linearly fitted according to

$$n_0 = c_3 n_{\mathrm{in}} + c_4, \qquad\qquad n_{\mathrm{n}} = c_5 n_{\mathrm{in}} + c_6, \tag{4.3}$$

where c_3, c_4, c_5 and c_6 are fit constants. This procedure enables us to extract the narrowband gain $G_{\mathrm{s}} = c_5/c_3$ and the total number of added noise photons $n_{\mathrm{f,n}} = c_6/G_{\mathrm{s}}$, referred to the JPA input. The experiment is repeated for signal gains ranging from $3\,\mathrm{dB}$ to $24\,\mathrm{dB}$. The measurement results as well as the linear fits are shown for JPA 2 as a logarithmic plot. For the fits, only data points following the expected linear amplifier response are considered to ensure that the determined noise corresponds to the linear regime. We find that for both narrowband and broadband amplification, this is the case for a large range of input parameters, although compression is already visible for gains $G \gtrsim 15\,\mathrm{dB}$. As shown in Fig. 4.2(a), this effect can be especially observed in the broadband regime. To quantify compression in this case, we determine the ratio $R(T_{\mathrm{a}}) = n_{\mathrm{b,det}}(T_{\mathrm{a}})/n_{\mathrm{b,fit}}(T_{\mathrm{a}})$ of the detected output photon number $n_{\mathrm{b,det}}(T_{\mathrm{a}})$ and the expected photon number $n_{\mathrm{b,fit}}(T_{\mathrm{a}})$ from the fit. This allows us to define the compression
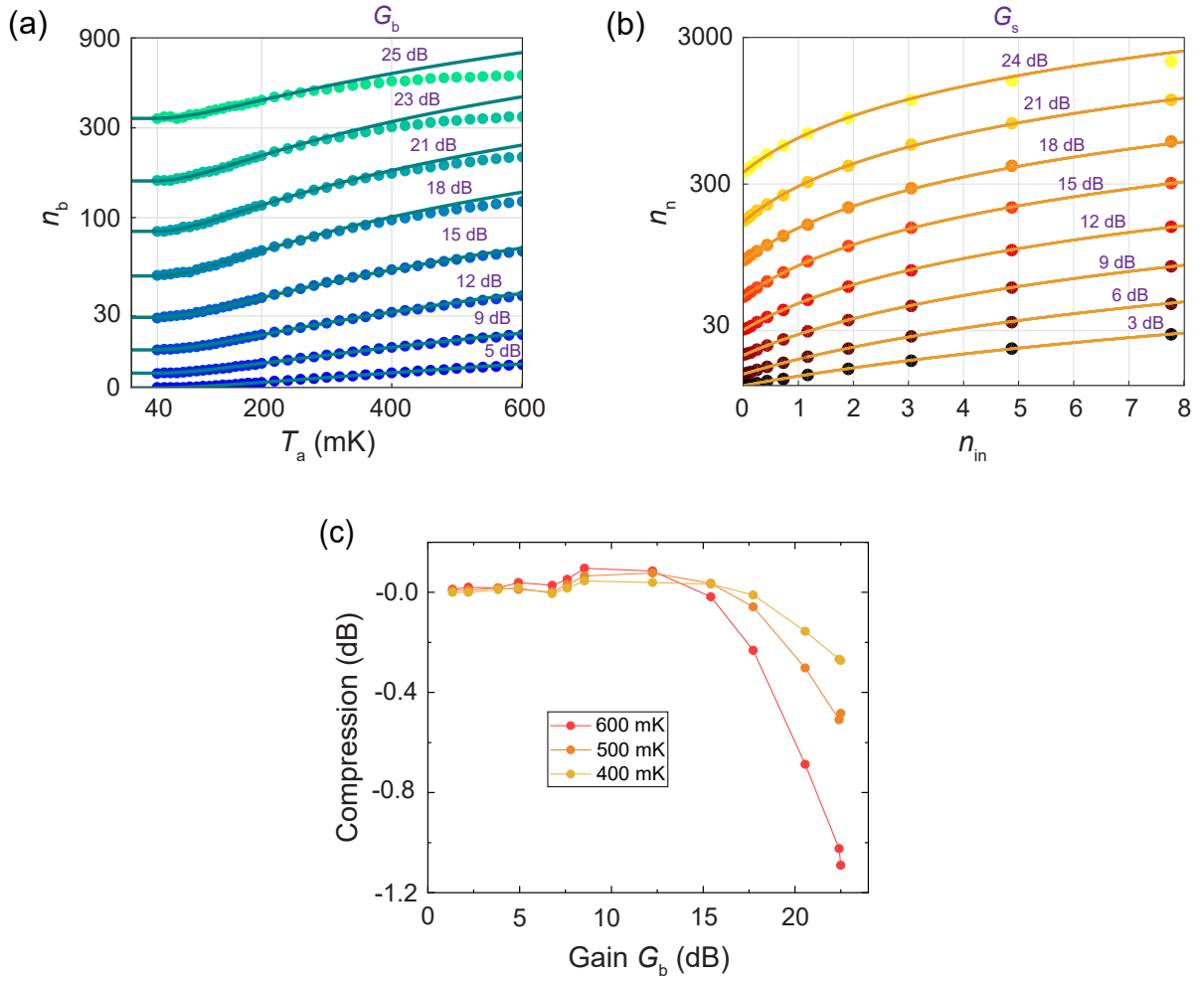
Figure 4.2: (a) Planck spectroscopy for various broadband gains G_b for JPA 2. The output photon number n_b at the reconstruction point is indicated by the dots. Each line corresponds to a fitted Planck curve. (b) Output photon number n_n for narrowband amplification for JPA 2 (dots). Input is a coherent state with photon number n_in. Each curve corresponds to a separate signal gain G_s and the lines corresponds to linear fits. (c) Compression $10\log_{10}\left[n_\mathrm{b,det}(T_\mathrm{a})/n_\mathrm{b,fit}(T_\mathrm{a})\right]$ as a function of broadband gain G_b for thermal input signals, corresponding to 400 mK, 500 mK, and 600 mK, respectively. Solid lines are a guide to the eye.

as $10\log_{10} R(T_\mathrm{a})$. Compression is plotted in Fig. 4.2(c) as a function of G_b and we observe that the 1 dB compression point is reached at $G_\mathrm{b} \simeq 22$ dB for $T_\mathrm{a} = 600$ mK, which corresponds to 2.3 thermal input photons. In addition, we find from Fig. 4.2(b) that, for 2.3 coherent input photons, no relevant compression can be observed in the narrowband case, implying that the narrowband and broadband regimes obey different compression constraints. The fact that the JPA enters compression at an earlier stage in the broadband scenario is consistent with the fact that the idler port acts as an additional port for the input signal which enhances the effective input power.

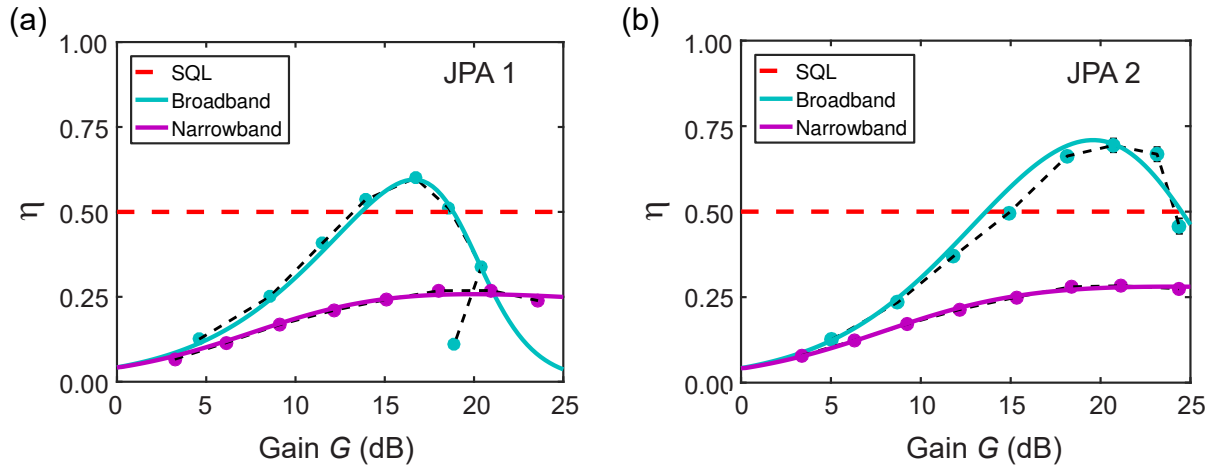Figure 4.3(a) shows the experimentally determined quantum efficiencies for JPA 1 for

Figure 4.3: Experimentally determined quantum efficiency for broadband (cyan dots) and narrowband (purple dots) amplification. Panel (a) shows the data for JPA 1 and panel (b) that for JPA 2. The red dashed line shows the SQL in the high gain limit. Solid lines are fits to the corresponding data using Eq. (4.5) for the broadband case and Eq. (4.6) for the narrowband case. Black dashed lines are guide to the eye.

amplification of broadband thermal states (cyan dots) and for narrowband coherent state amplification (purple dots). The respective results for JPA 2 are depicted in Fig. 4.3(b). For both JPAs, we find a gain region where we significantly exceed the SQL, indicated by the red dashed line, in the case of broadband amplification. We find a maximal quantum efficiency of 0.69 ± 0.02 for JPA 2, where the error has been determined from the fit error by Gaussian error propagation. This value is comparable to quantum efficiencies obtained with degenerate phase-sensitive JPAs. The deviation from the theoretically achievable value $\eta = 1$ can be explained by an interplay between constant HEMT amplifier noise n_{H} and gain-dependent JPA noise $n_{\mathrm{J}}(G_x)$, where $x \in \{\mathrm{s}, \mathrm{b}\}$. The Friis equation implies

$$n_{\mathrm{f},x}(G_x) = n_{\mathrm{J}}(G_x) + \frac{n_{\mathrm{H}}}{G_x}, \qquad \eta(G_x) = \frac{G_x}{G_x + 2 G_x n_{\mathrm{J}}(G_x) + 2 n_{\mathrm{H}}}. \tag{4.4}$$

Thus, the effect of the $n_{\mathrm{H}} = 11.3$ HEMT amplifier photons dominates at low gain but eventually decreases with $1/G_x$. On the other hand, as already indicated in Sec. 2.1.5, $n_{\mathrm{J}}(G_x)$ follows an empirical power law. Thus, the broadband quantum efficiency is fitted using

$$\eta_{\mathrm{b}}(G_{\mathrm{b}}) = \frac{G_{\mathrm{b}}}{G_{\mathrm{b}} + 2 G_{\mathrm{b}} \chi_{1,\mathrm{b}} (G_{\mathrm{b}} - 1)^{\chi_{2,\mathrm{b}}} + 2 n_{\mathrm{H}}}, \tag{4.5}$$

where $\chi_{1,\mathrm{b}}$ and $\chi_{2,\mathrm{b}}$ are treated as fit parameters. To fit the narrowband quantum efficiency, we additionally take the SQL into account and describe the noise by

$$n_{\mathrm{J},\mathrm{n}}(G_{\mathrm{s}}) = \underbrace{\chi_{1,\mathrm{n}} (G_{\mathrm{s}} - 1)^{\chi_{2,\mathrm{n}}}}_{\text{technical noise}} + \underbrace{\frac{1}{2}\left(1 - \frac{1}{G_{\mathrm{s}}}\right)}_{\text{SQL}}. \tag{4.6}$$
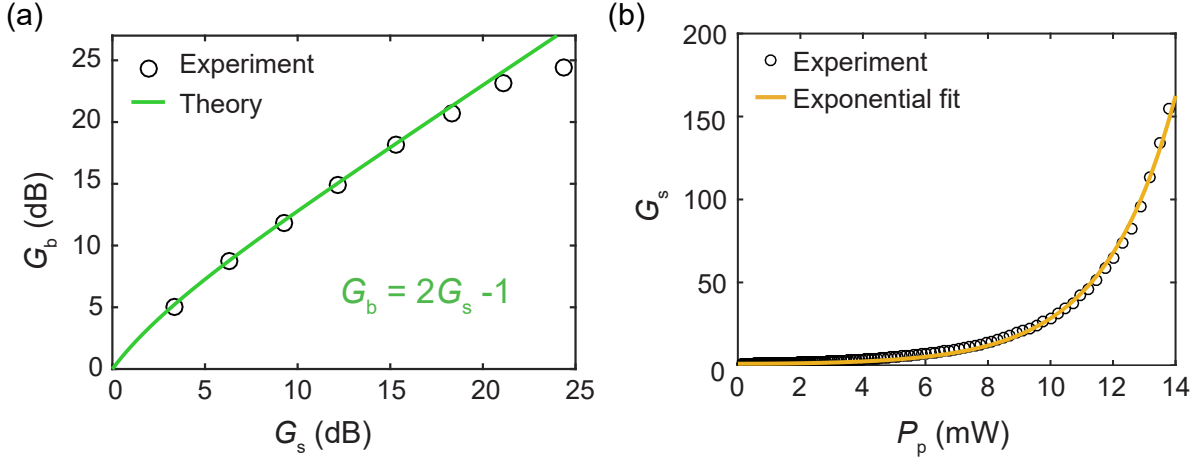
(a)

(b)

Figure 4.4: (a) Direct comparison between the experimentally determined broadband gain G_b and G_s for fixed pump power. The theoretical prediction $G_b = 2G_s - 1$ is accurately reproduced for most data points. (b) Narrowband signal gain G_s as a function of pump power P_p referred to the pump source at room temperature. The orange line corresponds to an exponential fit.

implying that we employ

$$\eta_n(G_s) = \frac{G_s}{2G_s - 1 + 2G_s\chi_{1,n}(G_s - 1)^{\chi_{2,n}} + 2n_H} \tag{4.7}$$

for the fit and use $\chi_{1,n}$ and $\chi_{2,n}$ as fit parameters. The respective fits are shown in Fig. 4.3(a) and Fig. 4.3(b). The corresponding fit parameters are listed in Tab. 4.1. The maximal value of quantum efficiency is determined by the optimal trade-off between constant HEMT amplifier noise and gain-dependent JPA noise. In a simple calculation, we can linearize the JPA gain, $n_J(G) \simeq n'_J G$ and find the optimal gain $G_{opt} = \sqrt{n_H/n'_J}$. The linear treatment in Ref. 66 provides $n'_J = 0.0059$, implying $G_{opt} = 16.4\,\mathrm{dB}$ in our case, which coincides well with the experimentally determined maxima in Fig. 4.3 and indicates that our JPAs behave in a comparably universal way. This result is useful in case we employ our system for applications which require high quantum efficiency such as qubit readout. In Fig. 4.4(a), we directly compare the experimentally determined G_b with G_s at fixed pump power and observe a good agreement with the theoretical prediction $G_b = 2G_s - 1$, indicated by the green solid line. This observation serves as an experimental verification that the input idler modes indeed effectively contribute to the signal.

Table 4.1: Fit parameters corresponding to the measured broadband and narrowband quantum efficiencies of JPA 1 and JPA 2.

Fit parameter	$\chi_{1,b}$	$\chi_{2,b}$	$\chi_{1,n}$	$\chi_{2,n}$
JPA 1	$6.03 \cdot 10^{-6}$	2.54	0.46	0.130
JPA 2	$8.48 \cdot 10^{-5}$	1.52	0.53	0.059

In the next step, we perform a Gedankenexperiment, where we amplify a broadband signal with a constant photon number n_s in the signal sideband. Now, we continuously reduce the photon number n_i of the idler input. At $n_i = 0$, we then expect to recover the SQL. However, our theory simultaneously predicts absence of the SQL for any infinitesimal $n_i > 0$, which is seemingly a contradiction. To solve this paradox, we have to distinguish between the "ideal" experimentalist, who has a detector at signal and idler frequency, and the "practical" experimentalist, as in our experiment, who only measures the signal sideband. For simplicity, we assume that the broadband signal consists of one signal mode and one idler mode. The theory in Sec. 2.1.4 is based on the assumption of the "ideal" experimentalist who detects two modes and can uniquely reconstruct input signal and input idler using a two-mode reference-state reconstruction. This works for arbitrary $n_i > 0$ (assuming perfect detection efficiency and sufficiently large gain). If $n_i = 0$, the "ideal" experimentalist would realize that the system of two equations for state tomography becomes redundant and reduces to a single equation, implying that one of the detectors effectively only measures noise. On the other hand, the "practical" experimentalist always only detects one mode and, thus, can never reconstruct n_s and n_i uniquely. However, when the "practical" experimentalist performs a power sweep, the ratio $\nu \equiv n_i/n_s$ remains constant and, effectively, a gain G_{eff} and noise n_{eff} given by

$$G_{\mathrm{eff}} = G_s + \nu(G_s - 1), \qquad n_{\mathrm{eff}} = \frac{1}{2}\left(\frac{2G_s - 1}{G_{\mathrm{eff}}} - 1\right) \tag{4.8}$$

will be measured. For $n_s = n_i$, the above equations reproduce our measurement results for broadband signals, and if we decrease n_i to zero, n_{eff} monotonically approaches the SQL.

The fact that the nondegenerate broadband and narrowband amplification regimes behave fundamentally different is of particular technical relevance for scenarios where Planck spectroscopy is used to calibrate the quantum efficiency of a detection setup. In addition, efficient broadband nondegenerate amplification can be exploited for parity detection of two superconducting qubits. In this case, the readout resonators of both qubits can be operated at the signal and idler frequencies of the JPA, respectively. The readout can be realized via a multiplexed broadband signal. Such a scheme can be especially relevant in the scope of stabilizer codes for quantum error correction [326, 327], where parity can be used as an error detection and correction syndrome [328]. In addition, broadband thermal states can be used for QKD [329]. Broadband signals can also be directly employed for the dispersive qubit readout. It can be shown using the Lindblad master equation that the equilibrium photon number inside a readout resonator can be well controlled by a thermal environment [297, 330]. Thus, from a fundamental point of view, the power spectral density of ambient thermal noise can be directly used as an indicator of the qubit state [331]. Such a scheme can potentially reduce a number of microwave readout lines needed for the operation of superconducting quantum processors.

As already discussed, the pump power dependence of G_s can be approximately described

by an exponential function in the limit of high gain, in accordance to Eq. (2.26). The result of such a calibration measurement and the corresponding exponential fit are shown in Fig. 4.4(b). This result is of particular interest for the next section, where pump-induced noise is considered as an origin of the gain-dependent JPA noise.

4.1.1 Gain-dependence of pump-induced noise

Here, we develop a phenomenological theory on how the pump-induced noise can lead to the observed power-law dependence of the gain-dependent JPA noise. To this end, we describe the coherent pump signal $\hat{A}(t)$ in a frame rotating with the pump frequency ω_p as

$$\hat{A}(t) = (\alpha_0 + \hat{f}_\mathrm{p}(t))e^{i\omega_\mathrm{p}t}, \tag{4.9}$$

where α_0 corresponds to the the amplitude of the pump field which is assumed to be real and $\hat{f}_\mathrm{p}(t)$ denotes the bosonic operator for the superposed fluctuations. Without loss of generality, we set the pump phase to zero, implying that α_0 is a real number. For the pump photon number operator $\hat{n}_\mathrm{p}(t)$ in the signal, we obtain

$$\hat{n}_\mathrm{p}(t) = \hat{A}^\dagger(t)\hat{A}(t) = |\alpha_0|^2 + \alpha_0(\hat{f}_\mathrm{p}(t) + \hat{f}_\mathrm{p}^\dagger(t)) + \hat{f}_\mathrm{p}^\dagger(t)\hat{f}_\mathrm{p}(t). \tag{4.10}$$

Thus, the noise contribution $\hat{n}_\mathrm{f,p}$ in the pump line is given by $\alpha_0(\hat{f}_\mathrm{p}(t) + \hat{f}_\mathrm{p}^\dagger(t)) + \hat{f}_\mathrm{p}^\dagger(t)\hat{f}_\mathrm{p}(t)$. The first term corresponds to the beating between the coherent pump tone and the noise mode and the second term provides the noise photon number associated with the mode $\hat{f}_\mathrm{p}(t)$. To find the corresponding noise spectral density, we calculate the autocorrelation function

$$\begin{aligned}
\langle \hat{n}_\mathrm{f,p}(t)\hat{n}_\mathrm{f,p}(t-\tau)\rangle = {}& \alpha_0^2\langle(\hat{f}_\mathrm{p}(t) + \hat{f}_\mathrm{p}^\dagger(t))(\hat{f}_\mathrm{p}(t-\tau) + \hat{f}_\mathrm{p}^\dagger(t-\tau))\rangle \\
& + \alpha_0\langle\hat{f}_\mathrm{p}(t)\hat{f}_\mathrm{p}^\dagger(t-\tau)\hat{f}_\mathrm{p}(t-\tau)\rangle + \alpha_0\langle\hat{f}_\mathrm{p}^\dagger(t)\hat{f}_\mathrm{p}^\dagger(t-\tau)\hat{f}_\mathrm{p}(t-\tau)\rangle \\
& + \alpha_0\langle\hat{f}_\mathrm{p}^\dagger(t)\hat{f}_\mathrm{p}(t)\hat{f}_\mathrm{p}(t-\tau)\rangle + \alpha_0\langle\hat{f}_\mathrm{p}^\dagger(t)\hat{f}_\mathrm{p}(t)\hat{f}_\mathrm{p}^\dagger(t-\tau)\rangle \\
& + \langle\hat{f}_\mathrm{p}^\dagger(t)\hat{f}_\mathrm{p}(t)\hat{f}_\mathrm{p}^\dagger(t-\tau)\hat{f}_\mathrm{p}(t-\tau)\rangle.
\end{aligned} \tag{4.11}$$

Next, we assume that the noise power spectrum is white, which implies

$$\begin{aligned}
\langle \hat{n}_\mathrm{f,p}(t)\hat{n}_\mathrm{f,p}(t-\tau)\rangle = {}& \underbrace{\alpha_0^2\langle(\hat{f}_\mathrm{p}(t) + \hat{f}_\mathrm{p}^\dagger(t))^2\rangle}_{(\mathrm{I})}\delta(\tau) + \underbrace{\alpha_0\langle\hat{f}_\mathrm{p}^{\dagger2}(t)\hat{f}_\mathrm{p}(t)\rangle}_{(\mathrm{II})}\delta(\tau) \\
& + \underbrace{\alpha_0\langle\hat{f}_\mathrm{p}^\dagger(t)\hat{f}_\mathrm{p}^2(t)\rangle}_{(\mathrm{III})}\delta(\tau) + \underbrace{\alpha_0\langle\hat{f}_\mathrm{p}^\dagger(t)\hat{f}_\mathrm{p}(t)\hat{f}_\mathrm{p}^\dagger(t)\rangle}_{(\mathrm{IV})}\delta(\tau) \\
& + \underbrace{\langle\hat{f}_\mathrm{p}^\dagger(t)\hat{f}_\mathrm{p}(t)\hat{f}_\mathrm{p}^\dagger(t)\hat{f}_\mathrm{p}(t)\rangle}_{(\mathrm{V})}\delta(\tau),
\end{aligned} \tag{4.12}$$

where $\delta(\tau)$ denotes the Dirac delta distribution. The contributions (II), (III), and (IV) vanish since they contain odd moments of $\hat{f}_\mathrm{p}(t)$ and we assume the probability distribution for $\hat{f}_\mathrm{p}(t)$ to have zero mean. This leads to

$$\langle \hat{n}_\mathrm{f,p}(t)\hat{n}_\mathrm{f,p}(t-\tau)\rangle = \left[\alpha_0^2 \langle (\hat{f}_\mathrm{p}(t) + \hat{f}_\mathrm{p}^\dagger(t))^2\rangle + \hat{f}_\mathrm{p}^\dagger(t)\hat{f}_\mathrm{p}(t)\hat{f}_\mathrm{p}^\dagger(t)\hat{f}_\mathrm{p}(t)\right]\delta(\tau). \qquad (4.13)$$

We apply the Wiener-Khinchine theorem to get the variance σ_p^2 of the noise power [332–334]

$$\sigma_\mathrm{p}^2 = \int_{-\infty}^{\infty} e^{i\omega\tau}\langle n_\mathrm{f,p}(t)n_\mathrm{f,p}(t-\tau)\rangle d\tau = \alpha_0^2\left[\langle \hat{f}_\mathrm{p}(t)^2\rangle + \langle \hat{f}_\mathrm{p}^\dagger(t)^2\rangle + \langle\{\hat{f}_\mathrm{p}(t),\hat{f}_\mathrm{p}^\dagger(t)\}\rangle\right]$$
$$+ \langle \hat{f}_\mathrm{p}^\dagger(t)\hat{f}_\mathrm{p}(t)\hat{f}_\mathrm{p}^\dagger(t)\hat{f}_\mathrm{p}(t)\rangle, \qquad (4.14)$$

where $\{\cdot,\cdot\}$ denotes the anticommutator. Equation (4.14) describes σ_p^2 in terms of statistical moments up to the fourth order. However, no further assumptions regarding the statistics of $\hat{f}_\mathrm{p}(t)$ have been made. Such a general description has the advantage that it allows one to describe conventional bosonic noise contributions. In principle, such an approach can also be used to describe fermionic noise [335], e.g., from quasiparticle formation [69, 336], by considering the fermionic anticommutation relations. In our case, we use the bosonic commutation relations and rewrite Eq. (4.14) in terms of normally ordered moments

$$\langle \hat{n}_\mathrm{f,p}(t)\hat{n}_\mathrm{f,p}(t-\tau)\rangle = \alpha_0^2\left[\langle \hat{f}_\mathrm{p}(t)^2\rangle + \langle \hat{f}_\mathrm{p}^\dagger(t)^2\rangle + 2\langle \hat{f}_\mathrm{p}^\dagger(t)\hat{f}_\mathrm{p}(t)\rangle + 1\right]\delta(\tau)$$
$$+ \left[\langle \hat{f}_\mathrm{p}^\dagger(t)^2\hat{f}_\mathrm{p}(t)^2\rangle + \langle \hat{f}_\mathrm{p}(t)^\dagger\hat{f}_\mathrm{p}(t)\rangle\right]\delta(\tau). \qquad (4.15)$$

We assume that $\hat{f}_\mathrm{p}$ obeys thermal statistics, $\langle \hat{f}_\mathrm{p}^\dagger(t)^n\hat{f}_\mathrm{p}(t)^m\rangle = n!\delta_{nm}n_\mathrm{th}^n$, where n_th denotes the average thermal photon number in the pump line. Furthermore, we set $\alpha_0^2 = \bar{n}_\mathrm{p}$, where $\bar{n}_\mathrm{p}$ is the expectation value for the coherent photons in the pump signal. The pump power fluctuations then correspond to a displaced thermal state with photon number variance

$$\sigma_\mathrm{p}^2 = \bar{n}_\mathrm{p}(2n_\mathrm{th} + 1) + 2n_\mathrm{th}^2 + n_\mathrm{th}. \qquad (4.16)$$

For $n_\mathrm{th} = 0$, Eq. (4.16) reproduces the Poissonian photon number fluctuations in the coherent pump tone, manifesting as shot noise emerging from the discreteness of photons [48, 337, 338]. Since we assume the JPA to be operated close to criticality, we use the exponential approximation Eq. (2.26) [cf. Fig.4.4(b)] and make the ansatz

$$G_\mathrm{s}(t) = Ce^{an_\mathrm{p}(t)}, \qquad (4.17)$$

with not further specified constants C and a. We now assume that the fluctuations in the pump photon number translate to fluctuations in gain. Thus, we calculate the statistical moments $\langle G_\mathrm{s}(t)^k\rangle$, $k \in \mathbb{N}$. We define $\zeta(t) \equiv n_\mathrm{p}(t) - \bar{n}_\mathrm{p}$ and assume that this quantity

describes a centralized normal distribution with variance $\sigma_{\rm p}^2$.[4] According to Eq. (2.98), we then have

$$\langle \zeta(t)^n \rangle = \sigma_{\rm p}^n \frac{2^{\frac{n}{2}} \Gamma\left(\frac{n+1}{2}\right)}{\sqrt{\pi}} \frac{1-(-1)^n}{2} = \begin{cases} 0 & \text{if } n \text{ is odd} \\ \sigma_{\rm p}^n (n-1)!! & \text{if } n \text{ is even} \end{cases}, \qquad (4.18)$$

where !! denotes the double factorial. As a result, we find

$$\langle G_{\rm s}(t)^k \rangle = C^k e^{ak\bar{n}_{\rm p}} \langle e^{ak\zeta(t)} \rangle = C^k e^{ak\bar{n}_{\rm p}} \sum_{j=0}^{\infty} \frac{(ak)^j}{j!} \langle \zeta(t)^j \rangle$$

$$= C^k e^{ak\bar{n}_{\rm p}} \left[1 + \sum_{j=1}^{\infty} \frac{(ak\sigma_{\rm p})^{2j}(2j-1)!!}{(2j)!} \right] = C^k e^{ak\bar{n}_{\rm p}} e^{\frac{a^2\sigma_{\rm p}^2 k^2}{2}} = G_{\rm s}^k e^{\frac{a^2\sigma_{\rm p}^2}{2}(k^2-k)}, \qquad (4.19)$$

where $G_{\rm s} \equiv \langle G_{\rm s}(t) \rangle$ is the average gain. The JPA noise $n_{\rm J}(G_{\rm s})$ then satisfies $G_{\rm s} n_{\rm J}(G_{\rm s}) = f\left(\sqrt{\text{Var}[G_{\rm s}(t)]}\right)$, where f is a function of the gain fluctuations.[5] To first order, we then obtain

$$n_{\rm J}(G_{\rm s}) = f'(0) \frac{\sqrt{\text{Var}[G_{\rm s}(t)]}}{G_{\rm s}}. \qquad (4.20)$$

The normalization with respect to the gain $G_{\rm s}$ is chosen to refer the noise to the amplifier input. From Eq. (4.19), we find

$$n_{\rm J}(G_{\rm s}) = f'(0) \sqrt{\frac{\langle G_{\rm s}(t)^2 \rangle}{G_{\rm s}^2} - 1} = f'(0) \sqrt{e^{a^2\sigma_{\rm p}^2} - 1}. \qquad (4.21)$$

From Eq. (4.14) and Eq. (4.19), we observe that we can always find constants β_1 and β_2 such that $\sigma_{\rm p}^2 = \beta_1 \ln G_{\rm s} + \beta_2$. Thus, we can write

$$n_{\rm J}(G_{\rm s}) = f'(0) \sqrt{e^{a^2\beta_2} G_{\rm s}^{\beta_1 a^2} - 1} \xrightarrow{G_{\rm s} \gg 1} \chi_1 G_{\rm s}^{\chi_2}, \qquad (4.22)$$

where $\chi_1 = f'(0) \exp\left(\frac{1}{2}a^2\beta_2\right)$ and $\chi_2 \equiv \beta_1 a^2/2$. The last approximation in Eq. (4.22) is justified since it is equivalent to the exponential approximation for the pump power dependence of the gain. To interpolate to the condition $n_{\rm J}(1) = 0$, we rewrite Eq. (4.22)

---

[4]Although the coherent pump tone obeys a Poissonian distribution, $\hat{f}_{\rm p}$ can obey different statistics. The ansatz of a normal distribution for $\zeta(t)$ is always a reasonable assumption since we use the approximation of high energy, $G_{\rm s} \gg 1$, which enables us to exploit that a Poissonian distribution can be well approximated by a normal distribution according to the central limit theorem.

[5]Note that gain fluctuations may also lead to a contribution to multiplicative noise. However, e.g., in the scope of mathematical image processing, it has been demonstrated that multiplicative noise can be approximated by an effective additive contribution [339]. Within our treatment, we assume that the gain fluctuations effectively manifest as additive noise.

as

$$n_\mathrm{J}(G_\mathrm{s}) = \chi_1(G_\mathrm{s} - 1)^{\chi_2}. \tag{4.23}$$

We neglect the resulting uncertainty from this interpolation since, due to the requirement $G_\mathrm{s} \gg 1$, Eq. (4.23) is anyways less accurate in the low gain regime. However, since the HEMT amplifier noise is the dominant contribution for $G_\mathrm{s} \simeq 1$, only the JPA noise in the high-gain regime is relevant for us. In addition, our pump-induced noise model is fully compatible with the model of a linear amplifier, in contrast to noise models resulting from higher order nonlinearities. In conclusion, our theory phenomenologically explains the observed noise dependence. However, regarding Eq. (4.14), we do not make any assumptions about the noise bandwidth. Thus, more accurate models can be obtained by considering suitable filter functions. To reduce the impact of pump-induced noise one could employ additional cavity filters for the pump lines [340].

4.1.2 Phase dependence of the amplified output power

As we have seen in Sec. 2.1.4, the broadband nondegenerate regime can be regarded as a hybrid of the conventional degenerate amplification and narrowband nondegenerate phase-preserving regimes. In this section, we want to analyze the dependence of the power of the amplified output state on the potentially correlated phases of the signal and idler input states. In addition, we experimentally demonstrate the fundamental difference to degenerate amplification. First, we consider phase-coherent tones at signal and idler ports

$$\hat{A}_\mathrm{s}(t) = \hat{a}_\mathrm{s} e^{i(\omega_\mathrm{s} t - \varphi_\mathrm{s})}, \qquad \hat{A}_\mathrm{i}(t) = \hat{a}_\mathrm{i} e^{i(\omega_\mathrm{i} t - \varphi_\mathrm{i})}, \tag{4.24}$$

where $\hat{a}_\mathrm{s}$ ($\hat{a}_\mathrm{i}$) is the bosonic amplitude operator for the signal (idler) input mode and φ_s (φ_i) corresponds to the input signal (idler) phase with respect to a common phase reference. Since we operate in the nondegenerate regime, we have $\omega_\mathrm{s} = \omega_0 + \Delta$ and $\omega_\mathrm{i} = \omega_0 - \Delta$ with $\Delta > 0$ and $\omega_0 = \omega_\mathrm{p}/2$. Resulting from our previous considerations, we conclude that, for such a scenario, we can in principle achieve amplification with a quantum efficiency of unity. The corresponding spectrum for Eq. (4.24) is given by

$$\hat{A}_\mathrm{s}(\tilde{\omega}) = \hat{a}_\mathrm{s} e^{-i\varphi_\mathrm{s}} \delta(\tilde{\omega} - \omega_\mathrm{s}), \qquad \hat{A}_\mathrm{i}(\tilde{\omega}) = \hat{a}_\mathrm{i} e^{-i\varphi_\mathrm{i}} \delta(\tilde{\omega} - \omega_\mathrm{i}). \tag{4.25}$$

We insert these expressions into Eq. (2.35) and find

$$\hat{c}(\omega) = \int_\mathcal{I} d\tilde{\omega} \left[M(\omega, \tilde{\omega}) \hat{a}_\mathrm{s} e^{-i\varphi_\mathrm{s}} \delta(\tilde{\omega} - \omega_\mathrm{s}) + L(\omega, \tilde{\omega}) \hat{a}_\mathrm{i}^\dagger e^{i\varphi_\mathrm{i}} \delta(\tilde{\omega} - \omega_\mathrm{i}) \right] + \hat{f}(\omega), \tag{4.26}$$

which we can directly evaluate

$$\hat{c}(\omega) = M(\omega, \omega_\mathrm{s}) \hat{a}_\mathrm{s} e^{-i\varphi_\mathrm{s}} + L(\omega, \omega_\mathrm{i}) \hat{a}_\mathrm{i}^\dagger e^{i\varphi_\mathrm{i}} + \hat{f}(\omega). \tag{4.27}$$

We now apply Eq. (2.38) and use the relation $\omega_i = 2\omega_0 - \omega_s$. We obtain

$$M(\omega, \omega_s) = M(\omega_s)\delta(\omega - \omega_s), \qquad\qquad L(\omega, \omega_i) = L(\omega_s)\delta(\omega - \omega_s), \qquad (4.28)$$

where the second expression contains a partial frequency conversion $\omega_i \to \omega_s$ during the amplification process. Using the corresponding Bogoliubov transformation, we have

$$\hat{c}(\omega) = \left[\sqrt{G_s}e^{-i\varphi_s}\hat{a}_s + \sqrt{G_s - 1}e^{i\varphi_i}\hat{a}_i^\dagger \right] \delta(\omega - \omega_s) + \hat{f}(\omega). \qquad (4.29)$$

Integration over an infinitesimally small measurement bandwidth around ω_s gives

$$\hat{c}(\omega_s) = \sqrt{G_s}e^{-i\varphi_s}\hat{a}_s + \sqrt{G_s - 1}e^{i\varphi_i}\hat{a}_i^\dagger + \hat{f}(\omega_s). \qquad (4.30)$$

In the following, we write $\hat{c} \equiv \hat{c}(\omega_s)$ and $\hat{f} \equiv \hat{f}(\omega_s)$ and calculate

$$
\begin{aligned}
\langle \hat{c}^\dagger\hat{c} + \hat{c}\hat{c}^\dagger \rangle = {}& G_s\langle \hat{a}_s^\dagger\hat{a}_s \rangle + \sqrt{G_s}\sqrt{G_s - 1}e^{i(\varphi_s+\varphi_i)}\langle \hat{a}_s^\dagger\hat{a}_i^\dagger \rangle + \underbrace{\sqrt{G_s}e^{i\varphi_s}\langle \hat{a}_s^\dagger \rangle\langle \hat{f} \rangle}_{=0} \\
& + \sqrt{G_s}\sqrt{G_s - 1}e^{-i(\varphi_s+\varphi_i)}\langle \hat{a}_i\hat{a}_s \rangle + (G_s - 1)\langle \hat{a}_i\hat{a}_i^\dagger \rangle + \underbrace{\sqrt{G_s - 1}e^{-i\varphi_i}\langle \hat{a}_i \rangle\langle \hat{f} \rangle}_{=0} \\
& + \underbrace{\sqrt{G_s}e^{-i\varphi_s}\langle \hat{f}^\dagger \rangle\langle \hat{a}_s \rangle}_{=0} + \underbrace{\sqrt{G_s - 1}e^{i\varphi_i}\langle \hat{f}^\dagger \rangle\langle \hat{a}_i^\dagger \rangle}_{=0} + \langle \hat{f}^\dagger\hat{f} \rangle + G_s\langle \hat{a}_s\hat{a}_s^\dagger \rangle \\
& + \sqrt{G_s}\sqrt{G_s - 1}e^{-i(\varphi_i+\varphi_s)}\langle \hat{a}_s\hat{a}_i \rangle + \underbrace{\sqrt{G_s}e^{i\varphi_s}\langle \hat{a}_s \rangle\langle \hat{f}^\dagger \rangle}_{=0} \\
& + \sqrt{G_s}\sqrt{G_s - 1}e^{i(\varphi_s+\varphi_i)}\langle \hat{a}_i^\dagger\hat{a}_s^\dagger \rangle + (G_s - 1)\langle \hat{a}_i^\dagger\hat{a}_i \rangle + \underbrace{\sqrt{G_s - 1}e^{i\varphi_i}\langle a_i^\dagger \rangle\langle \hat{f}^\dagger \rangle}_{=0} \\
& + \underbrace{\sqrt{G_s}e^{i\varphi_s}\langle \hat{f} \rangle\langle \hat{a}_s^\dagger \rangle}_{=0} + \underbrace{\sqrt{G_s - 1}e^{-i\varphi_i}\langle \hat{f} \rangle\langle \hat{a}_i \rangle}_{=0} + \langle \hat{f}\hat{f}^\dagger \rangle,
\end{aligned}
\qquad (4.31)
$$

where we assume that the $\hat{f}$ mode is uncorrelated with $\hat{a}_s$ and $\hat{a}_i$. By calculating the total power according to Eq. (2.30), we find

$$\langle |\hat{c}|^2 \rangle = G_s\langle |\hat{a}_s|^2 \rangle + (G_s - 1)\langle |\hat{a}_i|^2 \rangle + \langle |\hat{f}|^2 \rangle + \sqrt{G_s}\sqrt{G_s - 1}\langle \hat{a}_s\hat{a}_ie^{-i(\varphi_s+\varphi_i)} + \hat{a}_i^\dagger\hat{a}_s^\dagger e^{i(\varphi_s+\varphi_i)} \rangle. \qquad (4.32)$$

We observe that the last term in Eq. (4.32) is of the structure of a two-mode squeezing operation between the input signal and idler modes [315]. Under the assumption that $\langle \hat{a}_s \rangle = \langle \hat{a}_i \rangle = 0$, this two-mode squeezing term vanishes in the case of uncorrelated amplitudes $\hat{a}_s$ and $\hat{a}_i$ and we have

$$\langle |\hat{c}|^2 \rangle = G_s\langle |\hat{a}_s|^2 \rangle + (G_s - 1)\langle |\hat{a}_i|^2 \rangle + \langle |\hat{f}|^2 \rangle. \qquad (4.33)$$
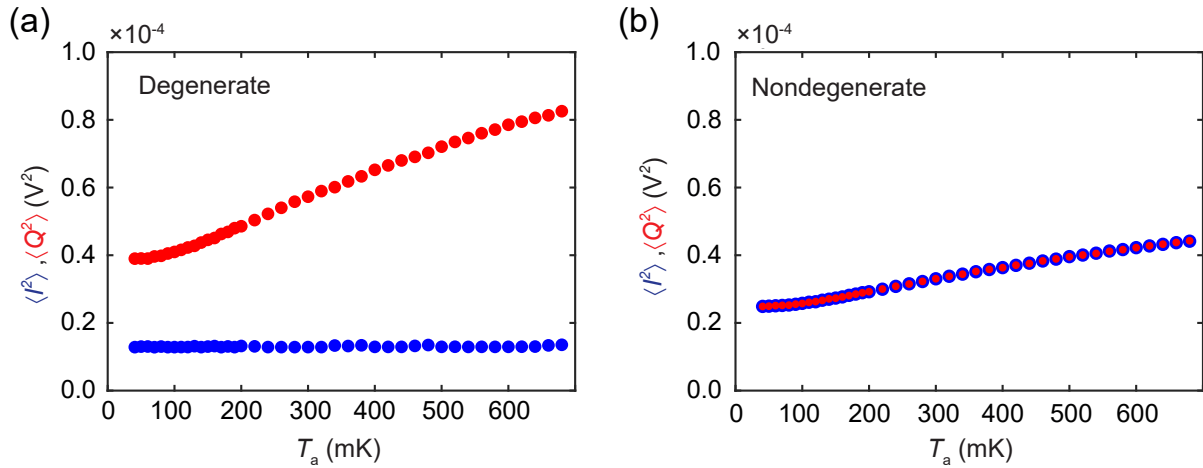
Figure 4.5: (a) Experimental quadrature-resolved Planck spectroscopy for a degenerate JPA. We observe phase-sensitive amplification of Q and simultaneous deamplification of I. (b) Quadrature-resolved Planck spectroscopy for the broadband nondegenerate amplification regime. In this case, the output power is equally distributed over both quadratures.

We now investigate the case when $\langle \hat{a}_\text{s} \rangle = \langle \hat{a}_\text{i} \rangle \neq 0$. Furthermore, we assume that we apply the same input power on the signal and idler sides, implying that $\langle |\hat{a}_\text{s}|^2 \rangle = \langle |\hat{a}_\text{i}|^2 \rangle$ and ideal signal-idler correlations. We obtain

$$\langle \hat{a}_\text{s}\hat{a}_\text{i}e^{-i(\varphi_\text{s}+\varphi_\text{i})} + \hat{a}_\text{i}^\dagger\hat{a}_\text{s}^\dagger e^{i(\varphi_\text{s}+\varphi_\text{i})} \rangle = \underbrace{\langle \hat{a}_\text{s}\hat{a}_\text{i} + \hat{a}_\text{i}^\dagger\hat{a}_\text{s}^\dagger \rangle}_{=2\langle|\hat{a}_\text{s}|^2\rangle} \cos(\varphi_\text{s}+\varphi_\text{i}) - i\underbrace{\langle \hat{a}_\text{s}\hat{a}_\text{i} - \hat{a}_\text{i}^\dagger\hat{a}_\text{s}^\dagger \rangle}_{=0} \sin(\varphi_\text{s}+\varphi_\text{i}),$$

$$(4.34)$$

and obtain the expression

$$\langle |\hat{c}|^2 \rangle = \left[2G_\text{s} - 1 + 2\sqrt{G_\text{s}}\sqrt{G_\text{s}-1}\cos(\varphi_\text{s}+\varphi_\text{i}) \right] \langle |\hat{a}_\text{s}|^2 \rangle + \langle |\hat{f}|^2 \rangle. \qquad (4.35)$$

The broadband gain is then given by

$$G_\text{b} = 2G_\text{s} - 1 + 2\sqrt{G_\text{s}}\sqrt{G_\text{s}-1}\cos(\varphi_\text{s}+\varphi_\text{i}) = \left| \sqrt{G_\text{s}}e^{i\varphi_\text{s}} + \sqrt{G_\text{s}-1}e^{-i\varphi_\text{i}} \right|^2. \qquad (4.36)$$

Here, we reproduce the expression for the phase-sensitive degenerate gain given in Ref. 90 when the input signal and idler coincide, $\varphi_\text{s} = \varphi_\text{i}$. However, in contrast to the degenerate regime ($\Delta = 0$), the phases φ_s and φ_i can be controlled independently.[6] As an example, if we anticorrelate the signal and idler phases, $\varphi_\text{s} = -\varphi_\text{i}$, we lose the phase-dependence in Eq. (4.36). Next, we investigate a possible phase-dependence for our scenario of thermal state amplification. In this case, possible temporal correlations between the input signal and idler modes can be taken into account by determining the inverse Fourier transform, $\mathcal{C}(t)$, of the Planck distribution. The result can be expressed in terms of

---

[6]We want to remark that stabilizing a phase relation between signal and idler can be challenging from a technical point of view if the respective frequencies are non-commensurable.

a single dimensionless parameter $\tau \equiv tT/(t_{\mathrm{p}}T_{\mathrm{p}})$, where time t and temperature T are compared with the respective Planck time $t_{\mathrm{p}} = 5.4 \times 10^{-44}\,\mathrm{s}$ and the Planck temperature $T_{\mathrm{p}} = 1.4 \times 10^{32}\,\mathrm{K}$. The normalized temporal correlation function is then given by

$$\mathcal{C}(\tau) = \frac{3}{\pi^2}\left[\zeta\left(2, 1 + i\tau\right) + \zeta\left(2, 1 - i\tau\right)\right] = \frac{3}{\pi^2\tau^2} - \frac{3}{\sinh^2\left(\pi\tau\right)}, \qquad (4.37)$$

where $\zeta(s, a) = \sum_{j=0}^{\infty}[j + a]^{-s}$ denotes the Hurwitz function [297, 341]. The Planck-scales determine the half-life time of the initial correlation, which is given by $t_{1/2} \simeq 0.662\hbar/k_{\mathrm{B}}T$. For $T = 50\,\mathrm{mK}$, we find $t_{1/2} \simeq 0.1\,\mathrm{ns}$, implying that correlations between φ_{s} and φ_{i} only exist in a sub-nanosecond time scale. As a result, we measure an effective average

$$\overline{\cos(\varphi_{\mathrm{s}} + \varphi_{\mathrm{i}})} = 0, \qquad (4.38)$$

implying that, for thermal states, the expression for the broadband gain reduces to our experimentally determined value $G_{\mathrm{b}} = 2G_{\mathrm{s}} - 1$.

Explicit experimental evidence for Eq. (4.38), as well as for the difference between degenerate amplification and nondegenerate broadband amplification, is given in Fig. 4.5. In this measurement, we perform a quadrature-resolved Planck spectroscopy. We vary the temperature T_{a} of the heatable 30 dB attenuator between 40 mK and 600 mK and amplify the respective thermal states with a degenerate JPA. The measurement is then
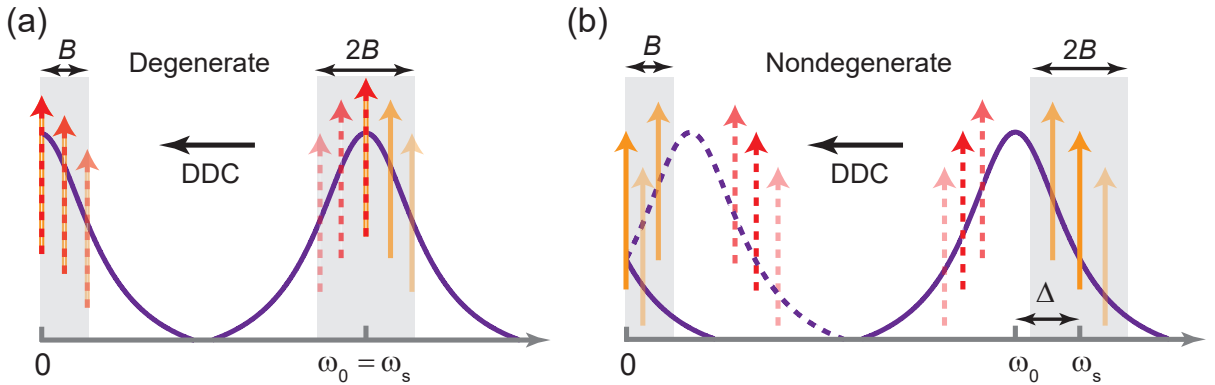
Figure 4.6: Scheme for digital downconversion (DDC). The arrows indicate the correlated output signal (orange solid) and idler (red dashed) modes, which are symmetrically distributed around the resonance frequency ω_0. The purple curves corresponds to the spectral JPA gain function and the gray shaded regions indicate the detection bandwidth. In the degenerate case, conversion of the RF signal to a DC signal symmetrically superposes the output signal and idler sidebands, as indicated in (a). This superposition leads to phase-sensitive amplification, resulting from interference between signal and idler. The scenario for nondegenerate amplification is shown in panel (b). In this case, the symmetry is broken due to $\Delta \neq 0$, causing superposition of uncorrelated output signal and output idler modes. For $\Delta > B$, no idler modes remain within the detection bandwidth and the amplifier becomes phase-insensitive.

repeated in the nondegenerate regime. The signal is reconstructed at $\omega_s/2\pi = 5.435\,\text{GHz}$. Figure 4.5(a) shows the detected output power in the I- and Q-quadrature for degenerate amplification, characterized by $\Delta = 0$. In this case, the signal input and idler input modes coincide, resulting in quadrature-dependent amplification and, eventually, squeezed state generation. Since the pump phase is stabilized to $0°$ in this measurement, the Q-quadrature is amplified while the I-quadrature is attenuated. In Fig. 4.5(b), we plot the result from the nondegenerate measurement, $\Delta \neq 0$ and find that the output power is equally distributed among both quadratures, despite the fact that we employ the same stable pump phase as in the degenerate case. This result can be regarded as an experimental proof that degenerate and broadband nondegenerate regimes are fundamentally different.

To gain further understanding of this result, we follow the consideration from Ref. 112 and compare degenerate and nondegenerate amplification with respect to downconversion and demondulation. Here, we skip the technically relevant heterodyne downconversion into the intermediate frequency regime, as all signal and idler correlations are preserved during this step. Figure 4.6(a) schematically depicts the digital downconversion process for the degenerate case. The correlated output signal and idler modes are symmetrically distributed around the resonance frequency ω_0. Within the digital downconversion, the RF signal is transformed into a digital DC signal and the frequency spectrum is effectively mirrored at the signal reconstruction frequency, implying overlapping signal and idler modes [112]. Depending on the relative phase with respect to the pump signal, this leads to either constructive or destructive interference and, thus, phase-sensitive amplification. On the other hand, in the nondegenerate scenario, as shown in Fig. 4.6(b), the symmetry is broken due to $\Delta \neq 0$. As long as $\Delta > B$, the output idler modes are not detected and the phase is preserved due to the absence of the interference effect. In the case of broadband nondegenerate amplification, instead of the idler modes, generated from the input signal, the input signal modes at idler frequency are superposed with the incoming modes in the signal band. As shown in Eq. (4.37), these modes are not phase coherent in the case of thermal input states, which explains the difference between the measurement results in Fig. 4.5.

4.2 Chained Josephson parametric amplifiers

In Sec. 2.1.5, we have investigated how we can increase quantum efficiency by connecting two JPAs in series. As can be seen in Fig. A.1, our setup for measuring quantum efficiency enables us to realize such an experiment. We choose the JPA pump powers such that we divide the desired total gain of the chain equally among both JPAs. Following that, we repeat the broadband quantum efficiency measurement from Sec. 4.1 when both JPAs are operated simultaneously. To access the properties of the individual JPAs, all experiments are performed using a four-pulse scheme. The first pulse serves as the vacuum reference, during the second (third) pulse we apply pump to JPA 1 (JPA 2) and during the last pulse

both JPAs are pumped simultaneously. The result of this chained measurement, in direct comparison with the quantum efficiency of JPA 1 and JPA 2 from Fig. 4.3, is shown in Fig. 4.7(a). We do not observe the expected improvement in quantum efficiency. Instead, we find that the maximal quantum efficiency of the JPA chain lies between the individual maximal quantum efficiencies of the employed JPAs. There are two explanations for this behavior. The first one is a pump crosstalk, since the employed JPA circulators are effectively transparent at pump frequencies. The second reason is the fact that JPA 1 has a worse noise scaling than JPA 2. To understand this effect in more detail, we assume that both JPAs follow a different noise scaling

$$n_1(G_{\mathrm{s}}) \simeq \alpha_1 G_{\mathrm{s}}^{\nu_1}, \qquad n_2(G_{\mathrm{s}}) \simeq \alpha_2 G_{\mathrm{s}}^{\nu_2}, \tag{4.39}$$

where index 1 (2) corresponds to JPA 1 (JPA 2). As condition to obtain an advantage by chaining the JPAs under the assumption $\nu_1 > \nu_2$, we find from Eq. (2.66) for the case of $N = 2$ JPAs with unequal noise scaling

$$\sqrt{G_{\mathrm{s}}} \frac{\alpha_1}{\alpha_2} G_{\mathrm{s}}^{\frac{\nu_1-\nu_2}{2}} + 1 \simeq \sqrt{G_{\mathrm{s}}} \frac{\alpha_1}{\alpha_2} G_{\mathrm{s}}^{\frac{\nu_1-\nu_2}{2}} \leq \sqrt{G_{\mathrm{s}}} G_{\mathrm{s}}^{\frac{\nu_2}{2}}. \tag{4.40}$$

By comparing the scaling on the left and right hand sides, we observe that, for sufficiently large G_{s}, this inequality can never be valid if $\nu_1 \geq 2\nu_2$. Thus, in the case where the JPAs have significantly different gain-dependent noise scaling, chaining is disadvantageous. This is consistent with the exponents found in Tab. 4.1. In agreement with the experiment, this scaling model predicts that the quantum efficiency in the chained case is always higher than the quantum efficiency of the worst performing single JPA in the chain. When chaining JPAs with different quantum efficiencies, it is always beneficial to use the best JPA as the first amplifier in the chain [93].

Next, we analyze chained phase-sensitive JPAs. First, we consider the case where the JPAs amplify orthogonal quadratures. Such a squeezed state balancing can potentially enable us to directly determine the JPA noise photons or the losses between both JPAs. This would be the case if the balanced variance v_* of the final state becomes independent of the squeeze factor r, since such a balancing procedure only involves a relative comparison of variances and can be assumed to be independent of the exact PNCF. Let v_{xy} denote the variance of the resulting state where JPA 1 performs operation x and JPA 2 performs operation y, with $x, y \in \{\mathrm{s}, \mathrm{a}\}$. Index s (a) implies that the respective variance is squeezed (antisqueezed). We have

$$v_{\mathrm{as}} = \frac{1}{4}e^{2r_2}[2n_2(r_2) + e^{-2r_1}(2n_1(r_1) + 1)], \qquad v_{\mathrm{sa}} = \frac{1}{4}e^{-2r_2}[2n_2(2) + e^{2r_1}(2n_1(r_1) + 1)], \tag{4.41}$$

where $n_i(r_i)$ is the noise photon number, added by the ith JPA. To realize this balancing experiment, we first perform a calibration measurement to compensate for a phase
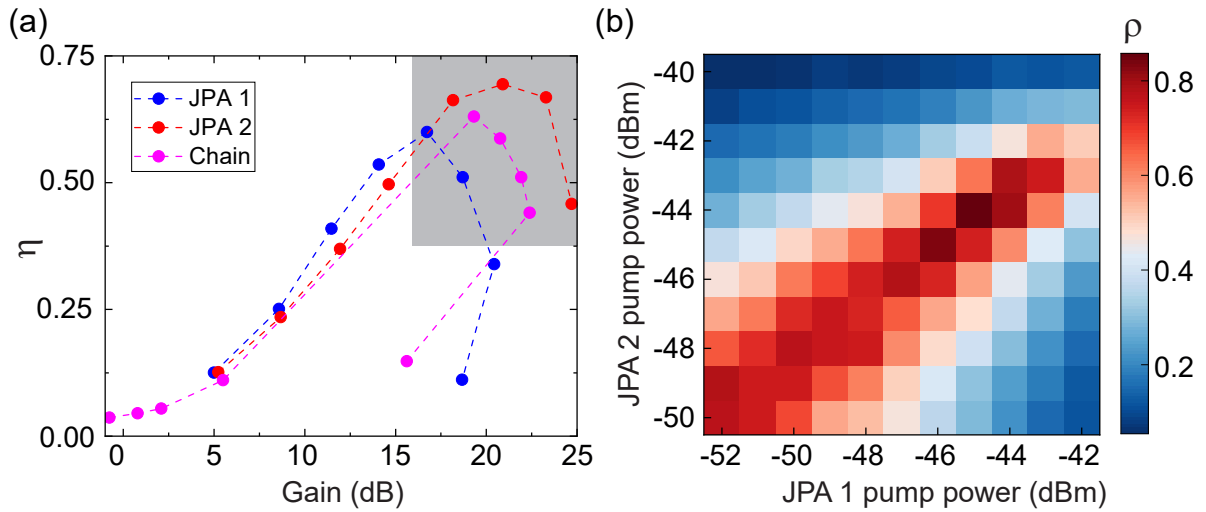
Figure 4.7: (a) Experimentally determined gain dependence of quantum efficiency η, as defined in Sec. 2.1.3, for individual and chained JPAs. Magenta dots show the experimentally determined quantum efficiency for chained JPAs. It can be seen that in the region around the optimum, indicated in gray, quantum efficiency for the chained case lies between the individual quantum efficiencies of JPA 1 and JPA 2. Dashed lines are guide to the eye. (b) Balancing measurement with the chained JPAs, where phase-sensitive amplification is performed on orthogonal quadratures. The color code corresponds to the variance ratio $\rho = v_{\mathrm{sa}}/v_{\mathrm{as}}$.

crosstalk between the JPAs as well as for possible phase delays. We fix the pump powers and the JPA 1 pump phase to 45° and vary the JPA 2 phase until the variance ratio $\rho \equiv v_{\mathrm{sa}}/v_{\mathrm{as}}$ becomes closest to 1, which is the case for 142°. At this optimum, we perform a simultaneous sweep of the JPA 1 and JPA 2 pump powers for fixed orthogonal amplification angles. In Fig. 4.7(b), we show the result of this measurement and reach an optimal $\rho = 0.86$, which demonstrates that such a balancing procedure can be successfully realized. For proof of principle, we assume r-independent noise $n = n_1(r_1) = n_2(r_2)$, such that any r-dependence solely emerges from the squeezing operation. When the variances are balanced, $\rho = 1$, the noise is described by a quadratic equation

$$16v_*^2 = 4n^2 + (2n + 1)^2 + 4n(2n + 1)\cosh 2r_1, \tag{4.42}$$

from which we find

$$n = \left(v_* - \frac{1}{4}\right) + \frac{1 - 16v_*}{32v_*}r_1^2 + \mathcal{O}(r_1^4). \tag{4.43}$$

Thus, measuring the balanced variance reduces the r-dependence to $\mathcal{O}(r^2)$, as compared to the case where we directly measure either the squeezed or antisqueezed quadrature in a single-JPA measurement, where we have a dependence scaling with $\mathcal{O}(r)$. However, the balancing method does not provide any benefits compared to direct full state reconstruction of both squeezed and antisqueezed variance. A similar problem occurs if we want to use such a balancing scheme for measurement of losses. The desired independence of r can
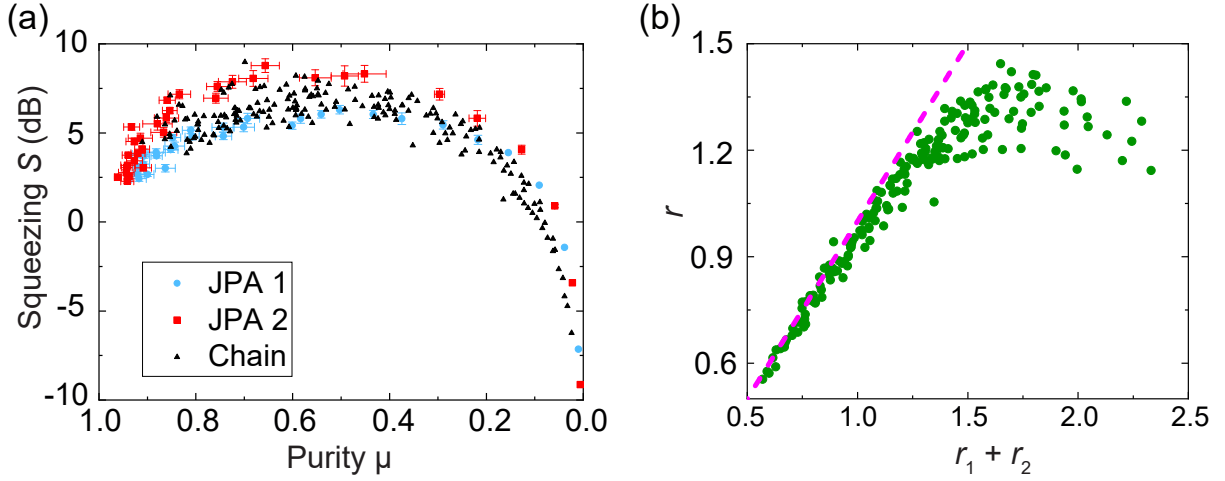
Figure 4.8: (a) Experimentally determined squeezing levels as a function of purity. Blue dots (red squares) correspond to individual measurements with JPA 1 (JPA 2) and black triangles show the result from serially connected JPAs. Most of the data points for chained JPAs lie in between the respective values of JPA 1 and JPA 2. (b) Comparison of the sum of individual squeeze factors r_1 (r_2) of JPA 1 (JPA 2) with the final squeeze factor r for the chained measurement. For low squeezing, we observe the expected behavior $r_1 + r_2 = r$, indicated by the magenta dashed line. In the case of high squeezing, we have $r_1 + r_2 > r$, which can be a result of the pump crosstalk between the JPAs or from compression.

only be achieved if we add a third JPA to the chain, as discussed in Appendix B. However, the balancing scheme with two JPAs, with special focus on Eq. (4.41), becomes of high practical relevance for understanding the principle of the analog phase space projection measurement. This is of particular importance for the quantum teleportation experiment described in chapter 6.

Next, we investigate the case where both JPAs amplify the same quadrature and analyze whether we can increase the purity of squeezed states with such a scheme as this is a particularly important quantity when these states are employed as a quantum resource. In analogy to Eq. (4.41), we have

$$v_{\mathrm{ss}} = \frac{1}{4}e^{-2r_2}[2n_2(r_2) + e^{-2r_1}(2n_1(r_1) + 1)], \qquad v_{\mathrm{aa}} = \frac{1}{4}e^{2r_2}[2n_2(2) + e^{2r_1}(2n_1(r_1) + 1)]. \tag{4.44}$$

Under the assumption that both JPAs show identical noise scaling, a combination of squeeze factors r_1, r_2 with $r_1 + r_2 = r$ improves the purity $\mu = 1/(4\sqrt{v_{\mathrm{ss}}v_{\mathrm{aa}}})$ if

$$n(r_1) + n(r_1)^2 + n(r_2)\cosh 2r_1 + n(r_2)^2 \le n(r) + n(r)^2. \tag{4.45}$$

The optimal combination of r_1 and r_2 for maximizing μ for a given squeezing level S can

be determined by minimizing the Lagrangian

$$\mathcal{L}(r_1, r_2, \lambda) = v_{\mathrm{ss}} v_{\mathrm{aa}} + \lambda \left(v_{\mathrm{ss}} - \frac{1}{4} 10^{-\frac{S}{10}} \right). \tag{4.46}$$

However, even in the simple case of linear gain dependence of the noise, the optimal distribution for the gain $G_i = \exp(2r_i)$ is described by a polynomial of 4th order which cannot be solved analytically in a reasonable way. In the experiment, we approach this problem in an empirical way by performing a 2D pump power sweep. Before the actual experiment, we perform a phase calibration in an analogous way as for the balancing measurement. Figure 4.8(a) shows the measured squeezing levels as a function of the reconstructed purity for individual JPAs and for the chained case. We observe that most of the squeezing levels for the chained case lie in between the respective individual squeezing levels of JPA 1 and JPA 2. Furthermore, we find that the squeezing level becomes maximal at a certain purity. This maximum is determined by the optimal trade-off between variance broadening due to the gain-dependent noise and attenuation of the squeezed quadrature variance with the inverse degenerate gain. The corresponding optimal squeeze factor is then determined by maximizing $S(r) = 10 \log_{10}[\mu(r) e^{2r}]$. If we assume that gain-dependent noise is described by the power law of Eq. (4.23), it can be shown that such an extremum exists if $\chi_2 \gtrsim 1$. From a least square fit, we find $(\chi_1, \chi_2) = (0.01, 2.01)$ for JPA 1 and $(\chi_1, \chi_2) = (0.01, 1.42)$ for JPA 2. The corresponding prediction for the purity dependence of the squeezing level is given in Fig. 4.9(a). Similar as in Fig. 4.7(a), one possible explanation on why we do not see any improvement by chaining the amplifiers is the fact that JPA 1 shows a disadvantageous gain scaling of the noise, compared to JPA 2. However, if we plot the theoretically expected purity-dependence of S based on the fit parameters of the respective JPA noise, we find that we would actually expect an advantage by chaining. In addition, we observe that in case JPA 1 obeys the same noise scaling as JPA 2 (i.e. identical χ_1, χ_2), only a slight improvement of squeezing would be expected in the chained measurement. This scenario is depicted by the gray dashed line.

To understand the difference between the experimental results in Fig. 4.8(a) and the simple model beneath Fig. 4.9(a), we investigate the effect of pump crosstalk. To this end, we exploit that for fixed pump powers, our four-pulsed measurement scheme enables us to reconstruct the individual squeeze factor r_1 (r_2), of JPA 1 (JPA 2) as well as the squeeze factor r of the final state in case both JPAs are operated. Following that, we plot r as a function of $r_1 + r_2$ in Fig. 4.8(b). The measurement results then follow the linear expectation $r_1 + r_2 = r$ until $r \simeq 1$. However, we observe $r_1 + r_2 > r$ for sufficiently high squeezing. In the next step, we introduce a simple qualitative model which explains how this crosstalk can lower the purity of the squeezed state. To do so, we introduce a new quantity $\kappa \equiv (r_1 + r_2)/r$. For $\kappa = 1$, we have no crosstalk between the JPAs, whereas the effect of crosstalk increases monotonically with κ. Thus, crosstalk implies that we need to pump with an effectively higher pump power strength, compared to single JPA
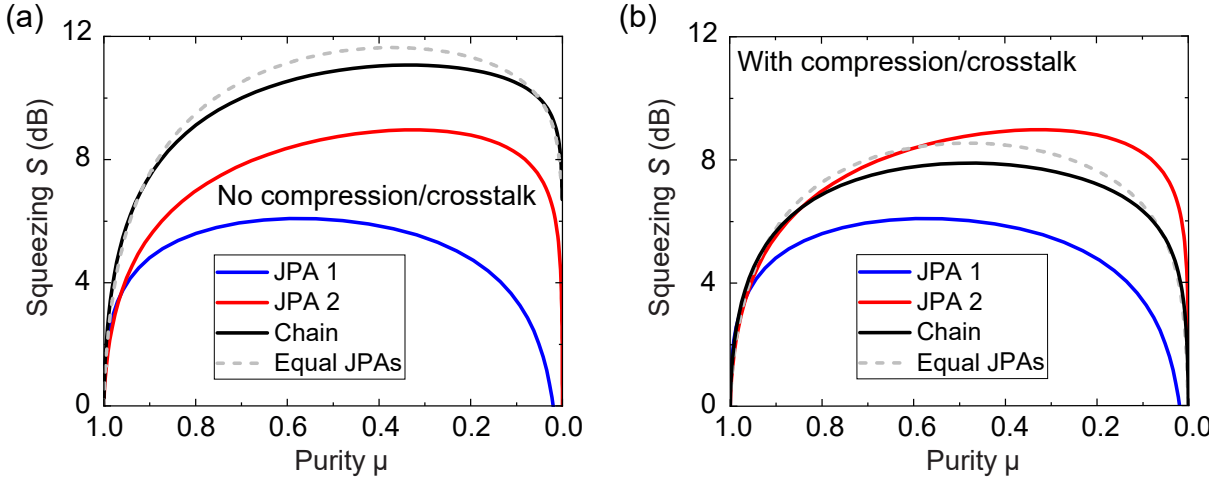
Figure 4.9: (a) Predicted purity-dependence of the squeezing level for individual and chained JPAs, based on the fit parameters for the gain-dependent noise. The gray dashed line shows the expected outcome in case JPA 1 shows identical noise scaling as JPA 2. In panel (b), we plot the expected result for chained JPAs with the pump crosstalk taken into account. For comparison, the (unaffected) squeezing levels for the individual JPAs from panel (a) are replotted.

squeezing. In order to achieve a given squeeze factor r in the chained case, each JPA needs to amplify with squeeze factor $\kappa r/2$, adding the noise contribution $n_J(\kappa r/2) > n_J(r/2)$. From Fig. 4.8(b), we find $\kappa \simeq 1.3$ in the high squeezing limit and in Fig. 4.9(b), we replot the expected squeezing for the chained case and take our crosstalk model into account. We observe that in this case, we qualitatively reproduce the experimental result. In addition, it is remarkable that even in the case where JPA 1 obeys the same noise scaling as JPA 2, crosstalk suppresses any improvement by chaining the JPAs, as indicated by the gray dashed line. In conclusion, we expect improvement of our results if we avoid any pump leakage. One possible realization is either the integration of superconducting on-chip bandpass filters [342] or the use of broadband circulators which provide nonreciprocity at $\simeq 11\,\text{GHz}$. In case of squeezed state generation, we can additionally attempt to increase the squeezing level by squeezing the pump signal itself, using a second JPA. However, we are eventually limited by compression in this case since the pump signal is required to be sufficiently powerful. We mention that for chained JPAs additional care needs to be taken to account for compression effects, which are neglected so far. In practice, it is beneficial to employ the JPA with highest quantum efficiency as the first amplifier and the JPA with the highest 1 dB compression point as the last amplifier. In addition, compression effects significantly increase the complexity with respect to the problem of finding an optimal gain distribution, since the 1 dB compression point sets additional power dependent inequality constraints to Eq. (2.80) and Eq. (4.46). In first order approximation, compression can be modelled by an AC Stark shift of the resonator [343], leading to power-dependent gain $G(n_{\text{in}}) = G_0 - \alpha(G_0 - 1)n_{\text{in}}$, where the constant $0 < \alpha \ll 1$ determines the compression strength, G_0 is the linear gain, and n_{in} is the input power. In this case, the output powers

of subsequently chained equal amplifiers are connected by a quadratic map [344]. In the noiseless case, these output powers are connected via the well-known logistic map, leading to potential chaotic dependence on the input power [345].

Chapter 5

Quantum discord and locally inaccessible information

In quantum communication protocols, entanglement is often employed as a nonclassical resource to enhance the capacity of communication channels, to achieve a quantum speed-up in information processing or to guarantee unconditional security [47]. However, as we have seen in Sec. 2.2.3, entanglement only describes a specific set of quantum correlations and a more general measure of nonclassical correlations is provided by quantum discord [176]. In this chapter, we study how local noise injection into a bipartite quantum system affects the corresponding quantum correlations. In Sec. 5.1, we demonstrate [1] the asymptotic robustness of quantum discord against environmental noise and its relation to entanglement in mixed tripartite systems [49]. In particular, our investigation reveals that the noise suppresses quantum correlations in the bipartite system and simultaneously increases correlations between one of the subsystems and the environment. This effect is closely related to the concept of locally inaccessible information (LII) [88] and investigated in Sec. 5.2. In addition, in Sec. 5.3, we demonstrate that LII is related to the unconditional security of a certain class of quantum key distribution (QKD) protocols [346]. In the context of the quantum teleportation experiment presented in chapter 6, analyzing quantum discord allows us to investigate how efficiently quantum correlations are consumed in quantum communication experiments, even if entanglement is already lost [347]. The results of this chapter have been published in Ref. 86. Parts of the figures as well as from the text have been adopted from this publication.

5.1 Entanglement of formation and quantum discord

In this section, we investigate the effect of noise injection into one local mode of a propagating TMS state. The corresponding experimental scheme is depicted in Fig. 5.1(a). The TMS state is distributed between two parties A and B and uncorrelated broadband

---

[1]The experimental results shown in this chapter have been measured by my former office colleague S. Pogorzalek using the setup, described in Ref. 112. With friendly permission, we use this experimental data to interpret it in the context of information flow.

noise is injected into path B. Following that, we reconstruct the resulting two-mode state and extract the quantum correlations between path A and path B. In the experiment, we form the TMS state by superimposing two orthogonally squeezed microwave states using a microwave hybrid ring beam splitter.[2] The squeezed states are obtained using two NEC JPAs operated at frequency $\omega_0/2\pi = 5.323\,\mathrm{GHz}$. The noise signal is generated using an arbitrary function generator (AFG)[3] which produces white Gaussian noise with a specified bandwidth of $160\,\mathrm{MHz}$ which is upconverted to the carrier frequency $\omega_0/2\pi$. We implement the actual noise injection into one of the entangled paths with a directional coupler with a coupling constant $\beta = -20\,\mathrm{dB}$.[4] More details about the experimental setup can be found in Ref. 86. The final covariance matrix of the system can be expressed as

$$\boldsymbol{V}_{\mathrm{AB}} = \frac{1 + 2n_{\mathrm{J}}(G)}{4} \begin{pmatrix} \cosh 2r\,\mathbb{1}_2 & \sqrt{1-\beta}\,\sinh 2r\,\sigma_z \\ \sqrt{1-\beta}\,\sinh 2r\,\sigma_z & \left[(1-\beta)\cosh 2r + \beta\frac{1+2\bar{n}}{1+2n_{\mathrm{J}}(G)}\right]\mathbb{1}_2 \end{pmatrix}, \quad (5.1)$$

where $n_{\mathrm{J}}(G)$ represents the gain-dependent noise added by the JPAs and $\bar{n}$ is the number of noise photons at the input of the coupled port of the directional coupler. As two distinct measures for bipartite quantum correlations, we use EoF and quantum discord. We choose this specific entanglement measure since it exactly coincides with quantum discord for pure states [204]. In addition, EoF and quantum discord can be directly compared since they are related to each other via various monogamy relations [348]. First, we analyze the ideal scenario of noiseless JPAs, corresponding to $n_{\mathrm{J}}(G) = 0$ and $\beta \to 0$ in Eq. (5.1). To this end, we define the rescaled injected noise $n \equiv \beta\bar{n}$ under the assumption that the injected noise satisfies $\bar{n} \gg 1$. To calculate Gaussian EoF, we define the auxiliary quantities

$$\kappa = 512 I_4 - 64 n^2 + 2 \quad (5.2)$$

and

$$\lambda_{\pm} = 16[I_1 + I_2 - 2I_3 + 2\left(\sqrt{I_1 I_2} - I_3\right) \pm 2\sqrt{I_3}\left(\sqrt{I_1} + \sqrt{I_2}\right)], \quad (5.3)$$

where I_1, I_2, I_3 and I_4 are the symplectic invariants of the covariance matrix from Eq. (5.1). For the quantity γ in Eq. (2.135), we then find [194]

$$\gamma = \frac{1}{2}\ln\sqrt{\frac{\kappa - \sqrt{\kappa^2 - \lambda_+\lambda_-}}{\lambda_-}} = \frac{1}{2}\ln\left[\frac{e^{2r} + n}{1 + e^{2r}n}\right]. \quad (5.4)$$

The resulting lower bound E_{F} for EoF as a function of injected noise is plotted in Fig. 5.1(b) for various squeezing levels S of the individual JPAs. We use S as an approximation for the two-mode squeezing level S_{T} in the TMS state. The relative deviation between these quantities due to the hybrid ring beam splitter losses is approximately $10\,\%$ [78].

---

[2]We use `CPL-5850-100B` hybrid ring beam splitters from `Miteq` for this purpose.
[3]We use a `Keysight` `81160A` AFG for that purpose.
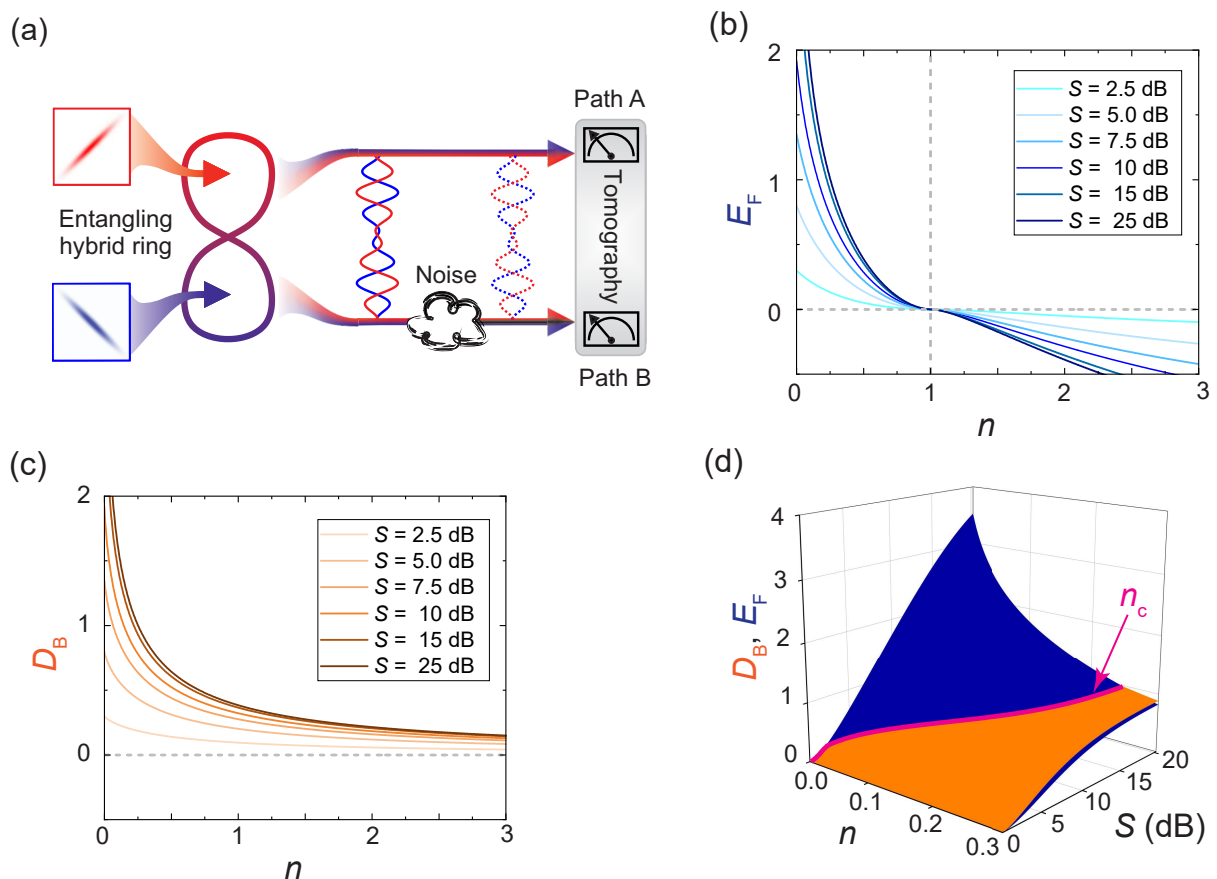[4]We use a `Miteq/Sirius` `CPL-4000-8000-20-C` coupler for that purpose.

Figure 5.1: (a) Scheme for two-mode squeezing generation and noise injection. Nonlocal correlations between path A and path B are generated by superimposing two orthogonally squeezed microwave state using a symmetric hybrid ring beam splitter, leading to the generation of a frequency-degenerate path entangled TMS state. (b) Theoretical prediction of the lower bound E_F for EoF as a function of the rescaled injected noise for various JPA squeezing levels S. As indicated by the vertical gray dashed line, we reproduce the sudden death of entanglement at $n = 1$. (c) Theoretical prediction for quantum discord D_B as a function of the rescaled injected noise for various squeezing levels. In contrast to EoF, we always observe positive $D_B(n) > 0$, demonstrating the asymptotic robustness of quantum discord against noise. (d) E_F and D_B in the regime $n \ll 1$. A crossover between EoF and quantum discord occurs at a certain rescaled noise photon number n_c.

As expected, we observe that for the pure TMS state, $n = 0$, EoF increases monotonically with S. In addition, we find that we lose all entanglement at $n = 1$, which can be seen from Eq. (5.4) since $\gamma(r, 1) = 0$ independently of r. This so-called sudden death of entanglement is a well-known phenomenon in literature [217].[5] Next, we investigate the noise dependence of quantum discord. For the quantities $E_{A|B}^{min}$ and $E_{B|A}^{min}$, describing the

---

[5]Note that E_F actually bounds the kernel $\mathcal{E}_k$ of EoF $\mathcal{E}_F$, satisfying $\mathcal{E}_F = \max[\mathcal{E}_k, 0]$. Consequently, we find $E_F < 0$ for noise exceeding the sudden death of entanglement threshold. From a practical point of view, we use the kernel for the fit routine since it enables us include data points where entanglement is already lost.

minimized conditional entropy according to Eq. (2.140), we find

$$E_{A|B}^{\min} = \frac{1}{16}\left[\frac{1+(1+2n)\cosh 2r}{1+2n+\cosh 2r}\right]^2, \qquad E_{B|A}^{\min} = \frac{1}{16}(1+2n)^2. \qquad (5.5)$$

We observe that $E_{B|A}^{\min}$, and, thus, the optimal Gaussian POVM in Eq. (2.137) does not depend on the squeeze factor r, in contrast to $E_{A|B}^{\min}$. This fact already indicates the locality of noise injection, i.e., that the noise injected into path B keeps the state in path A unaffected before the measurement. We plot the quantum discord D_B as a function of n in Fig. 5.1(c) and observe that, in strong contrast to EoF, quantum discord shows asymptotic robustness against noise [209]. We obtain a similar result for D_A. In Fig. 5.1(d), we combine plots from (b) and (c) in the limit $n \ll 1$, which reveals a crossover region between EoF and quantum discord. In the following, we denote this crossover point in terms of a corresponding noise photon number n_c. This crossover $n_c > 0$ exists for any squeeze factor r. To show this, we define the difference $\Delta_B(r,n) \equiv D_B - \mathcal{E}_F \simeq D_B - E_F$. Since EoF and quantum discord coincide for pure states, we always have $\Delta_B(r,0) = 0$. Furthermore, we have $\Delta_B(r,n) > 0$ for $n > 1$ as a result from the sudden death of entanglement and the asymptotic robustness. A direct calculation for fixed $r > 0$ in the limit $n \ll 1$ gives

$$\frac{\partial}{\partial n}\Delta_B(r,n) = \frac{1}{4}\operatorname{sech}^2 r (3 + \cosh 4r)\ln n + \mathcal{O}(n) \implies \left.\frac{\partial}{\partial n}\Delta_B(r,n)\right|_{n\to 0} < 0 \qquad \forall r > 0. \tag{5.6}$$

As a result, there needs to be a zero satisfying $0 < n_c < 1$.

Next, we show that we can reproduce these predictions in experiment. The experimentally extracted D_A and D_B as well as corresponding fits are plotted in Fig. 5.2(a) and Fig. 5.2(b). The experimentally determined lower bound E_F for EoF is shown in Fig. 5.2(c), together with a fit. In our approach we model the gain-dependent JPA noise by the power law dependence of Eq. (2.78), where we treat χ_1 and χ_2 as the only fit parameters. The effective squeeze factor r can be extracted from the reconstructed squeezed (antisqueezed) variance v_s (v_a) via $e^{4r} = v_a/v_s$. The degenerate gain can then be expressed as $G = e^{2r}$. For the fit, we let $\boldsymbol{\chi} \equiv (\chi_1, \chi_2)^T$ and define the weighted least-square cost function

$$T(\boldsymbol{\chi}) = \sum_{S,n}\left(w_1\left|D_A(S,n,\boldsymbol{\chi}) - \tilde{D}_A(S,n)\right|^2 + w_2\left|D_B(S,n,\boldsymbol{\chi}) - \tilde{D}_B(S,n)\right|^2 + \right.$$
$$\left. w_3\left|E_F(S,n,\boldsymbol{\chi}) - \tilde{E}_F(S,n)\right|^2\right), \tag{5.7}$$

where the sum is evaluated over all experimentally chosen squeezing levels S and noise numbers n and the quantities w_i are the weights, attributed to the respective contribution. The quantities $\tilde{D}_A(S,n)$, $\tilde{D}_B(S,n)$, and $\tilde{E}_F(S,n)$ are the experimentally determined data
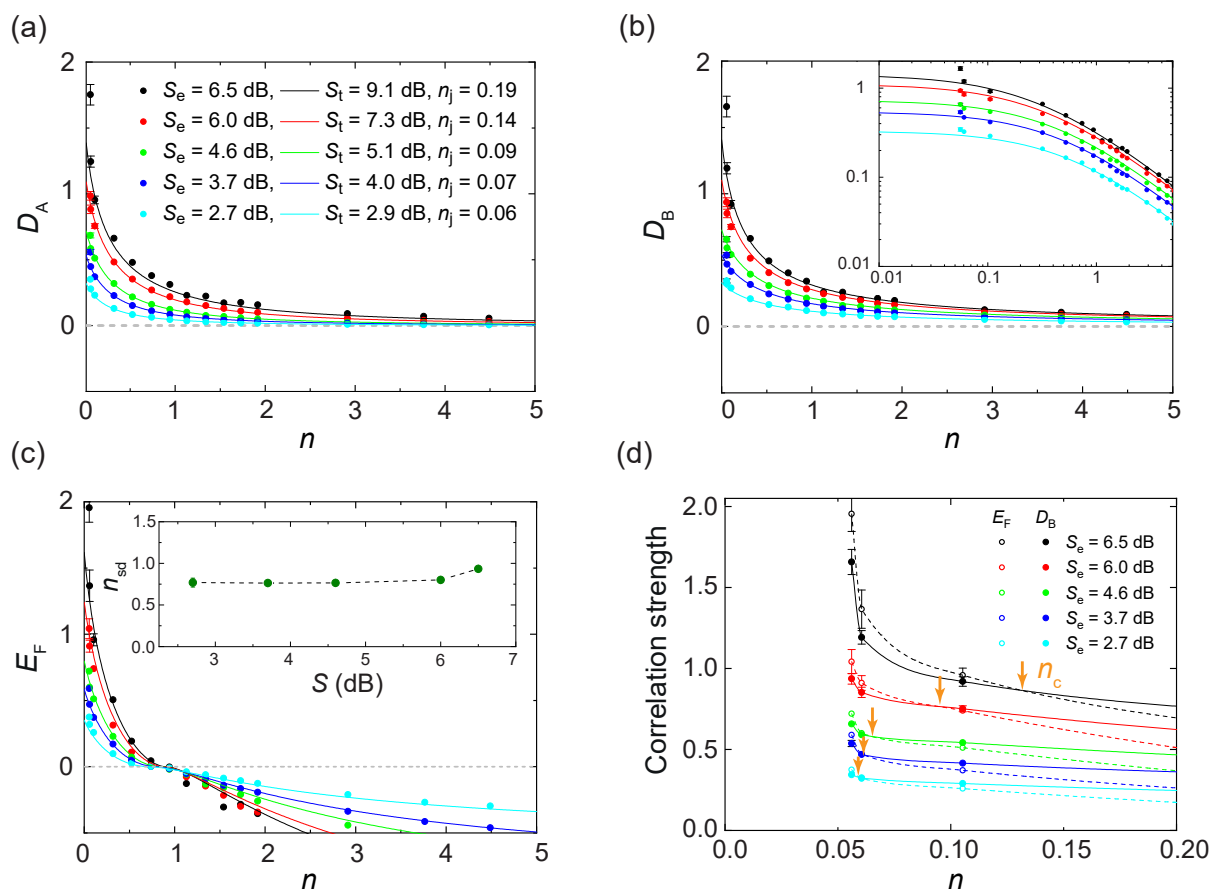
Figure 5.2: (a) Experimentally determined quantum discord values D_A as a function of the noise photon number n for various experimental squeezing levels S_e. Dots represent the measured data points. Solid lines correspond to a fit model based on Eq. (2.139) and Eq. (5.1) which takes gain-dependent JPA noise into account. The quantity S_t corresponds to the theoretically determined squeezing level from the fit and n_J is the JPA noise. Although we show S_t and n_J only in panel (a), the same values for S_e, S_t and n_J also correspond to D_A and E_F. (b) Experimentally determined quantum discord D_B as function of injected noise n for various squeezing levels. The inset shows the same data as a double logarithmic plot. (c) Experimentally determined lower bound E_F for EoF (dots) and corresponding fits (lines) for various squeezing levels. For the fit, we employ Eq. (2.135). We clearly observe the sudden death of entanglement at $n_{sd} \simeq 1$. In the inset, we plot n_{sd} as function of S_e which demonstrates that n_{sd} is independent of the squeezing level. The values n_{sd} are obtained from the experimental data using cubic Hermite spline interpolation. The error bars are obtained from the statistical measurement error and only plotted if the symbol size is exceeded. (d) Expanded view of the experimental results for D_B and E_F for noise photon number $n \leq 0.2$. Solid (dashed) lines correspond to cubic Hermite spline interpolation of the data points for D_B (E_F). We clearly observe the predicted crossover behavior of quantum discord and EoF, indicated by orange arrows.

points for A-quantum discord, B-quantum discord and EoF, respectively, corresponding to S and n. The functions $D_A(S, n, \chi)$, $D_B(S, n, \chi)$ and $E_F(S, n, \chi)$ are obtained by

inserting Eq. (5.1) into the theoretical expressions for quantum discord and EoF. To balance the contributions of quantum discord and EoF in the cost function, we choose the weights $w_1 = w_2 = 1/2$ and $w_3 = 1$. From the fit, we find $\chi_1 = 0.05$ and $\chi_2 = 0.56$. Our experimental results demonstrate positive quantum discord for all noise photon numbers n, which proves the asymptotic robustness of quantum discord. Furthermore, we measure the sudden death of entanglement at $n_{\mathrm{sd}} \simeq 1$. The quantity n_{sd} as a function of squeezing is shown in the inset of Fig. 5.2(d) and has been extracted from the measurement data using cubic Hermite spline interpolation [349]. We use cubic Hermite splines instead of conventional cubic splines to increase the precision by avoiding overshoots. The experimentally determined values for n_{sd} are smaller than the theoretical prediction due to the finite noise added by the JPAs themselves. Despite not being included in the fit model, further deviations from ideal theory are caused by path losses and crosstalk between the JPAs. In Fig. 5.2(d), we replot D_{B} and E_{F} for noise photon numbers $n \leq 0.2$, which reveals that we measure the predicted crossover between EoF and quantum discord in experiment, especially well observable for $S_{\mathrm{e}} = 6.5\,\mathrm{dB}$. The solid (dashed) lines correspond to a cubic Hermite spline interpolation for D_{B} (E_{F}). We provide the detailed analysis as well as the physical interpretation of this crossover in Sec. 5.2. So far, we have experimentally demonstrated that due to this robustness against noise, it would be beneficial to use quantum discord as a resource for quantum protocols. Possible quantum discord based protocols are deterministic quantum computing with one qubit (DQC1) [350, 351], quantum sensing [151], and quantum illumination [352]. An outstanding quantum communication protocol which exploits quantum discord as a quantum resource is RSP [347]. In addition, quantum discord is an ideal quantifier for how efficient quantum correlations are exploited in a noisy environment, where entanglement is already lost. We make use of this property in the next chapter, where we use quantum discord to investigate the correlation consumption in microwave quantum teleportation.

5.2 Flow of locally inaccessible information

In Sec. 2.2.3, we have introduced quantum discord as a general correlation measure, which implies that entanglement forms a subset of quantum discord. Thus, it seems contradictory that EoF can exceed quantum discord. This at first glance paradox situation can be resolved by considering that, so far, we assume that AB is an isolated bipartite quantum system. However, for a correct quantum mechanical description of noise injection, the quantum system needs to be coupled to an environmental bath E, thereby implying that we effectively measure bipartite quantum correlations in a multipartite system [49]. In such a system, a possible crossover between EoF and quantum discord has been predicted [353, 354]. As described in the following, regions where EoF exceeds quantum discord occur if we have a positive information flow from E to AB.

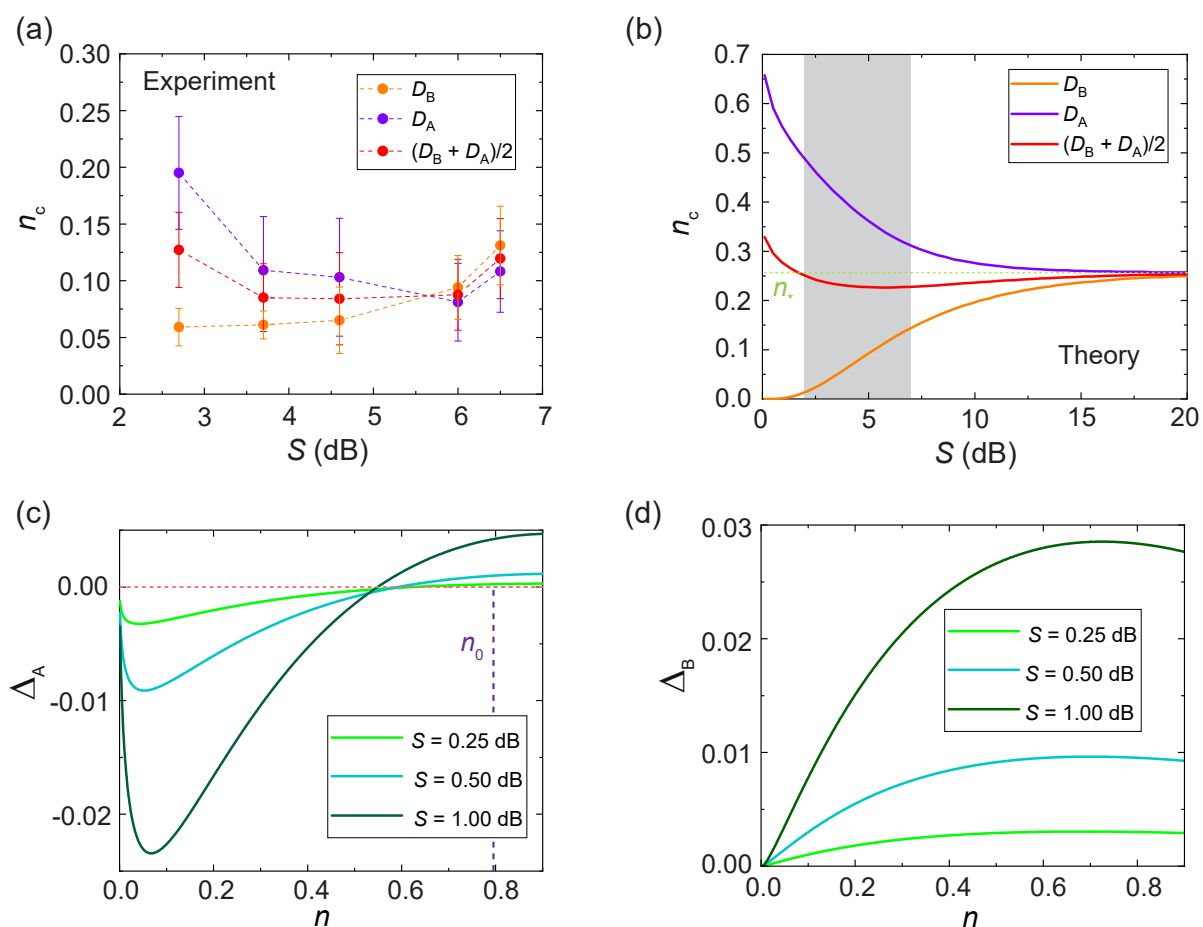According to the Stinespring dilation theorem [210, 355], the environment can always

Figure 5.3: (a) Experimentally determined crossover noise photon number n_c as a function of S for D_A (purple) and D_B (orange). Red dots correspond to the arithmetic mean of n_c, where we observe a minimum at approximately 5 dB squeezing. The error bars are determined from the respective experimental uncertainties of quantum discord and EoF using randomized error sampling. (b) Prediction of n_c from ideal theory. For D_A (D_B), n_c decreases (increases) monotonically with S. The red curve corresponds to the arithmetic mean of the purple and orange curve and shows a minimum at $S_{\mathrm{min}} = 5.73$ dB. In the limit $S \to \infty$, the curves converge to $n_* \simeq 0.26$. The gray dashed region shows the experimentally investigated regime of squeezing. Ideal theory qualitatively reproduces the experimental data. (c) Difference Δ_A between D_A and E_F as a function of n for various squeezing levels. The quantity $n_0 \simeq 0.79$ corresponds to n_c in the limit $S \to 0$. (d) Difference Δ_B between D_B and E_F as a function of n for various squeezing levels.

be chosen such that the system ABE is pure, implying a joint entropy $S_{\mathrm{ABE}} = 0$ [88]. The Araki-Lieb inequality then implies $S_{\mathrm{AB}} = S_E$ [356], which implies that EoF and quantum discord need to satisfy monogamy relations of the form

$$E_{XY} + E_{XZ} = D_{XY} + D_{XZ} \tag{5.8}$$

with distinct $X, Y, Z \in \{\mathrm{A, B, E}\}$ [348]. In Eq. (5.8), E_{XY} denotes the bipartite super-additive EoF shared between system X and Y and $D_{XY} = I(X : Y) - J(X|Y)$ is the corresponding quantum discord. In Ref. 88, a flow of LII is then defined as

$$\mathcal{L}_{X \to Y \to Z} = D_{YZ} + D_{XZ} + D_{YX}. \tag{5.9}$$

For the asymmetric differences Δ_A, Δ_B and Δ_AB between quantum discord and EoF, it can then be shown that

$$\Delta_\mathrm{A} \equiv D_\mathrm{A} - \mathcal{E}_\mathrm{F} = \frac{1}{2}(D_\mathrm{BE} - D_\mathrm{EB}) = \frac{1}{2}\left(\mathcal{L}_{\mathrm{B}\to\mathrm{A}\to\mathrm{E}} - \mathcal{L}_{\mathrm{E}\to\mathrm{A}\to\mathrm{B}}\right), \tag{5.10}$$

$$\Delta_\mathrm{B} \equiv D_\mathrm{B} - \mathcal{E}_\mathrm{F} = \frac{1}{2}(D_\mathrm{AE} - D_\mathrm{EA}) = \frac{1}{2}\left(\mathcal{L}_{\mathrm{A}\to\mathrm{B}\to\mathrm{E}} - \mathcal{L}_{\mathrm{E}\to\mathrm{B}\to\mathrm{A}}\right), \tag{5.11}$$

$$\Delta_\mathrm{AB} \equiv \frac{D_\mathrm{A} + D_\mathrm{B}}{2} - \mathcal{E}_\mathrm{F} = \frac{1}{2}\left(\mathcal{L}_{\binom{\mathrm{A}}{\mathrm{B}}\to\mathrm{E}} - \mathcal{L}_{\mathrm{E}\to\binom{\mathrm{A}}{\mathrm{B}}}\right), \tag{5.12}$$

where $\mathcal{L}_{\binom{X}{Y}\to Z}$ $\left(\mathcal{L}_{Z\to\binom{X}{Y}}\right)$ is the LLI flow from (to) the bipartite system XY to (from) Z. Thus, resulting from of Eq. (5.12), more LII flows from the bipartite system AB to the environment E than vice versa if $\Delta_\mathrm{AB} > 0$ [88]. As a result, the crossover n_c determines whether LII flows to ($n > n_\mathrm{c}$) or LLI is received from ($n < n_\mathrm{c}$) the environment.

Next, we investigate the squeezing dependence of n_c. In Fig. 5.3(a), we plot the experimentally determined crossover noise from the interpolation in Fig. 5.2(d). The same procedure is repeated for Δ_A and Δ_AB. The corresponding predictions from ideal theory are shown in Fig. 5.3(b). We observe that ideal theoretical plots qualitatively reproduce the measured squeezing dependence of n_c. However, we observe that, especially for Δ_A, the experimentally determined values are lower than predicted by ideal theory. Similar as for the sudden death of entanglement, this artifact can be explained by finite JPA noise, losses, and pump crosstalk. The gain-dependent noise is also the reason why we cannot experimentally investigate the full region shown in Fig. 5.3(b) since squeezing is restricted by 7 dB. As indicated by the red line, the crossover noise n_c for Δ_AB has a minimum at the numerically determined value $n_\mathrm{min} \simeq 0.23$ at $S_\mathrm{min} = 5.7$ dB. As a result, it is not always beneficial to increase the squeezing level when one attempts to maximize n_c. This minimum of n_c is also qualitatively reproduced in experiment, as seen in Fig. 5.3(a). Next, we analyze the limit $S \to \infty$, where ideal theory predicts the asymptotic expressions

$$D_\mathrm{A} = D_\mathrm{B} = (1 + n) \ln\left(1 + \frac{1}{n}\right) - 1 = (n + 1) \ln\frac{1}{n} + n - 1 + \mathcal{O}(n^2) \tag{5.13}$$

and

$$E_\mathrm{F} = -2 \ln 2 + \frac{(1+n)^2 \ln\left(2 + \frac{1}{n} + n\right) - (1-n)^2 \ln\left(\frac{1}{n} + n - 2\right)}{4n} = \ln\left(\frac{1}{4n}\right) + 1 + \mathcal{O}(n^2). \tag{5.14}$$

By comparing Eq. (5.13) and Eq. (5.14), we find that the crossover point n_c converges to
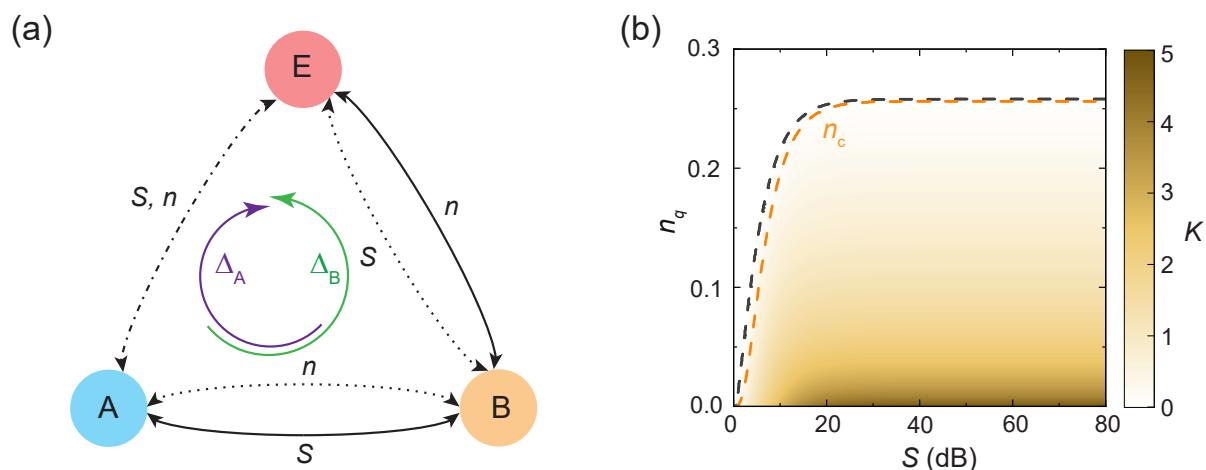
Figure 5.4: (a) Schematic illustration of bipartite correlation flow in the tripartite system ABE. Solid (dotted) black arrows indicate a monotonic increase (decrease) of the correlation with the respective quantity. The dotted-dashed arrow between path A and path E indicates that correlations between these two subsystems do not necessarily have to show monotonic dependence on S and n. The curved purple (green) arrow indicates the LII flow $B \to A \to E$ ($A \to B \to E$), according to Δ_A (Δ_B), described by Eq. (5.10) [Eq. (5.11)]. (b) Theoretically determined secret key K as a function of squeezing S and noise photon number n_q in the measured quadrature. Here, we assume a Gaussian CV QKD protocol between path A and path B, where environment acts as an eavesdropper. The black dashed line corresponds to the noise threshold at which the protocol becomes insecure, $K = 0$. The orange dashed line shows the crossover noise n_c, corresponding to Δ_B as a function of S, which provides an intuitive explanation for the security of the QKD protocol in the framework of LII flow.

a universal constant n_*, which can be analytically expressed as

$$n_* \simeq \frac{2(\ln 2 - 1)}{W_{-1}\left(\frac{2(\ln 2 - 1)}{e}\right)} \simeq 0.26, \tag{5.15}$$

where $W_{-1}(x)$ is the analytical continuation of the product logarithm function. As shown in the numerical treatment in Fig. 5.3(b) without any approximations, we find $n_* \simeq 0.2564$. In the next step, we investigate Δ_A, Δ_B, and Δ_{AB} as a function of n. The theoretically expected noise dependence of Δ_A and Δ_B is shown in Fig. 5.3 for various squeezing levels. We observe that these quantities behave fundamentally different in the limit $n \to 0$. In particular, n_c decreases (increases) monotonically with increasing S for Δ_A (Δ_B), as shown in Fig. 5.3(b). As already discussed above, this behavior is experimentally reproduced in Fig. 5.3(a). We can understand the fundamentally different behavior of Δ_A and Δ_B by the fact that noise injection in path B is a local process which directly leads to bipartite correlations between path B and environment E, but only indirectly correlates path A and E. Hence, the bipartite correlations between path B and E increase monotonically with n, whereas the correlations between path A and path B decrease due to the monogamy

relations. In constrast to that, the information flow between A and E can only result from tripartite correlations caused by an interplay between S and n. These correlations are not required to be monotonic in these quantities. The LII flow is schematically depicted in Fig. 5.4(a). We see that the fundamentally different behavior of Δ_A and Δ_B as a function of n can be explained by the fact that in the case of Δ_B no direct correlations between path A and path E are required to establish an LII flow, in contrast to the case described by Δ_A. This becomes especially clear if we take the low-squeezing limit $0 < r \ll 1$. In this limit, we have $n_c \to n_0$. A numerical investigation shows that $n_0 = 0$ for Δ_B, whereas we obtain the nontrivial result $n_0 \simeq 0.79$ in the case of Δ_A, as can be seen in Fig. 5.3(c). The existence of this nontrivial zero can be directly related to the fact that the LII flow $A \to E$ is only indirectly controlled by the parameters r and n. For a qualitative proof, we employ a simplistic model for the LII flow and assume that the LII flow capacity between two systems X and Y is described by a function $G_{XY}(r, n)$. Although the exact functional behavior is unknown, we certainly have $G_{AB}(0, n) = G_{BE}(r, 0) = 0$ and simultaneously for $r, n > 0$, we have $G_{AB}(r, 0) \neq 0$ and $G_{BE}(0, n) \neq 0$. The most relevant function for our purpose is $G_{AE}(r, n)$, which satisfies $G_{AE}(0, n) = G_{AE}(r, 0) = 0$. We then model the LII flow capacities for $A \to B \to E$ and $B \to A \to E$ by [6]

$$G_{ABE}(r, n) = G_{AB}(r, n)G_{BE}(r, n), \qquad G_{BAE}(r, n) = G_{AB}(r, n)G_{AE}(r, n). \tag{5.16}$$

To obtain behavior for small squeezing, we perform a Taylor expansion around $r = 0$ and find

$$G_{ABE}(r, n) = \underbrace{\left(\frac{\partial G_{AB}}{\partial r}\right)_{r=0}}_{>0} G_{BE}(0, n)r + \mathcal{O}(r^2), \tag{5.17}$$

$$G_{BAE}(r, n) = \underbrace{\left(\frac{\partial G_{BA}}{\partial r}\right)_{r=0}}_{>0} \left(\frac{\partial G_{AE}}{\partial r}\right)_{r=0} r^2 + \mathcal{O}(r^3), \tag{5.18}$$

where we assume that there are no divergences in the first and second order derivatives at $r \to 0$. Since we have $G_{BE}(0, 0) = 0$, we have a trivial zero in first order for G_{ABE} at $n_0 = 0$, as expected. Furthermore, we find that, in contrast to $G_{ABE}(r, n)$, $G_{BAE}(r, n)$ can only be described in quadratic order in r and not linearly. As a result, the lowest order coefficient is not simply $G_{AE}(0, n)$, similar as in Eq. (5.17), but the respective first order derivative, which can have nontrivial functional shape and allows for the possibility of a nontrivial zero $n_0 > 0$. Thus, measuring $n_0 > 0$ for D_A implies that noise injection in B leads to direct correlations as a function of $x \in \{r, n\}$ [i.e., $\mathcal{O}(x)$] between E and B. In contrast, the subsystems A and E are only correlated in higher order [i.e., $\mathcal{O}(x^2)$].

---

[6]Note that in an electrical circuit analogy, conductance would add reciprocally for a serial connection. Here, we do not use this analogy and neglect the sum of the respective individual conductances in the denominator as this would lead to divergences. By implicitly assuming a normalization $0 \leq G_{XY} \leq 1$, we rule out the unphysical case that the serial connection increases the overall capacity.

5.3 Relation of locally inaccessible information to quantum key distribution

Here, we show that LII is related to the security of certain QKD protocols. In particular, we focus on the Gaussian CV implementation of BB84 under reverse reconciliation, as described in Ref. 357 and Ref. 346. In this protocol, squeezing and displacement operations are used for a basis choice and encryption. Although the treatment of this specific protocol in Ref. 346 does not require entanglement, we can assume that an equivalent entanglement-based version exists by employing the concept of virtual entanglement [358, 359]. In order to investigate the relation between the LII flow and QKD, we assume that path A and path B exploit quantum correlations to securely share a common secret key [360]. The environment E can then be associated to an eavesdropper controlling loss and noise [361]. Thus, noise injection can be related to an entangling cloner attack from E [358]. As discussed in Sec. 5.2, the eavesdropper needs to add at least n_c noise photons to get a positive LII flow. For a perfect reconciliation efficiency, the amount of exchanged unconditionally secure information is then determined by the secret key [263, 362]

$$K = I_s(A : B) - \chi_E, \tag{5.19}$$

where the Shannon mutual information $I_s(A : B)$ is compared with the eavesdropper's Holevo quantity χ_E [276].[7] To determine K, we assume that path A and path B initially share an ideal TMS state with squeezing factor r, described by a covariance matrix V_{AB}. For the entangling cloner attack, the eavesdropper prepares a second TMS state [263]

$$\boldsymbol{V}_{E_1E_2} = \frac{1}{4} \begin{pmatrix} W\mathbb{1}_2 & \sqrt{W^2-1}\,\sigma_z \\ \sqrt{W^2-1}\,\sigma_z & W\mathbb{1}_2 \end{pmatrix}, \tag{5.20}$$

where the quantity W is determined by the eavesdropper's initial two-mode squeezing. As a result, the four-mode covariance matrix

$$\boldsymbol{V}_{ABE_1E_2} = \boldsymbol{V}_{AB} \oplus \boldsymbol{V}_{E_1E_2} \tag{5.21}$$

describes a pure state. Next, the eavesdropper couples the mode E_1 to B by an asymmetric beam splitter operation $\boldsymbol{C}$ with reflectivity β. The resulting covariance matrix is given by

$$\boldsymbol{V}'_{ABE_1E_2} = (\mathbb{1}_2 \oplus \boldsymbol{C} \oplus \mathbb{1}_2)\boldsymbol{V}_{ABE_1E_2}(\mathbb{1}_2 \oplus \boldsymbol{C} \oplus \mathbb{1}_2)^\dagger, \tag{5.22}$$

---

[7]The technically relevant quantity is the secret key rate. The secret key rate can be determined by multiplying K with the bandwidth of our system, which is determined by our digital FIR filter.

which can be expressed as

$$\boldsymbol{V}'_{\mathrm{ABE_1E_2}} = \frac{1}{4} \begin{pmatrix} \boldsymbol{V}'_{11} & \boldsymbol{V}'_{12} & \boldsymbol{V}'_{13} & \mathbb{0}_2 \\ \boldsymbol{V}'_{12}{}^{\mathrm{T}} & \boldsymbol{V}'_{22} & \boldsymbol{V}'_{23} & \boldsymbol{V}'_{24} \\ \boldsymbol{V}'_{13}{}^{\mathrm{T}} & \boldsymbol{V}'_{23}{}^{\mathrm{T}} & \boldsymbol{V}'_{33} & \boldsymbol{V}'_{34} \\ \mathbb{0}_2 & \boldsymbol{V}'_{24}{}^{\mathrm{T}} & \boldsymbol{V}'_{34}{}^{\mathrm{T}} & \boldsymbol{V}'_{44} \end{pmatrix}, \tag{5.23}$$

where the 2×2 matrices $\boldsymbol{V}'_{ij}$ can be straightfowardly calculated. Since the matrix $\boldsymbol{V}'_{22}/4$ corresponds to the final local noisy TMS state in system B, we demand

$$\frac{1}{4}(\cosh 2r + 2n)\mathbb{1}_2 = \frac{1}{4}[(1 - \beta)\cosh 2r\,\mathbb{1}_2 + \beta W \mathbb{1}_2]. \tag{5.24}$$

In the limit $\beta \ll 1$, we find the relation $\beta W = 2n$. We consider reverse reconciliation [358] and assume that we perform a homodyne detection on B in the next step. We define the number of noise photons added to the measured quadrature as $n_q = n/2$. We only consider the noise n_q since homodyne detection is equivalent to phase-sensitive amplification and measurement of a certain quadrature, which implies that the orthogonal quadrature is strongly deamplified. Consequently, only half of the added noise is of relevance since we assume that the noise is symmetrically added to both field quadratures. For the final state of the eavesdropper, we have

$$\boldsymbol{V}'_{\mathrm{E|B}} = \boldsymbol{V}'_{\mathrm{E}} - \frac{1}{4\sqrt{\det \boldsymbol{V}'_{22}}} \boldsymbol{V}'_{\mathrm{C}} \boldsymbol{\Pi}_q \boldsymbol{V}'_{\mathrm{C}}{}^{\mathrm{T}}, \qquad \boldsymbol{V}'_{\mathrm{E}} = \frac{1}{4} \begin{pmatrix} \boldsymbol{V}'_{33} & \boldsymbol{V}'_{34} \\ \boldsymbol{V}'_{34}{}^{\mathrm{T}} & \boldsymbol{V}'_{44} \end{pmatrix}, \tag{5.25}$$

where $\boldsymbol{V}_{\mathrm{C}} = (\boldsymbol{V}'_{23}, \boldsymbol{V}'_{24})^{\mathrm{T}}$ and $\boldsymbol{\Pi}_q$ denotes the phase space projector on the q-quadrature [49]. The corresponding Holevo quantity χ_E is then obtained as

$$\chi_{\mathrm{E}} = S_{\mathrm{E}} - S_{\mathrm{E|B}}, \tag{5.26}$$

where S_{E} ($S_{\mathrm{E|B}}$) denotes the von Neumann entropy, corresponding to $\boldsymbol{V}'_{\mathrm{E}}$ ($\boldsymbol{V}'_{\mathrm{E|B}}$).[8] For a Gaussian codebook of input states with variance σ^2, the Shannon mutual information Eq. (2.128) can be calculated by [263]

$$I_{\mathrm{s}}(\mathrm{A:B}) = \frac{\nu}{2} \log_2 [1 + \mathrm{SNR}(\nu)].$$

Here we choose $\nu = 1$ for a homodyne (projection onto squeezed states) detection and $\nu = 2$ for a heterodyne measurement (projection onto coherent states). For homodyne

---

[8]In this specific case, we calculate von Neumann entropies using the binary logarithm in Eq. (2.131) since this is common convention in QKD for the definition of K.

detection, we find

$$I_s(\text{A} : \text{B}) = \frac{1}{2}\log_2\left(1 + \frac{4(1-\beta)\sigma^2}{(1-\beta)e^{-2r} + 4n_q}\right) \simeq \frac{1}{2}\log_2\left(1 + \frac{\sigma^2}{n_q}\right), \qquad (5.27)$$

where, for the last expression, we use the approximations $r \gg 1$ and $\beta \ll 1$. For the calculation of SNR in the detected quadrature, we have considered the protocol described in Ref. 346, implying a noise of $e^{-2r}/4 + n_q$ per quadrature and an optimal codeboook variance $\sigma^2 = \sinh(2r)/2$. We plot $\max(K, 0)$ in Fig. 5.4(b) as a function of squeezing and noise for $\beta = 10^{-4}$. The black dashed line corresponds to the noise threshold beyond which the secret key becomes zero. For comparison, the orange dashed line shows n_c according to Δ_B in Eq. (5.11). Although we do not provide proof that both curves are identical, we observe that the threshold for the secret key and n_c approximately coincide, implying that the QKD protocol becomes insecure if the eavesdropper obtains a positive LII flow. One possible explanation for the deviation of both curves is the fact that we do not calculate the actual EoF but only the lower bound E_F. Thus, the quantities Δ_A, Δ_B, and Δ_AB can become of practical interest as security quantifiers in QKD, with the advantage that these quantities are easier to compute than the Holevo information. Equation (5.23) also allows us to substantiate our argumentation about the different behavior of Δ_A and Δ_B in Sec. 5.2. It can be shown that bipartite mutual information between path A and the respective modes E_1 and E_2 is always zero, implying that any LII flow between these systems needs to be caused by multipartite correlations. Although Eq. (5.23) is only one specific purification, this result is generally valid since the Stinespring dilation theorem states that the purification is unique up to a unitary transformation, which does not impact entropy [210, 355].

Finally, we want to note one relation of quantum discord to dense coding protocols, as discussed in Sec. 2.3.2, with respect to the entanglement-assisted channel capacity [363, 364]. We consider a bosonic thermal channel, carrying n_s of signal photons and n_n of noise photons. As shown by Holevo and Werner [365], the asymptotic ratio of the entanglement-assisted channel capacity C_ea and classical channel capacity can be expressed as

$$\lim_{n_n \to \infty} \frac{C_\text{ea}}{C} = (1 + n_s)\ln\left(1 + \frac{1}{n_s}\right). \qquad (5.28)$$

This equation has structural similarity to our result for the asymptotic quantum discord, Eq. (5.13). Indeed, if we relate the environment to an eavesdropper, the communication channel between the subsystem AB and E carries n photons on average. For the eavesdropper, enhancing the squeezing level S in the TMS state effectively looks like thermal noise. In this analogy, we then observe that the quantum discord between path A and path B corresponds to a relative entanglement-assisted enhancement of the channel capacity C between AB and E,

$$\lim_{S \to \infty} D_\text{A} = \lim_{S \to \infty} D_\text{B} = \frac{C_\text{ea} - C}{C}. \qquad (5.29)$$

Thus, quantum discord, describing LII between path A and path B, simultaneously increases the entanglement-assisted channel capacity C_{ea} between AB and the environment.

Chapter 6

Experimental quantum teleportation of coherent microwave states

In this chapter, we discuss our experimental realization of quantum teleportation with propagating microwaves. Although over the last decades successful experimental quantum teleportation has been demonstrated with discrete-variable systems and with propagating waves in the optical frequency regime [9, 67, 219], a realization with propagating microwave states has been missing so far. In the following, we demonstrate the first implementation of deterministic quantum teleportation of coherent microwave states by exploiting two-mode squeezing and an analog feedforward channel over a macroscopic distance of $d = 0.42\,\mathrm{m}$. In Sec. 6.1, we introduce our experimental setup. Next, discuss our calibration procedure for the TMS resource and the JM in Sec. 6.2. Following that, we present our experimental results in Sec. 6.3. A systematic experimental study of the teleportation fidelity as a function of resource squeezing and feedforward gain, is provided in Sec. 6.3.2. In addition, we introduce a theory model for our experiment in Sec. 6.3.3. In Sec. 6.4, we demonstrate in an outlook how analog quantum teleportation can be used for Gaussian error correction [218].[1] Parts of the results of this chapter have been published in Ref. 78. Parts of the figures as well as from the text have been adopted from this publication.

6.1 Setup for intra-fridge quantum teleportation

In this section, we provide a detailed discussion of the microwave quantum teleportation setup. A schematic illustration of this setup is provided in Fig. 6.1 and we briefly review our teleportation scheme in the following. The setup consists of four JPAs.[2] We employ two JPAs for entanglement generation and two other JPAs for analog Bell measurement. The two measurement JPAs in the JM geometry form the Alice part of the setup and the Bob part is realized with a directional coupler with coupling $\beta = -15\,\mathrm{dB}$. The

---

[1]The investigation of our analog quantum teleportation protocol with respect to Gaussian error correction has been collaboratively performed within a Master's project together with W. Yam. The resulting Master's thesis can be found in Ref. 238.

[2]We use NEC JPAs for the experiments presented in this chapter.
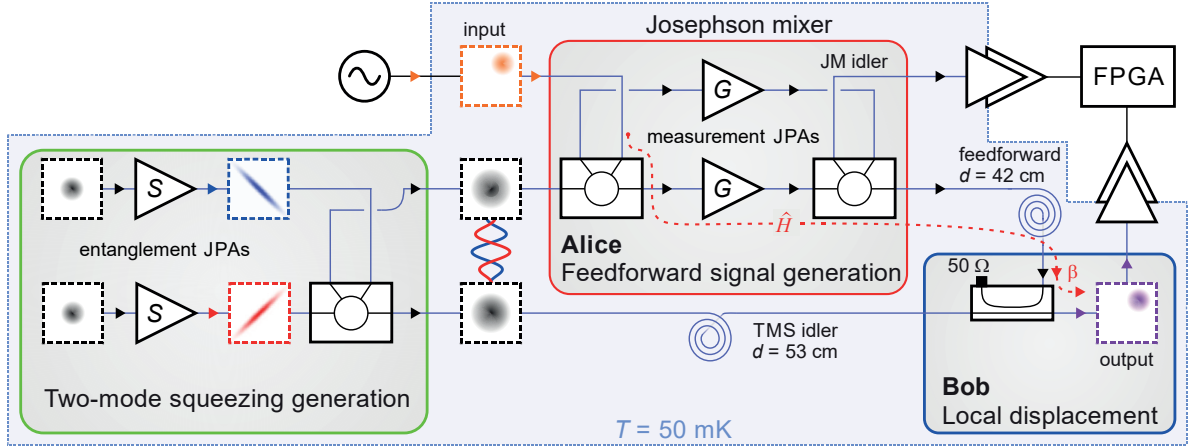
Figure 6.1: Schematic setup for quantum teleportation with propagating microwaves, consisting of two entanglement JPAs and two measurement JPAs. The TMS idler and the feedforward are distributed to Bob via superconducting coaxial cables. We employ a cable length of 53 cm for the TMS idler mode and of 42 cm for the feedforward. The classical feedforward is generated by the measurement JPAs with gain G and coupled to Bob's TMS idler via a directional coupler with coupling $\beta = -15$ dB. The combined action $\hat{H}$ of measurement JPAs and directional coupler implements an analog projective phase space measurement in the projective limit, $G \to \infty$, $\beta \to 0$, $G\beta = \text{const}$.

two entanglement JPAs generate orthogonally squeezed single-mode states which are superposed at a symmetric hybrid ring beam splitter. Then, the outputs of this hybrid ring beam splitter emit a TMS resource state. One mode of the resource state is distributed to Alice and the second mode (TMS idler) is sent to Bob's directional coupler over a distance of 53 cm. Alice uses a second hybrid ring beam splitter to entangle her resource mode with an unkown coherent input state, generated at room temperature, and employs the JM to realize the Bell measurement. Following that, Alice transmits the analog feedforward signal to Bob over a distance of 42 cm. Bob uses his directional coupler to couple the feedforward signal to his resource mode. As discussed in Sec. 2.3, in the projective limit, the joint action $\hat{H}$ of the JM and the directional coupler implements a phase space projection. As an example, for the q-quadrature, this joint action yields the phase space transformation [cf. Eq. (2.177)]

$$\boldsymbol{H} = \frac{\sqrt{\beta}}{2}\boldsymbol{J}_q \xrightarrow[G\cdot\beta\to 4]{\beta\to 0} \boldsymbol{\Pi}_q = \begin{pmatrix} 0 & 0 \\ 0 & 1 \end{pmatrix}, \qquad \boldsymbol{J}_q = \begin{pmatrix} 1/\sqrt{G} & 0 \\ 0 & \sqrt{G} \end{pmatrix}. \tag{6.1}$$

A similar expression can be found for the p-quadrature. In the next step, we perform quantum state tomography of the resulting state and compare the result to the precharacterized input state. Simultaneously, we measure the second JM output (JM idler) for phase stabilization. Figure 6.2 shows a photograph of our experimental setup. The central mechanical component of the experimental setup is formed by a silver rod which is directly

attached to the MC plate and allows for flexible mounting of microwave components. To improve a thermal contact between the silver rod and various components, we have chemically removed the silver tarnish Ag_2S prior to installation. This is done by boiling the sample rod together with aluminum foil and sodium hydrogencarbonate in saturated saline solution, leading to the redox reaction [366]

$$3Ag_2S + 2Al \longrightarrow 6Ag + Al_2S_3. \tag{6.2}$$
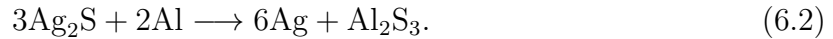
At the bottom, the sample rod is extended by an OFHC-Cu holder. The JPA samples and the passive microwave components are fixed on opposite sides of the sample rod. Each of the cylindrical Al boxes shown in Fig. 6.2(a) contains a single JPA, which is prepared as described in Sec. 3.2.1. In comparison with Ref. 112, the Al boxes are designed in a way that they can be directly attached to the sample rod from the back side without additional L-shaped holders. The motivation behind this new design is space optimization, since the teleportation setup needs to fit inside a cryoperm shield (not shown here) with a diameter of 13.5 cm and a length of 42.2 cm for protection from external magnetic fields. The DC flux of each JPA can be controlled by an individual superconducting coil inside of the respective Al shield. The two lower Al shields contain the entanglement JPAs, which can be individually temperature-stabilized.[3] During all our experiments described in this chapter, the temperature of the entanglement JPAs has been set to 50 mK. The top two Al boxes contain the measurement JPAs. In contrast to the entanglement JPAs, the measurement JPAs are not temperature-stabilized. The central Al box houses an additional JPA in Alice's input line which can be used for squeezed state generation and teleportation or for potential crosstalk correction in future experiments. As passive RF components, we employ circulators,[4] hybrid ring beam splitters,[5] and a directional coupler.[6] Most of these passive components are visible in Fig. 6.2(b) and some of those components are fixed with L-shaped OFHC-Cu holders to the front side of the sample rod. The JPAs and RF components are connected with custom-made superconducting coaxial NbTi/NbTi cables with crimped SMA connectors. These cables are desgined individually to fit inside of the cryoperm shield and satisfy the $50\,\Omega$ standard with tolerance $\pm 2\,\Omega$. Simultaneously, the cable lengths are chosen to minimize mismatches in the effective electrical path lengths between all three signal lines. For each of the JPAs, we install a circulator at the signal line to separate input and output modes. The first hybrid ring beam splitter (HR 1) is employed for TMS state generation. Hybrid ring beam splitters HR 2 and HR 3 belong to Alice's JM. We couple a coherent to-be-teleported signal into the setup via HR 2. Wherever possible, we employ direct connections between different

---

[3] We use two `AVS-47B` resistance bridges, combined with two `TS-530A` temperature controllers from `Picowatt` for this purpose.

[4] We use `CTH1184-KS18` circulators from `Quinstar` for this purpose.

[5] We use `CPL-5850-100B` hybrid ring beam splitters from `Miteq` for this purpose.

[6] We use a `CPL-4000-8000-15-C` coupler from `Miteq` for this purpose.
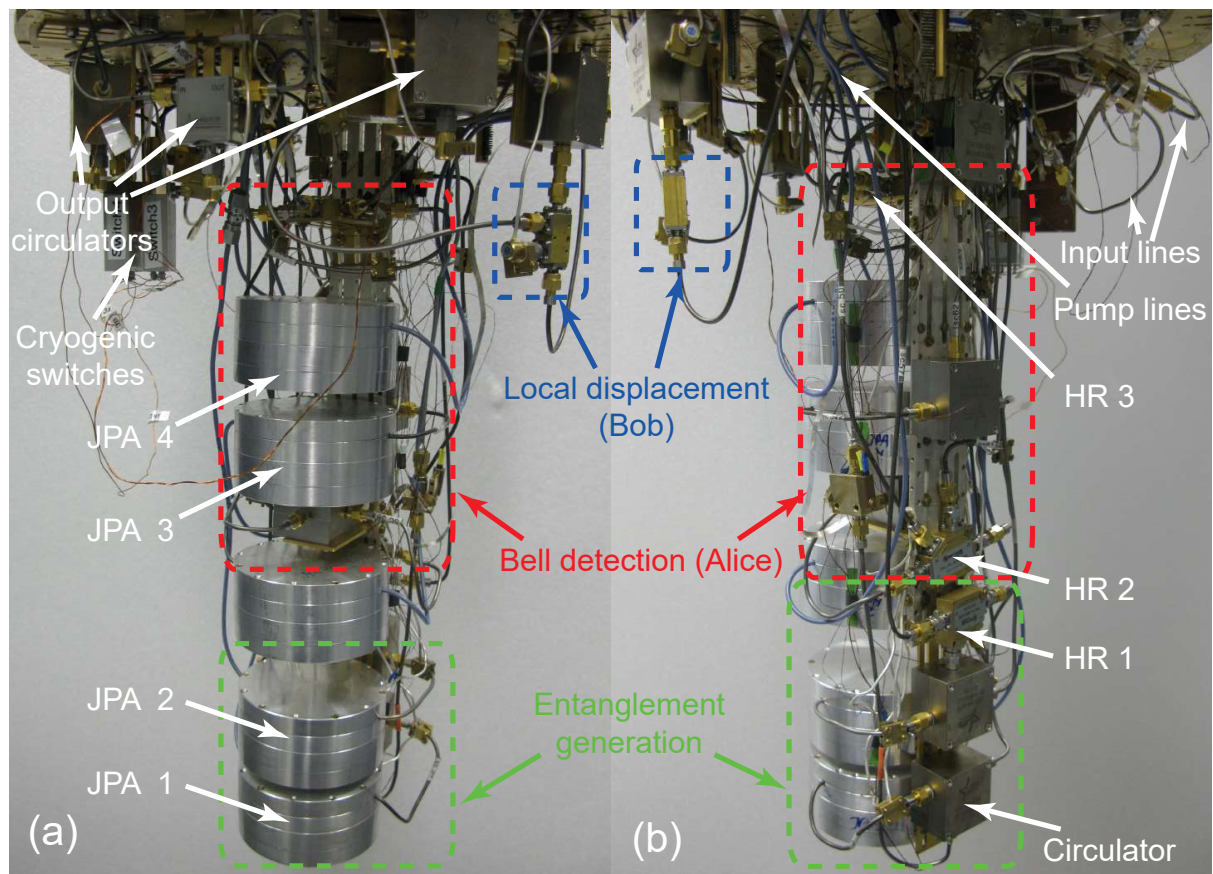
Figure 6.2: (a) Photograph showing the front view of the experimental teleportation setup. The two lowest aluminum boxes contain the entanglement JPAs (JPA 1 and JPA 2) and the two top boxes contain the measurement JPAs (JPA 3 and JPA 4). The aluminum box in the center contains a fifth JPA at Alice's input for potential teleportation of squeezed states. At the top of the photograph, the output circulators and cryogenic switches are visible. The pump lines can be recognized by the blue `minibend` cables. (b) Photograph showing the back view of the experimental teleportation setup and revealing the hybrid ring beam splitters ("HR 1", "HR 2", "HR 3") and circulators for entanglement and measurement JPAs. During the teleportation experiment, signals flow from bottom to top.

microwave components. As an example, we directly connect the JPA 2 circulator and HR 1, since minimizing losses is especially important to avoid degradation of entanglement. Bob's directional coupler is mounted outside of the cryoperm shield and the coupled port is connected to Alice via a 42 cm long superconducting coaxial cable. The input port is directly connected to an output of HR 1 via a 53 cm long superconducting coaxial cable. We thermalize all JPAs, cables, and microwave components with annealed silver wires. In addition, the second coupled port of Bob's directional coupler and unused ports of the circulators, are terminated by 50 Ω impedance loads, which are thermally anchored to the MC plate with annealed silver strips. The 50 Ω impedance effectively injects the respective signals at this port into an infinitely long transmission line and

dissipates the energy to cryogenic environment [93]. For our teleportation experiment, we use eight input lines and four output lines. We employ five of these input lines as pump lines for our JPAs. Two of the remaining input lines are connected to JPA 1 and JPA 2, respectively, and the last input line is used to inject the coherent input signal into HR 2. Each of these three input lines contains heatable 30 dB attenuators for Planck spectroscopy, as described in Sec. 3.1.4. To guarantee reliable photon number calibration, it is important to establish a weak thermal contact for these lines and to avoid any touches with other components. The four output lines are employed for TMS state characterization, calibration of the coherent input state, phase stabilization, and reconstruction of the teleported state. We generate the pump tones and the coherent input signal with room temperature `SGS100A` RF sources and measure the output signals with our FPGA-based microwave receiver setup as described in Sec. 3.1.3. For the teleportation protocol, we divide a single measurement trace of 400 µs into eight different parts (pulses). The first pulse provides a reference for the state tomography. The remaining pulses control the JPA pump sources as well as the RF input source. The pulse pattern is designed such that we can simultaneously reconstruct all individual JPA parameters as well as the coherent input signal and the teleported state within one single measurement trace. In addition, during one of the pulses, we perform the teleportation protocol without pumping the entanglement JPAs ("'classical teleportation"). During the last pulse, we realize the complete quantum teleportation protocol by simultaneously switching on the pump tones for the entanglement and measurement JPAs, as well as enabling the coherent input signal. A complete setup drawing is provided in Fig. A.2 in Appendix A.

To switch between different output lines, we use two cryogenic RF switches.[7] The location of these switches is indicated in the full setup drawing in Fig. A.2. The RF switches contain ferromagnetic components which can lead to trapping of magnetic flux vortices in the JPA ground planes. This flux trapping may degrade internal quality factors of the JPAs [367, 368]. In addition, switching requires application of a short current pulse and the induced magnetic field can destroy the DC flux calibration. Since it is necessary to switch both RF switches during the experiment, we ensure that the switches do not interact with our JPAs by mounting them outside of the cryoperm shield using a separate OFHC-Cu holder, as shown in Fig. 6.2(a). To avoid any magnetic crosstalk between the switches, we space them apart by 6 mm distance using an additional OFHC-Cu slab. The switches are controlled by a custom-built switch driver described in Ref. 158. We ground the cryogenic switches directly to the cryostat mass to save input lines. To change between different input and output lines in our teleportation experiment, we use additional switches at room temperature .[8]

---

[7]We use `N1812UL` 5-port switches from `Agilent` for this purpose.

[8]We use `N1810TL` 3-port switches from `Agilent` for this purpose. The switches are controlled by a `L4445A` switch driver via a TCP connection to our measurement CPU.
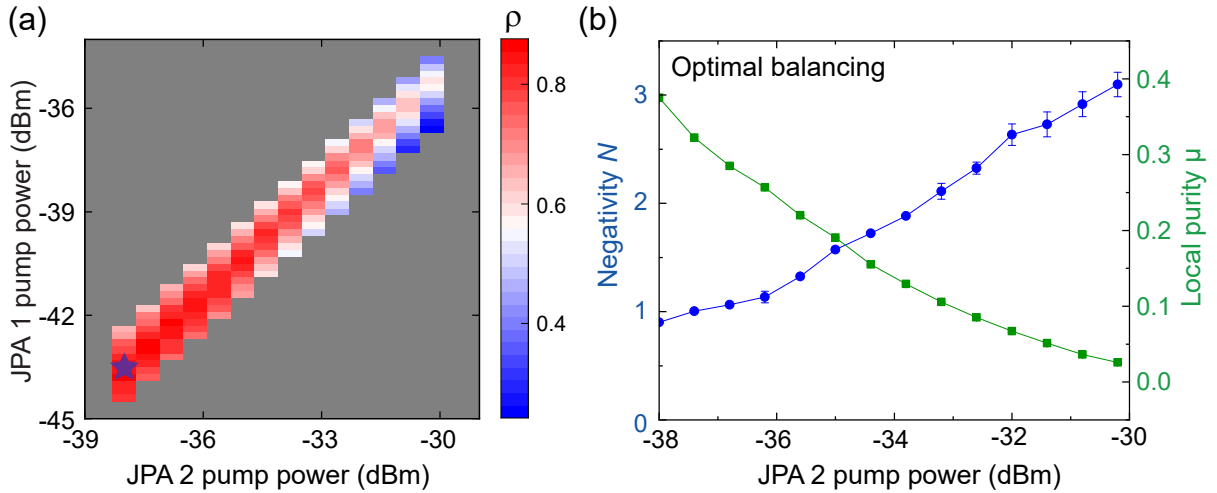
Figure 6.3: (a) Balancing of the TMS resource for microwave quantum teleportation. We fix the squeezing angles of the entanglement JPAs, perform a two-dimensional pump power sweep and optimize for maximal variance ratio $\rho = v_{s,1}v_{s,2}/(v_{a,1}v_{a,2})$, where $v_{s,i}$ ($v_{a,i}$) denotes the squeezed (antisqueezed) variance in path $i \in \{1,2\}$. To reduce the measurement time, we restrict ourselves to the region where we expect this optimum to appear. This measurement has been performed at $\omega_0/2\pi = 5.45\,\text{GHz}$. Here, we observe a maximal variance ratio of $\rho = 0.86$ (purple star) for JPA input squeezing $S = 4.5\,\text{dB}$. (b) Local purity μ of one TMS mode and negativity N, quantifying the entanglement strength between both modes, as a function of the JPA 2 pump power. For each JPA 2 pump power, the JPA 1 pump power is chosen such that we reach maximal ρ. We observe the expected monotonic decrease of the local purity μ as the TMS state locally coincides with thermal noise. Simultaneously, N increases monotonically. In the high pump power limit, we would approach a maximally entangled state, $\mu \to 0$ and $N \to \infty$ in the absence of practical experimental limitations. Solid lines connecting data points are a guide to the eye.

6.2 Calibration and balancing procedure

Before we can realize the actual teleportation experiment, we need to perform multiple calibration steps. These measurements include Planck spectroscopy for all four output lines, as described in Sec. 3.1.4. To minimize the measurement time, we use our two-path tomography setup for simultaneous detection of two Planck curves, implying that we need to run two Planck sweeps. In addition, we perform characterization routines for all involved JPAs, as described in Sec. 3.2.2. Next, we run a more advanced calibration routine to correct for a finite pump crosstalk between the JPAs as well as for differences in the electric path lengths. Finally, we calibrate the coherent photon number in the input to-be-teleported signal to eventually calculate the teleportation fidelity.

Two-mode squeezing balancing   As discussed in Sec. 2.2.2, an ideal TMS state locally looks like a symmetric thermal state. Since we experimentally create our TMS states by superposing two independent squeezed states, it is not guaranteed that both variances of

the resulting TMS state coincide, e.g., due to asymmetries in the JPAs or in the involved microwave components. In particular, since our circulators are effectively transparent at the pump frequency $2\omega_0$, the entanglement JPAs weakly affect each other via pump crosstalk. Since quantum teleportation works best with a symmetric TMS resource, we need to carefully balance our states. During this balancing routine, we fix the squeezing angle for JPA 1 (JPA 2) to $\gamma_1 = 45°$ ($\gamma_2 = 135°$). Next, we estimate the required pump powers to achieve a desired two-mode squeezing level from the individual squeezing characterization of both JPAs. Following that, we sweep the pump power of both JPAs in the region of expected balance and measure the variance ratio, $\rho = v_{s,1} v_{s,2}/(v_{a,1} v_{a,2})$, where $v_{s,i}$ ($v_{a,i}$) denotes the squeezed (antisqueezed) variance in path $i \in \{1, 2\}$.[9] For fixed JPA 2 pump power, we choose the JPA 1 pump power which maximizes ρ. To enable proper stabilization of the squeezing angles, we employ four pulses each having a temporal length $\tau = 107\,\mu s$. Results of such balancing at $\omega_0/2\pi = 5.45\,\text{GHz}$ are shown in Fig. 6.3(a), where each data point is averaged over 1.25×10^6 time traces. We clearly observe that, for each JPA 2 pump power, there is a corresponding JPA 1 pump power at which we reach maximal ρ. At this maximum, we measure typical values $\rho = 0.86$.[10] The pump powers, chosen for Fig. 6.3(a), correspond to squeezing levels ranging from $4.5\,\text{dB}$ to $6.5\,\text{dB}$. Figure 6.3(b) shows negativity and local purity at the point of optimal balancing as a function of JPA 2 pump power. We clearly observe that the entanglement strength increases with increasing pump power. In case of noiseless JPAs and perfect balancing, the increase in negativity is described by $N = \max[0, e^{-r} \sinh r]$, according to Eq. (2.133). Simultaneously, purity of the local mode decreases, as expected. For an ideal TMS state, this decay is given by $\mu = \text{sech}\, 2r$. In case we neglect all losses and noise, the two-mode squeezing level S_T coincides with the squeezing level S of the input squeezed states. However, our cryogenic hybrid ring beam splitters have an insertion loss of $\varepsilon_\text{HR} = 0.4\,\text{dB}$. These losses lead to $S_\text{T} \lesssim S$, where the relative difference between S and S_T is approximately $10\,\%$ [78]. The deviation is sufficiently small to treat S as a direct quantifier for the amount of two-mode squeezing in our resource.

Coherent photon number calibration   Next, we calibrate the coherent photon number in our teleportation setup, as described in Sec. 4.1. We choose the input of HR 2 as a reference point, indicated by the red dot in Fig. 6.4(a). First, we perform Planck spectroscopy to obtain a photon number calibration for our reconstruction point. Following that, we sweep the coherent signal power in a two-pulse measurement with a corresponding pulse length of $208\,\mu s$. Here, we perform averaging over 1.8×10^6 time traces. For each signal power, we perform reference-state reconstruction to determine the number of coherent photons in the signal. The result of this experiment is shown in Fig. 6.4(a). As a consistency check,

---

[9]We balance the TMS resource state via the outputs "Out 1" and "Out 2" shown in Fig. A.2.
[10]To the best of our knowledge, equality of this maximal ρ to the previous value found in Sec. 4.2 is a coincidence.
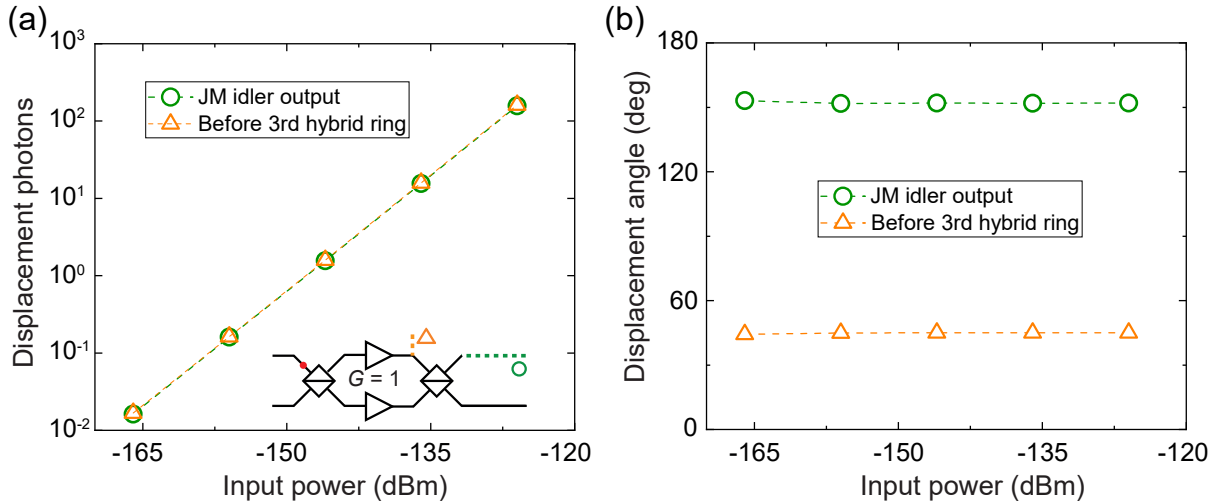
Figure 6.4: (a) Coherent photon number calibration of to-be-teleported signals. We vary the input power of a coherent signal in a two-pulse measurement and use reference-state reconstruction to obtain a calibration curve for the displacement photon number $|\alpha|^2$. To check for consistency, we perform the measurement via two distinct outputs, as indicated in the inset and observe a good agreement between them. (b) Reconstructed displacement phase. The calibration measurement is performed with the target phase $\theta = 45°$, which corresponds to orange triangles. The phase offset between both outputs results from different electrical path lengths. Dashed lines are a guide to the eye.

we simultaneously measure the calibration curve via two different outputs, as indicated in the inset.[11] From a linear fit, we extract a relation of $1.54\,\text{aW}$ per coherent photon within our measurement bandwidth. We also observe an excellent agreement between both signal paths. Figure 6.4(b) shows the reconstructed displacement angles. During this measurement, the coherent phase is stabilized to $\theta = 45°$. In the second path, we record a stable phase of $152 \pm 0.6°$, indicating a relative phase shift of $107°$ due to the phase offset of the hybrid ring beam splitter and differences in the electric path lengths.

Balancing of the Josephson mixer   Analogous to the TMS state balancing, the quasiprobability distributions of the JM output states are supposed to be symmetric as well. In this case, the combined action of the two phase-sensitive measurement JPAs corresponds to a TMS operation and the JM can be regarded as a single phase-preserving amplifier with spatially separated signal and idler ports. Before performing balancing of the JM, we toggle both cryogenic switches to a configuration which enables us to reconstruct Bob's output state at the directional coupler, as well as the JM idler.[12] In order to reconstruct our quantum states at the output of the directional coupler, we need to compensate for additional losses of $3.7\,\text{dB}$ in our photon number calibration, relative to HR 1 input.

---

[11]This calibration measurement requires switching to the output lines "Out 3" and "Out 4" in Fig. A.2.

[12]Bob's state is reconstructed via output line "Out 1" and the JM idler is measured via "Out 4" in Fig. A.2.
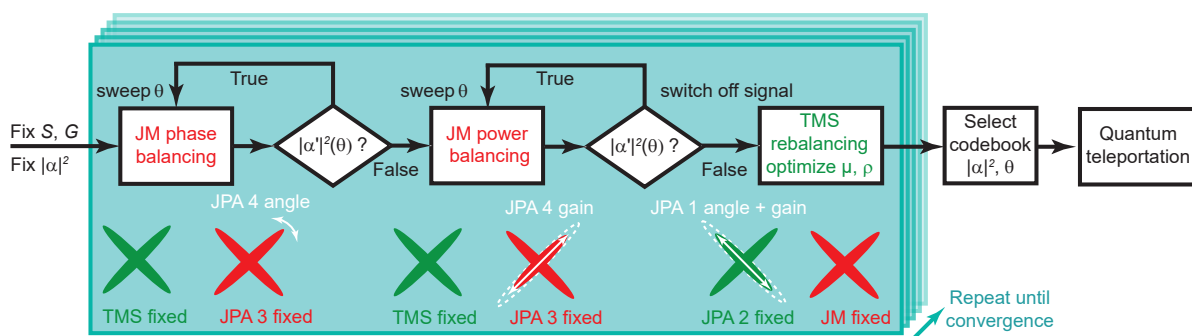
Figure 6.5: Balancing and calibration scheme for microwave quantum teleportation. Following this scheme, we balance the JM and the TMS resource states and take mutual JPA crosstalk into account. First, we fix resource squeezing S, feedforward gain G, and input photon number $|\alpha|^2$. In addition, we fix all JPA amplification angles close to their expected values. For fixed TMS state parameters, we vary the JPA 4 angle until we find an optimum φ_4^* at which the JM response, $|\alpha'|^2$, is independent of the displacement angle θ. Subsequently, we repeat the same procedure with the pump power of JPA 4. Next, we optimize the TMS resource with respect to variance ratio and purity by varying the angle and gain values of JPA 1. We repeat the whole procedure until we converge to steady parameters.

Simultaneously, we shift the reconstruction point from the input of HR 2 to the output of HR 3, which enables us to directly measure the JM idler. This is done by correcting the respective PNCF by estimating extra 8.2 dB of losses. Since we operate both measurement JPAs at large gain values, $G \gg 1$, we expect the effect of pump crosstalk to be significantly larger, as compared to the entanglement JPAs. Thus, we perform the JM balancing in two steps. In the first step, we roughly balance the JM in an analogous way as the TMS resource by amplifying a coherent signal with approximately $|\alpha|^2 = 4$ coherent photons. Within this procedure, we keep the pump power of JPA 3 and JPA 4 fixed and sweep the respective amplification phases around the expected optimum. We reach a maximal variance ratio $\rho = 0.93$. During this measurement, we keep the entanglement JPAs switched on to account for their pump crosstalk. We measure a phase mismatch of 58° between both JM paths. Correcting for the difference in electric path lengths is especially relevant for our Bell measurement setup, since the JM only acts as a proper interferometer in case of propagating waves in both paths under the same phase evolution [246, 247]. Thus, we need to correct for a possible phase mismatch by adjusting relative amplification angles of the measurement JPAs. We perform this sensitive balancing within a set of additional fine calibration measurements. The corresponding calibration protocol is depicted in Fig. 6.5 and consists of multiple steps. The main scope of this calibration routine is to remove any dependence of Bob's teleportation fidelity on the coherent phase θ, which is assumed to be unknown in our experiment since we employ polar symmetric codebooks. Prior to calibration, we fix the desired resource squeezing S, the feedforward gain G, and the displacement photon number $|\alpha|^2$. In the first calibration step, we fix

the pump power of both measurement JPAs, the amplification angle of JPA 3, as well as the TMS state parameters. Next, we simultaneously sweep the displacement phase θ and the JPA 4 phase. We then aim for the target phase φ_4^* at which the displacement photon number $|\alpha'|^2$, reconstructed at the output of the directional coupler, becomes independent of θ. If such a region does not exist, we repeat the same measurement for a different JPA 3 phase. In case we find such an optimal phase, we fix the JPA 4 phase at φ_4^*. The result of such a calibration measurement at $\omega_0/2\pi = 5.435\,\text{GHz}$ is shown in Fig. 6.6(a). In the second calibration step, we vary the pump power of JPA 4 and measure the amplitude response $|\alpha'|^2$. As in the first step, we aim for the target pump power P_4^* at which $|\alpha'|^2$ becomes independent of θ. Figure 6.6(b) depicts the outcome of such a calibration step. In Fig. 6.6(c), we plot the result from the same measurement in a 2D plot. We clearly observe that sinusoidal oscillations become flat at the pump power of $-34.4\,\text{dBm}$. During the third calibration step, we fix all JM parameters at their respective optimal values. Since changing the JM parameters affects the TMS state balancing due to the pump crosstalk, we need to recalibrate the TMS resource. This is done by fixing the JPA 2 parameters while we simultaneously vary the JPA 1 pump power and squeezing angle. Following that, we choose the JPA 1 parameters such that variance ratio and purity of the local single-mode states are maximized. The corresponding result is plotted in Fig. 6.6(d). Since each calibration step affects all other steps, the whole procedure needs to be repeated until we reach a steady state. However, we observe that, for most of our JPA working points, one calibration cycle is sufficient in practice. To find an optimal common working point for our JPAs, we repeat these measurements for various resonance frequencies and simultaneously optimize for squeezing S generated by the entanglement JPAs and for the degenerate gain G produced by the measurement JPAs.

6.3 Quantum teleportation results

In the following, we discuss results of our quantum teleportation experiment. In Sec. 6.3.1, we demonstrate a successful coherent state quantum teleportation by exceeding the no-cloning limit. In addition, we systematically investigate the fidelity dependence on the resource squeezing and feedforward gain in Sec. 6.3.2. Next, we introduce a theory model of our teleportation protocol which includes experimental imperfections in Sec. 6.3.3, and determine various technically relevant quantifiers of our protocol, such as a classical bit rate and practical Bell efficiency. In Sec. 6.4, we demonstrate that our quantum teleportation protocol implements a scheme for Gaussian error correction [218].

6.3.1 Experimental teleportation fidelities

From our JPA calibration measurements, we find that $\omega_0/2\pi = 5.435\,\text{GHz}$ represents a suitable working point. Following a proper calibration cycle, we run the complete
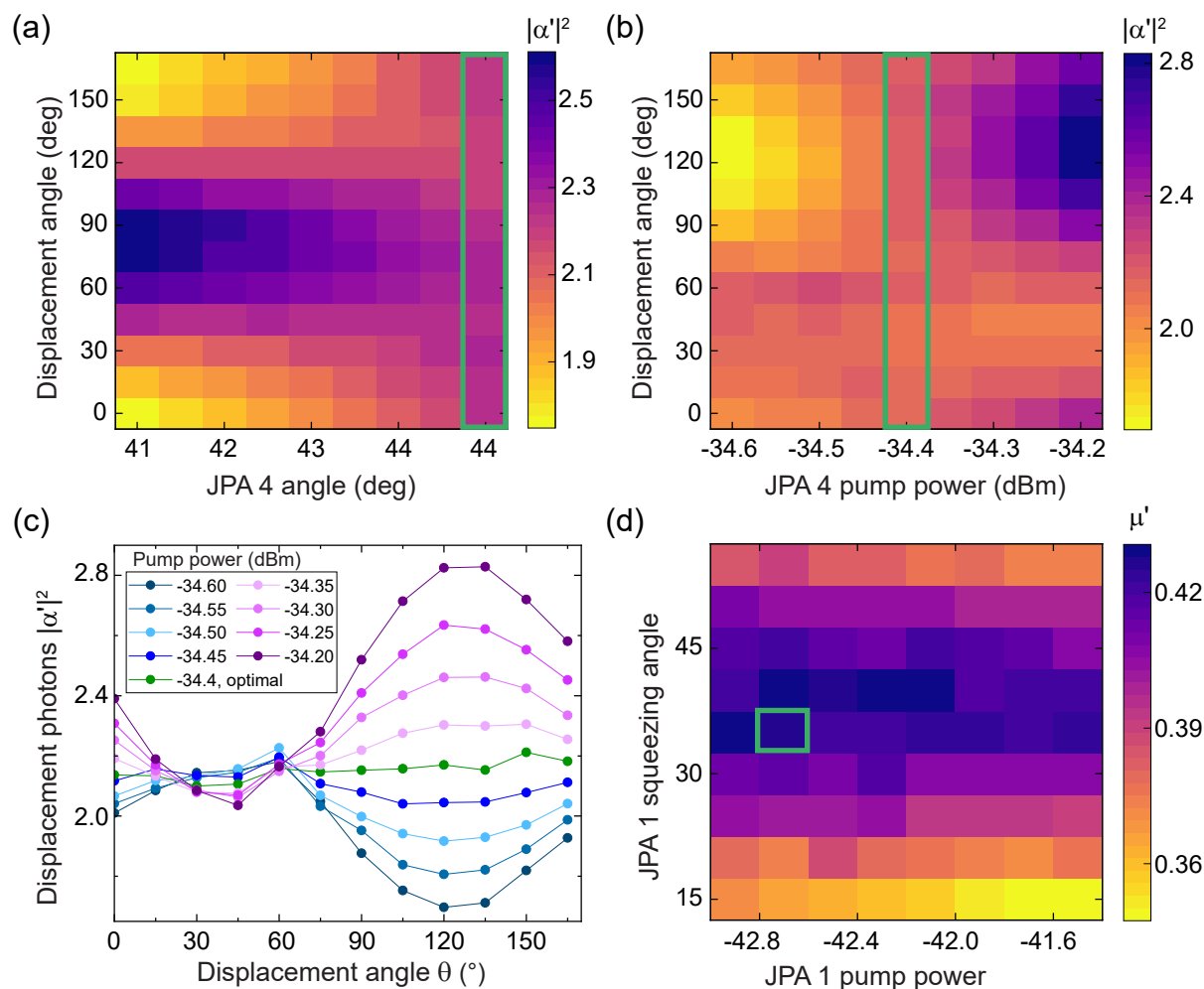
Figure 6.6: Experimental results according to the calibration scheme, described in Fig. 6.5. (a) First, we vary the JPA 4 angle φ_4 around the expected optimum and measure the JM interference pattern. For $\varphi_4^* = 44°$, indicated by the green box, the measurement JPAs effectively amplify orthogonal quadratures, implying that the JM acts like a phase-insensitive amplifier. (b) JPA 4 pump power calibration. Phase-independence is achieved at power $P_4^* = -34.4\,\mathrm{dBm}$, as indicated by the green box. (c) Data from panel (b) replotted as stacked lines. Solid lines are a guide to the eye. (d) Recalibration of the TMS resource. We vary the JPA 1 amplification parameters and optimize for purity μ' and variance ratio (not shown here). The green box corresponds to the optimal calibration setting.

teleportation protocol and reconstruct the Wigner function of the teleported state at the output of the directional coupler at Bob's side. A particular result of such a measurement for $|\alpha|^2 = 2.7$, $\theta = 45°$, $G = 23\,\mathrm{dB}$, and $S = 4.5\,\mathrm{dB}$, is plotted in Fig. 6.7. In this parameter regime, the entanglement (measurement) JPAs have a corresponding bandwidth of 11 MHz (4 MHz). We record the signal with our two-mode receiver with a SSB of 200 kHz. Figure 6.7(a) shows the Wigner function of the target state reconstructed at the input of the JM within the coherent state calibration measurement. In Fig. 6.7(b) we plot
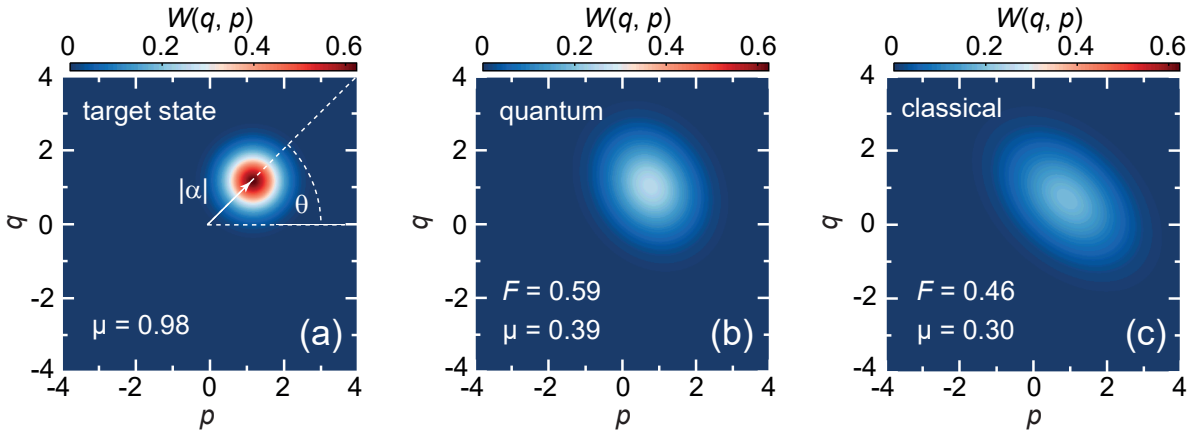
Figure 6.7: Results of the Gaussian Wigner tomography for the quantum teleportation of coherent microwave states. Panel (a) shows the Wigner function of the input state with $|\alpha|^2 = 2.7$ coherent input photons. Panel (b) shows the Wigner function of the teleported state with the teleportation fidelity $F = 0.59$, significantly exceeding the classical threshold $F_c = 1/2$. In panel (c), we plot the corresponding Wigner function of the same protocol without the entangled resource. In this classical scenario, we measure $F = 0.46$. In addition, we observe that the state gets purified in the quantum case, manifesting in the narrower output Wigner function.

the Wigner function of the teleported state and Fig. 6.7 (c) illustrates the classical result without employing entanglement. Before measuring classical teleportation, we repeat the calibration procedures for the JM, described in Sec. 6.2, but with the entanglement JPAs switched off. We clearly observe that the final quasiprobability distribution becomes sharper if we employ entanglement, which implies that our TMS resource purifies the state. In fact, the final state in the quantum case has purity $\mu = 0.39$ and we measure fidelity $F = 0.596 \pm 0.004$ with respect to the target state [78]. In the classical scenario, we measure $F = 0.46 < F_c$ and $\mu = 0.30$. This result demonstrates successful quantum teleportation of a single coherent state.

However, in case we attempt to employ quantum teleportation for applications including information transfer, we need to employ a codebook, consisting of various input states. As discussed in Sec. 2.2.6, this codebook forms a communication alphabet. Thus, we perform a systematic study of the fidelity dependence on $|\alpha|^2$. Corresponding results for $G = 21\,\mathrm{dB}$ and $G = 23\,\mathrm{dB}$ are shown in Fig.6.8 for $S = 4.5\,\mathrm{dB}$. We observe that for $G = 21\,\mathrm{dB}$, we exceed the no-cloning limit for $|\alpha|^2 \leq 1.1$. For larger photon numbers, the teleportation fidelity decreases due to compression of the measurement JPAs [107]. For $G = 23\,\mathrm{dB}$, we exceed F_c for the codebook of coherent states with up to 7 displacement photons and arbitrary displacement phases. In Fig. 6.9, we show the teleportation fidelity results as a function of displacement phase, θ, for an input codebook consisting of up to $\simeq 11$ input photons. In this measurement, phase and power are discretized over an 18×11 grid and Fig. 6.9 depicts an interpolation between respective measurement outcomes. For

$G = 23\,\text{dB}$ ($21\,\text{dB}$) we obtain an average fidelity $F \simeq 0.61 \pm 0.01$ ($F \simeq 0.72 \pm 0.05$) for $|\alpha|^2 \leq 1.8$. For both gain values, we significantly exceed the classical limit within statistical error bounds. For $G = 21\,\text{dB}$, we find an average fidelity of $F = 0.689 \pm 0.004 > F_{\text{nc}}$ for fixed $n_{\text{d}} = 1.1$. If we assume a truncated Gaussian codebook, restricted to $|\alpha|^2 = 2$ photons, Eq. (2.167) predicts a no-cloning threshold of $F_{\text{TG}} \simeq 0.98$. As a result, in order to reach unconditional security in our current quantum teleportation scheme, we would need to improve the $1\,\text{dB}$ compression point of our JPAs to higher values, $|\alpha|^2 \gg 1$, such that $F_{\text{TG}} \to F_{\text{nc}}$ while preserving $F > F_{\text{nc}}$ [312, 369]. As described in Sec. 3.2.2, this can be achieved by employing multi-SQUID JPAs. Although the performance of ideal quantum teleportation is not supposed to depend on the displacement phase θ, we observe a weak oscillatory phase dependence of F in Fig. 6.9. This phase dependence is an artifact from the imperfect balancing of the JM. As a result, the JM does not resemble a phase-insensitive amplifier but shows a weak phase dependence. By inserting a relative angle calibration error φ for each measurement JPAs with respect to its target quadrature, an analogous calculation as in Sec. 2.3 reveals phase modulation of the displacement photon number $|\alpha'|^2$ in the teleported state, according to

$$|\alpha'|^2 = |\alpha|^2 \underbrace{k(1 + \sin^2 2\varphi - 2\sin 2\varphi \cos 2\theta)}_{\equiv G(\theta)}. \tag{6.3}$$

By using the transformations

$$\tanh u = \frac{1 - \sin 2\varphi}{1 + \sin 2\varphi}, \qquad \epsilon = 2\sqrt{k \sin 2\varphi}, \tag{6.4}$$
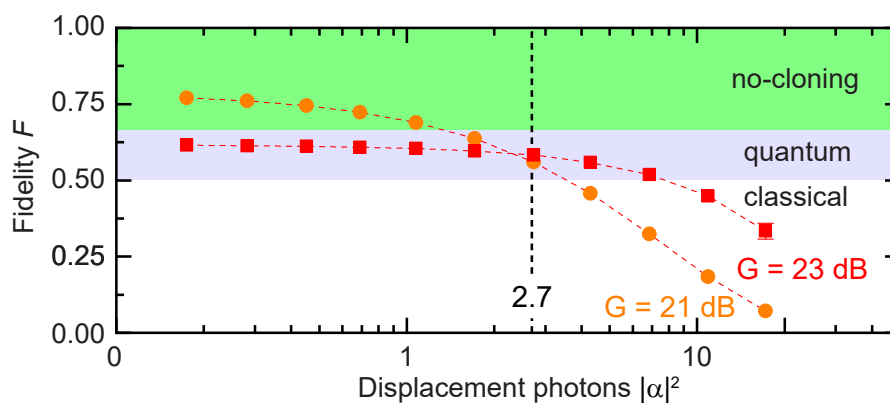
Figure 6.8: Experimentally determined quantum teleportation fidelity as a function of input displacement power $|\alpha|^2$ for feedforward gain $G = 21\,\text{dB}$ (orange) and $23\,\text{dB}$ (red). For $G = 21\,\text{dB}$, we exceed the asymptotic no-cloning bound and the classical threshold for a broad range of input states. The black dashed line corresponds to the particular input state used for the Wigner function reconstructions shown in Fig. 6.7. Orange and red dahes lines are guides to the eye.
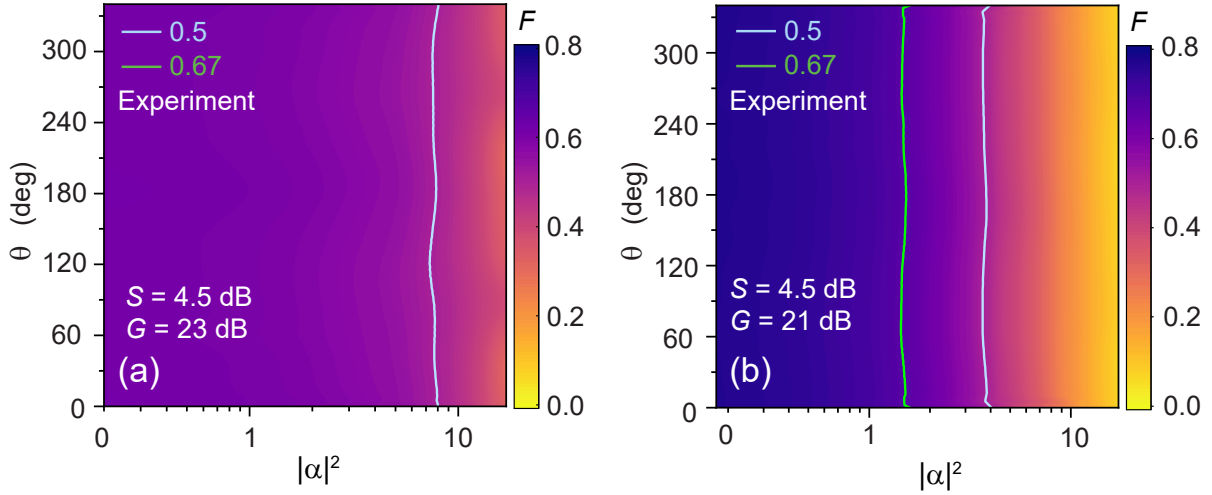
Figure 6.9: Experimental teleportation fidelity F for $S = 4.5\,\text{dB}$ as a function of displacement power and phase for feedforward gain (a) $G = 23\,\text{dB}$ and (b) $G = 21\,\text{dB}$. Green and blue lines indicate the no-cloning and classical limits, respectively. We observe that the fidelity is nearly independent of θ due to our previous calibration procedure.

the angle dependent gain $G(\theta)$ can be expressed in elliptical coordinates according to [370]

$$G(\theta) = \epsilon^2 \cosh^2 u \cos^2 \theta + \epsilon^2 \sinh^2 u \sin^2 \theta, \tag{6.5}$$

where we observe that the gain curves correspond to ellipses with linear eccentricity ϵ. Maximal and minimal gain values are given by

$$G_{\text{max}} = \epsilon \cosh u = k(1 + \sin 2\varphi)^2, \qquad G_{\text{min}} = \epsilon \sinh u = k(1 - \sin 2\varphi)^2. \tag{6.6}$$

 Since we determine our teleportation fidelities with respect to the same input state, this phase-dependent gain modulates fidelity with π-periodicity. This periodicity is reflected by weak oscillations in Fig. 6.9. According to Eq. (2.157), this phase dependence affects fidelity exponentially, which stresses the necessity of a proper calibration. A special case occurs for $\varphi = 45°$. In this case, both measurement JPAs amplify the same field quadrature. The displacement vector then transforms as

$$\mathbf{d}' = \sqrt{\beta}\boldsymbol{\Lambda}\mathbf{d}, \qquad \boldsymbol{\Lambda} = \begin{pmatrix} \cosh \phi & -\sinh \phi \\ -\sinh \phi & \cosh \phi \end{pmatrix}, \tag{6.7}$$

where $G = e^{2\phi}$ denotes the JM gain. In this case, the transformation of $\mathbf{d}$ is analogous to the coordinate transformation of a relativistic particle moving with a Lorentz factor and γ and effective velocity v

$$\gamma = \frac{G + 1}{2\sqrt{G}}, \qquad v = c\frac{G - 1}{G + 1}, \tag{6.8}$$

up to the square root of the coupling β [371]. Resulting from the careful balancing in our experiment, we have $\varphi \gtrsim 0$, indicating $G_{\max} \gtrsim G_{\min}$ and, thus, only a weak angle dependence. In Fig. 6.9, we specifically observe that the phase dependence becomes larger in the limit of high $|\alpha|^2$, where the measurement JPAs already undergo compression. This effect can be explained by the fact that, due to the phase-dependent gain, amplifier compression itself becomes phase-dependent.

6.3.2 Fidelity dependence on feedforward gain and squeezing

So far, we have studied quantum teleportation for fixed resource squeezing and two different feedforward gain values. However, as it can be seen from Fig. 6.8, the gain amplitude sensitively determines the teleportation fidelity F. Thus, we perform a systematic experimental study of teleportation fidelities on the gain and squeezing values. This task can be straightforwardly achieved in our experimental setup by tuning the JPA pump powers according to the prerecorded calibration curves for degenerate gain and squeezing. The experimental results, corresponding to $|\alpha|^2 = 1.1$, are shown in Fig. 6.10(a) for four gain and four squeezing values. The blue (green) plane corresponds to the classical (no-cloning) fidelity limit. We exceed both thresholds in a broad range of parameters. In addition, the teleportation fidelity strongly decays for $G > 23\,\mathrm{dB}$, which stresses the importance of realizing the projection condition, $k = G\beta/4 = 1$. In contrast, the fidelity only shows a weak dependence on S in our parameter regime. We find a maximal teleportation fidelity of $F = 0.689 \pm 0.004$ at $G = 21\,\mathrm{dB}$, where the gain value coincides with the naive ideal theory prediction, $G_{\mathrm{opt}} \simeq \beta + 6\,\mathrm{dB}$, as discussed in Sec. 2.3. However, this optimum relies on the assumption $S \to \infty$. In addition, microwave losses ε in the signal path correct this optimal gain to $G'_{\mathrm{opt}} = G_{\mathrm{opt}} + \varepsilon$. From the impedance mismatch of our RF cables, as well as from the technical specification of the corresponding passive RF components, we estimate $\varepsilon \simeq 2\,\mathrm{dB}$, implying that we expect the optimum to be located at $G'_{\mathrm{opt}} = 23\,\mathrm{dB}$. The observation that the optimal feedforward gain is lower than expected confirms the theoretical expectation that the optimal gain increases with the increasing entanglement strength [250], as can be seen in Fig. 2.16(b). Since our quantum teleportation fidelity sensitively depends on the photon number calibration, we can estimate how uncertainties in the PNCF κ translate to errors in fidelity. In case we change $\kappa \to \kappa \pm 10\,\%\kappa$ and for the exemplary working point $S = 6\,\mathrm{dB}$, $G = 21\,\mathrm{dB}$, we find $F = 0.685^{+0.0014}_{-0.004}$, implying that the relative error in fidelity is less than $1\,\%$. To take into account the more realistic loss estimates and the gain-dependent JPA noise [cf. Eq. (2.78) and Ref. 85], we fit our experimental results with a theory model which accounts for signal losses and JPA noise and is based on the steady-state input-output formalism. This fit is depicted by the purple plane in Fig. 6.10(b) and reproduces the experimental data as well as the observed maximum with reasonable accuracy. We note that measuring Fig. 6.10 took us approximately two months. This stresses the necessity of
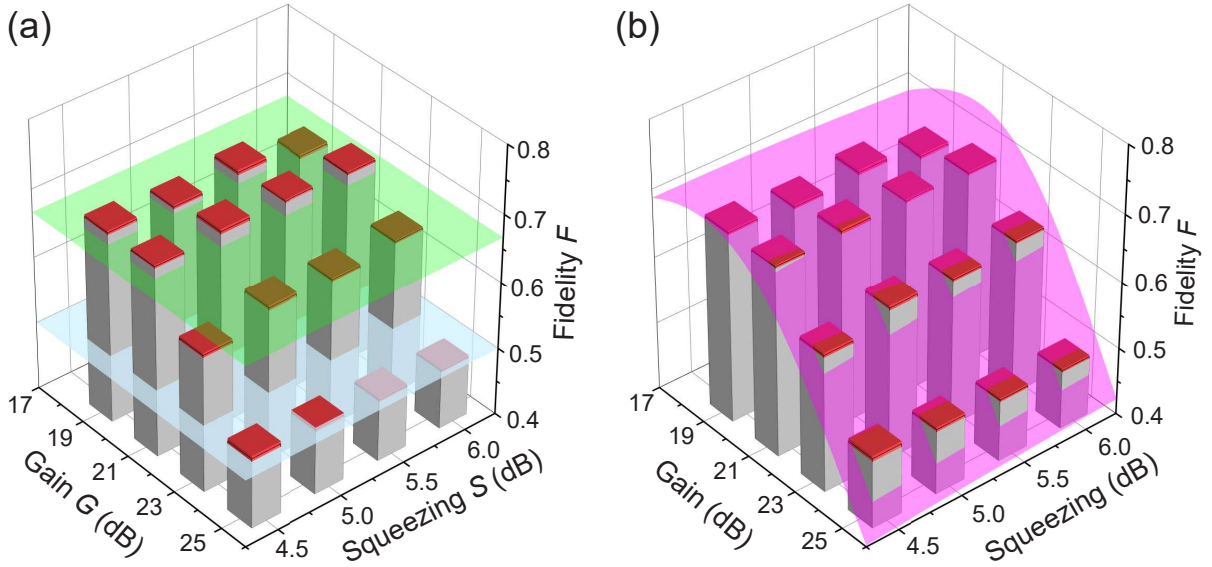
Figure 6.10: (a) Experimental quantum teleportation fidelities F as a function of squeezing S and gain G for $|\alpha|^2 = 1.1$ input displacement photons. Red bars correspond to the experimental uncertainty. The light blue plane corresponds to the classical threshold $F = 1/2$ and the green plane shows the asymptotic no-cloning limit, $F = 2/3$. Fidelity is maximal for $G = 21\,\mathrm{dB}$ and $S = 6\,\mathrm{dB}$. (b) Same data as in (a), but fitted with the theory model described in Sec. 6.3.3 (magenta plane). We use the JPA noise and environmental temperature as fit parameters. The model reproduces the location of the maximum.

our FPGA-based detection setup, described in Sec. 3.1.3. With the Acqiris card, acquiring the measurement with the same precision would take more than one year, which is an unrealistic cooldown time for our cryostats.

We provide a description of our simulation model as well as details about the fit in the following paragraph. Before that, however, we verify that our teleported quantum states are Gaussian. We do this by determining the corresponding cumulants κ_{mn}, according to Eq. (3.6). As can be seen in Fig. 6.11, the Gaussian approximation is valid since cumulants of order $m + n \leq 2$ exceed the higher order cumulants by an average factor of 7.2. In fact, many of the cumulants of order $m + n \geq 3$ vanish within the error bars.

The quantum advantage in fidelity is directly related to the interference mechanism between both TMS resource modes at Bob's directional coupler. The quality of this interference process depends on the consumption of quantum correlations in the protocol. However, classical feedforward and Bob's mode are not entangled after Bell detection. Consequently, this correlation consumption needs to be quantified via the noise-robust quantum discord D between JM idler and Bob's final state (cf. chapter 5) according to Eq. (2.138) [112]. We plot quantum discord in Fig. 6.12(a) and observe that D behaves differently as a function of S for $G = 25\,\mathrm{dB}$, as compared to lower gain values. This observation can be explained by the fact that $G = 25\,\mathrm{dB}$ corresponds to the regime $k > 1$. According to Eq. (2.188), this gain regime exhibits a significant deterioration of the
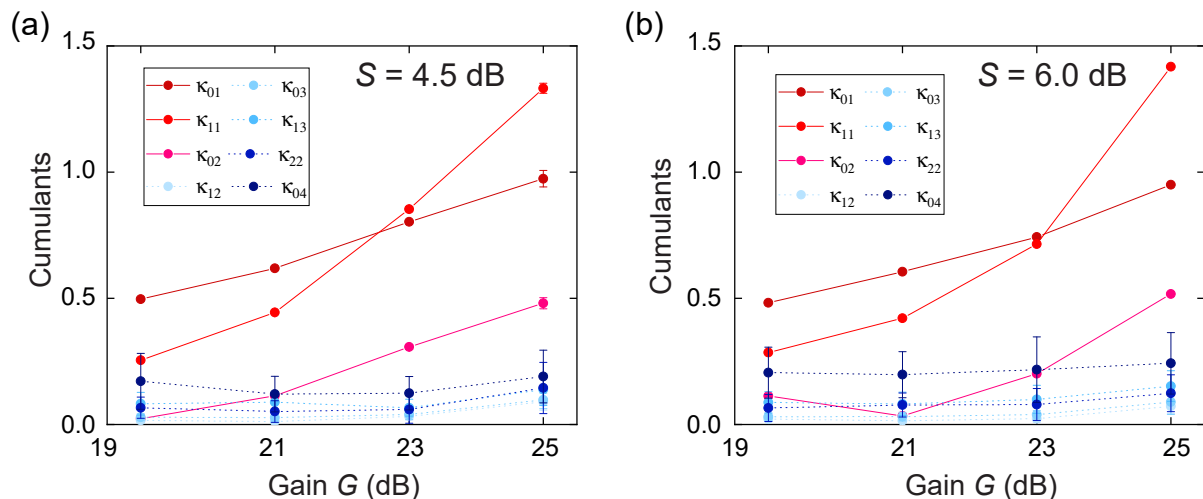
Figure 6.11: Absolute values of cumulants κ_{mn} as a function of the measurement gain G and squeezing levels for (a), $S = 4.5\,\mathrm{dB}$ and (b), $S = 6\,\mathrm{dB}$. Error bars correspond to the respective standard deviations. If not shown, the error bar is smaller than the symbol size. We observe that cumulants of order $m + n \geq 3$ are significantly smaller than cumulants of order $m + n \leq 2$, implying that the Gaussian approximation is valid. The solid and dashed lines are guides to the eye.

interference mechanism between both TMS resource modes. As a result, a lower amount of quantum correlations is consumed at the directional coupler, which eventually implies larger residual quantum discord. For $G \leq 23\,\mathrm{dB}$, we are in the regime $k < 1$, which is reflected by decreasing of D with increasing S, especially visible for $G = 19\,\mathrm{dB}$. Thus, increasing the squeezing improves the destructive interference in this case.

In the following, we analyze security of the protocol for the case where Alice employs quantum teleportation for the transfer of a known coherent state $|\alpha\rangle$ to Bob, similar as it is done in RSP for squeezed states [66]. In this case, we do not need to average over a codebook of unknown input states, like in Eq. (2.164), and can directly determine how much information about $|\alpha\rangle$ can be extracted by a potential eavesdropper Eve. In this regard, we can draw an analogy between quantum teleportation and the one-time pad encryption scheme. In this context, we interpret the teleported state as a message (M), the entanglement distribution as a key and the feedforward signal as a publicly available cipher (F) [221]. The protocol can then be considered as unconditionally secure if the von Neumann entropy S_{M}, associated with the message M, coincides with the conditional von Neumann entropy $S_{\mathrm{M|F}}$ in case we assume complete knowledge about the cipher F. Similar as in Ref. 66 and in Ref. 112, we determine a normalized deviation

$$\delta = \frac{S_{\mathrm{M}} - S_{\mathrm{M|F}}}{S_{\mathrm{M}}} = \frac{I(\mathrm{M} : \mathrm{F})}{S_{\mathrm{M}}}, \tag{6.9}$$

where we have employed Eq. (2.136). According to this quantifier, the protocol is secure if

(a)

(b)
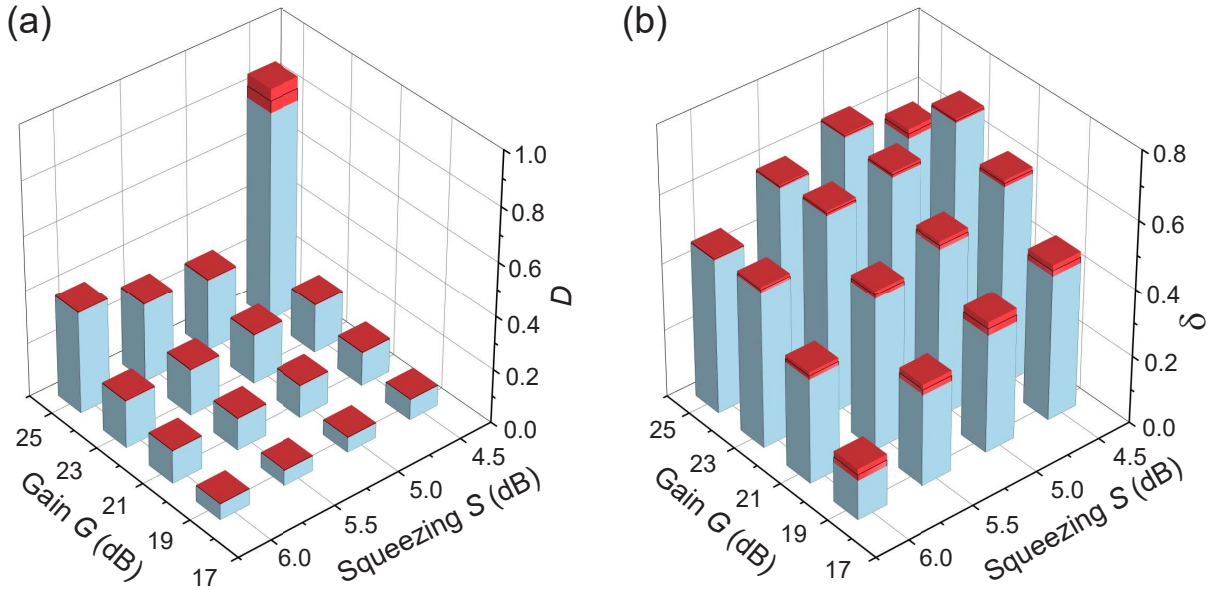
Figure 6.12: (a) Experimentally obtained D, shared by the teleported states from Fig. 6.10 and the feedforward signal, corresponding to the data shown in Fig. 6.10. Note that the gain axis is reverted compared to Fig. 6.10. For $G < 25\,\mathrm{dB}$, D decreases with increasing S, which is especially visible for $G = 19\,\mathrm{dB}$. Consequently, quantum correlations are consumed to purify the teleported state. (b) Normalized mutual information δ between the teleported state and the feedforward signal. We find that δ decreases with increasing S, implying that larger squeezing allows for less information about the teleported state to be extracted by eavesdropping the feedforward signal. By comparing to Fig. 6.10, we observe that the point of optimal fidelity does not lead to minimal δ. Red bars correspond to the experimental uncertainty.

$\delta = 0$, implying that mutual information $I(\mathrm{M}:\mathrm{F})$ between the message and the cipher vanishes. We plot δ in Fig. 6.12(b) and find that the quantum teleportation security increases with increasing S. However, minimal δ within our investigated parameter regime is reached for $G = 19\,\mathrm{dB}$. Despite being close to each other, the regions of maximal fidelity and minimal δ do not coincide. This finding indicates that despite Bob only achieves a non-optimal fidelity, the fidelity of a potential eavesdropper can be disproportionally smaller.

6.3.3 Simulation model including transmission losses and JPA noise

In this section, we discuss a theory model which takes signal losses and noise into account. We model our quantum teleportation scheme in a stepwise way, as illustrated in Fig. 6.13. The input state of the protocol in each path i is modelled by an operator $\hat{f}_i$, describing a weak thermal state with noise photon number n_i. The input noise photon numbers n_1 and n_2 are defined by a combination of the environmental thermal noise and the gain-dependent noise added by the entanglement JPAs. In the third path, $i = 3$, we start
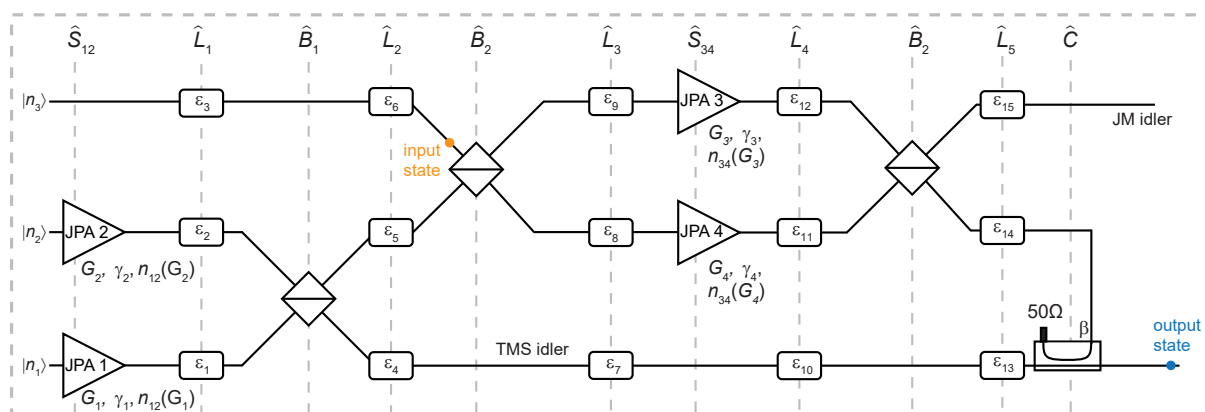
Figure 6.13: Scheme for simulation of the real-world quantum teleportation protocol. Each step consists of either a unitary squeezing operation ($\hat{S}_{12}$, $\hat{S}_{34}$), a beam splitter operation ($\hat{B}_1$, $\hat{B}_2$, $\hat{C}$), or a non-unitary operation such as path losses ($\hat{L}_1$, $\hat{L}_2$, $\hat{L}_3$, $\hat{L}_4$, $\hat{L}_5$) or a JPA noise transformation. The path losses are labelled with ε_i. The squeeze factors of the entanglement JPAs are r_1, r_2 with the respective squeezing angles are γ_1, γ_2. The degenerate gain of the measurement JPAs is G_3, G_4 and γ_3, γ_4 denote the amplification angles for the Bell measurement. The input state is reconstructed at the position, indicated by the orange dot. The blue dot denotes the reconstruction point for the teleported state.

with the displaced thermal state

$$\hat{a} = \hat{D}(\alpha)^\dagger \hat{f}_3 \hat{D}(\alpha) = \hat{f}_3 + \alpha. \tag{6.10}$$

The number of noise photons n_3 in the coherent input is related to purity $\mu = 1/(1 + 2n_3)$. Thus, we can formally write the 3-mode input state of the quantum teleportation protocol as $|n_1; n_2; \alpha, \mu\rangle \equiv |n_1\rangle \otimes |n_2\rangle \otimes |\alpha, \mu\rangle$.[13] We divide the teleportation protocol into a block structure consisting of alternating unitary and non-unitary operations. Between each unitary operation in the ideal protocol, as seen in Fig. 2.15, we insert a non-unitary block to model imperfections. The complete block structure is shown in Fig. 6.13, where experimentally relevant parameters are written next to each operation. The losses are modelled with a beam splitter model according to the operators [66]

$$\hat{L}_j^\dagger \begin{pmatrix} \hat{a}_1 \\ \hat{a}_2 \\ \hat{a}_3 \end{pmatrix} \hat{L}_j = \begin{pmatrix} \sqrt{1 - \varepsilon_{3(j-1)+1}}\, \hat{a}_1 + \sqrt{\varepsilon_{3(j-1)+1}}\, \hat{v}_{3(j-1)+1} \\ \sqrt{1 - \varepsilon_{3(j-1)+2}}\, \hat{a}_2 + \sqrt{\varepsilon_{3(j-1)+2}}\, \hat{v}_{3(j-1)+2} \\ \sqrt{1 - \varepsilon_{3(j-1)+3}}\, \hat{a}_3 + \sqrt{\varepsilon_{3(j-1)+3}}\, \hat{v}_{3(j-1)+3} \end{pmatrix}, \tag{6.11}$$

with $j \in \{1, 2, 3, 4, 5\}$. The bosonic bath modes $\hat{v}_{3(j-1)+1}$ model environment, which we assume to be in a weak thermal state with photon number n_{th}. The power losses are

---

[13]Note that here, we do not use $|n\rangle$ to denote photon number states but rather employ a symbolic notation for a thermal state with photon number n which is assumed to be purified by a suitably chosen environment.

denoted by $\varepsilon_{3(j-1)+3}$. The amplification process by the measurement JPAs is modelled with a noisy squeezing operator acting on mode two and mode three, according to

$$\hat{S}_{34}^{\dagger} \begin{pmatrix} \hat{a}_1 \\ \hat{a}_2 \\ \hat{a}_3 \end{pmatrix} \hat{S}_{34} = \begin{pmatrix} \hat{a}_1 \\ (\hat{a}_2 + \zeta_3)\cosh r_3 - (\hat{a}_2^{\dagger} + \zeta_3^{*})e^{-2i\gamma_3}\sinh r_3 \\ (\hat{a}_3 + \zeta_4)\cosh r_4 - (\hat{a}_3^{\dagger} + \zeta_4^{*})e^{-2i\gamma_4}\sinh r_4 \end{pmatrix}, \tag{6.12}$$

where the squeezing parameters r_3 (r_4) are related to the degenerate gain via $G_3 = e^{2r_3}$ $(G_4 = e^{2r_4})$ and the squeezing angle of JPA 3 (JPA 4) is denoted by γ_3 (γ_4). In the following, we assume equal degenerate gain for both JPAs, $G_3 = G_4 = G$. The noise added by JPA 3 (JPA 4) is modelled with a classical random variable ζ_3 (ζ_4). We assume that JPA 3 and JPA 4 have equal noise properties, $\zeta_3 = \zeta_4 = \zeta$, and assume ζ to obey a zero mean Gaussian distribution with $\langle \zeta\zeta^{*} \rangle = n_{34}(G)$ and $\langle \mathrm{Re}(\zeta^2) \rangle = \langle \mathrm{Im}(\zeta^2) \rangle = n_{34}(G)/2$. According to Fig. 2.15, the non-ideal teleportation protocol can be eventually expressed by the operator

$$\hat{T} = \hat{C}\hat{L}_5\hat{B}_2\hat{L}_4\hat{S}_{34}\hat{L}_3\hat{B}_2\hat{L}_2\hat{B}_1\hat{L}_1\hat{S}_{12}. \tag{6.13}$$

The final state $|\Psi\rangle$ of the three signal modes and the environment is given by

$$|\Psi\rangle = \hat{T}|n_1; n_2; \alpha, \mu\rangle \otimes |n_{\mathrm{th}}\rangle^{\otimes 15}. \tag{6.14}$$

In the following, we drop the terms corresponding to the environment. The moments of the output signal $\hat{b}$ can then be determined by [112]

$$\begin{pmatrix} \langle (\hat{b}^{\dagger})^n \hat{b}^m \rangle_1 \\ \langle (\hat{b}^{\dagger})^n \hat{b}^m \rangle_2 \\ \langle (\hat{b}^{\dagger})^n \hat{b}^m \rangle_3 \end{pmatrix} = \langle \Psi | \begin{pmatrix} (\hat{a}^{\dagger})^n \hat{a}^m \\ (\hat{a}^{\dagger})^n \hat{a}^m \\ (\hat{a}^{\dagger})^n \hat{a}^m \end{pmatrix} |\Psi\rangle, \tag{6.15}$$

We assume that all quantum states are Gaussian, which implies that we only require moments up to the second order. By defining the input covariance matrix

$$\boldsymbol{V}^{(0)} = \boldsymbol{V}_1 \oplus \boldsymbol{V}_2 \oplus \boldsymbol{V}_3, \qquad \boldsymbol{V}_j = \frac{1 + 2n_j}{4}\mathbb{1}_2, \tag{6.16}$$

we can write the transformation of $\boldsymbol{V}$ for a non-ideal teleportation protocol in analogy to the ideal protocol from Sec. 2.3.1 as a Gaussian channel. To this end, we define the beam splitter matrices $\boldsymbol{B}_1 = \boldsymbol{B}^{(1,2)}(1/\sqrt{2})$, $\boldsymbol{B}_2 = \boldsymbol{B}^{(2,3)}(1/\sqrt{2})$ as well as the matrices

$$\boldsymbol{J}_{12} = \boldsymbol{J}_q \oplus \boldsymbol{J}_p \oplus \mathbb{1}_2, \qquad \boldsymbol{J}_{34} = \mathbb{1}_2 \oplus \boldsymbol{J}_q \oplus \boldsymbol{J}_p, \tag{6.17}$$

which describe phase-sensitive amplification of entanglement JPAs ($\boldsymbol{J}_{12}$) and measurement JPAs ($\boldsymbol{J}_{34}$). Furthermore, we define the rotation matrices

$$\boldsymbol{R}_{12} = \boldsymbol{R}_1(\gamma_1) \oplus \boldsymbol{R}_2(\gamma_2) \oplus \mathbb{1}_2, \qquad \boldsymbol{R}_i(\gamma_i) = \begin{pmatrix} \cos\gamma_i & \sin\gamma_i \\ -\sin\gamma_i & \cos\gamma_i \end{pmatrix}, \tag{6.18}$$

$$\boldsymbol{R}_{34} = \mathbb{1}_2 \oplus \boldsymbol{R}_3(\gamma_3) \oplus \boldsymbol{R}_4(\gamma_4). \tag{6.19}$$

To model the transmission losses, we define the corresponding matrices

$$\boldsymbol{L}_j = \left(\sqrt{1 - \varepsilon_{3(j-1)+1}}\mathbb{1}_2 \right) \oplus \left(\sqrt{1 - \varepsilon_{3(j-1)+2}}\mathbb{1}_2 \right) \oplus \left(\sqrt{1 - \varepsilon_{3(j-1)+3}}\mathbb{1}_2 \right), \tag{6.20}$$

and

$$\boldsymbol{A}_j = \frac{1}{4}(1 + 2n_{\text{th}}) \left[\left(\varepsilon_{3(j-1)+1}\mathbb{1}_2 \right) \oplus \left(\varepsilon_{3(j-1)+2}\mathbb{1}_2 \right) \oplus \left(\varepsilon_{3(j-1)+3}\mathbb{1}_2 \right) \right], \tag{6.21}$$

with $j \in \{1, 2, 3, 4, 5\}$. Finally, we model the noise of the measurement JPAs according to

$$\boldsymbol{N}_{34} = \frac{n_{34}(G)}{2} \left[\mathbb{0}_2 \oplus \mathbb{1}_2 \oplus \mathbb{1}_2 \right]. \tag{6.22}$$

We can express the imperfect teleportation protocol in Eq. (6.13) as a Gaussian channel

$$\boldsymbol{T} = \boldsymbol{C}\boldsymbol{L}_5\boldsymbol{B}_2\boldsymbol{L}_4\boldsymbol{R}_{34}\boldsymbol{J}_{34}\boldsymbol{R}_{34}^\dagger\boldsymbol{L}_3\boldsymbol{B}_2\boldsymbol{L}_2\boldsymbol{B}_1\boldsymbol{R}_{12}\boldsymbol{J}_{12}\boldsymbol{R}_{12}^\dagger, \tag{6.23}$$

$$\begin{aligned} \boldsymbol{A} = &\boldsymbol{C}\boldsymbol{L}_5\boldsymbol{B}_2\boldsymbol{L}_4\boldsymbol{R}_{34}\boldsymbol{J}_{34}\boldsymbol{R}_{34}^\dagger\boldsymbol{L}_3\boldsymbol{B}_2\boldsymbol{L}_2\boldsymbol{B}_1\boldsymbol{A}_1\boldsymbol{B}_1^\dagger\boldsymbol{L}_2^\dagger\boldsymbol{B}_2^\dagger\boldsymbol{L}_3^\dagger\boldsymbol{R}_{34}\boldsymbol{J}_{34}^\dagger\boldsymbol{R}_{34}^\dagger\boldsymbol{L}_4^\dagger\boldsymbol{B}_2^\dagger\boldsymbol{L}_5^\dagger\boldsymbol{C}^\dagger \\ &+ \boldsymbol{C}\boldsymbol{L}_5\boldsymbol{B}_2\boldsymbol{L}_4\boldsymbol{R}_{34}\boldsymbol{J}_{34}\boldsymbol{R}_{34}^\dagger\boldsymbol{L}_3\boldsymbol{B}_2\boldsymbol{A}_2\boldsymbol{B}_2^\dagger\boldsymbol{L}_3^\dagger\boldsymbol{R}_{34}\boldsymbol{J}_{34}^\dagger\boldsymbol{R}_{34}^\dagger\boldsymbol{L}_4^\dagger\boldsymbol{B}_2^\dagger\boldsymbol{L}_5^\dagger\boldsymbol{C}^\dagger \\ &+ \boldsymbol{C}\boldsymbol{L}_5\boldsymbol{B}_2\boldsymbol{L}_4\boldsymbol{R}_{34}^\dagger\boldsymbol{J}_{34}\boldsymbol{R}_{34}(\boldsymbol{A}_3 + \boldsymbol{N}_{34})\boldsymbol{R}_{34}^\dagger\boldsymbol{J}_{34}^\dagger\boldsymbol{R}_{34}\boldsymbol{L}_4^\dagger\boldsymbol{B}_2^\dagger\boldsymbol{L}_5^\dagger\boldsymbol{C}^\dagger \\ &+ \boldsymbol{C}\boldsymbol{L}_5\boldsymbol{B}_2\boldsymbol{A}_4\boldsymbol{B}_2^\dagger\boldsymbol{L}_5^\dagger\boldsymbol{C}^\dagger \\ &+ \boldsymbol{C}\boldsymbol{A}_5\boldsymbol{C}^\dagger. \end{aligned} \tag{6.24}$$

The resulting final displacement vector $\mathbf{d}'$ and the covariance matrix $\boldsymbol{V}'$ are given by

$$\mathbf{d}' = \boldsymbol{T}\mathbf{d}^{(0)}, \qquad \boldsymbol{V}' = \boldsymbol{T}\boldsymbol{V}^{(0)}\boldsymbol{T}^\dagger + \boldsymbol{A}, \tag{6.25}$$

where $\mathbf{d}^{(0)}$ denotes the initial displacement vector of the to-be-teleported state. The transformations to obtain the reference displacement vector $\mathbf{d}$ and covariance matrix $\boldsymbol{V}$ from $\mathbf{d}^{(0)}$ and $\boldsymbol{V}^{(0)}$

$$\mathbf{d} = \tilde{\boldsymbol{T}}\mathbf{d}^{(0)}, \qquad \boldsymbol{V} = \tilde{\boldsymbol{T}}\boldsymbol{V}_0\tilde{\boldsymbol{T}}^\dagger + \tilde{\boldsymbol{A}}, \tag{6.26}$$

with

$$\tilde{\boldsymbol{T}} = \boldsymbol{L}_2\boldsymbol{B}_1\boldsymbol{R}_{12}\boldsymbol{J}_{12}\boldsymbol{R}_{12}^\dagger, \qquad \tilde{\boldsymbol{A}} = \boldsymbol{L}_2\boldsymbol{B}_1\boldsymbol{A}_1\boldsymbol{B}_1^\dagger\boldsymbol{L}_2^\dagger + \boldsymbol{A}_2. \tag{6.27}$$

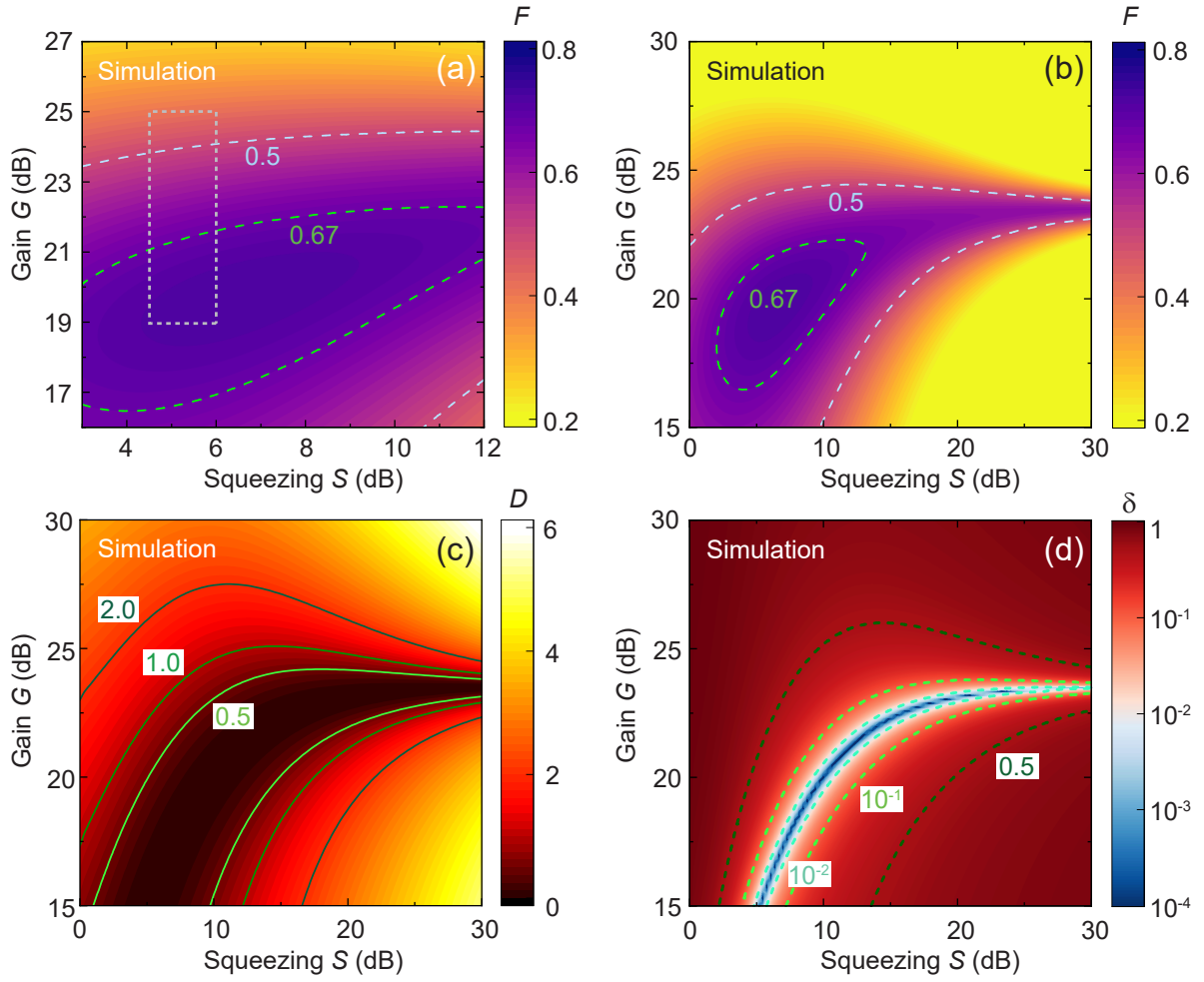In the next step, we determine a theoretically expected teleportation fidelity F_{t} between

Figure 6.14: (a) quantum teleportation fidelity predictions from our theory model, using the experimental parameters from Tab. 6.1. The gray dashed box indicates the experimentally investigated regime. We observe that this regime is close to the expected optimum. We expect further increase of fidelity by improving the resource squeezing. (b) Prediction of the quantum teleportation fidelity for an extended parameter space. In the limit of $S \gg 1$, the region of high fidelities narrows down around the projection condition, $G\beta/4 = 1$. (c) Predicted quantum discord D for an extended parameter space. The values of D are approximately anticorrelated to fidelity, since high fidelity requires consumption of quantum correlations. (d) Normalized mutual information δ between a teleported state and feedforward signal. In regions of high fidelity, δ becomes small since mutual information is reduced due to correlation consumption. In agreement with the experimental results in Fig. 6.12(b), regions for maximal F and minimal δ are close to each other but do not coincide.

input state, corresponding to the third mode of the state $(\mathbf{d}, \mathbf{V})$, and the first mode of $(\mathbf{d}', \mathbf{V}')$, according to Eq. (2.157). To produce the fit shown in Fig. 6.10(b), we use the least-square approach, where we model the JPA noise dependence by Eq. (2.78) and treat the coefficients χ_1, χ_2, and the environmental temperature T as fit parameters. As a result, we minimize the distance between the experimentally determined fidelities

Table 6.1: Model parameters used for the quantum teleportation protocol fit described in the main text. The loss values ε_i are estimated from individual losses of various components. The quantities χ_1, χ_2, and T are used as fit parameters and extracted by minimizing Eq. (6.28).

χ_1	χ_2	T (mK)	β (dB)	ε_1 (dB)	ε_2 (dB)	ε_3 (dB)
0.0158	0.2271	71.7	-15	0.36	0.35	0

ε_4 (dB)	ε_5	ε_6 (dB)	ε_7 (dB)	ε_8 (dB)	ε_9 (dB)	ε_{10} (dB)
0.5	1.1	0	0	0.64	0.63	0

ε_{11} (dB)	ε_{12} (dB)	ε_{13} (dB)	ε_{14} (dB)	ε_{15} (dB)	f_0 (GHz)	n_{d}
0.84	0.88	0	0.5	0.7	5.435	1.1

μ
0.98

$\{F(S_i, G_i)\}$ for squeezing S_i and degenerate gain G_i and the theoretically predicted values $F_{\mathrm{t}}(\chi_1, \chi_2, T, \{x\})$. Here $\{x\}$ is the parameter set including the JPA 1 and JPA 2 squeezing S_i, the degenerate measurement gain G_i the amplification angles γ_i as well as the constant system parameters such as path losses and coupling strength β. Thus, we fit the measurement data by minimizing the function

$$\mathcal{L}(\chi_1, \chi_2, T, \{x\}, \{F_i\}) = \sum_i |F_{\mathrm{t}}(\chi_1, \chi_2, T, \{x\}) - F(S_i, G_i)|^2. \qquad (6.28)$$

The parameters used in the numerical model are summarized in Tab. 6.1. The parameters χ_1, χ_2, and T are extracted from the fit routine and losses are estimated from the data sheets of the respective passive microwave components. The loss values ε_3, ε_6, ε_7, ε_{10} and ε_{13} are set to zero since they have been artificially introduced to keep the block matrix structure which simplifies the numerical analysis. As can be seen from Tab. 6.1, RF losses are non-negligible and eventually limit the teleportation fidelity. In future experiments, these losses can be significantly decreased by employing superconducting RF components. In particular, superconducting hybrid ring beam splitters [372] would improve the maximal fidelity of 0.72, predicted by our theory model, to 0.78. These beam splitters can be fabricated using conventional superconducting thin film technology and would require a modified circuit design for our samples as well as a proper even/odd mode analysis [158, 373, 374]. Since we observe reasonable agreement between data and model in Fig. 6.10(b), we use our theoretical model to predict teleportation outcomes for squeezing and gain regimes which are not yet reachable in experiment. The corresponding results are shown in Fig. 6.14. We clearly observe that we expect a further increase of the fidelity to $F \simeq 0.8$ in case we increase squeezing to $S \simeq 8\,\mathrm{dB}$. Figure 6.14(b) shows the simulated extrapolation of our teleportation experiment for up to 30 dB squeezing. We see that the optimal gain converges towards the expected value of 23 dB in the limit $S \to \infty$. With increasing S, the high-fidelity region becomes narrower due to the increasing impact of the e^{2r} terms [cf. Eq. (2.190)] in case of a finite gain mismatch from the optimum. The
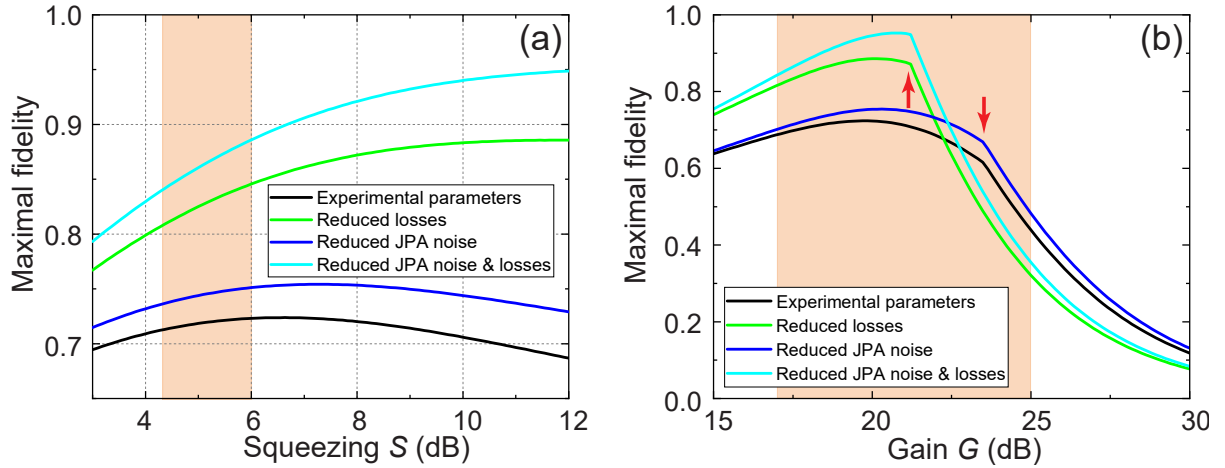
Figure 6.15: Maximal teleportation fidelity as a function of (a) resource squeezing S and (b) feedforward gain G. Experimental parameters correspond to those listed in Tab. 6.1. "Reduced" parameters correspond to ten-fold reduction $\varepsilon_i \to \varepsilon_i/10$, $\chi_i \to \chi_i/10$. We observe that our theory model reproduces the non-differentiable behavior predicted in Sec. 2.3 if the condition $k = 1$ is met. The transition gain between attenuation and amplification regime is indicated by the red arrows. The orange areas indicate the experimentally investigated regime.

calculated quantum discord between the feedforward and teleported states is shown in Fig. 6.14(c) and the δ-quantity, Eq. (6.9), is plotted in Fig. 6.14(d). We observe that the behavior of quantum discord and δ qualitatively coincides with our experimental results shown in Fig. 6.12.

Next, we analyze the error budget of our quantum teleportation protocol using the theory model. From our fit, we determine a fidelity $F = 0.682$ for $S = 6\,\mathrm{dB}$, $G = 21\,\mathrm{dB}$ [78], which is close to the experimentally determined value. We describe the input state as a pure coherent state, containing $|\alpha|^2 = 1.1$ photons. We now employ our theory model to iteratively idealize the protocol at this specific working point, which enables us to determine the loss in fidelity due to each imperfection. In case we would perform the experiment at zero temperature, fidelity would increase to 0.689. If we neglect all losses, fidelity further increases to $F = 0.738$. Without any JPA noise, we would reach $F = 0.80$. The difference to unity is then mainly limited by finite squeezing. For $S = 20\,\mathrm{dB}$, we would obtain $F = 0.984$. In case we further decrease β and assume the perfect projection criterion $G\beta = 4$, we obtain $F = 0.99$.

Finally, we numerically analyze how to increase the fidelity F at the optimal point. We employ our theory to algorithmically determine the maximally achievable fidelity as a function of squeezing [Fig. 6.15(a)] and gain [Fig. 6.15(b)]. We compare the fidelity for our experimental parameters with the case of reduced losses ($\varepsilon_i \to \varepsilon_i/10$) and noise ($\chi_i \to \chi_i/10$), as well as with the combined case ($\varepsilon_i \to \varepsilon_i/10$ and $\chi_i \to \chi_i/10$). We observe that a maximal fidelity of $\simeq 0.95$ can be reached in case we reduce losses and noise parameters by a factor of 10. In particular, we observe that for our current parameters,

reducing microwave losses improves the quantum teleportation fidelity stronger than suppressing the JPA noise. In Fig. 6.15(b), we reproduce the non-differential behavior predicted in Sec. 2.3.1 and demonstrate that the corresponding phase transition-like behavior is resilient against losses and noise. As expected, the transition gain depends on the losses but not on noise, and is located within the experimentally accessible gain range.

Projection condition including JPA noise In our theoretical treatment of quantum teleportation in Sec. 2.3.1, we have discussed how we can asymptotically implement a projective phase space measurement if we combine multiple Gaussian operations in the projective limit, Eq. (2.176). However, since in the ideal protocol all involved operations are Gaussian and unitary, this method only enables us to approximate a projective measurement with an arbitrary accuracy. In a practical realization of analog quantum teleportation, finite noise of the measurement JPAs turns the JM into a non-unitary device, which indicates that we indeed effectively implement a projective measurement already at finite gains $G \gg 1$. This fact is directly linked to our investigation of the chained orthogonal phase-sensitive JPAs in Sec. 4.2, in particular to Eq. (4.42), where we observe that the JPA noise plays a crucial role for balancing the power in both signal quadratures. We now perform a Gedankenexperiment and chain two of our actual measurement JPAs. The first JPA performs a strong phase-sensitive amplification $\boldsymbol{J}$ on the Gaussian input state $(\mathbf{d}, \boldsymbol{V})$ and thereby approximates a projection with respect to the amplified quadrature. Displacement then transforms like $\mathbf{d}' = \boldsymbol{J}\mathbf{d}$. With the second JPA, we reverse the operation of the first JPA such that we obtain a final displacement $\mathbf{d}' = \mathbf{d}$. However, in case both JPAs add n noise photons, the covariance matrix transforms as

$$\boldsymbol{V}' = \boldsymbol{V} + \frac{n}{2}\mathbb{1}_2 + \frac{n}{2}(\boldsymbol{J}^\dagger\boldsymbol{J})^{-1}. \tag{6.29}$$

In case $n \neq 0$, the variance of the quadrature deamplified by the first JPA is disproportionately amplified by the second amplifier, implying that the phase space distribution of the fluctuations in the final state is elliptically distorted. We specifically observe that, in case the large axis of this ellipse covers the variance σ^2 of the input codebook, we effectively lose all information about the initially deamplified quadrature. According to Eq.(6.29), this is the case if $nG \gtrsim 2\sigma^2$. For our current experimental parameters, we obtain $\sigma^2 \leq 2.96$, which is in reach with current experimental parameters. Consequently, the finite JPA noise can be regarded as essential for performing a phase space projection already at finite gains $G \gg 1$.

Bell efficiency of the Josephson mixer So far, we have introduced the JM as an analog Bell measurement device which enables the detection of two-mode symmetric (antisymmetric) quadradure superpositions p_+ (q_-) [cf. Eq. (2.179)]. In the following, we investigate a Bell efficiency of the JM, which quantifies how well our detector can

distinguish between different CV Bell states. Since our protocol is fully deterministic, we can distinguish between all possible input directions and reach the Bell efficiency of unity in case of ideal quantum efficiency $\eta = 1$ of our measurement JPAs [219]. However, the Bell efficiency decreases as a function of η. We demonstrate the impact of quantum efficiency on the Bell efficiency within a simplistic geometric model. A fundamental idea behind this model is depicted in Fig. 6.16. Within this model, we assume that the input of our Bell detection setup is a symmetric state with variance v_{in} and zero displacement. We operate the JM with orthogonal amplification angles and large gain, $G \gg 1$. As indicated in Fig. 6.16(a), for any global phase (rotation angle) of the JM measurement JPAs, the output of the JM is a symmetric state. Next, we consider the Bell measurement along the phase φ, relative to the q-axis, as shown in Fig. 6.16(b). We assume the JM to be in the steady state. Thus, broadening of the variance by Δv due to the finite JPA noise leads to an extra uncertainty $\Delta\varphi$ in the detected direction, which can be expressed, as

$$(v_{\text{in}} + \Delta v)\cos(\varphi + \Delta\varphi) = v_{\text{in}}\cos\varphi, \tag{6.30}$$

according to Fig. 6.16(b). Within this model, two directions for Bell detection, indicated in Fig. 6.16(c), become indistinguishable. Next, we use Eq. (2.32), to express quantum efficiency of the measurement JPAs as $\eta = v_{\text{in}}/(v_{\text{in}} + \Delta v)$ [107]. From the condition $\cos\varphi \leq 1$, we find from Eq. (6.30) that there is a critical angle $\cos\varphi_{\text{c}} = \eta$ so that only directions $\varphi_{\text{c}} \leq \varphi \leq \pi/2$ can be reliably distinguished. Then, a relative angle deviation is given by

$$\frac{\varphi + \Delta\varphi}{\varphi} = \frac{\arccos(\eta\cos\varphi)}{\varphi}. \tag{6.31}$$

Now, we can define the Bell efficiency $\mathcal{B}$ as a normalized average relative angle uncertainty. By exploiting the polar symmetry of the JM output with respect to $\pi/2$, we can express $\mathcal{B}$ by the integral

$$\mathcal{B}(\eta) = \frac{2}{\pi} \int_{\arccos(\eta)}^{\frac{\pi}{2}} \frac{\arccos(\eta\cos z)}{z} dz, \tag{6.32}$$

which needs to be evaluated numerically. From our fit parameters in Tab. 6.1, we find $\eta = 0.914$ for $G = 21\,\text{dB}$, leading to a reasonably large Bell efficiency $\mathcal{B} = 0.802$ in our experiment.

Teleportation bit rate   Next, we would like to quantify an amount of classical information which can be sent via our quantum teleportation protocol and calculate an associated classical bit rate R. We focus on the phase θ of our coherent states, since in a practical application, we would fix the power $|\alpha|^2$ and employ phase modulation for information encoding. To estimate R in our protocol, we use the Shannon-Hartley equation for the channel capacity, $R = 2B\log_2(1 + \text{SNR})$, where the bandwidth $B/2\pi = 200\,\text{kHz}$ is determined by our SSB FIR filter [78, 277, 375]. We express SNR as $\text{SNR} = \Delta\theta^2/\sigma_\theta^2$, where $\Delta\theta$ is the available range of coherent phases and σ_θ is the standard deviation of
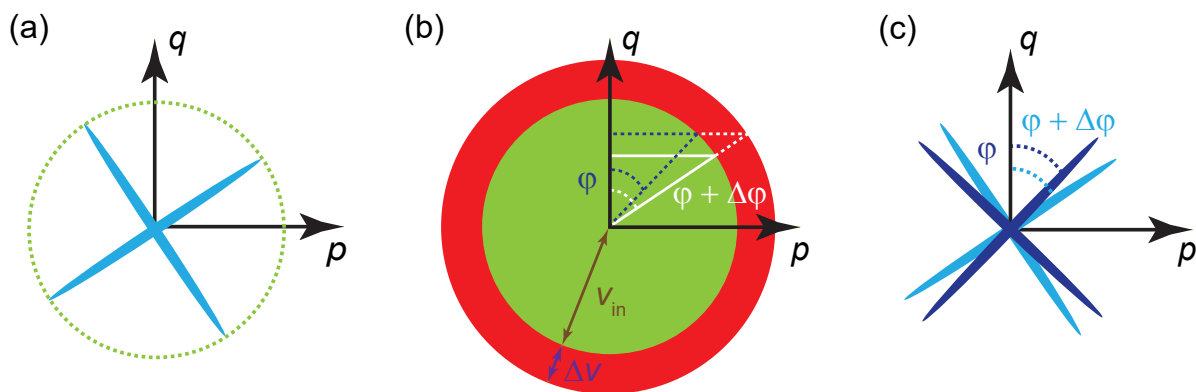
Figure 6.16: Scheme for modelling the Bell efficiency of the Josephson mixer (JM). We attempt to employ the JM to distinguish between two orthogonal phase space directions, as shown in panel (a). Finite JPA noise leads to an uncertainty of $\Delta\varphi$ for phase detection, as shown in panel (b). In this simplified geometric picture, R corresponds to the variance of the phase space distribution, which is broadened by d due to imperfect quantum efficiency. Consequently, the detector cannot distinguish among the directions φ and $\varphi + \Delta\varphi$, as shown in panel (c).

θ. We find a lower bound for σ_θ, using the quantum Cramér-Rao bound [376], which relates the quantum Fisher information $\mathcal{F}_\mathrm{Q}$ to a lower bound of the estimation error of θ as $\sigma_\theta^2 \geq 1/\mathcal{F}_\mathrm{Q}$ and can be saturated by a suitable measurement choice. The quantum Fisher information $\mathcal{F}_\mathrm{Q}$ for phase estimation for a Gaussian state is given by

$$\mathcal{F}_\mathrm{Q} = 4\mu|\alpha|^2 \left(\lambda \cos^2\gamma + \frac{1}{\lambda}\sin^2\gamma\right) + \frac{1}{1+\mu^2}\frac{(1-\lambda^2)^2}{\lambda^2}, \tag{6.33}$$

where $\lambda = e^{-2r}$ and γ denotes the squeezing angle [377]. For our working point, we find $\mathcal{F}_\mathrm{Q} = 4\mu|\alpha|^2 \simeq 0.85$. Since we employ a polar symmetric codebook, we have $\Delta\theta = 2\pi$, which results into the upper bound for the achievable bit rate $R = 1.95\,\mathrm{Mbit\,s^{-1}}$. In the fidelity region $1 > F > F_\mathrm{nc}$, we can achieve an unconditionally secure bit rate R_us, satisfying $R > R_\mathrm{us} > 0$. For $F < F_\mathrm{nc}$, we have $R_\mathrm{us} = 0$ [378]. Since R depends on the measurement bandwidth, which is a purely technical quantity, an alternative measure to quantify the classical channel capacity of our protocol is the spectral efficiency $\eta_\mathrm{s} = R/(2B)$, which solely depends on our protocol and the chosen operation point. Consequently, we obtain $\eta_\mathrm{s} = 4.88$. We can compare this number to the spectral density associated with the Gaussian QKD protocol investigated in Sec. 5.3. In this case, we consider a noiseless scenario and rewrite Eq. (5.27) as [263, 379]

$$R = 2BI_\mathrm{s}(\mathrm{A:B}) = B\log_2\left(1 + \frac{4\sigma^2}{e^{-2r}}\right) = B\log_2\left(1 + \frac{2RE_\mathrm{b}}{Be^{-2r}}\right), \tag{6.34}$$

where E_b corresponds to the required energy per classical bit. Assuming an irreversible protocol due to the reconciliation procedure in QKD, the fixed signal power leads to

maximal R if we operate at the Landauer-limit, $E_\text{b} = k_\text{B} T \ln 2 / (\hbar \omega)$ [380]. In the latter expression, we express E_b in units of signal photons at frequency ω. From Eq. (6.34), we obtain the implicit equation

$$\eta_\text{s} = \frac{1}{2} \log_2 \left[1 + \eta_\text{s} \frac{4 k_\text{B} T \ln 2}{e^{-2r} \hbar \omega} \right]. \tag{6.35}$$

To obtain a nontrivial solution $\eta_\text{s} > 0$, we require squeezing of at least $e^{2r} > \hbar \omega / (2 k_\text{B} T)$, which corresponds to the Shannon-limit [379]. In other words, we need to "squeeze" the crossover temperature $T_\text{cr} = \hbar \omega / (2 k_\text{B})$ of the Planck curve below T. For our quantum teleportation working point, according to Tab. 6.1, we find $\eta_\text{s} \simeq 0.8$. In particular, reaching the same spectral efficiency as for our quantum teleportation protocol would require squeezing of $S \simeq 23.7\,\text{dB}$. Thus, we conclude that our determined maximal spectral efficiency for quantum teleportation is significantly larger than for Gaussian QKD protocols which involve less ancillary modes for comparable squeezing level.

6.4 Teleportation-based Gaussian error correction

In Sec. 6.3.2, we have demonstrated that losses in the signal path act as a renormalization of the optimal measurement gain G. In this section, we demonstrate that quantum teleportation can be employed to correct for arbitrary Gaussian errors in the feedforward channel [65]. We exploit the JM for amplification with gain $G \gg 1$, which implies that the analog feedforward signal contains $n_\text{ff} \gg 1/2$ photons and can be regarded as a classical signal. For such classical states, loss channels can be fully compensated by amplification channels, as shown in Sec. 2.2.4. In addition, as demonstrated in chapter 4, the Friis equation implies that, in the high gain limit, the overall noise level is dominated by the noise added before the first amplification stage. To verify this intuition, we reconsider the quantum teleportation protocol in the framework of Sec. 2.3.1, but with finite losses ε_ent in the entanglement distribution to Bob and finite losses ε_ff in the feedforward channel (corresponding to ε_{13} and ε_{14} in Fig. 6.13) [238]. In fact, we find that, in the projective limit, displacement transforms as $\mathbf{d}_\text{out} = \sqrt{k_{\varepsilon_\text{ff}}} \mathbf{d}_\text{in}$, where $k_{\varepsilon_\text{ff}} = (1 - \varepsilon_\text{ff}) k$. Thus, displacement matching requires $k_{\varepsilon_\text{ff}} = 1$. In this case, teleportation fidelity can then be expressed as

$$F = \frac{2}{C(r, 1 - \varepsilon_\text{ent}) + 2 + \coth \left(\frac{\hbar \omega}{2 k_\text{B} T} \right) (\varepsilon_\text{ent} + \beta \varepsilon_\text{ff})}. \tag{6.36}$$

We observe that the losses ε_ent in the entanglement distribution channel directly enter the interference function $C(r, k)$ and effectively lead to a gain mismatch between both modes in the TMS resource. As considered in Sec. 2.3.1, the resulting power mismatch degrades the efficiency of the destructive interference process for the quduties at Bob's directional coupler and quantum physics forbids to compensate for ε_ent by using local operations.

In the limit $\varepsilon_{\text{ent}} \to 1$ and $T \to 0$, we find $F = 2/(3 + \cosh 2r) \leq 1/2$ [cf. Eq. (8.8)]. In contrast, we observe that feedforward losses ε_{ff} enter Eq. (6.36) only in combination with the coupling β. In fact, for $r \to \infty$ and $\varepsilon_{\text{ent}} = 0$, Eq. (6.36) reduces to

$$F = \frac{2}{2 + \beta\varepsilon_{\text{ff}} \coth\left(\frac{\hbar\omega}{2k_{\text{B}}T}\right)} = \frac{1}{1 + \beta\varepsilon_{\text{ff}}\mathcal{S}(\omega,T)}, \tag{6.37}$$

where $\mathcal{S}(\omega,T)$ denotes the thermal noise spectral density, coupled into the feedforward channel. We observe from Eq. (6.37) that we can decrease the impact from $\mathcal{S}(\omega,T)$ by decreasing β while maintaining $k_{\varepsilon_{\text{ff}}} = 1$. This result even holds in the high loss limit, $\varepsilon_{\text{ff}} \to 1$. In fact, according to Eq. (6.37) we can achieve quantum teleportation beyond the classical limit for temperatures below

$$T_{\text{c}} = \frac{\hbar\omega}{2k_{\text{B}}\text{arcoth}\,(2/\beta)} \simeq \frac{\hbar\omega}{k_{\text{B}}\beta}. \tag{6.38}$$

 Furthermore, Eq. (6.37) can be employed to determine the bath temperature T_{nc}, corresponding to the asymptotic no-cloning limit, $T_{\text{nc}} \simeq T_{\text{c}}/2$. For our actual experimental parameters, $\beta = -15\,\text{dB}$ and $\omega/2\pi = 5\,\text{GHz}$, we find $T_{\text{c}} \simeq 7.6\,\text{K}$. We predict that, even in the high loss limit, it is possible to transmit the feedforward signal though a liquid Helium bath with our setup. We observe from Eq. (6.38) that the value of T_{c} can be raised to arbitrarily high values by further decreasing β. In fact, we observe that when the feedforward signal is transmitted through a thermal channel, according to Eq. (2.147), quantum teleportation enables us to send coherent states with fidelity $F \to 1$. Thus, if Alice and Bob have access to a suitable quantum memory [381, 382] for storing the TMS resource, our quantum teleportation protocol enables both parties to establish an ideal quantum channel, although they might be physically separated within a noisy environment. This result demonstrates the advantage of quantum teleportation as compared to direct quantum state transfer, since the latter would rely on a physically lossless and noiseless quantum channel. The technical limitation of the quantum teleportation protocol is the maximization of the degenerate gain G of the measurement JPAs, which is necessary to satisfy the projection condition $k_{\varepsilon_{\text{ff}}} = 1$. In practice, we are eventually limited by compression of the measurement JPAs. Corresponding predictions based on our theory model described in Sec. 6.3.2 are shown in Fig. 6.17. We treat the protocol as ideal and only consider loss and noise in the feedforward channel. In addition, we assume that the JM gain is always chosen such that $k_{\varepsilon_{\text{ff}}} = 1$. Figure 6.17(a) corresponds to $\beta = -15\,\text{dB}$ and it can be seen that, in the high loss limit, fidelity becomes independent of ε_{ff} as described by Eq. (6.38). Figure 6.17(b) corresponds to $\beta = -30\,\text{dB}$ and demonstrates that we can shift the tolerable bath temperatures to values exceeding the liquid nitrogen (LN$_2$) threshold by further decreasing the coupling β. In Fig. 6.17(c), we demonstrate that we can increase the overall fidelity if we increase the resource squeezing S, whereas
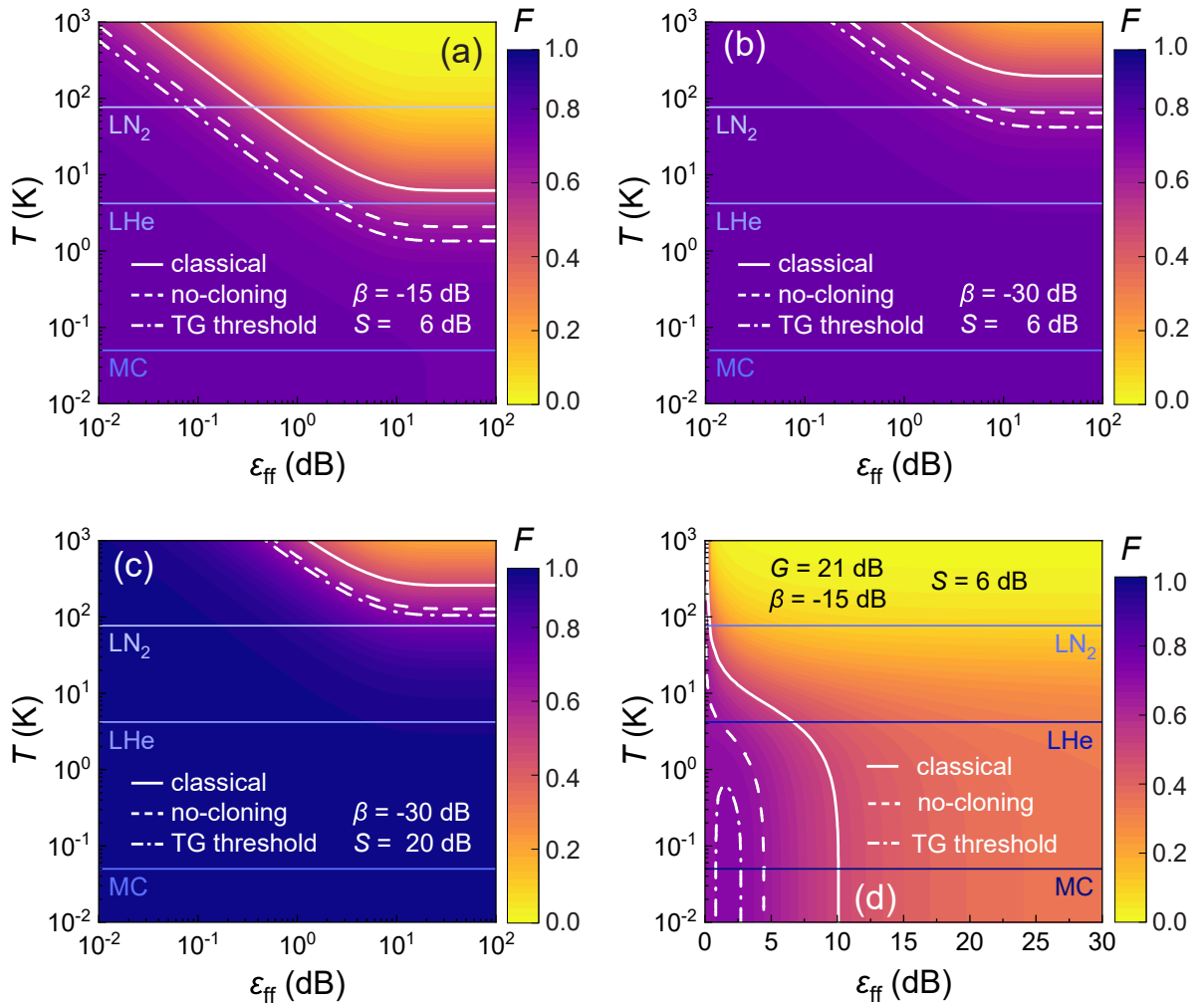
Figure 6.17: Teleportation fidelity as a function of environmental feedforward temperature T and feedforward losses ε_{ff}. Solid blue lines indicate temperatures corresponding to liquid nitrogen (LN_2), liquid Helium (LHe), and the mixing chamber (MC) of a dilution cryostat. Solid white line, dashed white line, and dotted-dashed white line, respectively, correspond to the classical fidelity threshold, the asymptotic no-cloning limit, and the upper bound for the truncated Gaussian no-cloning limit for the case $N_s = 100$ with optimized σ according to Eq. (2.166). In panels (a)-(c), we treat the protocol as ideal apart from the feedforward imperfections. In addition, we assume that we always meet the projection criterion $k = 1$. Panel (a) corresponds to our experimental values for resource squeezing and Bob's coupling, $S = 6\,\text{dB}$, $\beta = -15\,\text{dB}$. We find that, in the high loss limit, the critical temperature at which we exceed the classical fidelity threshold is already higher than the technically relevant threshold of LHe. We can push this threshold to even higher temperatures by further decreasing β, as it can be seen in (b). Panel (c) shows that by increasing S, we can improve the overall fidelity. For the plot shown in panel (d), we employ our theory model with the parameters from Tab. 6.1 for fixed gain $G = 21\,\text{dB}$. Even in this non-ideal scenario, we can achieve resilience towards losses and noise in the analog feedforward signal.

S only slightly affects the functional dependence of fidelity on ε_{ff} and T. In Fig. 6.17(d), we simulate our protocol including JPA noise and realistic losses using the parameters listed in Tab. 6.1. In constrast to the ideal scenario, we do not fix $k_{\varepsilon_{\text{ff}}} = 1$, but keep G and S constant, as we would also do in experiment. In this situation, fidelity still shows a certain resilience towards ε_{ff} and T, but we observe a cutoff in the region $\varepsilon_{\text{ff}} \simeq 10\,\text{dB}$, which results from residual e^{2r} terms in the interference function since feedforward losses implicitly change the power balance in the resource state if we do not adjust the JM gain properly. Thus, satisfying the projection condition is crucial in case we employ our protocol for Gaussian error correction.

Correction of phase shifts in the feedforward Next, we investigate whether we can correct for phase errors in the feedforward channel in coherent state teleportation. Such phase shifts would include operations such as the analog Fourier gate, which would transform $p \to q$, $q \to -p$ [47, 383]. We generally describe such a phase shift by a rotation $\boldsymbol{R}(\phi)$ in the feedforward channel and investigate whether such a phase error can be corrected if we change the amplification angle of the measurement JPAs. We allow for a general rotation $\boldsymbol{M}(\varphi)$ in Eq. (2.171), according to

$$\boldsymbol{J}_p \to \boldsymbol{M}(\varphi)\boldsymbol{J}_p\boldsymbol{M}(\varphi)^\dagger, \qquad \boldsymbol{J}_q \to \boldsymbol{M}(\varphi)\boldsymbol{J}_q\boldsymbol{M}(\varphi)^\dagger. \tag{6.39}$$

For the final displacement, we the find

$$\mathbf{d}_{\text{out}} = \frac{\sqrt{\beta}}{2}\boldsymbol{M}(\varphi)(\boldsymbol{J}_p + \boldsymbol{J}_q)\boldsymbol{M}(\varphi)^\dagger\boldsymbol{R}(\phi)d_{\text{in}} = \sqrt{k}\boldsymbol{R}(\phi)\mathbf{d}_{\text{in}}, \tag{6.40}$$

implying that we cannot correct for $\boldsymbol{R} = \boldsymbol{R}(\phi)$. This result is intuitive since the measurement JPAs amplify orthogonal quadratures, so that the complete JM acts as a phase-insensitive amplifier. Thus, its action should not depend on φ, since it takes the role of a global phase. The situation changes for the covariance matrix transformation at the directional coupler since, within the interference process, φ can be regarded as a relative phase shift with respect to the TMS state phase and should influence Bob's final covariance matrix. Indeed, we find

$$\boldsymbol{V}_{\text{out}} = \frac{1}{4}\left[(1+k)\cosh 2r \mathbb{1}_2 + k\mathbb{1}_2 - \sqrt{k}\sinh 2r(\boldsymbol{R}\boldsymbol{M}\sigma_z\boldsymbol{M}^\dagger\sigma_z + \sigma_z\boldsymbol{M}\sigma_z\boldsymbol{M}^\dagger\boldsymbol{R}^\dagger)\right]. \tag{6.41}$$

A direct calculation shows

$$\left[\sigma_z\boldsymbol{M}(\varphi)\sigma_z\boldsymbol{M}(\varphi)^\dagger\boldsymbol{R}(\phi)^\dagger\right]^\dagger = \boldsymbol{R}(\phi)\boldsymbol{M}(\varphi)\sigma_z\boldsymbol{M}(\varphi)^\dagger\sigma_z = \boldsymbol{R}(\phi)\boldsymbol{M}(2\varphi). \tag{6.42}$$

Thus, by choosing $\varphi = -\phi/2$, it is possible to perfectly compensate for phase errors in the feedforward channel regarding the interference process in the covariance matrix. Thus,

a quantum advantage by employing entanglement is still possible, since we can purify the final state with respect to the two quduties under the condition $k = 1$. In this case, fidelity depends on the phase error according to

$$F = \exp\left[-4|\alpha|^2 \sin^2 \frac{\phi}{2}\right]. \tag{6.43}$$

For a Gaussian codebook, the average fidelity is given by $\bar{F} = 1/(8\sigma^2 \sin^2 \frac{\phi}{2} + 1)$, which eventually approaches zero for $\sigma^2 \to \infty$. Thus, due to the phase modulation in Eq. (6.43), phase errors cannot be fully compensated.

Chapter 7

Microwave quantum local area network based on a cryogenic link

In this chapter, we discuss our cryogenic hardware platform to realize a quantum channel for microwave quantum communication experiments conducted between two separated laboratories. This hardware platform consists of a cryogenic millikelvin link which connects two dry dilution refrigerators, Alice and Bob, over a distance of 6.6 m between the center points of the cryostats. The cryogenic link has been designed and assembled in collaboration with `Oxford Instruments NanoScience` (`OINT`) within the European Quantum Flagship Project "Quantum Microwave Communication and Sensing" (QMiCS). In Sec. 7.1, we introduce the system and discuss its design and installation. Next, in Sec. 7.3, we discuss operation, as well as the cooldown performance, of the cryogenic link and investigate heat transfer in the system.[1] This system can be used for Bell tests [384] or for applications which require magnetic components and superconducting circuits, well decoupled from each other, within the same cryogenic environment. Potential applications are interferometric experiments regarding detection of gravitational waves [385] or dark matter axions [324, 386]. In addition such a cryogenic link can be employed for implementing experiments requiring localized heating.

7.1 System design and assembly

Our cryogenic link has been developed and fabricated at `OINT` in close collaboration with WMI. In Sec. 7.1.1, we discuss design and assembly of the entire system at WMI. In Sec. 7.1.2, we describe modifications of the thermometry for the Bob cryostat, which enables reliable temperature readout and control. Section 7.1.3 is dedicated to the technical modifications of the Alice cryostat, which were required to sustain an additional heat load from the cryogenic link.

---

[1]The first full assembly and the first successful cooldown has been collaboratively realized within two Master's projects together with W. Yam and S. Gandorfer. The corresponding Master's theses can be found in Ref. 238 and Ref. 282.
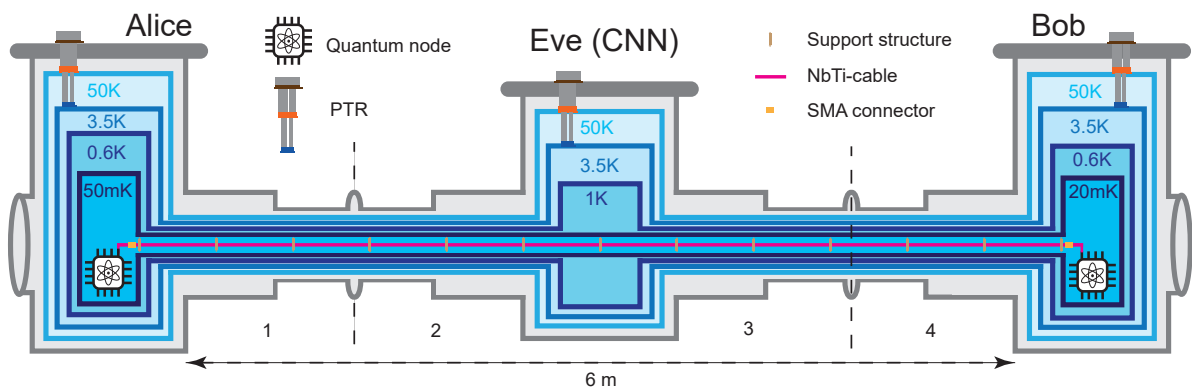
Figure 7.1: Schematic illustration of the cryogenic link connecting two dilution refrigerators over a distance of 6.6 m, measured between the center points of the respective cryostats. The center tube of the link contains a 6 m long superconducting transmission line. A third auxiliary cryostat, Eve, helps reducing the temperature of the important 50 K and 3.5 K shields via an additional PTR and allows for future extensions to a star-shaped QLAN.

7.1.1 Design and assembly of the cryogenic link

Figure 7.1 schematically illustrates the structure of our cryogenic link. The link consists of four segments and a cold network node (CNN) in the center, which we refer to as Eve in the following. The tube structure of the link segments resembles the respective shield structure of our dilution refrigerators. Eve contains an additional pulse tube refrigerator (PTR) to stabilize temperatures of the first PTR stage (PT1) and second PTR stage (PT2) segments in the center.[2] In addition, Eve is equipped with a radiation shield connected to the still segment of the cryogenic link. However, in contrast to Alice and Bob, Eve neither has a dilution unit, nor a Joule-Thomson (JT) or 1 K stage. Including Eve, the total link length corresponds to 6 m from flange to flange. The innermost tube, connected to the respective mixing chamber (MC) shields of Alice and Bob, is planned to host three superconducting coaxial cables, which form the microwave quantum channels between distant communication parties. A computer-aided design (CAD) drawing of the system is provided in Fig. 7.2(a). The drawing shows the outer vacuum (OVC) shield structure of Alice, Bob, and Eve as well as the stainless steel (SS) OVC tube of the cryogenic link which has an outer diameter of 20.5 cm. Each segment of the link arm is supported by a height-adjustable frame, constructed from aluminum profile rods [3]. In addition, Fig. 7.2(a) shows the corresponding `item` frames for Bob and Eve. A photograph of the assembled cryogenic link is shown in Fig. 7.2(b). The fully assembled system consists of 60 shield segments, 60 adapter components, ∼ 2200 screws, 14 large O-rings, 26 medium sized O-rings and ∼ 50 small O-rings.[4]

---

[2]Eve features a `PT415-RM` PTR from Cryomech, operated with a `CPA1110` compressor.

[3]We use aluminum profiles from item Industrietechnik GmbH for this purpose.

[4]The large O-rings correspond to the `BS389` standard. A reference for the medium sized O-rings is the `BS270` standard.

In the following, we discuss the relevant steps to assemble the link. We start from the center of the cryogenic link, which contains three 6 m long coaxial superconducting transmission lines, which we each realize by joining three 2 m long superconducting coaxial NbTi cables.[5] The coaxial cables and related superconducting joints for connection have been developed and provided by `KEYCOM Corp.` and exhibit an attenuation coefficient of $\alpha = 2.1\,\mathrm{dB\,km^{-1}}$ at 6 GHz [387]. This loss value is currently limited by the joints connecting the coaxial cables and not by fundamental limitations, such as the surface resistance R_s of NbTi superconductors [69, 388]. Due to the comparably high critical temperature of NbTi, $T_\mathrm{c} \simeq 10\,\mathrm{K}$, we can approximate $R_\mathrm{s} \sim \exp\left(-1.764 T_\mathrm{c}/T\right)$ [389], which means that R_s becomes negligibly small in our temperature range $T \simeq 100\,\mathrm{mK}$. The superconducting transmission line is supported by 13 holders, which are equidistantly spaced inside the mixing chamber tube at intervals of 0.5 m. The central support structure, positioned directly underneath Eve, is shown in Fig. 7.3(a). The frame of each support holder consists of polyether ether ketone (PEEK). PEEK has been chosen due to its comparably low thermal conductivity at low temperatures, which enables excellent thermal decoupling of the cables from the MC tube [390]. At the same time, the rigidness of PEEK guarantees stable mechanical support and, in terms of machining, is beneficial over alternative low thermal conductivity polymers such as polytetrafluoroethylene (PTFE) [283]. Top and bottom of the PEEK holder are tip-shaped to minimize the contact surface to the MC tube, which further reduces the thermal coupling and minimizes respective mechanical friction. The superconducting cables are clamped into supports made from gold-plated oxygen-free high conductance (OFHC) copper. This OFHC copper support is connected to the PEEK bearing structure by SS joints, which guarantees additional thermal decoupling. The whole structure is thermalized by two silver wires with a diameter of 1.5 mm which are screwed to each OFHC copper support and attached to the MC plate of Alice and Bob. The silver wires run in parallel to the coaxial cables and are made from segments, each connecting consecutive copper supports. As a result, thermal coupling of the transmission line to the MC stage is sufficiently weak to allow for a localized heating of the center. We employ a PID control architecture, consisting of a $100\,\Omega$ and a $\mathrm{RuO_2}$ thermometer on the central support holder, as shown in Fig. 7.3(a). This setup turns our QLAN cables into a well controlled thermal channel. During insertion of the superconducting coaxial cables, the support structures and thermalization wires have been attached to the cables *in-situ*. In addition, the procedures of cutting the cables to the correct length, crimping the SMA connectors to the cable ends, and performing proper time-domain reflectometry (TDR) tests have been realized directly following the insertion process. Figure 7.3(b) shows the SMA connectors of the superconducting coaxial lines, as well as the two silver wires used for thermalization. A photograph showing the insertion process of the transmission line, which has been realized via a push and pull method, is

---

[5]The transmission lines and the support structure have been developed in close collaboration with Dr. Matti Partanen.

Figure 7.2: (a) CAD drawing of the cryogenic link and the OVC shields of Alice, Bob, and Eve. Image courtesy of Oxford Instruments. (b) Photograph of the installed cryogenic link, taken in the Eve lab. More details regarding a lab plan are provided in Fig. 7.5. The Eve cryostat is designed with four ports to enable potential connection of additional link arms. One of these ports, covered by a blind flange, is visible on the photograph ("QLAN port").

provided in Fig. 7.3(c). To properly design the length of the thermalizations as well as of the NbTi cables, connecting the superconducting transmission lines to our experimental setup, we need to compensate for thermal contraction during the system cooldown. For this, we compare the contraction of NbTi, silver, and OFHC copper. For NbTi, thermal length contraction can be accurately predicted by empirical relations of the form

$$\frac{L_T - L_{293}}{L_{293}} = \left(a + bT + cT^2 + dT^3 + eT^4\right) \times 10^{-5}, \tag{7.1}$$

where L_T (L_{293}) denotes the length at room temperature T (293 K) and the polynomial
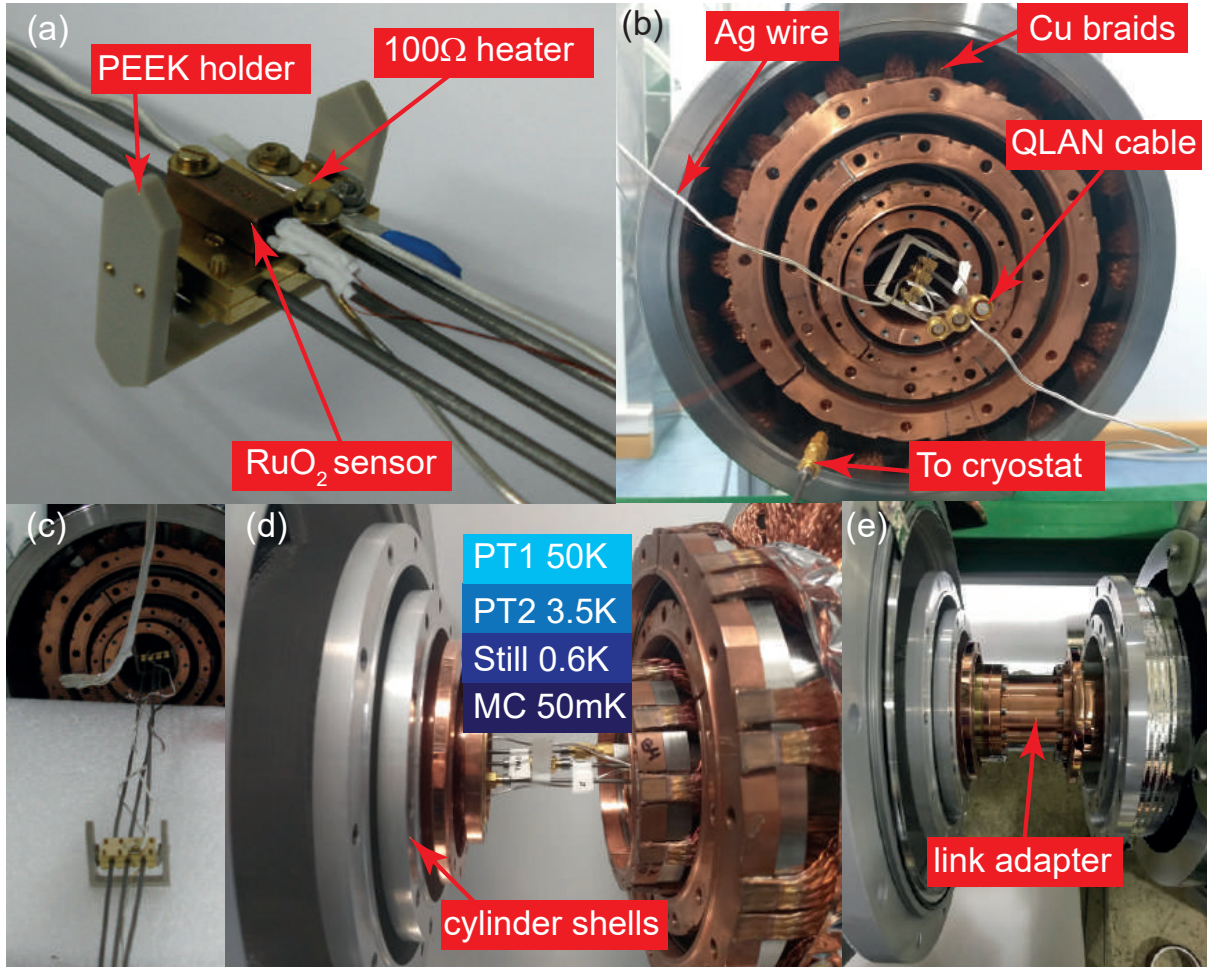
Figure 7.3: (a) PEEK holder for the superconducting coaxial cables passing through the cryogenic link. A RuO$_2$ sensor and a $100\,\Omega$ heater are installed for controlled local heating. (b) Cross section of the cryogenic link, reveiling the shield structure. This photograph shows the SS OVC shield, the four inner radiation shields (PT1, PT2, Still, MC), the crimped SMA connectors of the superconducting transmission line, as well as the two silver wires used for thermalization. (c) Photograph taken during the insertion process of the cables into the link. (d) Photograph showing the microwave connection between one of the dilution fridges and the cryolink transmission line. (e) Photograph showing the principle of connecting the cryogenic link to the cryostat shields via half cylindrical shells ("link adapter").

coefficients are known from literature [391]. A similar expression exists for OFHC copper [392]. Since such a relation is not available for silver, we determine the thermal contraction within the Grüneisen theory [393], where we determine internal energy E and phononic heat capacity C using the Debye model. We define $x_\mathrm{D} \equiv \Theta_\mathrm{D}/T$, where Θ_D is the Debye temperature [69]. The relative length contraction for a given temperature T, compared to $T = 0\,\mathrm{K}$, can be expressed as

$$\frac{L_T - L_0}{L_0} = \alpha_T \frac{E(x_\mathrm{D})}{C(x_\mathrm{D})} = \alpha_T \frac{\Theta_\mathrm{D}}{x_\mathrm{D}} \frac{D_3(x_\mathrm{D})}{4D_3(x_\mathrm{D}) - 3B(x_\mathrm{D})}, \tag{7.2}$$

where $D_3(x)$ is the third Debye function [69, 394] and $B(x) = x/(e^x - 1)$ is the Bernoulli generating function [163]. The expected relative thermal contraction, as a function of the cryogenic link temperature, is plotted in Fig. 7.4(a). We use silver for thermalizing the transmission line due to its higher thermal conductivity at low temperature compared to OFCH copper. The length of the thermalization wires is chosen appropriately to compensate for the contraction mismatch of 1.6 cm with respect to NbTi. In addition to thermal contraction, we plot the temperature dependent thermal conductivity λ of PEEK and of our transmission line in Fig. 7.4(b). For PEEK, we employ the empirical relation $\lambda_P[W/(m \cdot K)] = 18.7 \times T^{1.47} \times 10^{-4}$ [390]. In case of silver and NbTi, we neglect the phononic contribution to heat transfer as it follows a cubic temperature dependence. For our NbTi cables, we furthermore take into account that, in the superconducting state, the energy gap $\Delta(T)$ modifies the electronic thermal conductance λ_n corresponding to the normal conducting state, since Cooper pairs do not contribute to electronic heat transport [389]. The modified heat conductivity can be expressed as $\lambda_s = y(T)\lambda_n$, where the index "s" ("n") denotes the superconducting (normal) state and the temperature dependent factor $y(T)$ can be determined within the BCS-theory (cf. Appendix E) [395–398].[6] As it can be seen from Fig. 7.4(b), thermal conductivity of our transmission line can be neglected at temperatures $T \lesssim 1$ K. At temperatures below 1 K, thermal conductivity of the superconducting coaxial cable is eventually determined by the PTFE dielectric [399], which is typically on the order of 1×10^{-3} W K^{-1} m^{-1} $\ll \lambda_{Ag}$. Consequently, thermalization of the transmission line is fully determined by the silver wires.

In the following, we discuss the shield structure inside of our cryogenic link. The corresponding cross section is shown in Fig. 7.3(b). The MC and still tubes are constructed from electropolished copper; the PT2 and PT1 tubes are fabricated from aluminum. All tubes are divided into four segments, as illustrated in Fig. 7.1, and thermally decoupled from each other by foam and spacers made from `G-10` glass epoxy. The MC tube containing our transmission line has an inner diameter of 5.2 cm. Below the Eve cryostat, the corresponding two segments of the MC tube have different cross sections, such that they can be plugged into each other. In this way, the effects of thermal contraction or expansion are compensated. These two MC shield segments are thermalized to each other by annealed silver. In contrast to the MC tube, still, PT2 and PT1 are directly attached to Eve's respective radiation shields. Mechanical flexibility of the tubes is ensured by SS bellows. Due to low thermal conductivity of SS, the bellows are thermally shorted by flexible copper braids, which are shown in Fig. 7.3(b) and Fig. 7.3(d) for the PT1 tube. To reduce the risk of thermal links between different shields, the braids are fixed to respective tubes using Kevlar strings and PTFE tapes.

Next, we describe how to close the system. In the first step, we mount the shields of the individual cryostats. Each set of shields contains proper orifices for connection of the link arms, which need to be carefully aligned. Then, we attach cylindrical adapter

---

[6]Here, I would like to thank Prof. Dr. Dietrich Einzel for fruitful discussions.
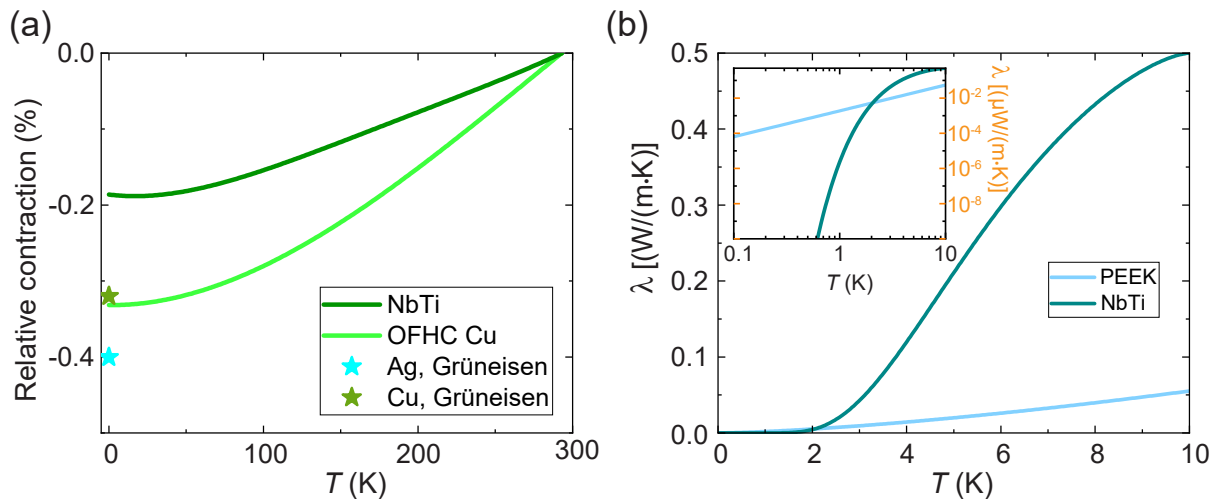
Figure 7.4: (a) Relative thermal contraction $(L_T - L_{293})/L_{293}$ for OFHC copper, NbTi, and silver as a function of temperature. When cooling from room temperature (293 K) to MC temperature, the superconducting transmission line contracts by $1 - 2$ cm. In case of silver, thermal contraction has been determined from the Grüneisen theory using the Debye model [69, 393]. For copper, the relative difference between the Grüneisen model and the empirical relation in Eq. (7.1) is 2.5 %. (b) Thermal conductivity of PEEK and electronic thermal conductivity NbTi as a function of temperature. For the calculation, we assume a critical temperature of 10 K and a corresponding $\lambda_n = 0.5\,\mathrm{W\,m^{-1}\,K^{-1}}$ [400].

shells with diameters matched to the respective tube size of the cryogenic link arm, as indicated in Fig. 7.3(d). Following that, we connect the experimental setups in Alice and Bob to the transmission line by gently bending the respective RF cables to fit through the MC adapters. In addition, we fix the silver thermalizing wires for the transmission line to the respective MC plates of Alice and Bob. After mounting the cables, we connect the cryogenic link arms using two half cylinder shells per shield. For the MC shield, we employ molybdenum washers to create a thermal contraction mismatch with respect to the SS screws, which keeps the connection tight at cryogenic temperatures. The gap between the respective shells is carefully covered with aluminum tape to minimize radiative heat leaks. In addition, we cover the PT1 connection with 40 layers of superinsulation foil. Following that, we close the OVC adapters using Viton O-rings, which we carefully grease prior to installation.[7] Since the OVC tube consists of rigid SS, the system requires careful prealignment which can be realized with a laser positioning system. In addition, the system is designed with additional degrees of freedom to adjust relative orientation between the link and the cryostats. Bob and Eve are mechanically suspended via an aluminum slab. The latter allows for approximately 1 cm of lateral position adjustment and can even compensate for height mismatches. The orientation of Alice can be changed by properly adjusting the height of the air bearings on top of the triangular support frame

---

[7]We use `BS270` Viton O-rings and silicone high vacuum grease from `Wacker AG` for this purpose.
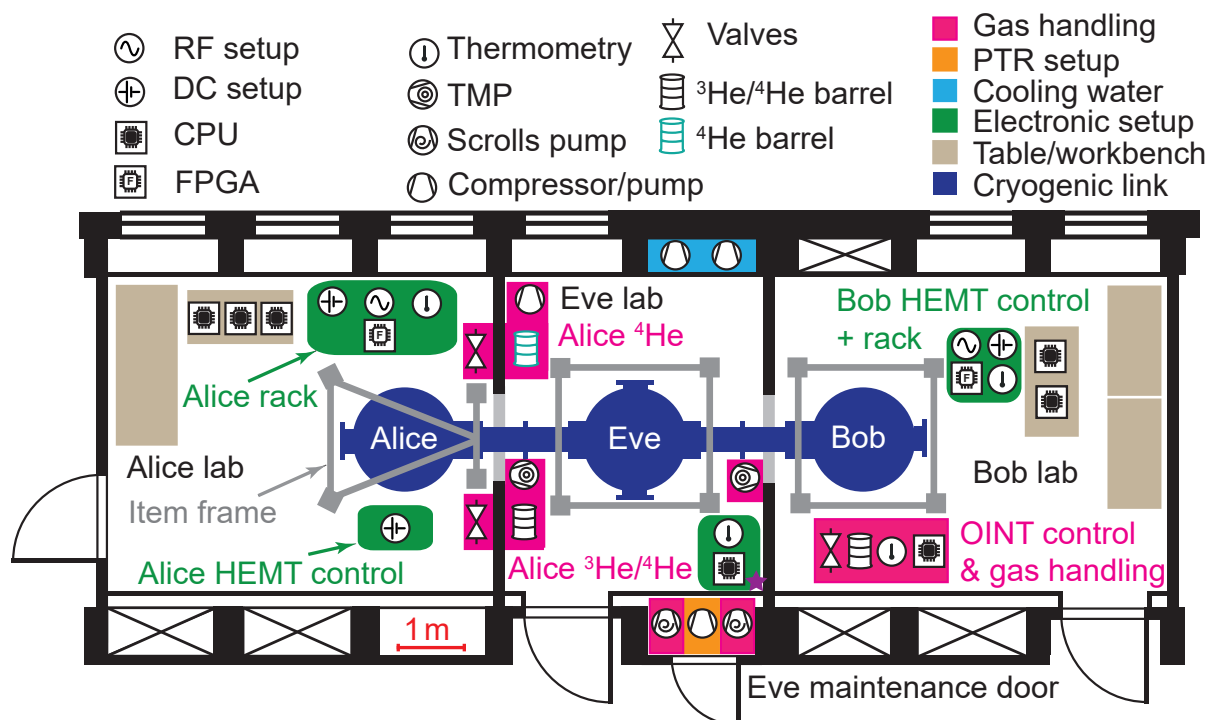
Figure 7.5: Schematic illustration of the cryogenic link installation, distributed over three laboratories. The spatial proportions of the room dimensions are real (scale 1:96). The purple star marks the position from which the photograph in Fig. 7.2(b) has been taken.

[288] and by exploiting the oversized washers at the connection to the support frame. In this way, the we can move Alice in lateral direction by multiple centimeters. For future scalability, e.g., for distributed quantum computing applications [401], the cryostat shields contain additional orifices for a potential connection of more link arms. We close these holes with suitable blanks and Viton O-rings. An additional connection port for Eve can be seen in Fig. 7.2(b) and allows for potential extension of the system to form star- or square-lattice shaped network geometries [402]. After properly closing the system, a careful leak test demonstrates that we can make the system tight up to a ^{4}He leak rate of $5 \times 10^{-8}\,\mathrm{mbar\,l\,s^{-1}}$. Since the full experimental setup covers three laboratories, it is difficult to display the overall system on a single photograph. Instead, we schematically illustrate the arrangement of our setup in Fig. 7.5.

7.1.2 Upgrading thermometry for the cryogenic link

We read out thermometers inside our cryogenic link via the resistance bridges in Alice and Bob lab, described in Sec. 3.1.1. For measuring of the center temperature T_{center} of the transmission line and for potential PID control, we employ an `AVS-48` resistance bridge in Bob lab. In addition to that, we read out the sensors inside the Eve cryostat using a `MercuryiTC` temperature controller from `OINT`, and the center temperature of the MC

tube below Eve is measured by a second `AVS-48` bridge. Since this elaborate thermometry requires a sufficient amount of sensors for millikelvin temperatures, we use the Bob fridge to calibrate additional RuO_2 sensors prior to the first cooldown of the cryogenic link. To this end, we apply a heater power P to sweep the MC temperature T_{mc} of Bob and compare the temperature dependence of the respective resistance values against a well calibrated reference sensor. The result of such a calibration measurement for five different sensors is shown in Fig. 7.6(a). We observe that sensors $2-4$ are suitable to be used as accurate resistance thermometers due to monotonic behavior and steep slope in the region $20-50\,\text{mK}$. On the other hand, sensor 1 is non-monotonic and sensor 5 is flat around $25\,\text{mK}$, implying that it is not optimal to employ these two sensors for thermometry at low temperatures. We can additionally use such a calibration run to check whether the MC thermometer in Bob is properly calibrated at low temperatures.

From the enthalpy balance in the MC, it can be shown that [285, 403, 404]

$$\dot{Q}_{mc} = \dot{n}_3 \left(95 T_{mc}^2 - 11 T_{hex}^2 \right) \left(\frac{\text{J}}{\text{mol} \cdot \text{K}^2} \right), \tag{7.3}$$

where $\dot{Q}_{mc}$ denotes the cooling power of the MC, $\dot{n}_3$ is the ^3He circulation rate, T_{mc} corresponds to the steady-state temperature, and T_{hex} denotes the temperature of the inflowing $^3\text{He}/^4\text{He}$ mixture from the counterflow heat exchangers. Base temperature T_0 of the cryostat is reached in case $\dot{Q}_{mc}$ exactly compensates for the heat leak $\dot{Q}_l$. In case we assume a proper precooling $T_{hex} \simeq T_{mc}$, the applied heater power P satisfies the relation

$$P(T_{mc}) = 84 \dot{n}_3 \left(T_{mc}^2 - T_0^2 \right). \tag{7.4}$$

Thus, if the MC thermometer is properly calibrated, we expect that P shows a parabolic dependence on the detected MC temperature. In case we know that the sensor is properly calibrated above a certain temperature threshold T_t, we can fit Eq. (7.4) to the temperatures beyond this threshold and check whether measured temperatures $T < T_t$ obey the predicted quadratic dependence. Deviations at lower temperatures indicate that the thermometer is not calibrated sufficiently well. In Fig. 7.4(b), we find that all detected temperature points lie on the parabola. From the fit, we find a base temperature $T_0 = 19\,\text{mK}$ and a circulation rate $\dot{n}_3 = 631\,\mu\text{mol s}^{-1}$. In addition, the parabola method enables us to detect the heat leak of Bob from the offset, $\dot{Q}_l \simeq 19.1\,\mu\text{W}$. Resulting from the large number of resistance bridges, pumps, and PTR compressors in the Eve lab, operated with strong currents, it is of crucial relevance to ensure that there is no crosstalk between different thermometry devices, e.g., due to ground loops. Such crosstalk has emerged between the two resistance bridges in the Bob lab. In addition, since the `Lakeshore` resistance bridge for Bob and the corresponding preamplifier initially have been positioned multiple meters away from the cryostat, the unshielded cables connecting cryostat and preamplifier can pick up sufficient noise to deteriorate thermometry results.
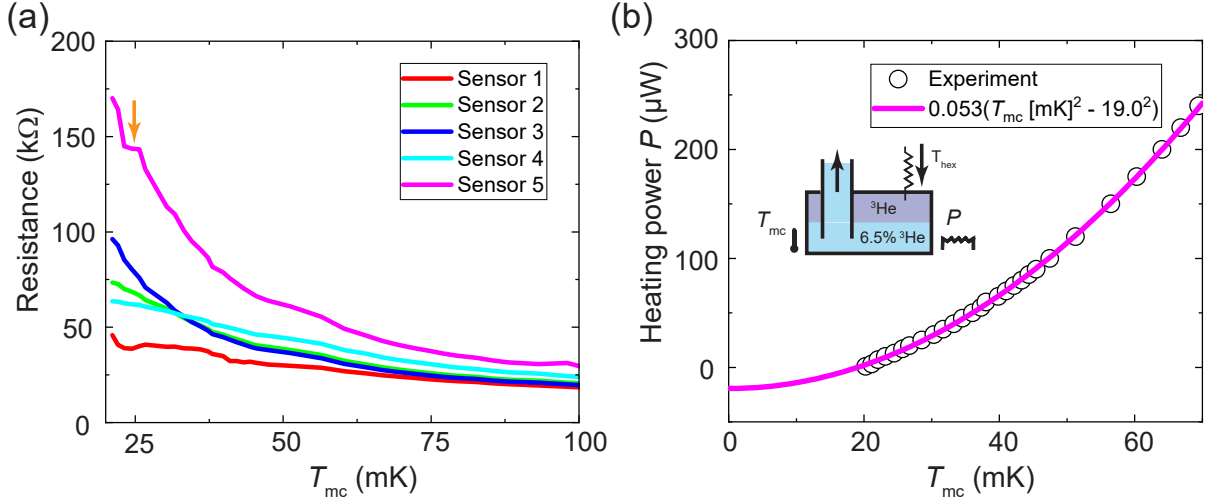
Figure 7.6: (a) Measured calibration curve for 5 new RuO_2 sensors. The orange arrow marks the flat region around $25\,mK$ rendering sensor 5 less useful. (b) Equilibrium MC temperature of Bob as a function of applied heater power (dots). The solid line corresponds to a fit based on the expected quadratic dependence, which enables one to extract the ^{3}He circulation rate and the MC base temperature.

Consequently, a reliable sensor readout is only possible with comparably high excitation voltage, $V_{ex} = 200\,\mu V$. At base temperature, this excitation voltage causes an increase of a few millikelvin in the thermometer readings. In case we want to reliably resolve low temperatures, we need to minimize this excitation voltage. For a well-coupled sensor at the MC plate, we obtain a temperature uncertainty

$$\Delta T = \frac{R_0 V_{ex}^2}{190 \dot{n}_3 T_{mc}^2 R_0^2 + V_{ex}^2 \left(\frac{\partial R}{\partial T} \right) \Big|_{T=T_{mc}}} + \mathcal{O}[(\Delta T)^2], \tag{7.5}$$

since the sensor voltage disturbs thermal equilibrium. Here, R_0 corresponds to resistance for the hypothetical $V_{ex} = 0$. The partial derivative of the sensor calibration curve $R(T)$, determines how a resistance change due to dissipated heat translates into an effective uncertainty in temperature. As a result, we install an analog low-pass filter for each twisted pair of thermometry wires on the fridge top, in analogy to Fig. 3.2. The filters are placed inside a shielded aluminum box and we mount the preamplifiers for our resistance bridges directly on top of these boxes. To manufacture the required PCBs for the filter, according to the design in Ref. 245 and Ref. 296, we print the circuit layout onto overhead transparencies and use the resulting pattern for optical lithography.[8] The circuit structure is developed in an NaOH bath and etched with $FeCl_3$. In addition, we shield all relevant cables using grounding wires and establish common ground between all preamplifiers, filters, and cryostat. These modifications eventually enable us to reduce the excitation

---

[8]We use a `Bungard` `120206E33 FR4 Photo Resist PCB` for this purpose.
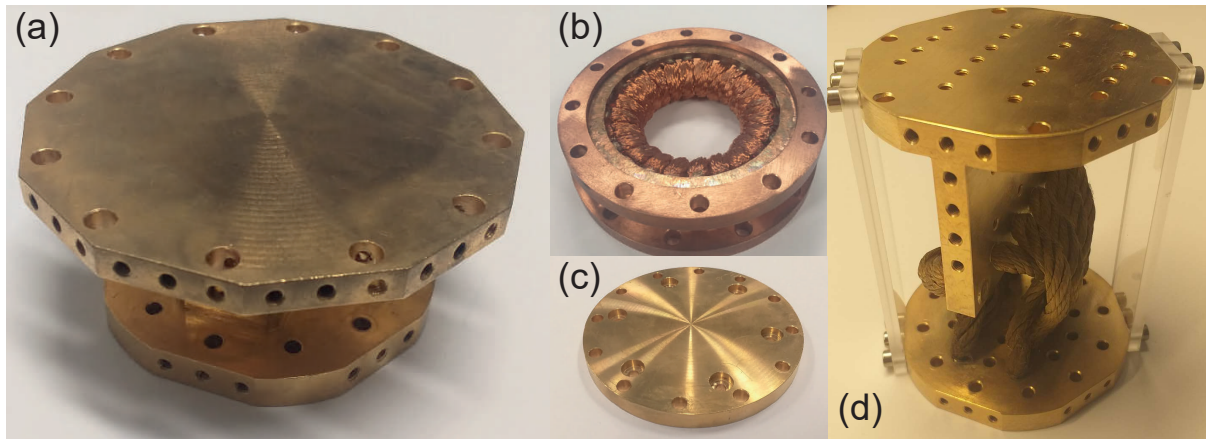
Figure 7.7: Alice fridge PTR upgrade. (a) Adapter component between the PT2 plate and the copper braids used for mechanical decoupling. A photograph of these braids is provided in panel (b). (c) Adapter plate between the second stage of the `PT420` cold head and the copper braids. (d) Photograph of the original thermal coupling component for comparison.

voltages for thermometry with our RuO_2 sensors by one order of magnitude, $V_{ex} = 20\,\mu V$.

7.1.3 Upgrading Alice with a PT420 cold head

According to estimations of `OINT`, the cryogenic link adds an additional heat load of $0.5\,W$ to each PT2 plate of Alice and Bob. This load comes on top of the precooling requirements for Alice's dry 1 K-pot and dilution circuit. Alice's `PT410-RM` cold head provides a PT2 cooling power of $1\,W$, which we have found to be insufficient to sustain a stable operation of the Alice fridge [288]. As a result, we have decided to upgrade Alice with a `PT420-RM` cold head to gain an additional $1\,W$ of PT2 cooling power. Since the new cold head has different geometric dimensions compared to the old one, we need to redesign the thermal coupling from the cold head to the PT2 plate of the cryostat. In addition, we need to open the precooling, 1 K, and mixture circuits. Photographs of the elements forming the new thermal coupling are provided in Fig. 7.7. The central component is shown in Fig. 7.7(a) and consists of a massive block of gold-plated OFHC copper with large surface areas to establish a strong thermal contact between cold head and PT2 plate. The top of the element is dodecagonally shaped to enable flexible mounting of additional components such as DC looms, which need to be properly thermalized at the PT2 stage. Since pressure oscillations in the PTR translate to mechanical vibrations of the cold head, we need to mechanically decouple the cold head from the cryostat, since our superconducting quantum chips might be susceptible to mechanical noise. We realize this mechanical decoupling at the PT2 stage using copper braids, which are shown in Fig. 7.7(b). These copper braids are twisted in a specific way to ensure quasi-metallic thermal contact. In this way, we maintain strong thermal coupling between the cold head
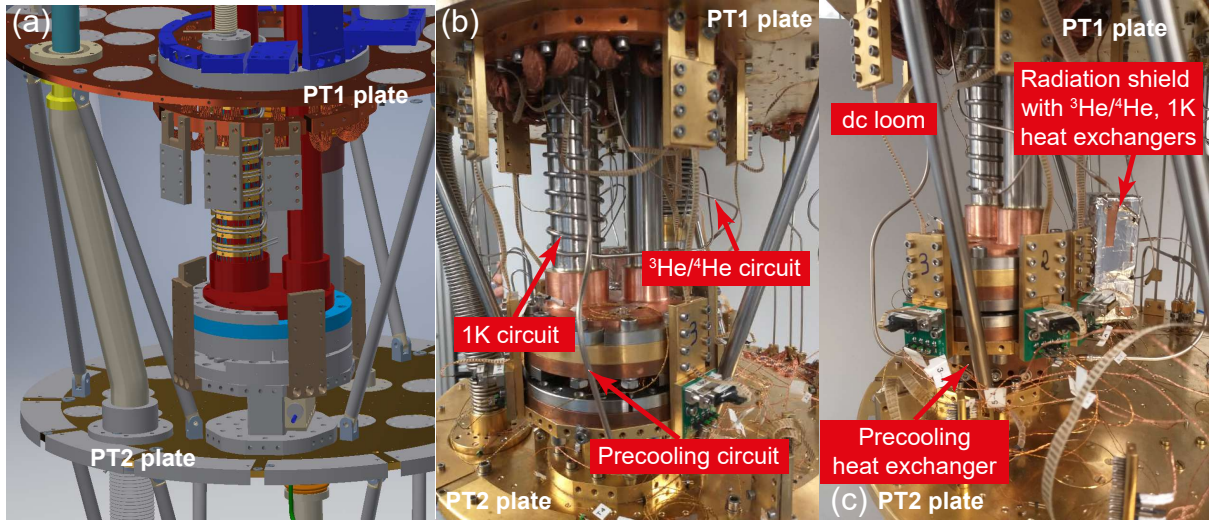
Figure 7.8: Alice fridge PTR upgrade. (a) CAD drawing for the integration of the `PT420` cold head into the cryostat. (b) Photograph showing the front view of the mounted `PT420` cold head as well as the resoldered helium circuits. (c) Photograph showing the corresponding back view.

and PT2 plate.[9] For the PT1 plate, we use the braids from the previous design of Alice [288]. Figure 7.7(c) shows the adapter plate connecting the cold head and the copper braids. Due to the restricted space resulting from the dense twisting of the braids, we employ counterbores for the screws, fixed to the cold head from the bottom. To establish optimal thermal contact, it is necessary to tighten these screws with sufficiently high torque. On the other hand, since the threads in the cold head consist of soft copper and we use SS M5 screws, it is possible to damage the thread in case one applies excessively strong torques. By conservation of energy, it can be shown that torque M relates to force F in the screw by [405]

$$M = F\frac{d_2}{2}\left[\tan\left(\varphi + \rho'\right) + \mu_{\mathrm{h}}\frac{d_{\mathrm{h}}}{d_2}\right],\tag{7.6}$$

where d_2 is the screw pitch diameter, d_{h} is the effective diameter of the screw head and μ_{h} is the friction coefficient related to the screw head surface. For a metric thread, the pitch angle φ and the friction angle ρ' can be expressed via $\tan\varphi = P/(\pi d_2)$ and $\tan\rho' = 2\mu_{\mathrm{t}}/\sqrt{3}$, where P denotes the slope of the screw and μ_{t} is the friction coefficient of the thread [406]. From Eq. (7.6), we can calculate the tension σ in the copper thread of the PT2 plate [407]. To avoid plastic deformation of the thread, we have to fulfill the condition $\sigma \leq \nu R_{\mathrm{e}}$, where R_{e} is the 0.2% elastic yield point of copper and $0 \leq \nu \leq 1$ is a safety factor [405]. The torque is then bounded by

---

[9]The copper braids have been provided by `OINT` and we acknowledge numerous fruitful discussions with `OINT` regarding the redesign of our cold head coupling.

$$M \leq \frac{\nu \gamma R_{\mathrm{e}}}{2} \frac{\pi D d_2 H_1 \left[d_2 \tan \left(\varphi + \rho' \right) + \mu_{\mathrm{k}} d_{\mathrm{k}} \right]}{P}, \tag{7.7}$$

where γ denotes the fraction of load-bearing threads, D is the thickness of the PT2 cold head plate and H_1 is the thread depth. By inserting the corresponding dimensions for an M5 screw and the PT2 plate under the conservative assumption $\mu_{\mathrm{t}} = \mu_{\mathrm{h}} = 0.2$, we find the relation $M[\mathrm{Nm}] \leq 0.101 \times \nu \gamma R_{\mathrm{e}}[\mathrm{MPa}]$. With the conventional choice $\gamma = 0.7$ and a relatively large safety margin $\nu = 0.5$, we find for soft copper (R_{e} typically $\sim 150\,\mathrm{MPa}$) that $M \lesssim 5.3\,\mathrm{N\,m}$ [405].[10] As a result, we tighten the screws with $5\,\mathrm{N\,m}$.[10] Apart from the copper braids, all the copper components have been annealed at $700\,^{\circ}\mathrm{C}$ for a time of $21\,\mathrm{h}$ at a pressure of $5 \times 10^{-5}\,\mathrm{bar}$ with atmospheric gas composition,[11] and gold-plated afterwards. Figure 7.7(d) shows our previous thermal coupling component, also visible in Fig. 3.1, for comparison [288].[12] A CAD drawing [13] for the redesigned coupling is provided in Fig. 7.8(a). A front view of the installed PT420 cold head is shown in Fig. 7.8(b) and Fig. 7.8(c) shows the corresponding back view. To optimize the thermal contact, we apply a thin layer of vacuum grease to all contact surfaces.[14] To evenly distribute the force over the whole surface, we additionally employ SS brackets for the screws instead of conventional washers. For optimal precooling of the inflowing gas, we install the heat exchangers for the 1 K pot and for the mixture circuit directly at the cold head adapter plate before the braids. Furthermore, to ensure sufficient precooling, the 1 K circuit is spirally coupled to the cold head. In addition, we cover the heat exchangers with a radiation shield as shown in Fig. 7.8(c) to protect them from radiation leaking from room temperature environment. This radiation leak is caused by the fact that the PT1 plate needs to be mechanically decoupled from the cold head. This requirement implies that it is not possible to install a rigid radiation shield for the gap between cold head and cryostat. To lower the impact of this heat leak, we clamp rolled superinsulation into this gap and fix it with aluminum tape. The heat exchanger for the precooling circuit is directly attached to the component shown in Fig. 7.7(a). In the next step, we resolder the precooling circuit, 1 K circuit, and $^3\mathrm{He}/^4\mathrm{He}$ circuit using Copper-nickel capillaries. The capillaries are connected using soldering sleeves fabricated from copper.[15] To properly place the CPA1114 compressor required for the operation of Alice's new cold head, we need to modify the structure of Eve lab and install an additional maintenance door, see Fig. 7.5. In addition, we coil up the 20 m long $^4\mathrm{He}$ SS flex-lines connecting compressor

---

[10]A torque of $5\,\mathrm{N\,m}$ has also been advised by Cryomech.

[11]The annealing has been performed at the Kristalllabor at the Physics Department of TU Munich.

[12]After dismantling, the component has been gold-plated at Metallveredelung Gebrueder Wigl GmbH and transformed into an exhibit.

[13]For CAD as well as for technical drawing, we use Autodesk Inventor 2019.

[14]We use Apiezon N high thermal conductivity vacuum grease for this purpose.

[15]We use L-PbSn40(Sb)/zh solder, together with Castolin flux for this purpose. To avoid formation of cold leaks in the long term, the soldering procedure requires careful handling and cleaning with distilled water. Tinol flux can be used as an alternative.

and cold head and fix them on the ceiling of Eve lab by an `item` frame.[16] Furthermore, we attach the motor for Alice's cold head to the cryostat frame using a suitable adapter plate.[17] After the soldering procedure, we perform ^{4}He throughput tests as well as careful leak tests. To measure the heat distribution over our redesigned thermal coupling, we install two additional RuO_2 thermometers at the PT2 stage, one on top of the cold head (T1) and the second one directly below the copper braids (T2). The conventional PT2 `Cernox` thermometer is located on the plate, far away of the cold head. The black RuO_2 probes for sensors T1 and T2 are directly exposed to radiation and not protected by a radiation shield, like for the radiation-shielded `Cernox` sensor. Thus, T1 and T2 enable us to directly measure the effect of the aforementioned radiation leak with respect to the OVC shields. In the next step, we perform a test cooldown for the Alice cryostat with the new cold head. We reach a minimal MC temperature of 12 mK and a steady-state PT1 (PT2) temperature of 49.2 K (3.1 K). With sensor T1 (T2), we reach a final temperature of 4.1 K (5.8 K). As expected, these temperatures are higher compared to the PT2 plate readings, due to thermal radiation. The temperature difference between T1 and T2 can be explained by the fact that the impact of radiation on both sensors depends on the view factor and thus the solid angle of the radiation leak with respect to the sensor. Since the sensors have a resistance of approximately 3 kΩ in the regime at 4 K, we can simultaneously employ them as heaters and investigate the resulting PT2 temperature as a function of the applied power.[18] The result of such a measurement is shown in Fig. 7.9(a) and we extract linear power dependence. This behavior can be understood by considering the result for the PT2 cooling power $\dot{Q}_{PT2}$ derived in Ref. 408. Using phasor analysis one obtains

$$\dot{Q}_{PT2} = \frac{Rp_1|\dot{m}|}{p_0 M} T_{PT2} \cos\theta, \tag{7.8}$$

with the gas constant $R = 8.314 \, \text{J} \, \text{mol}^{-1} \, \text{K}^{-1}$, molar mass M, equilibrium pressure p_0, pressure modulation amplitude p_1, and phase difference θ between mass flow and sinusoidal pressure oscillation. From the measurement, we find that in case the cryogenic link is attached and adds an additional heat load of 0.5 W, we expect a PT2 temperature of approximately 3.6 K, sufficiently low to condense ^{4}He. As a result, we expect the cooling power provided by the `PT420` cold head to be sufficient to enable stable operation of the cryogenic link. Since the result in Eq. (7.8) is valid for any quasi-ideal working gas with adiabatic index $\gamma = 5/3$, additional 33 % of cooling power could be gained by operating the PTR with ^{3}He [409, 410]. In practice, this approach is not chosen due to economic limitations. In addition, we determine the impact of the heat load added by our four HEMT amplifiers in Alice. As it can be seen from Fig. 7.9(b), the MC temperature increases to 21 mK and the steady-state PT2 temperature increases by 20 mK. As a

---

[16]For careful adjustment of the flex-line position at the ceiling, we have constructed a movable tripod using three hydraulic jacks.

[17]We use ten `5/16-24UNF` screws for this purpose.

[18]We use a `UNIWATT NG 304 Labor Netzgerät` from PEWA Messtechnik GmbH for this purpose.

(a)

(b)
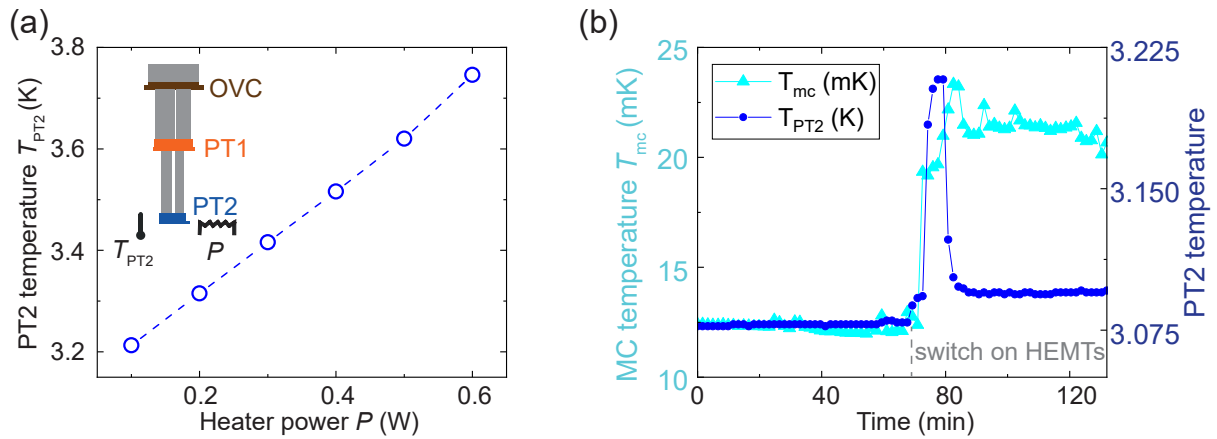
Figure 7.9: (a) Experimentally determined PT2 temperature as a function of applied heater power on the PT2 stage. The power $P = 0.5\,\text{W}$, estimated to be added by the cryogenic link, correspond to $T_{\text{PT2}} = 3.6\,\text{K}$. This temperature is expected to be sufficiently low to ensure stable operation of the system. Dashed lines are a guide to the eye. (b) Evolution of the MC and PT2 temperatures after we apply a heat load expected for the HEMT amplifiers. Lines are a guide to the eye.

result, the influence of the HEMT amplifiers on the effective precooling of the mixture can be neglected. To enable more heat load estimations during operation of the cryogenic link, we install separate heaters on the PT2 stage of Alice and Bob. Resulting from the comparably large targeted heating powers, we choose a significantly higher heater resistance of $1\,\text{k}\Omega$, compared to our conventional $100\,\Omega$ heaters. This choice is done to minimize power dissipation in the BeCu DC loom, which shows a typical resistance of $100\,\Omega$. In the Bob cryostat, we install a separate PT2 heater which is not integrated into the DC loom but separately connected to the OVC shield via manganin wire.

7.2 Cooldown procedure and operation

Here, we investigate the cooldown procedure and the performance of our cryogenic link. We compare four different types of cooldown, listed in Tab. 7.1. The first type of cooldown (CD 1) has been performed prior to the previously described modifications, using Alice's old `PT410` cold head. The second type of cooldown (CD 2) corresponds to Alice's test cooldown discussed in Sec. 7.1.3. The third cooldown type (CD 3) for the cryogenic link has been performed after installation of the `PT420` cold head. The fourth cooldown type (CD 4) corresponds to a repetition of CD 3 after further optimizing thermal isolation between adjacent cryostat shields and after attaching additional superinsulation foil layers at strategically relevant positions. Following a full assembly of the system as well as successful leak tests, we first start the PTRs for Alice, Eve and Bob. Eve and Bob are operated via a `Python` script running on Bob's control CPU. For Bob, the cooldown procedure follows the standard `Triton` cooldown protocol, implying that Bob

Table 7.1: List of different cooldown categories for Alice. Case CD 2 describes a test cooldown for Alice without the cryogenic link attached.

List of cooldown categories		
Category	Alice cold head	comment
CD 1	PT410	no further optimization
CD 2	PT420	Alice only
CD 3	PT420	no further optimization
CD 4	PT420	optimized regarding superinsulation and thermal isolation

starts precooling with the ^{3}He/^{4}He mixture as described in Sec. 3.1.1. Eve features a closed precooling circuit based on ^{4}He and cryogenic sorption pumps. Next, we start the precooling procedure for Alice, which we realize manually via a dedicated ^{4}He circuit and pressure up to 4.5 bar. The following precooling procedure takes approximately three days during which Alice's precooling pressure needs to be adjusted manually. The corresponding pressures, forming the optimal trade-off between proper coupling of the lower temperature stages to the PT2 stage and minimizing heat leaks to the room temperature stage, have been empirically determined over multiple cooldowns.

Figure 7.10 shows Alice's PTR temperatures during precooling for each cooldown, listed in Tab. 7.1. The sudden jumps in temperature correspond to a manual change of precooling pressure and insets show the respective final temperature in the steady-state regime. During our first cooldown of the entire cryogenic link with the PT420 cryocooler (CD 3), we reach a final temperature of 59 K (4.6 K) on the PT1 (PT2) stage. Despite significant improvement in comparison to the PT410 cold head, where we have reached a PT2 temperature of 6 K, the final PT2 temperature still exceeds the threshold for helium liquefication (4.15 K at normal pressure). As a result, the dilution cycle only starts up in Bob fridge, which has an efficient JT cooler in the mixture line. In Alice, the mixture condenses and the 1 K pot runs without external load, but the mixture cycle does not start up in a self-supporting way for higher throughputs. Thus, we further optimize the system by optimizing the thermal isolation between the link shields. In this regard, it turns out that the copper braids over the PT1 shield belllows, visible in Fig. 7.3(b), have touched the OVC shield, and have thus created a weak thermal short. To solve this problem, we have tightened the braids to the SS bellows using wax strings. Furthermore, we have reduced the impact of thermal radiation by covering the SS bellows with additional Mylar superinsulation. Following these modifications, the heat load is eventually sufficiently low to allow for stable circulation of the ^{3}He/^{4}He mixture. Cooldowns following these adaptations fall into category CD 4 and we observe that, in the scenario shown in Fig. 7.10, we reach a steady-state temperature of 49 K (3.6 K) for PT1 (PT2). We observe excellent agreement with the estimated heat load, added by the cryogenic link, as shown in Fig. 7.9(a). From the steady-state temperatures in Fig. 7.10,
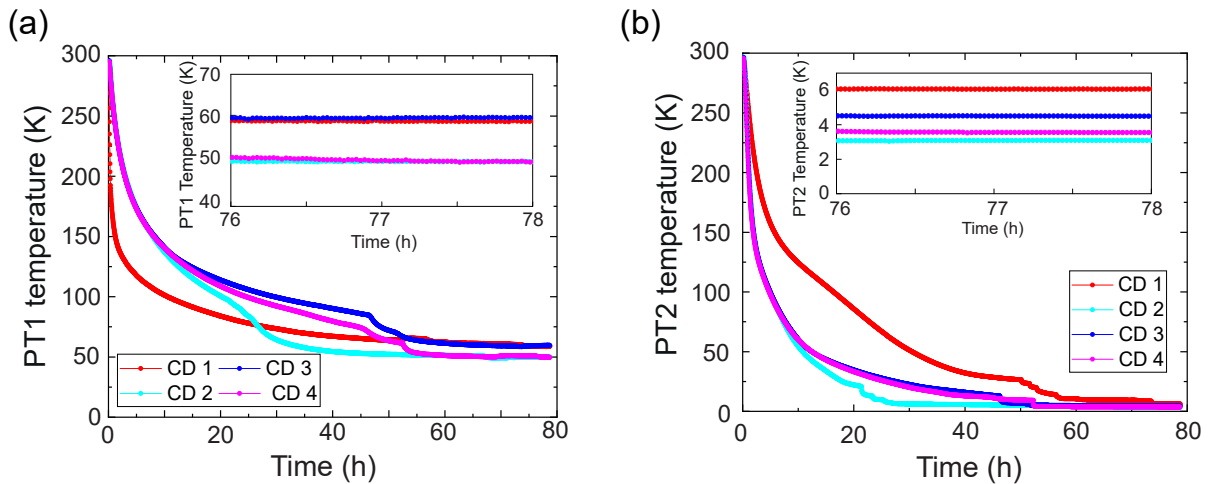
Figure 7.10: (a) Alice PT1 temperature for various cryolink cooldowns with the `PT410` cold head (red), the `PT420` cold head (blue), and the `PT420` cold head after optimizing thermal isolation (magenta). The cyan line shows data from the "Alice only" test cooldown with the `PT420` cold head described in Sec. 7.1.3. The inset shows steady-state temperatures. (b) Respective results for the Alice PT2 plate.

we observe that the final PT1 temperature is determined by the thermal leak to the OVC shield at the link adapter, whereas the final PT2 temperature is determined by the cooling power provided by the cold head. The temperature curves in Fig. 7.10 additionally reveal a different heat exchanger design for the `PT410` and `PT420` cryocoolers. For the `PT410` model, PT1 temperature drops significantly faster, as compared to PT2. The situation is reversed for the `PT420` cold head, which is crucial for our purposes, since we need to optimize for minimal PT2 temperatures. Following the precooling procedure, we start helium condensation as well as dilution cooling. Since Bob starts to empty his precooling circuit at a MC temperature of $\simeq 10\,\mathrm{K}$, it is crucial to properly evacuate Alice's precooling circuit at significantly higher temperatures, ideally above $15\,\mathrm{K}$. Otherwise, Bob liquefies the helium used for precooling on Alice's side and creates irreversible thermal shorts between the MC and still stage. After emptying Alice's precooling circuit, we keep Alice in idle mode and wait for Bob to start with JT cooling. Bob has sufficient cooling power to cool Alice's MC to $\simeq 500\,\mathrm{mK}$ over the link. A typical cooldown curve of the MC stage is provided in Fig. 7.11(a). After Bob has cooled Alice below LHe temperature, we can subsequently start the $1\,\mathrm{K}$ circulation of Alice and condense the $^3\mathrm{He}/^4\mathrm{He}$ mixture on Alice's side. This process typically takes approximately $6\,\mathrm{h}$. Alice's condensation is thereby effectively supported by the Bob cryostat. The overall cooldown procedure takes about $80\,\mathrm{h}$, as shown in Fig. 7.10. Figure 7.11(b) shows the final temperature profile of the MC section of the cryogenic link for CD 1, CD 3 and CD 4. In case of CD 1, the cooling power provided by the PTR is insufficient to operate Alice's $^3\mathrm{He}/^4\mathrm{He}$ cycle. Even in this case, Bob manages to hold Alice's MC at a steady temperature of $506\,\mathrm{mK}$ over
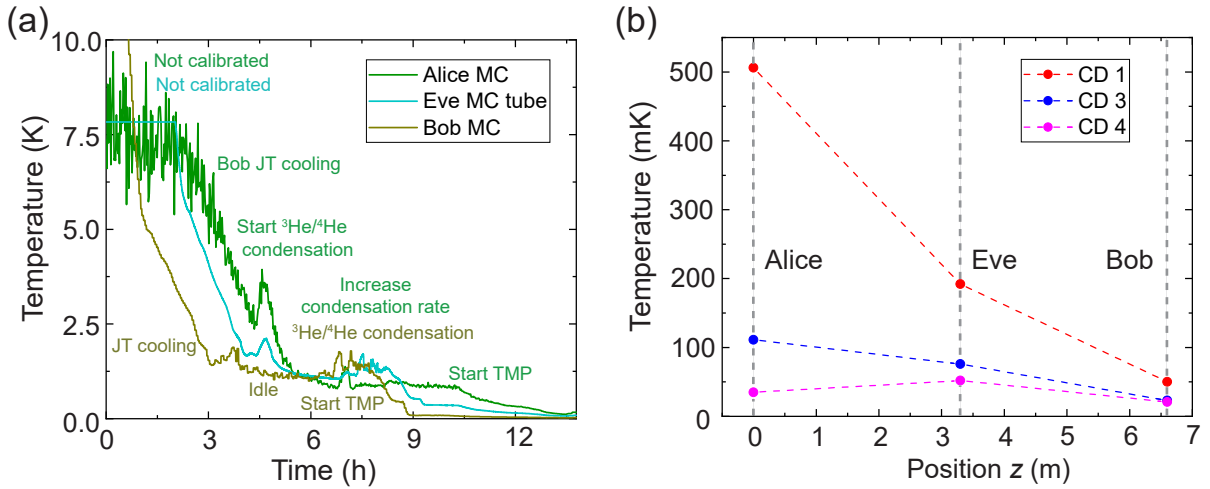
Figure 7.11: (a) Temperature evolution of the MC stage during a cooldown of category CD 4. Before we condense the ^{3}He/^{4}He mixture on Alice's side, we wait until Bob's JT cooler precools Alice to temperatures significantly below LHe. (b) MC temperature T_{mc} in the cryogenic link. In case of CD 1, it has not been possible to operate the dilution cycle of Alice. For CD 3, Alice could only be operated via the TMP backing pump, leading to significantly reduced cooling power. Red, blue, and magenta dashed lines are a guide to the eye.

the 6 m long MC tube. For CD 3, we have sufficient cooling power to sustain ^{3}He/^{4}He circulation, but only via Alice's TMP backing pump and not by the TMP itself, what leads to significantly lower cooling power compared to conventional operation. In this case, we reach a final temperature of 111 mK on Alice's side. By reducing the heat leaks at the link adapters prior to CD 4, we can operate Alice with the TMP, leading to a minimal MC temperature of 33 mK with a suitable still heater configuration. We reach a minimal temperature of 52 mK in the center of the cryogenic link, which coincides with the center of Eve. However, to stabilize the condensation pressures, we usually operate Alice without a still heater, leading to a steady-state temperature of approximately 50 mK. Bob reaches a base temperature of 21 mK.

7.3 Heat transfer over the cryogenic link

For the successful cooldown of the cryogenic link in CD 4, we investigate the heat transfer through the system by selective heating of specific sections. Such an investigation is of crucial relevance in case we apply our system to artificially generate thermal channels. In addition, such measurements can become of particular interest for potential future experiments to determine effects emerging from quantization of heat conductivity [411–413]. In addition, we investigate the lifetime limitations for our cryogenic system, which so far limit the length of particular cooldowns to approximately three weeks. The temperature $T(\mathbf{r}, t)$ of a specific temperature stage in the cryogenic link is determined by the heat

balance equation [414, 415]

$$\rho c \frac{\partial T(\mathbf{r},t)}{\partial t} - \nabla\left[\lambda(\mathbf{r})\nabla T(\mathbf{r},t)\right] = \underbrace{g_{\mathrm{r}}(\mathbf{r})\left[T_{\mathrm{r}}^4 - T(\mathbf{r},t)^4\right]}_{\text{radiation}} + \underbrace{\sum_{k,l} g_k\left[T_k - T(\mathbf{r}_l,t)\right]}_{\text{coupling to higher stages}}$$

$$+ \underbrace{g_{\mathrm{f}}\left[T_{\mathrm{f}} - T(\mathbf{r},t)\right]}_{\text{fluid}} + \underbrace{\sum_i \dot{q}_i \delta(\mathbf{r}-\mathbf{r}_i)}_{\text{local heating}}, \tag{7.9}$$

where ρ, c and $\lambda(\mathbf{r})$ denote density, specific heat, and thermal conductivity of the shield. The first term on the right side describes heat load via thermal radiation from the radiation shield with the temperature T_{r} which is assumed to be constant. The position-dependent geometric prefactor $g_{\mathrm{r}}(\mathbf{r})$ depends on the view factor with respect to the radiation leak, as well as on the emission coefficients of the respective material of the shield and its effective surface area [415]. In practice, we minimize $g_{\mathrm{r}}(\mathbf{r})$ by using superinsulation foil and by properly closing all radiation leaks. The second term on the right side describes heat added by direct thermal conduction between respective temperature stages, where index k labels the stage and index l denotes the location at which we couple to stage k. During precooling, we artificially increase this contribution whereas we attempt to minimize it during operation. The third term corresponds to convective heat flow due to a fluid with temperature T_{f} and the fourth term results from local heating with specific power $\dot{q}_i$ using, e.g., a PID control architecture. In the following, we experimentally study heat transfer within the MC stage. In this case, Eq. (7.9) needs to be solved under the boundary condition that the cooling power at the mixing chamber positions of Alice and Bob is determined by Eq. (7.3). In addition, we numerically solve Eq. (7.9) for heat transport over our QLAN cable. First, we vary the center temperature T_{center} of our superconducting transmission line inside of the cryogenic link. The results of this measurement are plotted in Fig. 7.12(a). We clearly observe that MC temperatures of Alice and Bob, as well as the temperature of the MC tube inside the Eve cryostat, show an approximately linear increase as a function of T_{center}. We conclude that thermal conduction via the MC tube is the dominant source of heat transfer in this case. We explain the deviation from linearity for the Eve MC tube by a comparably strong temperature dependence of the thermal conductivity of PEEK, as shown in Fig. 7.4(b). To realize a stable platform for quantum experiments, we stabilize our sample stage in Alice to $70\,\mathrm{mK}$. We choose a slightly higher value than the MC base temperature to achieve robustness towards temperature fluctuations in the cryogenic link. As it can be seen in Fig. 7.12(a), for our entanglement JPAs (JPA 1 and JPA 2) the sample stage temperature is independent of the temperature of the transmission line up to $T_{\text{center}} \simeq 300\,\mathrm{mK}$. Since within our frequency range, this temperature already corresponds to the Johnson-Nyquist regime [cf. Fig 3.7(b)], we can use the cryogenic link to verify influence of local environmental thermal noise in a superconducting environment. Following that, we stabilize the temperature in the
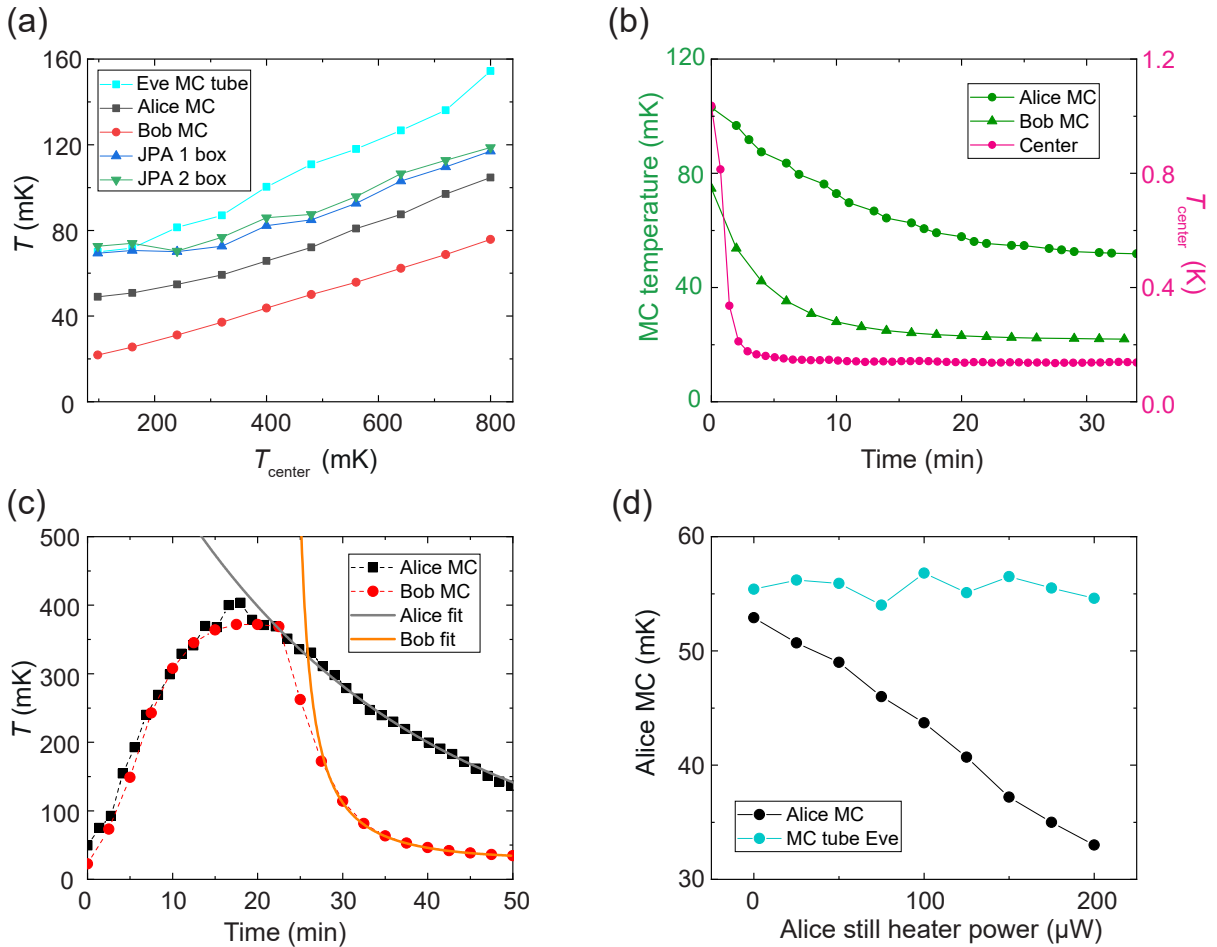
Figure 7.12: (a) Effect of PID stabilization of the center temperature T_{center} of our transmission line on the MC tube. The PID control architecture is installed on top of the central support holder [cf. Fig. 7.3(a)]. We detect the respective steady-state MC stage temperature and the Alice sample stage temperature (JPA 1 and JPA 2). Except for the latter, we observe an approximately linear increase of the steady-state temperatures, implying that heat transfer is dominated by thermal conductance. The thermometer "Eve MC tube" is fixed at the outside of the MC tube below Eve. Lines are a guide to the eye. (b) Time evolution of T_{center} and the MC temperature after heating to $T_{\text{center}}(t = 0) = 1\,\text{K}$ and then switching off the heater. Lines are a guide to the eye. (c) Stress test for the cryogenic link. We stabilize the center at $T_{\text{center}} = 4\,\text{K}$ and find that condensation of Alice breaks down after 20 min. We fit Alice's data with an exponential (solid gray line) and Bob's with Eq. (7.11) as described in the main text (orange line). Dashed lines are a guide to the eye. (d) Still heater test for Alice, demonstrating that we can reach a minimal MC temperature of 33 mK. Lines are a guide to the eye.

center of the transmission line to $T_{\text{center}} = 1\,\text{K}$ and measure temperature relaxation in the transmission line as well as at the MC in Alice and Bob after switching off the heating. The corresponding results are shown in Fig. 7.12(b). We find that the temperature of the transmission line relaxes to equilibrium within 10 min. In contrast, the MC stages of Alice

and Bob require approximately 30 min to reach equilibrium due to their comparably large heat capacity. The data shown in Fig. 7.12(c) corresponds to a stress test of our cryogenic link. During this test, we have investigated for how long we can stabilize the center temperature at $T_{\text{center}} = 4\,\text{K}$, such that the cryogenic link effectively forms a thermal channel resembling a LHe bath. We find that, within approximately 20 min, the MC stages in Alice and Bob heat up to 380 mK. At this point, we need to switch off the heater since the condensation pressure for Alice's 1 K circuit as well as for the $^3\text{He}/^4\text{He}$ circuit reach critical values.[19] Similar as in Fig. 7.12(b), Bob relaxes back to equilibrium within 30 min, whereas Alice cools down slower since a significant fraction of the $^3\text{He}/^4\text{He}$ needs to be recondensed on the Alice side. In addition, this finding indicates that our system is asymmetric regarding cooling power. In contrast, Alice and Bob show similar behavior during the warm-up (data not shown), implying that the cryogenic link is symmetric with respect to thermal conductivity and heat capacity. As it can be seen in Fig. 7.12(c), we can model the cooling curves of Alice and Bob. Alice can be accurately fitted by an exponential decay, implying approximately constant cooling power of the MC in the temperature regime $150 - 350\,\text{mK}$, which results in a Newton-like cooling law. For Bob, we fit the cooldown for temperatures below 100 mK. In this case, we consider Eq. (7.9), evaluated at the position of Bob's MC. Thus, we turn the corresponding boundary condition, Eq. (7.3), into an additional source term. In addition, we assume that the heat balance is dominated by conductive heat transfer. Consequently, the temperature of Bob's MC satisfies the differential equation

$$\frac{dT}{dt} = g[T_{\text{e}} - T(t)] - aT(t)^2, \tag{7.10}$$

where T_{e} corresponds to an effective environmental temperature associated with the heat leak. The constants a and g are used as fit parameters. By defining the auxiliary function $h(x) = x + g/(2a)$, the solution of this Riccatti type equation [163] can be expressed as

$$T(t) = h(T_*) \left[\frac{h(T_0) + h(T_*) \tanh[ah(T_*)t]}{h(T_*) + h(T_0) \tanh[ah(T_*)t]} - 1 \right] + T_*, \tag{7.11}$$

where T_* denotes the steady-state temperature and $T_0 = T(0)$. We observe from the fit in Fig. 7.12(c) that the asymptotic cooldown behavior of Bob follows Eq. (7.11). In a second stress test for the cryogenic link, we turn off Eve's PTR while not modifying Alice and Bob. We find that the system remains operational for 20 min under these circumstances. Figure 7.12(d) shows the result from a still heater test for Alice and we find that the base temperature of Alice can be significantly reduced by heating the still. The lowest observed temperature at still heater power of 200 µW is 33 mK and corresponds to the temperature value shown in Fig. 7.11(b) for CD 4. The temperature downtrend in Fig. 7.12(d) indicates possible lower temperatures for higher still heater power. The practical lower bound

---

[19]We are limited by the maximal exhaust pressure of 1 bar for the `NeoDry 60E Kashiyama` 1 K pump as well as for the `80C Edwards` scrolls pump in the mixture circuit.

for Alice's MC temperature is determined by the condensation pressure in the $1\,\mathrm{K}$ and $^3\mathrm{He}/^3\mathrm{He}$ circuits, which monotonically increases as a function of the still heater power and is required to be below $1\,\mathrm{bar}$. We find that the temperature T_{Eve}, measured at the outside of the MC tube below Eve, is effectively independent of Alice's base temperature. If we assume a constant specific heat load $\dot{q}$ over the MC tube, we find

$$T_{\mathrm{Eve}} = \frac{T_{\mathrm{A}} + T_{\mathrm{B}}}{2} + \frac{\dot{q}l^2}{8\lambda}, \tag{7.12}$$

where T_{A} (T_{B}) denotes the temperature of Alice (Bob), l corresponds to the link length, and λ denotes the thermal conductivity of the MC tube. Consequently, the heat load added by heating the still, approximately compensates for the reduction of Alice's temperature.

Heat transfer over the QLAN transmission line   Next, we investigate the spatial heat distribution along our superconducting transmission line. To enable photon number calibration over the cryogenic link, the QLAN cables are connected to heatable attenuators on the Alice side. During the first successful cooldown of category CD 4, we measure a steady-state attenuator temperature of $102\,\mathrm{mK}$, as well as $T_{\mathrm{center}} = 121\,\mathrm{mK}$ in the center of the transmission line. Since these temperatures are comparably high, we increase the thermal coupling of the attenuator to the MC plate before the following cooldown of type CD 4, leading to an attenuator temperature of $46\,\mathrm{mK}$. Following this modification, the temperature of the cable in the center reaches a steady value of $T_{\mathrm{center}} = 110\,\mathrm{mK}$. In general, the measured center temperature reaches its minimum shortly after cooldown, before we switch on our RF devices. The minimally recorded temperature corresponds to $T_{\mathrm{center}} = 97.4\,\mathrm{mK}$. These elevated temperatures, especially the attenuator temperatures prior to the increase of thermal coupling, indicate that the cryogenic link adds a significant level of thermal radiation inside the MC tube. The high attenuator temperature is then explained by the fact that the heatable $30\,\mathrm{dB}$ attenuator can be well approximated as a black body, whereas the copper MC shields almost perfectly reflect thermal radiation. Consequently, in case of a radiation leak of the MC shield structure, the heatable attenuators form the dominant heat sinks. To determine the temperature profile of the transmission line, we consider the steady state of Eq. (7.9) and treat the transmission line as quasi-1D object of length l. In addition, we assume that thermal coupling to the MC is dominated by the silver wires with thermal conductivity λ_{Ag} and cumulative cross section A_{Ag}. We have

$$-\lambda_{\mathrm{Ag}}A_{\mathrm{Ag}}\frac{\partial^2 T}{\partial z^2} = \underbrace{\sum_{n=-(N-1)/2}^{(N-1)/2} \dot{q}[T(z)]\delta\left(z - \frac{nl}{N-1}\right)}_{\text{coupling of PEEK to MC tube}} + \underbrace{P_{\mathrm{r}}[T(z)]}_{\text{radiation}} + \underbrace{P_{\mathrm{h}}\delta(z)}_{\text{center heating}} . \tag{7.13}$$

We model thermal coupling of the $N = 13$ PEEK support holders to the MC tube with a finite Dirac-comb due to their tip-shaped geometry. The radiative heat transfer $P_\mathrm{r}[T(z)]$ depends on the view factor $F_{\mathrm{r}\to\mathrm{t}}$ between radiation leak (r) and transmission line (t). The corresponding expressions are given by [415]

$$\dot{q}[T(z)] = \lambda_\mathrm{P}[T(z)]\frac{A_\mathrm{P}}{h_\mathrm{P}}[T_\mathrm{tube} - T(z)], \qquad P_\mathrm{r}[T(z)] = \frac{\sigma[T_\mathrm{r}^4 - T^4(z)]}{\left(\frac{1-\varepsilon_\mathrm{r}}{A_\mathrm{r}\varepsilon_\mathrm{r}}\right) + \left(\frac{1-\varepsilon_\mathrm{t}}{A_\mathrm{t}\varepsilon_\mathrm{t}}\right) + \frac{1}{A_\mathrm{r}F_{\mathrm{r}\to\mathrm{t}}}}, \quad (7.14)$$

where T_tube corresponds to the temperature of the MC tube, assumed to be constant, and A_P (h_P) denotes the respective cross section (height) of the PEEK support holders and $\sigma = 5.67 \times 10^{-8}\,\mathrm{W\,m^{-2}\,K^{-4}}$ is the Stefan-Boltzmann constant. The quantities A_r (A_t) and ε_r (ε_t) denote the area and integral emissivity associated with the radiation leak. The last term in Eq. (7.13) corresponds to possible heating of the center with power P_h. We numerically solve Eq. (7.13) using a finite-difference method. In this regard, we make two approximations. Since the conditions in Eq. (7.14) imply that Eq. (7.13) becomes nonlinear, we apply the approximation $P_\mathrm{r} = \langle P_\mathrm{r}[T(z)]\rangle$, where $\langle\cdots\rangle$ implies an average over the temperature profile of the cable. The effect of this approximation is small since radiation emitted by the transmission line can be neglected due to the low temperature of the cable. In addition, we approximate $\lambda_\mathrm{P}[T(z)] = \lambda_\mathrm{P}[\langle T(z)\rangle]$. We update these averages in an iterative approach and repeat the numerical routine for M times, where we determine the averages $\langle\cdots\rangle$ for iteration step j from the solution in step $j-1$. We repeat the procedure until we converge, which is sufficient for $M = 50$ in our case. A third approximation is related to boundary conditions. As previously mentioned, Eq. (7.13) needs to be solved for fixed MC cooling power, a quantity depending on the solution itself. For our numerical solution, we approximate these boundary conditions with Dirichlet conditions, implying that we fix temperature at the boundaries. To estimate the error made by this approximation, we compare our numerical routine to a special case where Eq. (7.9) can be solved analytically. This case corresponds to the dependence of the temperature T_center on local heating of the center with specific power $p \equiv P_\mathrm{h}/A_\mathrm{Ag}$. In case we neglect any energetic loss apart from direct thermalization to the MC stage, the respective cooling power $\dot{q}$ of Alice and Bob adjusts in a way that the global energy balance between sources and sinks is satisfied, $p = -2\dot{q}$. As a result, we can rewrite Eq. (7.9) without any boundary conditions as

$$\frac{\partial T}{\partial t} - \kappa\frac{\partial^2 T}{\partial z^2} = -\frac{p}{2\rho c}[\delta(z - l/2) + \delta(z + l/2)] + \frac{p}{\rho c}\delta(z), \qquad (7.15)$$

where $\kappa \equiv \lambda_\mathrm{Ag}/(\rho c)$. We assume that, prior to switching on the heater at $t = 0$, the system is in thermal equilibrium at $T = T_0$ for $-\infty < z < \infty$, where we neglect any boundary effects emerging from the finite link length in the initial condition. The solution

can be determined via the Green's function [416]

$$G(z, t) = \frac{1}{\sqrt{4\pi\kappa t}} e^{-\frac{z^2}{4\kappa t}} \tag{7.16}$$

as

$$T_{\text{center}}(t) = T_0 + \int_0^t dt' \int_{-\infty}^{\infty} dz' G(z', t - t') \left[\frac{p}{\rho c} \delta(z') - \frac{p}{2\rho c} (\delta(z' - l/2) + \delta(z' + l/2)) \right]$$
$$= T_0 + \frac{p}{\rho c} \int_0^t ds \left[G(0, s) - G(l/2, s) \right]. \tag{7.17}$$

The result can be expressed as

$$T_{\text{center}}(t) = T_0 + \frac{p}{\rho c} \sqrt{\frac{t}{\pi\kappa}} \left(1 - e^{-\frac{l^2}{16\kappa t}} \right) + \frac{pl}{4\kappa\rho c} \text{erfc} \left(\frac{l}{4\sqrt{\kappa t}} \right), \tag{7.18}$$

where $\text{erfc}(x)$ denotes the complementary error function. For the steady state, we find the simple expression

$$\lim_{t \to \infty} T_{\text{center}}(t) = T_0 + \frac{P_{\text{h}} l}{4\lambda_{\text{Ag}} A_{\text{Ag}}}. \tag{7.19}$$

The factor of 4 here results from the symmetry of the system: half of the heater power flows over each half of the link length. This result can be directly compared to the center temperature obtained with our numerical routine for this specific scenario. We find typical deviations of $1 - 2\,\%$, which correspond to the approximation error of the global energy balance by Dirichlet boundary conditions. Next, we use our numerical model to determine the temperature profile for the realistic parameters and geometry. The exact value of λ_{Ag} is not known in our case since it sensitively depends on the purity of the material, the annealing, as well as on the quality of the mechanically established thermal contacts. Consequently, we do not know the residual resistivity ratio (RRR) at low temperatures. For a conservative estimation, we assume $\lambda_{\text{Ag}} \simeq 1\,\text{W\,K}^{-1}\,\text{m}^{-1}$, which is significantly lower than values measured for high purity silver. We then find that our experimental observations can be reproduced in case we consider a radiative heat load of $P_{\text{r}} = 0.52\,\text{µW}$. The corresponding results are shown in Fig. 7.13(a), where we take Alice's heatable attenuator temperature and Bob's MC temperature as Dirichlet boundary conditions. Stars correspond to the measured temperature values. We have determined $P_{\text{r}} = 0.52\,\text{µW}$ such that the orange curve matches the experimental center temperature. Our calculation predicts a center temperature of $T_{\text{center}} = 111.9\,\text{mK}$, which is close to the measured value of $110\,\text{mK}$. In Fig. 7.13(b), we plot the expected temperature profile for the case where we apply an additional local heat load in the center. A possible origin for radiation leaks into the MC shield is the fact that the MC tube consists of two separate segments, as described in Sec. 7.1.1. Since these segments are only mechanically plugged
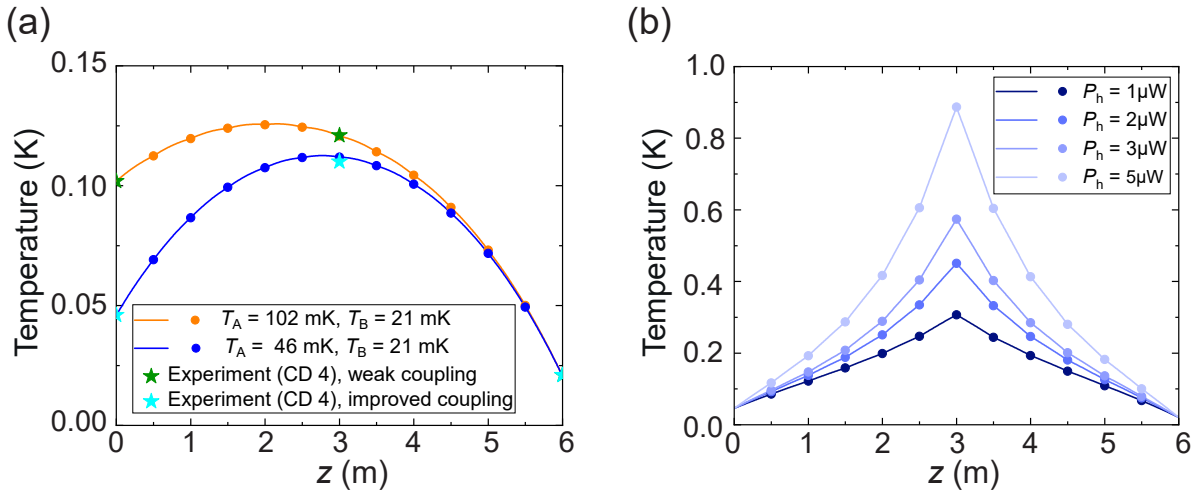
Figure 7.13: (a) Numerical solution of the heat equation for different thermal coupling of the transmission line on Alice's side. We take into account heat transfer by direct thermal conductivity as well as radiation. Stars correspond to experimentally measured temperatures for cooldowns of category CD 4 each. As Dirichlet boundary conditions, we employ the recorded heatable attenuator temperature for Alice and the MC temperature for Bob. (b) Numerically determined temperature profile under constant local heating of the link cable center with power P_h.

into each other, there is a significant gap at the connection point.

In future experiments, the impact of this radiative heat load can be reduced by covering the inside of the MC shields with SiC-based absorption coating [417]. Furthermore, we can insert additional black absorbers into the orifices for the link adapters. Note that it is expected that the center temperature of the transmission line is higher, as compared to the center temperature of the MC tube. The reason for this is a comparably weak coupling of the transmission line via the two silver wires establishing the thermal anchoring. In order to revert this situation and make the transmission line colder than the MC tube, we need to make the thermal anchoring stronger than the thermal contact established by the MC tube itself. For our geometry, this would require a silver rod with a thickness of 2 cm, which would be equivalent to 178 of our silver wires. This estimation is based on the assumption of equal RRR, implying that the corresponding thermal conductivities satisfy $\lambda_{Cu}/\lambda_{Ag} \simeq 55/76$ [283].

Within this work, the cooldown time of a single cryolink cooldown has been limited to three weeks. During an exemplary cooldown cycle of the cryogenic link, we observe a continuing loss of cooling power at the PT1 and PT2 stages. The corresponding PT1 temperature for three different cooldowns of category CD 4 is plotted in Fig. 7.14(a). We observe that, for cooldowns in April and March, slopes for the temperature uptrends approximately coincide. The offset between both curves results from the fact that we have added more superinsulation to multiple specific locations in the system between both cooldowns. In contrast, we find that the slope is significantly higher for the cooldown
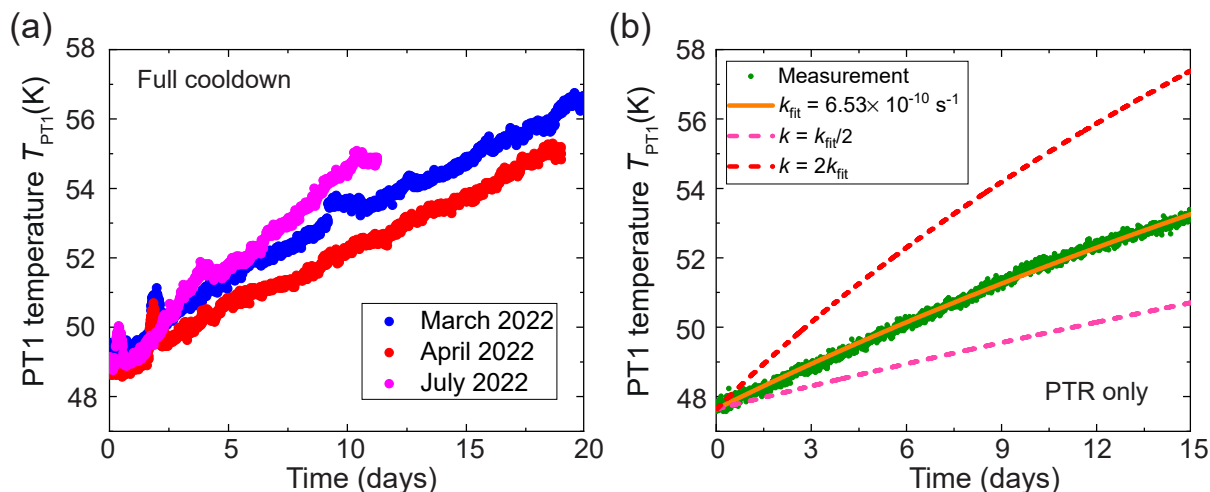
Figure 7.14: (a) Measured temperature uptrend of the PT1 stage for three cooldowns of category CD 4. The corresponding thermometer has been installed on top of Alice's PT1 plate. (b) Experimentally reproduced temperature uptrend in case we only operate the PTRs and keep all helium cycles evacuated (green dots). The orange line corresponds to a fit according to the model behind Eq. (7.27), where we treat the quantity k as the only fit parameter.

in July. After 3 weeks, the cooling power is not sufficient to operate our dry 1 K pot, which is necessary to provide precooling of the ^{3}He/^{4}He mixture. As an initial possible explanation, we assume that the effective loss of cooling power results from formation of a fluid which enters the heat balance, Eq. (7.9), as an additional source term. This idea has been ruled out by installing multiple custom-built charcoal sorption pumps in the system which have not led to any observable impact.[20] In the following, we give a possible alternative explanation for this effect. After warming up the system after three weeks, we detect an OVC pressure of 0.7 mbar at room temperature. In a careful analysis involving using an external cold trap followed by application of a mass spectrometer, we find that the largest fraction of this gas has a liquefication point above LN$_2$ temperature and only a small fraction of the gas consists of ^{4}He. By logging the OVC pressure of the evacuated system at room temperature, we find a comparable accumulation of gas over time which does not contain any ^{4}He. Cooling down the entire system only with the PTRs with evacuated helium cycles leads to the same result, this time with ^{4}He. Consequently, the helium emerges from a cold leak of the PTR cold head. Next, we analyse the origin of this gas. One explanation can be outgassing of the superinsulation, especially due to trapped moisture. An additional source for slow gas accumulation is diffusion through the significant amount of O-ring seals (cf. Sec. 7.1.1). From the diffusion equation, it can be

---

[20]The sorption pumps have been constructed from charcoal glued to an OFHC support using blue `stycast 2850 FT` mixed with OFHC copper powder. Before installation, we have removed trapped moisture by heating the sorption pumps to 150 °C, which is well below the autoignition temperature of our charcoal.

shown that the total gas permeation rate into the system can be expressed as

$$\dot{V} = \sum_y \sum_x gK_x p_x N_y f_y,$$ (7.20)

where p_x and K_x denote atmospheric partial pressure and permeation coefficient for gas x. The index y corresponds to the type of O-ring seal, where N_y denotes the number of O-rings of type y. The factor f_y takes the geometry of the O-ring trench into account, which determines the effective diffusion cross section and length. The grease factor g takes possible O-ring lubricant into account and takes typical values of $g = 0.7$ in case we properly apply vacuum grease [418]. Further assuming that the O-ring is pressed into an elliptical shape, we can express the form factor as

$$f_y = \frac{\pi^2}{2} \frac{D_y + d_y}{d_y^2 \arccos\left(\frac{h_y^2 + g_y^2 + 2h_y g_y}{d_y^2}\right)} \sqrt{d_y^4 - (h_y + g_y)^4},$$ (7.21)

where D_y is the diameter of the O-ring, d_y corresponds to the cross-sectional diameter of the O-ring, h_y denotes the trench depth and g_y denotes the clearance gap [419]. According to Ref. 420, the permeation rate strongly depends on ambient parameters such as temperature. For our Viton O-rings, permeation is especially high for polar molecules, such as water. In literature, we can find values up to $K_{H_2O} = 216 \times 10^{-8}\,\mathrm{sccm\,s^{-1}\,bar^{-1}\,cm^{-1}}$. We determine the partial atmospheric pressure of water by the August-Roche-Magnus equation [421]

$$p_{H_2O} = \varphi_{H_2O} p_v = 0.0061094 \cdot \varphi_{H_2O} \cdot \exp\left(\frac{17.625 T[^\circ\mathrm{C}]}{T[^\circ\mathrm{C}] + 243.04}\right)\,\mathrm{bar},$$ (7.22)

where p_v denotes the vapour pressure of water and φ_{H_2O} corresponds to the relative humidity. In the following, we assume $T = 25\,^\circ\mathrm{C}$ and $\varphi_{H_2O} = 0.67$ [422]. In addition, we investigate permeation of H_2O, N_2 and O_2 and neglect all remaining atmospheric gas contributions due to their low partial pressures. Using the permeation coefficients in Ref. 420, we find

$$\frac{\dot{V}_{N_2}}{\dot{V}_{H_2O}} = 0.119, \qquad \frac{\dot{V}_{O_2}}{\dot{V}_{H_2O}} = 0.078.$$ (7.23)

Increase in pressure over a time interval Δt is then given by

$$\Delta p = \frac{p_{\mathrm{atm}}}{V_l} \dot{V}_{H_2O} \left(1 + \frac{\dot{V}_{N_2}}{\dot{V}_{H_2O}} + \frac{\dot{V}_{O_2}}{\dot{V}_{H_2O}}\right) \Delta t,$$ (7.24)

where V_l denotes the volume of the cryogenic link. Using a well-defined test volume, we find $V_l = 870 \pm 291\,\mathrm{l}$, where the comparably large uncertainty results from the small size of the test volume and from the calibration uncertainty of our OVC pressure gauges. After three weeks, we thus expect an estimated pressure increase by $\Delta p = 1.3\,\mathrm{mbar}$. This

value exceeds our detected pressure increase. However, resulting from the corresponding simplifications and uncertainties, we expect our estimation to be reliable regarding the order of magnitude. Hence, this result is a strong indicator that gas accumulation in the OVC mainly results from a diffusion of water through the O-rings. Next, we investigate how a gas accumulation leads to effective loss of cooling power. We assume that the water vapor may form an ice layer on the PT1 shields, which degrades the effective reflection properties of our superinsulation. Since ice shows an integral emissivity of $\varepsilon_* = 0.98$ and thus resembles a black body [423],[21] it crucially changes the emissivity of our Mylar superinsulation, $\varepsilon_s = 0.05$. For our model, we employ the simplistic approximation that the ice layer forms on top of the superinsulation. In addition, we assume that the covering rate of ice is proportional to the uncovered surface, leading to an exponential relation. Consequently, we assume that the effective emissivity of the PT1 shield changes like

$$\varepsilon_f(t) = (1 - e^{-kt})\varepsilon_* + e^{-kt}\varepsilon_s, \tag{7.25}$$

where k corresponds to the ice formation rate. Next, we consider the net radiative heat fluxes $\dot{Q}_{r \to f}$ from the room temperature shield to the fluid film as well as $\dot{Q}_{f \to PT1}$ from the fluid film through the superinsulation. Since the trend is slow, we make an adiabatic approximation and assume that the system is in thermal equilibrium at any time, implying that these net heat fluxes are always in balance with the cooling power P_{PT1} on the PT1 stage [256], which we approximate to be independent of temperature within our temperature region of interest, $45 - 55\,\mathrm{K}$. Thus, we have

$$\dot{Q}_{r \to f} = \dot{Q}_{f \to PT1} = P_{PT1}. \tag{7.26}$$

Next, we employ the relation for net radiative heat transfer, Eq. (7.14), under the assumption that OVC shield and PT1 shield are close to each other such that their surface areas approximately coincide, which also implies a view factor of one. The time-dependent solution can be expressed as [285]

$$T_{PT1}(t)^4 = T_r^4 + (T_0^4 - T_r^4)\eta(t), \qquad \eta(t) = 1 - \frac{\varepsilon_r[\varepsilon_f(t) - \varepsilon_s]}{\varepsilon_f(t)[\varepsilon_s + \varepsilon_r(N + 2 - \varepsilon_s)]}, \tag{7.27}$$

where $N = 40$ denotes the number of superinsulation layers, $\varepsilon_r = 0.2$ denotes the emissivity of the OVC aluminum shields [423], and $T_r = 298\,\mathrm{K}$ corresponds to the lab temperature. We use Eq. (7.27) to fit the thermal uptrend for our test cooldown during which we have solely operated the PTRs and treat k as the only fit parameter. We choose this specific cooldown since, in this case, we do not need to take into account the heat load due to helium condensation, which would devalue our approximation that the heat load is dominated by radiation. The result is shown in Fig. 7.14(b) and we find $k_{\mathrm{fit}} = 6.53 \times 10^{-10}\,\mathrm{s^{-1}}$.

---

[21]Note that we perform a rough approximation by employing the bulk emissivity $\varepsilon_* = 0.98$ of ice. The realistic emissivity of a thin ice film could be notably different.

We find that our model is suitable to describe the experimental data and additionally reproduces the flattening of the temperature curve after $\simeq 9$ days. In addition, we plot the expected result for $k = k_{\text{fit}}/2$ and for $k = 2k_{\text{fit}}$. In the steady state, when all surfaces are is covered with ice, our model would predict a saturation temperature of 116 K. However, the realistic saturation value is expected to be significantly lower since our model does not take into account that the cooling power at the PT1 stage eventually increases with temperature. Interestingly, the now quite plausible assumption that the temperature uptrend results from ice explains the absence of any impact of our charcoal pumps. In addition, our model explains the different slopes in Fig. 7.14(a) due to higher ambient temperatures in July, which exponentially alter the atmospheric vapor pressure of water due to the August-Roche-Magnus equation.

To prolong the lifetime of our system, our system has undergone multiple modifications. As an example, to circumvent the problem that our 1 K circuit performance is limited by the maximally sustainable exhaust pressure of 1 bar of the pump, we have tested to operate the cryogenic link via an external ^{4}He bottle at the 1 K condensation line and have consequently connected the pump exhaust to our ^{4}He recovery line. This solution does not improve the cooling power of our 1 K pot. In addition, we have attempted to operate our 1 K pot with condensation pressures up to 3 bar, which has not improved the cooling performance either but has eventually led to instabilities in the suction pressure due to superfluid oscillations [285]. As a suitable long term solution to decrease the heat load on our 1 K pot in future experiments, we have installed an additional counterflow heat exchanger for the inflowing ^{3}He/^{4}He mixture on top of the still, with the intention to decouple the temperature of the mixture flowing into the 1 K pot from the PT2 temperature uptrend.[22] In a test cooldown with Alice only, we find that employing this heat exchanger reduces the temperature of the ^{3}He/^{4}He mixture at the input of the 1 K condensation line from 3 K to 2 K. In case we assume that this temperature difference acts as an offset and the heat exchanger does not affect the aforementioned temperature uptrend, we expect a lifetime improvement for our cryogenic link by roughly six weeks. However, during this test cooldown, we observe that the temperature uptrend rate at the exhaust of the heat exchanger is reduced by a factor of four. If the Alice cryostat would perform similarly in case we attach the cryogenic link, we would expect a lifetime improvement by multiple months which is sufficiently long for any state-of-the-art microwave quantum communication experiment.

---

[22]We thank Dr. Kurt Uhlig for numerous fruitful discussions and for coiling the heat exchanger.

Chapter 8

Microwave quantum communication over a quantum network

In this chapter, we combine results from chapter 6 and chapter 7 and realize microwave quantum teleportation over our cryogenic link. In Sec. 8.1, we introduce our experimental setup. Next, in Sec. 8.2, we demonstrate successful microwave entanglement distribution and quantum state transfer over the cryogenic link. We exploit the experimental capability for localized heating of separate parts of our experimental setup and prove that quantum properties are preserved for microwave signals propagating along thermal channels, as long as these channels stay superconducting. In Sec. 8.3, we present experimental results for microwave quantum teleportation between two remotely spaced dilution refrigerators with a teleportation fidelity of 0.55 ± 0.03 for coherent states with up to $|\alpha|^2 = 4.5$ displacement photons.[1]

8.1 Setup for inter-fridge quantum communication

Our experimental setup is schematically depicted in Fig. 8.1 and is similar to the one described in Sec. 6.1. In contrast to our intra-fridge experiment, we keep the JM setup in the Alice refrigerator and install the directional coupler ($\beta = -15\,\mathrm{dB}$) in the Bob cryostat, such that the feedforward signal generation and local displacement operation are realized in different laboratories, spaced apart from each other by 6.6 m. To enable quantum state transfer and classical communication between both parties, we transmit the TMS idler and the analog feedforward signal through our cryogenic link via our QLAN cable. The corresponding superconducting coaxial cables on Alice's and Bob's sides are designed with significant length redundancy and connected to the superconducting coaxial transmission lines in the cryogenic link *in-situ* after installation of the cryostat shields and the link adapters before attaching the link arms. These cables are bent in an S-shape to compensate for thermal contraction [cf. Fig. 7.4(a)] and the connection

---

[1]The measurements presented in this chapter have been collaboratively performed within two Master's projects together with W. Yam and S. Gandorfer. The corresponding Master's theses can be found in Ref. 238 and in Ref. 282.

is established via SMA female-female adapters. Following the directional coupler, the resulting signal is amplified by a HEMT amplifier in the Bob cryostat and guided back to Alice's lab using room temperature RF cables, where it is either detected by the heterodyne two-path receiver, described in Sec. 3.1.3, or by a VNA. The signal is then processed and reconstructed in Alice's lab. As indicated in Fig. 8.1, we can heat the entanglement distribution channel and the feedforward line during the experiment. Thus, by employing a PID control architecture, we can artificially create well defined thermal channels and systematically investigate effects emerging from thermal environment. During our work on inter-fridge quantum communication, we have replaced the NEC JPAs in the setup with VTT chips, where we employ double-SQUID JPAs as measurement JPAs and single-SQUID JPAs for entanglement generation. One of the main differences of this setup to the intra-fridge quantum teleportation experiment is the significant mismatch in propagation lengths regarding the entanglement distribution between Alice and Bob, since the TMS resource state is generated in the Alice cryostat. Thus, the mode arriving at Bob's directional coupler can be delayed, as compared to the TMS mode at Alice's detection setup. The effect of such finite-time delays and correlations has been investigated in Ref. 83. To investigate the effect of this retardation on teleportation fidelity, we consider the lossless and noiseless protocol with a propagation delay τ in the shared resource between Alice and Bob [83]. The interference function is then altered to

$$C(r, k, B, \tau) = (1 + k) \cosh 2r - 2\sqrt{k} \operatorname{sinc}(2B\tau) \sinh 2r, \tag{8.1}$$
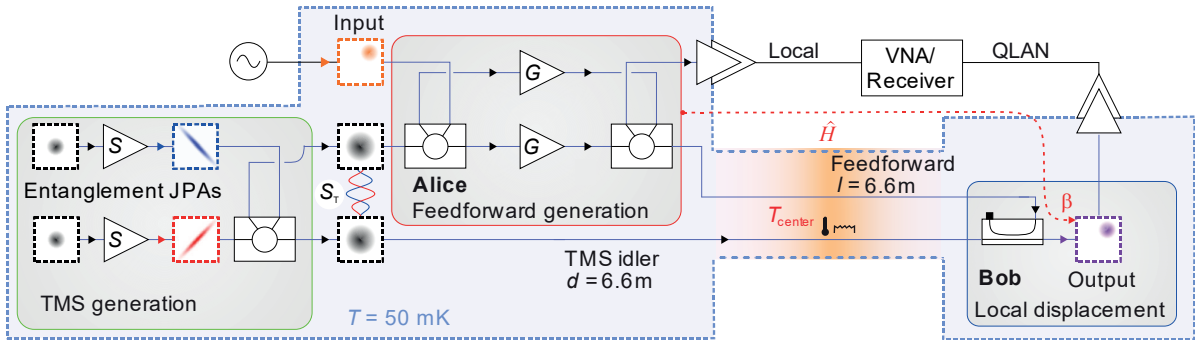
Figure 8.1: Experimental setup for the inter-lab microwave quantum teleportation experiment. The TMS idler and the analog feedforward signal are distributed from Alice to Bob via the superconducting NbTi transmission lines inside the cryogenic link. The receiver is physically located in Alice lab and can process both the teleported signal from Bob ("QLAN") and the feedforward signal from Alice ("Local"). The heater and thermometer symbols indicate the temperature control at the center of the link. All other symbols are as in Fig. 6.1 and Fig. A.2.

where B denotes the single-sideband (SSB) measurement bandwidth. Next, we let $k = 1$ and optimize Eq. (8.1) with respect to r, which leads to the final covariance matrix

$$\boldsymbol{V}_{\mathrm{out}} = \frac{1}{2} \sqrt{1 - \mathrm{sinc}^2 \left(2B\tau\right)} \mathbb{1}_2 + \frac{1}{4} \mathbb{1}_2. \qquad (8.2)$$

If we assume that τ corresponds to the full distance $l = 6.6\,\mathrm{m}$ between Alice and Bob, we obtain $\tau = n_{\mathrm{r}} l/c \simeq 30.2\,\mathrm{ns}$, where $n_{\mathrm{r}} = 1.37$ denotes the refractive index of PTFE [424] due to the dielectric in the superconducting transmission lines. According to Eq. (8.2), we obtain a teleportation fidelity of 0.98 in absence of any other imperfections, which implies that the finite length of the cryogenic link itself does not lead to a practically relevant fidelity limitation in contrast to the previously discussed losses or noise.

8.2   Quantum state transfer and entanglement distribution

Before realizing microwave quantum teleportation, we demonstrate that we can use our cryogenic link to perform standard JPA characterization measurements as discussed in Sec. 3.2.2. First, we measure the DC flux characteristic and the nondegenerate gain of one of our entanglement JPAs.[2] The hybrid ring beam splitter used to create the TMS resource enables us to simultaneously measure local transmission at Alice's side and transmission through the QLAN cable. A comparison between both measurements is shown in Fig. 8.2, where we find good agreement between the local and QLAN measurements of flux tuning of the JPA resonance frequency. In Fig. 8.2(b), we compare the detected nondegenerate gain as a function of applied pump power P_{p}, referred to the JPA input. We find that both curves coincide especially in the limit of $G \gg 1$. For low pump powers, we find that the gain for QLAN transmission is on average higher by $0.5\,\mathrm{dB}$ and shows significantly less scatter, as compared to Alice's local results. This result is due to the fact that the HEMT amplifier in Alice has been in use for multiple years prior to this measurement and degraded over time, adding $n_{\mathrm{H}} \simeq 25.82 \pm 1.11$ noise photons.[3] In contrast, we have installed a new HEMT amplifier with significantly lower noise photon number $n_{\mathrm{H}} \simeq 8.35 \pm 0.41$ in the Bob output line, implying that we would need to take at least three times more averages on the Alice side to achieve the same SNR between both paths. However, both measurements shown in Fig. 8.2 are obtained with identical VNA settings within a measurement bandwidth of $10\,\mathrm{Hz}$. Next, we demonstrate experimental transfer of squeezed microwave vacuum states over the QLAN cable. We do not correct the measured squeezing levels for the hybrid ring beam splitters in the setup to directly compare the locally reconstructed squeezing level on Alice's side and the squeezing level

---

[2]We use an NEC JPA for this purpose. The data shown in Fig. 8.3 and Fig. 8.4 has been measured in a separate cooldown before installation of the VTT JPAs.

[3]We remark that this photon number only corresponds to an effective amplifier noise since it has been determined within our standard photon number calibration procedure. To obtain a more accurate result, we would need to employ the 2D Planck spectroscopy, as described in Sec. 3.3.
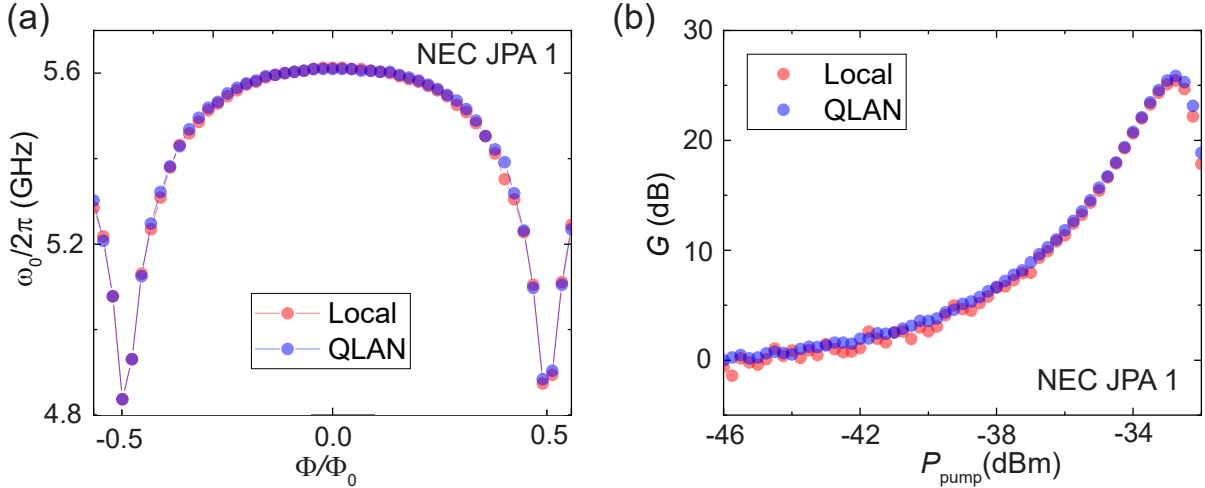
Figure 8.2: (a) Flux dependence of the resonant frequency ω_0 of one of our entanglement JPAs, simultaneously detected directly at Alice's side (local) and on Bob's side over the cryogenic link (QLAN). Lines are a guide to the eye. (b) Comparison of locally detected nondegenerate JPA gain G and nondegenerate gain measured over the cryogenic link. For both measurements, we find excellent agreement between both results, which demonstrates successful implementation of our QLAN microwave channel. Data scatter (red circles) in the local measurements in the regime of low gains results from degradation of the corresponding HEMT amplifier.

of the state transferred over the QLAN. The fluctuations coupled to the second input port of these hybrid ring beam splitters, set a fundamental limitation to the maximally observable squeezing level $S_{\max}$ as well as the maximal bath temperature $T_{\max}$ to detect squeezing. Assuming the squeezed signal passes ℓ symmetric beam splitters in a thermal quantum network, we have

$$S_{\max} = 10 \lg \left(1 + \frac{1}{M_\ell}\right), \qquad T_{\max} \leq \frac{\hbar \omega_{\mathrm{s}}}{k_{\mathrm{B}} \ln M_{\ell+1}}, \tag{8.3}$$

where $M_\ell = 2^\ell - 1$ are the Mersenne numbers. For our case, $\ell = 1$, we find $S_{\max} \simeq 3\,\mathrm{dB}$ and $T_{\max} \simeq 0.238\,\mathrm{K}$ at a signal frequency $\omega_{\mathrm{s}}/2\pi = 5.435\,\mathrm{GHz}$. Due to the additional heat load added by the cryogenic link, we stabilize our samples at $70\,\mathrm{mK} \ll T_{\max}$ instead of the $50\,\mathrm{mK}$ used in our intra-fridge experiments. Our results from quantum state transfer are plotted in Fig. 8.3, where we plot squeezing level and purity as a function of pump power. We measure a maximal squeezing level of $2.1 \pm 0.05\,\mathrm{dB}$ with corresponding purity $\mu = 0.320 \pm 0.002$. For the exemplary case where we allow for a PNCF uncertainty $\kappa \to \kappa \pm 0.2\kappa$, the uncertainty in squeezing level is given by $S = 2.1^{-0.6}_{+0.9}\,\mathrm{dB}$. Hence, our result of measuring a positive squeezing level is robust with respect to our photon number calibration. If we correct for a weak thermal state incident to the other hybrid ring port, we estimate squeezing levels of up to $8.3 \pm 0.5\,\mathrm{dB}$ at the JPA output (before the hybrid ring beam splitter). Note that the locally reconstructed squeezing level on Alice's side is
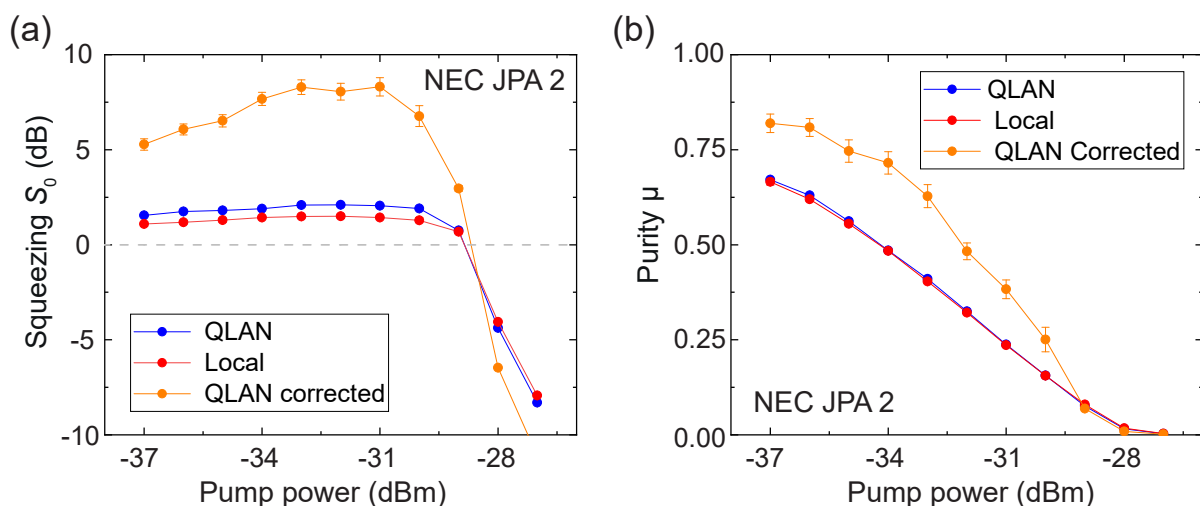
Figure 8.3: (a) Transfer of squeezed states over the cryogenic link. As in Fig. 8.2, we compare the local state (red) and the state transmitted via the transmission line (blue, orange). The directly detected squeezing level S_0 is limited to 3 dB due to vacuum incident to an idle port of the entangling hybrid ring beam splitter. The orange curve corresponds to the scenario where we correct for this beam splitter, indicating that we reach squeezing levels up to 8.3 dB. (b) Purity μ of the squeezed states from (a) as a function of the pump power, referred to the JPA input. Lines are a guide to the eye.

systematically lower by $\simeq 0.5$ dB, as compared to the squeezing level of the transmitted state. Since squeezing corresponds to phase-sensitive amplification with low gain, this artifact is consistent with the scatter of Alice's local gain observed in Fig. 8.2(b) and, again, results from Alice's degraded HEMT amplifier. This finding stresses the fact that a reliable reconstruction of small signal variances requires a stable detection chain. In contrast, the purity μ of both states coincides, as it can be seen in Fig. 8.3(b), because μ only depends on the product of both variances. Next, we repeat the squeezed quantum state transfer experiment for various temperatures of up to 1 K in the center of the QLAN transmission line. We employ the PID control architecture introduced in Sec. 7.1. The result of this measurement is shown in Fig. 8.4, where we show the squeezing level S and the purity μ. We quantify entanglement between Alice's and Bob's signals by means of negativity. Although, we do not distribute a balanced TMS state in this experiment, splitting a squeezed state via a hybrid ring beam splitter still results in entangled output modes due to the incident signal-idler correlations [77]. For noiseless JPAs, the negativity is related to the squeeze factor r via $N_{\mathrm{sq}} = (e^r - 1)/2$. When comparing to the negativity N_{TMS} of a TMS state with squeezing level r in Sec. 6.2, we find the relation

$$N_{\mathrm{TMS}} = 2N_{\mathrm{sq}}(N_{\mathrm{sq}} + 1). \tag{8.4}$$

As it can be seen in Fig. 8.4(d), we measure $N_{\mathrm{sq}} > 0$ within the entire temperature range of the QLAN center. Consequently, we do not observe the sudden death of entanglement
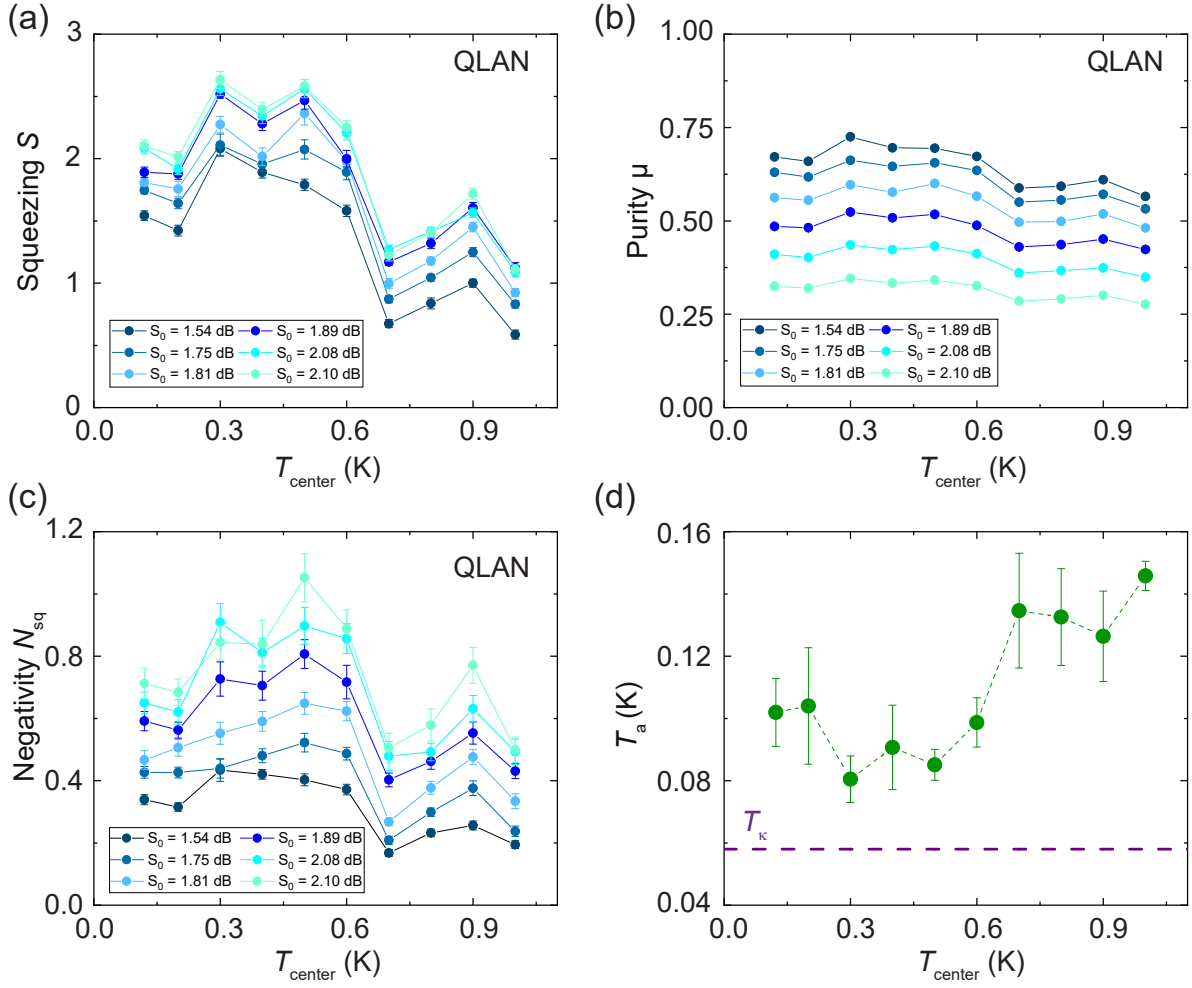
Figure 8.4: Squeezed state transfer with NEC JPAs. (a) Squeezing level S as a function the QLAN center temperature. The quantity S_0 thereby corresponds to the squeezing level at base temperature ($T_{\text{center}} = 120\,\text{mK}$) as in Fig. 8.3. Panel (b) shows the purity μ of the transmitted squeezed states and panel (c) the resulting negativity N_{sq} between Alice's and Bob's modes, demonstrating successful entanglement distribution over the QLAN. Panel (d) shows the temperature T_{a} of the heatable attenuator as a function of T_{center}. The comparably high T_{a} results from a weak thermal coupling to the MC plate. Attenuator temperature fluctuations directly translate to fluctuations of S, μ, and N_{sq}, since T_{a} lies significantly above the Johnson-Nyquist threshold T_κ. Solid and dashed lines connecting data points are a guide to the eye.

(cf. Sec. 5.1), expected at temperature $T_{\text{sd}} = \hbar\omega_{\text{s}}/(k_{\text{B}}\ln 2) \simeq 376\,\text{mK}$, within the entire investigated parameter space, although an ambient temperature of $1\,\text{K}$ corresponds to 3.4 photons at our signal frequency. This observation demonstrates that the superconductor isolates the electromagnetic modes in the cable from the environment, in agreement with the fluctuation-dissipation theorem, Eq. (2.148). As long as the environment is significantly colder than the critical temperature of our superconductor, $T \ll T_{\text{c}} \simeq 10\,\text{K}$, we can neglect
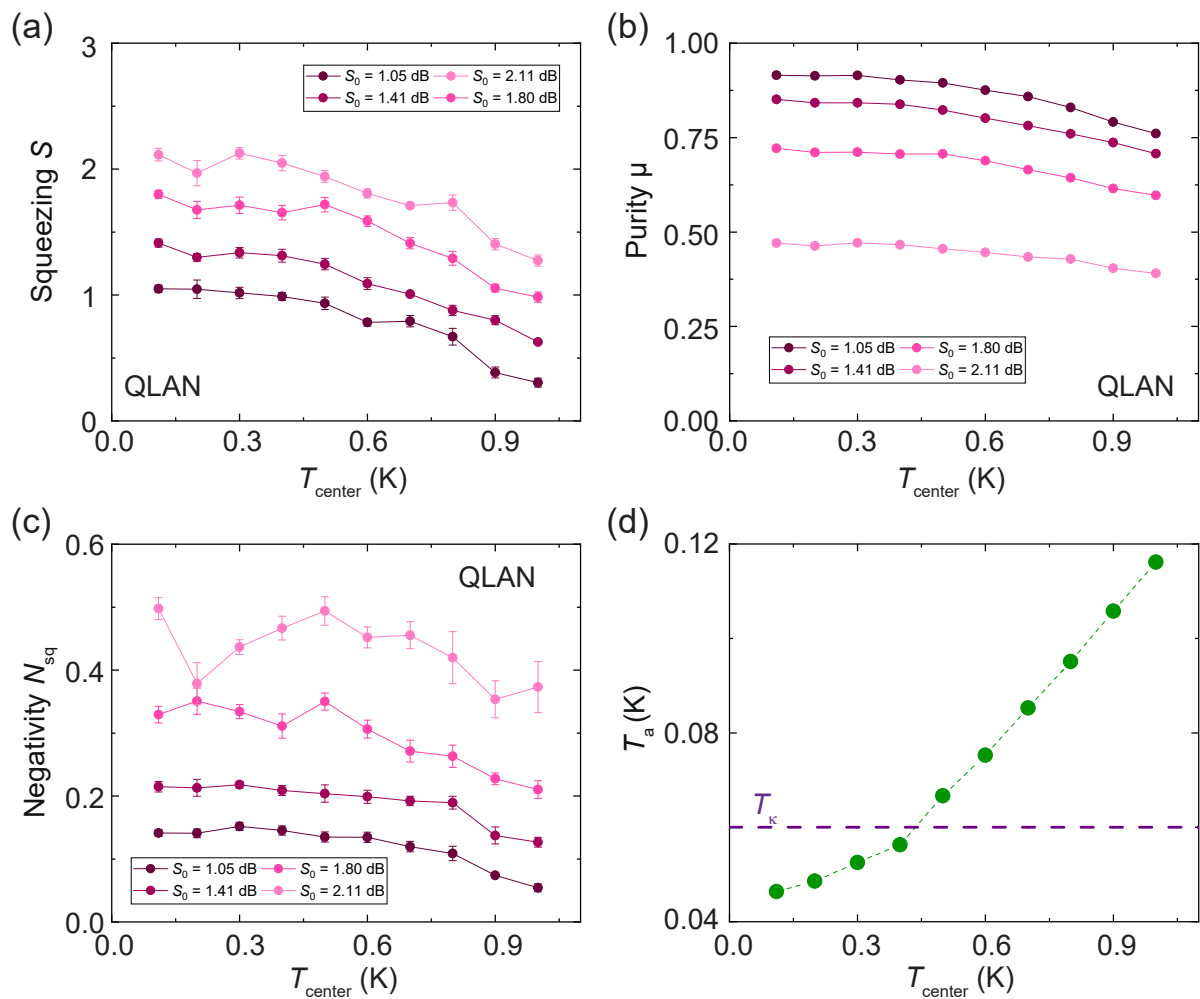
Figure 8.5: Squeezed state transfer with VTT JPAs and improved thermal coupling for the heatable attenuators (cf. Fig. 7.13). In this case, $T_\mathrm{a} < T_\kappa$ for $T_\mathrm{center} < 400\,\mathrm{mK}$. In this temperature regime, S, μ, and N_sq are approximately independent of the center temperature, even for $T_\mathrm{center} \gg T_\kappa$, as predicted by the fluctuation-dissipation theorem. Solid and dashed lines connecting data points are a guide to the eye.

the surface resistance of our transmission line, implying a vanishing dissipation spectrum $\varepsilon(\omega)$ for our propagating signals. Thus, the phononic environmental temperature and the mode temperature in the superconducting cable are decoupled from each other and the thermal fluctuation spectrum in the QLAN is effectively limited by the temperature T_a of the heatable attenuator. We observe that, up to temperatures of $T_\mathrm{center} \simeq 0.6\,\mathrm{K}$, the reconstructed state parameters fluctuate without any statistical correlation to T_center. We attribute these fluctuations to temperature fluctuations of the heatable $30\,\mathrm{dB}$ attenuator, implying that the JPA input state corresponds to a thermal state with varying photon number. These photon number fluctuations translate to fluctuations of the respective squeezing level for fixed pump power. For verification, we plot the corresponding average attenuator temperature T_a for each temperature set point T_center during the measurement

in Fig. 8.4(d). Since we are already in the Johnson-Nyquist regime, $T > T_\kappa$, as discussed in Sec. 3.1.4, we also need to account for these temperature changes in the reference-state reconstruction. In general, we observe that the heatable attenuators are comparably hot, $T_a > 100\,\text{mK}$. This result is due to the fact that we employ the same thermal coupling of our attenuators to the MC plate as in our intra-fridge experiments in Sec. 6.3. However, the employed silver ribbons connecting the heatable attenuators to the MC [cf. Fig. 3.7(a)] are too thin to bear the additional radiative heat load from the cryogenic link. For $T_{\text{center}} \gtrsim 0.6\,\text{K}$, we observe an overall degradation of all state parameters, since the sample stage starts to heat up [cf. Fig. 7.12(a)], implying that we increase thermal noise coupled via normal conducting RF components, such as circulators. At $T_{\text{center}} = 1\,\text{K}$, the sample stage has a temperature of 123 mK. Next, we improve the thermal contact of our heatable attenuators by using thicker annealed silver ribbons. In addition, we install cryogenic RF filters in our input lines to remove high frequency noise.[4] After replacing the NEC JPAs with VTT samples, we repeat the squeezed state transfer experiment. The corresponding results are shown in Fig. 8.5. As it can be seen in Fig. 8.5(d), T_a is significantly lower than in Fig. 8.4 and is well-correlated with the center temperature. As a result, we can resolve the saturation regime of the Planck curve in our photon number calibration. As long as we maintain $T_a \lesssim T_\kappa$, we are effectively limited by the quantum noise emitted by the attenuator, implying that S, μ, and N_{sq} are *de facto* temperature-independent, which is especially visible for $S_0 \lesssim 2\,\text{dB}$. This finding indicates that, for the realization of large thermal quantum networks [425], we do not necessarily require a millikelvin connection. As an important consequence, implementing a microwave link at significantly higher temperatures, potentially by exploiting high-T_c superconducting cables [426], can be regarded as an economic solution for large scale applications.

8.3 Analog inter-fridge quantum teleportation

In this section we demonstrate coherent state quantum teleportation over the QLAN prototype. In the first step, we discuss balancing of the TMS resource, as well as the JM over the cryogenic link. For all measurements presented in this section, we employ single-SQUID VTT JPAs for entanglement generation and double-SQUID VTT JPAs for Bell measurements. To suppress the pump crosstalk, we replace the respective circulators for entanglement JPAs and measurement JPAs by broadband circulators with 20 dB isolation over the frequency range $4 - 12\,\text{GHz}$.[5] The results from TMS state balancing between Alice and Bob over the cryogenic link are depicted in Fig. 8.6(a). We reach a maximal squeezing of 6.5 dB and a maximal variance ratio of $\rho = 0.93$. Due to the broadband circulators, this value is significantly higher compared to the value of 0.86 observed in Sec. 6.2 and is eventually limited by the intrinsic asymmetry of the used

---

[4]We use tubular low-pass filters with filter window $12 - 26\,\text{GHz}$ from `K&L Microwave` for this purpose.
[5]We use `QCY-G0401201AS` circulators from `Quinstar` for this purpose.
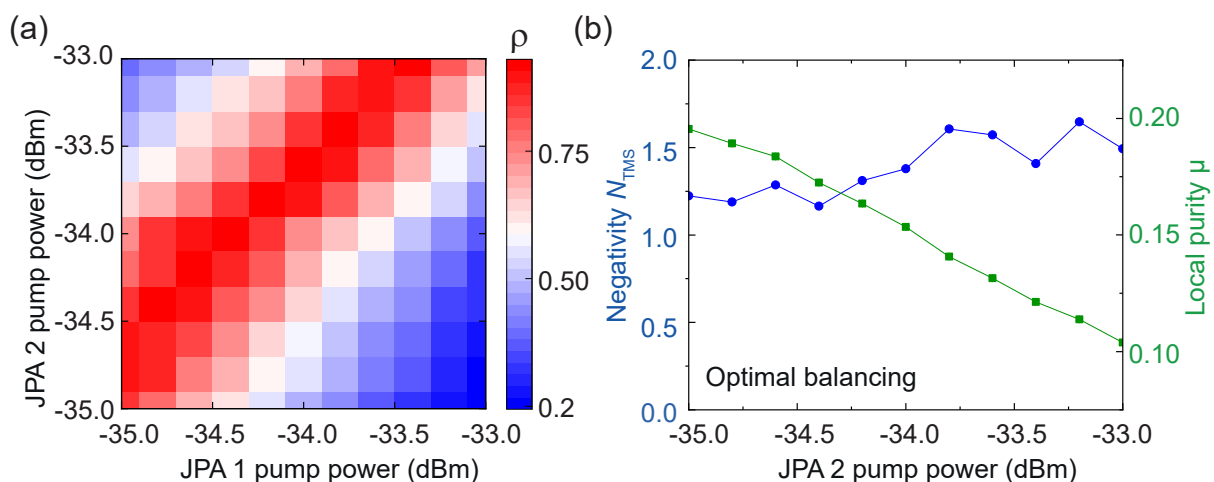
Figure 8.6: (a) Variance ratio ρ [cf. Fig. 6.3(a)] for the TMS resource state, distributed between Alice and Bob over the cryogenic link as a function of the JPA pump powers. (b) Local purity μ (green, filled boxes) and negativity N_{TMS} of the TMS state (blue, filled circles) as a function of the JPA 2 pump power, where the JPA 1 pump power is chosen such that ρ is maximized. We measure a decrease of μ and a simultaneous increase of N_{TMS}. This finding indicates that the TMS state asymptotically approaches a maximally entangled state. Lines are a guide to the eye.

hybrid ring beam splitter. In Fig. 8.6(b), we show purity and negativity of the TMS state as a function of the pump power. In analogy to Fig. 6.6(a), local purity decreases and, simultaneously, negativity increases with increasing pump power. Next, we measure the interference pattern of the JM over the cryogenic link, which is necessary for the realization of the JM balancing step. We apply an input signal with photon number $|\alpha|^2 = 2.1$ and phase $\theta_{\text{in}} = 45°$. Simultaneously, we fix the gain of the measurement JPAs at $G = 22\,\text{dB}$ and vary their respective amplification angles, φ_3 and φ_4. We reconstruct the resulting state at the output of Bob's directional coupler and calculate the fidelity with respect to a coherent state with displacement angle θ_{in}. The JM transforms the displacement vector via

$$M(\varphi_-, \varphi_+) = \begin{pmatrix} \cosh\phi + \sinh\phi\cos\varphi_-\cos\varphi_+ & -\sinh\phi\sin\varphi_+\cos\varphi_- \\ -\sinh\phi\sin\varphi_+\cos\varphi_- & \cosh\phi - \sinh\phi\cos\varphi_-\cos\varphi_+ \end{pmatrix}, \quad (8.5)$$

where $e^{2\phi} \equiv G$, $\varphi_- \equiv \varphi_3 - \varphi_4$, and $\varphi_+ \equiv \varphi_3 - \varphi_4$. The phase modulation of the displacement photon number at the directional coupler is given by

$$|\alpha'|^2 = |\alpha|^2 \frac{k}{2} \begin{cases} 3 + \cos(2\varphi_-) + 4\sin\varphi_+\cos\varphi_-, & \theta_{\text{in}} = \frac{\pi}{4} \\ 3 + \cos(2\varphi_-) - 4\sin\varphi_+\cos\varphi_-, & \theta_{\text{in}} = \frac{3\pi}{4} \end{cases}. \quad (8.6)$$

In case $\theta_{\text{in}} = \pi/4$, the maxima are located at $(\varphi_3, \varphi_4) = (\pi n + \pi/4, \pi m + \pi/4)$ and $(\varphi_3, \varphi_4) = (\pi n + \pi/4, \pi m + \pi/4)$, with $n, m \in \mathbb{Z}$. The minima can be found at $(\varphi_3, \varphi_4) =$

$(\pi n - \pi/4, \pi m - \pi/4)$ and $(\varphi_3, \varphi_4) = (\pi n + 3\pi/4, \pi m + 3\pi/4)$. In case $\theta_{\mathrm{in}} = 3\pi/4$, the respective maxima and minima are swapped. This result, combined with the $\pi-$periodicity of the interference pattern, can be observed in Fig. 8.7. Note that the predicted maxima in displacement, according to Eq. (8.6), do not exactly correspond to maxima in fidelity, which are determined by the condition $|\mathbf{d} - \mathbf{d}'| = 0$ for $|\alpha|^2 \gg 1$. In addition, we observe that the phase offsets for the maxima/minima do not reproduce the predicted value of $\pm\pi/4$, which results from different interferometric path lengths in the JM in this specific measurement. This observation stresses the necessity of the careful calibration procedure described in Sec. 6.2.

After performing this calibration, we perform coherent state quantum teleportation over the cryogenic link as described in Sec. 6.3.1. The result of this measurement for $S = 3\,\mathrm{dB}$ and $G = 22\,\mathrm{dB}$ is shown in Fig. 8.8(a). In the next step, we evaluate our teleportation results in the scope of practical security. We consider the attack depicted in Fig. 8.9. For this type of attack, we assume that the classical feedforward channel is public, whereas the quantum channel for entanglement distribution is not accessible for a potential eavesdropper, Evelyn. Alice's goal is to employ the teleportation protocol to securely transmit a coherent state $|\alpha\rangle$ to Bob. Evelyn can copy the feedforward signal using a beam splitter and subsequent amplification without changing Bob's result, as demonstrated in Sec. 6.4. Next, Evelyn copies Bob's setup and employs her own directional coupler with coupling β_{e}, but with vacuum instead of the resource state. In this way, she
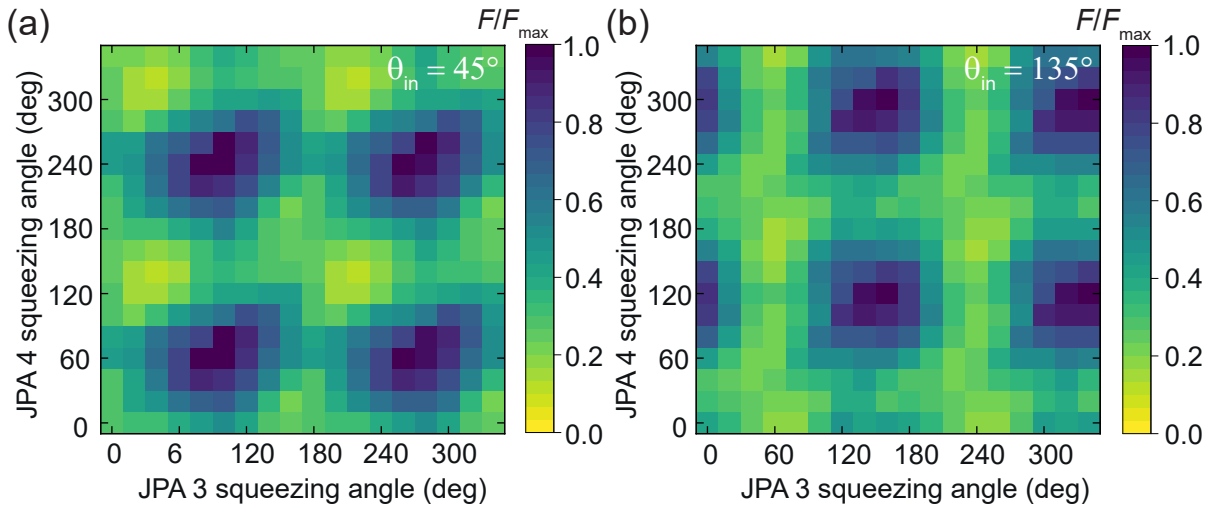
Figure 8.7: (a) Interference pattern for the JM as a function of the squeezing angles of the measurement JPAs, measured over the cryogenic link. We fix the coherent phase of the input state to $\theta_{\mathrm{in}} = 45°$ and determine modulation of fidelity between the input state and Bob's final state at the directional coupler. (b) Detected interference pattern for $\theta_{\mathrm{in}} = 135°$. In this case, maxima and minima are swapped.
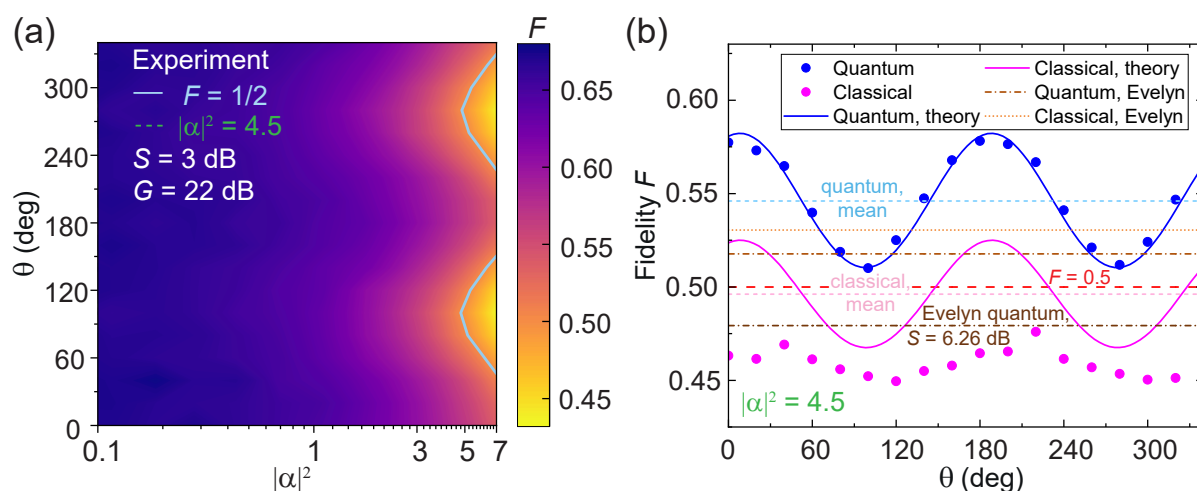
Figure 8.8: (a) Experimental fidelity for the inter-lab quantum teleportation of coherent microwave states as a function of displacement photon number $|\alpha|^2$ and displacement angle θ. The oscillatory phase dependence results from an imperfect balancing of the JM and the TMS state due to the limited cooldown time of three weeks (see Fig. 7.14). (b) Phase dependence of the fidelity for quantum teleportation (blue dots) and classical teleportation (magenta dots) for $|\alpha|^2 = 4.5$. The blue solid line corresponds to our theory model introduced in Sec. 6.3.3. We adjust the respective relative phase mismatch between the measurement and entanglement JPAs, as well as the JPA noise, such that we reproduce the quantum teleportation data. The corresponding predicted classical fidelity exceeds the measured data, which we attribute to the fact that we do not include any compression effects into the theory model. The dashed blue and magenta lines correspond to the average fidelity according to the theory model. The dashed light brown (orange) line corresponds to the maximal average fidelity which Evelyn can achieve in the quantum (classical) case. The dark brown curve shows the reduced maximal fidelity achievable by Evelyn in case we increase resource squeezing to 6.26 dB.

obtains her final state

$$\boldsymbol{V}_{\mathrm{e}} = \frac{1}{4}\left[2k_{\mathrm{e}}\cosh^2 r + 1\right]\mathbb{1}_2, \qquad \mathbf{d}_{\mathrm{e}} = \sqrt{k_{\mathrm{e}}}\mathbf{d}, \tag{8.7}$$

where $k_{\mathrm{e}} \equiv G\beta_{\mathrm{e}}/4$. The fidelity with respect to Alice's input state is given by

$$F_{\mathrm{e}} = \frac{1}{k_{\mathrm{e}}\cosh^2 r + 1}\exp\left[-\frac{(\sqrt{k_{\mathrm{e}}}-1)^2}{k_{\mathrm{e}}\cosh^2 r + 1}|\alpha|^2\right]. \tag{8.8}$$

In case Evelyn chooses $k_{\mathrm{e}} = 1$, she obtains $F_{\mathrm{e}} = 2/(\cosh 2r + 3)$. Evelyn's fidelity is related to Bob's teleportation fidelity F_{b} via

$$F_{\mathrm{e}} = 1 - \frac{1}{1 + 4F_{\mathrm{b}}(1 - F_{\mathrm{b}})}. \tag{8.9}$$

In the classical scenario, Evelyn measures $F_{\mathrm{e}} = 1/2$. In this case, Bob's and Evelyn's

settings are fully symmetric and both of them suffer from two quduties. However, since Evelyn has no access to the nonlocal $\sinh 2r$ terms in the TMS resource, the situation between Bob and Evelyn becomes asymmetric in case we employ entanglement. Since the nonlocal terms of the TMS resource act as a unique "key" for the interference mechanism, Evelyn cannot purify the state at her directional coupler. Instead, Evelyn is forced to amplify the local $\cosh 2r$ contribution which superposes the feedforward signal. Thus, the purity of Evelyn's state drastically reduces with increasing r. In the asymptotic case, $r \gg 1$, Evelyn's fidelity in Eq. (8.8) is given by $F_e \simeq 4e^{-2r}/k$ and asymptotically approaches zero, implying that, from a practical point of view, the protocol becomes secure in case F drops below the measurement uncertainty of Evelyn. In addition, Evelyn's fidelity is directly related to the mutual information between the analog feedforward and teleported signals as described by Eq. (6.9). We observe that $F_e \to 0$ when $\delta \to 0$. At the same time, Evelyn's fidelity is inversely correlated to Bob's teleportation fidelity. In addition, Alice and Bob can distribute their phase reference publicly since security solely relies on the resource squeezing, which asymptotically degrades Evelyn's SNR to zero. Although the realistic type of attack in Fig. 8.9 is of high relevance for quantum communication over long distances, unconditional security is not yet guaranteed if we attempt to employ analog teleportation in combination with cryptographic wrapper protocols, e.g., for QKD applications. In this case, in order to achieve a finite bit rate, Alice needs to sample her unkown input states from a specified codebook, implying that the no-cloning limit quantifies whether communication is secure.

As a verification, we plot our quantum teleportation results for $|\alpha|^2 = 4.5$ input photons in Fig. 8.8(b) in direct comparison to the classical result, where entanglement is absent. The observed π-periodic oscillations are described by Eq. (8.5) and correspond to the phase modulation due to imperfect balancing of the JM.[6] We measure an average quantum teleportation fidelity of $F_q = 0.55 \pm 0.03$ and a classical fidelity $F_c = 0.46 \pm 0.01$. In comparison, in our intra-fridge teleportation experiment with the NEC JPAs in chapter 6, comparable squeezing and gain parameters correspond to a significantly lower fidelity $F = 0.476 \pm 0.004$ for $|\alpha|^2 = 4.3$ due to compression. This finding reveals the advantage of using double-SQUID JPAs in the JM. Solid lines in Fig. 8.8(b) correspond to the theory model, as described in Sec. 6.3.3. We find a good agreement between the experiment and theory for noise parameters $\chi_1 = 0.0315$ and $\chi_2 = 0.315$. From the phase modulation, we extract a deviation by $12.3\,\%$ from orthogonality for the measurement/entanglement JPAs. We observe that the theory model predicts a higher classical fidelity as well as larger oscillation amplitude as compared to our measurements. This finding originates from the fact that the power of the TMS state adds to the power of the coherent input state, which enhances the impact of phase-dependent compression and is not included in

---

[6]Within this experiment, it has not been possible to ensure more accurate calibration of the JM since our measurement time has been restricted to three weeks, resulting from the continuous loss of cooling power for the pulse tube stages, as described in Sec. 7.3.
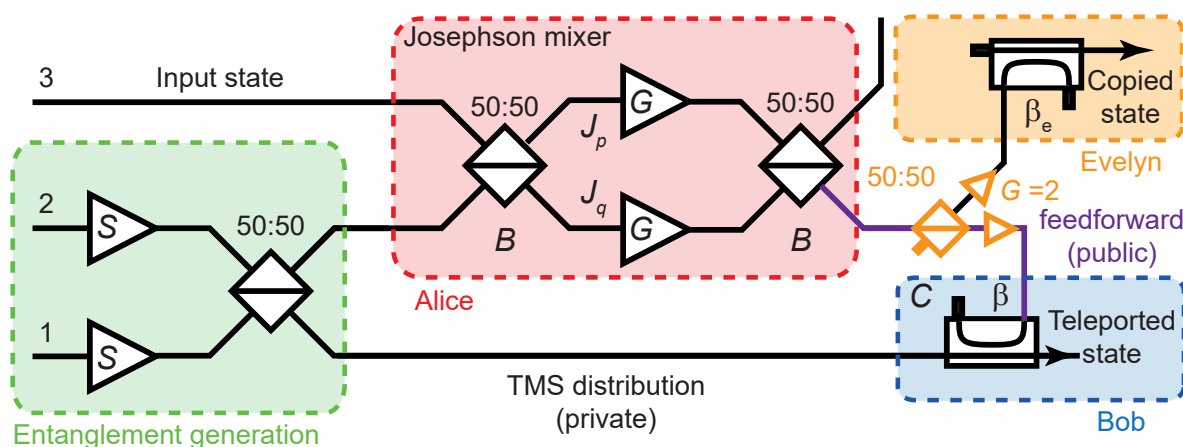
Figure 8.9: Scheme for practical security analysis of inter-lab microwave quantum teleportation. We consider the teleportation setup for secure transmission of a coherent state $|\alpha\rangle$. We treat the entanglement distribution as private and the feedforward as public channels. A potential eavesdropper, Evelyn, can interact with the feedforward signal via a symmetric beam splitter followed by a phase-insensitive amplifier, in order to extract information on the teleported state. Evelyn then attempts to copy Bob's setup by employing her own directional coupler with coupling β_e.

the linear theory model. In addition, we integrate Evelyn into our simulation and optimize her maximally achievable average fidelity with respect to her coupling β_e. We find this optimum to be $\beta_e = -16.9\,\text{dB}$. We plot Evelyn's fidelity for the quantum case as well as for the classical case in Fig. 8.8(b). We observe that Evelyn's classical fidelity (0.530) exceeds the classical teleportation fidelity, implying that the classical protocol is not secure. Note that the fact that Evelyn can realistically detect a fidelity slightly above $1/2$ is a result from losses and noise as well as from the projective limit approximation ($\beta \to 0$). Additional deviations from ideal model conditions originate from the imperfect purity, $\mu = 0.96$, of the coherent input state. However, in case we employ entanglement, the teleportation fidelity increases as expected, whereas Evelyn's average fidelity (0.518) drops below Bob's mean teleportation fidelity. Thus, although we do not exceed the no-cloning limit in our inter-lab quantum teleportation experiment, the protocol can be regarded as secure with respect to the attack described in Fig. 8.9. If we theoretically assume that we could optimize Bob's fidelity with respect to squeezing for our experimental parameters, we find a maximal $F_b = 0.592$. This fidelity corresponds to the squeezing level $S = 6.26\,\text{dB}$ and is limited by the gain-dependent JPA noise. Evelyn's corresponding fidelity is given by $F_e = 0.479$, see Fig. 8.8(b). As shown in Sec. 2.3.1, for ideal quantum teleportation, switching on entanglement increases fidelity for any displacement as long as we ensure $k = 1$. On the other hand, this is not necessarily true if $k \neq 1$. In this case, we have to take into account that resource squeezing impacts fidelity via two competing mechanisms. On the one hand, increasing the squeezing optimizes the destructive interference of the two quduties. On the other hand, detuning $k \neq 1$ implies that we cannot perfectly remove

the local quasi-thermal noise of the TMS resource, which manifests as a e^{2r} dependence. This effect becomes larger in case the TMS state itself is noisy. It can then appear that it is more beneficial to accept pure vacuum fluctuations at the directional coupler input, compared to an impure TMS mode.

In the following, we experimentally demonstrate that the working point choice crucially affects the relation between quantum fidelity F_q and classical fidelity F_c as a function of input power $|\alpha|^2$. We define a relative quantum advantage of our teleportation protocol as $\Psi = (F_q - F_c)/F_q$. In Fig. 8.10(a) we plot the experimentally determined Ψ corresponding to the experimental results shown in Fig. 8.8(a). Figure 8.10(b) shows the results from an inter-lab teleportation experiment, performed with $S = 3.7\,\mathrm{dB}$ and $G = 30\,\mathrm{dB}$, corresponding to a significant detuning from the ideal projection condition, $k > 1$. By comparing the results of both experiments, we observe that Ψ increases with $|\alpha|^2$ in one case, but decreases in the other case. To understand this effect, we express the power dependence of Ψ as

$$\Psi(r, k, n_0, |\alpha|^2) = 1 - B(r, k, n_0) \exp\left[-|\alpha|^2 \frac{(\sqrt{k} - 1)^2}{1 + k} \left(\frac{B(r, k, n_0) - 1}{B(r, k, n_0)}\right)\right], \qquad (8.10)$$

where the function

$$B(r, k, n_0) \equiv \frac{1}{2}\left[1 + \frac{1 + 2n_0}{1 + k}C(r, k)\right] \qquad (8.11)$$

depends on the squeeze parameter r, the noise n_0 in the TMS state, and the renormalized gain k. Apart from that, we treat the teleportation protocol as ideal throughout this investigation. The function $B(r, k, n_0) \in [1/2, \infty)$ determines the qualitative behavior of quantum advantage. In addition, we observe from Eq. (8.10) that, in case $k \neq 1$, we always find $|\alpha|^2 > 0$ where $\Psi = 0$, i.e., quantum advantage changes sign. In case we employ an infinitely large input codebook, we aim for an increase of relative quantum advantage with $|\alpha|^2$. This is the case if we employ the quantum correlations in a sufficiently efficient way to gain more purity by destructive interference of the quduties, compared to antithetical effects which degrade the purity. These effects include the noise added by the entanglement JPAs and the amplified e^{2r} contributions from the resource state due to detuning of k from one. From Eq. (8.10), we find that the quantum advantage increases as a function of the displacement photon number if we exploit the quantum correlations in the TMS state in a sufficiently efficient way to satisfy $1/2 \leq B(r, k, n_0) \leq 1$. In combination with the result $C(r, k) \geq C(r_*, k) = |k - 1|$ from Sec. 2.3.1, we find the noise threshold

$$n_t = \frac{1}{2}\left(\frac{k + 1}{|k - 1|} - 1\right). \qquad (8.12)$$

Thus, Ψ can only increase as a function of $|\alpha|^2$ in case the noise in the TMS state satisfies $n_0 \leq n_t$. We find that if we meet the exact condition $k = 1$, Ψ becomes independent of $|\alpha|^2$ and we can reach $\Psi > 0$ for any finite n_0. In this from a practical point of view artificial
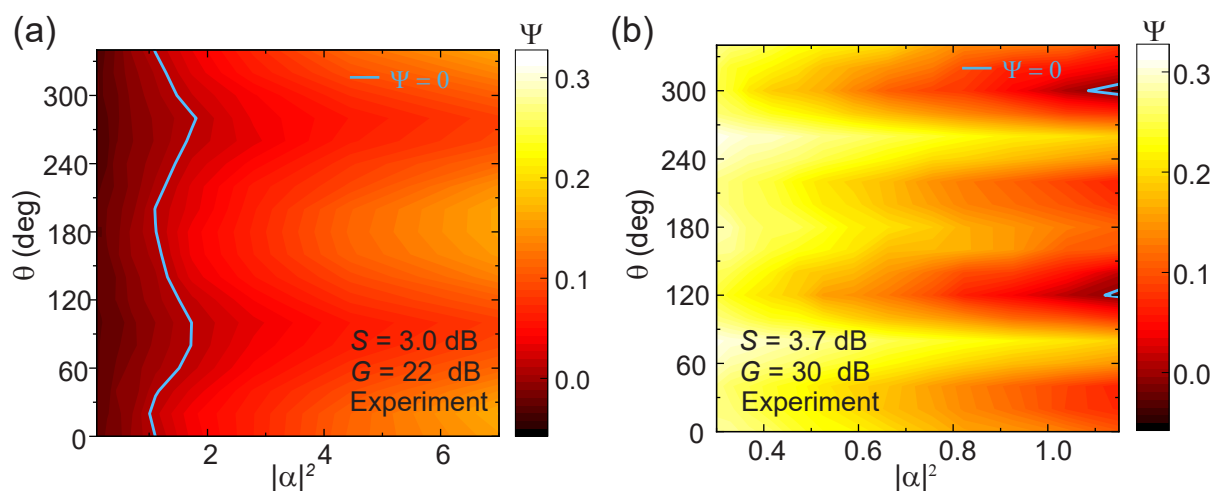
Figure 8.10: (a) Experimental quantum advantage Ψ in case of sufficiently low noise in the TMS resource and sufficiently good gain matching, $k \simeq 1$. In this case, quantum advantage increases with increasing input power. The blue line correspond to the transition threshold at which quantum advantage changes sign (b) Experimental quantum advantage Ψ for a sufficiently large gain mismatch, leading to a decreasing quantum advantage with increasing input power.

case, the JPA noise simply acts as a renormalization of the squeezing level, implying that in case $0 < C(r,1) = 2e^{-2r} < \varepsilon$ for $\varepsilon > 0$, we can reach $0 < (1 + 2n_0)C(r,1) < \varepsilon$ by increasing the squeeze factor $r \to r + \ln \sqrt{1 + 2n_0}$. However, this is not generally true for $k \neq 1$ since in this case, the $\cosh 2r$ and $\sinh 2r$ contributions in the interference function are not balanced. In this general case, the purity of the TMS resource matters significantly and noise cannot be compensated by simply increasing r. Throughout most of our teleportation experiments, we find a monotonic increase of quantum advantage Ψ with $|\alpha|^2$, which implies that we exploit quantum correlations in the TMS resource in our favor.

In summary, we have employed a cryogenic link connecting two dilution cryostats over a distance of $6.6\,\mathrm{m}$ to demonstrate successful inter-lab quantum teleportation of coherent microwave states. We have performed the experiment for up to $|\alpha|^2 = 7$ displacement photons and measure a quantum advantage for our protocol within most of the investigated parameter regimes. For the specific input photon number $|\alpha|^2 = 4.5$, we find a quantum teleportation fidelity of 0.55 ± 0.03 and a corresponding classical fidelity of 0.46 ± 0.01 in the absence of entanglement. We have demonstrated a security advantage of our protocol in case we employ entanglement. Furthermore, we have proven robustness of entanglement distribution via superconducting cables towards thermal environmental noise. Our experiments show the practical feasibility of microwave quantum communication over thermal quantum networks. As a result, our work forms a building block towards distributed quantum computing applications, e.g., by employing continuous-variable states to generate Gottesman-Kitaev-Preskill (GKP) qubits [383]. An alternative approach

are hybrid protocols such as quantum teleportation of qubit states with TMS states as entangled quantum resource [265, 266].

Chapter 9

Conclusion and outlook

9.1 Summary

In this thesis, we have experimentally demonstrated successful quantum teleportation of propagating continuous-variable microwave states between two separated laboratories. We have employed the Josephson parametric amplifier (JPA) as our main microwave quantum building block, which enables the implementation of three-wave mixing via a nonlinear Josephson inductance. We have exploited the resulting phase-sensitive amplification process to produce squeezed microwave vacuum states. We have subsequently exploited this process to generate two-mode squeezed (TMS) states and, thus, generated an entangled quantum resource for microwave quantum communication protocols. Due to the low energy of the microwave photons, compared to photons in the optical regime, we have decided to realize our experiments in a fully analog configuration. The complex microwave teleportation experiments have required a number of preparatory steps in theory and experiment. From a theoretical point of view, we have first derived how the interplay between phase-sensitive JPAs and directional couplers can be used to realize an analog phase space projection operation. On this basis, we have formulated quantum teleportation in the framework of the Gaussian analog projector formalism. In addition, we have investigated quantum teleportation for various different types of communication alphabets. Regarding experimental techniques we have realized an FPGA-based setup for efficient Wigner tomography. This approach has improved the averaging rate in our measurements by a factor of 8 as compared to our previous implementations with analog-to-digital converters and data postprocessing on a CPU. Furthermore, we have investigated single- and multi-SQUID JPAs, demonstrating improved compression properties of the latter. Due to the importance of the amplification process for advanced microwave quantum communication experiments, we have investigated the quantum efficiency of our JPAs. This number is of high relevance for quantum communication applications, since it determines many practically important quantities, such as bit rates, fidelities, or Bell efficiency. Our results reveal that, in contrast to nondegenerate amplification of narrowband signals, quantum efficiency is not bound by the standard quantum limit (SQL) if the input signal is sufficiently broadband. This observation matches our theoretical prediction. For an

amplification of broadband thermal states, we have experimentally found a maximal quantum efficiency of 0.69 ± 0.02 with nondegenerate JPAs. Here, we have also studied how serially concatenated JPAs can improve quantum efficiency of the overall amplification chain. Finally, we have investigated 2D Planck spectroscopy as an accurate method for photon number calibration.

Another topic of central relevance to quantum communication is the understanding of quantum correlations. In addition to entanglement, which has been thoroughly investigated in previous works [83], we have employed quantum discord as a more general and robust measure for quantum correlations. We have studied information flow between the TMS modes and environment. In quantum communication experiments, quantum discord can be employed to measure consumption of quantum correlations, which is directly related to how efficiently quantum resources are being exploited.

In the next step, we have demonstrated the, to the best of our knowledge, first experimental implementation of deterministic intra-fridge quantum teleportation of propagating microwave states. Specifically, we have used a TMS quantum resource to teleport coherent states with a displacement photon number of 1.1 over a distance of 42 cm. For the Bell measurement, we have employed two separate JPAs in the Josephson mixer configuration. The achieved teleportation fidelity of $F = 0.689 \pm 0.004$ significantly exceeds the asymptotic no-cloning limit. We have performed a systematic experimental study of teleportation fidelity as a function of the resource squeezing and feedforward gain. Furthermore, we have used the input-output formalism to develop a theory model which enables us to reproduce the experimental data with reasonable accuracy. In addition, we have analyzed bit rate, security, and correlation consumption of our protocol and interpreted the analog quantum teleportation protocol in the scope of Gaussian error correction.

As a crucial prerequisite for extending our teleportation range over multiple laboratories, we have set up two new laboratories for quantum communication experiments (Eve lab and Bob lab). Together with the preexisting Alice lab, we have connected all three laboratories by constructing a 6 m long cryogenic link containing three superconducting transmission lines. By carefully optimizing the cryogenic setup, we have reached a minimal center temperature of 52 mK for the mixing chamber stage of our cryogenic link. To enable stable operation of the system, we have upgraded our home-built dilution cryostat in Alice lab with a more powerful pulse-tube refrigerator. To benchmark the performance of the system, we have performed multiple heat transport tests. Eventually, we have combined the intra-fridge quantum teleportation setup and the cryogenic link to realize inter-lab quantum communication. We have implemented successful entanglement distribution over the cryogenic link and verified the fluctuation-dissipation theorem. In the end, we have realized the inter-lab quantum teleportation with fidelity of 0.55 ± 0.03 for a coherent state with a displacement photon number of 4.5. In a practical security analysis, we have demonstrated that the security of the protocol improves in case we increase the entanglement strength.

9.2 Outlook

The work done within the framework of this thesis, both in terms of cryogenic installations and propagating quantum microwave communication technology, forms a basis for future realization of larger scale superconducting microwave quantum networks. In a first step, we could employ our experimental setup to teleport displaced squeezed thermal states, which can be interpreted as universal Gaussian quantum teleportation. This approach could then be used for cryptographic Gaussian protocols, such as teleportation-based quantum key distribution (QKD). In addition, we could realize analog dense coding by reverting the direction of signal flow in our setup. Furthermore, our demonstration of entanglement preservation in a superconducting system, even at elevated temperatures, motivates further research in the direction of thermal quantum networks. In such a scenario, one would implement quantum channels at temperatures exceeding, e.g., the LHe threshold, which would be an important step for many real-world applications of microwave quantum networks. In this way, one could significantly simplify our quantum communication hardware what is relevant from an economic point of view.

So far, we have focused on continuous variable (CV) quantum systems. However, in case we want to use our quantum communication protocols for distributed quantum computing, we require an interface to the discrete variable (DV) regime. In future experiments, we could modify our setup to realize hybrid quantum teleportation, where one employs the TMS resource for teleportation of DV quantum states, such as qubit or Fock states [265, 266]. One way to generate such a CV-DV interface is to exploit a TMS state for the generation of entanglement between remote qubits using a quantum steering protocol [427, 428]. In conclusion, our research has demonstrated the experimental feasibility of unconditionally secure microwave quantum local area networks (QLAN). Such a QLAN could ultimately be employed for distributed superconducting quantum computing. In the long term, we envision that superconducting quantum networks can be eventually employed for quantum internet applications by linking the microwave QLAN to long-range quantum channels. Despite the more demanding cryogenic setup, microwave QLAN technology naturally overcomes one key bottleneck for networked superconducting quantum computing: the microwave-to-optics conversion. Despite massive efforts over the last decade, actual quantum efficienies are still in the 10^{-5} range here [70], orders of magnitude away from gate fidelities with multiple nines required for quantum error correction.
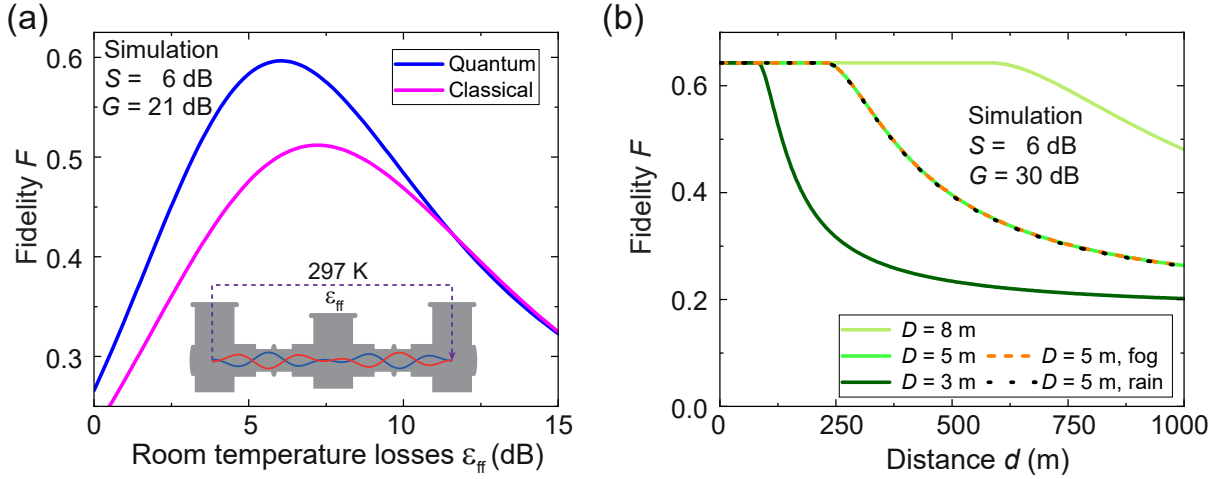
Figure 9.1: (a) Simulation results for inter-lab quantum teleportation over our cryogenic link with an analog room temperature feedforward. The plot shows the expected teleportation fidelity as a function of the feedforward losses ε_{ff} at room temperature. The maximum corresponds to $k \sim 1$. For the simulation, we use the parameters from Tab. 6.1. In addition, we assume realistic input attenuation for the cryostat as well as a state-of-the-art HEMT amplifier adding 7 noise photons. The simulation predicts a maximal quantum (classical) fidelity of 0.596 (0.51). (b) Expected quantum teleportation fidelity with open-air feedforward. The quantity D denotes the aperture of the parabolic transmitter (Alice) and receiver (Bob) antenna. The antenna aperture determines the maximal antenna gain according to Eq. (9.3). In case a lower gain is required to satisfy the projection, we can always achieve $k = 1$ by adding more attenuation at Bob's receiver. This gain regime is indicated by the flat plateaus. In case the parabolic antenna gain is insufficient to reach $k = 1$, we find rabid decay of the teleportation fidelity. We find a maximal teleportation fidelity of $F = 0.64$ in this case. Furthermore, fidelity is limited by geometric effects due to isotropic propagation in free space and shows no significant dependence on weather conditions. The atmospheric path losses for different weather conditions are modelled based on the information in Ref. 429, as described in Appendix G.

In the near term, we suggest two follow-up experiments related to coherent state quantum teleportation. In the first experiment, we consider using a room temperature microwave feedforward for quantum teleportation. For the second experiment, one can go one step further and perform an open-air feedforward distribution.

Quantum teleportation with room temperature feedforward   Here, we propose to perform a modified version of the inter-fridge quantum teleportation experiment described in chapter 8, but with the analog feedforward signal being transmitted through a coaxial cable at room temperature as shown in Fig. 9.1(a). At the same time, we implement the entanglement distribution via a cryogenic superconducting link. Nevertheless, the room temperature feedforward significantly simplifies the experimental set-up and open interesting use cases in the area of QKD. In this context, the entangled resource is treated

as a private, secure channel, while the feedforward signal represents the public channel. We combine the results from the security analysis presented in Sec. 8.3 with the error-correction interpretation from Sec. 6.4. To maintain coherence of our quantum states, we need to protect the setup from thermal noise entering through the RF lines. Thus, before we couple the feedforward to Bob's directional coupler, the signal needs to undergo a significant input attenuation $\varepsilon_{\mathrm{in}} = 50\,\mathrm{dB}$, discussed in Sec. 3.1.1. This attenuation needs to be compensated on Alice's side by cryogenic amplifiers. In our case, we assume that the corresponding gain is provided by the JM with $G = 21\,\mathrm{dB}$ and a cryogenic HEMT amplifier [84] with $G_{\mathrm{H}} = 40\,\mathrm{dB}$ and $n_{\mathrm{H}} = 7$ noise photons. In addition, we employ a room temperature RF amplifier with $G_{\mathrm{rt}} = 15\,\mathrm{dB}$, which we for now assume to be noiseless. In linear units, the projection condition to match input and output displacement is given by

$$\beta G G_{\mathrm{H}} G_{\mathrm{rt}} = 4(1 - \varepsilon_{\mathrm{A}})(1 - \varepsilon_{\mathrm{ff}})(1 - \varepsilon_{\mathrm{in}}), \tag{9.1}$$

where ε_{A} corresponds to the losses on Alice's side, before the JM and $\varepsilon_{\mathrm{ff}}$ are the feedforward losses. In our theory, we use the loss and noise parameters listed in Tab. 6.1, and assume $6\,\mathrm{dB}$ of resource squeezing. In addition, we assume $\varepsilon_{\mathrm{ff}}$ of feedforward losses which couple to a thermal bath at room temperature and the cryostat attenuations forming $\varepsilon_{\mathrm{in}}$ to their respective cryostat stage temperatures. Figure 9.1(a) shows the result of this model for teleportation of a coherent microwave state with $|\alpha|^2 = 2$ displacement photons. Maximal fidelity is obtained in the regime where we meet the condition $k = 1$. Our model predicts that we can reach a maximal quantum teleportation fidelity of 0.606 and a maximal classical fidelity of 0.512 with state-of-the-art parameters. To further optimize fidelity, it can be beneficial to chain different types of cryogenic amplifiers. As investigated in Sec. 2.1.5, the gain distribution between these amplifiers determines the overall noise in the feedforward.

Quantum teleportation with open-air feedforward In a more advanced future experiment, Alice does not need to transmit the feedforward signal through a cable, but could directly emit it through open-air using a suitable antenna [430, 431]. This scenario is especially relevant in case Alice and Bob have the capability to store their entangled resource modes in a quantum memory for consumption during the protocol, implying that establishing a cryogenic connection between both communication parties becomes obsolete [218]. We assume that Bob uses an equivalent antenna on his side as a receiver. Since the feedforward signal can be regarded as classical, it can be described using the Maxwell equations, implying that Bob's detected power at the receiver is determined by the Friis antenna equation [362, 432]

$$P_{\mathrm{r}} = \frac{P_{\mathrm{t}} G_{\mathrm{t}} G_{\mathrm{r}}}{L_{\mathrm{p}}} \left(\frac{\lambda}{4\pi d} \right)^2, \tag{9.2}$$

where P_{t} is Alice's transmitted power, G_{t} (G_{r}) is the transmitter (receiver) antenna gain, L_{p} denotes the path losses, λ the wavelength and d corresponds to the transmission distance. The dependence $P_{\mathrm{r}} \propto 1/d^2$ indicates a strong decrease of power with the transmission distance and results from the isotropic emission of the signal into open-air environment. Since these losses result from a purely geometric effect and do not couple to any bath, we assume that they can be fully compensated by increasing the antenna gain [362]. For our estimations, we assume that Alice's and Bob's antennae are parabolic, implying [93]

$$G_{\mathrm{r}} = G_{\mathrm{t}} = e_{\mathrm{A}} \left(\frac{D\omega}{2c} \right)^2, \tag{9.3}$$

where we assume an aperture efficiency $e_{\mathrm{A}} = 0.67$ and an effective antenna diameter D. In addition, we assume that the antenna is designed to perfectly compensate for the impedance mismatch between free space ($377\,\Omega$) and the circuit impedance ($50\,\Omega$) [433]. The atmospheric losses $\varepsilon_{\mathrm{ff}}$ are related to the distance d by the Lambert-Beer law, $\varepsilon_{\mathrm{ff}} = 10^{-\gamma_{\mathrm{a}}d/10}$, where γ_{a} denotes the atmospheric absorption coefficient. This coefficient depends on the weather conditions and is determined in Appendix G by the information provided in Ref. 429 and Ref. 362. Figure 9.1(b) shows the result from our model for antenna apertures ranging between $3 - 8\,\mathrm{m}$ and communication distances up to $1\,\mathrm{km}$. We assume a signal frequency $\omega/2\pi = 5.5\,\mathrm{GHz}$, resource squeezing $S = 6\,\mathrm{dB}$ and JM gain $G = 30\,\mathrm{dB}$. In addition, we use the parameters from Tab. 6.1. Solid lines correspond to ideal weather conditions, whereas the orange dashed (black dotted) line corresponds to fog (rain) for an aperture $D = 5\,\mathrm{m}$. Thus, in accordance with Sec. 6.4, our protocol is robust towards weather-induced imperfections in the feedforward channel. In fact, after a distance of $1.2\,\mathrm{km}$, fidelity is reduced by a factor of $0.46\,\%$ in case of rain, as compared to ideal conditions. Similar as in Fig. 9.1(a), the fidelity is maximal in case the gain compensates for the feedforward losses. In case the required gain is lower than the maximal antenna gain, Eq. (9.3), we can always lower the effective gain by attenuating the signal at the receiver antenna. This scenario corresponds to the flat plateaus in Fig. 9.1(b). In case the projection condition $k = 1$ requires a higher gain than Eq. (9.3), the fidelity decays rapidly with increasing distance. Consequently, the antenna aperture eventually determines the maximal communication range. In the open-air scenario, the dominant loss contribution arises from geometric factors and losses resulting from different weather conditions can be neglected for intermediate distances. This stresses the robustness of our protocol for open-air applications.

Appendix A

Detailed setup drawings

Figure A.1: Full setup drawing for the measurements related to quantum efficiency and chained JPAs, as described in chapter 4.
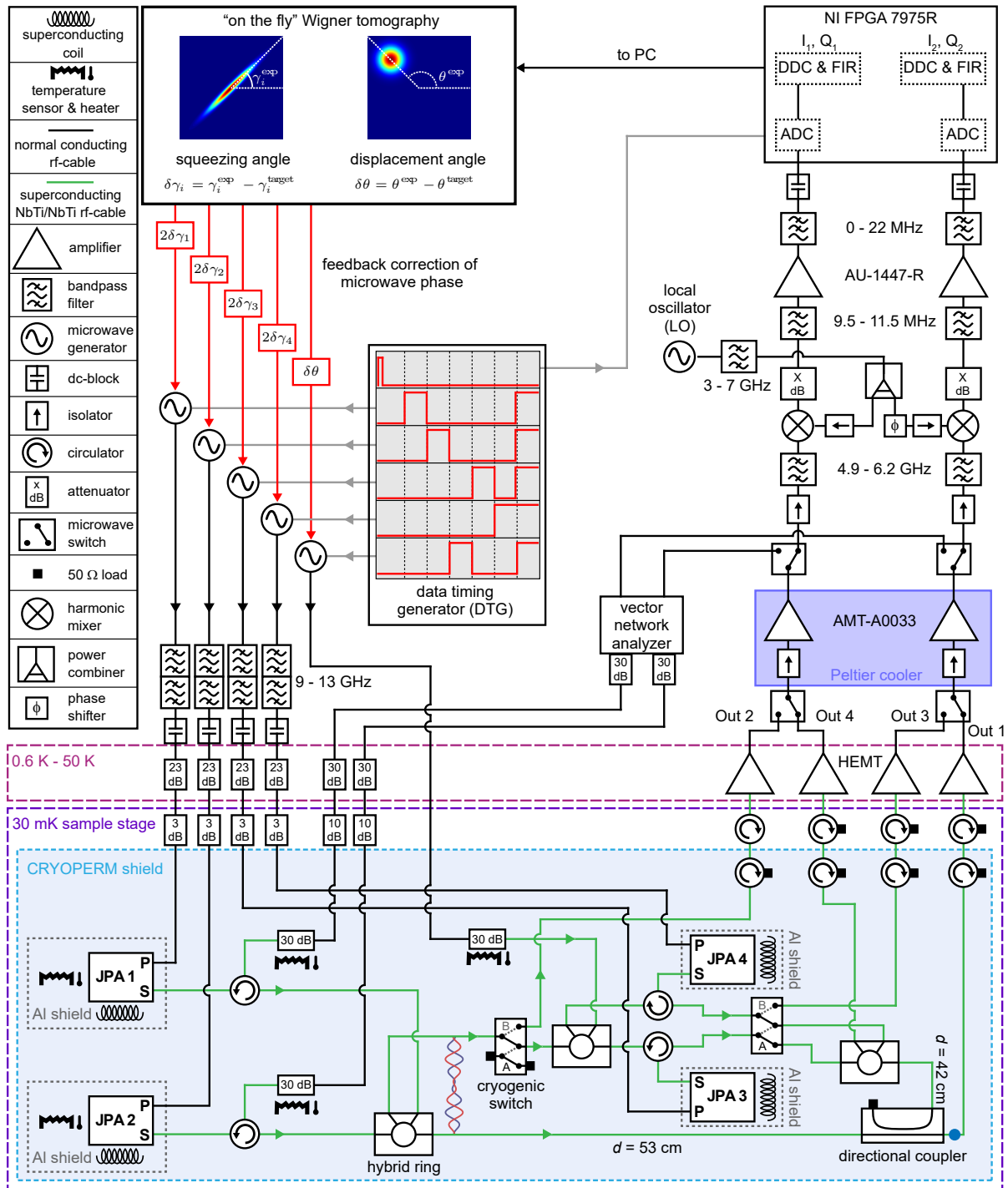
Figure A.2: Full setup drawing for the quantum teleportation experiment presented in chapter 6. The complete scheme for inter-lab quantum teleportation, as described in chapter 8, is analogous and differs only by the fact that feedforward and TMS idler are transmitted over the cryogenic link. The teleported state is measured via output line "Out 1". "Out 2" is used for TMS state characterization and balancing, "Out 3" is employed for characterization of the coherent to-be-teleported state and "Out 4" is used for stabilization of squeezing and amplification phases. The blue dot indicates the reconstruction point for teleported states.

Appendix B

Loss measurements with chained JPAs

We consider a scenario where we chain 3 noiseless and JPAs with equal properties, operated in degenerate mode. As we will see in the following, such an amplification chain in principle allows us to detect unkown losses ε_x between the second JPA and the third JPA by adjusting the known losses ε between the first JPA and the second JPA. The advantage of this procedure is independence of the exact PNCF. We assume that all 3 JPAs amplify with the same squeeze factor r. Furthermore, we assume that the first 2 JPAs amplify with the same squeezing angle and that the third JPA amplifies with an orthogonal squeezing angle. We now adjust ε independently such that the variances of the final state coincide. Thus, if we manage to calibrate ε and control it via an external control parameter (e.g., magnetic flux, temperature), we can use this configuration to accurately determine losses at millikelvin temperatures. The operation principle of such a device, depicted in Fig. B.1(b), resembles that of the Wheatstone resistance bridge [434],
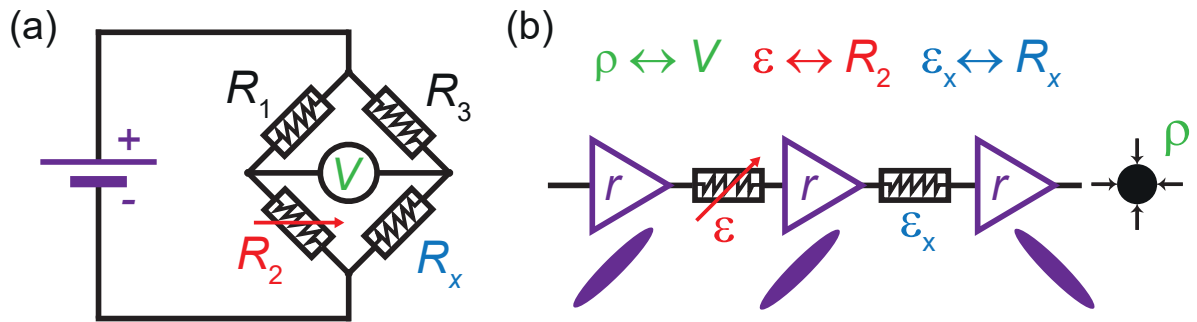
Figure B.1: (a) Wheatstone bridge setup for sensitive measurement of an unknown resistance R_x. In this setup, we tune the resistance R_2 until we balance electric potential, $V = 0$. Consequently, R_x can be determined only from R_1, R_3 and R_2. (b) Setup for sensitive loss measurement using 3 chained JPAs. Losses ε between the first and second JPA are assumed to be well known and tunable and losses ε_x are assumed to be unknown. We operate all 3 JPAs with same squeeze factor r. The first two JPAs amplify with the same squeezing angle and the third JPA is operated with orthogonal squeezing angle. In analogy to the Wheatstone bridge, we tune ε until the output state is balanced. This enables us to determine ε_x from ε, independently of r and thus of any potentially imprecise PNCF.

shown in Fig. B.1(a). In the Wheatstone bridge setup, we attempt to determine R_x and therefore vary R_2 to balance the electric potential such that we have $V = 0$, independently of the bias voltage. The resistances then satisfy the condition $R_x R_1 = R_2 R_3$. In our suggested setup, voltage V is therefore analogous to the variance ratio ρ, the squeeze factor r corresponds to the bias voltage and ε and ε_x assume the role of the tunable known resistance R_2 and the unkonwn resistance R_x, respectively. In the following, we determine the squeezing-independent relation between losses at the balancing point. After the first JPA, we obtain the variances

$$v_{\mathrm{s}} = \frac{e^{-2r}}{4}(1 - \varepsilon) + \frac{\varepsilon}{4}, \tag{B.1}$$

$$v_{\mathrm{a}} = \frac{e^{2r}}{4}(1 - \varepsilon) + \frac{\varepsilon}{4}, \tag{B.2}$$

and after the second JPA

$$v_{\mathrm{ss}} = e^{-2r}\left[\frac{e^{-2r}}{4}(1 - \varepsilon) + \frac{\varepsilon}{4}\right](1 - \varepsilon_x) + \frac{\varepsilon_x}{4}, \tag{B.3}$$

$$v_{\mathrm{aa}} = e^{2r}\left[\frac{e^{2r}}{4}(1 - \varepsilon) + \frac{\varepsilon}{4}\right](1 - \varepsilon_x) + \frac{\varepsilon_x}{4}. \tag{B.4}$$

After the third JPA, we find

$$v_{\mathrm{ssa}} = \left[\frac{e^{-2r}}{4}(1 - \varepsilon) + \frac{\varepsilon}{4}\right](1 - \varepsilon_x) + e^{2r}\frac{\varepsilon_x}{4}, \tag{B.5}$$

$$v_{\mathrm{aas}} = \left[\frac{e^{2r}}{4}(1 - \varepsilon) + \frac{\varepsilon}{4}\right](1 - \varepsilon_x) + e^{-2r}\frac{\varepsilon_x}{4}. \tag{B.6}$$

We now tune ε such that the resulting state is balanced in phase space (this condition is analogous to choosing the resistances such that the voltage $V = 0$ in the Wheatstone-setup). We then obtain the condition

$$v_{\mathrm{ssa}} = v_{\mathrm{aas}}, \tag{B.7}$$

which can be rewritten as

$$2\sinh 2r\left[\varepsilon_x - (1 - \varepsilon)(1 - \varepsilon_x)\right] = 0. \tag{B.8}$$

We observe that for any $r > 0$ we then have

$$\varepsilon_x = \frac{1 - \varepsilon}{2 - \varepsilon}, \tag{B.9}$$

independently of r. Since we can assume that variance balancing is independent of the exact value of the PNCF, we find a condition for ε_x which only depends on ε.

Appendix C

Optimal gain distribution for noise reduction of N chained JPAs

In this section, we analyze the optimal way to subdivide a gain g to N JPAs with equal noise properties. Let g_j denote the gain of the jth JPA. We then have the constraint

$$\prod_{j=1}^{N} g_j = g. \tag{C.1}$$

From the Friis equation, we find the Lagrangian

$$\mathcal{L}(\{g_j\}, \lambda) = \sum_{j=1}^{N} n_{\text{J}}(g_j) \prod_{i=j}^{N} g_i + \lambda \left(\prod_{j=1}^{N} g_j - g \right). \tag{C.2}$$

We calculate the gradient. $\partial\mathcal{L}/\partial\lambda$ then reproduces the constraint Eq. (C.1). We furthermore obtain

$$\frac{\partial\mathcal{L}}{\partial g_k} = \sum_{j=1}^{N} \frac{\partial}{\partial g_k} \left[n_{\text{J}}(g_j) \prod_{i=j}^{N} g_i \right] + \lambda \prod_{i=j, i \neq k}^{N} g_i$$

$$= \sum_{j=1}^{N} \left(\frac{\partial n_{\text{J}}(g_j)}{\partial g_k} \prod_{i=j}^{N} g_i + n_{\text{J}}(g_j) \frac{\partial}{\partial g_k} \prod_{i=j}^{N} g_i \right) + \lambda \prod_{i=j, i \neq k}^{N} g_i \tag{C.3}$$

$$= \frac{\partial n_{\text{J}}(g_k)}{\partial g_k} \prod_{i=k}^{N} g_i + \sum_{j=1}^{N} n_{\text{J}}(g_j) \prod_{i=j, j \neq k}^{N} g_i + \lambda \prod_{i=j, i \neq k}^{N} g_i. \tag{C.4}$$

If we assume a linear dependence of the noise on the gain, $n_{\text{J}}(g_i) = n' g_i$, we can solve the systems of equations Eq. (C.4) analytically. We find

$$0 = 2n' g_1 \cdots g_N + \lambda g_2 \cdots g_N, \tag{C.5}$$

implying

$$\lambda = -2n' g_1. \tag{C.6}$$

235

Furthermore, we find

$$0 = n' g_1^2 \cdots g_{i-1} g_{i+1} \cdots g_N + n' g_2^2 \cdots g_{i-1} g_{i+1} \cdots g_N$$
$$+ \cdots + n' g_{i-1}^2 g_{i+1} \cdots g_N + 2n' g_1 g_{i+1} \cdots g_N + \lambda g_1 \cdots g_{i-1} g_{i+1} \cdots g_N. \tag{C.7}$$

Via induction, we find the recursion relation

$$g_i^2 = 2 g_{i+1}. \tag{C.8}$$

Thus, from $g_i = \sqrt{2 g_{i+1}}$, we find

$$g_1 = 2^{1 - 2^{1-i}} g_i^{\left(\frac{1}{2}\right)^{i-1}}, \tag{C.9}$$

and inverted

$$g_i = 2 \left(\frac{g_1}{2} \right)^{2^{i-1}}. \tag{C.10}$$

This result allows us to write down a relation between the desired total gain g and the gain g_1 of the first amplifier

$$g = \prod_{i=1}^{N} g_i = \prod_{i=1}^{N} 2 \left(\frac{g_1}{2} \right)^{2^{i-1}} = (M_N + 1) \left(\frac{g_1}{2} \right)^{M_N}, \tag{C.11}$$

with the Mersenne numbers $M_N = 2^N - 1$. In addition, we can determine all gains g_i via Eq. (C.10).

Appendix D

Hybrid quantum teleportation

We study the theory of hybrid quantum teleportation. Within such a hybrid protocol, we employ a TMS resource to teleport a qubit state. The description is based on Wigner functions and follows the argumentation in Ref. 273. We assume that we operate in the projective limit, Eq. (2.176). In this case, the loss- and noiseless quantum teleportation protocol transforms the Wigner function of the to-be-teleported state according to Eq. (2.231). In case we insert the TMS Wigner function, Eq. (2.116), for the first two modes, we can rewrite Eq. (2.231) as a convolution integral [273]

$$W_{\text{out}}(q,p) = \frac{1}{k}\left[W_{\text{in}} \star G_{\frac{\xi(r,k)}{2}}\right]\left(\frac{q}{\sqrt{k}}, \frac{p}{\sqrt{k}}\right) \tag{D.1}$$

with the normalized interference function $\xi(r,k) \equiv C(r,k)/k$ and a bivariate Gaussian distribution

$$G_\tau(q,p) = \frac{1}{2\pi\tau}\exp\left(-\frac{q^2 + p^2}{2\tau}\right). \tag{D.2}$$

In the next step, we combine the density matrix formulation of qubit teleportation with the Wigner function formulation. We assume we want to teleport a target state described by density operator

$$\hat{\rho}_{\text{in}} = \sum_{m,n}\langle m|\hat{\rho}_{\text{in}}|n\rangle|m\rangle\langle n|. \tag{D.3}$$

We furthermore describe the Gaussian teleportation protocol by a superoperator $\hat{T}$, connecting input state and Bob's final output state $\hat{\rho}_{\text{out}}$ via

$$\hat{\rho}_{\text{out}} = \hat{T}(\hat{\rho}_{\text{in}}) = \sum_{m,n}\langle m|\hat{\rho}_{\text{in}}|n\rangle\hat{T}(|m\rangle\langle n|). \tag{D.4}$$

We expand each operator $\hat{T}(|m\rangle\langle n|)$ in the photon number basis

$$\hat{T}_{mn} \equiv \hat{T}(|m\rangle\langle n|) = \sum_{j,l}T_{mn\to jl}|j\rangle\langle l|. \tag{D.5}$$

The coefficient $T_{mn \to jl}$ describes the complex probability amplitude that the protocol $\hat{T}$ maps the input density matrix element $|m\rangle\langle n|$ to density matrix element $|j\rangle\langle l|$ [273]. Density matrix formulation is transformed to Wigner function description via Weyl correspondence [147]. For the input state, we obtain

$$W_{\text{in}}(q,p) = \frac{1}{2\pi} \int dx e^{ipx} \langle q - x/2|\hat{\rho}_{\text{in}}|q + x/2\rangle = \sum_{m,n} \langle m|\hat{\rho}_{\text{in}}|n\rangle W^{|m\rangle\langle n|}(q,p), \qquad (D.6)$$

where we define

$$W^{|m\rangle\langle n|}(q,p) \equiv \frac{1}{2\pi} \int dx e^{ipx} \langle q - x/2|m\rangle\langle n|q + x/2\rangle. \qquad (D.7)$$

These integrals can be found in literature [435],

$$W^{|m\rangle\langle n|}(q,p) = \frac{1}{2\pi} \begin{cases} (-1)^n \sqrt{\frac{n!}{m!}} 2^{m-n} (\alpha^*)^{m-n} L_n^{m-n}(4|\alpha|^2) \exp(-2|\alpha|^2) & 0 \leq n \leq m, \\ (-1)^m \sqrt{\frac{m!}{n!}} 2^{n-m} \alpha^{n-m} L_m^{n-m}(4|\alpha|^2) \exp(-2|\alpha|^2) & 0 \leq m < n, \end{cases} \qquad (D.8)$$

where $\alpha \equiv p + iq$ denotes the complex displacement and $L_c^{a-b}(x)$ are the generalized Laguerre functions. We furthermore apply Weyl correspondence to the output state,

$$W_{\text{out}}(q,p) = \frac{1}{2\pi} \int dx e^{ipx} \langle q - x/2|\hat{\rho}_{\text{out}}|q + x/2\rangle \qquad (D.9)$$

$$= \sum_{m,n} \langle m|\hat{\rho}_{\text{in}}|n\rangle \frac{1}{2\pi} \int dx e^{ipx} \langle q - x/2|\hat{T}(|m\rangle\langle n|)|q + x/2\rangle \qquad (D.10)$$

$$= \sum_{m,n} \sum_{j,l} \langle m|\hat{\rho}_{\text{in}}|n\rangle T_{mn \to jl} \frac{1}{2\pi} \int dx e^{ipx} \langle q - x/2|j\rangle\langle l|q + x/2\rangle \qquad (D.11)$$

$$= \sum_{m,n} \sum_{j,l} \langle m|\hat{\rho}_{\text{in}}|n\rangle T_{mn \to jl} W^{|j\rangle\langle l|}(q,p). \qquad (D.12)$$

From Eq. (D.1), we find

$$W_{\text{out}}(q,p) = \frac{1}{k} \left[W_{\text{in}} \star G_{\frac{\xi(r,k)}{2}} \right] \left(\frac{q}{\sqrt{k}}, \frac{p}{\sqrt{k}} \right) \qquad (D.13)$$

$$= \sum_{m,n} \langle m|\hat{\rho}_{\text{in}}|n\rangle \frac{1}{k} \left[W^{|m\rangle\langle n|} \star G_{\frac{\xi(r,k)}{2}} \right] \left(\frac{q}{\sqrt{k}}, \frac{p}{\sqrt{k}} \right). \qquad (D.14)$$

Since the expansions in Eq. (D.9) and Eq. (D.13) hold for arbitrary states, we obtain from equating the coefficients

$$\sum_{j,l} T_{mn \to jl} W^{|j\rangle\langle l|}(q,p) = \frac{1}{k} \left[W^{|m\rangle\langle n|} \star G_{\frac{\xi(r,k)}{2}} \right] \left(\frac{q}{\sqrt{k}}, \frac{p}{\sqrt{k}} \right). \qquad (D.15)$$

It then follows from orthogonality of the Laguerre functions that the transition probability amplitudes are determined by the integral

$$T_{mn \to jl} = 2\pi \int dq \int dp \, W^{|j\rangle\langle l|}(q,p) \frac{1}{k} \left[W^{|m\rangle\langle n|} \star G_{\frac{\xi(r,k)}{2}} \right] \left(\frac{q}{\sqrt{k}}, \frac{p}{\sqrt{k}} \right). \tag{D.16}$$

Next, we restrict to teleportation of pure qubit states

$$|\psi\rangle = \cos\frac{\theta}{2}|0\rangle + e^{i\varphi}\sin\frac{\theta}{2}|1\rangle. \tag{D.17}$$

We formally split off the state leakage contribution

$$\hat{T}_{mn} = \sum_{j,l} T_{mn \to jl}|j\rangle\langle l| = T_{mn \to 00}|0\rangle\langle 0| + T_{mn \to 01}|0\rangle\langle 1| + T_{mn \to 10}|1\rangle\langle 0| + T_{mn \to 11}|1\rangle\langle 1|$$
$$+ \sum_{j,l \geq 2} T_{mn \to jl}|j\rangle\langle l|, \tag{D.18}$$

where the last contribution corresponds to leaking out off the qubit Hilbert space, induced by the teleportation protocol. The output state is then formally described by the density matrix

$$\hat{\rho}_{\text{out}} = \rho_{00}|0\rangle\langle 0| + \rho_{10}|1\rangle\langle 0| + \rho_{01}|0\rangle\langle 1| + \rho_{11}|1\rangle\langle 1| + \hat{\rho}_{\geq 2}, \tag{D.19}$$

where the coefficients are determined by the product of the initial qubit density matrix elements and the probability of teleportation-induced mapping between respective density matrix contributions, i.e.,

$$\rho_{00} = T_{00 \to 00}\cos^2\frac{\theta}{2} + T_{10 \to 00}e^{i\varphi}\cos\frac{\theta}{2}\sin\frac{\theta}{2} + T_{01 \to 00}e^{-i\varphi}\cos\frac{\theta}{2}\sin\frac{\theta}{2} + T_{11 \to 00}\sin^2\frac{\theta}{2}, \tag{D.20}$$

$$\rho_{10} = T_{00 \to 10}\cos^2\frac{\theta}{2} + T_{10 \to 10}e^{i\varphi}\cos\frac{\theta}{2}\sin\frac{\theta}{2} + T_{01 \to 10}e^{-i\varphi}\cos\frac{\theta}{2}\sin\frac{\theta}{2} + T_{11 \to 10}\sin^2\frac{\theta}{2}, \tag{D.21}$$

$$\rho_{01} = T_{00 \to 01}\cos^2\frac{\theta}{2} + T_{10 \to 01}e^{i\varphi}\cos\frac{\theta}{2}\sin\frac{\theta}{2} + T_{01 \to 01}e^{-i\varphi}\cos\frac{\theta}{2}\sin\frac{\theta}{2} + T_{11 \to 01}\sin^2\frac{\theta}{2}, \tag{D.22}$$

$$\rho_{11} = T_{00 \to 11}\cos^2\frac{\theta}{2} + T_{10 \to 11}e^{i\varphi}\cos\frac{\theta}{2}\sin\frac{\theta}{2} + T_{01 \to 11}e^{-i\varphi}\cos\frac{\theta}{2}\sin\frac{\theta}{2} + T_{11 \to 11}\sin^2\frac{\theta}{2}. \tag{D.23}$$

The state leakage contribution is given by

$$\hat{\rho}_{\geq 2} = \sum_{j,l \geq 2} a_{jl}|j\rangle\langle l|, \tag{D.24}$$

where

$$a_{jl} = T_{00 \to jl}\cos^2\frac{\theta}{2} + T_{10 \to jl}e^{i\varphi}\cos\frac{\theta}{2}\sin\frac{\theta}{2} + T_{01 \to jl}e^{-i\varphi}\cos\frac{\theta}{2}\sin\frac{\theta}{2} + T_{11 \to jl}\sin^2\frac{\theta}{2}. \tag{D.25}$$

The exact functional shape of $\hat{\rho}_{\geq 2}$ is not yet of interest and the effect of state leakage manifests as a contribution to teleportation infidelity. Next, we determine the transition probabilities $T_{mn \to jl}$ for $j, l, m, n \leq 1$. In this case, we can explicitly integrate the quasiprobability distributions and find for the population contributions

$$T_{00 \to 00} = \frac{2}{k + 1 + C(r,k)}, \qquad T_{00 \to 11} = 2\frac{C(r,k) + k - 1}{[C(r,k) + k + 1]^2}, \tag{D.26}$$

$$T_{11 \to 00} = 2\frac{C(r,k) - k + 1}{[C(r,k) + k + 1]^2}, \tag{D.27}$$

and

$$T_{11 \to 11} = \frac{2}{[C(r,k) + k + 1]^3}\left[(C(r,k) - k + 1)(C(r,k) + k - 1) + 4k\right]. \tag{D.28}$$

For the coherences, we find

$$T_{00 \to 01} = T_{00 \to 10} = 0, \qquad T_{00 \to 01} = T_{00 \to 10} = 0, \tag{D.29}$$

$$T_{01 \to 00} = T_{10 \to 00} = T_{01 \to 11} = T_{10 \to 11} = 0, \tag{D.30}$$

$$T_{10 \to 01} = T_{01 \to 10} = 0, \tag{D.31}$$

and

$$T_{10 \to 10} = T_{01 \to 01} = \frac{4\sqrt{k}}{[C(r,k) + k + 1]^2}. \tag{D.32}$$

We find that for transitions between coherences, we have $T_{mn \to jl} = 0$ as long as $m \neq j$ and $n \neq l$, implying that the ideal teleportation protocol is phase-preserving and does not induce phase flip errors. The Uhlmann fidelity between input and output is given by

$$F = \langle \psi | \hat{\rho}_{\text{out}} | \psi \rangle = \cos^2\frac{\theta}{2}\rho_{00} + \cos\frac{\theta}{2}\sin\frac{\theta}{2}e^{i\varphi}\rho_{01} + \cos\frac{\theta}{2}\sin\frac{\theta}{2}e^{-i\varphi}\rho_{10} + \sin^2\frac{\theta}{2}\rho_{11}. \tag{D.33}$$

A simple calculation shows

$$\rho_{00} = \frac{2}{C(r,k) + k + 1} - \frac{4k\sin^2\frac{\theta}{2}}{[C(r,k) + k + 1]^2}, \tag{D.34}$$

$$\rho_{11} = \frac{2}{[C(r,k) + k + 1]^3}\left[C^2(r,k) - 1 + k(C(r,k) + 3) + k(C(r,k) + k - 3)\cos\theta\right], \tag{D.35}$$

$$\rho_{01} = \rho_{10}^* = \frac{4\sqrt{k}}{[C(r,k) + k + 1]^2}e^{-i\varphi}\cos\frac{\theta}{2}\sin\frac{\theta}{2}. \tag{D.36}$$

The resulting fidelity can then be expressed as

$$F(r, k, \theta) = f_1(r, k) + f_2(r, k) \cos \theta + f_3(r, k) \cos 2\theta, \tag{D.37}$$

where

$$f_1(r, k) = \frac{k^{\frac{3}{2}} + \sqrt{k}[C(r, k) + 1] + 2C(r, k)[C(r, k) + 1] + 2k[C(r, k) + 3]}{[C(r, k) + k + 1]^3}, \tag{D.38}$$

$$f_2(r, k) = \frac{2[C(r, k)(1 + k) + (k - 1)^2]}{[C(r, k) + k + 1]^3}, \tag{D.39}$$

$$f_3(r, k) = -\sqrt{k} \frac{C(r, k) + (\sqrt{k} - 1)^2}{[C(r, k) + k + 1]^3}. \tag{D.40}$$

We assume arbitrary pure qubit states for the input codebook. Thus, the average fidelity is given by integration over the Bloch sphere surface

$$\bar{F}(r, k) = \frac{1}{4\pi} \int_0^{2\pi} d\varphi \int_0^{\pi} d\theta F(r, k, \theta) \sin \theta = f_1(r, k) - \frac{1}{3} f_3(r, k). \tag{D.41}$$

We then have

$$\bar{F}(0, 1) = \frac{5}{12}, \qquad \bar{F}(r \to \infty, 1) = 1. \tag{D.42}$$

We have to compare to the no-cloning/classical threshold for conventional qubit teleportation [233, 436]

$$F_c = \frac{2}{3}, \qquad F_{nc} = \frac{5}{6}. \tag{D.43}$$

In the following, we look at four special cases.

Case 1: $k = 1$ In this case of ideal projection, we find

$$F(r, 1, \theta) = \frac{1 + \tanh r}{32 \cosh r} [8 \cosh 2r + 5 + 4 \cos \theta - \cos 2\theta]. \tag{D.44}$$

For the ground state, we obtain

$$F(r, 1, 0) = \frac{1 + \tanh r}{2}. \tag{D.45}$$

For teleporting the excited qubit state, we find

$$F(r, 1, \pi) = \frac{1}{4} (1 + \tanh r) (1 + \tanh^2 r). \tag{D.46}$$

This result coincides with our previous result of Fock state $|1\rangle$ teleportation [cf. Eq. (2.237)]. The average fidelity over the Bloch sphere surface is given by

$$\bar{F}(r,1) = \frac{e^{2r}(3 + 4e^{2r} + 3e^{4r})}{3(e^{2r} + 1)^3}. \tag{D.47}$$

Case 2: $k \neq 1, r = r_*(k)$ This case discusses the symmetry-broken regime $k \neq 1$ of coexisting solutions. In this case, the energy within Bob's and Alice's TMS modes is asymmetrically distributed. We find

$$F(r_*, k, \theta) = \frac{1}{4} \begin{cases} 2 + \sqrt{k} + k + 2(1-k)\cos\theta + \sqrt{k}(\sqrt{k}-1)\cos 2\theta & 0 \leq k \leq 1, \\ \frac{1}{k^2}\left[1 + \sqrt{k} + 2k + 2(k-1)\cos\theta - (\sqrt{k}-1)\cos 2\theta\right] & k > 1. \end{cases} \tag{D.48}$$

For the ground state, we have

$$F(r_*, k, 0) = \begin{cases} 1 & 0 \leq k \leq 1, \\ \frac{1}{k} & k > 1. \end{cases} \tag{D.49}$$

For the excited state, we furthermore find

$$F(r_*, k, \pi) = \begin{cases} k & 0 \leq k \leq 1, \\ \frac{1}{k^2} & k > 1. \end{cases} \tag{D.50}$$

The average is given by

$$F(r_*, k, \pi) = \frac{1}{6} \begin{cases} 3 + 2\sqrt{k} + k & 0 \leq k \leq 1, \\ \frac{1 + 2\sqrt{k} + 3k}{k^2} & k > 1. \end{cases} \tag{D.51}$$

We observe that also for hybrid teleportation, the optimal teleportation fidelity shows non-differentiable behavior at $k = 1$.

Case 3: $r = 0$. In this classical case, we find

$$F(0, k, \theta) = \frac{2k^2 + k^{\frac{3}{2}} + 7k + 2 + 2(k^2 + 1)\cos\theta - \sqrt{k}(k - \sqrt{k} + 1)\cos 2\theta}{4(k+1)^3}. \tag{D.52}$$

For ideal classical teleportation, $k = 1$, we have

$$F(0, 1, \theta) = \frac{1}{32}(13 + 4\cos\theta - \cos 2\theta). \tag{D.53}$$

Case 4: $k = 0$ In this case Alice switches off her measurement devices. We find

$$F(r, 0, \theta) = \frac{\cos \theta + \cosh 2r}{2 \cosh^4 r}. \tag{D.54}$$

The average fidelity is given by

$$\bar{F}(r, 0) = \frac{\cosh 2r}{2 \cosh^4 r}. \tag{D.55}$$

For ground and excited state, we find

$$F(r, 0, 0) = \frac{1}{\cosh^2 r}, \qquad F(r, 0, \pi) = \frac{\tanh^2 r}{\cosh^2 r}. \tag{D.56}$$

For the excited state, we find a nontrivial maximum at

$$\max F(r, 0, \pi) = \frac{1}{4}, \qquad r = \frac{1}{2} \ln(3 + 2\sqrt{2}) \simeq 0.88. \tag{D.57}$$

This maximum occurs due to the fact that for $r = 0$, we have $F(r, 0, \pi) = \langle 0|1 \rangle = 0$ due to orthogonality, whereas $F > 0$ for $r > 0$ since the TMS resource contains contributions from all possible photon numbers. Furthermore, we asymptotically have $F(r, 0, \pi) \to 0$ for $r \to \infty$ since the local TMS mode asymptotically suppresses the SNR of the reconstructed state to zero.

In the next step, we consider losses ε in the distribution paths for the TMS state [266]. For sake of simplicity, assume equal losses ε in both paths. Consequently, both local TMS modes contain the same amount of energy. Resulting from this preserved symmetry, teleportation still works optimally for $r \to \infty$, $k = 1$ in this scenario. The losses alter the interference function, according to

$$C(r, k) \to C_\varepsilon(r, k) = (1 - \varepsilon)C(r, k) + \varepsilon(1 + k). \tag{D.58}$$

Apart from replacing $C(r, k) \to C_\varepsilon(r, k)$, the calculation coincides with the aforementioned consideration. We find the optimal fidelity

$$F(\theta, \varepsilon) \equiv F(r \to \infty, k = 1, \theta, \varepsilon) = \frac{4 + \varepsilon(5 + 4\varepsilon) + 4\varepsilon \cos \theta - \varepsilon \cos 2\theta}{4(\varepsilon + 1)^3}. \tag{D.59}$$

For ground state and excited state, Eq. (D.59) takes the simple form

$$F(0, \varepsilon) = \frac{1}{1 + \varepsilon}, \qquad F(\pi, \varepsilon) = \frac{1 + \varepsilon^2}{(1 + \varepsilon)^3}. \tag{D.60}$$

The average fidelity is given by

$$\bar{F}(\varepsilon) = \frac{1}{4\pi} \int_0^{2\pi} d\varphi \int_0^{\pi} d\theta F(\theta, \varepsilon) \sin\theta = \frac{4 + \varepsilon(5 + 4\varepsilon)}{4(\varepsilon + 1)^2} + \frac{\varepsilon}{12(\varepsilon + 1)^3} = \frac{3 + 4\varepsilon + 3\varepsilon^2}{3(\varepsilon + 1)^3}. \tag{D.61}$$

We observe that even for the optimal parameter regime, assumed in Eq. D.59, there exists a respective loss threshold beyond which we can no longer exceed the classical or no-cloning limit [266]. For the classical limit of $F_c = 2/3$, we find

$$F(0, \varepsilon) : \varepsilon \leq \frac{1}{2} \to 3\,\text{dB}, \tag{D.62}$$

$$F(\pi, \varepsilon) : \varepsilon \leq \frac{1}{2} \left(\sqrt[3]{7 + 2\sqrt{19}} - \frac{3}{\sqrt[3]{7 + 2\sqrt{19}}} - 1 \right) \simeq 0.15 \to 0.71\,\text{dB}, \tag{D.63}$$

$$\bar{F}(\varepsilon) : \varepsilon \leq \frac{1}{2} \left(\sqrt[3]{\frac{27 + 2\sqrt{183}}{9}} - \frac{1}{\sqrt[3]{3(27 + 2\sqrt{183})}} - 1 \right) \simeq 0.32 \to 1.67\,\text{dB}. \tag{D.64}$$

For the no-cloning threshold F_{nc}, we find

$$F(0, \varepsilon) : \varepsilon \leq \frac{1}{5} \to 0.97\,\text{dB}, \tag{D.65}$$

$$F(\pi, \varepsilon) : \varepsilon \leq \frac{1}{5} \left(\sqrt[3]{2(49 + 5\sqrt{137})} - 8\sqrt[3]{\frac{4}{49 + 5\sqrt{137}}} - 3 \right) \simeq 0.064 \to 0.29\,\text{dB}, \tag{D.66}$$

$$\bar{F}(\varepsilon) : \varepsilon \leq \frac{1}{5} \left(\sqrt[3]{\frac{2(171 + 5\sqrt{1185})}{9}} - 8\sqrt[3]{\frac{4}{3(171 + 5\sqrt{1185})}} - 3 \right) \simeq 0.12 \to 0.56\,\text{dB}. \tag{D.67}$$

Consequently, it can be expected that we need to suppress the microwave losses in the entanglement distribution paths to values significantly below 1 dB.

As an outlook for the description of generally imperfect hybrid quantum teleportation including arbitrary loss components and JPA noise, we can employ a similar block structure as in Sec. 6.3.3. In a multimode description in terms of with Wigner functions, a loss block ε can be modelled by the convolution integral [273]

$$W'(q, p) = \frac{1}{1 - \varepsilon} \left[W \star G_{\frac{\varepsilon}{2(1-\varepsilon)}} \right] \left(\frac{q}{\sqrt{1 - \varepsilon}}, \frac{p}{\sqrt{1 - \varepsilon}} \right). \tag{D.68}$$

Phase-insensitive amplification by a JPA, adding gain-dependent noise $n_J(g)$, can be modelled by

$$W'(q, p) = \frac{1}{g} \left[W \star G_{\frac{1}{2}\left(1 - \frac{1}{g}\right) + n_J(g)} \right] \left(\frac{q}{\sqrt{g}}, \frac{p}{\sqrt{g}} \right). \tag{D.69}$$

Added noise n by a classical noise channel [cf. Eq. 2.149], leading to broadening of the

Wigner function, can be modelled via the convolution

$$W'(q,p) = [W \star G_n] (q,p).$$
<div align="right">(D.70)</div>

Appendix E

Thermal conductivity of superconducting QLAN cable

We neglect any phononic contribution to heat conductivity in our temperature regime of interest as this contribution decreases with a T^3-law. According to the Wiedemann-Franz law, the electronic thermal conductivity λ_{n} of the NbTi cable in the normal conducting state can be calculated by [69]

$$\frac{\lambda_{\mathrm{n}}}{\sigma_{\mathrm{n}}} = LT, \qquad L = \frac{\pi^2}{3}\left(\frac{k_{\mathrm{B}}}{e}\right)^2 \simeq 2.44 \times 10^{-8}\,\mathrm{V^2\,K^{-2}}, \tag{E.1}$$

where σ_{n} denotes the electrical conductivity in the normal conducting state. In the superconducting state, the thermal conductivity is reduced due to the energy gap $\Delta(T)$ in the excitation spectrum, where T corresponds to the effective electronic temperature of the cable. We define the dimensionless parameter $z = \Delta(T)/k_{\mathrm{B}}T$, which is related to the temperature T by [437]

$$\frac{T}{T_{\mathrm{c}}} = e^{-b(z)}, \qquad b(z) = 2\sum_{n=0}^{\infty}\left[\frac{1}{2n+1} - \frac{1}{\sqrt{(2n+1)^2 + \frac{z^2}{\pi^2}}}\right]. \tag{E.2}$$

According to BCS-theory, the resulting thermal conductivity of the superconducting cable is then given by $\lambda_{\mathrm{s}} = y(T)\lambda_{\mathrm{n}}$, where

$$y(z) = \frac{3}{2\pi^2}\int_z^{\infty}\frac{t^2}{\cosh^2\left(\frac{t}{2}\right)}dt. \tag{E.3}$$

By taking the substitution $t'^2 = (t^2 + z^2)/4$, the integral can be rewritten as a generalized version of the Yosida function [438], which can be analytically expressed as

$$y(z) = \frac{3z}{\pi^2}\left[4\ln\left(2\cosh\frac{z}{2}\right) - z - z\tanh\frac{z}{2}\right] - \frac{12}{\pi^2}\mathrm{Li}_2(-e^{-z}), \tag{E.4}$$

where $\mathrm{Li}_2(x) \equiv -\int_0^x \frac{\ln(1-y)}{y} dy$ denotes the dilogarithm function. For a practical calculation of z, we use the interpolation formula [396]

$$z = \delta_{\mathrm{sc}} \frac{T_{\mathrm{c}}}{T} \tanh \frac{\pi}{\delta_{\mathrm{sc}}} \sqrt{\frac{2}{3} \frac{\Delta C}{C_{\mathrm{N}}} \left(\frac{T_{\mathrm{c}}}{T} - 1 \right)}, \tag{E.5}$$

with $\delta_{\mathrm{sc}} = \pi/e^\gamma$ and $\Delta C/C_{\mathrm{N}} = 12/7\zeta(3)$, where $\gamma = 0.577...$ denotes the Euler-Mascheroni constant and $\zeta(3) \simeq 1.202...$ is Apéry's constant.

Appendix F

JPA compression model

In the following, we provide a simple model to describe how compression effects affect our amplified quantum states. We assume that we employ our JPA to amplify a coherent state $|\alpha|$ and treat the amplifier as nonlinear. We start with the state

$$|\alpha, 0\rangle = (\hat{D}(\alpha)|0\rangle)|0\rangle = e^{-\frac{|\alpha|^2}{2}} \sum_{n=0}^{\infty} \frac{\alpha^n}{\sqrt{n!}}|n\rangle|0\rangle \tag{F.1}$$

and describe the amplification process via the TMS operator $\hat{S}_{\mathrm{TMS}}(\xi)$, where we set the global phase to zero for simplicity. For our model, we assume that compression is sufficiently high that the JPA only acts as an amplifier in case the input state contains either $n = 0$ or $n = 1$ photons. Contributions with higher power, $n \leq 2$, are not affected by the JPA. Consequently, we generate the state

$$|\alpha', \xi\rangle = e^{-\frac{|\alpha|^2}{2}} \left[\hat{S}_{\mathrm{TMS}}(\xi)|0, 0\rangle + \alpha \hat{S}_{\mathrm{TMS}}(\xi)|1, 0\rangle + \sum_{n \geq 2} \frac{\alpha^n}{\sqrt{n!}}|n, 0\rangle \right]. \tag{F.2}$$

we can rewrite Eq. (F.2) as

$$|\alpha', \xi\rangle = e^{-\frac{|\alpha|^2}{2}} \left[|\mathrm{TMS}\rangle + \alpha \hat{S}_{\mathrm{TMS}}(\xi)\hat{a}^{\dagger}\hat{S}_{\mathrm{TMS}}^{\dagger}|\mathrm{TMS}\rangle + \sum_{n \geq 2} \frac{\alpha^n}{\sqrt{n!}}|n, 0\rangle \right], \tag{F.3}$$

where $|\mathrm{TMS}\rangle$ corresponds to a TMS state, represented in the Fock basis by Eq. (2.114). Next, we use the Bogoliubov transformation

$$\hat{S}_{\mathrm{TMS}}(\xi)\hat{a}^{\dagger}\hat{S}_{\mathrm{TMS}}^{\dagger} = \cosh r \hat{a}_1^{\dagger} + \sinh r \hat{a}_2. \tag{F.4}$$

To trace out environment, we employ the Fock basis $|l\rangle$ and investigate

$$(\mathbb{1} \otimes \langle l|)|\alpha', \xi\rangle = e^{-\frac{|\alpha|^2}{2}} \left[\frac{(-\tanh r)^l}{\cosh r}|l\rangle + \frac{\alpha\sqrt{l+1}(-\tanh r)^l}{\cosh^2 r}|l+1\rangle + \sum_{n \geq 2} \frac{\alpha^n}{\sqrt{n!}}|n\rangle \delta_{l,0} \right]. \tag{F.5}$$

The density operator can then be determined via

$$\hat{\rho} = \sum_l (\mathbb{1} \otimes \langle l|)|\alpha', \xi\rangle\langle\alpha', \xi|(\mathbb{1} \otimes |l\rangle), \tag{F.6}$$

from which the Wigner function can be determined via the characteristic function. The state described by Eq. (F.6) is non-Gaussian and we expect that it should be possible to find negative regions for the corresponding Wigner function.

Appendix G

Weather-dependent microwave losses

Throughout our investigation, we consider horizontal dependence, implying that we do not take any elevation angle into account. Under ideal conditions, the attenuation by atmospheric absorption γ_a is expressed as

$$\gamma_a = \gamma_o + \gamma_w, \tag{G.1}$$

where γ_o (γ_w) is the attenuation coefficient for oxygen (water vapor). In the horizontal dependence, these quantities are given by empirical relations [429]. In addition, we can take into account how different weather conditions affect our results. The effect of rain is taken into account according to the ITU rain attenuation model, which shows that total specific attenuation rate γ_R is a function of rain fall rate R as

$$\gamma_R = k(\omega)R^{\alpha(\omega)} \text{ dB/km}, \tag{G.2}$$

where the two coefficients α and k are functions of signal frequency and a potential elevation angle, which is not considered here. Both quantities have been empirically studied in Ref. 429. At approximately $5\,\text{GHz}$ and intermediate rainfall, the attenuation is $\gamma_R \simeq 0.1\,\text{dB/km}$. Attenuation due to clouds and fog can be expressed in terms of the total water content per unit volume based on the Rayleigh approximation,

$$\gamma_c = K_l M \text{ dB/km}, \tag{G.3}$$

where γ_c is the specific attenuation in dB/km within the cloud, K_l is the specific attenuation coefficient $[(\text{dB/km})/(\text{g/m}^3)]$ and M is the liquid water density in the cloud or fog in g/m^3. We choose the values $K_l \simeq (0.02\,\text{dB/km})/(\text{g/m}^3)$ and $M \simeq 0.5\,\text{g/m}^3$ and obtain $\gamma_c \simeq 0.01\,\text{dB/km}$. It can be seen that attenuation due to clouds and fog is not as influential as rain attenuation. We neglect effects from scintillation produced by turbulent air with variations in refractive index [429].

Bibliography

[1] R. Feynman, R. Leighton, and M. Sands, *The Feynman Lectures on Physics, Vol. III: The New Millennium Edition: Quantum Mechanics*, The Feynman Lectures on Physics (Basic Books, 2011), ISBN 9780465025015, URL https://books.google.de/books?id=KsnbNL_rh04C.

[2] L. D. Landau and L. M. Lifshitz, *Quantum Mechanics Non-Relativistic Theory, Third Edition: Volume 3* (Butterworth-Heinemann, 1981), 3rd ed., ISBN 0750635398, URL http://www.worldcat.org/isbn/0750635398.

[3] D. Griffiths and P. Griffiths, *Introduction to Quantum Mechanics*, Pearson international edition (Pearson Prentice Hall, 2005), ISBN 9780131118928, URL https://books.google.de/books?id=z4fwAAAAMAAJ.

[4] J. S. Bell, "On the Einstein Podolsky Rosen paradox", Physics Physique Fizika **1**, 195 (1964).

[5] A. Einstein, B. Podolsky, and N. Rosen, "Can Quantum-Mechanical Description of Physical Reality Be Considered Complete?", Phys. Rev. **47**, 777 (1935).

[6] Y. Aharonov and D. Rohrlich, *Quantum Paradoxes: Quantum Theory for the Perplexed*, Physics textbook (Wiley, 2008), ISBN 9783527619122, URL https://books.google.de/books?id=3PSHDohngVgC.

[7] J. Audretsch, *Verschränkte Systeme: Die Quantenphysik auf neuen Wegen*, Lehrbuch Physik (Wiley, 2008), ISBN 9783527618590, URL https://books.google.de/books?id=B_uFblp3tkYC.

[8] "Pioneering quantum information science", Nature Computational Science **2**, 687 (2022).

[9] D. Bouwmeester, J.-W. Pan, K. Mattle, M. Eibl, H. Weinfurter, and A. Zeilinger, "Experimental quantum teleportation", Nature **390**, 575 (1997).

[10] A. Aspect, P. Grangier, and G. Roger, "Experimental Realization of Einstein-Podolsky-Rosen-Bohm Gedankenexperiment: A New Violation of Bell's Inequalities", Phys. Rev. Lett. **49**, 91 (1982).

[11] Y. Aharonov and D. Bohm, "Significance of Electromagnetic Potentials in the Quantum Theory", Phys. Rev. **115**, 485 (1959).

[12] B. Misra and E. C. G. Sudarshan, "The Zeno's paradox in quantum theory", Journal of Mathematical Physics **18**, 756 (1977).

[13] H. B. G. Casimir and D. Polder, "The Influence of Retardation on the London-van der Waals Forces", Phys. Rev. **73**, 360 (1948).

[14] S. P. Walborn, M. O. Terra Cunha, S. Pádua, and C. H. Monken, "Double-slit quantum eraser", Phys. Rev. A **65**, 033818 (2002).

[15] M. A. Nielsen and I. L. Chuang, *Quantum Computation and Quantum Information* (Cambridge University Press, Cambridge, 2010).

[16] N. Meher and S. Sivakumar, "A review on quantum information processing in cavities", The European Physical Journal Plus **137**, 985 (2022).

[17] M. H. Devoret and R. J. Schoelkopf, "Superconducting Circuits for Quantum Information: An Outlook", Science **339**, 1169 (2013).

[18] A. Blais, S. M. Girvin, and W. D. Oliver, "Quantum information processing and quantum optics with circuit quantum electrodynamics", Nature Physics **16**, 247 (2020).

[19] F. Flamini, N. Spagnolo, and F. Sciarrino, "Photonic quantum information processing: a review", Reports on Progress in Physics **82**, 016001 (2018).

[20] G. Benenti, G. Casati, D. Rossini, and G. Strini, *Principles of Quantum Computation and Information* (WORLD SCIENTIFIC, 2018), https://www.worldscientific.com/doi/pdf/10.1142/10909, URL https://www.worldscientific.com/doi/abs/10.1142/10909.

[21] P. W. Shor, "Algorithms for quantum computation: discrete logarithms and factoring", Proceedings 35th Annual Symposium on Foundations of Computer Science pp. 124–134 (1994).

[22] P. W. Shor, "Polynomial-Time Algorithms for Prime Factorization and Discrete Logarithms on a Quantum Computer", SIAM Review **41**, 303 (1999).

[23] L. K. Grover, "A Fast Quantum Mechanical Algorithm for Database Search", in *Proceedings of the Twenty-Eighth Annual ACM Symposium on Theory of Computing* (Association for Computing Machinery, New York, NY, USA, 1996), STOC '96, p. 212, ISBN 0897917855, URL https://doi.org/10.1145/237814.237866.

[24] D. Deutsch and R. Jozsa, "Rapid solution of problems by quantum computation", Proceedings of the Royal Society of London. Series A: Mathematical and Physical Sciences **439**, 553 (1992).

[25] T. Monz, P. Schindler, J. T. Barreiro, M. Chwalla, D. Nigg, W. A. Coish, M. Harlander, W. Hänsel, M. Hennrich, and R. Blatt, "14-Qubit Entanglement: Creation and Coherence", Phys. Rev. Lett. **106**, 130506 (2011).

[26] P. Kok, W. J. Munro, K. Nemoto, T. C. Ralph, J. P. Dowling, and G. J. Milburn, "Linear optical quantum computing with photonic qubits", Rev. Mod. Phys. **79**, 135 (2007).

[27] D. Loss and D. P. DiVincenzo, "Quantum computation with quantum dots", Phys. Rev. A **57**, 120 (1998).

[28] B. E. Kane, "A silicon-based nuclear spin quantum computer", Nature **393**, 133 (1998).

[29] M. W. Doherty, N. B. Manson, P. Delaney, F. Jelezko, J. Wrachtrup, and L. C. Hollenberg, "The nitrogen-vacancy colour centre in diamond", Physics Reports **528**, 1 (2013).

[30] G. Wendin, "Quantum information processing with superconducting circuits: a review", Reports on Progress in Physics **80**, 106001 (2017).

[31] Y. Nakamura, Y. A. Pashkin, and J. S. Tsai, "Coherent control of macroscopic quantum states in a single-Cooper-pair box", Nature **398**, 786 (1999).

[32] M. H. Devoret, A. Wallraff, and J. M. Martinis, "Superconducting Qubits: A Short Review", (2004), URL https://arxiv.org/abs/cond-mat/0411174.

[33] Y. Wu et al., "Strong Quantum Computational Advantage Using a Superconducting Quantum Processor", Phys. Rev. Lett. **127**, 180501 (2021).

[34] K. Zhang, P. Rao, K. Yu, H. Lim, and V. Korepin, "Implementation of efficient quantum search algorithms on NISQ computers", Quantum Information Processing **20**, 233 (2021).

[35] K. Zeissler, "Controlling a superconducting quantum processor", Nature Electronics **6**, 181 (2023).

[36] A. Blais, R.-S. Huang, A. Wallraff, S. M. Girvin, and R. J. Schoelkopf, "Cavity quantum electrodynamics for superconducting electrical circuits: An architecture for quantum computation", Phys. Rev. A **69**, 062320 (2004).

[37] T. Niemczyk, F. Deppe, H. Huebl, E. P. Menzel, F. Hocke, M. J. Schwarz, J. J. Garcia-Ripoll, D. Zueco, T. Hümmer, E. Solano, A. Marx, and R. Gross, "Circuit quantum electrodynamics in the ultrastrong-coupling regime", Nat. Phys. **6**, 772 (2010).

[38] I. Buluta, S. Ashhab, and F. Nori, "Natural and artificial atoms for quantum computation", Reports on Progress in Physics **74**, 104401 (2011).

[39] F. Arute et al., "Quantum supremacy using a programmable superconducting processor", Nature **574**, 505 (2019).

[40] A. Grimm, N. E. Frattini, S. Puri, S. O. Mundhada, S. Touzard, M. Mirrahimi, S. M. Girvin, S. Shankar, and M. H. Devoret, "Stabilization and operation of a Kerr-cat qubit", Nature **584**, 205 (2020).

[41] R. Acharya et al., "Suppressing quantum errors by scaling a surface code logical qubit", Nature **614**, 676 (2023).

[42] J. Preskill, "Quantum Computing in the NISQ era and beyond", Quantum **2**, 79 (2018).

[43] B. Schumacher, "Quantum coding", Phys. Rev. A **51**, 2738 (1995).

[44] A. Robert, P. K. Barkoutsos, S. Woerner, and I. Tavernelli, "Resource-efficient quantum algorithm for protein folding", npj Quantum Information **7**, 38 (2021).

[45] C. Gross and I. Bloch, "Quantum simulations with ultracold atoms in optical lattices", Science **357**, 995 (2017).

[46] A. Eddins, M. Motta, T. P. Gujarati, S. Bravyi, A. Mezzacapo, C. Hadfield, and S. Sheldon, "Doubling the Size of Quantum Simulators by Entanglement Forging", PRX Quantum **3**, 010309 (2022).

[47] S. L. Braunstein and P. van Loock, "Quantum information with continuous variables", Rev. Mod. Phys. **77**, 513 (2005).

[48] D. F. Walls and G. J. Milburn, *Quantum Optics* (Springer, Berlin, 2008).

[49] C. Weedbrook, S. Pirandola, R. García-Patrón, N. J. Cerf, T. C. Ralph, J. H. Shapiro, and S. Lloyd, "Gaussian quantum information", Rev. Mod. Phys. **84**, 621 (2012).

[50] Y.-A. Chen et al., "An integrated space-to-ground quantum communication network over 4,600 kilometres", Nature **589**, 214 (2021).

[51] M. Pompili, S. L. N. Hermans, S. Baier, H. K. C. Beukers, P. C. Humphreys, R. N. Schouten, R. F. L. Vermeulen, M. J. Tiggelman, L. dos Santos Martins, B. Dirkse, S. Wehner, and R. Hanson, "Realization of a multinode quantum network of remote solid-state qubits", Science **372**, 259 (2021).

[52] S. L. N. Hermans, M. Pompili, H. K. C. Beukers, S. Baier, J. Borregaard, and R. Hanson, "Qubit teleportation between non-neighbouring nodes in a quantum network", Nature **605**, 663 (2022).

[53] J. Chung, G. Kanter, N. Lauk, R. Valivarthi, W. Wu, R. R. Ceballos, C. Peñ, N. Sinclair, J. Thomas, S. Xie, R. Kettimuthu, P. Kumar, P. Spentzouris, and M. Spiropulu, "Illinois Express Quantum Network (IEQNET): Metropolitan-scale experimental quantum networking over deployed optical fiber", (2021), 2104.04629, URL https://arxiv.org/abs/2104.04629.

[54] D. Awschalom, K. K. Berggren, H. Bernien, S. Bhave, L. D. Carr, P. Davids, S. E. Economou, D. Englund, A. Faraon, M. Fejer, S. Guha, M. V. Gustafsson, E. Hu, L. Jiang, J. Kim, B. Korzh, P. Kumar, P. G. Kwiat, M. Lončar, M. D. Lukin, D. A. Miller, C. Monroe, S. W. Nam, P. Narang, J. S. Orcutt, M. G. Raymer, A. H. Safavi-Naeini, M. Spiropulu, K. Srinivasan, S. Sun, J. Vučković, E. Waks, R. Walsworth, A. M. Weiner, and Z. Zhang, "Development of Quantum Interconnects (QuICs) for Next-Generation Information Technologies", PRX Quantum **2**, 017002 (2021).

[55] H. J. Kimble, "The quantum internet", Nature **453**, 1023 (2008).

[56] S.-K. Liao, W.-Q. Cai, W.-Y. Liu, L. Zhang, Y. Li, J.-G. Ren, J. Yin, Q. Shen, Y. Cao, Z.-P. Li, F.-Z. Li, X.-W. Chen, L.-H. Sun, J.-J. Jia, J.-C. Wu, X.-J. Jiang, J.-F. Wang, Y.-M. Huang, Q. Wang, Y.-L. Zhou, L. Deng, T. Xi, L. Ma, T. Hu, Q. Zhang, Y.-A. Chen, N.-L. Liu, X.-B. Wang, Z.-C. Zhu, C.-Y. Lu, R. Shu, C.-Z. Peng, J.-Y. Wang, and J.-W. Pan, "Satellite-to-ground quantum key distribution", Nature **549**, 43 (2017).

[57] T. van Leent, M. Bock, F. Fertig, R. Garthoff, S. Eppelt, Y. Zhou, P. Malik, M. Seubert, T. Bauer, W. Rosenfeld, W. Zhang, C. Becher, and H. Weinfurter, "Entangling single atoms over 33 km telecom fibre", Nature **607**, 69 (2022).

[58] S. L. Braunstein and H. J. Kimble, "Teleportation of Continuous Quantum Variables", Phys. Rev. Lett. **80**, 869 (1998).

[59] S. L. Braunstein and H. J. Kimble, "Dense coding for continuous variables", Phys. Rev. A **61**, 042302 (2000).

[60] S. Lloyd and S. L. Braunstein, "Quantum Computation over Continuous Variables", Phys. Rev. Lett. **82**, 1784 (1999).

[61] X. Wang, T. Hiroshima, A. Tomita, and M. Hayashi, "Quantum information with Gaussian states", Physics Reports **448**, 1 (2007).

[62] F. Grosshans, G. Van Assche, J. Wenger, R. Brouri, N. J. Cerf, and P. Grangier, "Quantum key distribution using gaussian-modulated coherent states", Nature **421**, 238 (2003).

[63] C. H. Bennett and S. J. Wiesner, "Communication via one- and two-particle operators on Einstein-Podolsky-Rosen states", Phys. Rev. Lett. **69**, 2881 (1992).

[64] O. Pfister, "Continuous-variable quantum computing in the quantum optical frequency comb", Journal of Physics B: Atomic, Molecular and Optical Physics **53**, 012001 (2019).

[65] C. H. Bennett, D. P. DiVincenzo, P. W. Shor, J. A. Smolin, B. M. Terhal, and W. K. Wootters, "Remote state preparation", Phys. Rev. Lett. **87**, 077902 (2001).

[66] S. Pogorzalek, K. G. Fedorov, M. Xu, A. Parra-Rodriguez, M. Sanz, M. Fischer, E. Xie, K. Inomata, Y. Nakamura, E. Solano, A. Marx, F. Deppe, and R. Gross, "Secure quantum remote state preparation of squeezed microwave states", Nat. Commun. **10**, 2604 (2019).

[67] A. Furusawa, J. L. Sørensen, S. L. Braunstein, C. A. Fuchs, H. J. Kimble, and E. S. Polzik, "Unconditional Quantum Teleportation", Science **282**, 706 (1998).

[68] E. Zeuthen, A. Schliesser, A. S. Sørensen, and J. M. Taylor, "Figures of merit for quantum transducers", Quantum Science and Technology **5**, 034009 (2020).

[69] R. Gross and A. Marx, *Festkörperphysik* (Oldenbourg Verlag, München, 2012).

[70] C. P. Sun, L. F. Wei, Y.-x. Liu, and F. Nori, "Quantum transducers: Integrating transmission lines and nanomechanical resonators via charge qubits", Phys. Rev. A **73**, 022318 (2006).

[71] M. Mirhosseini, A. Sipahigil, M. Kalaee, and O. Painter, "Superconducting qubit to optical photon transduction", Nature **588**, 599 (2020).

[72] M. Forsch, R. Stockill, A. Wallucks, I. Marinković, C. Gärtner, R. A. Norte, F. van Otten, A. Fiore, K. Srinivasan, and S. Gröblacher, "Microwave-to-optics conversion using a mechanical oscillator in its quantum ground state", Nature Physics **16**, 69 (2020).

[73] M. Mariantoni, E. P. Menzel, F. Deppe, M. A. Araque Caballero, A. Baust, T. Niemczyk, E. Hoffmann, E. Solano, A. Marx, and R. Gross, "Planck Spectroscopy and Quantum Noise of Microwave Beam Splitters", Phys. Rev. Lett. **105**, 133601 (2010).

[74] E. P. Menzel, F. Deppe, M. Mariantoni, M. A. Araque Caballero, A. Baust, T. Niem-
czyk, E. Hoffmann, A. Marx, E. Solano, and R. Gross, "Dual-Path State Reconstruc-
tion Scheme for Propagating Quantum Microwaves and Detector Noise Tomography",
Phys. Rev. Lett. **105**, 100401 (2010).

[75] L. Zhong, E. P. Menzel, R. D. Candia, P. Eder, M. Ihmig, A. Baust, M. Haeberlein,
E. Hoffmann, K. Inomata, T. Yamamoto, Y. Nakamura, E. Solano, F. Deppe,
A. Marx, and R. Gross, "Squeezing with a flux-driven Josephson parametric ampli-
fier", New J. Phys. **15**, 125013 (2013).

[76] K. G. Fedorov, L. Zhong, S. Pogorzalek, P. Eder, M. Fischer, J. Goetz, E. Xie,
F. Wulschner, K. Inomata, T. Yamamoto, Y. Nakamura, R. Di Candia, U. Las Heras,
M. Sanz, E. Solano, E. P. Menzel, F. Deppe, A. Marx, and R. Gross, "Displacement
of Propagating Squeezed Microwave States", Phys. Rev. Lett. **117**, 020502 (2016).

[77] E. P. Menzel, R. Di Candia, F. Deppe, P. Eder, L. Zhong, M. Ihmig, M. Haeberlein,
A. Baust, E. Hoffmann, D. Ballester, K. Inomata, T. Yamamoto, Y. Nakamura,
E. Solano, A. Marx, and R. Gross, "Path Entanglement of Continuous-Variable
Quantum Microwaves", Phys. Rev. Lett. **109**, 250502 (2012).

[78] K. G. Fedorov, M. Renger, S. Pogorzalek, R. D. Candia, Q. Chen, Y. Nojiri, K. Ino-
mata, Y. Nakamura, M. Partanen, A. Marx, R. Gross, and F. Deppe, "Experimental
quantum teleportation of propagating microwaves", Sci. Adv. **7**, eabk0891 (2021).

[79] T. Yamamoto, K. Inomata, M. Watanabe, K. Matsuba, T. Miyazaki, W. D. Oliver,
Y. Nakamura, and J. S. Tsai, "Flux-driven Josephson parametric amplifier", Appl.
Phys. Lett. **93**, 042510 (2008).

[80] B. Yurke, L. R. Corruccini, P. G. Kaminsky, L. W. Rupp, A. D. Smith, A. H. Silver,
R. W. Simon, and E. A. Whittaker, "Observation of parametric amplification and
deamplification in a Josephson parametric amplifier", Phys. Rev. A **39**, 2519 (1989).

[81] J. Y. Mutus, T. C. White, R. Barends, Y. Chen, Z. Chen, B. Chiaro, A. Dunsworth,
E. Jeffrey, J. Kelly, A. Megrant, C. Neill, P. J. J. O'Malley, P. Roushan, D. Sank,
A. Vainsencher, J. Wenner, K. M. Sundqvist, A. N. Cleland, and J. M. Martinis,
"Strong environmental coupling in a Josephson parametric amplifier", Applied Physics
Letters **104**, 263513 (2014).

[82] Z. R. Lin, K. Inomata, W. D. Oliver, K. Koshino, Y. Nakamura, J. S. Tsai, and
T. Yamamoto, "Single-shot readout of a superconducting flux qubit with a flux-driven
Josephson parametric amplifier", Appl. Phys. Lett. **103**, 132602 (2013).

[83] K. G. Fedorov, S. Pogorzalek, U. Las Heras, M. Sanz, P. Yard, P. Eder, M. Fischer,
J. Goetz, E. Xie, K. Inomata, Y. Nakamura, R. Di Candia, E. Solano, A. Marx,

F. Deppe, and R. Gross, "Finite-time quantum entanglement in propagating squeezed microwaves", Scientific Reports **8**, 6416 (2018).

[84] R. Di Candia, K. G. Fedorov, L. Zhong, S. Felicetti, E. P. Menzel, M. Sanz, F. Deppe, A. Marx, R. Gross, and E. Solano, "Quantum teleportation of propagating quantum microwaves", EPJ Quantum Technology **2**, 25 (2015).

[85] M. Renger, S. Pogorzalek, Q. Chen, Y. Nojiri, K. Inomata, Y. Nakamura, M. Partanen, A. Marx, R. Gross, F. Deppe, and K. G. Fedorov, "Beyond the standard quantum limit for parametric amplification of broadband signals", Npj Quantum Inf. **7**, 160 (2021).

[86] M. Renger, S. Pogorzalek, F. Fesquet, K. Honasoge, F. Kronowetter, Q. Chen, Y. Nojiri, K. Inomata, Y. Nakamura, A. Marx, F. Deppe, R. Gross, and K. G. Fedorov, "Flow of quantum correlations in noisy two-mode squeezed microwave states", Phys. Rev. A **106**, 052415 (2022).

[87] W. H. Zurek, "Quantum Darwinism", Nat. Phys. **5**, 181 (2009).

[88] F. F. Fanchini, L. K. Castelano, M. F. Cornelio, and M. C. de Oliveira, "Locally inaccessible information as a fundamental ingredient to quantum information", New Journal of Physics **14**, 013027 (2012).

[89] M. Renger, W. Yam, S. Gandorfer, O. Gargiulo, F. Fesquet, K. Honasoge, F. Kronowetter, D. Bazulin, Q. Chen, Y. Nojiri, A. Marx, R. Gross, K. G. Fedorov, and F. Deppe, "Towards Quantum Local Area Networks", in *Annual Report 2021* (2021), pp. 53–54, URL https://www.wmi.badw.de/fileadmin/WMI/Publications/Annual_Reports/2021.pdf.

[90] T. Yamamoto, K. Koshino, and Y. Nakamura, "Parametric Amplifier and Oscillator Based on Josephson Junction Circuitry", in *Principles and Methods of Quantum Information Technologies*, edited by Y. Yamamoto and K. Semba (Springer Japan, Tokyo, 2016), pp. 495–513.

[91] J. Clarke and A. Braginski, *The SQUID Handbook: Fundamentals and Technology of SQUIDs and SQUID Systems* (Wiley, 2006), ISBN 9783527604586, URL https://books.google.de/books?id=BsTTM-nU-JkC.

[92] R. Collin, *Foundations for Microwave Engineering*, IEEE Press Series on Electromagnetic Wave Theory (Wiley, 2001), ISBN 9780780360310, URL https://books.google.de/books?id=2SxoQgAACAAJ.

[93] D. M. Pozar, *Microwave Engineering* (Wiley, Hoboken, 2012), 4th ed.

[94] S. Gevorgian, L. Linner, and E. Kollberg, "CAD models for shielded multilayered CPW", IEEE Transactions on Microwave Theory and Techniques **43**, 772 (1995).

[95] M. Göppl, A. Fragner, M. Baur, R. Bianchetti, S. Filipp, J. M. Fink, P. J. Leek, G. Puebla, L. Steffen, and A. Wallraff, "Coplanar waveguide resonators for circuit quantum electrodynamics", J. Appl. Phys. **104**, 113904 (2008).

[96] M. Wallquist, V. S. Shumeiko, and G. Wendin, "Selective coupling of superconducting charge qubits mediated by a tunable stripline cavity", Phys. Rev. B **74**, 224506 (2006).

[97] W. Buckel and R. Kleiner, *Superconductivity* (Wiley, Weinheim, 2004).

[98] B. D. Josephson, "Possible new effects in superconductive tunnelling", Phys. Lett. **1**, 251 (1962).

[99] J. Bourassa, F. Beaudoin, J. M. Gambetta, and A. Blais, "Josephson-junction-embedded transmission-line resonators: From Kerr medium to in-line transmon", Phys. Rev. A **86**, 013814 (2012).

[100] O. Klein, "Quantentheorie und fünfdimensionale Relativitätstheorie", Zeitschrift für Physik **37**, 895 (1926).

[101] W. Gordon, "Der Comptoneffekt nach der Schrödingerschen Theorie", Zeitschrift für Physik **40**, 117 (1926).

[102] B. Peropadre, J. Lindkvist, I.-C. Hoi, C. M. Wilson, J. J. Garcia-Ripoll, P. Delsing, and G. Johansson, "Scattering of coherent states on a single artificial atom", New Journal of Physics **15**, 035009 (2013).

[103] R. Doll and M. Näbauer, "Experimental Proof of Magnetic Flux Quantization in a Superconducting Ring", Phys. Rev. Lett. **7**, 51 (1961).

[104] B. S. Deaver and W. M. Fairbank, "Experimental Evidence for Quantized Flux in Superconducting Cylinders", Phys. Rev. Lett. **7**, 43 (1961).

[105] S. Pogorzalek, K. G. Fedorov, L. Zhong, J. Goetz, F. Wulschner, M. Fischer, P. Eder, E. Xie, K. Inomata, T. Yamamoto, Y. Nakamura, A. Marx, F. Deppe, and R. Gross, "Hysteretic Flux Response and Nondegenerate Gain of Flux-Driven Josephson Parametric Amplifiers", Phys. Rev. Applied **8**, 024012 (2017).

[106] A. Blais, A. L. Grimsmo, S. M. Girvin, and A. Wallraff, "Circuit quantum electro-dynamics", Rev. Mod. Phys. **93**, 025005 (2021).

[107] S. Boutin, D. M. Toyli, A. V. Venkatramani, A. W. Eddins, I. Siddiqi, and A. Blais, "Effect of Higher-Order Nonlinearities on Amplification and Squeezing in Josephson Parametric Amplifiers", Phys. Rev. Appl. **8**, 054030 (2017).

[108] C. Eichler and A. Wallraff, "Controlling the dynamic range of a Josephson parametric amplifier", EPJ Quantum Technol. **1**, 2 (2014).

[109] J. Koch, T. M. Yu, J. Gambetta, A. A. Houck, D. I. Schuster, J. Majer, A. Blais, M. H. Devoret, S. M. Girvin, and R. J. Schoelkopf, "Charge-insensitive qubit design derived from the Cooper pair box", Phys. Rev. A **76**, 042319 (2007).

[110] M. Peskin and D. Schroeder, *An Introduction to Quantum Field Theory*, Advanced book classics (Avalon Publishing, 1995), ISBN 9780201503975, URL https://books.google.de/books?id=i35LALN0GosC.

[111] D. Kapec, M. Perry, A.-M. Raclariu, and A. Strominger, "Infrared divergences in QED revisited", Phys. Rev. D **96**, 085002 (2017).

[112] S. Pogorzalek, "Remote State Preparation of Squeezed Microwave States", Phd thesis, Technische Universität München (2020), URL https://mediatum.ub.tum.de/1540503.

[113] M. Sandberg, C. Wilson, F. Persson, T. Bauch, G. Johansson, V. Shumeiko, T. Duty, and P. Delsing, "Tuning the field in a microwave resonator faster than the photon lifetime", Applied Physics Letters **92**, 203501 (2008).

[114] D. Arweiler, "Multi-SQUID Josephson Parametric Amplifiers", Master's thesis, Technische Universität München (2018), URL http://www.wmi.badw.de/publications/theses/Arweiler,Daniel_Masterarbeit_2018.pdf.

[115] A. T. Baust, "Characterization of Flux-driven Josephson Parametric Amplifiers", Diploma thesis, Technische Universität München (2010), URL https://www.wmi.badw.de/fileadmin/WMI/Publications/Baust%2CAlexander_Diplomarbeit_2012.pdf.

[116] J. Goetz, F. Deppe, M. Haeberlein, F. Wulschner, C. W. Zollitsch, S. Meier, M. Fischer, P. Eder, E. Xie, K. G. Fedorov, E. P. Menzel, A. Marx, and R. Gross, "Loss mechanisms in superconducting thin film microwave resonators", Journal of Applied Physics **119**, 015304 (2016).

[117] E. Organick, *A Fortran IV Primer*, Addison-Wesley series in computer science and information processing (Addison-Wesley, 1966), URL https://books.google.de/books?id=36tQAAAAMAAJ.

[118] A. Kamal, A. Marblestone, and M. Devoret, "Signal-to-pump back action and self-oscillation in double-pump Josephson parametric amplifier", Phys. Rev. B **79**, 184301 (2009).

[119] W. Wustmann and V. Shumeiko, "Parametric resonance in tunable superconducting cavities", Phys. Rev. B **87**, 184501 (2013).

[120] N. N. Bogoljubov, "On a new method in the theory of superconductivity", Il Nuovo Cimento (1955-1965) **7**, 794 (1958).

[121] X. Guo, X. Li, N. Liu, and Z. Y. Ou, "Multimode theory of pulsed-twin-beam generation using a high-gain fiber-optical parametric amplifier", Phys. Rev. A **88**, 023841 (2013).

[122] B. Carter, "Chapter 13 - Understanding Op Amp Parameters", in *Op Amps for Everyone (Third Edition)*, edited by R. Mancini and B. Carter (Newnes, Boston, 2009), pp. 189–229, third edition ed., ISBN 978-1-85617-505-0, URL https://www.sciencedirect.com/science/article/pii/B9781856175050000132.

[123] P. Krantz, A. Bengtsson, M. Simoen, S. Gustavsson, V. Shumeiko, W. D. Oliver, C. M. Wilson, P. Delsing, and J. Bylander, "Single-shot read-out of a superconducting qubit using a Josephson parametric oscillator", Nature Communications **7**, 11417 (2016).

[124] C. M. Wilson, T. Duty, M. Sandberg, F. Persson, V. Shumeiko, and P. Delsing, "Photon Generation in an Electromagnetic Cavity with a Time-Dependent Boundary", Phys. Rev. Lett. **105**, 233907 (2010).

[125] D. J. Parker, M. Savytskyi, W. Vine, A. Laucht, T. Duty, A. Morello, A. L. Grimsmo, and J. J. Pla, "Degenerate Parametric Amplification via Three-Wave Mixing Using Kinetic Inductance", Phys. Rev. Applied **17**, 034064 (2022).

[126] D. F. Walls, "Squeezed states of light", Nature **306**, 141 (1983).

[127] Q.-M. Chen, M. Fischer, Y. Nojiri, M. Renger, E. Xie, M. Partanen, S. Pogorzalek, K. G. Fedorov, A. Marx, F. Deppe, and R. Gross, "Quantum behavior of a superconducting Duffing oscillator at the dissipative phase transition", (2022), URL https://arxiv.org/abs/2206.06338.

[128] H. A. Haus and J. A. Mullen, "Quantum Noise in Linear Amplifiers", Phys. Rev. **128**, 2407 (1962).

[129] C. M. Caves, "Quantum limits on noise in linear amplifiers", Phys. Rev. D **26**, 1817 (1982).

[130] C. M. Caves, J. Combes, Z. Jiang, and S. Pandey, "Quantum limits on phase-preserving linear amplifiers", Phys. Rev. A **86**, 063802 (2012).

[131] A. A. Clerk, M. H. Devoret, S. M. Girvin, F. Marquardt, and R. J. Schoelkopf, "Introduction to quantum noise, measurement, and amplification", Rev. Mod. Phys. **82**, 1155 (2010).

[132] A. A. Clerk, M. H. Devoret, S. M. Girvin, F. Marquardt, and R. J. Schoelkopf, "Introduction to quantum noise, measurement, and amplification", Rev. Mod. Phys. **82**, 1155 (2010).

[133] D. Kouznetsov, R. Ortega-Martínez, and D. Rohrlich, "Quantum noise limits for nonlinear, phase-invariant amplifiers", Phys. Rev. A **52**, 1665 (1995).

[134] A. Roy and M. Devoret, "Introduction to parametric amplification of quantum signals with Josephson circuits", C R Phys **17**, 740 (2016).

[135] P. Bhupathi, P. Groszkowski, M. P. DeFeo, M. Ware, F. K. Wilhelm, and B. L. T. Plourde, "Transient Dynamics of a Superconducting Nonlinear Oscillator", Phys. Rev. Appl. **5**, 024002 (2016).

[136] M. J. Feldman and M. T. Levinsen, "Gain-dependent noise temperature of Josephson parametric amplifiers", Applied Physics Letters **36**, 854 (1980).

[137] S. M. Anton, J. S. Birenbaum, S. R. O'Kelley, V. Bolkhovsky, D. A. Braje, G. Fitch, M. Neeley, G. C. Hilton, H.-M. Cho, K. D. Irwin, F. C. Wellstood, W. D. Oliver, A. Shnirman, and J. Clarke, "Magnetic Flux Noise in dc SQUIDs: Temperature and Geometry Dependence", Phys. Rev. Lett. **110**, 147002 (2013).

[138] Y. Yokotera and N. Yamamoto, "Sensitivity Analysis of Cascaded Quantum Feedback Amplifier", IEEE Control Systems Letters **3**, 156 (2019).

[139] M. Renger, K. G. Fedorov, S. Pogorzalek, Y. Nojiri, Q. Chen, M. Partanen, A. Marx, F. Deppe, and R. Gross, "Chained Josephson Parametric Amplifiers", in *Annual Report 2019* (2019), pp. 67–68, URL https://www.wmi.badw.de/fileadmin/WMI/Publications/Annual_Reports/2019.pdf.

[140] A. Pilotto, P. Palestri, L. Selmi, M. Antonelli, F. Arfelli, G. Biasiol, G. Cautero, F. Driussi, R. H. Menk, C. Nichetti, and T. Steinhartova, "A New Expression for the Gain-Noise Relation of Single-Carrier Avalanche Photodiodes With Arbitrary Staircase Multiplication Regions", IEEE Transactions on Electron Devices **66**, 1810 (2019).

[141] H. Friis, "Noise Figures of Radio Receivers", Proceedings of the IRE **32**, 419 (1944).

[142] H. Heuser, *Lehrbuch der Analysis. Teil 1* (Vieweg+Teubner Verlag, 2009), URL http://www.springer.com.emedien.ub.uni-muenchen.de/de/book/9783834807779.

[143] L. Landau and E. Lifshitz, *Mechanics: Volume 1*, Bd. 1 (Elsevier Science, 1982), ISBN 9780080503479, URL https://books.google.de/books?id=bE-9tUH2J2wC.

[144] W. Heisenberg, "Über den anschaulichen Inhalt der quantentheoretischen Kinematik und Mechanik", Zeitschrift für Physik **43**, 172 (1927).

[145] N. J. Cerf, G. Leuchs, and E. S. Polzik, *Quantum Information with Continuous Variables of Atoms and Light* (2007), https://www.worldscientific.com/doi/pdf/10.1142/p489, URL https://www.worldscientific.com/doi/abs/10.1142/p489.

[146] J. E. Moyal, "Quantum mechanics as a statistical theory", Mathematical Proceedings of the Cambridge Philosophical Society **45**, 99 (1949).

[147] H. Weyl, *The Theory of Groups and Quantum Mechanics*, Dover Books on Mathematics (Dover Publications, 1950), ISBN 9780486602691, URL https://books.google.de/books?id=jQbEcDDqGb8C.

[148] U. Leonhardt and H. Paul, "Measuring the quantum state of light", Progress in Quantum Electronics **19**, 89 (1995).

[149] E. Wigner, "On the Quantum Correction For Thermodynamic Equilibrium", Phys. Rev. **40**, 749 (1932).

[150] H. Carmichael, *Statistical Methods in Quantum Optics 1: Master Equations and Fokker-Planck Equations*, Physics and astronomy online library (Springer, 1999), ISBN 9783540548829, URL https://books.google.de/books?id=ocgRgM-yJacC.

[151] G. Adesso, S. Ragy, and A. R. Lee, "Continuous Variable Quantum Information: Gaussian States and Beyond", Open Systems & Information Dynamics **21**, 1440001 (2014).

[152] J. Radon, "On the determination of functions from their integral values along certain manifolds", IEEE Transactions on Medical Imaging **5**, 170 (1986).

[153] K. Husimi, "Some Formal Properties of the Density Matrix", Proceedings of the Physico-Mathematical Society of Japan. 3rd Series **22**, 264 (1940).

[154] R. J. Glauber, "Coherent and Incoherent States of the Radiation Field", Phys. Rev. **131**, 2766 (1963).

[155] E. C. G. Sudarshan, "Equivalence of Semiclassical and Quantum Mechanical Descriptions of Statistical Light Beams", Phys. Rev. Lett. **10**, 277 (1963).

[156] R. F. Werner and M. M. Wolf, "Bound Entangled Gaussian States", Phys. Rev. Lett. **86**, 3658 (2001).

[157] R. D. Candia, E. P. Menzel, L. Zhong, F. Deppe, A. Marx, R. Gross, and E. Solano, "Dual-path methods for propagating quantum microwaves", New Journal of Physics **16**, 015001 (2014).

[158] E. P. Menzel, "Propagating quantum microwaves: dual-path state reconstruction and path entanglement", Phd thesis, Technische Universität München (2013), URL https://mediatum.ub.tum.de/1177178.

[159] J. Eisert and M. B. Plenio, "Introduction to the basics of entanglement theory in continuous-variable systems", (2003).

[160] M. G. A. Paris, F. Illuminati, A. Serafini, and S. De Siena, "Purity of Gaussian states: Measurement schemes and time evolution in noisy channels", Phys. Rev. A **68**, 012314 (2003).

[161] A. Gut, *An Intermediate Course in Probability*, Springer Texts in Statistics (Springer New York, 2009), ISBN 9781441901620, URL https://books.google.de/books?id=ufxMwdtrmOAC.

[162] M. A. de Oliveira, E. P. de Política, and R. H. Ikeda, "Representation of the n-th Derivative of the Normal PDF Using Bernoulli Numbers and Gamma Function", (2012).

[163] G. Arfken, H. Weber, and F. Harris, *Mathematical Methods for Physicists: A Comprehensive Guide* (Elsevier Science, 2012), ISBN 9780123846549, URL https://books.google.de/books?id=qLFo_Z-PoGIC.

[164] G. C. Wick, "The Evaluation of the Collision Matrix", Phys. Rev. **80**, 268 (1950).

[165] M. Alexanian, "Temporal second-order coherence function for displaced-squeezed thermal states", Journal of Modern Optics **63**, 961 (2016).

[166] M. Ghasemkhani, A. A. Varshovi, and R. Bufalo, "Perturbative effective action for the photon in noncommutative QED_2 and exactness of the Schwinger mass", Phys. Rev. D **97**, 065005 (2018).

[167] M. Kliesch and A. Riera, *Properties of Thermal Quantum States: Locality of Temperature, Decay of Correlations, and More* (Springer International Publishing, Cham, 2018), pp. 481–502, ISBN 978-3-319-99046-0, URL https://doi.org/10.1007/978-3-319-99046-0_20.

[168] L. Landau and E. Lifshitz, *Statistical Physics*, Bd. 5 (Elsevier Science, 1980), ISBN 9780750633727, URL https://books.google.de/books?id=dEVtKQEACAAJ.

[169] M. J. Collett and C. W. Gardiner, "Squeezing of intracavity and traveling-wave light fields produced in parametric amplification", Phys. Rev. A **30**, 1386 (1984).

[170] M. O. Scully and M. S. Zubairy, *Quantum optics* (Cambridge University Press, Cambridge, 1997).

[171] J. Klauder and B. Skagerstam, *Coherent States* (WORLD SCIENTIFIC, 1985), https://www.worldscientific.com/doi/pdf/10.1142/0096, URL https://www.worldscientific.com/doi/abs/10.1142/0096.

[172] J.-W. Pan, D. Bouwmeester, H. Weinfurter, and A. Zeilinger, "Experimental Entanglement Swapping: Entangling Photons That Never Interacted", Phys. Rev. Lett. **80**, 3891 (1998).

[173] C. Gerry, P. Knight, and P. Knight, *Introductory Quantum Optics* (Cambridge University Press, 2005), ISBN 9780521527354, URL https://books.google.de/books?id=CgByyoBJJwgC.

[174] P. Yard, "Noncommutation and finite-time correlations with propagating quantum microwave states", Master's thesis, Technische Universität München (2016), URL https://www.wmi.badw.de/fileadmin/WMI/Publications/Yard%2CPatrick_Masterarbeit_2016.pdf.

[175] M. Esposito, A. Ranadive, L. Planat, S. Leger, D. Fraudet, V. Jouanny, O. Buisson, W. Guichard, C. Naud, J. Aumentado, F. Lecocq, and N. Roch, "Observation of Two-Mode Squeezing in a Traveling Wave Parametric Amplifier", Phys. Rev. Lett. **128**, 153603 (2022).

[176] H. Ollivier and W. H. Zurek, "Quantum Discord: A Measure of the Quantumness of Correlations", Phys. Rev. Lett. **88**, 017901 (2001).

[177] A. Ferraro, S. Olivares, and M. G. A. Paris, "Gaussian states in continuous variable quantum information", (2005).

[178] J. Williamson, "On the Algebraic Problem Concerning the Normal Forms of Linear Dynamical Systems", American Journal of Mathematics **58**, 141 (1936).

[179] A. Serafini, F. Illuminati, and S. D. Siena, "Symplectic invariants, entropic measures and correlations of Gaussian states", Journal of Physics B: Atomic, Molecular and Optical Physics **37**, L21 (2003).

[180] R. Simon, "Peres-Horodecki Separability Criterion for Continuous Variable Systems", Phys. Rev. Lett. **84**, 2726 (2000).

[181] G. Adesso, A. Serafini, and F. Illuminati, "Determination of Continuous Variable Entanglement by Purity Measurements", Phys. Rev. Lett. **92**, 087901 (2004).

[182] L. Landau and E. Lifshitz, *Statistical Physics: Volume 5*, Bd. 5 (Elsevier Science, 2013), ISBN 9780080570464, URL https://books.google.de/books?id=VzgJN-XPTRsC.

[183] C. E. Shannon, "A Mathematical Theory of Communication", Bell Syst. Tech. J. **27**, 379 (1948).

[184] T. Cover and J. Thomas, *Elements of Information Theory* (Wiley, 2012), ISBN 9781118585771, URL https://books.google.de/books?id=VWq5GG6ycxMC.

[185] A. Rényi, "On measures of entropy and information", in *Proceedings of the fourth Berkeley symposium on mathematical statistics and probability* (Berkeley, California, USA, 1961), vol. 1.

[186] M. Müller-Lennert, F. Dupuis, O. Szehr, S. Fehr, and M. Tomamichel, "On quantum Rényi entropies: A new generalization and some properties", Journal of Mathematical Physics **54**, 122203 (2013).

[187] J. Eisert, M. Cramer, and M. B. Plenio, "Colloquium: Area laws for the entanglement entropy", Rev. Mod. Phys. **82**, 277 (2010).

[188] F. P. M. Méndez-Córdoba, J. J. Mendoza-Arenas, F. J. Gómez-Ruiz, F. J. Rodríguez, C. Tejedor, and L. Quiroga, "Rényi entropy singularities as signatures of topological criticality in coupled photon-fermion systems", Phys. Rev. Research **2**, 043264 (2020).

[189] G. Adesso, D. Girolami, and A. Serafini, "Measuring Gaussian Quantum Information and Correlations Using the Rényi Entropy of Order 2", Phys. Rev. Lett. **109**, 190502 (2012).

[190] A. Peres, "Separability Criterion for Density Matrices", Phys. Rev. Lett. **77**, 1413 (1996).

[191] A. Sergeevich and V. I. Man'ko, "Scaling separability criterion: application to Gaussian states", Journal of Russian Laser Research **30**, 609 (2009).

[192] G. Adesso and F. Illuminati, "Gaussian measures of entanglement versus negativities: Ordering of two-mode Gaussian states", Phys. Rev. A **72**, 032334 (2005).

[193] M. M. Wolf, G. Giedke, O. Krüger, R. F. Werner, and J. I. Cirac, "Gaussian entanglement of formation", Phys. Rev. A **69**, 052320 (2004).

[194] S. Tserkis, S. Onoe, and T. C. Ralph, "Quantifying entanglement of formation for two-mode Gaussian states: Analytical expressions for upper and lower bounds and numerical estimation of its exact value", Phys. Rev. A **99**, 052337 (2019).

[195] S. Tserkis and T. C. Ralph, "Quantifying entanglement in two-mode Gaussian states", Phys. Rev. A **96**, 062338 (2017).

[196] S.-K. Chu, C.-T. Ma, R.-X. Miao, and C.-H. Wu, "Maximally entangled state and Bell's inequality in qubits", Annals of Physics **395**, 183 (2018).

[197] J. F. Clauser, M. A. Horne, A. Shimony, and R. A. Holt, "Proposed Experiment to Test Local Hidden-Variable Theories", Phys. Rev. Lett. **23**, 880 (1969).

[198] B. S. Cirel'son, "Quantum generalizations of Bell's inequality", Letters in Mathematical Physics **4**, 93 (1980).

[199] L. Borsten, K. Brádler, and M. J. Duff, "Tsirelson's bound and supersymmetric entangled states", Proceedings of the Royal Society A: Mathematical, Physical and Engineering Sciences **470**, 20140253 (2014).

[200] V. Lipinska, F. J. Curchod, A. Máttar, and A. Acín, "Towards an equivalence between maximal entanglement and maximal quantum nonlocality", New Journal of Physics **20**, 063043 (2018).

[201] A. Bera, T. Das, D. Sadhukhan, S. Singha Roy, A. Sen(De), and U. Sen, "Quantum discord and its allies: a review of recent progress", Rep. Prog. Phys. **81**, 024001 (2018).

[202] K. Modi, A. Brodutch, H. Cable, T. Paterek, and V. Vedral, "The classical-quantum boundary for correlations: Discord and related measures", Rev. Mod. Phys. **84**, 1655 (2012).

[203] L. Henderson and V. Vedral, "Classical, quantum and total correlations", J Phys A Math Gen **34**, 6899 (2001).

[204] G. Adesso and A. Datta, "Quantum versus Classical Correlations in Gaussian States", Phys. Rev. Lett. **105**, 030501 (2010).

[205] M. Neeley, M. Ansmann, R. C. Bialczak, M. Hofheinz, N. Katz, E. Lucero, A. O'Connell, H. Wang, A. N. Cleland, and J. M. Martinis, "Process tomography of quantum memory in a Josephson-phase qubit coupled to a two-level state", Nature Physics **4**, 523 (2008).

[206] M. Renger, "Quantum Process Tomography of a 3D Quantum Memory", Master thesis, Technische Universität München (2018), URL https://www.wmi.badw.de/fileadmin/WMI/Publications/Renger%2CMichael_Masterarbeit_2018.pdf.

[207] S. Rahimi-Keshari, A. Scherer, A. Mann, A. T. Rezakhani, A. I. Lvovsky, and B. C. Sanders, "Quantum process tomography with coherent states", New Journal of Physics **13**, 013006 (2011).

[208] E. Knill, D. Leibfried, R. Reichle, J. Britton, R. B. Blakestad, J. D. Jost, C. Langer, R. Ozeri, S. Seidelin, and D. J. Wineland, "Randomized benchmarking of quantum gates", Phys. Rev. A **77**, 012307 (2008).

[209] T. Werlang, S. Souza, F. F. Fanchini, and C. J. Villas Boas, "Robustness of quantum discord to sudden death", Phys. Rev. A **80**, 024103 (2009).

[210] S. Pirandola, S. L. Braunstein, and S. Lloyd, "On the Security and Degradability of Gaussian Channels", in *Theory of Quantum Computation, Communication, and Cryptography, 4th Workshop, TQC 2009, Waterloo, Canada, May 11-13, 2009, Revised Selected Papers*, edited by A. M. Childs and M. Mosca (Springer, 2009), vol. 5906 of *Lecture Notes in Computer Science*, pp. 47–55, URL https://doi.org/10.1007/978-3-642-10698-9_5.

[211] C. Lupo, S. Pirandola, P. Aniello, and S. Mancini, "On the classical capacity of quantum Gaussian channels", Physica Scripta **2011**, 014016 (2011).

[212] J. Eisert and M. M. Wolf, "Gaussian quantum channels", (2005).

[213] G. A. L. White, C. D. Hill, F. A. Pollock, L. C. L. Hollenberg, and K. Modi, "Demonstration of non-Markovian process characterisation and control on a quantum processor", Nature Communications **11**, 6301 (2020).

[214] I. Oppenheim, "A survey of thermodynamics", Journal of Statistical Physics **83**, 791 (1996).

[215] H. B. Callen and T. A. Welton, "Irreversibility and Generalized Noise", Phys. Rev. **83**, 34 (1951).

[216] R. Kubo, "Statistical-Mechanical Theory of Irreversible Processes. I. General Theory and Simple Applications to Magnetic and Conduction Problems", Journal of the Physical Society of Japan **12**, 570 (1957).

[217] T. Yu and J. H. Eberly, "Sudden death of entanglement.", Science **323**, 598 (2009).

[218] C. H. Bennett, G. Brassard, C. Crépeau, R. Jozsa, A. Peres, and W. K. Wootters, "Teleporting an unknown quantum state via dual classical and Einstein-Podolsky-Rosen channels", Phys. Rev. Lett. **70**, 1895 (1993).

[219] S. Pirandola, J. Eisert, C. Weedbrook, A. Furusawa, and S. L. Braunstein, "Advances in quantum teleportation", Nature Photonics **9**, 641 (2015).

[220] C. M. Caves and K. Wodkiewicz, "Fidelity of Gaussian channels", (2004), URL
https://arxiv.org/abs/quant-ph/0409063.

[221] P. O. Boykin and V. Roychowdhury, "Optimal encryption of quantum bits", Phys.
Rev. A **67**, 042317 (2003).

[222] B. Skoric and Z. Wolffs, "Diagrammatic security proof for 8-state encoding", arXiv
(2021).

[223] A. Uhlmann, "The "transition probability" in the state space of a *-algebra", Reports
on Mathematical Physics **9**, 273 (1976).

[224] H. Jeong, T. C. Ralph, and W. P. Bowen, "Quantum and classical fidelities for
Gaussian states", Journal of the Optical Society of America B **24**, 355 (2007).

[225] B. Schumacher, "Sending entanglement through noisy quantum channels", Phys.
Rev. A **54**, 2614 (1996).

[226] N. Takei, T. Aoki, S. Koike, K.-i. Yoshino, K. Wakui, H. Yonezawa, T. Hiraoka,
J. Mizuno, M. Takeoka, M. Ban, and A. Furusawa, "Experimental demonstration of
quantum teleportation of a squeezed state", Phys. Rev. A **72**, 042304 (2005).

[227] L. Banchi, S. L. Braunstein, and S. Pirandola, "Quantum Fidelity for Arbitrary
Gaussian States", Phys. Rev. Lett. **115**, 260501 (2015).

[228] S. L. Braunstein, C. A. Fuchs, and H. J. Kimble, "Criteria for continuous-variable
quantum teleportation", Journal of Modern Optics **47**, 267 (2000).

[229] P. T. Cochrane, T. C. Ralph, and A. Dolińska, "Optimal cloning for finite distribu-
tions of coherent states", Phys. Rev. A **69**, 042313 (2004).

[230] J. Fiurášek, "Optical Implementation of Continuous-Variable Quantum Cloning
Machines", Phys. Rev. Lett. **86**, 4942 (2001).

[231] S. L. Braunstein, C. A. Fuchs, H. J. Kimble, and P. van Loock, "Quantum versus
classical domains for teleportation with continuous variables", Phys. Rev. A **64**,
022321 (2001).

[232] S. L. Braunstein, N. J. Cerf, S. Iblisdir, P. van Loock, and S. Massar, "Optimal
Cloning of Coherent States with a Linear Amplifier and Beam Splitters", Phys. Rev.
Lett. **86**, 4938 (2001).

[233] H. Fan, Y.-N. Wang, L. Jing, J.-D. Yue, H.-D. Shi, Y.-L. Zhang, and L.-Z. Mu,
"Quantum cloning machines and the applications", Physics Reports **544**, 241 (2014).

[234] M. F. Sacchi, "Phase-covariant cloning of coherent states", Phys. Rev. A **75**, 042328 (2007).

[235] F. Grosshans and P. Grangier, "Quantum cloning and teleportation criteria for continuous quantum variables", Phys. Rev. A **64**, 010301 (2001).

[236] N. J. Cerf, O. Krüger, P. Navez, R. F. Werner, and M. M. Wolf, "Non-Gaussian Cloning of Quantum Coherent States is Optimal", Phys. Rev. Lett. **95**, 070501 (2005).

[237] A. Serafini, *Quantum Continuous Variables: A Primer of Theoretical Methods* (CRC Press, 2017), ISBN 9781351645003, URL https://books.google.de/books?id=bMItDwAAQBAJ.

[238] W. K. Yam, "Microwave Quantum Teleportation Over a Thermal Channel", Master's thesis, Technische Universität München (2022).

[239] P. van Loock and S. L. Braunstein, "Multipartite Entanglement for Continuous Variables: A Quantum Teleportation Network", Phys. Rev. Lett. **84**, 3482 (2000).

[240] N. Gisin, "Nonlocality criteria for quantum teleportation", Physics Letters A **210**, 157 (1996).

[241] G. Adesso and F. Illuminati, "Entanglement in continuous-variable systems: recent advances and current perspectives", Journal of Physics A: Mathematical and Theoretical **40**, 7821 (2007).

[242] N. Bergeal, F. Schackert, M. Metcalfe, R. Vijay, V. E. Manucharyan, L. Frunzio, D. E. Prober, R. J. Schoelkopf, S. M. Girvin, and M. H. Devoret, "Phase-preserving amplification near the quantum limit with a Josephson ring modulator", Nature **465**, 64 (2010).

[243] E. Flurin, N. Roch, J. D. Pillet, F. Mallet, and B. Huard, "Superconducting Quantum Node for Entanglement and Storage of Microwave Radiation", Phys. Rev. Lett. **114**, 090503 (2015).

[244] F. Kronowetter, F. Fesquet, M. Renger, K. Honasoge, Y. Nojiri, K. Inomata, Y. Nakamura, A. Marx, R. Gross, and K. G. Fedorov, "Quantum microwave parametric interferometer", (2023), URL https://arxiv.org/abs/2303.01026.

[245] S. Gandorfer, "Frequency-Degenerate Josephson Mixer Based on Josephson Parametric Amplifiers", Bachelor's thesis, Technische Universität München (2020), URL https://www.wmi.badw.de/fileadmin/WMI/Publications/thesis.pdf.

[246] P. Eder, T. Ramos, J. Goetz, M. Fischer, S. Pogorzalek, J. P. Martínez, E. P. Menzel, F. Loacker, E. Xie, J. J. Garcia-Ripoll, K. G. Fedorov, A. Marx, F. Deppe, and R. Gross, "Quantum probe of an on-chip broadband interferometer for quantum microwave photonics", Superconductor Science and Technology **31**, 115002 (2018).

[247] V. Vedral, *Introduction to Quantum Information Science*, Oxford Graduate Texts (OUP Oxford, 2006), ISBN 9780199215706, URL https://books.google.de/books?id=f4yI1eGSyIYC.

[248] Z. Y. Ou and X. Li, "Quantum SU(1,1) interferometers: Basic principles and applications", APL Photonics **5**, 080902 (2020).

[249] E. Flurin, "The Josephson mixer : a swiss army knife for microwave quantum optics",, URL https://tel.archives-ouvertes.fr/tel-01241123.

[250] P. Liuzzo-Scorpo, A. Mari, V. Giovannetti, and G. Adesso, "Optimal Continuous Variable Quantum Teleportation with Limited Resources", Phys. Rev. Lett. **119**, 120503 (2017).

[251] L. Mišta, R. Filip, and A. Furusawa, "Continuous-variable teleportation of a negative Wigner function", Phys. Rev. A **82**, 012322 (2010).

[252] A. Zubarev, M. Cuzminschi, and A. Isar, "Continuous variable quantum teleportation of a thermal state in a thermal environment", Results in Physics **39**, 105700 (2022).

[253] J. Fiurášek, "Improving the fidelity of continuous-variable teleportation via local operations", Phys. Rev. A **66**, 012304 (2002).

[254] L.-Y. Hu, Z. Liao, S. Ma, and M. S. Zubairy, "Optimal fidelity of teleportation with continuous variables using three tunable parameters in a realistic environment", Phys. Rev. A **93**, 033807 (2016).

[255] S. Qolibikloo and A. Ghodsi, "More on phase transition and Rényi entropy", The European Physical Journal C **79**, 406 (2019).

[256] W. Nolting, *Grundkurs Theoretische Physik 4/2: Thermodynamik*, Springer-Lehrbuch (Springer Berlin Heidelberg, 2016), ISBN 9783662490334, URL https://books.google.de/books?id=s1LNCwAAQBAJ.

[257] W. Nolting, *Theoretical Physics 8: Statistical Physics* (Springer International Publishing, 2018), ISBN 9783319738277, URL https://books.google.de/books?id=hd1ODwAAQBAJ.

[258] Z. Kurucz, P. Adam, Z. Kis, and J. Janszky, "Continuous variable remote state preparation", Phys. Rev. A **72**, 052315 (2005).

[259] M. G. A. Paris, M. Cola, and R. Bonifacio, "Remote state preparation and teleportation in phase space", Journal of Optics B: Quantum and Semiclassical Optics **5**, S360 (2003).

[260] J. Řeháček, Y. S. Teo, Z. Hradil, and S. Wallentowitz, "Surmounting intrinsic quantum-measurement uncertainties in Gaussian-state tomography with quadrature squeezing", Scientific Reports **5**, 12289 (2015).

[261] C. M. Caves and P. D. Drummond, "Quantum limits on bosonic communication rates", Rev. Mod. Phys. **66**, 481 (1994).

[262] H. P. Yuen and M. Ozawa, "Ultimate information carrying limit of quantum systems", Phys. Rev. Lett. **70**, 363 (1993).

[263] F. Laudenbach, C. Pacher, C. F. Fung, A. Poppe, M. Peev, B. Schrenk, M. Hentschel, P. Walther, and H. Hübel, "Continuous-Variable Quantum Key Distribution with Gaussian Modulation-The Theory of Practical Implementations", Adv. Quantum Technol **1**, 1800011 (2018).

[264] A. Patra, R. Gupta, S. Roy, T. Das, and A. S. De, "Quantum Dense Coding Network using Multimode Squeezed States of Light", (2022), URL https://arxiv.org/abs/2204.14147.

[265] U. L. Andersen, J. S. Neergaard-Nielsen, P. van Loock, and A. Furusawa, "Hybrid discrete - and continuous-variable quantum information", Nature Physics **11**, 713 (2015).

[266] S. H. Lie and H. Jeong, "Limitations of teleporting a qubit via a two-mode squeezed state", Photon. Res. **7**, A7 (2019).

[267] P. A. Bushev, J. Bourhill, M. Goryachev, N. Kukharchyk, E. Ivanov, S. Galliou, M. E. Tobar, and S. Danilishin, "Testing the generalized uncertainty principle with macroscopic mechanical oscillators and pendulums", Phys. Rev. D **100**, 066020 (2019).

[268] S. Başkal, Y. S. Kim, and M. E. Noz, *Physics of the Lorentz Group*, 2053-2571 (Morgan & Claypool Publishers, 2015), ISBN 978-1-6817-4254-0, URL https://dx.doi.org/10.1088/978-1-6817-4254-0.

[269] J. Zhang, C. Xie, and K. Peng, "The criterion for quantum teleportation of fock states", Optics Communications **207**, 213 (2002).

[270] A. Kenfack and K. Życzkowski, "Negativity of the Wigner function as an indicator of non-classicality", Journal of Optics B: Quantum and Semiclassical Optics **6**, 396 (2004).

[271] M. He, R. Malaney, and R. Aguinaldo, "Teleportation of discrete-variable qubits via continuous-variable lossy channels", Phys. Rev. A **105**, 062407 (2022).

[272] U. Schollwöck, "The density-matrix renormalization group in the age of matrix product states", Annals of Physics **326**, 96 (2011).

[273] S. Takeda, T. Mizuta, M. Fuwa, H. Yonezawa, P. van Loock, and A. Furusawa, "Gain tuning for continuous-variable quantum teleportation of discrete-variable states", Phys. Rev. A **88**, 042327 (2013).

[274] F. S. Luiz and G. Rigolin, "Teleportation-based continuous variable quantum cryptography", Quantum Information Processing **16**, 58 (2017).

[275] S. Tserkis, N. Hosseinidehaj, N. Walk, and T. C. Ralph, "Teleportation-based collective attacks in Gaussian quantum key distribution", Phys. Rev. Research **2**, 013208 (2020).

[276] A. S. Holevo, "Bounds for the quantity of information transmitted by a quantum communication channel", Probl. Inf. Transm. **9**, 177 (1973).

[277] C. Shannon, "Communication in the Presence of Noise", Proceedings of the IRE **37**, 10 (1949).

[278] I. S. Gradshteyn and I. M. Ryzhik, *Summen-, Produkt- und Integraltafeln* (VEB Deutscher Verlag der Wissenschaften, 1963), 2nd ed.

[279] I. N. Bronstein, K. A. Semendjajew, G. Musiol, and H. Mühlig, *Taschenbuch der Mathematik* (Verlag Harri Deutsch, 2001).

[280] P. Humbert, "Sur les fonctions hypercylindriques.", C. R. Acad. Sci., Paris **171**, 490 (1920).

[281] R. Neagu, "FPGA-based Tomography of Propagating Quantum Microwaves", Master's thesis, Technische Universität München (2019), URL https://www.wmi.badw.de/fileadmin/WMI/Publications/Neagu%2CRobert_Masterarbeit_2019.pdf.

[282] S. Gandorfer, "Distribution of quantum states in a microwave local area network", Master's thesis, Technische Universität München (2022).

[283] F. Pobell, *Matter and Methods at Low Temperatures* (Springer Berlin Heidelberg, 2007), ISBN 9783540463603, URL https://books.google.de/books?id=mRZOuPfiWTQC.

[284] A. T. A. M. de Waele, "Basic Operation of Cryocoolers and Related Thermal Machines", Journal of Low Temperature Physics **164**, 179 (2011).

[285] C. Enss and S. Hunklinger, *Low-Temperature Physics*, SpringerLink: Springer e-Books (Springer Berlin Heidelberg, 2005), ISBN 9783540266198, URL https://books.google.de/books?id=ufM7sPMTGdAC.

[286] C. R. Lawson, A. T. Jones, W. Kockelmann, S. J. Horney, and O. Kirichek, "Neutron imaging of an operational dilution refrigerator", Scientific Reports **12**, 1130 (2022).

[287] K. Uhlig and W. Hehn, "^{3}He^{4}He dilution refrigerator precooled by Gifford-McMahon refrigerator", Cryogenics **37**, 279 (1997).

[288] A. Marx, J. Hoess, and K. Uhlig, "Dry Dilution Refrigerator for Experiments on Quantum Effects in the Microwave Regime", ArXiv e-prints:1412.3619 (2014).

[289] C. Eichler, D. Bozyigit, C. Lang, L. Steffen, J. Fink, and A. Wallraff, "Experimental State Tomography of Itinerant Single Microwave Photons", Phys. Rev. Lett. **106**, 220503 (2011).

[290] K. Inomata, Z. Lin, K. Koshino, W. D. Oliver, J.-S. Tsai, T. Yamamoto, and Y. Nakamura, "Single microwave-photon detector using an artificial Λ-type three-level system", Nature Communications **7**, 12303 (2016).

[291] N. Roch, E. Flurin, F. Nguyen, P. Morfin, P. Campagne-Ibarcq, M. H. Devoret, and B. Huard, "Widely Tunable, Nondegenerate Three-Wave Mixing Microwave Device Operating near the Quantum Limit", Phys. Rev. Lett. **108**, 147701 (2012).

[292] B. Abdo, A. Kamal, and M. Devoret, "Nondegenerate three-wave mixing with the Josephson ring modulator", Phys. Rev. B **87**, 014508 (2013).

[293] K. G. Fedorov, R. Neagu, M. Renger, S. Pogorzalek, Y. Nojiri, Q. Chen, M. Partanen, A. Marx, F. Deppe, and R. Gross, "Fast FPGA-based Measurements of Quantum Microwaves", in *Annual Report 2019* (2019), pp. 65–66, URL https://www.wmi.badw.de/fileadmin/WMI/Publications/Annual_Reports/2019.pdf.

[294] S. Probst, F. B. Song, P. A. Bushev, A. V. Ustinov, and M. Weides, "Efficient and robust analysis of complex scattering data under noise in microwave resonators", Review of Scientific Instruments **86**, 024706 (2015).

[295] M. Hiebel, *Fundamentals of Vector Network Analysis* (Rohde & Schwarz, 2007), ISBN 9783939837060, URL https://books.google.de/books?id=jYG2PQAACAAJ.

[296] G. Wild, "Macroscopic quantum tunneling in Josephson junctions - a method to characterise a well-shielded low temperature setup", Diploma thesis, Technische Universität München (2004), URL https://www.wmi.badw.de/fileadmin/WMI/Publications/Wild_Diplomarbeit_2004.pdf.

[297] J. Götz, "The Interplay of Superconducting Quantum Circuits and Propagating Microwave States", Phd thesis, Technische Universität München (2017), URL `https://mediatum.ub.tum.de/doc/1326240/1326240.pdf`.

[298] H. Nyquist, "Certain Topics in Telegraph Transmission Theory", Transactions of the American Institute of Electrical Engineers **47**, 617 (1928).

[299] B. Shenoi, *Introduction to Digital Signal Processing and Filter Design* (Wiley, 2005), ISBN 9780471656388, URL `https://books.google.de/books?id=37g8oUqaS_AC`.

[300] N. Johnson and S. Kotz, *Urn Models and Their Application: An Approach to Modern Discrete Probability Theory*, Approach to Modern Discrete Probability Theory (Wiley, 1977), ISBN 9780471446309, URL `https://books.google.de/books?id=ZBfvAAAAMAAJ`.

[301] A. V. Oppenheim and R. W. Schafer, *Discrete-Time Signal Processing* (Prentice Hall Press, USA, 2009), 3rd ed., ISBN 0131988425.

[302] M. Avesani, D. G. Marangon, G. Vallone, and P. Villoresi, "Source-device-independent heterodyne-based quantum random number generator at 17 Gbps", Nature Communications **9**, 5365 (2018).

[303] L. Spietz, K. W. Lehnert, I. Siddiqi, and R. J. Schoelkopf, "Primary Electronic Thermometry Using the Shot Noise of a Tunnel Junction", Science **300**, 1929 (2003).

[304] C. Macklin, K. O'Brien, D. Hover, M. E. Schwartz, V. Bolkhovsky, X. Zhang, W. D. Oliver, and I. Siddiqi, "A near quantum-limited Josephson traveling-wave parametric amplifier", Science **350**, 307 (2015).

[305] M. Perelshtein, K. Petrovnin, V. Vesterinen, S. Hamedani Raja, I. Lilja, M. Will, A. Savin, S. Simbierowicz, R. Jabdaraghi, J. Lehtinen, L. Grönberg, J. Hassel, M. Prunnila, J. Govenius, G. Paraoanu, and P. Hakonen, "Broadband Continuous-Variable Entanglement Generation Using a Kerr-Free Josephson Metamaterial", Phys. Rev. Applied **18**, 024063 (2022).

[306] M. Mariantoni, "New trends in superconducting circuit quantum electrodynamics: two amplifiers, two resonators, and two photons: a not so short introduction to quantum circuits and signals", Ph.D. thesis, Tech. U., Munich (main) (2009), URL `https://www.wmi.badw.de/fileadmin/WMI/Publications/Mariantoni_Doktorarbeit_2009.pdf`.

[307] C. L. Hogan, "The Ferromagnetic Faraday Effect at Microwave Frequencies and its Applications", Rev. Mod. Phys. **25**, 253 (1953).

[308] E. Cheney and D. Kincaid, *Numerical Mathematics and Computing*, International student edition (Cengage Learning, 2007), ISBN 9780495114758, URL https://books.google.de/books?id=ZUfVZELlrMEC.

[309] D. Rieger, S. Günzler, M. Spiecker, A. Nambisan, W. Wernsdorfer, and I. M. Pop, "Fano Interference in Microwave Resonator Measurements", (2023), 2209.03036.

[310] R. C. Bialczak, R. McDermott, M. Ansmann, M. Hofheinz, N. Katz, E. Lucero, M. Neeley, A. D. O'Connell, H. Wang, A. N. Cleland, and J. M. Martinis, "$1/f$ Flux Noise in Josephson Phase Qubits", Phys. Rev. Lett. **99**, 187006 (2007).

[311] H. Meinke, K. Lange, F. Gundlach, and K. Löcherer, *Taschenbuch der Hochfrequenztechnik: Band 3: Systeme*, TASCHENBUCH der Hochfrequenztechnik (Springer, 1992), ISBN 9783540153962, URL https://books.google.com.na/books?id=xKUjSQAACAAJ.

[312] V. V. Sivak, S. Shankar, G. Liu, J. Aumentado, and M. H. Devoret, "Josephson Array-Mode Parametric Amplifier", Phys. Rev. Applied **13**, 024014 (2020).

[313] X. Zhou, V. Schmitt, P. Bertet, D. Vion, W. Wustmann, V. Shumeiko, and D. Esteve, "High-gain weakly nonlinear flux-modulated Josephson parametric amplifier using a SQUID array", Phys. Rev. B **89**, 214517 (2014).

[314] R. Schack and A. Schenzle, "Moment hierarchies and cumulants in quantum optics", Phys. Rev. A **41**, 3847 (1990).

[315] C. Eichler, Y. Salathe, J. Mlynek, S. Schmidt, and A. Wallraff, "Quantum-Limited Amplification and Entanglement in Coupled Nonlinear Resonators", Phys. Rev. Lett. **113**, 110502 (2014).

[316] S. N. Filippov and V. I. Man'ko, "Evolution of microwave quantum states in terms of measurable ordered moments of creation and annihilation operators", Optics and Spectroscopy **112**, 365 (2012).

[317] S. N. Filippov and V. I. Man'ko, "Measuring microwave quantum states: Tomogram and moments", Phys. Rev. A **84**, 033827 (2011).

[318] R. Rossi, *Mathematical Statistics: An Introduction to Likelihood Based Inference* (Wiley, 2018), ISBN 9781118771044, URL https://books.google.de/books?id=ehpfDwAAQBAJ.

[319] J. A. Nelder and R. Mead, "A simplex method for function minimization", Computer Journal **7**, 308 (1965).

[320] J. Kondo, "Resistance Minimum in Dilute Magnetic Alloys", Progress of Theoretical Physics **32**, 37 (1964).

[321] R. Movshovich, B. Yurke, P. G. Kaminsky, A. D. Smith, A. H. Silver, R. W. Simon, and M. V. Schneider, "Observation of zero-point noise squeezing via a Josephson-parametric amplifier", Phys. Rev. Lett. **65**, 1419 (1990).

[322] S. Lloyd, "Enhanced Sensitivity of Photodetection via Quantum Illumination", Science **321**, 1463 (2008).

[323] U. Las Heras, R. Di Candia, K. G. Fedorov, F. Deppe, M. Sanz, and E. Solano, "Quantum illumination reveals phase-shift inducing cloaking", Scientific Reports **7**, 9333 (2017).

[324] T. Braine et al. (ADMX Collaboration), "Extended Search for the Invisible Axion with the Axion Dark Matter Experiment", Phys. Rev. Lett. **124**, 101303 (2020).

[325] C. Braggio, G. Carugno, F. D. Valle, G. Galeazzi, A. Lombardi, G. Ruoso, and D. Zanello, "The measurement of a single-mode thermal field with a microwave cavity parametric amplifier", New J. Phys. **15**, 013044 (2013).

[326] A. Kitaev, "Fault-tolerant quantum computation by anyons", Annals of Physics **303**, 2 (2003).

[327] S. Krinner, N. Lacroix, A. Remm, A. Di Paolo, E. Genois, C. Leroux, C. Hellings, S. Lazar, F. Swiadek, J. Herrmann, G. J. Norris, C. K. Andersen, M. Müller, A. Blais, C. Eichler, and A. Wallraff, "Realizing repeated quantum error correction in a distance-three surface code", Nature **605**, 669 (2022).

[328] M. Takita, A. D. Córcoles, E. Magesan, B. Abdo, M. Brink, A. Cross, J. M. Chow, and J. M. Gambetta, "Demonstration of Weight-Four Parity Measurements in the Surface Code Architecture", Phys. Rev. Lett. **117**, 210505 (2016).

[329] C. Weedbrook, S. Pirandola, and T. C. Ralph, "Continuous-variable quantum key distribution using thermal states", Phys. Rev. A **86**, 022318 (2012).

[330] D. Manzano, "A short introduction to the Lindblad master equation", AIP Advances **10**, 025106 (2020).

[331] G. Liu, X. Cao, T.-C. Chien, C. Zhou, P. Lu, and M. Hatridge, "Noise Reduction in Qubit Readout with a Two-Mode Squeezed Interferometer", Phys. Rev. Appl. **18**, 064092 (2022).

[332] P. Kylemark, M. Karlsson, and P. A. Andrekson, "Gain and wavelength dependence of the noise-figure in fiber optical parametric amplification", IEEE Photon. Technol. Lett. **18**, 1255 (2006).

[333] N. A. Olsson, "Lightwave systems with optical amplifiers", J. Light. Technol. **7**, 1071 (1989).

[334] S. M. Rytov, Y. A. Kravtsov, and V. I. Tatarskii, *Principles of Statistical Radiophysics 2* (Springer-Verlag, 1988).

[335] R. L. Hudson and V. R. Struleckaja, "Fermionic quantum stochastic flows", Letters in Mathematical Physics **37**, 309 (1996).

[336] F. Henriques, F. Valenti, T. Charpentier, M. Lagoin, C. Gouriou, M. Martínez, L. Cardani, M. Vignati, L. Grünhaupt, D. Gusenkova, J. Ferrero, S. T. Skacel, W. Wernsdorfer, A. V. Ustinov, G. Catelani, O. Sander, and I. M. Pop, "Phonon traps reduce the quasiparticle density in superconducting circuits", Applied Physics Letters **115**, 212601 (2019).

[337] W. Schottky, "Über spontane Stromschwankungen in verschiedenen Elektrizitätsleitern", Annalen der Physik **362**, 541 (1918).

[338] A. Van Der Ziel and E. Chenette, "Noise in Solid State Devices", (Academic Press, 1978), vol. 46 of *Advances in Electronics and Electron Physics*, pp. 313–383, URL https://www.sciencedirect.com/science/article/pii/S006525390860414X.

[339] R. Nicholson and J. P. Kaipio, "An Additive Approximation to Multiplicative Noise", Journal of Mathematical Imaging and Vision **62**, 1227 (2020).

[340] T. J. Clark, V. Vadakkumbatt, F. Souris, H. Ramp, and J. P. Davis, "Cryogenic microwave filter cavity with a tunability greater than 5 GHz", Review of Scientific Instruments **89**, 114704 (2018).

[341] Y. Kano and E. Wolf, "Temporal Coherence of Black Body Radiation", Proc. Phys. Soc. **80**, 1273 (2002).

[342] D. D. Bai, J. Du, T. Zhang, and Y. S. He, "A compact high temperature superconducting bandpass filter for integration with a Josephson mixer", Journal of Applied Physics **114**, 133906 (2013).

[343] D. I. Schuster, A. Wallraff, A. Blais, L. Frunzio, R.-S. Huang, J. Majer, S. M. Girvin, and R. J. Schoelkopf, "ac Stark Shift and Dephasing of a Superconducting Qubit Strongly Coupled to a Cavity Field", Phys. Rev. Lett. **94**, 123602 (2005).

[344] P. Drazin, P. Drazin, M. Ablowitz, and D. Crighton, *Nonlinear Systems*, Cambridge Texts in Applied Mathematics (Cambridge University Press, 1992), ISBN 9780521406680, URL https://books.google.de/books?id=Spd9vxma24IC.

[345] S. H. Strogatz, *Nonlinear Dynamics and Chaos: With Applications to Physics, Biology, Chemistry and Engineering* (Westview Press, 2000).

[346] N. J. Cerf, M. Lévy, and G. V. Assche, "Quantum distribution of Gaussian keys using squeezed states", Phys. Rev. A **63**, 052311 (2001).

[347] B. Dakić, Y. O. Lipp, X. Ma, M. Ringbauer, S. Kropatschek, S. Barz, T. Paterek, V. Vedral, A. Zeilinger, Č. Brukner, and P. Walther, "Quantum discord as resource for remote state preparation", Nat. Phys. **8**, 666 (2012).

[348] F. F. Fanchini, M. F. Cornelio, M. C. de Oliveira, and A. O. Caldeira, "Conservation law for distributed entanglement of formation and quantum discord", Phys. Rev. A **84**, 012313 (2011).

[349] E. Kreyszig, H. Kreyszig, and E. J. Norminton, *Advanced Engineering Mathematics* (Wiley, Hoboken, NJ, 2011), tenth ed., ISBN 0470458364.

[350] A. Datta, A. Shaji, and C. M. Caves, "Quantum Discord and the Power of One Qubit", Phys. Rev. Lett. **100**, 050502 (2008).

[351] B. P. Lanyon, M. Barbieri, M. P. Almeida, and A. G. White, "Experimental Quantum Computing without Entanglement", Phys. Rev. Lett. **101**, 200501 (2008).

[352] C. Weedbrook, S. Pirandola, J. Thompson, V. Vedral, and M. Gu, "How discord underlies the noise resilience of quantum illumination", New J. Phys. **18**, 043027 (2016).

[353] S. Luo, "Quantum discord for two-qubit systems", Phys. Rev. A **77**, 042303 (2008).

[354] P. Marian, I. Ghiu, and T. A. Marian, "Decay of Gaussian correlations in local thermal reservoirs", Phys. Scr. **90**, 074041 (2015).

[355] W. F. Stinespring, "Positive Functions on C^*-Algebras", Proceedings of the American Mathematical Society **6**, 211 (1955).

[356] H. Araki and E. H. Lieb, "Entropy inequalities", Communications in Mathematical Physics **18**, 160 (1970).

[357] C. H. Bennett and G. Brassard, "Quantum cryptography: Public key distribution and coin tossing", in *Proceedings of the Conference on Computers, Systems and Signal Processing* (IEEE, New York, 1984), p. 175.

[358] F. Grosshans, N. J. Cerf, J. Wenger, R. Tualle-Brouri, and P. Grangier, "Virtual Entanglement and Reconciliation Protocols for Quantum Cryptography with Continuous Variables", Quantum Inf Comput **3**, 535 (2003).

[359] R. García-Patrón and N. J. Cerf, "Unconditional Optimality of Gaussian Attacks against Continuous-Variable Quantum Key Distribution", Phys. Rev. Lett. **97**, 190503 (2006).

[360] S. Pirandola, "Composable security for continuous variable quantum key distribution: Trust levels and practical key rates in wired and wireless networks", Phys. Rev. Research **3**, 043014 (2021).

[361] O. Ahonen, M. Möttönen, and J. L. O'Brien, "Entanglement-enhanced quantum key distribution", Phys. Rev. A **78**, 032314 (2008).

[362] F. Fesquet, F. Kronowetter, M. Renger, Q. Chen, K. Honasoge, O. Gargiulo, Y. Nojiri, A. Marx, F. Deppe, R. Gross, and K. G. Fedorov, "Perspectives of microwave quantum key distribution in open-air", https://arxiv.org/abs/2203.05530:2203.05530 (2022).

[363] C. H. Bennett, P. W. Shor, J. A. Smolin, and A. V. Thapliyal, "Entanglement-Assisted Classical Capacity of Noisy Quantum Channels", Phys. Rev. Lett. **83**, 3081 (1999).

[364] C. Adami and N. J. Cerf, "von Neumann capacity of noisy quantum channels", Phys. Rev. A **56**, 3470 (1997).

[365] A. S. Holevo and R. F. Werner, "Evaluating capacities of bosonic Gaussian channels", Phys. Rev. A **63**, 032312 (2001).

[366] H. Latscha and H. Klein, *Anorganische Chemie: Chemie-Basiswissen I*, Chemie-Basiswissen (Springer Berlin Heidelberg, 2007), ISBN 9783540698654, URL https://books.google.de/books?id=yhvnJHyEUCcC.

[367] A. Abrikosov, "The magnetic properties of superconducting alloys", Journal of Physics and Chemistry of Solids **2**, 199 (1957).

[368] B. Chiaro, A. Megrant, A. Dunsworth, Z. Chen, R. Barends, B. Campbell, Y. Chen, A. Fowler, I. C. Hoi, E. Jeffrey, J. Kelly, J. Mutus, C. Neill, P. J. J. O'Malley, C. Quintana, P. Roushan, D. Sank, A. Vainsencher, J. Wenner, T. C. White, and J. M. Martinis, "Dielectric surface loss in superconducting resonators with flux-trapping holes", Superconductor Science and Technology **29**, 104006 (2016).

[369] K. Jensen, W. Wasilewski, H. Krauter, T. Fernholz, B. M. Nielsen, M. Owari, M. B. Plenio, A. Serafini, M. M. Wolf, and E. S. Polzik, "Quantum memory for entangled continuous-variable states", Nature Physics **7**, 13 (2011).

[370] G. Korn and T. Korn, *Mathematical Handbook for Scientists and Engineers: Definitions, Theorems, and Formulas for Reference and Review*, Dover Civil and Mechanical Engineering Series (Dover Publications, 2000), ISBN 9780486411477, URL https://books.google.de/books?id=xHNd5zCXt-EC.

[371] J. Jackson, *Classical Electrodynamics* (Wiley, 2012), ISBN 9788126510948, URL https://books.google.de/books?id=8qHCZjJHRUgC.

[372] E. Hoffmann, F. Deppe, T. Niemczyk, T. Wirth, E. P. Menzel, G. Wild, H. Huebl, M. Mariantoni, T. Weißl, A. Lukashenko, A. P. Zhuravel, A. V. Ustinov, A. Marx, and R. Gross, "A superconducting 180° hybrid ring coupler for circuit quantum electrodynamics", Applied Physics Letters **97**, 222508 (2010).

[373] J. Reed and G. Wheeler, "A Method of Analysis of Symmetrical Four-Port Networks", IRE Transactions on Microwave Theory and Techniques **4**, 246 (1956).

[374] M. Fischer, "In situ tunable nonlinearity and competing signal paths in coupled superconducting resonators", Phd thesis, Technische Universität München (2022), URL https://www.wmi.badw.de/fileadmin/WMI/Publications/Fischer_Michael_Doktorarbeit_2022.pdf.

[375] R. V. L. Hartley, "Transmission of information", The Bell System Technical Journal **7**, 535 (1928).

[376] S. L. Braunstein and C. M. Caves, "Statistical distance and the geometry of quantum states", Phys. Rev. Lett. **72**, 3439 (1994).

[377] O. Pinel, P. Jian, N. Treps, C. Fabre, and D. Braun, "Quantum parameter estimation using general single-mode Gaussian states", Phys. Rev. A **88**, 040102 (2013).

[378] D. Lima and G. Rigolin, "Asymptotic security analysis of teleportation-based quantum cryptography", Quantum Information Processing **19**, 201 (2020).

[379] C. Berrou, A. Glavieux, and P. Thitimajshima, "Near Shannon limit error-correcting coding and decoding: Turbo-codes. 1", in *Proceedings of ICC '93 - IEEE International Conference on Communications* (1993), vol. 2, pp. 1064–1070 vol.2.

[380] R. Landauer, "Irreversibility and Heat Generation in the Computing Process", IBM Journal of Research and Development **5**, 183 (1961).

[381] Y. Y. Gao, B. J. Lester, Y. Zhang, C. Wang, S. Rosenblum, L. Frunzio, L. Jiang, S. M. Girvin, and R. J. Schoelkopf, "Programmable Interference between Two Microwave Quantum Memories", Phys. Rev. X **8**, 021073 (2018).

[382] E. Xie, F. Deppe, M. Renger, D. Repp, P. Eder, M. Fischer, J. Goetz, S. Pogorzalek, K. G. Fedorov, A. Marx, and R. Gross, "Compact 3D quantum memory", Appl. Phys. Lett. **112**, 202601 (2018).

[383] D. Gottesman, A. Kitaev, and J. Preskill, "Encoding a qubit in an oscillator", Phys. Rev. A **64**, 012310 (2001).

[384] P. Magnard, S. Storz, P. Kurpiers, J. Schär, F. Marxer, J. Lütolf, T. Walter, J.-C. Besse, M. Gabureac, K. Reuer, A. Akin, B. Royer, A. Blais, and A. Wallraff, "Microwave Quantum Link between Superconducting Circuits Housed in Spatially Separated Cryogenic Systems", Phys. Rev. Lett. **125**, 260502 (2020).

[385] A. Berlin, D. Blas, R. T. D'Agnolo, S. A. R. Ellis, R. Harnik, Y. Kahn, and J. Schütte-Engel, "Detecting high-frequency gravitational waves with microwave cavities", Phys. Rev. D **105**, 116011 (2022).

[386] R. Lasenby, "Microwave cavity searches for low-frequency axion dark matter", Phys. Rev. D **102**, 015008 (2020).

[387] M. Partanen, M. Pfeiffer, S. Pogorzalek, M. Renger, Q. Chen, Y. Nojiri, A. Marx, K. G. Fedorov, F. Deppe, and R. Gross, "Superconducting Cables for Microwave Quantum Communication over Kilometer Distances", in *Annual Report 2019* (2019), pp. 69–70, URL https://www.wmi.badw.de/fileadmin/WMI/Publications/Annual_Reports/2019.pdf.

[388] J. P. Turneaure and I. Weissman, "Microwave Surface Resistance of Superconducting Niobium", Journal of Applied Physics **39**, 4417 (1968).

[389] J. Bardeen, L. N. Cooper, and J. R. Schrieffer, "Theory of Superconductivity", Phys. Rev. **108**, 1175 (1957).

[390] E. Gottardi, G. Bianchini, I. Peroni, A. Peruzzi, and G. Ventura, "Thermal conductivity of polyetheretherketone at low", in *Proc. 8th Int. Symp. on Temperature and Thermal Measurements in Industry and Science (Berlin)* (2001), p. 1151, URL https://www.researchgate.net/publication/268055430_THERMAL_CONDUCTIVITY_OF_POLYETHERETHERKETONE_AT_LOW_TEMPERATURES.

[391] E. D. Marquardt, J. P. Le, and R. Radebaugh, "Cryogenic Material Properties Database", Presented at the 11th International Cryocooler Conference June 20-22, 2000 Keystone, Co (2000).

[392] N. Simon, E. Drexler, and R. Reed, "Properties of Copper and Copper Alloys at Cryogenic Temperatures", NIST Monograph **177** (1992).

[393] Y. Touloukian, *Thermal Expansion: Metallic Elements and Alloys*, TPRC data series (Springer US, 1975), ISBN 9780306670329, URL https://books.google.de/books?id=XR1NAQAAIAAJ.

[394] K. Thurnay, Tech. Rep. (1998), 32.21.02; LK 01, URL https://doi.org/10.5445/IR/270043419.

[395] A. V. Timofeev, M. Helle, M. Meschke, M. Möttönen, and J. P. Pekola, "Electronic Refrigeration at the Quantum Limit", Phys. Rev. Lett. **102**, 200801 (2009).

[396] D. Einzel, "Spin-independent transport parameters for superfluid ^{3}He-B", Journal of Low Temperature Physics **54**, 427 (1984).

[397] D. Einzel, "Interpolation of BCS Response Functions", Journal of Low Temperature Physics **130**, 493 (2003).

[398] D. Einzel, "Universal Parameters in the Response of Unconventional Superconductors", Journal of Low Temperature Physics **126**, 867 (2002).

[399] A. Kushino, S. Kasai, S. Kohjiro, S. Shiki, and M. Ohkubo, "Development of Superconducting Coaxial Cables for Cryogenic Detectors", Journal of Low Temperature Physics **151**, 650 (2008).

[400] G. Krainz and D. Hagedorn, "Quench Protection and Powering in a String of Superconducting Magnets for the Large Hadron Collider", (1997).

[401] H. R. H. Buhrman, *Distributed Quantum Computing* (2013), pp. 1–20.

[402] D. Poderini, I. Agresti, G. Marchese, E. Polino, T. Giordani, A. Suprano, M. Valeri, G. Milani, N. Spagnolo, G. Carvacho, R. Chaves, and F. Sciarrino, "Experimental violation of n-locality in a star quantum network", Nature Communications **11**, 2467 (2020).

[403] J. Kuerten, C. Castelijns, A. de Waele, and H. Gijsman, "Thermodynamic properties of liquid ^{3}He-^{4}He mixtures at zero pressure for temperatures below 250 mK and ^{3}He concentrations below 8%", Cryogenics **25**, 419 (1985).

[404] G. Chaudhry and J. G. Brisson, "Thermodynamic Properties of Liquid ^{3}He-^{4}He Mixtures Between 0.15K and 1.8K", Journal of Low Temperature Physics **155**, 235 (2009).

[405] *Technisches Taschenbuch* (Schaeffler Technologies AG & Co. KG, 2013), ISBN 978-1100223407.

[406] K. Kabus, F. Rieg, F. Weidermann, G. Engelken, and R. Hackenschmidt, *Decker Maschinenelemente-Formeln*, Physics textbook (Carl Hanser Verlag GmbH & Co. KG, 2011), 5th ed., ISBN 978-3-446-42620-7, URL https://books.google.de/books?id=3PSHDohngVgC.

[407] L. D. Landau, L. P. Pitaevskii, E. M. Lifshitz, and A. M. Kosevich, *Theory of Elasticity* (Butterworth-Heinemann, 1986), 3rd ed., ISBN 075062633X.

[408] N. Almtireen, J. J. Brandner, and J. G. Korvink, "Pulse Tube Cryocooler: Phasor Analysis and One-Dimensional Numerical Simulation", Journal of Low Temperature Physics **199**, 1179 (2020).

[409] M. Xu, A. De Waele, and Y. Ju, "A pulse tube refrigerator below 2 K", Cryogenics **39**, 865 (1999).

[410] I. A. Tanaeva and A. T. A. M. de Waele, *Helium-3 Pulse Tube Cryocooler* (Springer US, Boston, MA, 2003), pp. 283–292, ISBN 978-0-306-47919-9, URL https://doi.org/10.1007/0-306-47919-2_38.

[411] M. Partanen, K. Y. Tan, J. Govenius, R. E. Lake, M. K. Mäkelä, T. Tanttu, and M. Möttönen, "Quantum-limited heat conduction over macroscopic distances", Nature Physics **12**, 460 (2016).

[412] K. Schwab, E. A. Henriksen, J. M. Worlock, and M. L. Roukes, "Measurement of the quantum of thermal conductance", Nature **404**, 974 (2000).

[413] M. Banerjee, M. Heiblum, A. Rosenblatt, Y. Oreg, D. E. Feldman, A. Stern, and V. Umansky, "Observed quantization of anyonic heat flow", Nature **545**, 75 (2017).

[414] T. Bergman, T. Bergman, F. Incropera, D. DeWitt, and A. Lavine, *Fundamentals of Heat and Mass Transfer* (Wiley, 2011), ISBN 9780470501979, URL https://books.google.de/books?id=vvyIoXEywMoC.

[415] Y. Çengel and A. Ghajar, *Heat and Mass Transfer: Fundamentals & Applications*, Asia Higher Education Engineering/Computer Science Mechanica (McGraw Hill Education, 2015), ISBN 9789814595278, URL https://books.google.de/books?id=1YPhoAEACAAJ.

[416] J. Beck, K. Cole, A. Haji-Sheikh, and B. Litkouhl, *Heat Conduction Using Green's Function*, Series in Computational Methods and Physical Processes in Mechanics and Thermal Sciences (Taylor & Francis, 1992), ISBN 9781560320968, URL https://books.google.de/books?id=R7N7QgAACAAJ.

[417] T. Klaassen, J. Blok, J. Hovenier, G. Jakob, D. Rosenthal, and K. Wildeman, "Absorbing coatings and diffuse reflectors for the Herschel platform sub-millimeter spectrometers HIFI and PACS", in *Proceedings, IEEE Tenth International Conference on Terahertz Electronics* (2002), pp. 32–35.

[418] "O-Ring Leak Rate Equation and Calculator", https://www.engineersedge.com/fluid_flow/oring_leak_rate_13605.htm, accessed: 2022-11-21.

[419] O. Parker, "O-ring Handbook (ORD 5700)", Parker Hannifin Corporation, Cleveland (2007).

[420] P. Sturm, M. Leuenberger, C. Sirignano, R. E. M. Neubert, H. A. J. Meijer, R. Langenfelds, W. A. Brand, and Y. Tohjima, "Permeation of atmospheric gases through polymer O-rings used in flasks for air sampling", Journal of Geophysical Research: Atmospheres **109** (2004).

[421] O. A. Alduchov and R. E. Eskridge, Tech. Rep., United States (1997), research Org.: Department of Commerce, Asheville, NC (United States), URL https://www.osti.gov/biblio/548871.

[422] "Average humidity in Munich (Bavaria)", https://weather-and-climate.com/average-monthly-Humidity-perc,munich,Germany, Accessed: 2022-12-15.

[423] M. Brewster, *Thermal Radiative Transfer and Properties*, A Wiley-Interscience publication (Wiley, 1992), ISBN 9780471539827, URL https://books.google.de/books?id=z_anVNTmQLUC.

[424] R. H. French, J. M. Rodríguez-Parada, M. K. Yang, R. A. Derryberry, M. F. Lemon, M. J. Brown, C. R. Haeger, S. L. Samuels, E. C. Romano, and R. E. Richardson, "Optical properties of materials for concentrator photovoltaic systems", in *2009 34th IEEE Photovoltaic Specialists Conference (PVSC)* (2009), pp. 000394–000399.

[425] Z.-L. Xiang, M. Zhang, L. Jiang, and P. Rabl, "Intracity Quantum Communication via Thermal Microwave Networks", Phys. Rev. X **7**, 011035 (2017).

[426] Y. Zhang, Z. Luo, K. Yang, and Q. Zhang, "Measurement method of microwave surface resistance of high Tc superconductive thin films", Physica C: Superconductivity **385**, 473 (2003).

[427] B. Kraus and J. I. Cirac, "Discrete Entanglement Distribution with Squeezed Light", Phys. Rev. Lett. **92**, 013602 (2004).

[428] J. Agustí, Y. Minoguchi, J. M. Fink, and P. Rabl, "Long-distance distribution of qubit-qubit entanglement using Gaussian-correlated photonic beams", Phys. Rev. A **105**, 062454 (2022).

[429] C. M. Ho, C. Wang, K. Angkasa, and K. Gritton, "Estimation of Microwave Power Margin Losses Due to Earth's Atmosphere and Weather in the Frequency Range of 3–30 GHz", (2004).

[430] T. Gonzalez-Raya, M. Casariego, F. Fesquet, M. Renger, V. Salari, M. Möttönen, Y. Omar, F. Deppe, K. G. Fedorov, and M. Sanz, "Open-Air Microwave Entanglement Distribution for Quantum Teleportation", Phys. Rev. Applied **18**, 044002 (2022).

[431] M. Sanz, K. G. Fedorov, F. Deppe, and E. Solano, "Challenges in Open-air Microwave Quantum Communication and Sensing", in *2018 IEEE Conference on Antenna Measurements & Applications (CAMA)* (2018), pp. 1–4.

[432] H. Friis, "A Note on a Simple Transmission Formula", Proceedings of the IRE **34**, 254 (1946).

[433] T. Gonzalez-Raya and M. Sanz, "Coplanar Antenna Design for Microwave Entangled Signals Propagating in Open Air", Quantum **6**, 783 (2022).

[434] W. Chen, *The Electrical Engineering Handbook* (Elsevier Science, 2004), ISBN 9780080477480, URL https://books.google.de/books?id=qhHsSlazGrQC.

[435] W. Schleich, *Quantum Optics in Phase Space* (Wiley, 2011), ISBN 9783527635009, URL https://books.google.de/books?id=2jUjQPW-WXAC.

[436] S. Massar and S. Popescu, "Optimal Extraction of Information from Finite Quantum Ensembles", Phys. Rev. Lett. **74**, 1259 (1995).

[437] B. Mühlschlegel, "Die thermodynamischen Funktionen des Supraleiters", Zeitschrift für Physik **155**, 313 (1959).

[438] R. Gross, A. Marx, and D. Einzel, *Festkörperphysik. Aufgaben und Lösungen* (De Gruyter, 2013), ISBN 9783486858969, URL https://books.google.de/books?id=mn3pBQAAQBAJ.

List of publications

- F. Kronowetter, F. Fesquet, <u>M. Renger</u>, K. Honasoge, Y. Nojiri, K. Inomata, Y. Nakamura, A. Marx, R. Gross, K. G. Fedorov, "Quantum microwave parametric interferometer", arXiv https://doi.org/10.48550/arXiv.2203.05530 (2023).

- <u>M. Renger</u>, S. Gandorfer, W. Yam, F. Fesquet, K. Honasoge, F. Kronowetter, Y. Nojiri, M. Partanen, A. Marx, K. G. Fedorov, R. Gross, F. Deppe, "Entanglement distribution over a cryogenic microwave link", In preparation (2023).

- <u>M. Renger</u>, S. Pogorzalek, F. Fesquet, K. E. Honasoge, F. Kronowetter, Q. Chen, Y. Nojiri, K. Inomata, Y. Nakamura, A. Marx, F. Deppe, R. Gross, K. G. Fedorov, "Flow of quantum correlations in noisy two-mode squeezed microwave states", Phys. Rev. A **106**, 052415 (2022).

- F. Fesquet, F. Kronowetter, <u>M. Renger</u>, Q. Chen, K. E. Honasoge, O. Gargiulo, Y. Nojiri, , A. Marx, F. Deppe, R. Gross, K. G. Fedorov, "Perspectives of microwave quantum key distribution in open-air", arXiv https://doi.org/10.48550/arXiv.2203.05530 (2022).

- T. Gonzalez-Raya, M. Casariego, F. Fesquet, <u>M. Renger</u>, V. Salari, M. Möttönen, Y. Omar, F. Deppe, K. G. Fedorov, M. Sanz, "Open-Air Microwave Entanglement Distribution for Quantum Teleportation", Phys. Rev. Applied **18**, 044002 (2022).

- Q. Chen, M. Fischer, Y. Nojiri, <u>M. Renger</u>, E. Xie, M. Partanen, S. Pogorzalek, K. G. Fedorov, A. Marx, F. Deppe, R. Gross, "Quantum behavior of a superconducting Duffing oscillator at the dissipative phase transition", arXiv https://doi.org/10.48550/arXiv.2206.06338 (2022).

- Q. Chen, M. Partanen, F. Fesquet, K. E. Honasoge, F. Kronowetter, Y. Nojiri, <u>M. Renger</u>, K. G. Fedorov, A. Marx, F. Deppe, R. Gross, "Scattering coefficients of superconducting microwave resonators. II. System-bath approach", Phys. Rev. B **106**, 214506 (2022).

- Q. Chen, M. Pfeiffer, M. Partanen, F. Fesquet, K. E. Honasoge, F. Kronowetter, Y. Nojiri, <u>M. Renger</u>, K. G. Fedorov, A. Marx, F. Deppe, R. Gross, "Scattering coefficients of superconducting microwave resonators. I. Transfer matrix approach", Phys. Rev. B **106**, 214505 (2022).

- Q. Chen, F. Kronowetter, F. Fesquet, K. E. Honasoge, Y. Nojiri, S. Pogorzalek, , Y. Nojiri, M. Renger, K. G. Fedorov, A. Marx, F. Deppe, R. Gross, "Tuning and amplifying the interactions in superconducting quantum circuits with subradiant qubits", Phys. Rev. A **150**, 012405 (2022).

- M. Casariego, E. Zambrini Cruzeiro, S. Gherardini, T. Gonzalez-Raya, Rui André, G. Frazão, G. Catto, M. Möttönen, D. Datta, K. Viisanen, J. Govenius, M. Prunnila, K. Tuominen, M. Reichert, M. Renger, K. G. Fedorov, F. Deppe, H. van der Vliet, A. J. Matthews, Y. Fernández, R. Assouly, R. Dassonneville, B. Huard, M. Sanz, Y. Omar, "Propagating Quantum Microwaves: Towards Applications in Communication and Sensing", Quantum Sci. Technol. **8**, 023001 (2023).

- M. Renger, S. Pogorzalek, Q. Chen, Y. Nojiri, K. Inomata, Y. Nakamura, M. Partanen, A. Marx, R. Gross, F. Deppe, K. G. Fedorov, "Beyond the standard quantum limit for parametric amplification of broadband signals", Npj Quantum Inf. **7**, 160 (2021).

- K. G. Fedorov, M. Renger, S. Pogorzalek, R. Di Candia, Q. Chen, Y. Nojiri, K. Inomata, Y. Nakamura, M. Partanen, A. Marx, R. Gross, F. Deppe, "Experimental quantum teleportation of propagating microwaves", Sci. Adv. **7**, eabk0891 (2021).

- M. Fischer, Q. Chen, C. Besson, P. Eder, J. Goetz, S. Pogorzalek, M. Renger, E. Xie, M. J. Hartmann, K. G. Fedorov, A. Marx, F. Deppe, R. Gross, "In situ tunable nonlinearity and competing signal paths in coupled superconducting resonators", Phys. Rev. B **103**, 094515 (2021).

- Q. Chen, F. Deppe, R. Wu, L. Sun, Y. Liu, Y. Nojiri, S. Pogorzalek, M. Renger, M. Partanen, K. G. Fedorov, A. Marx, R. Gross, "Quantum Fourier Transform in Oscillating Modes", arXiv https://doi.org/10.48550/arxiv.1912.09861 (2019).

- E. Xie, F. Deppe, M. Renger, D. Repp, P. Eder, M. Fischer, J. Goetz, S. Pogorzalek, K. G. Fedorov, A. Marx, R. Gross, "Compact 3D quantum memory", Appl. Phys. Lett. **112**, 202601 (2018).

Acknowledgments

The previous four years during which this thesis has been created have been a formative experience, not only scientifically, but also from a personal point of view. Within this time, I enjoyed the diverse work in the interdisciplinary field of superconducting quantum information processing, ranging from theoretical derivations over experimental setup planning and measurement, to screwing, soldering, and hammering in the lab. It is my hope that this thesis contributes a small fragment of new physical insights into this increasingly growing field of research. However, one of the most important aspects in modern science is coordinated team work. In the following, I want to acknowledge and thank everyone who has delivered support during the creation of this work.

First, I want to thank my doctoral advisor *Dr. Frank Deppe* for accepting me as his first PhD student and for providing me the opportunity to contribute to the success of the QMiCS project. It has been a great pleasure to work on quantum teleportation and on the cryogenic link under your coordination. I admire your high-level practical knowledge in the lab, as well as your passion towards science, and I have enjoyed to construct Bob and Eve lab together with you. In addition, I want to thank you for our numerous fruitful discussions during which I have learnt the benefits of understanding physical problems from an intuitive point of view, compared to a pure mathematical formulation.

Next, I want to thank *Prof. Dr. Rudolf Gross* for giving me the opportunity to work in the WMI superconducting circuits group. I marvel at your broad and deep physical knowledge as well as at your open door whenever advice is needed. Your outstanding textbook about solid state physics has inspired me during my entire graduate studies and was among the main motivations for me to join WMI.

A special thanks goes to *Dr. Kirill G. Fedorov*, my everyday mentor, advisor, and later office colleague. I admire your remarkable physical intuition as well as your dedication to science and work. Thank you for sharing your knowledge about quantum physics, for teaching me how to do proper lab work, and for showing the benefit of finding analytical solutions by applying clever approximations. In addition I learnt from you the importance of patience and perseverance in science. Apart form our everyday discussions about physics and life in general, I enjoyed BBQ, doi cake baking as well as attending conferences with you. Special thanks as well for the сгущёнка supply during thesis writing.

I want to thank *Dr. Achim Marx* for his active support and the countless rewarding discussions regarding the cryogenic link. Without you, it would not have been possible to bring QMiCS to success. Thank you for sharing your knowledge about cryogenic engineering, especially with respect to the significant modifications which have been required for the Alice cryostat. From you, I learn a lot about cryogenic technology as well as practical lab work in general. In addition, I am grateful that I had the opportunity to learn practical fundamentals about dilution cryostat engineering from *Dr. Kurt Uhlig*, who delivered significant support for the cryogenic link with his decades of experience.

Thanks to all my office colleagues during my time as a PhD student. I thank *Dr. Michael Fischer* for his patience and mental support and *Dr. Philip Schmidt*, who was the senior PhD student in our office for a significant time, for always having a sympathetic ear for me as a beginner. I especially enjoyed your specially-brewed coffee as well as the nice GoT evenings. A special thanks goes to *Dr. Stefan Pogorzalek*, who delivered substantial subject-related and personal support. It was a great pleasure for me to proceed as successor of your work in the field of microwave quantum communication, which you helped to establish at WMI. Thanks for our evenings at Augustiner and at various conferences. I guess some mysteries like the "black cat" in Freiburg will remain unsolved forever. Thank you also for the nights we spent at the institute in attempt to theoretically and practically advance our nitrogen rocket technology. I want to thank your office-successor *Florian Fesquet*, who is among the pioneers of microwave QKD at WMI. It was a great pleasure to regularly philosophize about quantum physics with you as well as to work together with you in Bob lab. One can always rely on you - no matter whether it is about finding a common solution for a physical problem or about finishing the last deep dish pizza in Chicago. Thank you also for travelling to Grenoble with me and for familiarizing me with French culture, Monsieur. In addition, I want to thank my much sought colleague *Ivan Tsitsilin* for his friendly and calm nature, which led to many interesting discussions. Eventually, I want to thank *Manuel Müller* for facilitating my life not only during thesis writing. During this period, you have, in principle, always been around at the institute, which led to numerous helpful conversations and might also be one reason for your admirable scientific output. I enjoyed organizing multiple BBQs together with you, as well as the nice evenings at the institute and at Honghong.

Next, I want to thank all active and former WMI members. I want to thank my good sirs *Kedar Honasoge*, *Yuki Nojiri*, *Daniil Bazulin*, as well as *Maria-Teresa Handschuh*, not only for our regular conversations at the back of the institute building, but also for the nice time at Honghong, in Sonthofen, and on many other conferences. It is great to see that your dedication and productivity leads to successful fabrication of Josephson devices. Thanks to *Dr. Qi-Ming Chen* for our interesting discussions about quantum physics. It was a pleasure to go to the Wiesn with you. I thank *Fabian Kronowetter* for our numerous fruitful discussions about quantum radar and I wish you all the best for the